Elisa Fresta

Doctoral thesis

# BEYOND TRADITIONAL EMITTERS IN LIGHT-EMITTING ELECTROCHEMICAL CELLS

Autónoma University of Madrid

FACULTY OF SCIENCE

Madrid, 2020

Elisa Fresta

Tesis doctorales

# MÁS ALLÁ DE LOS EMISORES TRADICIONALES EN CÉLULAS ELECTROQUÍMICAS EMISORAS DE LUZ

Universidad Autónoma de Madrid

FACULTAD DE CIENCIAS

Madrid, 2020

This PhD thesis was elaborated in the period going from May 2017 to June 2020 at IMDEA Materials Institute and the Department of Applied Physics of the Universidad Autónoma de Madrid (UAM), under the supervision of Prof. Dr. Rubén D. Costa and the tutoring of Prof. Mariola Ramírez. In addition, a 3-month internship at the Department of Applied Chemistry and Physics of the University of Waseda (Tokyo, Japan), under the supervision of Prof. Dr. Takayuki Homma was realized in 2019.

El presente trabajo se elaboró en el período comprendido entre mayo de 2017 y junio de 2020 en el Instituto IMDEA Materiales y el departamento de física aplicada de la Universidad Autónoma de Madrid (UAM), bajo la supervisión del Catedrático Rubén D. Costa y la tutoría de la Profesora Mariola Ramírez. Además, se realizó una estancia de tres meses en el 2019 en el departamento de química y física aplicada en la Universidad de Waseda (Tokio, Japón) bajo la supervisión del Catedrático Takayuki Homma.

## Acknowledgments

I dedicate this work to my family, that always supported me during these three long years.

I would firstly like to thank my supervisor Rubén Costa, that accepted me in the group first as a master and then as a PhD student, and for patiently discussing, encouraging me and correcting my works, despite his busy schedule.

Then, I would like to thank Vero, that was with me from the beginning, when the laboratories where only empty rooms that we patiently filled with equipment and samples, to the end, when we sustained each other in the writing of the thesis.

Also, I thank all the people in our research group, that is, Alfonso, Carmen, Maria, Anna, Alba, Julio, Gilbert, Isabel, Sara, Yanyan, and Luca. It was a pleasure to see the group growing, to share coffee breaks, beer meetings and long talks in both labs and corridors.

Of course, I also thank all the people in IMDEA, especially Richard, Rudi, Thomas, Alvaro D., Daniel, Ahmed, Marco, Jaime, Pablo, David, Miguel, Alvaro M., Rosa, Clara, Miguel Monclús, JuanPe, Luis, Meijuan, Nana Chen, Kia, Javier, Na Li, Jon, Andrea, Maria, Anna, Yunfu, and Hugo, and the visiting students Jorge, Jiayin, Francesco, Mark, Fabien, Filippo, Antoine and Hugo. All of you contributed to render Madrid a place I can call home.

I furtherly thank the people from IMDEA Nanoscience that helped me with the thermal experiments, Juan Cabanillas, Chen and Ahmad.

Finally, a special thanks goes to all the people I met in Waseda University, especially Morten Bertz, Homma-sensei, Kunimoto-sensei, Nishikitani-sensei, Uchida-san, Keiko-san, Fujimura-san, Yusuke-san and Hikima-san. Thank you for welcoming me in your group, teaching me some Japanese language and traditions, helping me with the experiments or the bureaucracy, inviting me to dinners and parties, and giving me the Waseda sweater and towel as goodbye present.

## List of abbreviations

**$^{1}$H-NMR** proton nuclear magnetic resonance

**3-Medpa** 2,2′-bis-(3-methylpyridyl)amine

**$^{13}$C-NMR** carbon-13 nuclear magnetic resonance

**AFM** atomic force microscopy

**Ag-iTMCs** silver (I) ionic transition metal complexes

**Bpy** 2,2′-bipyridine

**CBP** 4,4′-bis(*N*-carbazolyl)-1,1′-biphenyl

**CIE** commission international de l'eclairage

**CPs** conjugated polymers

**Cu-iTMCs** copper (I) ionic transition metal complexes

**CT** charge transfer

**CV** cyclic voltammetry

**Dpa** 2,2′-bis-(3-methylpyridyl)amine

**ECD** electrochemical doping

**ED** electrodynamical doping

**EDLs** electric double layers

**$E_g$** energy bandgap

**EIS** electrochemical impedance spectroscopy

**EPR** electron paramagnetic resonance

**Fc/Fc$^{+}$** ferrocene/ferrocenium

**FWHM** full width to half maximum

**HOMO** highest occupied molecular orbital

**IL** ionic liquid

**IP** ionic polyelectrolyte

**IPr** 1,3-bis-(2,6-di-iso-propylphenyl)imidazole-2-ylidene

**Ir-iTMCs** iridium (III) ionic transition metal complexes

**ITO** indium Tin Oxide

**iTMCs** ionic transition metal complexes

**LC** ligand centered

**LECs** light-emitting electrochemical cells

**LEDs** light-emitting diodes

**LiOTf** lithium triflate

**LLCT** ligand-to-ligand charge transfer

**LUMO** lowest unoccupied molecular orbital

**MC** metal centered

**MLCT** metal-to-ligand charge transfer

**Nr.** number

**OLEDs** organic light-emitting diodes

**PBD** 2-(4-*tert*-butylphenyl)-5-(4-biphenylyl)-1,3,4-oxadiazole

**pECD** preferential electrochemical doping

**PEDOT:PSS** poly(3,4-ethylenedioxythiophene) polystyrene sulfonate

**POP** (bis(2-(diphenylphosphino)phenyl)ether)

**Ppy** 2-phenylpyridine

**PS** polystyrene

**RISC** reverse intersystem crossing

**RT** room temperature

**SSL** solid-state lighting

**SWV** square wave voltammetry

**TADF** thermally activated delayed fluorescence

**TMPE** trimethylol propane ethoxylate

**Xantphos** (4,5-bis(diphenylphosphino)-9,9-dimethylxanthene)

**XRD** X-ray powder diffraction

## Abstract

The future lighting devices should present high efficiency, excellent air-stability under storage/operation conditions, and low-cost fabrication and recycling. A leading example is light-emitting electrochemical cell (LECs) technology. This consists of two air-stable electrodes sandwiching a thin film of an electroluminescent material blended with an ionic electrolyte.

Among the device components, the electroluminescent material is the cornerstone of LECs as it rules both, device performance and sustainable aspects. In this context, this thesis focused on the study, implementation, and characterization of new sustainable emitters, that is, $d^{10}$ ionic transition metal complexes ($d^{10}$-iTMCs, Cu- or Ag-based) and small organic molecules (SMs).

Prior to the start of this PhD thesis, both families of emitters presented several limitations, namely i) low device performance with respect to efficiency and stability for yellow and green emitting devices, ii) lack of stable blue emitters, and iii) the lack of an efficient and stable white LEC. The main goal of this thesis is to overcome all these issues towards highly efficient LECs based on sustainable emitters.

In detail, this thesis is divided in 8 chapters that summarize the prior state of the art in LECs, theoretical aspects about emitter design, characterization techniques, device fabrication and analysis, our main advances in the field, and a critical conclusion and outlook.

In the first chapter, a short introduction about LECs and the most common electroluminescent materials is provided.

The second chapter provides a theoretical description of the characterization techniques and the measuring protocols.

The third chapter is focused on the presentation of the work done during the thesis to solve the above-presented challenges. In particular, it is divided in two sections: $d^{10}$-iTMCs and SMsOn one hand, we focused on blue-, yellow- and red-emitting Cu-iTMCs, and on green emitting Ag-iTMCs. For each family, we rationalized the reasons that led to an early performance loss, which was ascribed to either irreversible oxidation (Cu-iTMCs) or irreversible reduction (Ag-iTMCs) processes. As such, we modified the device architecture to decouple hole and electron transport. Additionally, the most promising red Cu-iTMCs were used to build the first Cu-iTMC-based white LEC.

On the other hand, we explored a new promising family of SMs, that is, nanographenes. In particular, we study the electroluminescent behavior of an archetype, a BN-doped and contorted nanographenes. These emitters showed outstanding performances compared to the state-of-art of SM-based LECs. Additionally, they also presented surprising behaviors that we thoroughly rationalized. In detail, the emission features of the archetype nanographene exhibited a strong dependence upon increasing pixel temperature. As such, it was employed to shed light for the first time on the impact of unavoidable self-heating upon device driving onto its color chromaticity and figures-of-merit. The BN-doped nanographene is a blue emitter in thin films that yielded white LECs with high efficiency and stabilities of days. The reason for this uncommon behavior was

ascribed to electric-field and a temperature induced ternary emission. Finally, the contorted nanographene showed an uncommon dependence of the electroluminescence band shape from the inner electric-field experienced across device active layer, reaching stabilities of 3600 h at efficiencies of 0.74 lm/W.

All these results are rationalized combining steady-state and time-resolved emission/absorption spectroscopy, electrochemical impedance spectroscopy, and microscopic assays applied to thin films and devices as well as a myriad of device architectures using different driving conditions – i.e. operation modes and ambient conditions.

The fourth chapter provides information about other works related to this thesis.

The fifth chapter summarizes the advances in $d^{10}$-iTMC- and SM-based LECs achieved by other research groups during this thesis. This will help the reader to contextualize the results presented in this thesis.

Finally, the sixth chapter discusses conclusions and future outlook in the field.

## Resumen

Los futuros dispositivos de iluminación deben cumplir con una alta eficiencia, una excelente estabilidad en condiciones ambientales de almacenamiento / operación y una fabricación y reciclaje de bajo coste. Un ejemplo destacado es la tecnología de células electroquímicas emisoras de luz (LEC de las siglas en inglés light-emitting electrochemical cell). Estos consisten en dos electrodos estables al aire entre los que se intercala una película delgada de un material electroluminiscente mezclado con un electrolito iónico. Entre los componentes del dispositivo, el material electroluminiscente es la piedra angular de los LEC, ya que rige tanto el rendimiento del dispositivo como los aspectos de sostenibilidad.

En este contexto, esta tesis se centró en el estudio, implementación y caracterización de nuevos emisores sostenibles, es decir, complejos de metales de transición iónicos $d^{10}$ como Cu(I) y Ag(I) ($d^{10}$-iTMCs de las siglas en inglés de ionic transition metal complexes) y pequeñas moléculas orgánicas (SMs de las siglas en inglés small molecules)Antes del comienzo de esta tesis doctoral, ambas familias de emisores presentaban varias limitaciones: i) bajo rendimiento del dispositivo con respecto a la eficiencia y la estabilidad de los dispositivos emisores amarillos y verdes, ii) falta de emisores azules estables, y iii) falta de LECs blancos eficientes y estables. El objetivo principal de esta tesis es abordar estos problemas para fabricar LECs altamente eficientes usando emisores sostenibles.

En detalle, esta tesis se divide en 8 capítulos que resumen el estado del arte en LECs, aspectos teóricos sobre diseño de emisores, técnicas de caracterización, fabricación y análisis de dispositivos, nuestros principales avances en el campo y una conclusión y perspectiva crítica.

En el primer capítulo, se proporciona una breve introducción sobre los LECs y los materiales electroluminiscentes más comunes. El segundo capítulo proporciona una descripción teórica de las técnicas de caracterización y los protocolos de medición.

El tercer capítulo se centra en la presentación de los resultados científicos. En particular, se divide en dos secciones: $d^{10}$-iTMCs y SMs. Por un lado, nos centramos en los Cu-iTMC emisores azules, amarillos y rojos, y en los Ag-iTMCs emisores verdes. Para cada familia, racionalizamos la pérdida de estabilidad, que se atribuyó a los procesos de oxidación (Cu-iTMCs) o de reducción (Ag-iTMCs) irreversibles. Como tal, modificamos la arquitectura del dispositivo para desacoplar el transporte de huecos y electrodos de la recombinación. Además, se utilizaron los Cu-iTMC rojos más prometedores para construir el primer LEC blanco basado en Cu-iTMCs.

Por otro lado, exploramos una nueva familia prometedora de SMs, es decir, nanographenes. En particular, estudiamos el comportamiento electroluminiscente de un miembro arquetipo, un nanografeno dopado con BN y otro retorcido. Dispositivos basados en estos emisores mostraron un rendimiento sobresaliente en comparación con el estado del arte de los LECs con SMs. Además, también presentaron comportamientos electroluminiscentes sorprendentes que racionalizamos usando una gran variedad de técnicas espectroscópicas y electroquímicas. En detalle, la emisión de dispositivos con el arquetipo de nanografeno exhibieron una fuerte dependencia del color con el aumento de la temperatura de los píxeles. Esto se empleó para arrojar luz por primera vez sobre el impacto del inevitable autocalentamiento al encender un dispositivo en su cromaticidad y las otras figuras de mérito. El nanografeno dopado con BN es un emisor azul en películas delgadas que produce LECs de emisión blanca con una alta eficiencia y estabilidad. La razón de este comportamiento poco común se atribuyó al campo eléctrico y a una emisión ternaria inducida por la temperatura. Finalmente, dispositivos con el nanografeno retorcido mostraron una dependencia poco común de la forma de la banda de electroluminiscencia con el campo eléctrico interno experimentado a través de la capa activa del dispositivo, alcanzando estabilidades de 3600 h con eficiencias de 0.74 lm/W. Todos estos resultados se racionalizaron combinando espectroscopia de emisión/absorción en estado estacionario y con resolución temporal, espectroscopia de impedancia electroquímica y ensayos microscópicos aplicados a películas y dispositivos delgados, así como una gran variedad de arquitecturas y condiciones de encendido, es decir, modos de operación y condiciones ambientales. El cuarto capítulo proporciona información sobre otros trabajos relacionados con esta tesis. El quinto capítulo resume los avances en LECs basados en $d^{10}$-iTMCs y SMs logrados por otros grupos de investigación durante esta tesis. Esto ayudará al lector a contextualizar los resultados presentados en esta tesis. Finalmente, el sexto capítulo discute las principales conclusiones de esta tesis y las perspectivas de este campo.

# Table of Content

# 1. Introduction

## 1.1 Electroluminescence and solid-state lighting

Electroluminescence is the emission of light upon application of an electrical current or an electric field to a compound. This basic concept led to the well-known solid-state lighting (SSL) technologies that are based on thin-film electroluminescent devices involving an inorganic or organic semiconductors.[1] Upon application of a bias, these compound hold holes and electron injection and transport through the bulk of the material, where they recombine forming an exciton that relaxes radiatively, yielding a photon in the visible region.[2] Through this approach, the primary product of these lighting devices is the photon itself. As a result, SSL creates visible light with reduced heat generation and increased efficiency (as high as 80%, compared to 10-20% for traditional lighting sources, such as incandescent- and discharge-based lamps and compact fluorescent tubes).[3,4] Thus, SSL represents the present and future of artificial illumination.

Traditionally, SSL is divided into light-emitting diodes (LEDs), organic light-emitting diodes (OLEDs), and light-emitting electrochemical cells (LECs). LEDs are made of a thin-film of inorganic semiconductors such as InGaN or GaN, as well as color converting filters. The latter can be either inorganic, usually phosphors doped with rare-earth metals like Y or Ce, or organic down-converters. This last case yields organic/inorganic structures known as hybrid LEDs.[5] LEDs have shown outstanding luminous efficiency and stability. They are, indeed, commonly found in TV screens, lightbulbs, traffic signaling, decorations, as well as in implantable lighting devices.[2,6]

Both OLEDs and LECs are organic based thin-film lighting technologies with active layers of few hundred nanometers thickness that employ small molecules, polymers, coordination complexes, *etc*. for carrier injection, carrier transport, and emission. OLEDs are multilayered architectures, in which each layer plays a specific function (*i.e*. electron/hole injection, electron/ hole transport, emission); this allows for outstanding color quality, high efficiency and stability.[7] However, their sensitivity to both oxygen and moisture, as well as the necessity to fabricate them using high vacuum deposition techniques, renders them highly expensive. Additionally, blue emitting OLEDs are by far less efficient and stable compared to LEDs.[8] LECs, by contrast, consist of single- or double-layered devices fabricated using solvent-based up-scalable techniques.[9,10] Their peculiarity is the presence of ions in the layers, which allows for a different working mechanism with performances that are independent from the working function of the cathode.[11,12] As such, low-

cost, air stable cathodes, such as Al or Ag, can be employed. Several practical applications of LECs have been demonstrated, among which the fabrication of moderate performing devices on 3D shaped substrates, such as kitchen forks,[13] wearable fibers,[14] light-emitting paper,[15] *etc*, stands out. Additionally, a record efficacy of 99.2 cd/A has been recently reported.[16] For more information, *Advanced Functional Materials* recently celebrated the 25$^{th}$ anniversary of the LEC technology with a special issue dedicated to past and recent achievements as well as the future challenges.

This thesis is focused on the named 3$^{rd}$ generation LECs, which will be described in details in the following sections.

### *1.1.1 LEC structure*

LECs contain one active layer sandwiched between two air-stable electrodes ─ Figure 1. Owing to the roughness of Indium Tin Oxide (ITO), a layer of poly(3,4-ethylenedioxythiophene) polystyrene sulfonate (PEDOT:PSS) is generally coated on top of it to ensure device reproducibility. Notably, the metal cathode is air stable Al, Ag, or Au. Finally, the active layer consists of a luminescent material, such as a polymer, an iTMC, perovskites, small molecules, *etc*. together with an electrolyte, which can be an ionic liquid such as buthyl methyl imidazolium hexafluorophosphate [BMIM][$PF_6$], or a polyelectrolyte matrix based, for instance, on the polymer trimethylolpropane ethoxylate (TMPE) and the inorganic salt lithium trifluoromethanesulfonate (LiOTf) ─ Figure 1. iTMCs do not need an electrolyte, as they already feature the necessary ion mobility to sustain charge injection and transport. However, an electrolyte can be added to increase the brightness and/or decrease the turn-on time of the device.[4,17,18]

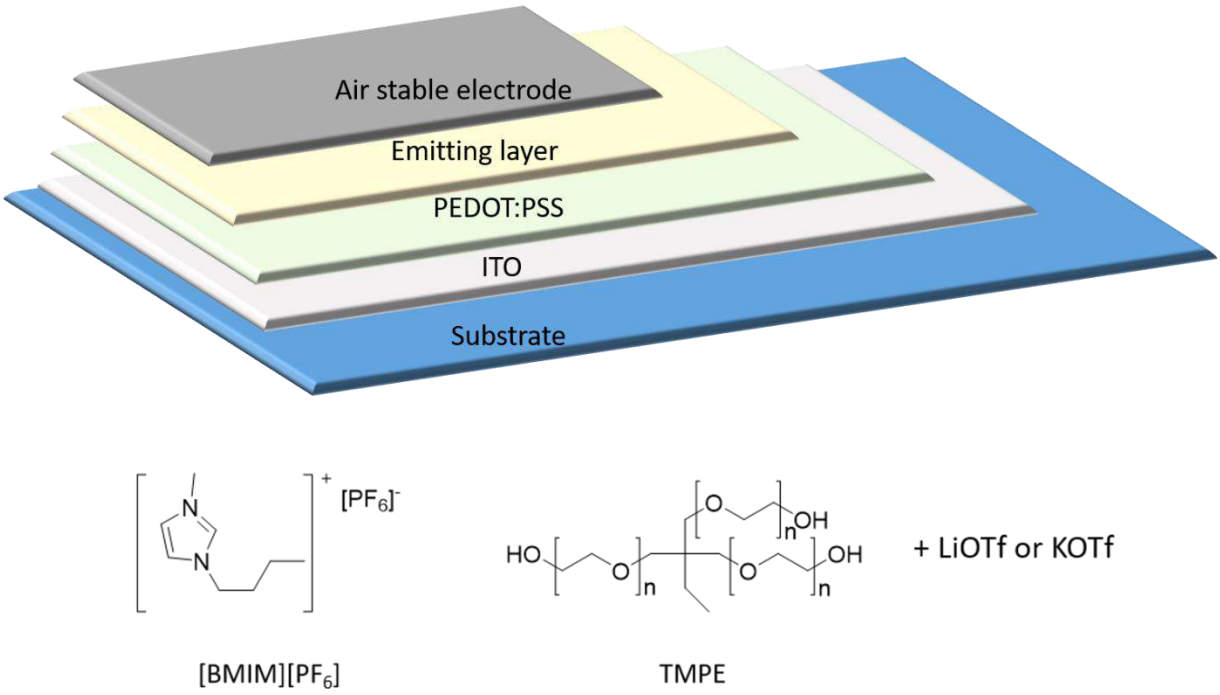


Figure 1. Schematic structure of a typical LEC (top), and most common additives employed in LECs (bottom).

### *1.1.2 LEC working mechanism*

Various working mechanisms have been proposed for LECs, depending on their device composition.[19–27] The electrochemical doping model (ECD, Figure 2, top) was firstly proposed by Pei *et. al.*[21] According to this model, the injection of holes and electrons leads to the formation of oxidized and reduced species at the electrodes. These form highly conductive p-doped and n-doped regions, respectively. The doped regions grow over time, creating a p-i-n junction, where i represents the undoped region, and is characterized by a sharp drop of the potential, leading to charge recombination and light emission.

The electrodynamical model (ED, Figure 2, center) was first proposed by DeMello *et al.*[23,26] According to this model, the application of a bias below the energy bandgap ($E_g$) leads to the formation of electronic double layers (EDLs), as a direct consequence of the ionic movements towards oppositely charged electrodes. This leads to the formation of p- and n-doped regions,

which are separated by an undoped region (the so-called field free region). The potential significantly drops at the electrodes, allowing for the injection of charge carriers into the active layer at voltages above $E_g$. Recombination and light emission happen in the field free region of the device.

Finally, the preferential electrochemical doping model (pECD, Figure 2, bottom) was firstly proposed by Leger *et al*.[28] This model can be described as a modified ECD model, in which only one type of doping efficiently occurs at the interfaces (either p-type or n-type), and leads to recombination and emission being very close to the interfaces.

All the three models were corroborated by both numerical models[29,30] and experimental assays.[29–31] As demonstrated by Edman's group in 2010, the three models are interchangeable, and they have different degrees of applicability depending on the ability to form Ohmic injecting contacts in the LEC.[32,33] In detail, if the LEC is able to efficiently form two Ohmic contacts higher than $E_g$, the ECD will be prevailing. By contrast, when no Ohmic contact is efficiently formed, while if carrier injection is the ED model will be dominant. Finally, if only one Ohmic contact is efficiently formed, the pECD will be dominant.

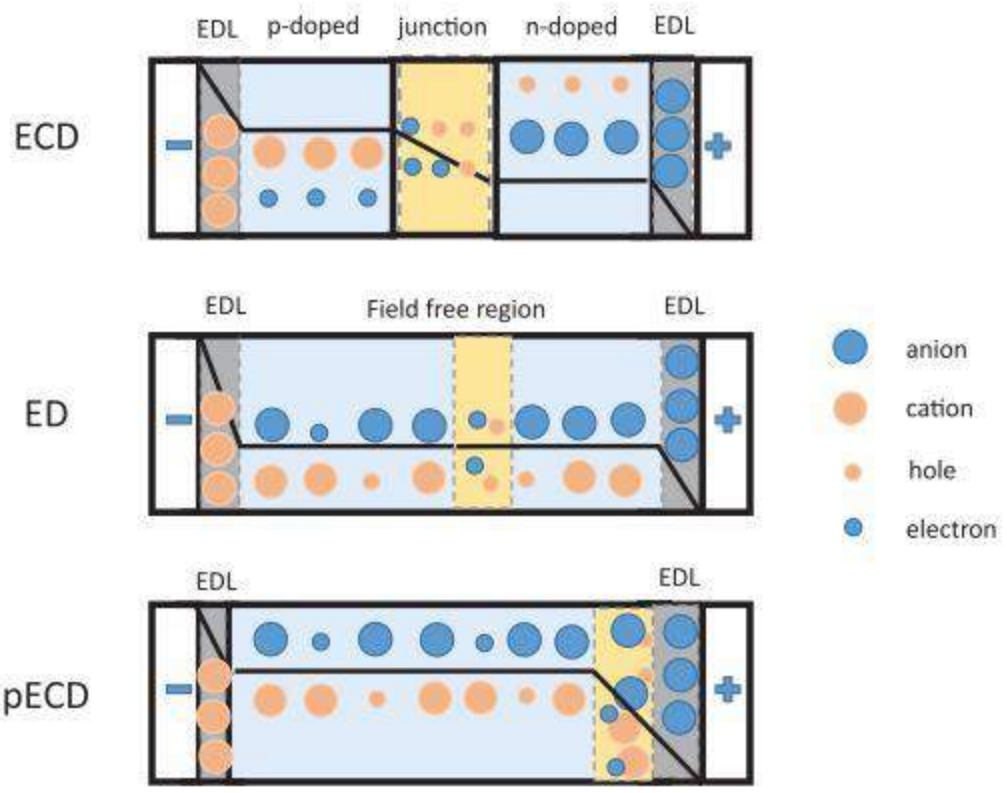


Figure 2. Electrochemical (top), electrodynamic (center), and preferential electrochemical (bottom) models proposed for the LEC operation. The black line indicates the potential within the device, the grey region indicates the EDLs, and the yellow region indicates the recombination region. Taken from reference[34].

## 1.2 Overview on the emitters employed in LECs

Three generations of materials have been under the focus of LECs: while the 1st and the 2nd generation focused on conjugated polymers (CPs)[35] and Ir(III) ionic transition metal complexes (Ir-iTMCs),[36] respectively, the 3rd one sees small molecules (SM), $d^{10}$-iTMCs (Cu-iTMCs and Ag-iTMCs), quantum dots and perovskites as protagonist.[11,35–37]

### *4.2.1 1st generation emitters*

Conjugated polymer-based LECs were firstly reported by Pei's group in 1995.[21] The first LECs consisted of a light-emitting CP mixed with an ionic polyelectrolyte (IP). CP representatives are polyphenylenes, vinylenes, such as the archetype poly(1,4-phenylene-1,2-ethenediyl) commercialized as Super Yellow shown in Figure 3.[38] The CP acts as a semiconductor due to the

presence of delocalized π electrons along the polymer chain. The IP is typically a polyethylene oxide (PEO) or trimethylolpropane ethoxylate (TMPE): lithium triflate salt complex. The active layer of a CP-LEC is therefore a mixed ionic/electronic conductor.[39]

This type of materials has provided interesting results, among which stabilities of more than 1000 h[40] and power efficiencies of 18.1 lm/W stand out.[41] Additionally, their easy color tunability resulted in single-layer blue, white, and near infrared (NIR) CP-LECs.[42–46] However, CPs present different bottlenecks, such as photo-oxidation issues[35,47], which is particularly severe in high energy bandgap CPs, sensitivity to air and moisture, as well as marked roll-off of efficiencies owing to increased level of doping that quenches the fluorescence of the polymer.[48]

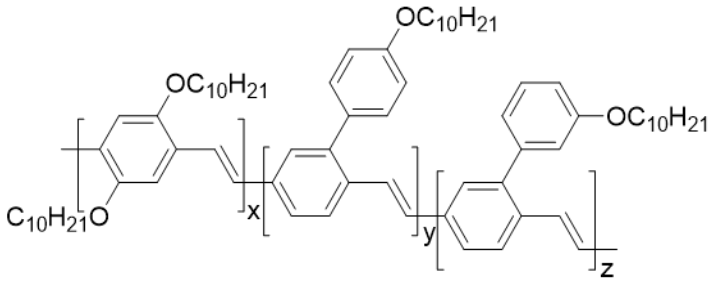


Figure 3. Chemical structure of the archetype CP Super Yellow.

### *1.2.2 2nd generation of emitters*

Luminescent materials based on ionic transition metal complexes (iTMCs) have become the ‘‘go to’’ material when designing emitters for SSL applications.[4,49,50] Among the iTMCs based-LECs, cationic Ir(III) complexes (Ir-iTMCs) cover a leading position owing to their short excited-state lifetimes, tuneable color, straight forward synthesis and purification, good solubility and high photoluminescence quantum yields (Φ).[4,36,51] In recent years, stabilities of > 6000 hours[52] and efficacies of ~60 cd/A[53] have been reported. Figure 4 shows the archetypal Ir-iTMC [4,4′-*Bis*(1,1-dimethylethyl)-2,2′-bipyridine-*N*1,*N*1′]*bis*[2-(2-pyridinyl-*N*)phenyl-C]iridium(III) hexafluorophosphate ([Ir(dtbbpy)$(ppy)_2$]$PF_6$).

Ir-iTMCs are highly stable toward substitution, as the electronic configuration of the metal center is always in a low-spin state ($t_2g$ 6 eg 0) and the ligand-field stabilization energy is maximized employing cyclometalating ligands. Moreover, the high spin-orbit coupling of the metal atom

allows for almost unitary intersystem crossing efficiency from the lowest singlet to the lowest triplet excited states, leading to an efficient spin-forbidden phosphorescence emission. The emitting excited state is the lowest-energy triplet ($T_1$), which is normally constituted by "mixed" triplet levels that involve contributions of $^3$MLCT (metal-to-ligand charge transfer), $^3$LC (ligand centered), and sometimes also $^3$LLCT (ligand-to-ligand charge transfer) states.[54]

Overall, these photophysical features renders Ir-iTMCs ideal candidates for LECs application. However, they also present major drawbacks. Iridium is one of the least abundant elements in the Earth's crust (0.001 ppm),[54] with a price currently around $50,000 per kg.[55] Additionally, independently of the type of emitter, the best performing LECs are yellow- and orange-emitting devices. Indeed, blue-emitting Ir-iTMCs LECs exhibit a low stability caused by a population of triplet metal centered (MC) degradative excited states upon electron–hole recombination states,[36,49,56–58] while red-emitting Ir-iTMCs usually present low Φ owing to the energy gap law.[59] In particular, no stable white emitting LEC has been reported so far.[60] Therefore, the search towards new emitters represent one of the most critical concerns.

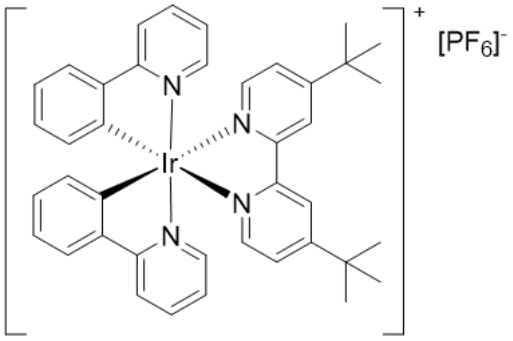


Figure 4. Chemical structure of[Ir(dtbbpy)(ppy)$_2$]PF$_6$.

### *1.2.3 3rd generation of emitters*

The third generation of emitters comprises SMs, Cu-iTMCs, Ag-iTMCs, QDs and perovskites. Cu-iTMCs present appealing properties due to their abundance, low cost (currently around $6 per kg),[55] well-known chemistry, and high Φ features spanning the whole visible spectrum.[61,62] The most desired feature of Cu-iTMCs their emission based on an efficient thermally activated delayed fluorescence (TADF) mechanism at room temperature (rt). This phenomenon allows to undergo reverse intersystem crossing (RISC) from a triplet state converting it to an emitting singlet state using thermal energy. Transitions in Cu-iTMCs often have MLCT character ($^3$MLCT and $^1$MLCT)

that allows for small energy gaps between the lowest singlet $S_1$ and triplet $T_1$ state, which is required for efficient TADF (<0.12 eV).[63,64] A predominant spatial separation of the highest occupied molecular orbital (HOMO) and lowest unoccupied molecular orbital (LUMO) reduces the energy gap and leads to short emission decay times.[65]

Since their first implementation in 2005,[66] Cu-iTMCs have attracted the attention of numerous research groups, whose joint efforts led to the implementation of blue,[67–69] green,[70] yellow[71–81] and red[82]-emitting Cu-iTMCs into LECs. The most studied Cu-iTMCs are related to the $[Cu(N^N)(P^P)]^+$ family, where the N^N ligand is usually bpy (2,2′-bipyridine) or phen (1,10-phenantroline) derivatives and P^P is usually POP (bis(2-(diphenylphosphino)phenyl)ether) or Xantphos (4,5-bis(diphenylphosphino)-9,9-dimethylxanthene).[62,83] Encouraging record efficacies of 5.2 cd/A[72] and stabilities up to hundreds of hours[75,82] were reported in the last decade. However, the commonly irreversible oxidation processes strongly limit the performance of these devices.

Ag-iTMCs also exhibit TADF emission, but have received less attention compared to Cu-iTMCs, owing to their light sensitivity, the easy decomposition to Ag(0),[84,85] and the higher oxidation potentials than the Cu(I) ion, which causes holes transport issues.[85–87] Even though Ag(I) ions can be found in different coordination geometries,[84,88] the geometry mostly described for TADF Ag-iTMCs is tetrahedral, as in Cu-iTMCs. In mononuclear Ag-iTMCs, the metal is often not involved in the formation of the HOMO, in contrast to mononuclear Cu(I), while it is usually attributed to ligand-centered (LC) $\pi$–$\pi^*$ transition or metal-centered in the case of metal–metal bonding.[89] This is mainly justified by the difficulty in oxidizing Ag-iTMCs; however, the choice of suitable ligands with strong acceptor abilities could generate MLCT emitting excited states, which show efficient photoluminescence.[87,89] In OLEDs, Ag-iTMCs based OLEDs achieved high external quantum efficiencies of 14%,[88] while LECs showed interesting green-emitting devices with $[Ag(bpy)(POP)]^+$ ($\lambda_{max}$ = 520 nm; compared to $\lambda_{max}$ = 590 nm for LECs with $[Cu(bpy)(POP)]^+$)[73,90], as well as stabilities of up to 80 hours.[85]

Hill and co-workers were the first ones proposing the use of SMs as emitters in LECs in 2008,[91] while Edman and co-workers demonstrated 5 years later that the mechanism of SM-based LECs is the same as that reported for CP- and iTMC-based LECs, thereby stating SMs as new types of emitters for LECs.[92] SMs are regarded as appealing as (i) their ease of chemical modification for

designing, for example, host–guest schemes, (ii) the high Φ spanning the whole visible range, (iii) the redox stability, and (iv) their easy processability and high stability in solution.[11,93] Up to date, SMs have been showing efficiencies of 1-3 cd/A and stabilities of up to 3600 h.[92–95] On average, their performances are, however, moderate compared to the older generation materials.

Finally, scattered literature on QDs- and perovskite-based LECs has appeared in the last decade.[96–99] The interest in this materials is justified by their compatibility with ionic additives like IP or IL in solution, allowing the preparation of thin-films from solution-based techniques.[11] In addition, their photoluminescence features – *i.e.*, emission color and Φ values, can be easily modified.[100–103] The first QD-based LECs were reported by Leger and co-workers in 2011.[96] Upon luminance-current-voltage (L-I-V) assays, they featured a turn-on voltage of 7 V, a maximum luminance of 200–300 cd $m^2$, and an EQE of 0.1% at 16 V. The first perovskite-based LECs was achieved by Costa's group in 2015,[99] and showed 2 cd/$m^2$ at a driving current of 14 mA/$cm^2$. Recently, Slinker and collaborators focused on enhancing the device stability utilizing an optimized amount of $LiPF_6$ salt additive and reaching 100 h of operation at high brightness (>800 cd/$m^2$), as well as an efficiency of 6.6 cd/A.[104] Despite these encouraging results, the presence of highly toxic materials, such as Cd and Pb, as well as their high sensitivity towards oxygen and moisture, renders them unideal candidates for future lighting applications.

## 1.3 Motivation of the thesis

This thesis focuses on the implementation of $d^{10}$-iTMCs and SMs in LECs as sustainable alternatives to older generation materials.

In May 2017, when this thesis started, 3rd generation emitters for LECs presented different challenges, such as:

i) The device stability, which is usually limited to a few hours or is accompanied by low brightness.
ii) The moderate device efficiency (<1 cd/A), especially at brightness> 10 cd/$m^2$.
iii) As for Cu-iTMCs, the limited color availability, such as the absence of red-emitting Cu-iTMCs, as well as the very low performances of blue-emitting Cu-iTMCs.
iv) As for Ag-iTMCs, lack of knowledge on the electroluminescence behavior in LECs.
v) As for SMs, the handful number of emitters so far explored.

These challenges will be addressed in section 3. At the beginning of each section, an overview of the drawbacks and challenges in LECs prior to this thesis is presented, clarifying the aim and strategies adopted.

# 2. Theoretical background and experimental methods

## 2.1 Spectroscopic, electrochemical and microscopy techniques

### *2.1.1 Ultraviolet-visible (UV-Vis) spectroscopy*

UV-Vis spectroscopy consists in irradiating the sample with light in the visible and UV (mostly near UV) range. Molecules containing π-electrons or non-bonding electrons can absorb UV or VIS light to excite these electrons to higher anti-bonding molecular orbitals. The absorption is proportional to the concentration of the absorbing specie in the sample, according to Lambert-Beer law: $A = \varepsilon bc$ where **A** is defined as the absorbance (-LogT, where T is the transmittance, that is the ratio between the transmitted light and the incident light), **ε** is the molar absorption coefficient, **c** is the molarity of the absorbing specie, and **b** is the path length through the sample. Steady-state absorption spectra were recorded with a Perkin Elmer Lambda 35.

### *2.1.2 Steady state fluorescence spectroscopy*

Fluorescence spectroscopy measures the emission of light from excited states, and it represents, therefore, a complementary technique to UV-Vis spectroscopy. In particular, excited state can be singlet (S) or triplet (T). In the first case, the emission of light is called fluorescence, and the electron in the excited state presents opposite spin orientation compared to the electron in the ground state. In the case of emission from triplet excited states, phosphorescence takes place. In this case, the electron in the excited state has the same spin orientation as in the ground state. Since the transitions to the ground state are forbidden, the emission rates are slower compared to those of fluorescence ($10^{-6}$ to 100 $s^{-1}$ compared to $10^{-8}$s), so that phosphorescence excited state lifetimes (τ) are typically microseconds to seconds. Noteworthy, the distinction between fluorescence and phosphorescence is not always clear. As an example, Ir-iTMCs display phosphorescence with intermediate τ values of hundreds of nanoseconds to several microseconds.[4]

The Φ of a sample is defined as $\Phi = \frac{Nr.\ of\ emitted\ photons}{Nr.\ of\ absorbed\ photons}$.

The average excited state lifetime can be obtained by using the $< \tau > = \frac{A_1\tau_1^2 + A_2\tau_2^2 + \cdots + A_n\tau_n^2}{A_1\tau_1 + A_2\tau_2 + \cdots + A_n\tau_n}$ formula reported in literature.[105]

Emission spectra, Φ values, and τ values were measured with a F5 Fluorimeter with integrating sphere SC-30 (Edinburgh Instruments). Excited states lifetimes (τ) were obtained with a TCSPC module ($\lambda_{exc}$ =377.6 nm).

### *2.1.3 Cyclic voltammetry*

Cyclic Voltammetry (CV) is an electrochemical technique that allows the determination of the redox properties of a compound. The setup consists of a working electrode, a counter electrode, and a reference electrode. The compound is dissolved in a solvent, which is electrochemically stable in the regime of the measurement and a reference (in our work, ferrocene) is added. To increase the conductivity an electrochemically inert electrolyte (*e.g.*, tert-butyl ammonium salts for non-aqueous solutions) is used. A triangular shaped potential is applied between the working electrode and the reference electrode, while the current between the two electrodes is detected. If the analyzed species is reduced or oxidized, a current is produced. Three different type of processes can be distinguished, namely reversible, *quasi*-reversible, and irreversible. In the first case, the peaks are symmetric to a central point and the maximum peak current is proportional to the square root of the scan rate. Additionally, the anodic and cathodic peak potentials have to be independent of the scan rate and the difference between them has to be $59/n$ mV, where $n$ is the number of transferred electrons. In *quasi*-reversible processes, the return peak has a lower intensity compared to the first peak. Irreversible processes do not show the return peak. CV measurements were carried out at rt using an AUTOLAB PGSTAT 204 potentiostat. A three-electrode system was used, consisting of a static glassy carbon working electrode, a platinum wire auxiliary electrode and an Ag/AgCl reference electrode.

### *2.1.4 Square wave voltammetry*

Square wave voltammetry (SWV) is an electrochemical technique in which a staircase potential ramp is applied with a square wave mode. The main parameters of the SWV potential modulation are the scan increment $\Delta E$ of the staircase ramp, the SWV amplitude and the duration of the potential pulse. The shape of the forward and reverse scan resembles that of the CV, and provides the same information, with the advantage of a higher sensitivity. Therefore, it is possible to calculate the reversibility ratio of a redox process by integrating and comparing the areas of the forward ($A_f$) and reverse peaks ($A_r$). In detail, reversibility ratio= $A_r/A_f$. SW measurements were carried out at rt using an AUTOLAB PGSTAT 204 potentiostat.

### *2.1.5 Electrochemical impedance spectroscopy*

Electrochemical Impedance Spectroscopy (EIS) is a frequency-domain-based approach, which measures the current response to the application of an AC voltage as a function of the frequency. In other words, an externally applied small perturbation of the system *via* an AC voltage amplitude

leads to a frequency-dependent resistance commonly referred to as "impedance".[106] The employed perturbation is small enough (mV range) to ensure a linear response from the investigated system. EIS yields information about electron transfer processes across interfaces in the active layer, and has emerged as a powerful tool, since electronic and ionic charge carriers of mixed conductors are easily distinguished by the probed frequency.[106,107] Furthermore, this technique allows two types of experiments, namely: (i) static, by performing EIS assays at different voltages; and (ii) dynamic, by applying a constant voltage and periodically performing EIS analysis over the driving time. Typically, Nyquist plots obtained from EIS assays consist of one semicircle whose diameter relates to the resistance associated to the dynamics of the electrical double layer (EDL) formation at the electrode interface under applied voltages lower than the band gap of the emitter (*i.e.*, 3–3.5 eV) and the reduction of the intrinsic undoped region when charge injection is effective (>3.5 eV). This is related to the formation of the EDLs due to the slow movement of the mobile anions towards the electrode interfaces until charge injection is efficient. At this point, the p- and n-doped regions start to grow reducing the p–i–n region and leading to a linear decrease of the resistance profile due to the ohmic charge injection.

In the static mode, measurements were performed at an applied voltage range from 0 to 4/5 V and fitted with the Nova 1.11 software using the circuit model shown in Figure 5. The AC signal amplitude was set to 10 mV and was monitored in a frequency range from 10 to 1 MHz. The Nova 1.11 software was used to obtain the parameters from the equivalent circuit. With this data at hand, the resistance of the intrinsic non-doped region ($R_{LEC}$) was directly obtained. The film conductivity (S/m) is measured at 0 V with the equation $\sigma = d\text{A} \times R_{LEC}$ where $d$ is the thickness of the layer, A is the area of the electrodes, and $R_{LEC}$ is the resistance of the active layer.[107–109] Assays were carried out with a potentiostat/galvanostat (Metrohm μAutolabIII) equipped with a frequency response analyzer module (FRA2).

In dynamic mode, the slow ionic distribution rearrangement and the growth of the doped regions over time are observed by measuring EIS at certain intervals, while keeping the device at an applied constant voltage. The fitting circuit is shown in Figure 5. Upon performing the fitting, the capacitance was replaced with a constant phase element (CPE), which is the equivalent electrical circuit component that models the behavior of an imperfect capacitor. This is assumed to be caused by non-uniform current density distribution and/or reaction rates along the electrode surface,

usually caused by an inhomogeneous surface.[108,110] The CPE's impedance is defined as $C= Q^{1/\alpha}$ x $R_{LEC}^{(1-\alpha)/\alpha}$, and $\alpha$ ($0 \leq \alpha \leq 1$). Q corresponds to $1/|Z|$ at $\omega = 1$ rad/s, where Z is the impedance; it represents no direct meaningful physical value. However, the CPE acts as pure resistor for $\alpha = 0$ and pure capacitor for $\alpha = 1$. The thickness of the doped regions is calculated taking into account that $d_{EDL}C_{EDL}=dC_{geo}$, where $d_{EDL}$=thickness of the doped regions, $C_{EDL}$=capacitance associated to the doped regions, d=device thickness and $C_{geo}$=geometric capacitance obtained by fitting the circuit at 0 V.[18,95,109] The intensity of the internal electric field is then calculated with $E=V/d_{EDL}$, where V is the constant applied voltage and $d_{EDL}$ the thickness of the doped regions.

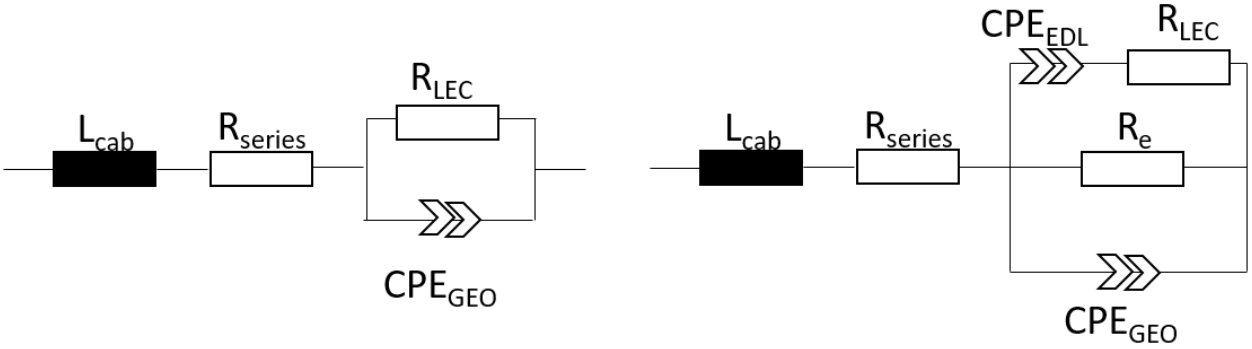


Figure 5. Simplified circuit model with inductance ($L_{Cab}$), external series resistor ($R_{series}$), internal electrical resistance ($R_{LEC}$, and constant phase element $CPE_{geo}$ used for static EIS assays (left), and integral circuit model with EDL related capacitance ($CPE_{EDL}$), ionic resistance ($R_{LEC}$), electrical resistance ($R_e$), and geometric capacitance ($CPE_{GEO}$) used for dynamic EIS assays (right).

### *2.1.6 Atomic force microscopy*

Atomic force microscopy (AFM) is a type of scanning probe microscopy with a sub-nanometer height resolution. A small tip attached to a cantilever fixed onto a piezoelectric crystal is used to touch the sample and to acquire a picture of the surface. The tip oscillates while touching the sample and this deflection is detected by a reflecting laser light from the top surface of the cantilever. This allows the determination of the exact position of the tip and, therefore, contains information about forces. In particular, it is possible to measure both the topography of a surface with a sub-nanometer resolution, as well as the root mean square roughness (RSM), which gives an indication of its homogeneity. AFM assays were performed with VEECO DIMENSION 5000 with a NanoScope V probe head and the Gwyddion evaluation software.

## 2.2 LECs measurement system

For the characterization of the LECs, a LED lifetime system was used to simultaneously measure luminescence, current, and voltage of the device. The luminescence is measured by a silicon detector placed onto the lighting area, while the current-voltage characteristics are determined by applying a stepwise increasing voltage and recording the current and the luminescence of the device (the so-called L-I-V, or luminance-current-voltage scan). In order to measure the lifetime of the device a pulsed voltage/current is used and voltage/current and luminescence are recorded as a function of time. The maximum sensibility of the light sensors is in the yellow-green region and blue or red emitting devices are generally measured by placing an integrated sphere connected to a spectrometer on top of the operating pixel. In the work at hand, measurements were performed with an Avantes spectrophotometer (Avaspec-ULS2048L-USB2) in conjunction with a calibrated integrated sphere Avasphere 30-Irrad and a BOTEST OLT2 LED lifetime system.

## 2.3 Layer deposition Techniques

The LEC fabrication requires the application of layers with defined thicknesses onto a substrate. To this end, different deposition methods were employed.

### *2.3.1 Doctor blading*

A doctor blader consists of a heated bottom plate and an adjustable doctor blade. By applying the coating solution in the gap between the blade and the substrate and moving the blade, it is possible to coat substrates with liquids and simultaneously evaporate the solvent to realize thin solid layers. The thickness and homogeneity of the coating depend on the viscosity and the drying speed of the liquid as well as the height and coating speed of the doctor blade. Thin films were fabricated with a Zehntner 2300 doctor blade.

### *2.3.2 Spin coating*

Spin coating is another deposition technique for uniform thin films, which is suitable for depositing solutions with different viscosities on a variety of substrates. The coating solution is applied to the center of the substrate, which is subsequently rotated with high speed. The centrifugal force spreads the solution and the rotating speed can be varied to obtain the desired layer thickness. It is also possible to apply the coating while the substrate is already rotating, thereby reducing the necessary solution and potentially increasing the layer quality. The solvent commonly evaporates during the spinning process, which results in a solid-state layer. Commonly used solvents are

tetrahydrofuran (THF), acetonitrile (MeCN) or toluene. Thin film layers were spin-coated with a Laurell WS-650-23 Spin Coater.

## 2.4 Figures-of-merit of LECs

The LEC characterization is based on the following figures-of-merit:

- Current density (J): flux of current that is flowing through the device and is measured in ampere per unit area ($A/m^2$).
- Irradiance (I) : radiant flux received by a surface per unit area and is measured in ($W/m^2$).
- Luminance (L): flux of emitted light by the LEC and is measured in candela per surface unit ($cd/m^2$). It is the photometric equivalent of irradiance. The maximum luminance ($L_{max}$) is the highest reached during the entire measurement.
- Turn-on time ($t_{on}$): the time needed to reach the maximum luminance.
- Lifetime ($t_{1/2}$): time until a device reaches half of its maximum luminance.
- Total emitted energy ($E_{tot}$): integrated area of the radiant flux of a device from the beginning of the application of bias until the luminance reaches 1/5 of its maximum value divided by the area of the electrode. The device stability can also be characterized using the $E_{tot}$ parameter (usually measured in mJ), taking the time needed to reach one fifth of the maximum luminance as the upper limit.
- Efficacy (or efficiency): the emitted light per electric flux and is measured in candela per ampere (cd/A).
- Power efficiency: flux of light per electric input and is measured in lumen per Watt (lm/W).
- External quantum efficiency (EQE): ratio of photons emerging from the device per injected electrons.
- Color coordinates: they are used to compare color in a standardized manner, according to the *Commission Internationale de l'Eclairage* (CIE) model ─ Figure 6, based on the fact that the human eye has three types of color sensors that respond to different ranges of wavelengths, and consequently a full plot of all visible colors is a three-dimensional figure.

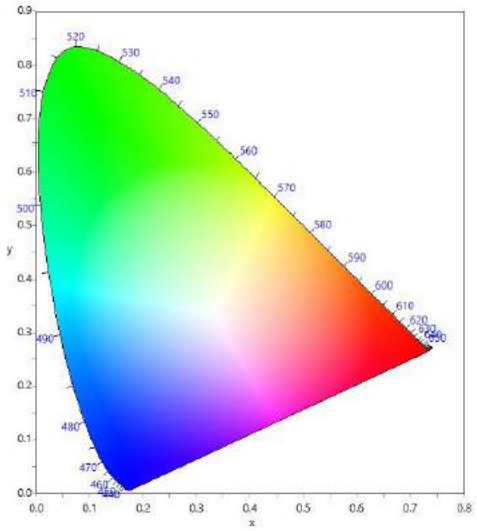


Figure 6. The CIE chromaticity diagram.

## 2.5 Common driving modes of LECs

- L-I-V mode: A ramp of voltage with a determined scan rate – *i.e.*, 500 mV/s, is applied until a suitable voltage is reached (usually from 6 V to 18 V). Repetitive scans are possible.
- Constant mode: A constant voltage or current (usually 3-5 V, 1-100 mA/cm$^2$) is selected and applied over time.
- Pulsed mode: A pulsed voltage or current is selected and applied over time. The pulse is characterized by a duty cycle (50%, if not specified otherwise) and a frequency (1 kHz in the presented contributions). The typical response of a standard LEC tested upon a certain applied current is shown in Figure 7.

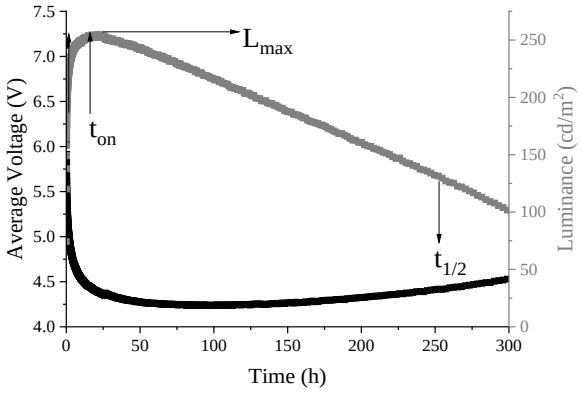


Figure 7. Typical response of the average voltage (black) and luminance (grey) over time of a standard LEC at a certain applied pulsed current. The points at which the $L_{max}$, $t_{on}$ and $t_{1/2}$ are reached are indicated in the graphs.

# 3. Results

## 3.1 $d^{10}$ complexes-based LECs

### *3.1.1 Copper (I) ionic transition metal complexes (Cu-iTMCs)*

Owing to the low cost and toxicity of copper, cationic luminescent Cu-iTMCs have been investigated since the 1970's, when McMillin and co-workers initially described their synthesis and photophysical properties.[111–114] The Cu(I) ion usually presents a tetrahedral geometry, while Cu(II) is more stable in a tetragonal coordination. The emissive state features a MLCT character, as long as empty π orbitals are easily accessible in the ligands, and the $d^{10}$ electronic configuration of the Cu(I) ions disfavors MC electronic transitions, which are generally non-emissive. These factors lead to long excited states lifetimes and potentially intense photoluminescence.

Surprisingly, the first report on Cu-iTMCs in LECs was published only in 2005, when Teng, Fu, and co-workers prepared a yellow-emitting ($\lambda_{em}$ = 570 nm) dinuclear Cu-iTMC that showed a maximum efficiency of 0.16 cd/A at 12 V.[115] In 2006, Armaroli's group proposed to work on an interesting family of heteroleptic copper(I) complexes, that is, $[Cu(N\hat{}N)(P\hat{}P)]^+$ in which N^N and P^P are diimine and diphosphine ligands. In the following years, much effort was put into designing new P^P and N^N ligands. In particular, sterically hindered ligands, such as bis(2-(diphenylphosphino)phenyl)ether (POP) or 4,5-Bis(diphenylphosphino)-9,9-dimethylxanthene (Xantphos), help to stabilize the geometry of the excited state, hindering complex degradation.[62] Concerning the N^N ligand design, important achievements have been realized attaching σ-donating groups or halogen atoms at the para position of the N^N ligands.[72,74–77,81] In particular, Keller *et al*. reported a record efficiency of 5.2 cd/A in LECs built as ITO/PEDOT:PSS/[Cu(6,6'-dimethyl-2,2'-bpy)(POP)][$PF_6$]:ethyl methyl imidazolium hexafluorophosphate ([EMIM][$PF_6$]) 1:1/Al driven at 10 mA/$cm^2$ pulsed current. This, however, came at the expense of a limited stability (0.5 h). By contrast, LECs bearing [Cu(6-methoxy-2,2'-bpy)(POP)][$PF_6$] showed record stability (200 h), but poor luminance (17 cd/$m^2$). It is, therefore, of utter importance to design new complexes and device architectures that feature simultaneous good brightness and stability levels. Furthermore, Cu-iTMCs, despite their well-known color tunability, failed in providing good performing blue-emitting LECs. Indeed, the stability of the first reported blue-emitting Cu-iTMC LEC was limited to a couple of minutes.[67] Additionally, no red-emitting Cu-iTMCs were reported prior to this thesis, hindering the achievement of white light.

The goal of this thesis is, therefore, i) to rationalize the reasons leading to the low stability in Cu-iTMC based LECs, ii) to design suitable N^N or P^P ligands towards enhanced device performance, and iii) to provide rainbow LECs, focusing on the obtainment of stable blue- and red-emitting Cu-iTMCs for the preparation of white-emitting Cu-iTMC based LECs.

### *3.1.2 Blue-emitting Cu-iTMCs-based LECs*

Michael D. Weber[+], Elisa Fresta[+], Margaux Elie, Matthias E. Miehlich, Jean-Luc Renaud, Karsten Meyer, Sylvain Gaillard, and Rubén D. Costa, Rationalizing Fabrication and Design Toward Highly Efficient and Stable Blue Light-Emitting Electrochemical Cells Based on NHC Copper(I) Complexes, *Adv. Funct. Mater*, **2018**, 17, 1704023.

*+ authors contributed equally*

Blue-emitting Cu-iTMCs have not been so far obtained by simply attaching electron withdrawing substituents to the ligands, as extensively reported in Ir-iTMCs. For example, the addition of fluorine groups leads to green-emitting complexes.[76] As such, new types of N^N ligands with high energy LUMO levels were introduced to blue-shift the emission. Costa, Barolo and coworkers firstly proposed a new [Cu(impy)(POP][$PF_6$] complex where impy is 3-(2-methoxyphenyl)-1-(pyridine-2-yl)imidazo[1,5-a]pyridine that showed a deep blue emission centered at ~450 nm in solution, powder, and thin film.[80] However, in LECs it presented a yellow electroluminescence response centered at ~ 550 nm. This was ascribed to the LC character of the emitting excited states that led to a lack of the TADF process under device operation conditions. In other words, the photoluminescence occurs from the singlet excited state and the electroluminescence from the triplet excited state, without having the chance to undergo TADF.
As expected, the device performance was poor, featuring a maximum luminance of 13.9 cd/$m^2$ and an efficacy of 0.03 cd/A at a pulsed driving current of 7.5 mA.

To obtain blue-emitting LECs, Costa and collaborators used a new family of Cu-iTMCs, that is, the NHC–copper(I) dipyridylamine [Cu(IPr)(dpa)][$PF_6$], where IPr: 1,3-bis-(2,6-di-iso-propylphenyl)imidazole-2-ylidene; dpa: 2,2′-bis-(3-methylpyridyl)amine.[67] The authors synthetized a series of Cu-iTMCs, in which the diimine (N^N) ligand was modified with different electron donating and electron withdrawing groups and the NHC ligand bears different bulky

groups. They reported that the combination of both electron-donating and electron-withdrawing type of substituents in a "push-pull" fashion leads to an increased CT character of the emitting excited state and a consequent higher Φ. Importantly, all these complexes exhibited TADF emission in both, solution and powder. The most promising blue-emitting copper(I) complex, [Cu(IPr)(3-Medpa)][$PF_6$] (**1**), where 3-Medpa: 2,2′-bis-(3-methylpyridyl)amine metal complex– Figure 8; $\lambda_{em}$ = 458 nm; Φ=0.86 – was applied into LECs built as ITO/PEDOT:PSS (90 nm)/ **1** (100 nm)/Al. It showed blue electroluminescence centered at 497 nm with x/y CIE color coordinates of 0.23/0.28. At the pulsed driving current of 9.97 mA/$cm^2$, luminances of 22.2 cd/$m^2$, lifetimes of 4 mJ, and efficacies of 0.2 cd/A were achieved–Table 1.[69] Unfortunately, all these devices are characterized by very short lifetimes.

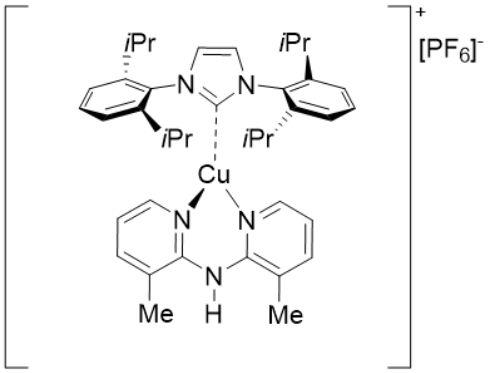


Figure 8. Chemical structure of **1**.

As such, we decided to thoroughly investigate the reasons leading to the poor stability. In fact, although NHC Cu-iTMCs show a sound stability in powder,[67,68,116] there is little known about their stability in solution. Here, three degradation mechanisms may, indeed, take place, namely i) the formation of homoleptic complexes,[117] ii) a solvent-assisted ligand exchange process as both solvents show coordination features,[70,118,119] and iii) the spontaneous formation of copper(II) compounds.[120–122] We selected THF and MeCN as suitable solvents to fabricate LECs with **1**, owing to its high solubility and the suitability of the solvents to yields homogeneous films. Firstly, the absorption features of fresh and aged solutions were analysed. The appearance of a new, well-structured band centered at 350-400 nm in THF evolves immediate, and it increases over time, reaching a plateau after 2 h. By contrast, the absorption features in MeCN solutions remain unchanged during a timeframe of a couple of days, when a significant band at 350-400 nm appears

– Figure 9. In THF, the same degradation band at 350-400 nm was also observed for [Cu(3-Medpa)$_2$][$PF_6$], the homoleptic analogue of **1**. As such, we could discard the formation of homoleptic species as possible degradation mechanism.

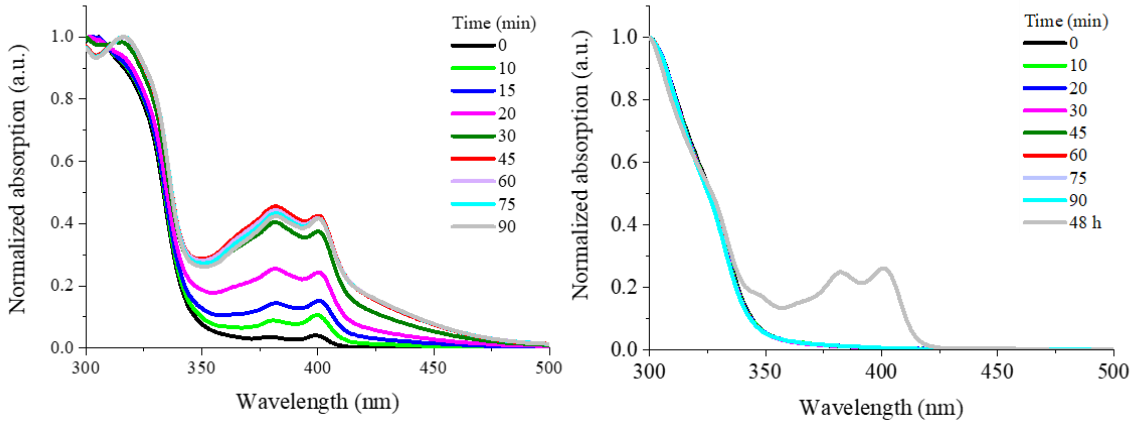


Figure 9. Changes over time in the UV-Vis absorption features of **1** in solution of THF (left) and MeCN (right).

Time-dependent $^1$H proton nuclear magnetic resonance ($^1$H-NMR) and electron paramagnetic resonance (EPR) spectroscopy experiments in both solvents further highlighted that the formation of Cu(II) was instantaneous in THF.[69] MeCN solutions, by contrast, showed that the formation of Cu(II) was taking place at a significantly slower rate than in THF. Those results highlighted the better suitability of MeCN over THF for thin film fabrication. However, a last experiment involved Φ measurements of thin films spin-coated from fresh and aged solution. Here, the Φ of films prepared from MeCN solutions reduced significantly faster than those with THF solutions. In particular, Φ changed from 78% to 30% for MeCN and from 85% to 75% in THF after 10 min, which is the minimum time required to process LECs. This was ascribed to the irreversible solvent-assisted ligand exchange reaction that leads to the formation of homoleptic species.[69,72] Therefore, we selected THF as solvent for LEC fabrication.

Next, we performed CV measurements. **1** shows two *quasi*-reversible oxidations at 0.95 and 1.40 V *vs* ferrocene/ferrocenium ($Fc/Fc^+$), while only one *quasi*-reversible reduction process at −2.00 V *vs* $Fc/Fc^+$. Both, oxidation and reduction processes, could be considered as *quasi*-reversible, but their impact on the photoluminescence features is unknown. Indeed, it is of utmost relevance to

determine if the redox processes have an impact on the photoluminescence features and whether this is reversible or irreversible. The latter would suggest the formation of quenching species that are the major reasons leading to fast luminance decay in LECs. Therefore, spectro-electrochemical assays were performed monitoring the emission features upon applying a cyclic voltage loop from 0 to either 1.0 or −2.0 V and back to 0 V – Figure 10. Upon reductive scan, the emission is decreased in intensity, but it is recovered once the potential goes back to 0 V. Upon oxidation, by contrast, the emission intensity is significantly reduced, and is not recovered upon decreasing potential. This highlights that the oxidation process might have a major impact on the LEC performances and, therefore, needs to be solved.

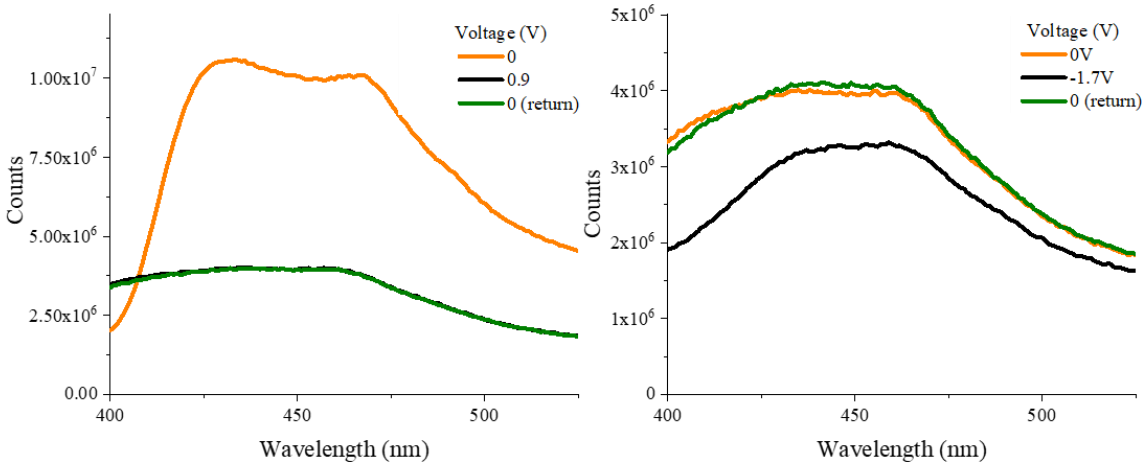


Figure 10. Spectro-electrochemical assays of **1** under oxidation (left) and reduction (right) applied voltage scan.

To this end, we opted for the commonly used hole transport material 4,4′-bis(*N*-carbazolyl)-1,1′-biphenyl (CBP) for preparing two sets of devices. The first set followed the common host–guest approach, namely a single-layered device architecture based on mixture of CBP as host and **1** as guest in mass ratio of 10, 20, 30, and 50 wt.% − Figure 11. The second set consisted in a multi-layered device architecture, that is, a device with the configuration indium tin oxide (ITO)/CBP/**1**/Al, in which CBP acts as a hole injection/transport layer and **1** acts as electron-transport as well as electron–hole recombination layer. Among various hole transporter, CBP was elected owing to its oxidation reversibility and the wide electrochemical band-gap, in which the

HOMO and LUMO levels of **1** are embedded, allowing energy transfer as the light emitted by of CBP can be absorbed by **1**. However, only a 50:50 CBP:**1** ratio led to for a complete energy conversion from host to guest −Figure 11. The device performance was encouraging, reaching comparable luminances (19 cd/m$^2$) and efficacies (0.15 cd/A), but a 6-fold enhanced stability (24.6 mJ) − Figure 12 and Table 1.

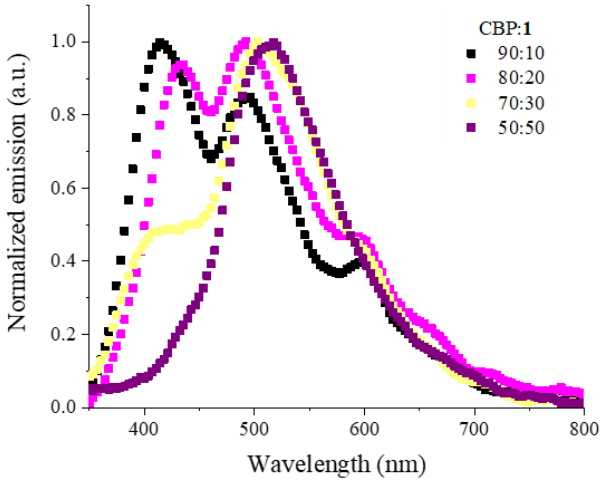


Figure 11. Electroluminescence spectra of LECs with different ratios of CBP to **1**.

Finally, multi-layered devices were fabricated and the thickness of the CBP layer was optimized to 25 nm. These devices showed 8-fold enhanced luminances (170 cd/m$^2$), efficacies (1.2 cd/A), and stabilities (32.7 mJ) at pulsed driving current of 2 mA − Figure 12 and Table 1.

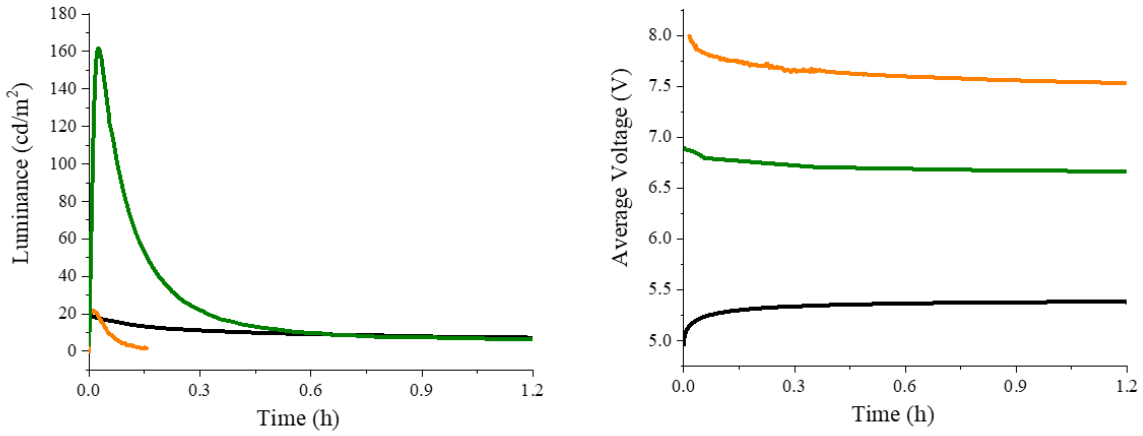

Figure 12. Luminance *vs* time (left) and average voltage *vs* time (right) of **1** (orange), CBP:**1** 50:50 (black), and CBP/**1** (green) LECs driven at different pulsed currents (see legend).

The electroluminescence response of CBP/**1** was comparable to that of **1**, indicating that electron transport and light emission were successfully happening at **1** layer, as there is no contribution for CBP. However, the enhanced stability of CBP/**1** LECs suggests that CBP acts as an effective hole transporter, hindering the oxidation on **1**− Figure 13. This is in line with the energy levels of CBP and **1**; here, CBP traps hole as it has the lowest lying HOMO, while the emission happens in **1** layer as it has the smaller bandgap.

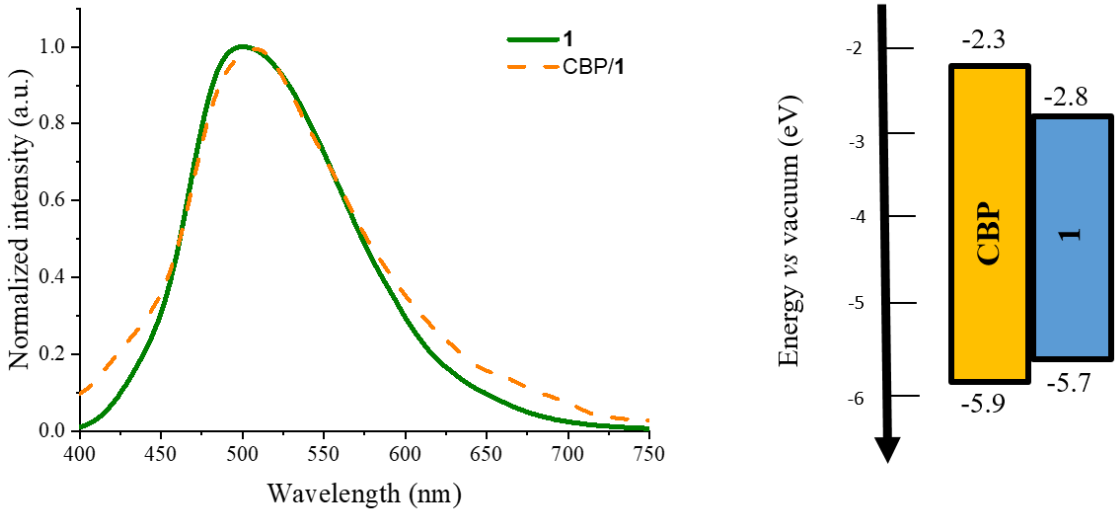


Figure 13. Electroluminescence spectra of **1** and CBP/**1** LECs (left), and schematic representation of the energy levels in CBP/**1** LECs (right).

To summarize, this work shed light onto the reasons leading to the poor performances of **1** LECs, which comprised a more careful solvent choice and the irreversibility of the oxidation process. As such, we enhanced the performances of **1** LECs by employing the small molecule CBP in i) single-layered devices with host-guest approach, and ii) multi-layered devices, in which CBP acted as a hole transporter. The best results were obtained with the second strategy, and consisted in an 8-fold enhancement of luminance, efficacy and stability compared to single-layered device.

Table 1. Figures-of-merit of single- and multi-layered **1** devices run at pulsed 2 mA.

| Device | $L_{max}$[a] ($cd/m^2$) | $t_{on}$[b] (h) | $E_{tot}$ (mJ) | Efficacy (cd/A) |
|---|---|---|---|---|
| **1** | 20 | 0.01 | 4 | 0.2 |
| CBP:**1** 50:50 | 19 | 0.01 | 24.6 | 0.2 |
| CBP/**1** | 168 | 0.03 | 32.7 | 1.2 |

a. Maximum luminance. b. Time to reach the maximum luminance.

### *3.1.3 Yellow- emitting Cu-iTMCs-based LECs*

Elisa Fresta, Giorgio Volpi, Marco Milanesio, Claudio Garino, Claudia Barolo and Rubén D. Costa, Novel Ligand and Device Designs for Stable Light-Emitting Electrochemical Cells Based on Heteroleptic Copper(I) Complexes, *Inorg Chem*., **2018**, 16, 10469–10479.

To enhance the performances of green- and yellow-emitting LECs, strategies have focused on the optimization of both the synthesis protocol (purification and yields)[123,124] and the ligand design (*para* or *ortho* substitutions of the N^N ligand).[74–76,81,125] Concerning the ligand design, encouraging results have been realized attaching σ-donating groups or halogen atoms at the *ortho* or *para* position of N^N ligands.[74,81] In particular, a major breakthrough was realized through the functionalization of the bpy ligand with two methyl groups in *ortho* position, which led to both enhanced Φ values (69% *vs* 6% in powder) and device performances (*i.e*., efficacy of 5.2 *vs* 0.6 cd/A) compared to the non-substituted Cu-iTMC.[75,125] This was ascribed to the positive effect of twisting of the bipyridyl units coupled with a tilting of the heterocyclic ring plane, that led to enhanced luminescence as the photo-induced flattening distortion was limited.[126] In this context, we turned our attention to further enhancement of Cu-iTMCs LECs performances by carefully designing the N^N ligand. We chose two yellow-emitting complexes, namely [Cu(bpy)(POP)]$PF_6$ (**2**), and [Cu(bpy)(POP)]$PF_6$ (**3**). They were synthetized according to literature procedures,[116,124] and their chemical structures are displayed in Figure 14. While **2** was already reported in literature,[73,127] **3** is a new complex featuring methoxy groups at the *ortho* position of the bipyridine ligand (6,6'-$OMe_2$bpy). The presence of the methoxy group should lead to enhanced performances, owing to the electron-donating character of such substituting groups, as well as a sterical hindrance and free rotation motion. As such, not only the coordination from solvent molecules should be

hindered, but also the molecule should possess enhanced rigidity and should not flatten in the excited state.[127,128]

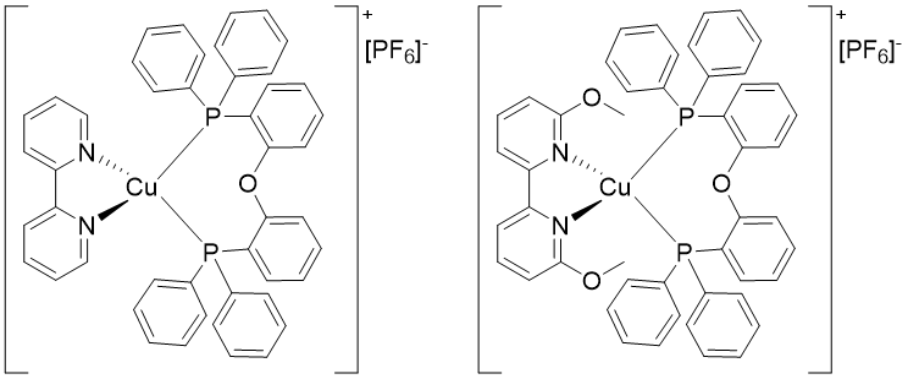


Figure 14. Chemical structures of **2** (left) and **3** (right).

A first confirmation came from the X-ray analysis of **2-3**, which pointed out that i) the O-$CH_3$ bond belonging to the methoxy group has the typical length of an aromatic bond (1.39 Å), which suggests a certain degree of electron delocalization, and ii) the geometry is closer to an ideal tetrahedron due to the enhanced rigidity of the bpy ligand.[71]

The expected positive effect of the substitution was firstly tested in solution. Indeed, LECs fabrication requires are prepared using solvent-based deposition techniques; however, this step can lead to degradation issues if the complex gets coordinated by the chosen solvent. In this case, we selected MeCN as solvent due to the high solubility of the Cu-iTMCs and the quality of the layer's morphology. MeCN is, however, known for its coordinative character.[125] Both thermal and photo-stabilities were tested, by keeping solutions of **2** and **3** at 70°C or under UV-light excitation over time, respectively, and monitoring the absorption features over time.

In detail, fresh MeCN solutions of both **2** and **3** show well-defined absorption bands transitions located at 280-300 nm and 380-400 nm regions ─ Figure 15. They correspond to LC and MLCT transitions, respectively. At 70°C, the archetypal **2** showed an evolution of a third absorption band after *ca*. one hour, while **3** showed no changes after 6 hours of continuous measurements. The band was ascribed to the formation of a homoleptic complex ─ Figure 15. Under UV excitation, both complexes feature a fast growth of additional absorption bands with **2** starting to degrade after one minute and **3** holding fresh absorption features for at least 10 minutes ─ Figure 14. This

experiment represents a first confirmation that the methoxy group has a positive effect towards solvent coordination both in the ground and excited state.

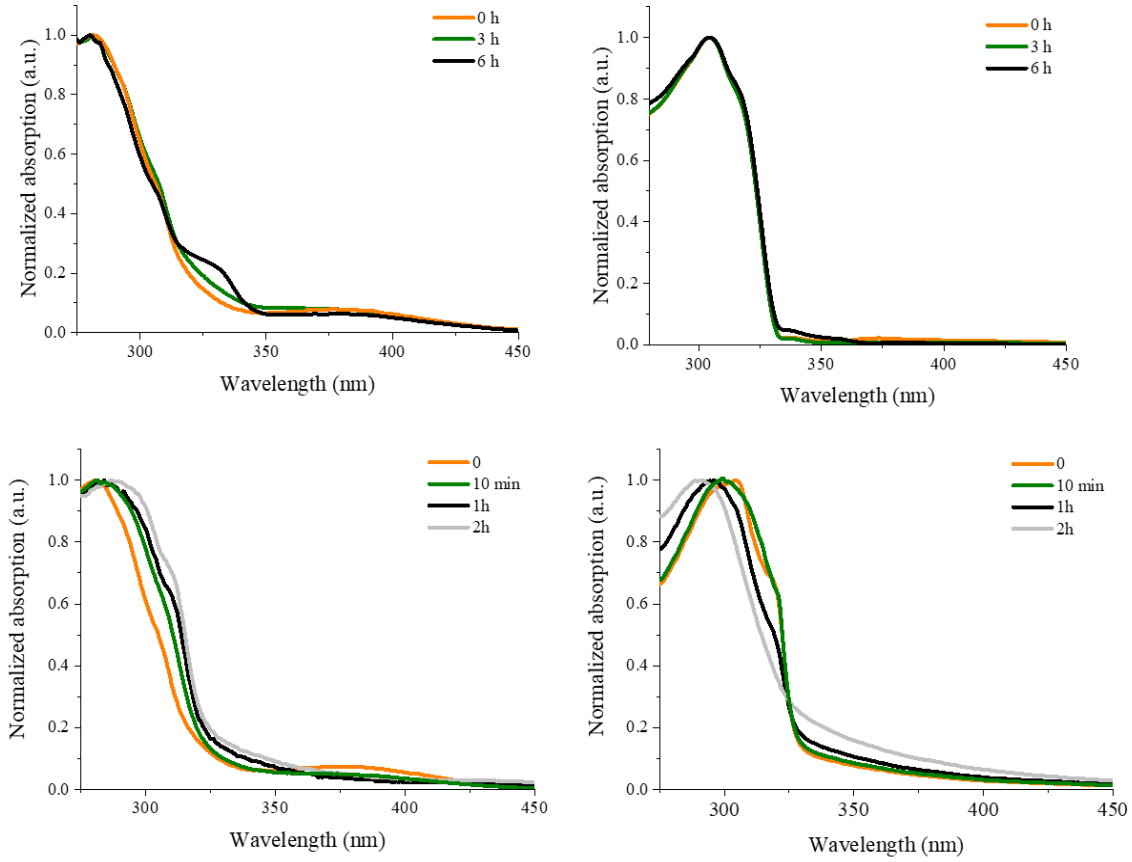


Figure 15. Change in the UV-Vis absorption spectra of **2** (left) and **3** (right) MeCN solution (10^-4 M) under thermal (70°C, top) and UV irradiation (302 nm, 640 μW/cm$^2$, bottom) stress.

Next, thin films of **2** and **3** were processed; their photoluminescence features showed shapeless emission centered at $\lambda_{max}$ of 583 (**2**) and 571 (**3**) nm. Importantly, the Φ value of **3** (20%) more than double that of **2** (9%). Thus, we proceed to study their electroluminescence features in standard single-layered LECS. The complexes showed yellow electroluminescence with $\lambda_{max}$ of 589 (**2**) and 571 (**3**) nm and x/y CIE color coordinates of 0.49/0.53 (**2**) and 0.46/0.52 (**3**). Regardless of the applied pulsed driving current, which was varied from 2.5 to 7.5 mA, the LEC performances of **3** resulted up to 3- to 4-times higher compared to those of **2** ─ Figure 16 and Table

2, in that they showed simultaneously enhanced brightness, shorter turn-on times, and longer stabilities. Noteworthy, all the devices show a rise of the voltage over time, accompanied by luminance loss. Importantly, this happens within a shorter time for **2** compared to **3**, *i.e.*, 0.5 h compared to 1.5 h at 7.5 mA pulsed driving current. This points out that degradation processes are taking place, generating quenching species.

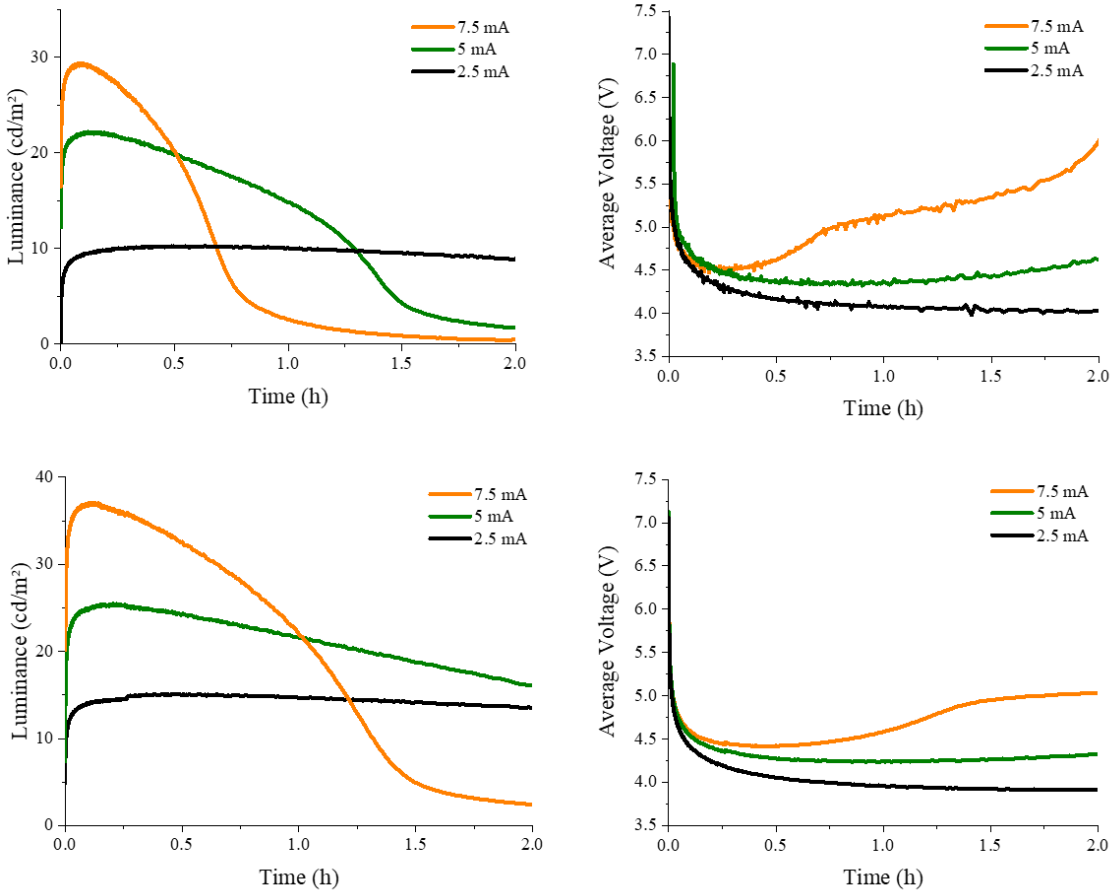


Figure 16. Luminance *vs* time (left) and average voltage *vs* time (right) of **2** (top) and **3** (bottom) single-layered LECs driven at different pulsed currents (see legend).

As such, we turned our attention to cyclic voltammetry assays. Both **2** and **3** showed a *quasi*-reversible oxidation at ~ 1 V, and two totally reversible reductions at around -2 V and -2.5 V — Figure 17. We could, therefore, assume that the oxidation process was responsible for the luminance decay and the voltage rise, as also described for **1**. Indeed, this is a common issue for Cu-iTMCs.[129]

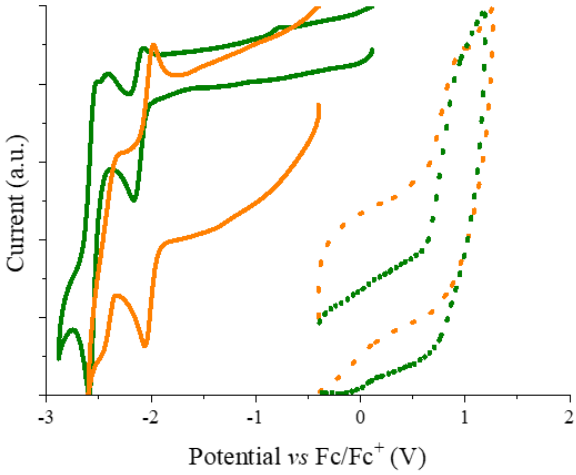


Figure 17. Cyclic voltammogram of **2** (green) and **3** (orange) in MeCN solution. The straight line indicates the reduction scan, while the dotted line the oxidation scan.

Following the successful strategy achieved with **1**,[69] we opted for a multi-layered architecture strategy, in which a pure CBP layer works as a hole transporter, and the Cu-iTMC as an electron transporter and emissive layer. The optimized CBP layer thickness was found to be 15 nm, and the pulsed driving current of 7.5 mA was chosen, as it was the most prone to fast performance loss. The device stability was enhanced for both complexes by one order of magnitude compared to that of single-layered LECs without affecting the other figures-of-merit ─ Figure 17 and Table 2. As a further proof of the positive effect of the methoxy substitution, **3** multi-layered devices showed better performances compared to those with **2**. Importantly, the electroluminescence features of the multi-layered devices show no relevant difference with regard to the single-layered one, highlighting that recombination and emission were successfully happening at **2** and **3** layers ─ Figure 18.

Finally, the enhanced stability confirmed that the hole transport role of the CBP layer was efficiently contributing in hindering the oxidation issues. This is also corroborated by the favorable energy levels on CBP and **2** or **3**; indeed, CBP has the lowest HOMO and therefore collects hole, while recombination happens in the Cu-iTMC layer as it has the smaller bandgap.

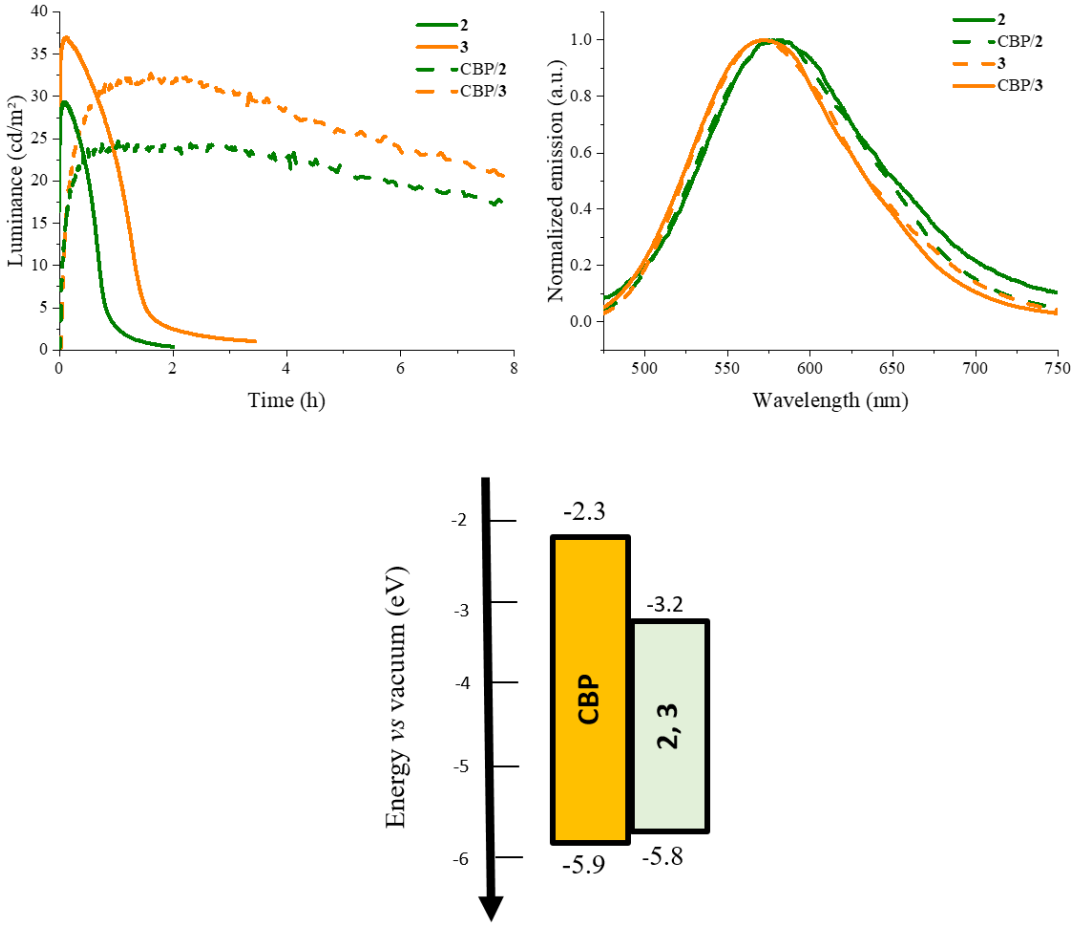


Figure 18. Comparison between luminance *vs* time (top left) and electroluminescence spectra (top right) of **2** and **3** single-layered and multi-layered devices driven at pulsed 7.5 mA, and schematic representation of the energy levels of the multi-layered device (bottom).

Overall, this work firstly provides a ligand design, in which the methoxy substitution in the *ortho* position of the bpy ligand allows for improved photophysical and device properties. Secondly, the multi-layered device strategy that we used for **1**, led to 10-fold enhanced stabilities compared to single-layered devices, without affecting the other figure-of-merits. As such, we can state the universal character of this approach towards stable and efficient Cu-iTMC based LECs.

Table 2. Figures-of-merit of single-layered and multi-layered **2** and **3** devices.

| Device | Driving current (mA) | Average Voltage (V) | $L_{max}$[a] ($cd/m^2$) | $t_{on}$[b] (h) | $t_{1/2}$[c] (h) | Efficacy (cd/A) |
|---|---|---|---|---|---|---|
| **2** | 2.5 | 4.0 | 10.2 | 0.90 | 5.5 | 0.1 |
| **2** | 5.0 | 4.3 | 22.1 | 0.25 | 0.5 | 0.1 |
| **2** | 7.5 | 4.5 | 28.5 | 0.20 | 0.6 | 0.1 |
| CBP/**2** | 7.5 | 3.7 | 24.7 | 1.1 | 13 | 0.1 |
| **3** | 2.5 | 3.9 | 15.2 | 0.31 | 7.2 | 0.4 |
| **3** | 5.0 | 4.2 | 25.1 | 0.12 | 2.6 | 0.3 |
| **3** | 7.5 | 4.4 | 36.4 | 0.05 | 1.1 | 0.3 |
| CBP/**3** | 7.5 | 3.4 | 32.9 | 1.6 | 10.8 | 0.3 |

a. Maximum luminance. b. Time to reach the maximum luminance. c. Time to decay to the half of the maximum luminance.

### *3.1.4 Red-emitting Cu-iTMCs-based LECs*

Elisa Fresta, Michael D. Weber, Julio Fernandez-Cestau, Rubén D. Costa, White light-emitting electrochemical cells based on deep-red Cu(I) complexes, *Adv. Opt. Mater*, **2019**, 7, 1900830.

Although there have been scattered reports of red-emitting Cu-iTMCs employed in OLEDs,[130,131] they have not been reported for LECs so far. This is a critical concern, as it also implies the lack of Cu-iTMCs based white-emitting LECs, that is necessary for indoor lighting. In order to red-shift the emission, we decided to substitute the common N^N ligand bpy, that gives rise to yellow-emitting LECs, with the highly conjugated dcbq (= 4,4′-diethylester-2,2′-biquinoline). Additionally, we opted for different P^P ligands, that is, $(PPh_3)_2$ or bis-triphenylphosphine, POP or (bis(2-(diphenylphosphino)phenyl)ether), and Xantphos or (4,5-Bis(diphenylphosphino)-9,9-dimethylxanthene), named **4**, **5**, and **6**, respectively ─ Figure 19. The rigidity of the P^P ligand increases from **4** to **6**, which should imply enhanced chemical and electrochemical stability, as well as higher Φ values due to the reduced structural distortion in the excited state. This strategy, therefore, allows to shed light on a possible effect of the increased P^P ligand rigidity onto **4**–**6** photophysical properties as well as their device performances.

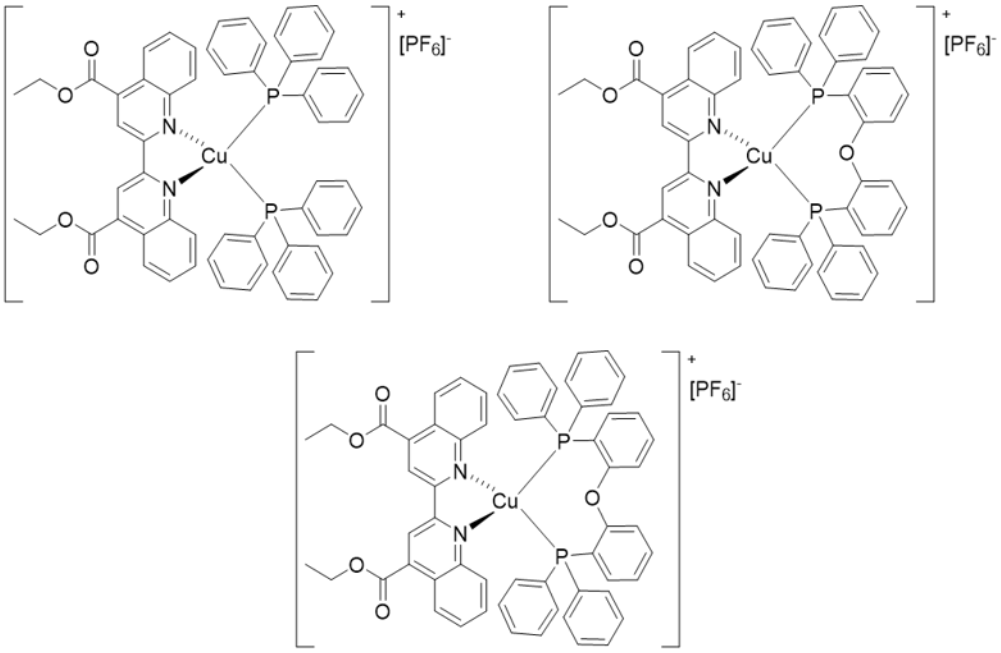


Figure 19. Chemical structure of **4** (top left), **5** (top right), and **6** (bottom).

**4**–**6** exhibit strong deep-red photoluminescence in $CH_2Cl_2$ solution, featuring broad emission bands centered at $\lambda_{max}$ = 704 nm (**4**), 709 nm (**5**), and 701 nm (**6**), and blue-shifted emission in powder ($\lambda_{max}$ = 669 nm **4**; 676 nm **5**; 671 nm **6**) –Figure 20. The reasons underlying the blue-shift are ascribed to the hypsochromic shift following a change in the molecular geometry in the excited state.[132] The Φ values in powder follow the same trend as the rigidity of the P^P ligand, increasing from 26% (**4**), 36% (**5**), and 56% (**6**).

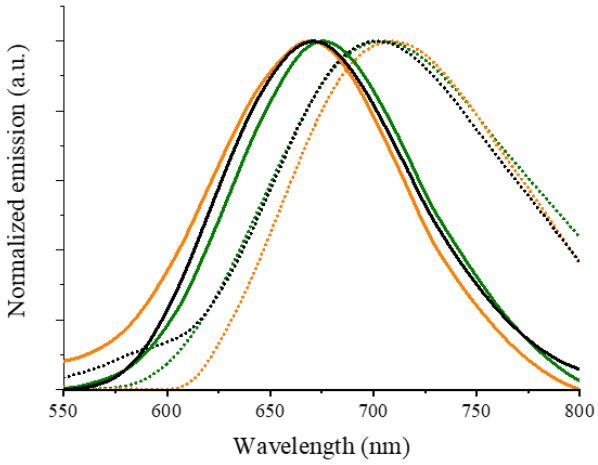

Figure 20. Emission spectra in $CH_2Cl_2$ solution (straight line) and powder (dotted line) of **4** (orange), **5** (black), and **6** (green).

Next, devices with LECs **4**–**6** were prepared in a standard single-layered device architecture. Firstly, five cyclic L–I–V assays with scan rate 300 mV/s were performed. Here, the current density does not vary and the luminance increases upon the scans for **5** and **6**, while devices with **4** show current density increase and luminance loss upon the scans – Figure 21. This suggests that **4**, in contrast to **5** and **6**, shows a limited stability upon applied voltage. Moreover, the maximum irradiance displayed increases from **4** (0.89 µW/cm$^2$) to **5** (29 µW/cm$^2$), and to **6** (40 µW/cm$^2$). The light output can be described as deep-red with x/y CIE color coordinates of 0.52/0.33 (**4**), and 0.66/0.32 (**5** and **6**).

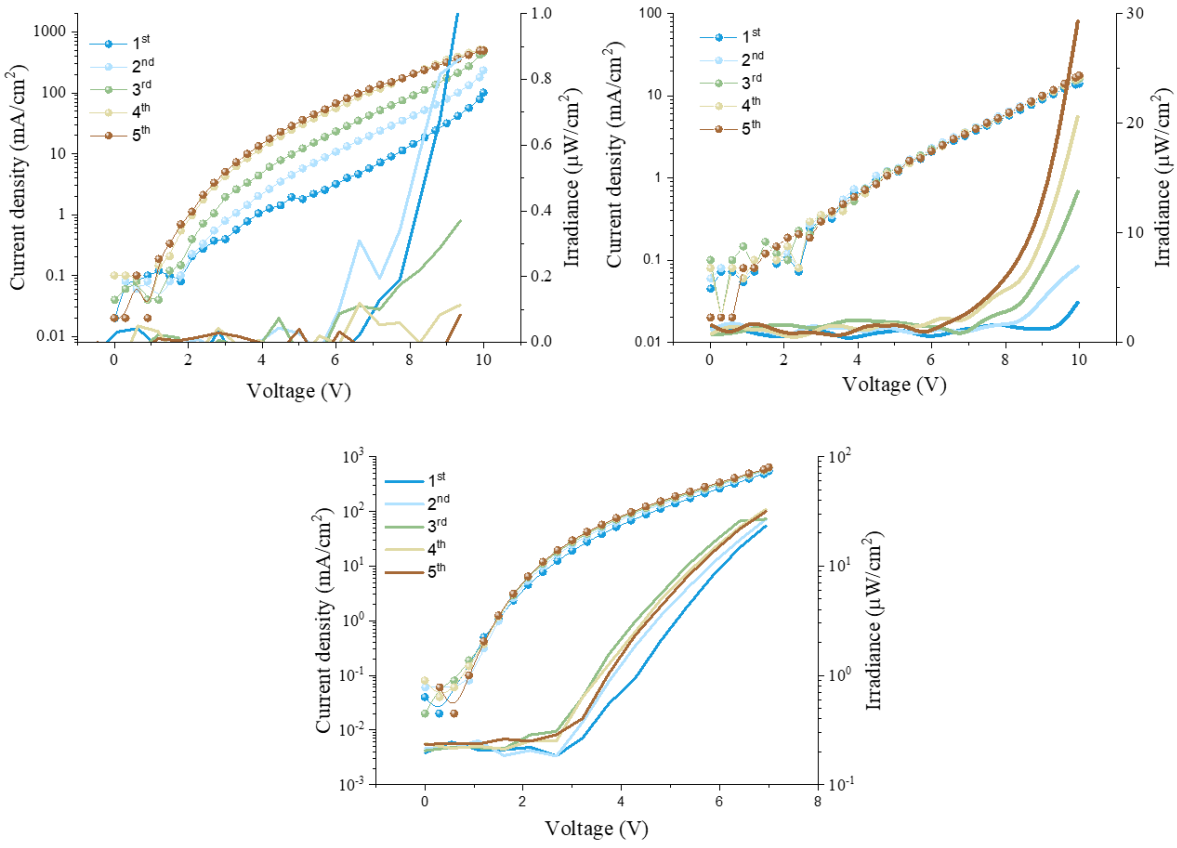


Figure 21. Consecutive L-I-V scans (see legend) of **4**-(top left), **5**-(top right) and **6**-(bottom) LECs.

This trend is also kept when the devices are measured in pulsed mode at 15 mA (97.9 μW/cm$^2$, 20.9 h **6**; 41.5 μW/cm$^2$, 6.5 h **5**; 0.77 μW/cm$^2$, 1.7 × 10$^{-3}$ h **4**). More strikingly, **6** also shows the longest lifetime (20.3 h compared to 6.5 h for **5** and 0.0017 h for **4**) – Figure 22 and Table 3.

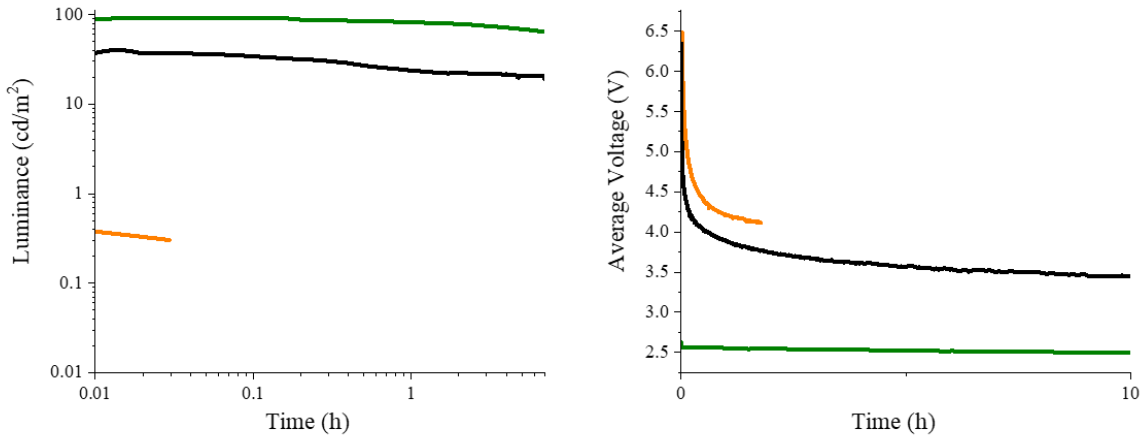


Figure 22. Luminance *vs* time (left) and average voltage *vs* time (right) of **4** (orange), **5** (black), and **6** (green) single-layered LECs driven at 15 mA pulsed current.

In an attempt to further improve the device performances, we turned our attention to CV and SWV studies, as a tool to study degradative processes. – Figure 23. These complexes show a *quasi*-reversible oxidation going from 0.91 V (**4**), to 0.87 V (**5**), and to 0.83 V (**6**) *vs* Fc/Fc$^+$, a first reduction wave at -1.3 V *vs* Fc/Fc$^+$, which is ascribed to the N^N ligand (dcbq), and a second reduction wave at -1.51 V (**4**), -1.70 V (**5**), and -1.76 V (**6**). However, the level of *quasi*-reversibility of the processes may vary significantly. To this end, we performed SWV assays by scanning in forward and reverse directions and integrating the observed peaks. This allowed us to calculate the reversibility ratio, which increases linearly from **4** to **6** for both the oxidation and reduction processes. This highlights the crucial role of the P^P ligand in affecting both the complex and device stability. Indeed, among the three complexes, **6** appears as the most promising candidate for LECs. As such, we decided to concentrate on **6** to further improve the device performances.

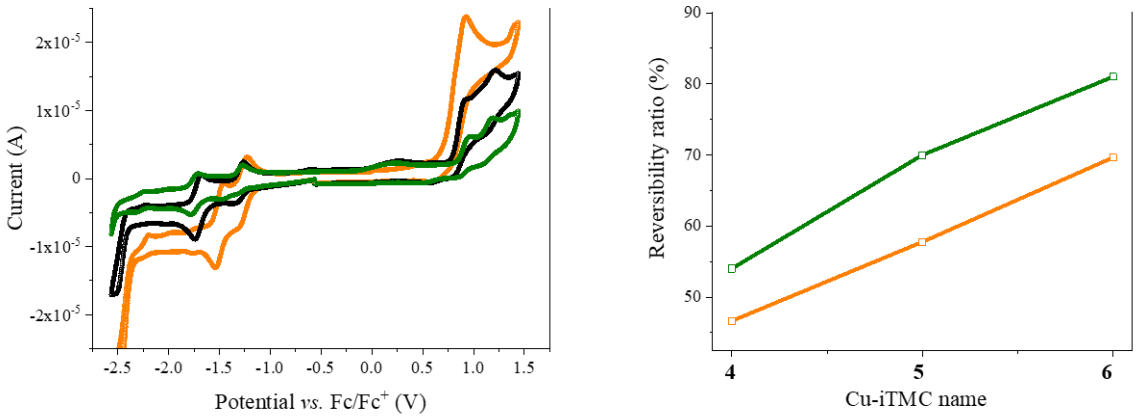


Figure 23. Cyclic voltammogram of **4** (orange), **5** (black), and **6** (green) in THF solutions (left), and reversibility ratio for oxidation (orange) and reduction (green) processes for complexes **4**–**6** (right).

Following the success obtained with the previously reported complexes **1**–**3**,[69,71] a host-guest system with the blue-emitting molecule CBP was tested. Indeed, the energy level of **6** are embedded in these of CBP and the electroluminescence response of the latter fit to the absorption of **6**. The device architecture ITO/PEDOT:PSS/**6**:CBP/Al was analyzed by changing the blending ratio in a range 1%–30% wt. of **6**. With a 15% wt of **6**, proof-of-concept white LECs featuring 4 cd/m$^2$ at 25 mA pulsed driving current, x/y CIE color coordinates of 0.31/0.32 and a high CRI of 92. These represent the first Cu-iTMCs based white LECs – Figure 24 and Table 3.

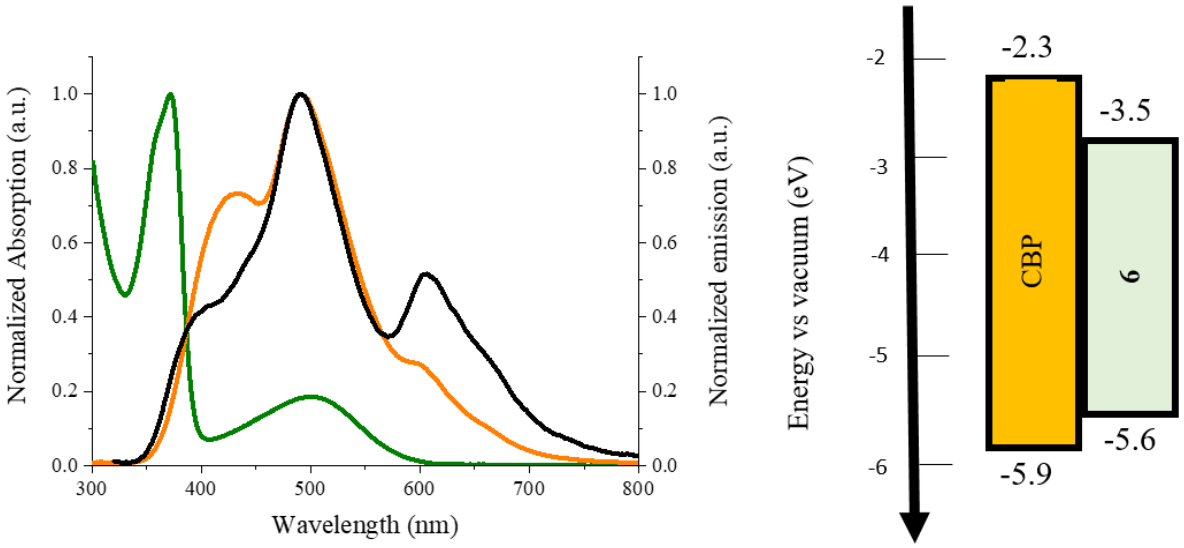


Figure 24. Normalized absorption of **6** (green) overlapping to the normalized electroluminescence of CBP (orange), and electroluminescence of the white CBP:**6** 85:15 LEC (black), (left); schematic representation of the energy levels of CBP and **6** (right).

Noteworthy, when increasing the concentration of **6** to 30%, only deep-red emission from **6** is noted, along with slightly lower irradiances (79 μW/cm$^2$) compared to pure **6** devices, but with an outstanding stability of 170 h, which represents one of the most stable Cu-iTMC-LECs so far reported, and a 9-fold improvement compared to the device with **6** pristine– Figure 25.

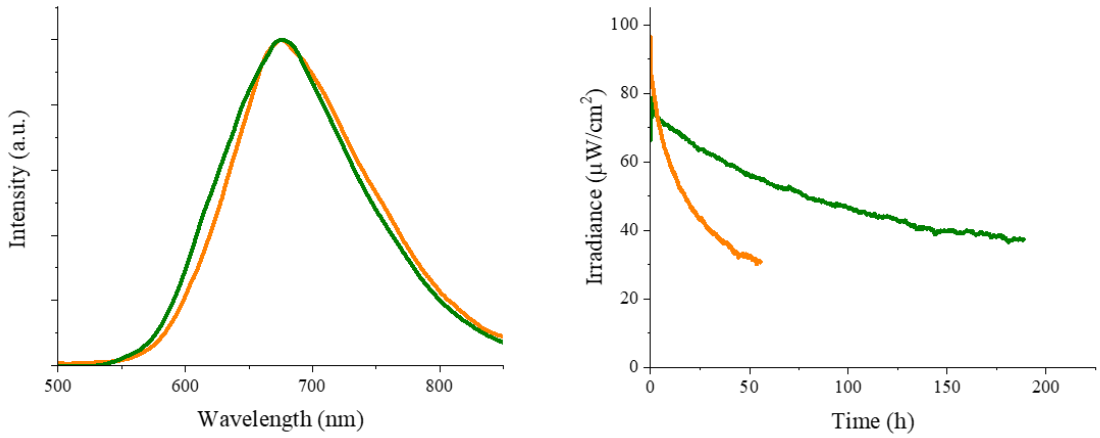

Figure 25. Electroluminescence spectrum (left) and irradiance *vs*. time (right) of pristine **6** (orange) and CBP: **6** 70:30 (green) LECs.

To conclude, the first deep red-emitting Cu-iTMCs bearing different P^P ligand are realized. The type of P^P ligand has a huge impact in determining Φ value, redox reversibility and device properties. In particular, all these properties are enhanced with enhanced rigidity of the P^P ligand. To further enhance the stability of the most promising complex, that is, **6**, host-guest devices with the hole transporter CBP are fabricated. Here, a CBP:**6** ratio of 85:15 leads to the first Cu-based white emitting LECs, while a CBP:**6** ratio of 30:70 to 9-fold enhanced stability compared to **6** devices, without negatively affecting the other performances.

Table 3. Figures-of-merit of **4**–**6** devices driven at pulsed 15 mA

| Device | Irradiance$_{max}$ [a] ($\mu W/cm^2$) | $t_{1/2}$ [b] (h) | $t_{1/5}$ [c] (h) | $E_{tot}$ [d] (J) | Eff [e] (lm/W) | $\lambda_{max}$ (nm) | x/y CIE |
|---|---|---|---|---|---|---|---|
| **4** | 0.90 | 1.7E-3 | 4.7E-3 | 7.15E-05 | 1.00E-4 | 670 | 0.52/0.33 |
| **5** | 41.1 | 6.5 | 20.0 | 1.39E+02 | 0.05 | 672 | 0.66/0.33 |
| **6** | 97.9 | 20.9 | 81.2 | 1.34E+03 | 0.23 | 675 | 0.66/0.32 |
| CBP:**6** 85:15 | 3.8 $cd/m^2$ | 0.8 | - | - | - | 490,653 | 0.31/0.32 |
| CBP:**6** 70:30 | 78.8 | 170 | 659 | 8.75E+03 | 0.18 | 673 | 0.66/0.32 |

a. Maximum irradiance. b. Time to reach 50% of the initial irradiance. c. Time to reach 20% of the initial irradiance. d. Total emitted energy. e. Power efficiency.

### *3.1.6 Ag-iTMCs*

Ag-iTMCs are a much less explored alternative to Cu-iTMCs, despite belonging to group 11 and having a $d^{10}$ configuration as Cu(I) ions.[70,133] However, the Ag(I) ion features a larger ionic ratio than the Cu(I) ion,[65] which translates in very stable 2-coordinate linear complexes instead of tetrahedral complexes. Besides, they are more difficult to be oxidized,[134] hampering the hole transport in thin-film devices. Additionally, the emission mechanism of Ag-iTMCs has not been entirely clarified yet.[86] Indeed, their emission usually attributed to ligand-centered (LC) π–π* transition or metal-centered in the case of metal-metal bonding, while Cu-iTMCs show MLCT character.[89] Nonetheless, the presence of a MLCT emission is possible in opportunely functionalized Ag-iTMCs.

The first Ag-iTMCs-based LEC is dated 2015, as Moudam *et al*. reported on [Ag(bpy)(POP)][$BF_4$], whose emission had mixed MLCT/LLCT and intra-ligand character.[135] LECs built as (ITO/PEDOT:PSS/Ag-iTMC:[BMIM][$PF_6$]/LiF:Ag showed encouraging performances (395 cd/$m^2$ at 5.5 V) and warm-white, broad emission. However, the device stability was not commented. This leaves the quest of the possible substitution of Cu(I) by Ag(I) open, and motivates our studies towards this purpose.

### 3.1.7 *Ag-iTMCs-based LECs*

Elisa Fresta, José M. Carbonell-Vilar, Jiayin Yu, Donatella Armentano, Joan Cano, Marta Viciano-Chumillas, and Rubén D. Costa, Deciphering the Electroluminescence Behavior of Silver(I)-Complexes in Light-Emitting Electrochemical Cells: Limitations and Solutions toward Highly Stable Devices, *Adv. Funct. Mater*, **2019**, 29, 1901797.

With the aim of thoroughly studying the electroluminescent behavior of Ag-iTMCs, the green-emitting Ag-iTMC, namely [Ag(4,4′-$(MeO)_2$-bipy)(Xantphos)]X (**7·X**, X = $BF_4$, $PF_6$, and $ClO_4$ and 4,4′-$(MeO)_2$-bipy = 4,4′-dimethoxy-2,2′-bipyridine) was chosen – Figure 26.

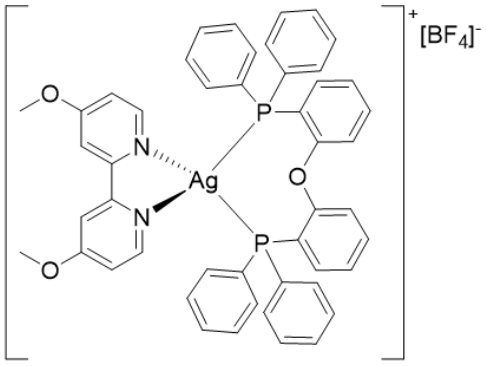


Figure 26. Chemical structure of **7·$BF_4$**.

Firstly, we decided to investigate the stability of the reference **7·$BF_4$** in MeCN, monitoring the changes of the absorption features over time under different conditions – *i.e.*, dark or UV-irradiation and thermal stress. Indeed, the previous reports on complexes **1**–**3** pointed out that this step may be crucial for device performances, if the complex is not robust enough. Fresh **7·$BF_4$** solutions featured an absorption band centered at 254 nm with a shoulder at 277 nm, which do not change over time, suggesting a good suitability of **7·$BF_4$** to be processed in LEC devices. However, this may change when the temperature is increased up to 60 °C, which is a temperature that is

commonly reached in LECs under operation,[136] and they are simultaneously irradiated by UV-light. In detail, two new absorption bands at 310 and 346 nm were noticed after 4 h– Figure 27. These were attributed to the formation of silver nanoclusters. Indeed, as reported by Mulvaney and Henglein, the absorption features at around 300 and 350 nm are characteristic of nonmetallic $Ag_n$ nanoclusters with $n = 3$, and $n >> 3$, respectively.[137]

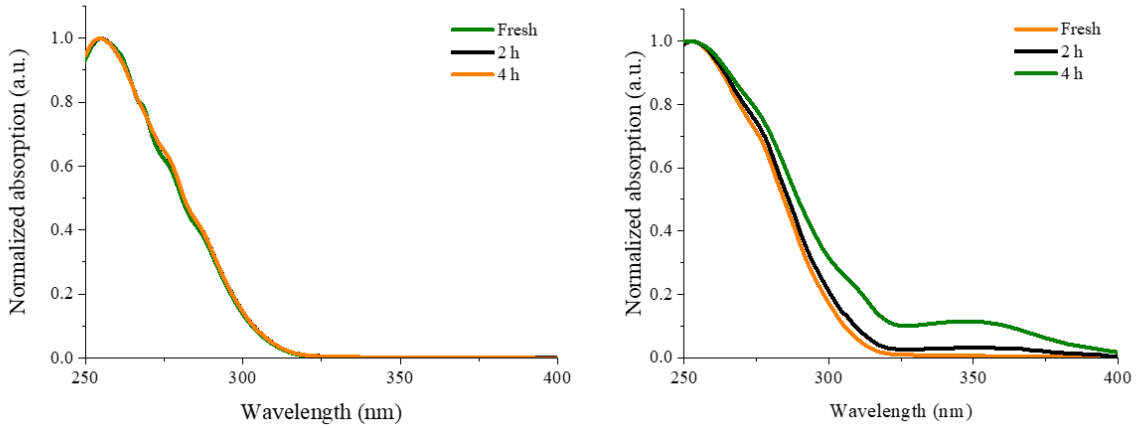


Figure 27. Changes of the UV−vis absorption spectra of **7·BF4** measured in MeCN over time (see legend) at 60 °C in dark (left) and under UV-irradiation (right).

The next step consisted in fabricating thin films, which showed good morphology, Φ values of 20%, and a broad photoluminescence emission centered at 520 nm. We then proceeded with a standard single-layered device fabrication and its consequent testing.

The electroluminescence response of the devices results in a broad, shapeless band centered at around 520 nm and x/y CIE color coordinates of 0.29/0.45, *i.e.*, green devices. They were then measured at different pulsed currents, among which an optimized driving current of 15 mA was selected for further measurements. Indeed, it resulted in the most well performing devices, that showed luminances of 40 cd/m$^2$, efficacies of 0.2 cd/A, and very poor stability of 30 s – Figure 28 and Table 4.

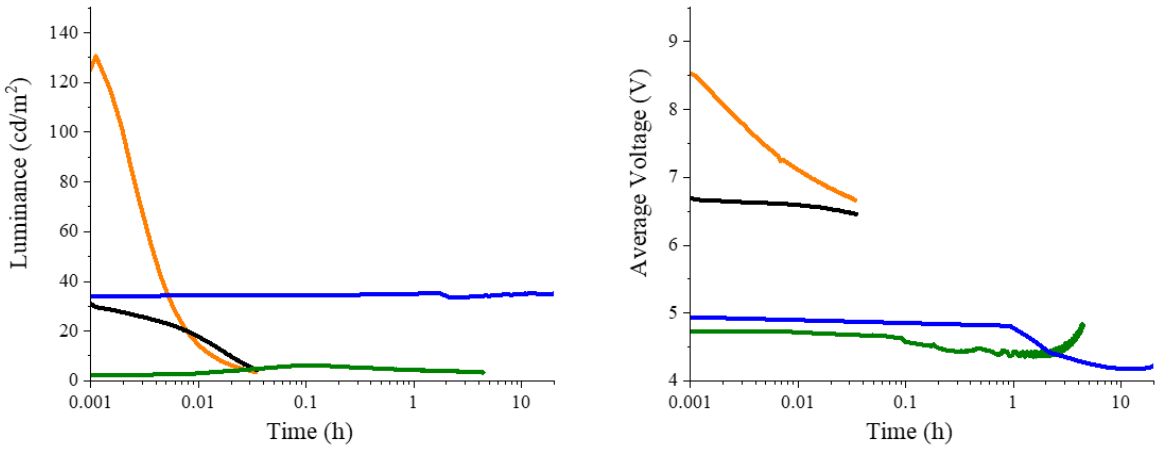


Figure 28. Luminance (left) and average voltage (right) over time of **7·BF$_4$** (black), **7·PF$_6$** (orange), **7·BF$_4$**/PBD (green) and **7·PF$_6$**/PBD (blue) LECs driven at pulsed 15 mA.

As already highlighted for above-reported Cu-iTMCs, CV is a key technique to understand which processes are the most impacting on the device performances. **7·BF$_4$** shows a broad quasi-reversible oxidation peak at 1.1 V and one irreversible reduction wave at -2.05 V (both *vs* Fc/Fc$^+$ couple) – Figure 29. Importantly, an additional peak at -0.09 V was noted on a second scan. This may be ascribed to the deposition of metallic silver onto the working electrode. We further confirmed this phenomenon by employing X-ray powder diffraction (XRD) assays. Indeed, while fresh devices showed peaks coming exclusively from ITO, used devices also feature diffraction peaks at 2θ values of 38.1°, 44.4°, 64.5°, 77.5°, and 81.6°, which are attributed to Ag(0) nanoclusters–Figure 29. [138]

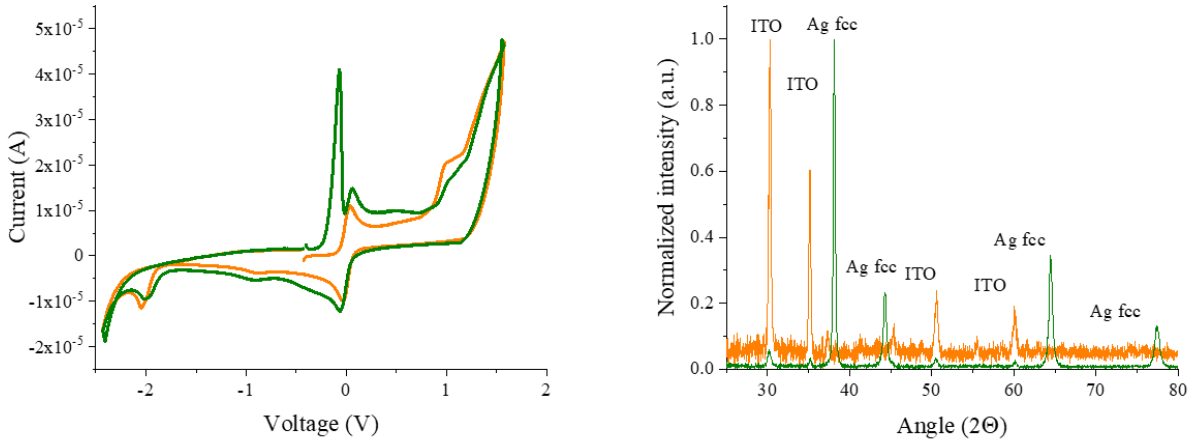


Figure 29. First (orange) and second (green) consecutive cyclic voltammogram of **7·BF$_4$** in acetonitrile (left), and XRD measurements of fresh (orange) and used (green) **7·BF$_4$** devices (right). The peaks related to ITO and to metallic Ag with fcc crystalline cell are labelled correspondingly.

As Ag(0) nanoclusters may be highly conductive, we turned our attention to EIS assays in the range 0-5 V. The first relevant information of this measurement consists in a linear decrease of the resistance in Ag-iTMC-LECs, highlighting the lack of efficient charge injection. More strikingly, used devices also show an unusual behavior with a significant decrease in the active layer ionic resistance ($1.7 \times 10^4$ Ω compared to $1.26 \times 10^5$ Ω for fresh ones). The resistance further decreases during the voltage scan, approaching very low values (≈1000 Ω) at only 1 V, which is far below the bandgap of **7·BF$_4$** – Figure 30. The significant resistance drop may be justified by i) the need of a more suitable counter-ion/electrolyte matrix that leads to standard charge transport and injection, and/or ii) the formation of conductive metallic Ag(0) nanoclusters upon charge injection.

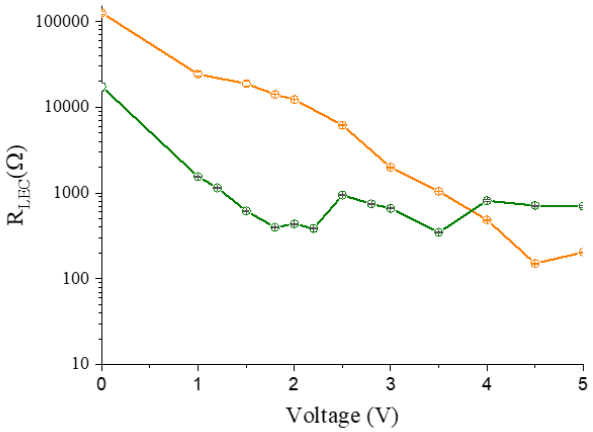


Figure 30. Change in the resistance upon applied voltage in static EIS assays (0-5 V) of fresh (orange) and used (green) **7·BF$_4$** devices.

Firstly, the impact of different electrolyte matrices (that, the standard IL [BMIM[$PF_6$] and the TMPE:LiOTf IP were used to fabricate thin films. However, the resulting bad morphology highlighted the unavailability of this strategy. Next, the impact of different counter-ions on the device performances was studied. Surprisingly, **7·PF$_6$** devices featured higher luminances of ≈130 cd/m$^2$, while **7·ClO$_4$** devices showed lower brightness (4 cd/m$^2$) compared to **7·BF$_4$** – Table 4. However, the lifetimes of all the devices are comparable (~30 s), suggesting that the role of the **BF$_4$** counter-ion has no damaging impact on the device stability, as well as the reason for the resistance drop of the EIS assays.

Overall, these measurements pointed, indeed, out that the key strategy to improve device performances lies on hindering the irreversible reduction process that generates irreversible formation of Ag(0) nanoclusters. Following the strategies pursued in Cu-iTMCs **1**–**6**, we decided to employed a multi-layered architecture in which, this time, an electron transporter is deposited on top of the Ag-iTMCs layer. We selected electron transporter 2-(4-*tert*-butylphenyl)-5-(4-biphenylyl)-1,3,4-oxadiazole (PBD), which is well-known for OLEDs,[139] and fabricated device with the architecture ITO/**7·BF$_4$**/PBD/Al. The optimized devices driven at 15 mA featured luminances of 7 cd/m$^2$, but a three orders of magnitude enhanced stability of 7.2 h–Figure 28 and Table 4. These devices also featured broad whitish electroluminescence with a full width to half-maximum (FWHM) of 206 nm that is centered at 540 nm, as well as x/y CIE coordinates of

0.40/0.44 and a good CRI of 85 –Figure 31. This emission feature is ascribed to the formation of an exciplex as already reported in literature for multi-layered devices.[34,43,140] Indeed, the energy levels of both **7·BF4** and PBD highlight the possibility of an exciplex formation with a $\lambda_{max}$~540 nm –Figure 31.

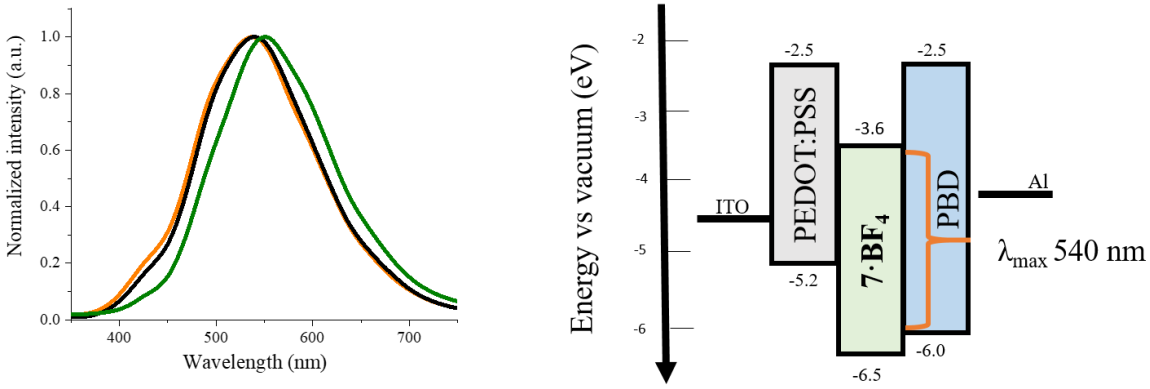


Figure 31. Normalized electroluminescence spectra (left) of **7·BF4** at t=0 (orange), t=$L_{max}$ (black), and at t=$t_{1/2}$ (green) of **7·BF4**/PBD devices driven at pulsed 15 mA, and schematic representation of the energy levels in the device (right). The emission from the exciplex is highlighted by an orange bracket.

Upon further changing the counter-ion to **7·PF6** the multi-layered devices showed maximum brightness of 35 cd/m$^2$ and an extrapolated stability of ≈80 h, which represents an outstanding four order of magnitude stability enhancement compared to both **7·PF6** and **7·BF4** pristine devices– Figure 28 and Table 4.

Overall, this work provides the first insights into the electroluminescent properties of a barely studied family of iTMCs. Single-layered devices show scarce stability of 30 s that is ascribed to the formation of metallic silver nanoparticles upon reduction process. This issue is tackled by both changing the counter-ion (from **BF4** to **PF6**) and decoupling electron transport and emission

processes by employing a multi-layered device architecture with the electron transporter BDP. The so-fabricated devices show comparable luminance and $10^4$ enhanced stability compared to single-layered **7·PF$_6$** LECs, and exciplex-based whitish emission.

Table 4. Figures-of-merit of single- and multi-layered **7·X** devices.

| Device | Average Voltage (V) | $L_{max}$[a] (cd/m$^2$) | $t_{on}$[b] (s) | $t_{1/2}$[c] (h) | Efficacy (cd/A) |
|---|---|---|---|---|---|
| **7·BF$_4$** | 6.5 | 40 | subsec | 0.008 | 0.2 |
| **7·PF$_6$** | 6.9 | 131 | 4.0 | 0.003 | 0.6 |
| **7·ClO$_4$** | 6.0 | 4 | subsec | 0.01 | 0.1 |
| **7·BF$_4$**/PBD | 4.5 | 7 | 0.12h | 7.2 | 0.04 |
| **7·PF$_6$**/PBD | 4.2 | 35 | 1.5h | 35 | 0.1 |

a. Maximum luminance; b. Time to reach the maximum luminance; c. Time to decay to the half of the maximum luminance

## 3.2 Nanographene-based LECs

Among all the types of 3$^{rd}$ generation emitters, SMs are particularly interesting owing to the high versatility, the solubility in organic solvents, the usually reversible redox stability, their robustness, their high Φ values.[11,37]

Different types of families have been employed in SM-based LECs, realizing encouraging results. For instance, the green-emitting benzothiadiazole was employed by Edman and collaborators to yield LECs with high efficiencies of 2.25 cd/A at a moderate luminance of 45 cd/m$^2$,[92] while Costa and co-workers reported a stability of more than 1000 h with a porphyrin-bodipy dyad.[141] Moreover, a single-component porphyrin-based white LECs was reported by the same group.[142] The major weakness of SM-LECs is, indeed, the lack of simultaneously bright and stable SM-LECs, which represents an crucial problem for white SM-LECs featuring luminances barely visible by human-eye. This may be ascribed to the limited families of emitters so far tested. Indeed, the necessity of robust, efficient emitters with optimal n- and p-doping properties represents a key

role in this context. This motivated us to widen the spectrum of families that were considered for LECs, and we turned our attention to the family of nanographenes. This appealing yet neglected class of compounds, indeed, possess i) high Φ values, ii) good solubility in organic solvents, iii) sound stability in solution and upon heating, iv) ambipolar transport properties, and v) easy color tunability.[143] In particular, we tested firstly a reference archetype hexa-peri-hexabenzocoronene with strong green emission. The emitter was further modified through a bandgap enlarging boron-nitrogen doping-obtaining a $B_3N_3$-doped nanographene with strong blue emission in solution and thin film. Finally, we turned our attention to a contorted nanographene, whose distortion from a planar shape hinders aggregation issues and strongly enhances the solubility in organic solvents, allowing for a fast and homogeneous deposition of thin films.

### *3.2.1 LECs based on archetype nanographenes*

Elisa Fresta, Jacopo Dosso, Juan Cabanillas-Gonzalez, Davide Bonifazi and Rubén D. Costa, Revealing the impact of heat generation using nanographene based light-emitting electrochemical cells**,** *ACS Appl. Mater. Inter.*, **2020**, DOI:10.1021/acsami.0c06783.

As already mentioned above, nanographenes are an interesting family of emitters that have barely been investigated in lighting application.[144] As they show great color tunability, we decided to start exploring their electroluminescence behavior by selecting a green-emitting archetype hexaperihexabenzocoronene (**8**)– Figure 32.[145] The color selection was motivated by the lack of green-emitting SMs-LECs,[92,146–149] that contrast to the large number of blue-[150–158] or red-emitting[91,92,142,159–165] SMs-LECs. Moreover, device stability barely reaches 20 minutes. In this context, **8** may provide interesting results, owing to its high robustness, its good ambipolar transport properties, and its reversibility upon redox processes.[144,145]

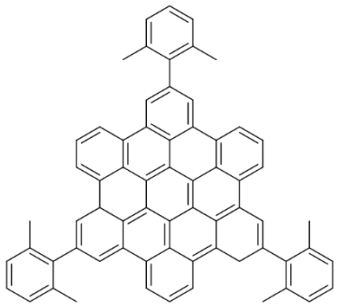

Figure 32. Chemical structure of **8**.

As a standard step before the fabrication of devices, thin films of pristine **8** and of **8** with the IP mixture used in devices were prepared – *i.e.*, **8**:PS:PEO:LiOTf in a mass ratio 10:0.9:2.6:0.78. This IP matrix is has been reported only sporadically for SM-LECs,[166] while the IP TMPE:LiOTf is usually favored. The latter had to be discarded owing to layer morphology issues. They exhibited a well-structured green emission centered at *ca*. 500 nm, and Φ values of 23.1% and 14 % with and without ionic polyelectrolyte – Figure 33.

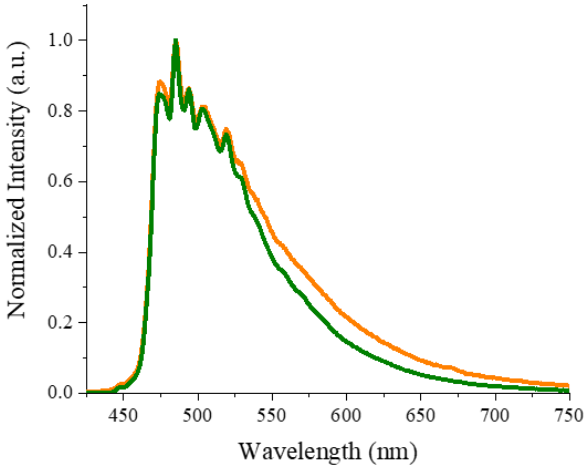


Figure 33. Photoluminescence spectrum of **8** thin films ($\lambda_{exc}$ 405 nm) without (orange) and with polyelectrolyte matrix.

Standard single-layered LECs were fabricated and driven at the pulsed current of 15, 25, and 55 mA. They exhibited luminances of 157, 233, and 343 cd/m$^2$, and lifetimes of 5.8 h, 3.8 h, and 3 h for 15, 25, and 55 mA, respectively – Figures 34 and Table 5. Noteworthy, the performances of **8**-LECs stand out compared to the previous state-of-art of green-emitting SM-LECs, highlighting

the important role of nanographenes in widening the horizons of possible emitter families for SM-LECs.[92,147–149]

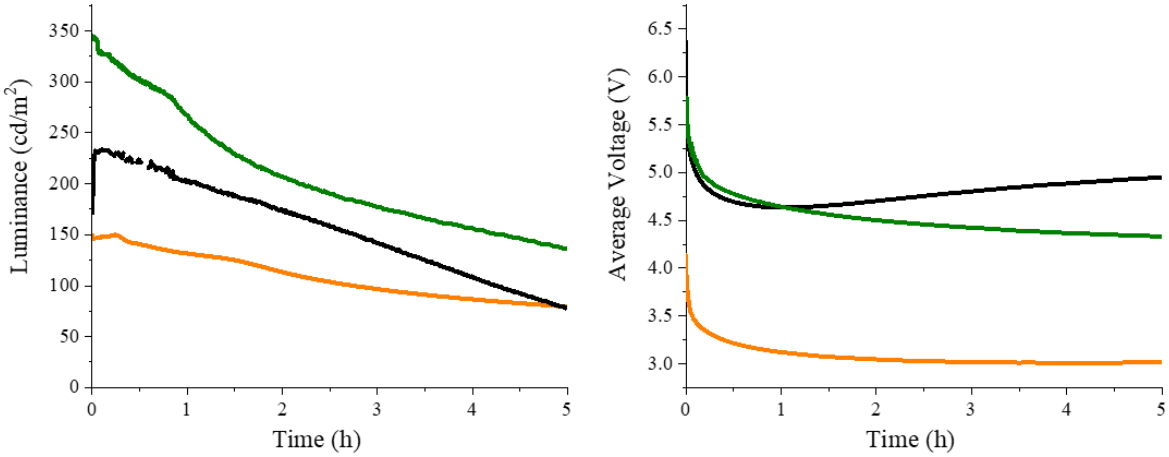


Figure 34. Luminance (left) and average voltage (right) over time of **8** devices driven at pulsed 15 mA (orange), 25 mA (black), and 55 mA (green).

The electroluminescence response shows, however, unexpected changes over time. Regardless of the applied current, at the very beginning a broad emission band centered at $\lambda_{max}$= 525 nm yields a green emission with x/y CIE color coordinates of 0.31/0.49 – Figures 35. However, the electroluminescence maximum red-shifts over time, reaching 545 nm with a shoulder at 505 nm that is associated to x/y CIE color coordinates of 0.34/0.50 or a green-yellow emission.

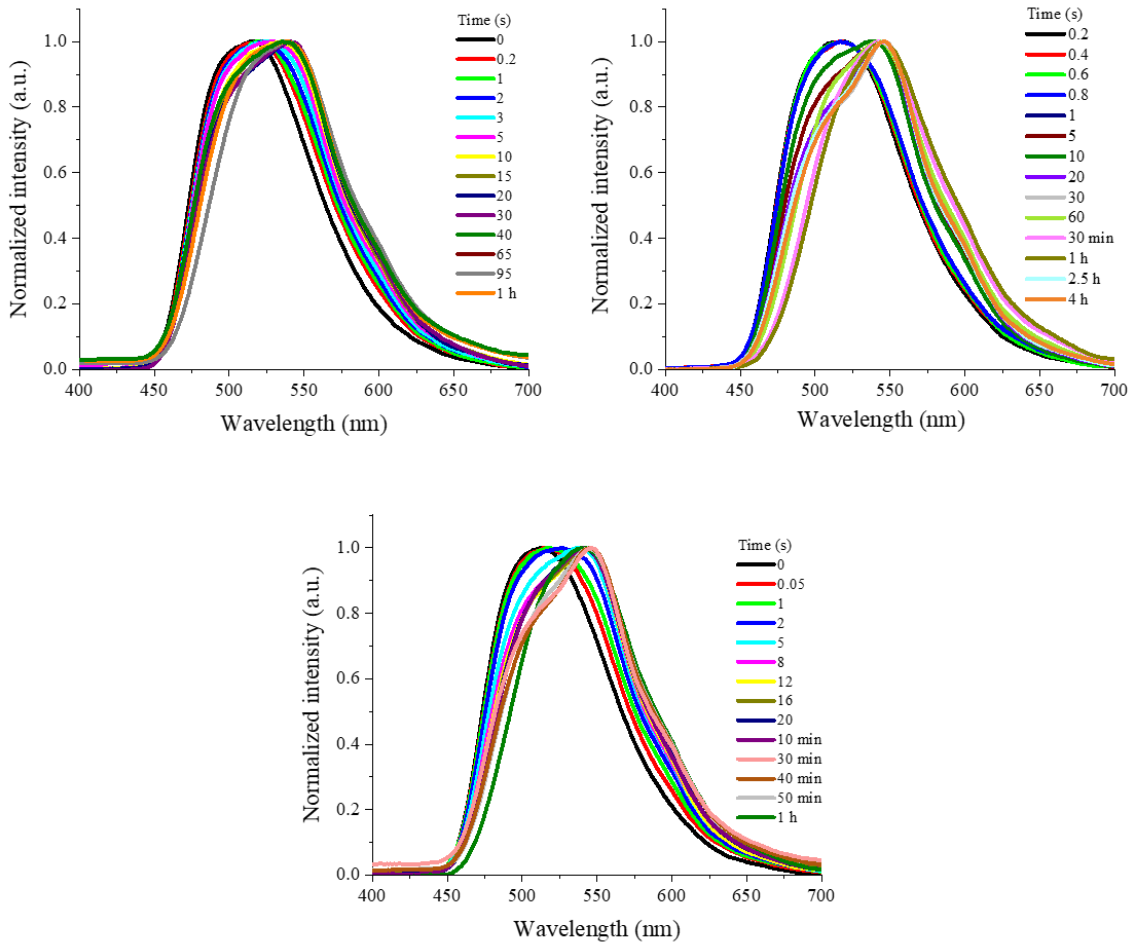


Figure 35. Change over time in the electroluminescence spectra of **8** devices driven at pulsed 15 mA (top left), 25 mA (top right), and 55 mA (bottom).

Interestingly, both the time to reach a stable electroluminescence spectrum and its shape depend on the applied current. In detail, the electroluminescence spectrum does not show remarkable changes after 120 s, 30 s, and 8 s for devices driven at 15, 25, and 55 mA, respectively. However, the emission energy onset ($E_{0,0}$) remains unchanged, suggesting that the emission is coming from the same excited state. Overall, the electroluminescence emission appears to be very different from the photoluminescence; however, this divergence is put into context upon close inspection of the photoluminescence features, which show a fine vibrational structure covering all the spectral range from 476 to 590 nm – Figure 33. The latter can be altered by both the electric field and the temperature increase due to self-heating processes under operation conditions.

Indeed, self-heating is generated by a combination of both Joule effect and the non-radiative decay of excitons.[136] In particular, the internal temperature of the devices may reach values higher than 80 ºC.[136,167] The temperature increase also affects the device chromaticity, as it renders upper vibrational states available, thereby broadening the emission band. Thus, the higher the applied current is, the higher the heat generation is.

At first, the temperature dependency of the photoluminescence of **8**-films was analysed, performing the measurement under vacuum upon increasing temperature from rt to 475 K (202 °C) – Figure 36. Unusually, the emission intensity rises with increased temperature, reaching a value that is 5-fold increased at temperatures of 152 °C. This may be due by a change in the layer morphology. More strikingly, the emission band shape changes over time, promoting emission from the low-energy vibrational peaks at higher temperatures. This leads to a color emission change from green to green-yellow that resembles those in the devices. We can discard the presence of phosphorescence processes as the τ for both the emission maxima (at $\lambda_{max}$ of 486 and 600 nm) are of 3 ns.

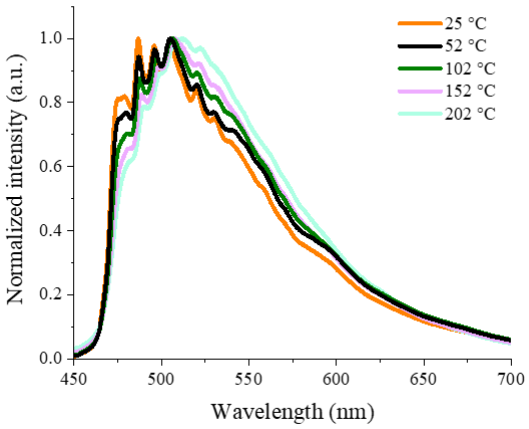


Figure 36. Photoluminescence spectrum of **8** thin films at different temperatures (see legend) under vacuum.

Next, we measured the temperature rise trend in devices driven at different currents by using a thermal camera, finding a strong correlation between the increase of the pixel temperature and the spectral changes regardless of the driving conditions. The temperature increases abruptly in the very first phase of the measurement, reaching a plateau after 2 minutes, 20 s, and 8 s for devices

driven at 15, 25 and 55 mA, respectively. In parallel, the temperatures reached are of 42°, 47° and 83° C. Interestingly, the time to reach the plateau temperature nicely fits with the time to stabilize the electroluminescence response under pulsed driving mode – *i.e.*, 2 min, 20 s, 8 s, for 15, 25, 55 mA, respectively–Figure 37.

Finally, we tested devices driven at constant applied voltage of 3.5, 4.5, and 6 V, which exhibited similar efficiencies and both lower luminance and stability values compared to those driven at pulsed current – Table 5. The electroluminescence response, however, exhibited the same initial green and broad electroluminescence spectrum – *i.e.*, $\lambda_{max}$= 520 nm; x/y CIE color coordinates of 0.29/0.44 – regardless of the applied voltage, while a slow change until a stable yellowish green electroluminescence band is reached – *i.e.*, $\lambda_{max}$ = 548 nm; x/y CIE color coordinates of 0.44/0.53. The time to reach a stable emission band decreases linearly from 32 min, to 13.2 min, to 7.2 min for devices driven at 3.5, 4.5, and 6 V, respectively, which, again, corresponds to the time to reach the plateau temperature observed in devices – Figure 37. These are accompanied by maximum temperatures of 35 °C, 36 °C, and 59 °C for 3.5 V, 4.5 V, and 6 V, respectively – Figure 6. The reason underlying the lower temperatures may be the reduced current density compared to the pulsed driving mode – *i.e.*, 12.5 mA at 6 V.

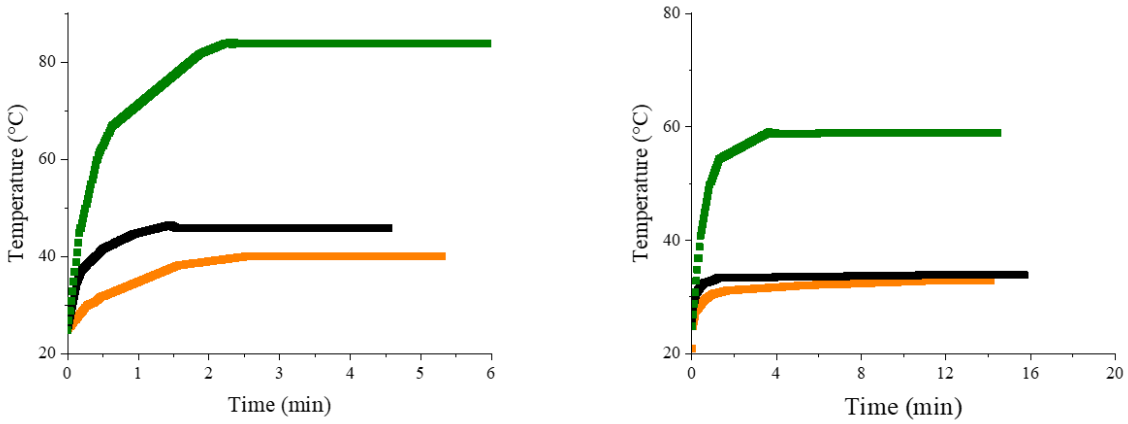


Figure 37. Left: Temperature rise over time for **8**-LECs driven at pulsed 15 (orange), 25 (black), and 55 mA (green). Right: Temperature rise over time for **8**-LECs driven at constant 3.5 (orange), 4.5 (black), and 6 V (green).

Importantly, we confirmed that the changes of the electroluminescence spectra were generated exclusively by the electric field and the temperature rise, and not by degradation processes. To this end, we performed i) L-I-V scans, in which **8** demonstrated a sound stability upon electrical stress, ii) EIS assays, in which both fresh and used devices showed an ideal LEC response, highlighting the absence of degraded species, and iii) absorption and emission of fresh and used device, that showed no important difference.

Here, it was above mentioned that **8** shows a usual enhancement of the emission intensity upon increased temperature. This was also reflected in an enhancement of the Φ values, as calculated by the ratio of the integrated area of absorption and emission peaks at the corresponding temperature. Indeed, considering the Φ of *ca*. 23 % at 25 ºC as reference, a significantly enhanced Φ of to 37 % is measured at 83 ºC – Figure 38.

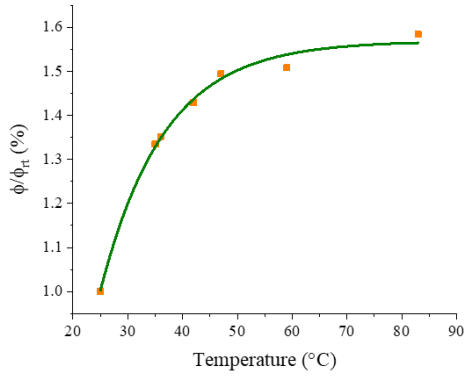


Figure 38. Change in the $\Phi/\Phi_{rt}$ values at different temperatures. The fitting is indicated by a green line.

This should also lead to an increase of the radiative decay (φ) in devices. **8**-LECs only presents fluorescent emission, which means that the maximum φ is ¼ of Φ in thin films, as, statistically, ¼ of the electron-hole recombination produces singlets. Here, the EQE is defined as EQE= $b\varphi/2n^2$, where *b* is the recombination efficiency (equal to 1 for two ohmic contacts), and *n* is the refractive index of the glass substrate and is equal to 1.5 (the factor $1/2n^2$ represents the light out-coupling of the device). That implies that the EQE is also temperature-dependent, assuming that *b* and *n* do not change significantly with temperature. Thus, this should follow the same trend of Φ. As an example, at 83 ºC the theoretical EQE significantly increases– Figure 39. Counterintuitively,

experimental EQE values feature important decrease with the increasing temperature, regardless of the driving mode and conditions– Figure 39.

To shed light on this curious phenomenon, we calculated the ratio between experimental and theoretical EQE values ($\eta = EQE_{exp}/EQE_{theo}$). At pulsed currents of 15, 25, and 55 mA, η values are 0.067, 0.019, and 0.0057 considering Φ at 25 ºC, while η values of 0.047, 0.013, and 0.0036 are recalculated taking into account the pixel working temperature. Likewise, devices driven at constant bias of 3.5, 4.5 and 6 V show a η value of 0.27, 0.15, 0.010 as well as 0.20, 0.11, and 0.0067 with and without considering pixel temperature, respectively. Next, we can get an estimation of the % error – *i.e.*, $((\eta_{nc}-\eta_c)/\eta_{nc}) \times 100$ – between the uncorrected ($\eta_{nc}$) and corrected ($\eta_c$) values with the temperature, regardless of the driving mode – Figure 39. Importantly, this error can be as high as 35 % at usual working temperatures (50 °C).

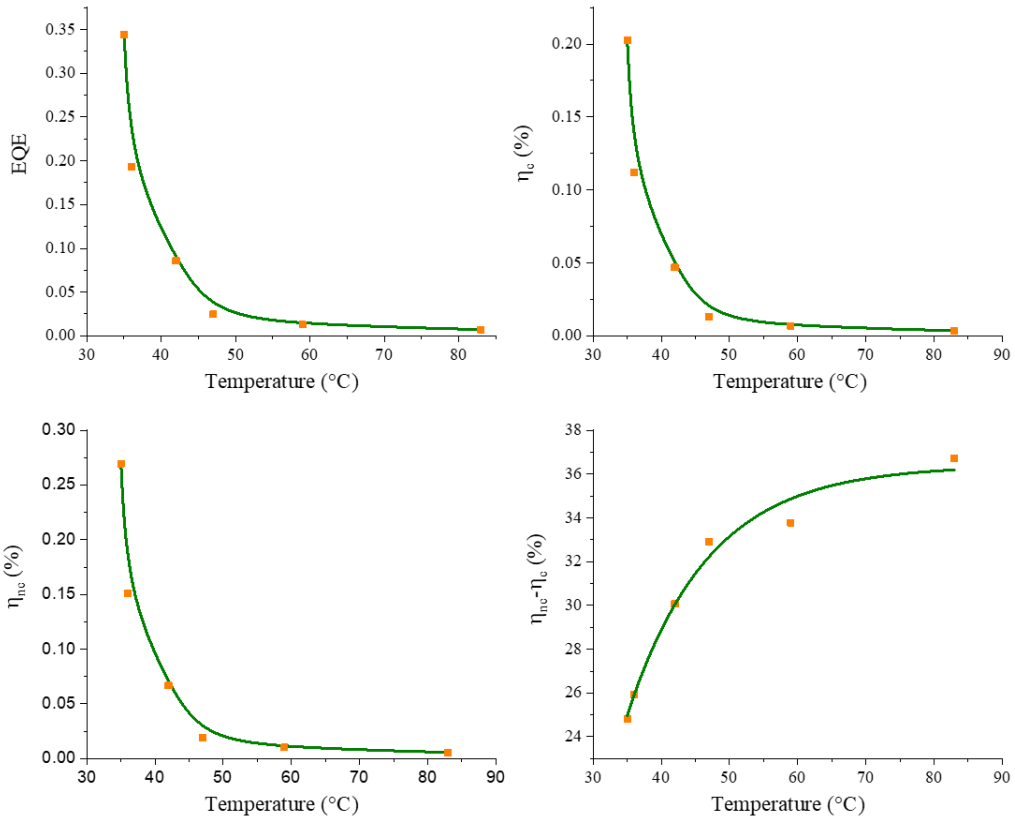


Figure 39. EQE% (top left), $\eta_c$ % (top right), $\eta_{nc}$ % (bottom left), and difference $\eta_{nc}$ - $\eta_c$ % (bottom right) *vs.* measured **8** devices temperatures. The green lines display the fittings.

Overall, this contribution provides two important findings. Firstly, it illustrated the positive role in nanographenes in providing SMs-LECs with excellent balance between brightness and stability. Secondly, it shed light onto a previously neglected topic, that is, self-heating in LECs, pointing out the necessity of taking temperature rise into account when performing device optimization.

Table 5. Figures-of-merit of **8** devices.

| Driving mode (mA) | $L_{max}$[a] (cd/m$^2$) | $t_{on}$[b] (h) | $t_{1/2}$[c] (h) | $E_{tot}$ (J) | Efficacy (cd/A) | EQE (%) | x/y CIE color coordinates ( $t_0$- $t_{1/2}$) |
|---|---|---|---|---|---|---|---|
| 15 mA[a] | 157 | 0.008 | 5.8 | 483 | 0.20 | 8.6E-2 | 0.31-0.37/0.49-0.52 |
| 25 mA[a] | 233 | 0.004 | 3.8 | 469 | 0.18 | 2.3E-2 | 0.31-0.38/0.49-0.52 |
| 55 mA[a] | 343 | 0.003 | 3.0 | 545 | 0.12 | 7.2E-3 | 0.31-0.36/0.49-0.54 |
| 3.5 V | 12 | 0.20 | 5.5 | 35 | 0.12 | 3.4E-1 | 0.29-0.32/0.44-0.44 |
| 4.5 V | 36 | 0.05 | 0.23 | 4.4 | 0.20 | 1.9E-1 | 0.30-0.33/0.44-0.46 |
| 6 V | 133 | 0.01 | 0.17 | 12 | 0.11 | 1.3E-2 | 0.30-0.34/0.44-0.53 |

a. Maximum luminance; b. Time to reach the maximum luminance; c. Time to decay to the half of the maximum luminance.

### *3.2.2 LECs based on BN-doped nanographenes*

Elisa Fresta, Jacopo Dosso, Juan Cabanillas-Gonzalez, Davide Bonifazi and Rubén D. Costa, Origin of the exclusive ternary electroluminescent behavior of BN-doped nanographenes in efficient single-component white light-emitting electrochemical cells, *Adv. Funct. Mater*, **2020**, DOI:10.1002/adfm.201906830.

In the context of white LECs, multi-emissive white emitters are highly desired. Here, there are four different approaches to achieve white LECs. First, a host:guest strategy in which a large band gap host is mixed with a smaller band gap guest. They are, however, highly sensitive to i) the applied voltage/current, ii) the phase separation over time, iii) the ratio between the emitters, and iv) the relative stability of each component. Second, multi-layered architectures based on either tandem or color down-converting schemes are commonly employed. However, they often show complicated and high-cost fabrication processes, which render them less reproducible and sustainable.[168,169] The third strategy regards to white-emitting excimers or exciplex species.[43,170]

This has, however, yielded poorly efficient devices due to the low Φ of these emitting species. Finally, the fourth strategy focused on designing white-emitting molecules for single-component WLECs. Various examples have already been reported in literature.[34,140] For instance, Edman and Pei groups have reported on CPs with multi-fluorophoric units that led to white LECs with encouraging performances, *i.e.*, efficiencies of *ca*. 3 cd/A, color rendering index (CRI) of *ca*. 80, and stabilities of few hours. Costa and co-workers reported on single-component white SM-LECs with TIPs-functionalized pentacenes[160] and free-base porphyrins[142], whose performances, however, showed low efficacy (<0.1 cd/A). Herein, we report the first example of a single-component white-emitting SM-LEC with high efficacy and good stability.

In particular, we turned our attention to a promising class of emitters, namely BN-doped nanographenes with the $B_3N_3$ doping pattern – *i.e.*, hexa-peri-hexabenzoborazinocoronene or **9** as shown in Figure 40.

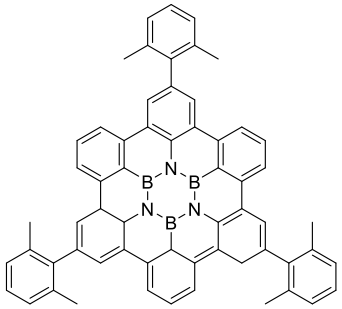

Figure 40. Chemical structure of **9**.

The emitter shows blue fluorescence in solution and thin films, featuring a well-structured band centered at $\lambda_{max}$ 415 nm, Φ = 22.1%, and excited state lifetimes ($\tau$) of *ca*. 3 ns– Figure 41. This encouraged us to further proceed in the fabrication of **9**-based LECs built as ITO/PEDOT:PSS(70 nm)/**9**:polystyrene(PS):polyethylene oxide (PEO):LiOTf 10:0.9:2.6:0.78 (100 nm)/Al(90 nm). Surprisingly, devices run at pulsed 5 mA showed white electroluminescence covering the entire visible range and peaking at 435, 505, and 695 nm with shoulders at 550 and 750 nm, x/y CIE coordinates of 0.28/0.31, and a high CRI of 89 – Figure 41. Upon device driving, the emission color varies slightly to final x/y CIE coordinates of 0.31/0.38. Importantly, the device performances stand out compared to other SM-LECs, exhibiting luminances of 48.6 cd/m$^2$ efficiency of 2.1 cd/A, and stability of a day – Figure 41 and Table 6.

The reasons of this unusual white electroluminescence could be related to several aspects, namely i) an interaction with the ionic matrix that is added to the layer to give it the necessary ion mobility, ii) the presence of degradative species, iii) aggregation phenomena, iv) the formation of exciplexes or electromeric species, and v) thermally-induced emission.

We therefore started analyzing if there is a possible interaction between **9** and the electrolyte matrix. To this end, we performed $^{1}$H-NMR assay of **9**, the electrolyte matrix, and the combination of the two in solution at increasing concentration of the matrix (up to 100 times), in order to produce a *quasi*-solid state, in which the component may easily interact. However, the $^{1}$H-NMR spectra still showed a pattern that was the exact sum of the two components.

Noteworthy, as the electroluminescence is white since the very beginning of the device lifetime, indicating the lack of degradation, as the presence of degradative species should increase over time. However, we compared absorption and emission spectra of fresh and after-lifetime devices, which do not show relevant differences, highlighting the absence of degradation.[167]

Additionally, we used EIS assays to analyze the resistance behavior of both fresh and after lifetime devices. The ionic resistance ($\sigma$) values are of of $1 \times 10^6$ Ω and $1 \times 10^5$ Ω at 0 V for fresh and after lifetime devices, respectively. The decrease in the ionic resistance can be attributed to the remaining polarization obtained after biasing the device, and suggests that no degradative event took place. Furthermore, the value of $\sigma$ is significantly recovered (78% or $0.78 \times 10^6$ Ω) after heating up the devices at 90 °C, which indicates a good electrochemical reversibility.[142,171,172]

Next, we turned our attention to the possibility of aggregation issues. This is not a satisfactory explanation as aggregated species usually show broad and shapeless emission bands and low efficiencies, which contrast with the high efficiencies (1-3 cd/A) and the well-structured emission shape of **9**-LECs. Aggregates also yields broad photoluminescence spectra, which is not the case of **9**, that shows blue emission and no peaks in the red region. Moreover, the use of the electrolyte matrix with a high amount of polystyrene hinders the formation of aggregated species.

The exciplex emission was discarded preparing a single-layer device with Ag cathode as a replacement for the standard Al cathode.[170,173] The electroluminescence response, however, still corresponds to a white emission. These devices also exhibit good luminances of 69.1 cd/m$^2$ and high efficiencies of 3.1 cd/A– Figure 42.

Exciplex or electromeric species may be generated by a pair of **9** molecules in ionic and cationic form. Electromers are formed only upon the application of an electrical field.[43,85,170,174] As such, new devices with increased PS amount and thickness were prepared, in an attempt to reduce the inner electric field. These devices were also driven at 9V pulsed voltage to assess the driving mode influence on the electroluminescence response. Once again, the electroluminescence response was white, featuring a broad band peaking at 435, 560, 690, and 750 nm – Figure 42.

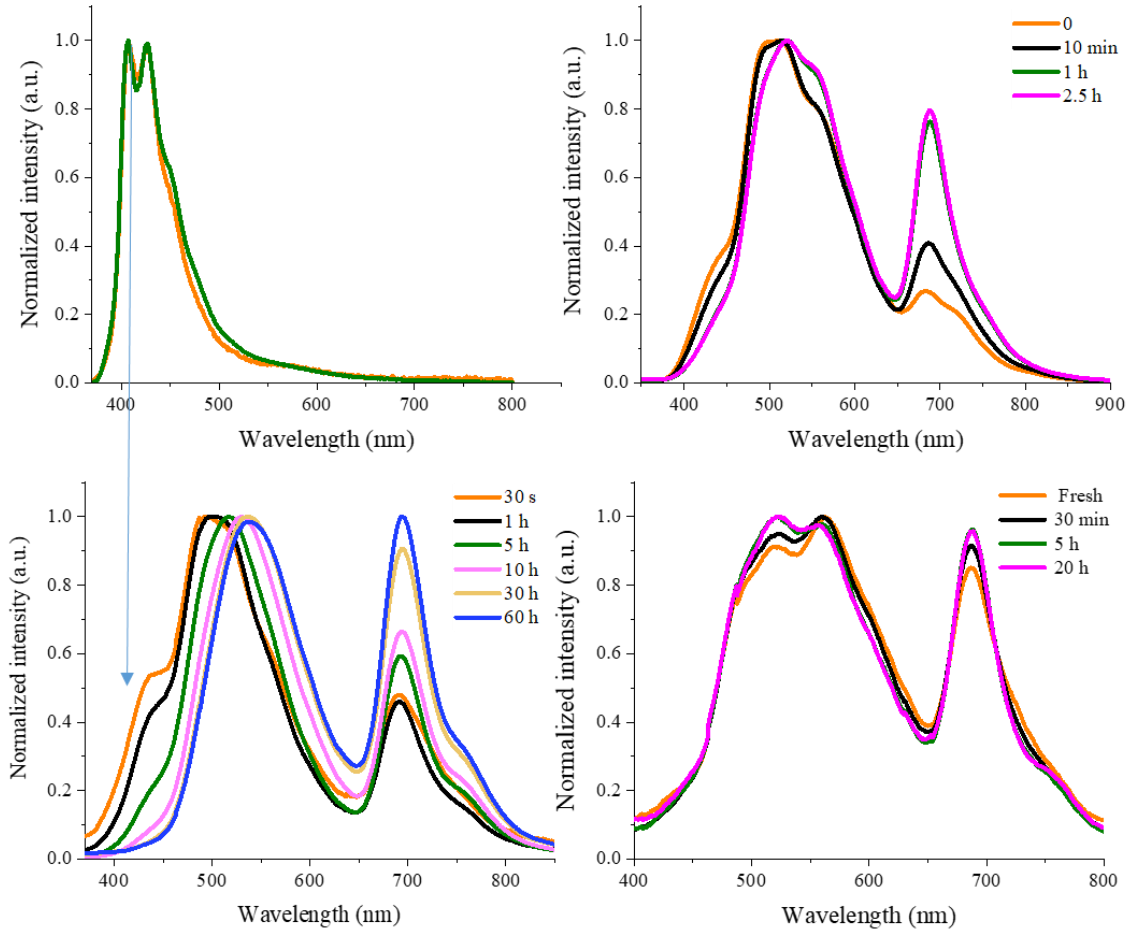


Figure 41. Photoluminescence spectrum of **9** thin films with electrolyte matrix (orange) and without (green), (top left), and electroluminescence spectra at different times (see legend) of **9** devices with Al cathode measured at pulsed 5 mA (bottom left), with Ag cathode measured at pulsed 5 mA (top right), and with Al cathode measured at pulsed 9 V (bottom right). The light blue arrow indicates a correspondence between the emission maxima in the photoluminescence

spectrum and the shoulder in the electroluminescence spectrum of **9** devices with Al cathode measured at pulsed 5 mA.

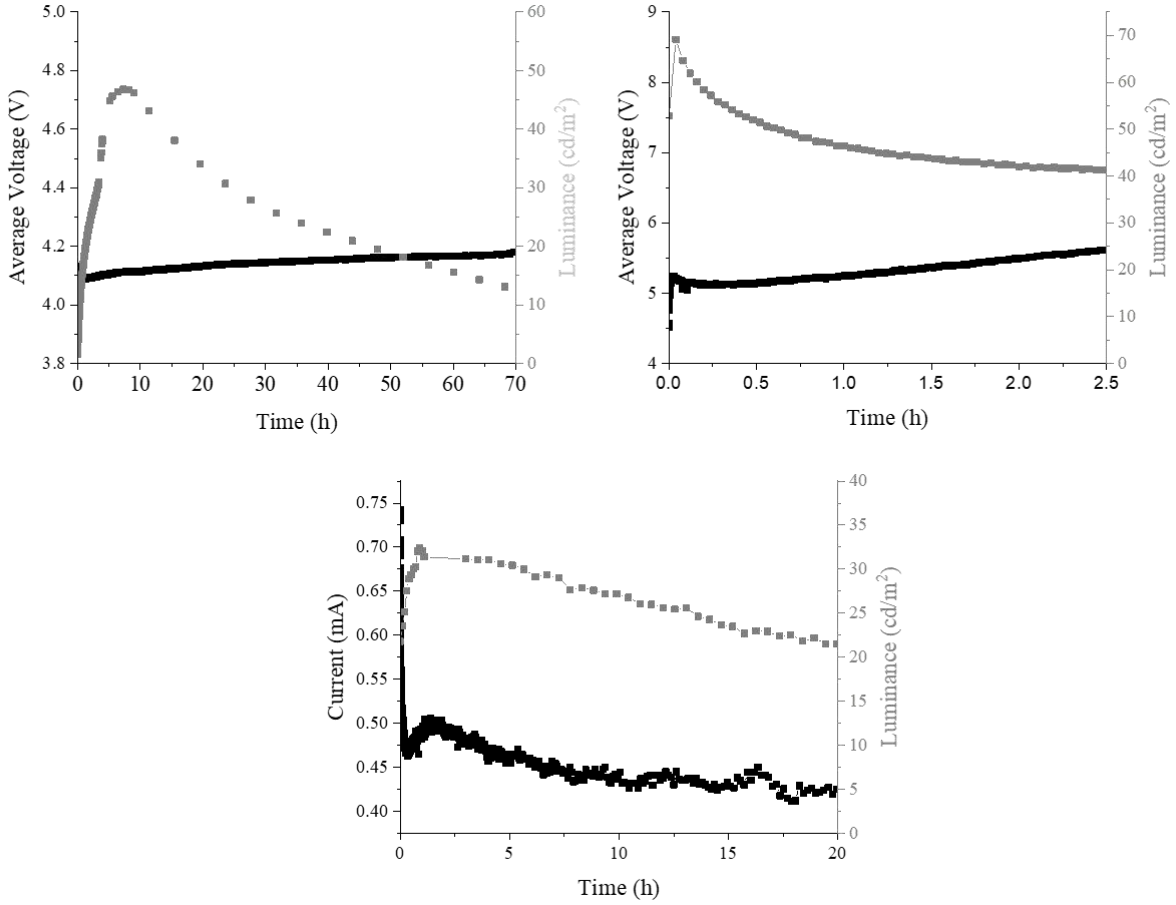


Figure 42. Average voltage and luminance *vs* time for **9** devices with Al cathode run at pulsed 5 mA (top left), with Ag cathode run at pulsed 5 mA (top right), and current and luminance *vs* time for thick **9** devices driven at constant 9 V (bottom).

Finally, we focused on a possible thermally induced emission. First, we studied the photoluminescence dependency upon increasing temperature of **9** thin films. Upon heating, two well-structured bands appear at 530 and 700 nm, yielding a broad whitish photoluminescence that is similar to that observed in device – Figure 43.

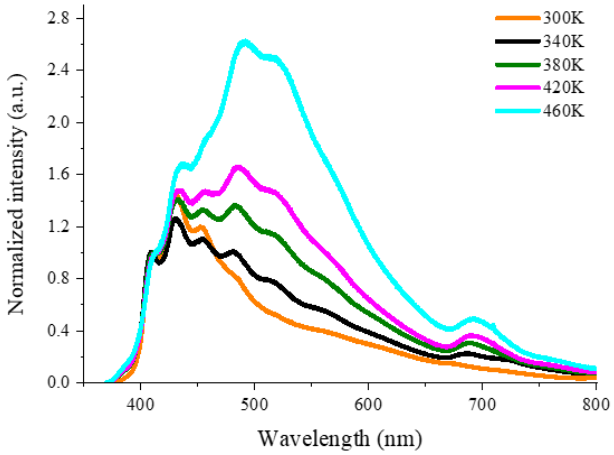


Figure 43. Photoluminescence spectra of **9** thin films at different temperatures (see legend).

Next, the nature of the excited states was determined by measuring the average <τ> at 400 nm, 525 nm, and 700 nm, which corresponds to 3.2 ns, 5.8 μs, and 12.3 μs. While the first τ involves pure fluorescence, the other two are related to phosphorescence, and, in particular, to different triplet states. Importantly, ternary emission is more prominent in devices, as statistically triplets are formed 3-times as often as singlets. Additionally, the temperature of the devices can reach up to ~80 °C, as highlighted in the previous section.[175] This further contributes to the promotion of triplet excited states. In this context, differences in temperature due to various device driving modes can explain the slight change of the electroluminescence in different devices and over time.

To summarize, we implemented a blue-emitting BN-doped nanographene in LECs that showed good luminance (50-70 cd/m$^2$) and efficiency (2-3 cd/A), and white electroluminescence with x/y CIE coordinates of 0.29-31/0.31-38 and average color rendering index (CRI) of 87. We attributed the rare electroluminescence behavior to a ternary emission mechanism involving fluorescence and thermally activated dual phosphorescence. The latter is enhanced by both temperature, which can be as high as 80 °C upon device driving, and electric field. This represents the first example of ternary emission activated in lighting devices.

Table 6. Figures-of-merit of **9** devices.

| Driving mode (mA) | Cathode | $L_{max}$[a] (cd/m$^2$) | $t_{on}$[b] (h) | $t_{1/2}$[c] (h) | Efficacy (cd/A) | x/y CIE color coordinates ( $t_0$- $t_{1/2}$) |
|---|---|---|---|---|---|---|
| 5 mA[a] | Al | 48.6 | 4.7 | 32.9 | 2.1 | 0.28-0.31/0.31-0.38 |
| 9 V | Al | 32.7 | 1.1 | 25.6 | 1.0 | 0.30-0.35/0.31-0.39 |
| 5 mA | Ag | 69.1 | 0.05 | 4.4 | 3.1 | 0.27-0.31/0.31-0.37 |

a. Maximum luminance; b. Time to reach the maximum luminance; c. Time to decay to the half of the maximum luminance.

### *3.2.3 LECs based on contorted nanographenes*

Elisa Fresta, Kevin Baumgärtner, Juan Cabanillas-Gonzalez, Michael Mastalerz, and Rubén D. Costa, Bright, Stable, and Efficient Red Light-emitting Electrochemical Cells using Contorted Nanographenes, *Nanoscale Horiz.*, **2020**, 5, 473–480.

Stable and efficient third-generation red-emitters are highly desired. Numerous research groups have investigated red-emitting SMs like perylenes, benzothiadiazoles, pentacenes, porphyrins, BODIPY-porphyrin dyads, and cyanines.[91,92,159–161,164] However, SM-LECs combining high irradiances along with stabilities of hundreds of hours have not been realized yet. Indeed, while the best stabilities (~1000 hours) are accompanied by low irradiances (0.1-1 μW/cm$^2$),[159,164] the best luminances (750 cd/m$^2$) come at the price of low stabilities (15 hours).[92]

In this context, we turned our attention to a highly contorted nanographene, that is, a hexabenzoovalene (HBO) – *i.e.*, **10** as shown in Figure 44, as a promising candidate for red-emitting SM-LECs. Indeed, the family of contorted nanographenes has attracted enormous interest as it holds the positive features of the nanographene family, but feature enhanced solubility in common organic solvents compared to rigid nanographenes.[176,177] However, to the best of our knowledge, no report on its electroluminescent behavior was provided prior to this thesis.

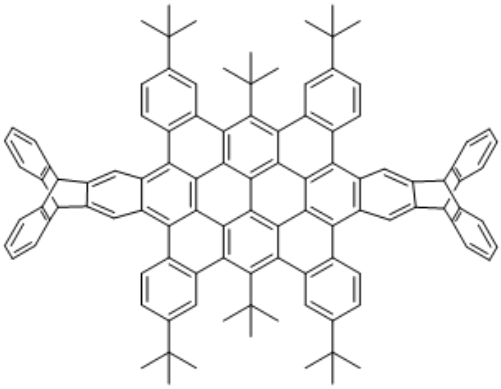

Figure 43. Chemical structure of **10**.

We firstly investigated the photoluminescence features of **10** thin-films, which consist of a broad, well-structured emission band with peaks at $\lambda_{max}$ of 598 nm and 647 nm, as well as a $\Phi$ value of 23% and $\tau$ of 3.2 ns – Figure 45. Next, we fabricated devices with the architecture ITO/PEDOT:PSS(70 nm)/**10**:TMPE:LiOTf 1:0.15:0.05(70 nm)/Al(90 nm).

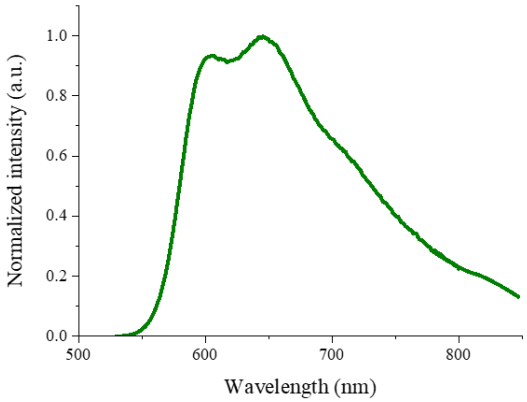


Figure 45. Photoluminescence spectrum of **10** thin films.

These devices were driven at pulsed currents of 25 mA and showed the typical LEC features, that is, an initial decrease of the applied voltage along with an increase of the luminance as the EDLs start to build up and assist charge injection. The devices achieved irradiances of *ca*. 220 $\mu W/cm^2$ along with stabilities over 200 h, as well as power efficiency and EQE values of 0.74 lm/W and 0.78% were noted – Figure 46 and Table 7. Remarkably, the EQE value represents the 76% of the

theoretical EQE (1.15%), which is an outstand result considering that no host-guest optimization has been performed. Overall, **10**-LECs represent the first bright and stable red-emitting SM-LECs. The electroluminescence response of **10**-LECs features a broad emission peaking at 600 and 650 nm. However, the device chromaticity changes over time. In detail, the intensity ratio between the high-energy vibrational peak (h-peak; 600 nm) and low-energy vibrational peak (l-peak; 650 nm), herein called h/l, changes over time, increasing from 0.99 to 1.23 during the first 40 hours, holding constant up to 100 h, and then abruptly decreasing (1.13) until the device lifetime was reached – Figure 46. Consequently, a slight change in the x/y CIE color coordinates follows, namely 0.59/0.40 to 0.59/0.41, and finally to 0.61/0.39. It is important to remark that these changes are barely noted by the human eye.

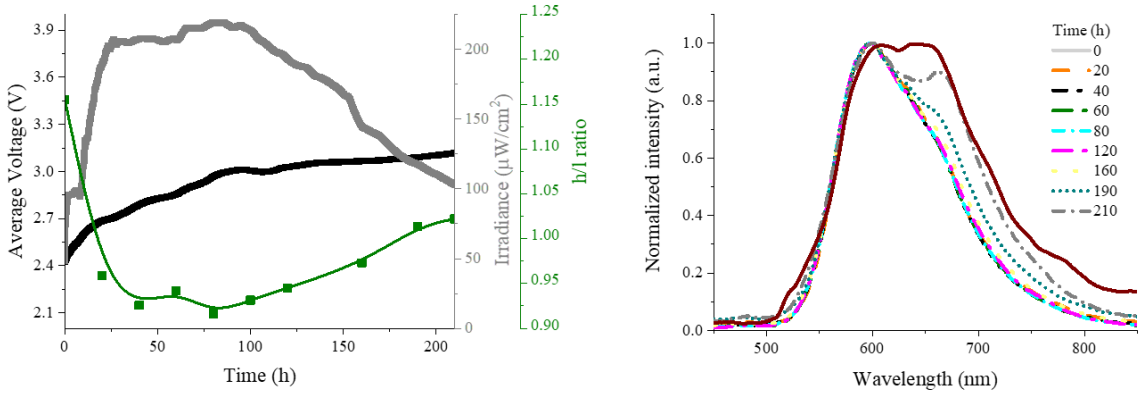


Figure 46. Average voltage, irradiance, and h/l ratio (left), as well as electroluminescence spectra (right) over time (see legend) for **10** devices driven at pulsed 25 mA current.

The reason of the chromaticity change over time may be ascribed to different causes, such as degradation,[142,178] phase separation or changes in the layer's morphology,[85,179] and/or changes of the local electric field distribution and intensity.[180–183]

Firstly, we investigated the possible presence of degradative species. Here, new quenching species would affect the h- and l- peaks in a different measure. However, the intensity changes of the two peaks are equally affected over time, while the $E_{0\text{-}0}$ band does not shift over time, remaining

constant at 2.38 eV (520 nm).[95] Moreover, fresh and used devices show comparable absorption and emission features.[95]

Therefore, we turned our attention to the relationship between electrical and chromaticity changes over time. Indeed, changes of the local electric field may influence the dipole moment and orientation of the emitter, which may favor different vibronic states and emission quenching over time. We selected four different strategies to increase the externally applied electric field, namely i) measuring consecutive L-I-V scans in which the voltage is changed over time in a ramp manner, ii) increasing the driving current, and, consequently, the average driving voltage, iii) changing the duty cycle, thereby affecting the duration of the applied voltage, and iv) decreasing the active layer thickness from 70 nm (thick) to 30 nm (thin)[142,184,185]

As a first step, L-I-V scans in the range of 0-6 V with a scan rate of 300 mV/s were performed. The devices showed a red emission response starting at low applied voltages of ~2.5 V. Importantly, the maximum irradiance does not change over time, highlighting the sound stability of **10** upon bias – Figure 47.

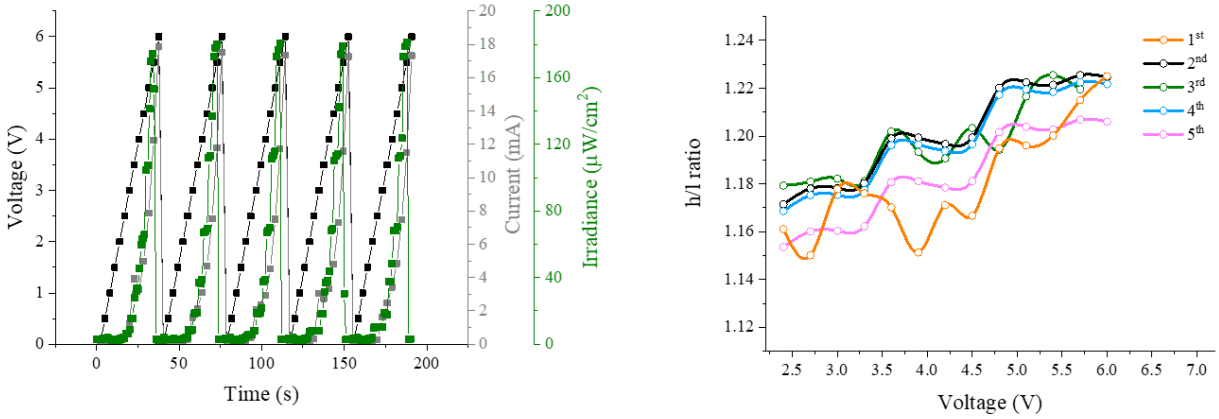


Figure 47. Repetitive 0-6 V L-I-V scans of 10 devices (left), and h/l ratio upon applied voltage (right, the legend indicates the scan number).

The electroluminescence spectrum consists of a broad emission band with two peaks at 600 nm and 650 nm, as already noticed for devices driven at pulsed mode. Importantly, the h/l ratio changes slightly over time (< 0.1 unit), exhibiting the same values at each steps of the five L-I-V scans, which suggests a reversible effect of the voltage on the electroluminescence behavior.

Next, the driving current was increased to 50 mA, leading to devices with irradiances of 370 μW/cm$^2$, EQEs of 0.52%, and stabilities of 24 h – Figure 48 and Table 7. The electroluminescence behavior shows the same trend in the h/l peak intensity ratio as commented before. In detail, a higher h/l value compared to for devices driven at 25 mA (1.25 *vs* 1.40) was noted. This reinforces the hypothesis on a correlation between chromaticity change and electrical field intensity.

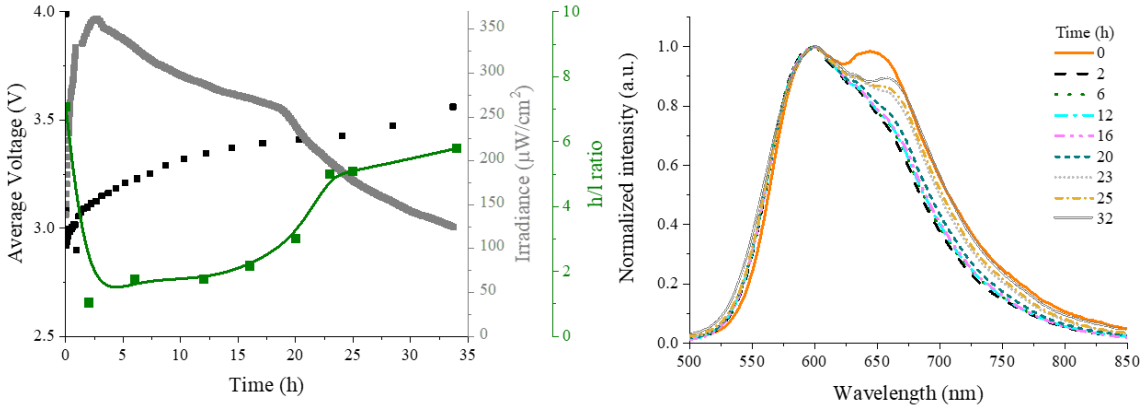


Figure 48. Average voltage, irradiance, and h/l ratio (left), as well as electroluminescence spectra (right) over time (see legend) for **10** devices driven at pulsed 50 mA current.

Next, the duty cycle was varied by driving devices for three times at four different duty cycle values (25, 50, 75, and 100%) for a short time (<5 minutes), in order not to generate over oxidized/reduced species that could hamper the measurement. This measurement provided two relevant pieces of information, that is, i) the h/l ratio varies with the duty cycle, spanning from 1.02 (25% duty cycle), to 0.90 (50%), 0.87 (75%), and 0.85 at 100% duty cycle, and ii) h/l showed always similar values for the different duty cycles in each scan. This confirms both the influence of the external electric field onto the electroluminescence, and the reversibility of this effect on the devices.

Finally, thin devices (30 nm) driven at pulsed current of 25 mA were studied –Figures 49 and Table 7. They feature lower irradiance of~ 30 μW/cm$^2$, along with an outstanding stability of 3600 h (measured) and >13.000 h (extrapolated). These represents one of the most stable LECs ever reported. Once again, the same behavior in the h/l ratio over time was noted. In detail, the h/l ratio

value increases up to 1.90. The color chromaticity changes more significantly, with x/y CIE coordinates that range from 0.59/0.40 to 0.63/0.36, while the emission response shows a shoulder at 670 nm appearing after 1000 h of measurement and rising over time.

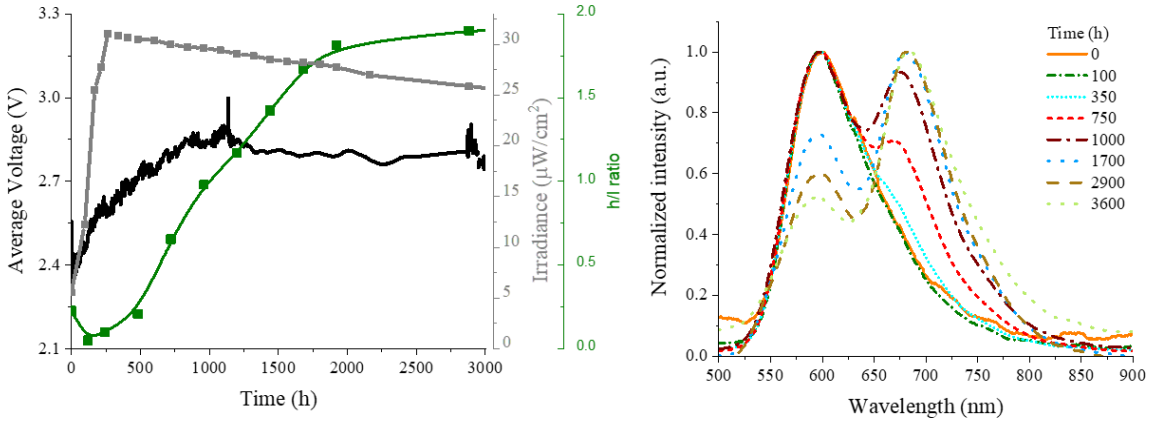


Figure 49. Average voltage, irradiance, and h/l ratio (left), as well as electroluminescence spectra (right) over time (see legend) for thin (30 nm) **10** devices driven at pulsed 25 mA current.

After isolating the external electric field effect as the major cause of the device chromaticity, we proved it with dynamic EIS assays held at constant voltage of 3 V. As shown in Figure 50, both the h/l peak intensity ratios and the internal electric field experienced by the emitters show similar trends over time. Indeed, the internal electric field is high at the beginning, but it rapidly decreases as the building up of the doped regions take place, until it reaches a minimum value after 0.42 h. This is accompanied by both the reduction of the resistance from 86.8 Ω to 25.9 Ω and the increase of the capacitance $C_{geo}$ from 8.35 x $10^{-9}$ to 8.85 x $10^{-9}$ F. Importantly, this perfectly corresponds to the time required to reach the maximum in the h/l peak intensity ratio. Then, the internal electric field starts slowly rising over time, as the neutral region shrinks and the h/l ratio decrease over time. This is flanked by both a constant increase of the resistance and a decrease in the irradiance intensity.

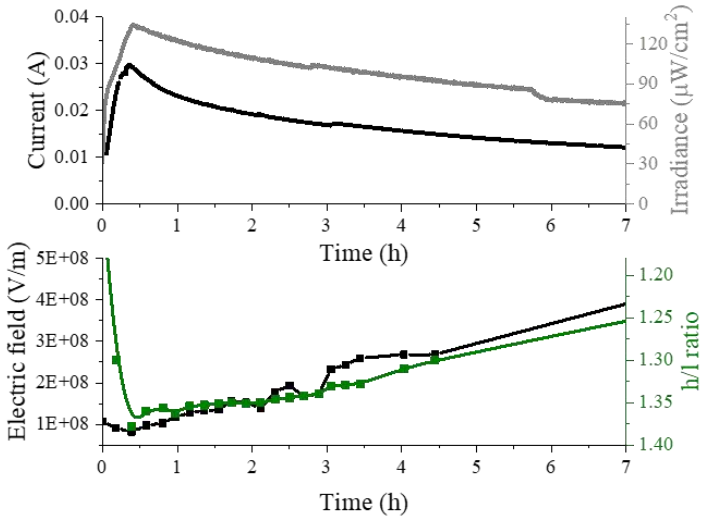


Figure 50. Current and irradiance over time (top), and internal electric field and h/l ratio over time (bottom) of **10** devices driven at constant 3V.

Overall, this work reports on a contorted nanographene that simultaneously provides bright (221 μW/cm$^2$) and stable (>200 h) devices, while an optimized device featured record stabilities of 3,600 h (measured) and 13,000 h (extrapolated). Its electroluminescence response shows an interplay between a high-energy ($\lambda_{max}$ 600 nm) and a low-energy ($\lambda_{max}$ 650 nm) vibrational state. This is ascribed to the changes in the inner electric field that is felt by the molecule.

Table 7. Figures-of-merit of **10** devices.

| Driving mode (mA) | Thickness[a] (nm) | Irradiance$_{max}$[b] (cd/m$^2$) | $t_{on}$[c] (h) | $t_{1/2}$[d] (h) | Efficiency (lm/W) | EQE (%) | x/y CIE color coordinates ( $t_0$- $t_{1/2}$) |
|---|---|---|---|---|---|---|---|
| 25 mA | 70 | 218 | 23.9 | 204.8 | 0.74 | 0.78 | 0.59-0.40/0.61-0.39 |
| 50 mA | 70 | 371 | 2.4 | 24.6 | 0.48 | 0.52 | 0.59-0.40/0.61-0.39 |
| 25 mA | 30 | 31 | 257 | 13,000[e] | 0.12 | 0.10 | 0.59-0.40/0.63-0.36 |

a. Of the active layer. b. Maximum luminance; c. Time to reach the maximum luminance; d. Time to decay to the half of the maximum luminance. e. Extrapolated.

# 4. Other works related to this thesis

## 4.1 Original papers

1. Elisa Fresta, Giorgio Volpi, Marco Milanesio, Claudio Garino, Claudia Barolo and Rubén D. Costa, Contextualizing Yellow Light-Emitting Electrochemical Cells Based on a Blue-Emitting Imidazo-Pyridine Emitter, *Polyhedron*, **2018**, 140, 129–137.

We investigated a promising blue emitting pirydilimidazopirydine SM featuring a low-cost and facile synthesis, excellent redox properties, and a high Φ of 0.4 associated to a blue emission ($\lambda_{max}$ 436 nm) in solution.[186] However, it yielded low-performing yellow-emitting devices due to aggregation. The phenomenon was firstly rationalized by studying absorption and photo/electroluminescence responses of both the emitter alone and diluted in a polymeric matrix. Then, it was put into context by obtaining a comparable efficacy with a LEC comprising an Ir-iTMC bearing the small molecule as ancillary ligand.

2. Asterios Charisiadis, Anthis Bagaki, Elisa Fresta, Katharina T. Weber, Georgios Charalambidis, Christina. Stangel, Anthonios G. Hatzidimitriou, Panagiotis A. Angaridis, Athanassios Coutsolelos and Rubén D. Costa, Peripheral Substitution of Tetraphenyl Porphyrins: Fine-Tuning of the Self-Assembling towards Enhanced Electroluminescence, *Chem Plus Chem*, **2018**, 83, 254–265.

We studied the change of electroluminescence in zinc porphyrins by changing their side chains, *i.e.*, with the length of the chains ranging from 2, to 6, and to 12 carbon atoms.[187] The molecules were processed into thin films. Depending on the length of the lateral chains, they were classified into ordered or disordered films. As a consequence, the electroluminescence response of the ordered films occurred at lower bias and was almost one order of magnitude higher compared to the disordered ones.

3. Elisa Fresta, Miguel A. Monclús, Morten Bertz, Cintia Ezquerro, Jon M. Molina-Aldareguia, Jesús R. Berenguer, Masahiro Kunimoto, Takayuki Homma and Rubén D. Costa, Key Ionic Electrolytes for Highly Self-Stable Light-Emitting Electrochemical Cells Based on Ir(III) Complexes, *Adv. Opt. Mater*., **2020**, DOI:10.1002/adom.202000295.

Another important neglected point in LECs is the optimization of the electrolyte matrix to achieve improved self-stabilities of both flexible and traditional glass-substrate LECs. Self-stability is defined as how changes in morphology, photoluminescence, and ionic/electrical conductivities of the active layers, stored under ambient/ inert atmospheres or exposed to mechanical stress, affect device performances at different driving modes. Therefore, we performed a comprehensive study on the impact of the ionic electrolyte on the self-stability upon storage and mechanical stress of rigid and flexible Ir-iTMC-based LECs.[188] In contrast to previous literature reports, devices with ionic polyelectrolyte featured higher brightness, stability, and storage stability compared to devices with only the Ir-iTMC or with ionic liquid. These findings are supported by steady-state and time-resolved emission spectroscopy, electrochemical impedance spectroscopy, microscopic, and mechanical assays, along with the analysis of fresh and aged devices driven at different modes under inert/ambient conditions. Overall, this work opens a new debate regarding new emitter: electrolyte combinations towards realizing highly self-stable LECs.

4. Cintia Ezquerro,[+] Elisa Fresta,[+] Elena Serrano, Elena Lalinde, Javier García-Martínez, Jesús R. Berenguer and Rubén D. Costa, White-Emitting Organometallo-Silica Nanoparticles for Sun-Like Light-Emitting Diodes, *Mater. Horiz.,* **2019**, 6, 130–136.

*+ authors contributed equally*

Another important field covered during this thesis regards hybrid LEDs. Our group achieved the first white-emitting organometallo-silica nanoparticles, in which blue-, green- and red-alcoxysilane Ir-iTMCs are simultaneously included as the core of the silica nanoparticle.[189] The combination of the emission features of the three complexes leads to a white emission that is stable under different stress scenarios. As such, the nanoparticles were used as color down-converters to develop single-component hybrid organic-inorganic white LEDs featuring sun-like color quality with stabilities of more than two thousand hours. This represents one of the most stable white hybrid LEDs reported so far.

5. Elisa Fresta, Julio Fernández-Cestau, Belén Gil, Patricia Montaño, Jesús R. Berenguer, Maria Teresa Moreno, Pedro B. Coto, Elena Lalinde, and Rubén D. Costa, Versatile Homoleptic Naphthyl-Acetylide Heteronuclear $[Pt_2M_4(C{\equiv}C\text{-}Np)_8]$ (M = Ag, Cu) Phosphors for Highly Efficient White and NIR Hybrid Light-Emitting Diodes, *Adv. Opt. Mater.*, **2020**, 8, 1901126.

Orange- and red-emitting Platinum (Pt)-based clusters, namely $[Pt_2Ag_4(C{\equiv}C\text{-}1\text{-}Np)8]C_{96}H_{56}Ag_4Pt_2$ $[Pt_2Ag_4(C{\equiv}C\text{-}1\text{-}Np)8]C_{96}H_{56}Cu_4Pt_2$, where Np is 1-methylnaphtalene, were for the first time reported.[190] They were used as color down-converters to yield hybrid LEDs with NIR emission centered at 730 nm, color purity close to 0.99, and remarkable efficiencies of ≈1.5 lm/W, that is comparable to commercial NIR-LEDs, and ii) daylight white LEDs with efficiencies of 75 lm/W and stabilities of >500 h.

## 4.2 Reviews and book chapters

As a complement to the research work, I have participated in the writing of five reviews focused on:

1. New emitters and device designs for LECs: Elisa Fresta, Rubén D. Costa, Beyond Traditional Light-Emitting Electrochemical Cells-a Review of New Device Designs and Emitters, *J. Mater. Chem. C*, **2017**, 5, 5643–5675.

2. Recent advances in white LECs: Elisa Fresta, Rubén D. Costa, Advances and Challenges in White Light-Emitting Electrochemical Cells, *Adv. Funct. Mater.*, **2020**, DOI: 10.1002/adfm.201908176.

3. White perovskite based lighting devices: Maria Bidikoudi[+], Elisa Fresta[+], Rubén D. Costa, White-Emitting Perovskite Based Lighting Devices, *Chem comm.*, **2018**, 54, 8150–8169.

*+ authors contributed equally*

4. Biogenic and bio-inspired materials for solid-state lighting: Elisa Fresta, Veronica F. Luna, Pedro B. Coto and Rubén D. Costa, Merging Biology and Solid-State Lighting: Recent Advances in Light-Emitting Diodes Based on Biological Materials, *Adv. Funct. Mater.*, **2018**, 28, 1707011.

5. Polypyridyl ligands employed in solid-state light-emitting devices: Babak Pashaei, Soheila Karimi, Hashem Shahroosvand, Parisa Abbasi, Melanie Pilkington, Antonino Bartolotta, Elisa Fresta, Julio Fernández-Cestau, Rubén D. Costa and Francesco Bonaccorso, Polypyridyl Ligands as a Versatile Platform for Solid-State Light-Emitting Devices, *Chem. Soc. Rev.*, **2019**, 48, 5033–5139.

In addition, a book chapter regarding the application of the best iTMCs in LECs: Elisa Fresta, Rubén D. Costa, Applying Ionic Transition Metal Complexes to Light-Emitting Electrochemical Cells, accepted.

## 5. Progress achieved by others during this thesis

Other research groups have actively contributed to progress the field of $d^{10}$-iTMCsand SMs based LECs over the period of this PhD.

Regarding Cu-iTMCs, Bolink and collaborators reported on the positive effect of biphosphane and halogen functionalization of the N^N ligand.[83] The champion device with [Cu(6,6'-$Cl_2$bpy)(xantphos)][$PF_6$] showed high luminances of 259 cd/$m^2$ and EQEsof 1.2% upon driving at pulsed 100 mA/$cm^2$. This was, however, accompanied by a low stability of 5 minutes. The same year, this group investigated the effect of the$CF_3$-substitution in [Cu(bpy)(P^P)][$PF_6$] on the device performances, obtaining the best results with [Cu(xantphos)(6-$CF_3$bpy)][$PF_6$]. This device exhibited luminances of 131 cd/$m^2$ along with a good stability of 31 h upon driving at pulsed current of 10 mA/$cm^2$.[76] In a further contribution, they analyzed the impact of 6-alkoxy, 6-alkylthio,6-phenyloxy and 6-phenylthio-substitution at the bpy ligand on the device figures-of-merit.[77] The most performing complex,[Cu(6-phenylObpy)(POP)][$PF_6$] realized devices with luminances of 80 cd/$m^2$ and stabilities of 45 h when driven at pulsed 50 mA/$cm^2$. Finally, they combined the functionalization of Xantphos with bidentate phosphane groups and the employment of a PEDOT:PSS with reduced ionic conductivity to achieve outstanding luminances of 355 cd/$m^2$, efficiencies of 3.6 cd/A, and EQE of 1.2% upon driving the devices at 100 mA/$cm^2$.[191] Nonetheless, the device stability was limited to 14 minutes.

To the best of our knowledge, no other group reported progress in the Ag-iTMCs field during this thesis. However, Yersin *et al*. have started to explored the TADF features of Ag-iTMCs indicating that this type of complexes could be of high interest for thin film lighting.[86,192]

In SM-LECs field, much research efforts were put into exploring the field of deep-red and NIR-emitting LECs.[193,194] In 2017, Jenatsch *et al*. reported on a highly optimized host-guest system with commercially available cyanines peaking at $\lambda_{max}$ of 625 and 675 nm. The devices were driven

at 10 mA/cm$^2$, featuring luminances of 30 cd/m$^2$, stabilities of 0.25 h, and EQEs of 0.36%, which is nearly half of the theoretical one (0.81).

In 2019, Edman's group implemented a star-shaped diketopyrrolopyrrole–Zn-porphyrin compound in LECs featuring $\lambda_{max}$ 900 nm and a remarkable irradiance of 36 μW/cm$^2$.[195] This represents the most red-shifted emission reported so far in LECs.

Another appealing topic is the implementation of TADF emitters into LECs. Edman's group firstly reported on a host-guest system with CBP and 2,4,5,6-tetra(9H-carbazol-9-yl)isophthalonitrile (4CzIPN), a commercially available TADF emitter that delivered 228 cd/m$^2$ at pulsed current density of 77 mA/cm$^2$. This represented an important step forwards compared to previous contributions, in which the luminance was limited to 30 cd/m$^2$.[149,196,197]

In a follow-up work, the group proved the effective presence of TADF in devices, as they achieved EQE of 7.0%, which would be superior to the theoretical limit if TADF would not take place.[166] This result was achieved by employing 4CzIPN as emitter and a rationalized device architecture and polymer electrolyte blend.

Finally, Choe's group reported various contribution in the field of blue and green-emitting SMs. In 2017, they reported on two novel blue-emitting phenantroimidazole-based ionic emitters, with pyrene and naphtalene as fluorophores, respectively.[198] Single layered devices showed $\lambda_{max}$ 485 and 450 nm, luminances of 277 and 160 cd/m$^2$ at 8 V, and x/y CIE color coordinates of 0.17/0.26 and 0.17/0.16, respectively. The latter is very close to the x/y CIE color coordinates assigned to pure blue (0.15/0.06). In a follow-up work, they characterized two ionic pyrene imidazole derivatives that featured LECs with $\lambda_{max}$ 446 and 487 nm, luminances of 180 and 72 cd/m$^2$ and x/y CIE color coordinates of 0.17/0.18 and 0.18/0.25 at constant driving currents of 55 and 27 mA/cm$^2$, respectively.[158] They also reported on an ionic phenothiazine derivative that featured green emission centered at $\lambda_{max}$ 499 nm, x/y CIE color coordinates of 0.28/0.43 and luminances of 129 cd/m$^2$ at 9 V.[199] The low efficiency of the device was ascribed to the incapability of the emitter to perform efficient n-doping. In 2019, the group reported on the implementation of a carbazole in blue-emitting devices, showing $\lambda_{max}$ 485 nm, luminances of 454 cd/m$^2$, efficacies of 1.3 cd/A, and x/y CIE color coordinates of 0.17/0.33 upon L-I-V scan.[154] No information on the device stability was supplied. In 2020, the group tested phenanthrene–imidazole-based SMs in single-layered

LECs that showed blue emission (e.g., $\lambda_{max}$ 459 nm, x/y CIE 0.21/0.22), good efficiencies of 1.85 cd/A and EQEs of 1.7% for the best emitting compound.[157]

## 6. Conclusions and Outlook

In section 3.1, Cu-iTMCs and Ag-iTMCs have been analyzed as promising, sustainable alternatives to Ir-iTMCs.

In particular, we firstly focused on i) the complex coordination geometry, (*e.g.*, tri- or tetracoordination), ii) ligand sets rationalizing the N^N or P^P ligand functionalization, and iii) counter-ions (**7·X**), to obtain emission color spanning all the visible range along with enhanced stability properties. The superior properties of one N^N (**2**,**3**) or P^P (**4**–**6**) ligand compared to the others were assessed by analyzing their photophysical properties (e.g., Φ, thermal stability, complex coordination geometry in both ground and excited state), as well as the device performances. The latter were firstly investigated in a single-layered architecture, where they showed scarce to moderate stabilities. This was ascribed to the irreversible oxidation (**4**–**6**) or reduction process (**7·X**), as corroborated with cyclic voltammetry (**1**–**6**) spectro-electrochemistry (**1**), and square wave voltammetry (**4**–**6**). As such, we proposed a one-fits-all strategy that is based on decoupling hole and electron transport from recombination with the use of a multi-layered device architecture (**1**–**3**, **7·X**) or a host guest system (**1**, **6**). In the case of the Cu-iTMCs, the oxidation process was hindered by selecting CBP as hole transporter, while Ag-iTMCs required the opposite strategy, that is, the employment of an electron transporter (PBD) to avoid the reduction process on the emitter. Here, 8-, 10- and 9-fold improved stabilities for blue, yellow- and red-emitting Cu-iTMCs, and ~$10^4$–fold improved stabilities with green emitting Ag-iTMCs were achieved compared to single-layered reference devices. While **1** also presented 8-fold improvement in luminance and efficiency, **2**–**6** showed comparable figures-of merits. Additionally, the most promising red Cu-iTMC (**6)** was used to build the first Cu-iTMCs-based white LECs, while the interaction of **7·X** with the PDB layer gave rise to an exciplex emission with whitish electroluminescence.

Although these results are encouraging, there are still several issues that will need to be tackled in the future. First, the stability of Cu-iTMCs, in general, and of blue-emitting Cu-iTMCs, in particular, is still low to allow the achievement of color stable all-Cu-iTMCs based white LECs. Additionally, deep-blue emitting Cu-iTMCs have not been reported yet. Moreover, the maximum efficiencies reached by Cu-iTMCs LECs (5.2 cd/A) still lag behind that of the older emitter

generations (60 cd/A). In this context, an in-depth study on the impact of the TADF emission mechanism upon device driving may yield interesting information.

Regarding Ag-iTMCs, the field is still in its infancy, and the characterization of differently functionalized Ag-iTMCs for LECs is very appealing. However, efficient ways to prevent the irreversible reduction impact on the performances, while preserving the device chromaticity features needs to be implemented. Positive results may be obtained, for instance, by testing other electron transporters. Another solution would be to synthetize Ag-iTMCs that are more robust towards the reduction process.

In section 3.2, different types of nanographenes have been selected as promising candidates for LECs. As first take-home message, **8**–**10** devices all showed excellent performances compared to the state-of-art of SM-LECs. In particular, **8** achieved a good balance of high luminances (343 cd/m$^2$) along with good stability (3 h). **9** showed good luminances of 50-70 cd/m$^2$ and efficacies of 2-3 cd/A, which are among the highest reported for SMs-LECs. Finally, **10** showed simultaneous high irradiance (>200 μW/cm$^2$) and stability (>200 h) and, in a furtherly optimized device, a record stability of 3,600 h (measured) and 13,000 h (extrapolated), at a moderate irradiance of 31 μW/cm$^2$. As interesting findings, each one of these emitters exhibited particular electroluminescence behaviors related to the temperature and electric field phenomena. In detail, **8** showed electroluminescence color changes that were ascribed to the rapid rise of temperature upon device driving. This provided us a useful tool to study the impact of self-heating onto both device chromaticity and performances - *e.g.*, the EQE of a device can be overestimated of a factor of 1/3 if temperature rise is not taken into account. **9**, a blue-emitter in thin films and solution, showed stable white emission regardless of the device architecture, driving condition, and active layer composition. This phenomenon was ascribed to a ternary emission involving both fluorescence and phosphorescence that is activated by temperature- and electric field. Finally, **10** exhibited a change in the chromaticity owing to the interplay between a high and a low energy excited vibrational modes that was proved to nicely follow the changes of the inner electric field felt by the molecule.

In the future, further efforts have to be performed to achieve better stabilities and luminances. Despite the improvement compared to the previous state-of-art, they are not comparable to those

of the older generation emitters. A possible strategy would be the employment of charged molecules, which do not need an electrolyte matrix, or of a more suitable electrolyte matrix. Additionally, further investigations in TADF SMs in LECs using a host:guest approach could be seen as a powerful tool to enhance the device efficiency.

Finally, the search of SM-based white LECs based either on host-guest systems or on single-component emitters is barely explored, and much more efforts are needed in the near future.

Overall, our results constitute a major improvement in the field of sustainable emitters for LECs, giving important guidelines about both device architecture and emitter optimization. Both aspects are key towards paving the way to meet stable, bright, and efficient LECs.

## 6. Conclusiones y prospectivas futuras

En la sección 3.1, se han analizado los Cu-iTMCs y Ag-iTMCs como alternativas prometedoras y sostenibles a los Ir-iTMCs.

En particular, nos hemos centrado en i) la geometría de coordinación del complejo (p. Ej., Tri- o tetracoordinación), ii) conjuntos de ligandos que racionalizan la funcionalización de los ligandos N^N y P^P, y iii) los contraiones (**7·X**), para obtener un color de emisión que abarque todo el rango visible junto con estabilidades mejoradas. Las mejoras obtenidas usando nuevos ligandos N^N (**2**,**3**) y P^P (**4**–**6**) en comparación con los ligandos de referencia se apoyaron analizando las propiedades fotofísicas (Φ, estabilidad térmica, geometría de coordinación del complejo en estados fundamental y excitado) y el rendimiento de los dispositivos. Estos últimos fueron investigados en primer lugar con una arquitectura de una sola capa, alcanzando estabilidades moderadas. Esto se atribuyó al proceso irreversible de oxidación (**4**–**6**) o reducción (**7·X**), como se corroboró usando voltametría cíclica (**1**–**6**), espectroelectroquímica (**1**) y voltametría de onda cuadrada (**4**–**6**). Por tanto, propusimos una estrategia única basada en el desacoplamiento del transporte de huecos y electrones de la recombinación usando una arquitectura multicapa (**1**–**3**, **7·X**) y un estrategia anfitrión:huésped (**1**,**6**). En el caso de los Cu-iTMCs, el proceso de oxidación fue asistido usando CBP como transportador de huecos, mientras que los Ag-iTMCs requerían una estrategia opuesta, es decir, el empleo de un transportador de electrones (PBD) para evitar el proceso de reducción en el emisor. Se lograron mejorar las estabilidades en un factor de 8, 10 y 9 para los Cu-iTMCs emisores azules, amarillos y rojos, respectivamente. Esta mejora fue aún mucho más superior ( ~ $10^4$ veces) para los Ag-iTMCs emisores verdes en comparación con los dispositivos de referencia de una sola capa. Mientras que **1** también presentó una mejora de 8 veces en luminancia y eficiencia, **2**–**6** mostraron mejoras comparables. Finalmente, se usó el Cu-iTMC emisor rojo más prometedor (**6**) para construir los primeros LEC blancos basados en Cu-iTMCs, mientras que la interacción de **7·X** con la capa de PDB dio lugar a una emisión de tipo exciplex con una electroluminiscencia blanquecina.

Aunque estos resultados son alentadores, todavía hay varios problemas que deberán abordarse en el futuro. Primero, las estabilidades de Cu-iTMCs, en general, y de Cu-iTMCs emisores de azul, en particular, todavía son bajas para fabricar LECs blancos eficientes y estables con solo Cu-

iTMCs. Además, aún no se ha publicado LECs azules oscuros con Cu-iTMCs. Finalmente, las eficiencias máximas alcanzadas por los LECs de Cu-iTMCs (5.2 cd / A) todavía están por detrás aquellos basados en Ir-iTMCs (60 cd / A). En este contexto, un estudio en profundidad sobre el impacto del mecanismo de emisión de TADF durante el funcionamiento del dispositivo podrías ser crucial para entender las limitaciones en eficiencia de los LECs con Cu-iTMCs.

Con respecto a los Ag-iTMCs, el campo aún está en su infancia. Por tanto, el diseño y caracterización de nuevos Ag-iTMCs es muy atractivo. Sin embargo, se deben implementar formas eficientes para evitar el impacto de la reducción irreversible en las prestaciones de los dispositivos. Se pueden obtener resultados positivos, por ejemplo, probando otros transportadores de electrones. Otra solución sería sintetizar Ag-iTMCs que sean más robustos frente al proceso de reducción.

En la sección 3.2, se han seleccionado diferentes tipos de nanografenos como prometedores candidatos para LECs. Como primera conclusión, los dispositivos hechos con **8**–**10** mostraron excelentes desempeños en comparación con el estado del arte de los SMs-LECs. En particular, dispositivos con **8** logró un buen balance mostrando una alta luminancia (343 cd/m$^2$) junto con una buena estabilidad (3 h). Dispositivos con **9** mostraron luminancia de 50-70 cd/m$^2$ y eficacia de 2-3 cd/A, que se encuentran entre las más altas reportadas para SMs-LEC. Finalmente, dispositivos con **10** mostraron simultáneamente altas irradiancias (>200 μW/cm$^2$) y estabilidades (>200 h). Mientras que una con una optimización posterior se alcanzaron estabilidades récord de 3,600 h (medida) y 13,000 h (extrapolada) con una irradiancia moderada de 31 μW/cm$^2$. Como hallazgos interesantes, cada uno de estos emisores exhibió comportamientos particulares de electroluminiscencia relacionados con la temperatura y campo eléctrico que experimentan los dispositivos en funcionamiento. En detalle, dispositivos con **8** mostraron cambios de color de electroluminiscencia que se atribuyeron al rápido aumento de la temperatura al encender el dispositivo. Esto nos proporcionó una herramienta útil para estudiar el impacto del autocalentamiento en la cromaticidad y el rendimiento de los dispositivos; por ejemplo, el EQE de un dispositivo se puede sobreestimar en un factor de 1/3 si no se tiene en cuenta el aumento de temperatura. Otro interesante ejemplo son los dispositivos con **9**, un emisor azul en capas delgadas y solución, que mostraron una emisión blanca estable independientemente de la arquitectura del dispositivo, las condiciones de conducción y la composición de la capa activa. Este fenómeno se atribuyó a una emisión ternaria que involucra fluorescencia y fosforescencia que se activa por

temperatura y campo eléctrico. Finalmente, **10** exhibió un cambio en la cromaticidad debido a la interacción entre los modos vibracionales excitados de alta y baja energía. Estos cambios de intensidad se correlacionaron muy bien con los cambios del campo eléctrico interno del dispositivo.

En el futuro, se deben realizar más esfuerzos para combinar mejores estabilidades y luminancias. A pesar de la mejora en comparación con el estado del arte, no son comparables con LECs basados en emisores tradicionales. Una posible estrategia sería el empleo de moléculas cargadas, que no necesitan una matriz de electrolitos, o del uso de una matriz de electrolitos más adecuada. Además, nuevas investigaciones en SMs con TADF en LECs que utilizan un enfoque anfitrión:huésped podría conducir a mejoras interesantes como ha demostrado recientemente el grupo del Prof. Edman.

Finalmente, la investigación sobre LEC blancos basados en SMs con sistemas anfitrión-huésped o en emisores que muestran una emisión multicomponente no se ha explorado necesitándose más esfuerzos en el futuro.

En general, nuestros resultados constituyen una mejora importante en el campo de nuevos emisores sostenibles para LECs, dando pautas importantes sobre la arquitectura del dispositivo y la optimización del diseño de los emisores. Ambos aspectos son clave para preparar el camino hacia LECs estables, brillantes y eficientes.

## 7. References


(1) Shur, M. S.; Žukauskas, A.; Solid-State Lighting: Toward Superior Illumination *Proc. IEEE* **2005**, *93*, 1691–1703.

(2) Humphreys, C. J.; Solid-State Lighting *MRS Bull.* **2008**, *33*, 459–470.

(3) Fresta, E.; Luna, V. F.; Coto, P. B.; Costa, R. D.; Merging Biology and Solid-State Lighting: Recent Advances in Light-Emitting Diodes Based on Biological Materials *Adv. Funct. Mater.* **2018**, *28*, 1707011.

(4) Costa, R. D.; Ortí, E.; Bolink, H. J.; Monti, F.; Accorsi, G.; Armaroli, N.; Luminescent Ionic Transition-Metal Complexes for Light-Emitting Electrochemical Cells *Angew. Chem.- Int. Ed.* **2012**, *51*, 8178–8211.

(5) Schlotter, P.; Schmidt, R.; Schneider, J.; Luminescence Conversion of Blue Light Emitting Diodes *Appl. Phys. A Mater. Sci. Process.* **1997**, *64*, 417–418.

(6) Nardelli, A.; Deuschle, E.; de Azevedo, L. D.; Pessoa, J. L. N.; Ghisi, E.; Assessment of Light Emitting Diodes Technology for General Lighting: A Critical Review *Renew. Sustain. Energy Rev.* **2017**, *75*, 368–379.

(7) Kalyani, N. T.; Swart, H.; Dhoble, S. J.; Principles and Applications of Organic Light Emitting Diodes (OLEDs) . In *Woodhead Publishing Series in Electronic and Optical Materials*; Woodhead Publishing, 2017; pp 171–203.

(8) Lee, J. H.; Chen, C. H.; Lee, P. H.; Lin, H. Y.; Leung, M. K.; Chiu, T. L.; Lin, C. F.; Blue Organic Light-Emitting Diodes: Current Status, Challenges, and Future Outlook *J. Mater. Chem. C* **2019**, *7*, 5874–5888.

(9) Tang, S.; Edman, L.; Light-Emitting Electrochemical Cells: A Review on Recent Progress *Top Curr Chem* **2016**, *374*, 40.

(10) Auroux, E.; Sandström, A.; Larsen, C.; Lundberg, P.; Edman, L.; Solution-Based Fabrication of the Top Electrode in Light-Emitting Electrochemical Cells *Org. Electron.* **2020**, DOI: 10.1016/j.orgel.2020.105812.

(11) Fresta, E.; Costa, R. D.; Beyond Traditional Light-Emitting Electrochemical Cells-a Review of New Device Designs and Emitters *J. Mater. Chem. C* **2017**, *5*, 5643–5675.

(12) Xu, J.; Sandström, A.; Lindh, E. M.; Yang, W.; Tang, S.; Edman, L.; Challenging Conventional Wisdom: Finding High-Performance Electrodes for Light-Emitting Electrochemical Cells *ACS Appl. Mater. Interfaces* **2018**, *10*, 33380–33389.

(13) Sandstroem, A.; Asadpoordarvish, A.; Enevold, J.; Edman, L.; Spraying Light: Ambient-Air Fabrication of Large-Area Emissive Devices on Complex-Shaped Surfaces *Adv. Mater.* **2014**, *26*, 4975–4980.

(14) Zhang, Z.; Li, Y.; Guan, G.; Li, H.; Luo, Y.; Zhao, F.; Zhang, Q.; Wei, B.; Pei, Q.; Peng, H.; et al.; A Colour-Tunable, Weavable Fibre-Shaped Polymer Light-Emitting Electrochemical Cell *Nat. Photonics* **2015**, *9*, 233–238.

(15) Asadpoordarvish, A.; Sandström, A.; Larsen, C.; Bollström, R.; Toivakka, M.; Österbacka, R.; Edman, L.; Light-Emitting Paper *Adv. Funct. Mater.* **2015**, *25*, 3238–3245.

(16) Tang, S.; Sandström, A.; Lundberg, P.; Lanz, T.; Larsen, C.; Van Reenen, S.; Kemerink, M.; Edman, L.; Design Rules for Light-Emitting Electrochemical Cells Delivering Bright Luminance at 27.5 Percent External Quantum Efficiency *Nat. Commun.* **2017**, *8*, 1190.

(17) Slinker, J.; Bernards, D.; Houston, P. L.; Abruña, H. D.; Bernhard, S.; Malliaras, G. G.; Solid-State Electroluminescent Devices Based on Transition Metal Complexes *Chem. Commun.* **2004**, 2392–2399.

(18) Lin, K. Y.; Bastatas, L. D.; Suhr, K. J.; Moore, M. D.; Holliday, B. J.; Minary-Jolandan, M.; Slinker, J. D.; Influence of Lithium Additives in Small Molecule Light-Emitting Electrochemical Cells *ACS Appl. Mater. Interfaces* **2016**, *8*, 16776–16782.

(19) Matyba, P.; Maturova, K.; Kemerink, M.; Robinson, N. D.; Edman, L.; The Dynamic Organic P-n Junction. *Nat. Mater.* **2009**, *8*, 672–676.

(20) Slinker, J. D.; DeFranco, J. A.; Jaquith, M. J.; Silveira, W. R.; Zhong, Y. W.; Moran-Mirabal, J. M.; Craighead, H. G.; Abrũa, H. D.; Marohn, J. A.; Malliaras, G. G.; Direct

Measurement of the Electric-Field Distribution in a Light-Emitting Electrochemical Cell *Nat. Mater.* **2007**, *6*, 894–899.

(21) Pei, Q.; Yu, G.; Zhang, C.; Yang, Y.; Heeger, A. J.; Polymer Light-Emitting Electrochemical Cells *Science* **1995**, *269*, 1086–1088.

(22) Pei, Q.; Yang; Yu, G.; Zhang, C.; Heeger, A. J.; Polymer Light-Emitting Electrochemical Cells: In Situ Formation of a Light-Emitting P−n Junction *J. Am. Chem. Soc.* **1996**, *118*, 3922–3929.

(23) deMello, J. C.; Tessler, N.; Graham, S. C.; Friend, R. H.; Ionic Space-Charge Effects in Polymer Light-Emitting Diodes *Phys. Rev. B* **1998**, *57*, 12951–12963.

(24) deMello, J. C.; Interfacial Feedback Dynamics in Polymer Light-Emitting Electrochemical Cells *Phys. Rev. B* **2002**, *66*, 235210.

(25) Smith, D. L.; Steady State Model for Polymer Light-Emitting Electrochemical Cells *J. Appl. Phys.* **1997**, *81*, 2869–2880.

(26) deMello, J. C.; Halls, J. J. M.; Graham, S. C.; Tessler, N.; Friend, R. H.; Electric Field Distribution in Polymer Light-Emitting Electrochemical Cells *Phys. Rev. Lett.* **2000**, 421–424.

(27) van Reenen, S.; Matyba, P.; Dzwilewski, A.; Janssen, R. A. J.; Edman, L.; Kemerink, M.; A Unifying Model for the Operation of Light-Emitting Electrochemical Cells *J. Am. Chem. Soc.* **2010**, *132*, 13776–13781.

(28) Leger, J. M.; Carter, S. A.; Ruhstaller, B.; Recombination Profiles in Poly[2-Methoxy-5-(2-Ethylhexyloxy)-1,4- Phenylenevinylene] Light-Emitting Electrochemical Cells *J. Appl. Phys.* **2005**, *98*, 124907.

(29) Pei, Q.; Heeger, A. J.; Operating Mechanism of Light-Emitting Electrochemical Cells *Nat. Mater.* **2008**, *7*, 167.

(30) Bychkov, V.; Matyba, P.; Akkerman, V.; Modestov, M.; Valiev, D.; Brodin, G.; Law, C. K.; Marklund, M.; Edman, L.; Speedup of Doping Fronts in Organic Semiconductors through Plasma Instability *Phys. Rev. Lett.* **2011**, *107*, 016103.

(31) Gao, J.; Dane, J.; Visualization of Electrochemical Doping and Light-Emitting Junction Formation in Conjugated Polymer Films *Appl. Phys. Lett.* **2004**, *84*, 2778–2780.

(32) Rodovsky, D. B.; Reid, O. G.; Pingree, L. S. C.; Ginger, D. S.; Concerted Emission and Local Potentiometry of Light-Emitting Electrochemical Cells *ACS Nano* **2010**, *4*, 2673–2680.

(33) van Reenen, S.; Matyba, P.; Dzwilewski, A.; Janssen, R. A. J.; Edman, L.; Kemerink, M.; A Unifying Model for the Operation of Light-Emitting Electrochemical Cells *J. Am. Chem. Soc.* **2010**, *132*, 13776–13781.

(34) Fresta, E.; Costa, R. D.; Advances and Challenges in White Light-Emitting Electrochemical Cells *Adv. Funct. Mater.* **2020**, DOI:10.1002/adfm.201908176.

(35) Gao, J.; Polymer Light-Emitting Electrochemical Cells—Recent Advances and Future Trends *Curr. Opin. Electrochem.* **2018**, *7*, 87–94.

(36) Housecroft, C. E.; Constable, E. C.; Over the LEC Rainbow: Colour and Stability Tuning of Cyclometallated Iridium(III) Complexes in Light-Emitting Electrochemical Cells *Coord. Chem. Rev.* **2017**, *350*, 155–177.

(37) Costa, R. D.; *Light-Emitting Electrochemical Cells. Concepts, Advances and Challenges.* , 1st ed.; Springer International Publishing: Basel, 2017.

(38) Sun, Q.; Li, Y.; Pei, Q.; Polymer Light-Emitting Electrochemical Cells for High-Efficiency Low-Voltage **2007**, *3*, 211–224.

(39) Hu, S.; Gao, J.; Polymer Light-Emitting Electrochemical Cells with Bipolar Electrode-Dynamic Doping and Wireless Electroluminescence *Adv. Funct. Mater.* **2019**, *1907003*, DOI: 10.002/adfm.1907003.

(40) Shao, Y.; Gong, X.; Heeger, A. J.; Liu, M.; Jen, A. K. Y.; Long-Lifetime Polymer Light-Emitting Electrochemical Cells Fabricated with Crosslinked Hole-Transport Layers *Adv. Mater.* **2009**, *21*, 1972–1975.

(41) Mindemark, J.; Tang, S.; Wang, J.; Kaihovirta, N.; Brandell, D.; Edman, L.; High-Performance Light-Emitting Electrochemical Cells by Electrolyte Design *Chem. Mater.*

**2016**, *28*, 2618–2623.

(42) Nishikitani, Y.; Takizawa, D.; Nishide, H.; Uchida, S.; Nishimura, S.; White Polymer Light-Emitting Electrochemical Cells Fabricated Using Energy Donor and Acceptor Fluorescent π-Conjugated Polymers Based on Concepts of Band-Structure Engineering *J. Phys. Chem. C* **2015**, *119*, 28701–28710.

(43) Nishikitani, Y.; Takeuchi, H.; Nishide, H.; Uchida, S.; Yazaki, S.; Nishimura, S.; White Polymer Light-Emitting Electrochemical Cells Using Emission from Exciplexes with Long Intermolecular Distances Formed between Polyfluorene and π-Conjugated Amine Molecules *J. Appl. Phys.* **2015**, *118*, 225501.

(44) Geng, Z. M.; Sato, G.; Marumoto, K.; Kijima, M.; D–π–A Polysulfones for Blue Electroluminescence *J. Polym. Sci. Part A Polym. Chem.* **2016**, *54*, 3454–3461.

(45) Tang, S.; Murto, P.; Xu, X.; Larsen, C.; Wang, E.; Edman, L.; Intense and Stable Near-Infrared Emission from Light-Emitting Electrochemical Cells Comprising a Metal-Free Indacenodithieno[3,2-b]Thiophene-Based Copolymer as the Single Emitter *Chem. Mater.* **2017**, *29*, 7750–7759.

(46) Tang, S.; Buchholz, H. A.; Edman, L.; White Light from a Light-Emitting Electrochemical Cell: Controlling the Energy-Transfer in a Conjugated Polymer/Triplet-Emitter Blend *ACS Appl. Mater. Interfaces* **2015**, *7*, 25955–25960.

(47) Altal, F.; Gao, J.; Long-Term Testing of Polymer Light-Emitting Electrochemical Cells: Reversible Doping and Black Spots *Org. Electron.* **2015**, *18*, 1–7.

(48) Van Reenen, S.; Janssen, R. A. J.; Kemerink, M.; Fundamental Tradeoff between Emission Intensity and Efficiency in Light-Emitting Electrochemical Cells *Adv. Funct. Mater.* **2015**, *25*, 3066–3073.

(49) Henwood, A. F.; Zysman-Colman, E.; Luminescent Iridium Complexes Used in Light-Emitting Electrochemical Cells (LEECs) *Top. Curr. Chem.* **2016**, *374*, 36.

(50) Slinker, J. D.; Rivnay, J.; Moskowitz, J. S.; Parker, J. B.; Bernhard, S.; Abruña, H. D.; Malliaras, G. G.; Electroluminescent Devices from Ionic Transition Metal Complexes *J.*

*Mater. Chem.* **2007**, *17*, 2976–2988.

(51) Ma, D.; Tsuboi, T.; Qiu, Y.; Duan, L.; Recent Progress in Ionic Iridium(III) Complexes for Organic Electronic Devices *Adv. Mater.* **2017**, *29*, 1603253.

(52) Ertl, C. D.; Momblona, C.; Pertegás, A.; Junquera-Hernández, J. M.; La-Placa, M.-G.; Prescimone, A.; Ortí, E.; Housecroft, C. E.; Constable, E. C.; Bolink, H. J.; Highly Stable Red-Light-Emitting Electrochemical Cells *J. Am. Chem. Soc.* **2017**, *139*, 3237–3248.

(53) Zanoni, K. P. S.; Coppo, R. L.; Amaral, R. C.; Murakami Iha, N. Y.; Ir(III) Complexes Designed for Light-Emitting Devices: Beyond the Luminescence Color Array. *Dalt. Trans.* **2015**, *44*, 14559–14573.

(54) Flamigni, L.; Barbieri, A.; Sabatini, C.; Ventura, B.; Barigelletti, F.; Photochemistry and Photophysics of Coordination Compounds: Iridium *Top. Curr. Chem.* **2007**, *281*, 143–203.

(55) http://www.infomine.com/investment/metal-prices/.

(56) Costa, R. D.; Ortí, E.; Bolink, H. J.; Graber, S.; Schaffner, S.; Neuburger, M.; Housecroft, C. E.; Constable, E. C.; Archetype Cationic Iridium Complexes and Their Use in Solid-State Light-Emitting Electrochemical Cells *Adv. Funct. Mater.* **2009**, *19*, 3456–3463.

(57) Bolink, H. J.; Coronado, E.; Costa, R. D.; Ortì, E.; Sessolo, M.; Graber, S.; Doyle, K.; Neuburger, M.; Housecroft, C. E.; Constable, E. C.; Long-Living Light-Emitting Electrochemical Cells - Control through Supramolecular Interactions *Adv. Mater.* **2008**, *20*, 3910–3913.

(58) Bai, R.; Meng, X.; Wang, X.; He, L.; Blue-Emitting Iridium(III) Complexes for Light-Emitting Electrochemical Cells: Advances, Challenges, and Future Prospects *Adv. Funct. Mater.* **2020**, *1907169*, DOI:10.1002/adfm.201907169.

(59) Englman, R.; Jortner, J.; The Energy Gap Law for Radiationless Transitions in Large Molecules *Mol. Phys.* **1970**, *18*, 285–287.

(60) Fresta, E.; D.Costa, R.; White Light-Emitting Electrochemical Cells *Adv. Funct. Mater.* **2020**, DOI:10.1002/adfm.201908176.

(61) Armaroli, N.; Accorsi, G.; Cardinali, F.; Listorti, A.; *Photochemistry and Photophysics of Coordination Compounds: Copper* ; Balzani, V., Campagna, S., Eds.; Springer Berlin Heidelberg, 2007; Vol. 280.

(62) Elie, M.; Gaillard, S.; Renaud, J. L.; Luminescent Cationic Copper(I) Complexes: Synthesis, Photophysical Properties and Application in Light-Emitting Electrochemical Cells . In *Light-Emitting Electrochemical Cells: Concepts, Advances and Challenges*; Springer International Publishing: Basel, 2017; pp 287–327.

(63) Leitl, M. J.; Krylova, V. A.; Djurovich, P. I.; Thompson, M. E.; Yersin, H.; Phosphorescence versus Thermally Activated Delayed Fluorescence. Controlling Singlet-Triplet Splitting in Brightly Emitting and Sublimable Cu(I) Compounds *J. Am. Chem. Soc.* **2014**, *136*, 16032–16038.

(64) Czerwieniec, R.; Leitl, M. J.; Homeier, H. H. H.; Yersin, H.; Cu(I) Complexes – Thermally Activated Delayed Fluorescence. Photophysical Approach and Material Design *Coord. Chem. Rev.* **2016**, *325*, 2–28.

(65) Bizzarri, C.; Hundemer, F.; Busch, J.; Bräse, S.; Triplet Emitters versus TADF Emitters in OLEDs: A Comparative Study *Polyhedron* **2018**, *140*, 51–66.

(66) Wang, Y. M.; Teng, F.; Hou, Y. B.; Xu, Z.; Wang, Y. S.; Fu, W. F.; Copper(I) Complex Employed in Organic Light-Emitting Electrochemical Cells: Device and Spectra Shift *Appl. Phys. Lett.* **2005**, *87*, 233512.

(67) Elie, M.; Sguerra, F.; Di Meo, F.; Weber, M. D.; Marion, R.; Grimault, A.; Lohier, J.-F.; Stallivieri, A.; Brosseau, A.; Pansu, R. B.; et al.; Designing NHC–Copper(I) Dipyridylamine Complexes for Blue Light-Emitting Electrochemical Cells *ACS Appl. Mater. Interfaces* **2016**, *8*, 14678–14691.

(68) Elie, M.; Weber, M. D.; Di Meo, F.; Sguerra, F.; Lohier, J.-F.; Pansu, R. B.; Renaud, J.-L.; Hamel, M.; Linares, M.; Costa, R. D.; et al.; Role of the Bridging Group in Bis-Pyridyl Ligands: Enhancing Both Photo- and Electro-Luminescent Features of Cationic (IPr)Cu(I) Complexes *Chem. - A Eur. J.* **2017**, *23*, 16328–16337.

(69) Weber, M. D.; Fresta, E.; Elie, M.; Miehlich, M. E.; Renaud, J.-L.; Meyer, K.; Gaillard, S.; Costa, R. D.; Rationalizing Fabrication and Design Toward Highly Efficient and Stable Blue Light-Emitting Electrochemical Cells Based on NHC Copper(I) Complexes *Adv. Funct. Mater.* **2018**, *28*, 1707423.

(70) Kaeser, A.; Moudam, O.; Accorsi, G.; Séguy, I.; Navarro, J.; Belbakra, A.; Duhayon, C.; Armaroli, N.; Delavaux-Nicot, B.; Nierengarten, J. F.; Homoleptic Copper(I), Silver(I), and Gold(I) Bisphosphine Complexes *Eur. J. Inorg. Chem.* **2014**, *2014*, 1345–1355.

(71) Fresta, E.; Volpi, G.; Milanesio, M.; Garino, C.; Barolo, C.; Costa, R. D.; Novel Ligand and Device Designs for Stable Light-Emitting Electrochemical Cells Based on Heteroleptic Copper(I) Complexes *Inorg. Chem.* **2018**, *57*, 10469–10479.

(72) Keller, S.; Constable, E. C.; Housecroft, C. E.; Neuburger, M.; Prescimone, A.; Longo, G.; Pertegás, A.; Sessolo, M.; Bolink, H. J.; [Cu(Bpy)(P^P)] + Containing Light-Emitting Electrochemical Cells: Improving Performance through Simple Substitution *Dalt. Trans.* **2014**, *43*, 16593–16596.

(73) Costa, R. D.; Tordera, D.; Ortí, E.; Bolink, H. J.; Schönle, J.; Graber, S.; Housecroft, C. E.; Constable, E. C.; Zampese, J. A.; Copper(I) Complexes for Sustainable Light-Emitting Electrochemical Cells *J. Mater. Chem.* **2011**, *21*, 16108–16118.

(74) Brunner, F.; Martínez-Sarti, L.; Keller, S.; Pertegás, A.; Prescimone, A.; Constable, E. C.; Bolink, H. J.; Housecroft, C. E.; Peripheral Halo-Functionalization in [Cu(N^N)(P^P)](+) Emitters: Influence on the Performances of Light-Emitting Electrochemical Cells. *Dalt. Trans.* **2016**, *45*, 15180–15192.

(75) Keller, S.; Pertegás, A.; Longo, G.; Martínez, L.; Cerdá, J.; Junquera-Hernández, J. M.; Prescimone, A.; Constable, E. C.; Housecroft, C. E.; Ortí, E.; et al.; Shine Bright or Live Long: Substituent Effects in [Cu(N^N)(P^P)]+-Based Light-Emitting Electrochemical Cells Where N^N Is a 6-Substituted 2,2′-Bipyridine *J. Mater. Chem. C* **2016**, *4*, 3857–3871.

(76) Keller, S.; Brunner, F.; Junquera-Hernández, J. M.; Pertegás, A.; La-Placa, M.-G.; Prescimone, A.; Constable, E. C.; Bolink, H. J.; Ortí, E.; Housecroft, C. E.; CF 3

Substitution of [Cu(P^P)(Bpy)][PF 6 ] Complexes: Effects on Photophysical Properties and Light-Emitting Electrochemical Cell Performance *Chempluschem* **2018**, *83*, 217–223.

(77) Alkan-Zambada, M.; Keller, S.; Martínez-Sarti, L.; Prescimone, A.; Junquera-Hernández, J. M.; Constable, E. C.; Bolink, H. J.; Sessolo, M.; Ortí, E.; Housecroft, C. E.; [Cu(P^P)(N^N)][PF $_6$ ] Compounds with Bis(Phosphane) and 6-Alkoxy, 6-Alkylthio, 6-Phenyloxy and 6-Phenylthio-Substituted 2,2′-Bipyridine Ligands for Light-Emitting Electrochemical Cells *J. Mater. Chem. C* **2018**, *6*, 8460–8471.

(78) Bizzarri, C.; Strabler, C.; Prock, J.; Trettenbrein, B.; Ruggenthaler, M.; Yang, C. H.; Polo, F.; Iordache, A.; Brüggeller, P.; De Cola, L.; Luminescent Dinuclear Cu(I) Complexes Containing Rigid Tetraphosphine Ligands *Inorg. Chem.* **2014**, *53*, 10944–10951.

(79) Asil, D.; Foster, J. A.; Patra, A.; Dehatten, X.; Delbarrio, J.; Scherman, O. A.; Nitschke, J. R.; Friend, R. H.; Temperature- and Voltage-Induced Ligand Rearrangement of a Dynamic Electroluminescent Metallopolymer *Angew. Chem- Int. Ed.* **2014**, *53*, 8388–8391.

(80) Weber, M. D.; Garino, C.; Volpi, G.; Casamassa, E.; Milanesio, M.; Barolo, C.; Costa, R. D.; Origin of a Counterintuitive Yellow Light-Emitting Electrochemical Cell Based on a Blue-Emitting Heteroleptic Copper(I) Complex *Dalt. Trans.* **2016**, *45*, 8984–8993.

(81) Weber, M. D.; Viciano-Chumillas, M.; Armentano, D.; Cano, J.; Costa, R. D.; σ-Hammett Parameter: A Strategy to Enhance Both Photo- and Electro-Luminescence Features of Heteroleptic Copper(I) Complexes *Dalt. Trans.* **2017**, *46*, 6312–6323.

(82) Fresta, E.; Weber, M. D.; Fernández-Cestau, J.; Costa, R. D.; White Light-Emitting Electrochemical Cells Based on Deep-Red Cu(I) Complexes *Adv. Opt. Mater.* **2019**, *7*, 1900830.

(83) Housecroft, C. E.; Constable, E. C.; Orti, E.; Bolink, H. J.; Keller, S.; Prescimone, A.; Sessolo, M.; Longo, G.; Martinez-Sarti, L.; Junquera-Hernandez, J. M.; Luminescent Copper(I) Complexes with Bisphosphane and Halogen-Substituted 2,2'-Bipyridine Ligands *Dalt. Trans.* **2018**, *47*, 14263–14276.

(84) Chen, J.; Teng, T.; Kang, L.; Chen, X. L.; Wu, X. Y.; Yu, R.; Lu, C. Z.; Highly Efficient Thermally Activated Delayed Fluorescence in Dinuclear Ag(I) Complexes with a Bis-Bidentate Tetraphosphane Bridging Ligand *Inorg. Chem.* **2016**, *55*, 9528–9536.

(85) Fresta, E.; Carbonell-Vilar, J.-M.; Yu, J.; Armentano, D.; Cano, J.; Viciano-Chumillas, M.; Costa, R. D.; Deciphering the Electroluminescence Behaviour of Silver (I)-Complexes in Light-Emitting Electrochemical Cells: Limitations and Solutions toward Highly Stable Devices *Adv. Funct. Mater.* **2019**, *29*, 1901797.

(86) Shafikov, M. Z.; Suleymanova, A.; Schinabeck, A.; Yersin, H.; A Di-Nuclear Ag(I) Complex Designed for Highly Efficient Thermally Activated Delayed Fluorescence *J. Phys. Chem. Lett.* **2018**, *9*, 702–709.

(87) Carbonell-Vilar, J. M.; Fresta, E.; Armentano, D.; Cano, J.; Costa, R. D.; Viciano-Chumillas, M.; Photoluminescent Cu(I) vs Ag(I) Complexes: Slowing down Emission in Cu(I) Complexes by Pentacoordinate Low-Lying Excited States *Dalt. Trans.* **2019**, *48*, 9765–9775.

(88) Romanov, A. S.; Jones, S. T. E.; Yang, L.; Conaghan, P. J.; Di, D.; Linnolahti, M.; Credgington, D.; Bochmann, M.; Mononuclear Silver Complexes for Efficient Solution and Vacuum-Processed OLEDs *Adv. Opt. Mater.* **2018**, *6*, 1801347.

(89) Barbieri, A.; Accorsi, G.; Armaroli, N.; Luminescent Complexes beyond the Platinum Group: The D10 Avenue *Chem. Commun.* **2008**, 2185–2193.

(90) Moudam, O.; Tsipis, A. C.; Kommanaboyina, S.; Horton, P. N.; Coles, S. J.; First Light-Emitting Electrochemical Cell with [Ag( I )(N^N)(P^P)] Type Complex *RSC Adv.* **2015**, *5*, 95047–95053.

(91) Hill, Z. B.; Rodovsky, D. B.; Leger, J. M.; Bartholomew, G. P.; Synthesis and Utilization of Perylene-Based n-Type Small Molecules in Light-Emitting Electrochemical Cells *Chem. Commun.* **2008**, 6594–6596.

(92) Tang, S.; Tan, W.-Y.; Zhu, X.-H.; Edman, L.; Small-Molecule Light-Emitting Electrochemical Cells: Evidence for in Situ Electrochemical Doping and Functional

Operation *Chem. Commun.* **2013**, *49*, 4926–4928.

(93) Kanagaraj, S.; Puthanveedu, A.; Choe, Y.; Small Molecules in Light-Emitting Electrochemical Cells: Promising Light-Emitting Materials *Adv. Funct. Mater.* **2019**, DOI:10.1002/adfm.201907126.

(94) Subeesh, M. S.; Shanmugasundaram, K.; Sunesh, C. D.; Chitumalla, R. K.; Jang, J.; Choe, Y.; Host-Dopant System to Generate Bright Electroluminescence from Small Organic Molecule Functionalized Light-Emitting Electrochemical Cells *J. Phys. Chem. C* **2016**, *120*, 12207–12217.

(95) Fresta, E.; Baumgärtner, K.; Cabanillas-Gonzalez, J.; Mastalerz, M.; Costa, R. D.; Bright, Stable, and Efficient Red Light-Emitting Electrochemical Cells Using Contorted Nanographenes *Nanoscale Horiz* **2020**, *5*, 473–480.

(96) Norell Bader, A. J.; Ilkevich, A. A.; Kosilkin, I. V.; Leger, J. M.; Precise Color Tuning via Hybrid Light-Emitting Electrochemical Cells *Nano Lett.* **2011**, *11*, 461–465.

(97) Frohleiks, J.; Wepfer, S.; Kelestemur, Y.; Demir, H. V.; Bacher, G.; Nannen, E.; Quantum Dot/Light-Emitting Electrochemical Cell Hybrid Device and Mechanism of Its Operation *ACS Appl. Mater. Interfaces* **2016**, *8*, 24692–24698.

(98) Frohleiks, J.; Gellner, S.; Wepfer, S.; Bacher, G.; Nannen, E.; Design and Realization of White Quantum Dot Light-Emitting Electrochemical Cell Hybrid Devices *ACS Appl. Mater. Interfaces* **2018**, *10*, 42637–42646.

(99) Aygüler, M. F.; Weber, M. D.; Puscher, B. M. D.; Medina, D. D.; Docampo, P.; Costa, R. D.; Light-Emitting Electrochemical Cells Based on Hybrid Lead Halide Perovskite Nanoparticles *J. Phys. Chem. C* **2015**, *119*, 12047–12054.

(100) Veldhuis, S. A.; Boix, P. P.; Yantara, N.; Li, M.; Sum, T. C.; Mathews, N.; Mhaisalkar, S. G.; Perovskite Materials for Light-Emitting Diodes and Lasers *Adv. Mater.* **2016**, *28*, 6804–6834.

(101) Docampo, P.; Bein, T.; A Long-Term View on Perovskite Optoelectronics *Acc. Chem. Res.* **2016**, *49*, 339–346.

(102) Zhang, Y.; Liu, J.; Wang, Z.; Xue, Y.; Ou, Q.; Polavarapu, L.; Zheng, J.; Qi, X.; Bao, Q.; Synthesis, Properties, and Optical Applications of Low-Dimensional Perovskites *Chem. Commun.* **2016**, *52*, 13637–13655.

(103) Bidikoudi, M.; Fresta, E.; Costa, R. D.; White-Emitting Perovskite Based Lighting Devices *Chem. Commun.* **2018**, *54*, 8150–8169.

(104) Mishra, A.; Alahbakhshi, M.; Haroldson, R.; Bastatas, L. D.; Gu, Q.; Zakhidov, A. A.; Slinker, J. D.; Enhanced Operational Stability of Perovskite Light-Emitting Electrochemical Cells Leveraging Ionic Additives **2020**, DOI:10.1002/adom.202000226.

(105) Luk, C. M.; Tang, L. B.; Zhang, W. F.; Yu, S. F.; Teng, K. S.; Lau, S. P.; An Efficient and Stable Fluorescent Graphene Quantum Dot–agar Composite as a Converting Material in White Light Emitting Diodes *J. Mater. Chem.* **2012**, *22*, 22378.

(106) Munar, A.; Sandström, A.; Tang, S.; Edman, L.; Shedding Light on the Operation of Polymer Light-Emitting Electrochemical Cells Using Impedance Spectroscopy *Adv. Funct. Mater.* **2012**, *22*, 1511–1517.

(107) Van Reenen, S.; Janssen, R. A. J.; Kemerink, M.; Dynamic Processes in Sandwich Polymer Light-Emitting Electrochemical Cells *Adv. Funct. Mater.* **2012**, *22*, 4547–4556.

(108) Meier, S. B.; Hartmann, D.; Winnacker, A.; Sarfert, W.; The Dynamic Behavior of Thin-Film Ionic Transition Metal Complex-Based Light-Emitting Electrochemical Cells *J. Appl. Phys.* **2014**, *116*, 104504.

(109) Puscher, B. M. D.; Aygüler, M. F.; Docampo, P.; Costa, R. D.; Unveiling the Dynamic Processes in Hybrid Lead Bromide Perovskite Nanoparticle Thin Film Devices *Adv. Energy Mater.* **2017**, *7*, 1602283.

(110) Meier, S. B.; Van Reenen, S.; Lefevre, B.; Hartmann, D.; Bolink, H. J.; Winnacker, A.; Sarfert, W.; Kemerink, M.; Dynamic Doping in Planar Ionic Transition Metal Complex-Based Light-Emitting Electrochemical Cells *Adv. Funct. Mater.* **2013**, *23*, 3531–3538.

(111) Buckner, M. T.; McMillin, D. R.; Photoluminescence from Copper(I) Complexes with Low-Lying Metal-to-Ligand Charge Transfer Excited States *J. Chem. Soc. Chem.*

*Commun.* **1978**, *29*, 759–761.

(112) Ichinaga, A. K.; Kirchhoff, J. R.; McMillin, D. R.; Dietrich-Buchecker, C. O.; Marnot, P. A.; Sauvage, J. P.; Charge-Transfer Absorption and Emission of Cu(NN)2+ Systems *Inorg. Chem.* **1987**, *26*, 4290–4292.

(113) McMillin, D. R.; Buckner, M. T.; Ahn, B. T.; A Light-Induced Redox Reaction of Bis(2,9-Dimethyl-1,10-Phenanthroline)Copper(I) *Inorg. Chem.* **1977**, *16*, 943–945.

(114) Blaskie, M. W.; McMillin, D. R.; Photostudies of Copper(I) Systems. 6. Room-Temperature Emission and Quenching Studies of Bis(2,9-Dimethyl-1,10-Phenanthroline)Copper(I). *Inorg. Chem.* **1980**, *19*, 3519–3522.

(115) Wang, Y.-M.; Teng, F.; Hou, Y.-B.; Xu, Z.; Wang, Y.-S.; Fu, W.-F.; Copper(I) Complex Employed in Organic Light-Emitting Electrochemical Cells: Device and Spectra Shift *Appl. Phys. Lett.* **2005**, *87*, 233512.

(116) Marion, R.; Daniellou, R.; Renaud, J.; Linares, M.; Hamel, M.; Gaillard, S.; NHC Copper(I) Complexes Bearing Dipyridylamine Ligands: Synthesis, Structural, and Photoluminescent Studies *Inorg. Chem.* **2014**, *53*, 9181–9191.

(117) Díez-González, S.; Scott, N. M.; Nolan, S. P.; Cationic Copper(I) Complexes as Efficient Precatalysts for the Hydrosilylation of Carbonyl Compounds *Organometallics* **2006**, *25*, 2355–2358.

(118) Kuang, S.-M.; Cuttell, D. G.; McMillin, D. R.; Fanwick, P. E.; Walton, R. A.; Synthesis and Structural Characterization of Cu(I) and Ni(II) Complexes That Contain the Bis[2-(Diphenylphosphino)Phenyl]Ether Ligand. Novel Emission Properties for the Cu(I) Species *Inorg. Chem.* **2002**, *41*, 3313–3322.

(119) Yuasa, J.; Dan, M.; Kawai, T.; Phosphorescent Properties of Metal-Free Diphosphine Ligands and Effects of Copper Binding *Dalt. Trans.* **2013**, *42*, 16096–16101.

(120) Chen, L. X.; Shaw, G. B.; Jennings, G.; Chen, L. X.; Shaw, G. B.; Novozhilova, I.; Liu, T.; Jennings, G.; Attenkofer, K.; Meyer, G. J.; et al.; MLCT State Structure and Dynamics of a Copper ( I ) Diimine Complex Characterized by Pump − Probe X-Ray and

Laser Spectroscopies and DFT Calculations *J. Am. Chem. Soc.* **2003**, *125*, 7022–7034.

(121) Gunaratne, T.; Rodgers, M. A. J.; Felder, D.; Nierengarten, J.-F.; Accorsi, G.; Armaroli, N.; Ultrafast Dynamics of Cu(I)-Phenanthrolines in Dichloromethane *Chem. Commun.* **2003**, 3010–3011.

(122) Shaw, G. B.; Grant, C. D.; Shirota, H.; Castner, E. W.; Meyer, G. J.; Chen, L. X.; Ultrafast Structural Rearrangements in the MLCT Excited State for Copper(I) Bis-Phenanthrolines in Solution *J. Am. Chem. Soc.* **2007**, *129*, 2147–2160.

(123) Mohankumar, M.; Monti, F.; Holler, M.; Niess, F.; Delavaux-Nicot, B.; Armaroli, N.; Sauvage, J. P.; Nierengarten, J. F.; Combining Topological and Steric Constraints for the Preparation of Heteroleptic Copper(I) Complexes *Chem. - A Eur. J.* **2014**, *20*, 12083–12090.

(124) Kaeser, A.; Mohankumar, M.; Mohanraj, J.; Monti, F.; Holler, M.; Cid, J.-J.; Moudam, O.; Nierengarten, I.; Karmazin-Brelot, L.; Duhayon, C.; et al.; Heteroleptic Copper(I) Complexes Prepared from Phenanthroline and Bis-Phosphine Ligands *Inorg. Chem.* **2013**, *52*, 12140–12151.

(125) Keller, S.; Constable, E. C.; Housecroft, C. E.; Neuburger, M.; Prescimone, A.; Longo, G.; Pertegás, A.; Sessolo, M.; Bolink, H. J.; [Cu(Bpy)(P^P)] + Containing Light-Emitting Electrochemical Cells: Improving Performance through Simple Substitution *Dalt. Trans.* **2014**, *43*, 16593–16596.

(126) Czerwieniec, R.; Leitl, M. J.; Homeier, H. H. H.; Yersin, H.; Cu(I) Complexes – Thermally Activated Delayed Fluorescence. Photophysical Approach and Material Design *Coord. Chem.Reviews* **2016**, *325*, 2–28.

(127) Keller, S.; Constable, E. C.; Housecroft, C. E.; Neuburger, M.; Prescimone, A.; Longo, G.; Pertegás, A.; Sessolo, M.; Bolink, H. J.; [Cu(Bpy)(P^P)] + Containing Light-Emitting Electrochemical Cells: Improving Performance through Simple Substitution *Dalt. Trans.* **2014**, *43*, 16593–16596.

(128) Linfoot, C. L.; Leitl, M. J.; Richardson, P.; Rausch, A. F.; Chepelin, O.; White, F. J.;

Yersin, H.; Robertson, N.; Thermally Activated Delayed Fluorescence (TADF) and Enhancing Photoluminescence Quantum Yields of [Cu(I) (Diimine)(Diphosphine)] + Complexes—Photophysical, Structural, and Computational Studies *Inorg. Chem.* **2014**, *53*, 10854–10861.

(129) Balzani, C.; Campagna, S.; Armaroli, N.; Accorsi, G.; Cardinali, F.; Listorti, A.; Photochemistry and Photophysics of Coordination Compounds **2007**, *281*, 143–203.

(130) Zhang, Q.; Ding, J.; Cheng, Y.; Wang, L.; Xie, Z.; Jing, X.; Wang, F.; Novel Heteroleptic Cu1 Complexes with Tunable Emission Color for Efficient Phosphorescent Light-Emitting Diodes *Adv. Funct. Mater.* **2007**, *17*, 2983–2990.

(131) So, G. K. M.; Cheng, G.; Wang, J.; Chang, X.; Kwok, C. C.; Zhang, H.; Che, C. M.; Efficient Color-Tunable Copper(I) Complexes and Their Applications in Solution-Processed Organic Light-Emitting Diodes *Chem. - An Asian J.* **2017**, *12*, 1490–1498.

(132) Yersin, H.; Rausch, A. F.; Czerwieniec, R.; Hofbeck, T.; Fischer, T.; The Triplet State of Organo-Transition Metal Compounds. Triplet Harvesting and Singlet Harvesting for Efficient OLEDs *Coord. Chem. Rev.* **2011**, *255*, 2622–2652.

(133) Hsu, C.-W.; Lin, C.-C.; Chung, M.-W.; Chi, Y.; Lee, G.-H.; Chou, P.-T.; Chang, C.-H.; Chen, P.-Y.; Systematic Investigation of the Metal-Structure–Photophysics Relationship of Emissive d $^{10}$ -Complexes of Group 11 Elements: The Prospect of Application in Organic Light Emitting Devices *J. Am. Chem. Soc.* **2011**, *133*, 12085–12099.

(134) Igawa, S.; Hashimoto, M.; Kawata, I.; Hoshino, M.; Osawa, M.; Photoluminescence Properties, Molecular Structures, and Theoretical Study of Heteroleptic Silver(I) Complexes Containing Diphosphine Ligands *Inorg. Chem. Commun.* **2012**, *51*, 5805–5813.

(135) Moudam, O.; Tsipis, A. C.; Kommanaboyina, S.; Horton, P. N.; Coles, S. J.; First Light-Emitting Electrochemical Cell with [Ag(I)(N^N)(P^P)] Type Complex *RSC Adv.* **2015**, *5*, 95047–95053.

(136) Ràfols-Ribé, J.; Robinson, N. D.; Larsen, C.; Tang, S.; Top, M.; Sandström, A.; Edman,

L.; Self-Heating in Light-Emitting Electrochemical Cells *Adv. Funct. Mater.* **2020**, DOI:10.1002/adfm.201908649.

(137) Mulvaney, P.; Henglein, A.; Long-Lived Nonmetallic Silver Clusters in Aqueous Solution: A Pulse Radiolysis Study of Their Formation *J. Phys. Chem.* **1990**, *94*, 4182–4188.

(138) Yang, W.; Wang, C.; Arrighi, V.; An Organic Silver Complex Conductive Ink Using Both Decomposition and Self-Reduction Mechanisms in Film Formation *J. Mater. Sci. Mater. Electron.* **2018**, *29*, 2771–2783.

(139) Schwab, T.; Lüssem, B.; Furno, M.; Gather, M. C.; Leo, K.; 18 - Organic Light-Emitting Diodes Handbook of Organic Materials for Optical and (Opto)Electronic Devices . In *Woodhead Publishing Series in Electronic and Optical Materials*; Woodhead Publishing, 2013; pp 508–534.

(140) Su, H.; Chen, Y.; Wong, K.; Recent Progress in White Light-Emitting Electrochemical Cells *Adv. Funct. Mater.* **2019**, DOI:10.1002/adfm.201906898.

(141) Weber, M. D.; Nikolaou, V.; Wittmann, J. E.; Nikolaou, A.; Angaridis, P. A.; Charalambidis, G.; Stangel, C.; Kahnt, A.; Coutsolelos, A. G.; Costa, R. D.; Benefits of Using BODIPY–porphyrin Dyads for Developing Deep-Red Lighting Sources *Chem. Commun.* **2016**, *52*, 1602–1605.

(142) Weber, M. D.; Wittmann, J. E.; Burger, A.; Malcıoğlu, O. B.; Segarra-Martí, J.; Hirsch, A.; Coto, P. B.; Bockstedte, M.; Costa, R. D.; From White to Red: Electric-Field Dependent Chromaticity of Light-Emitting Electrochemical Cells Based on Archetypal Porphyrins *Adv. Funct. Mater.* **2016**, *26*, 6737–6750.

(143) Lorenzo-García, M. M.; Bonifazi, D.; Renaissance of an Old Topic: From Borazines to BN-Doped Nanographenes *Chim. Int. J. Chem.* **2017**, *71*, 550–557.

(144) Seyler, H.; Purushothaman, B.; Jones, D. J.; Holmes, A. B.; Wong, W. W. H.; Hexa-Peri-Hexabenzocoronene in Organic Electronics *Pure Appl. Chem.* **2012**, *84*, 1047–1067.

(145) Dosso, J.; Tasseroul, J.; Fasano, F.; Marinelli, D.; Biot, N.; Fermi, A.; Bonifazi, D.;

Synthesis and Optoelectronic Properties of Hexa-Peri-Hexabenzoborazinocoronene *Angew. Chem., Int. Ed.* **2017**, *56*, 4483–4487.

(146) Subeesh, M. S.; Shanmugasundaram, K.; Sunesh, C. D.; Won, Y. S.; Choe, Y.; Utilization of a Phenanthroimidazole Based Fluorophore in Light-Emitting Electrochemical Cells *J. Mater. Chem. C* **2015**, *3*, 4683–4687.

(147) Shanmugasundaram, K.; Subeesh, M. S.; Sunesh, C. D.; Chitumalla, R. K.; Jang, J.; Choe, Y.; Green Electroluminescence from Charged Phenothiazine Derivative *J. Phys. Chem. C* **2016**, *120*, 20247–20253.

(148) Chen, H.-F.; Liao, C.-T.; Su, H.-C.; Yeh, Y.-S.; Wong, K.-T.; Highly Efficient Exciplex Emission in Solid-State Light-Emitting Electrochemical Cells Based on Mixed Ionic Hole-Transport Triarylamine and Ionic Electron-Transport 1,3,5-Triazine Derivatives *J. Mater. Chem. C* **2013**, *1*, 4647–4654.

(149) Wong, M. Y.; Hedley, G. J.; Xie, G.; Kölln, L. S.; Samuel, I. D. W.; Pertegás, A.; Bolink, H. J.; Zysman-Colman, E.; Light-Emitting Electrochemical Cells and Solution-Processed Organic Light-Emitting Diodes Using Small Molecule Organic Thermally Activated Delayed Fluorescence Emitters *Chem. Mater.* **2015**, *27*, 6535–6542.

(150) Chen, H.-F.; Liao, C.-T.; Chen, T.-C.; Su, H.-C.; Wong, K.-T.; Guo, T.-F.; An Ionic Terfluorene Derivative for Saturated Deep-Blue Solid State Light-Emitting Electrochemical Cells *J. Mater. Chem.* **2011**, *21*, 4175–4181.

(151) Chen, H. F.; Liao, C. T.; Kuo, M. C.; Yeh, Y. S.; Su, H. C.; Wong, K. T.; UV Light-Emitting Electrochemical Cells Based on an Ionic 2,2′-Bifluorene Derivative *Org. Electron.* **2012**, *13*, 1765–1773.

(152) Wong, M. Y.; La-Placa, M.-G.; Pertegas, A.; Bolink, H. J.; Zysman-Colman, E.; Deep-Blue Thermally Activated Delayed Fluorescence (TADF) Emitters for Light-Emitting Electrochemical Cells (LEECs) *J. Mater. Chem. C* **2017**, *5*, 1699–1705.

(153) Shanmugasundaram, K.; Subeesh, M. S.; Sunesh, C. D.; Chitumalla, R. K.; Jang, J.; Choe, Y.; Synthesis and Photophysical Characterization of an Ionic Fluorene Derivative for

Blue Light-Emitting Electrochemical Cells *Org. Electron.* **2015**, *24*, 297–302.

(154) Shanmugasundaram, K.; John, J. C.; Chitumalla, S.; Jang, J.; Choe, Y.; Carbazole Based Ionic Small Molecule Emitter for Non-Doped Light-Emitting Electrochemical Cells *Org. Electron.* **2019**, *67*, 141–145.

(155) Shanmugasundaram, K.; Subeesh, M. S.; Sunesh, C. D.; Choe, Y.; Non-Doped Deep Blue Light-Emitting Electrochemical Cells from Charged Organic Small Molecules *RSC Adv.* **2016**, *6*, 28912–28918.

(156) Subeesh, M. S.; Shanmugasundaram, K.; Sunesh, C. D.; Nguyen, T. P.; Choe, Y.; Phenanthroimidazole Derivative as an Easily Accessible Emitter for Non-Doped Light-Emitting Electrochemical Cells *J. Phys. Chem. C* **2015**, *119*, 23676–23684.

(157) Choi, J.; Kanagaraj, S.; Choe, Y.; Utilization of Novel Phenanthrene-Imidazole-Based Ionic Small Molecules for Blue Light-Emitting Electrochemical Cells *J. Mater. Chem. C* **2020**, *8*, 4580–4587.

(158) Lee, H.; Sunesh, C. D.; Subeesh, M. S.; Choe, Y.; Blue-Light Emitting Electrochemical Cells Comprising Pyrene-Imidazole Derivatives *Opt. Mater.* **2018**, *78*, 44–51.

(159) Weber, K. T.; Karikis, K.; Weber, M. D.; Coto, P. B.; Charisiadis, A.; Charitaki, D.; Charalambidis, G.; Angaridis, P.; Coutsolelos, A. G.; Costa, R. D.; Cunning Metal Core: Efficiency/Stability Dilemma in Metallated Porphyrin Based Light-Emitting Electrochemical Cells *Dalt. Trans.* **2016**, *45*, 13284–13288.

(160) Weber, M. D.; Adam, M.; Tykwinski, R. R.; Costa, R. D.; Controlling the Chromaticity of Small-Molecule Light-Emitting Electrochemical Cells Based on TIPS-Pentacene *Adv. Funct. Mater.* **2015**, *25*, 5066–5074.

(161) Pertegás, A.; Tordera, D.; Serrano-Pérez, J.; Light-Emitting Electrochemical Cells Using Cyanine Dyes as the Active Components *J. Am. Chem. Soc.* **2013**, *135*, 18008–18011.

(162) Jenatsch, S.; Wang, L.; Leclaire, N.; Hack, E.; Steim, R.; Anantharaman, S. B.; Heier, J.; Ruhstaller, B.; Penninck, L.; Nüesch, F.; et al.; Visible Light-Emitting Host-Guest Electrochemical Cells Using Cyanine Dyes *Org. Electron.* **2017**, *48*, 77–84.

(163) Jenatsch, S.; Wang, L.; Bulloni, M.; Véron, A. C.; Ruhstaller, B.; Altazin, S.; Nüesch, F.; Hany, R.; Doping Evolution and Junction Formation in Stacked Cyanine Dye Light-Emitting Electrochemical Cells *ACS Appl. Mater. Interfaces* **2016**, *8*, 6554–6562.

(164) Weber, M. D.; Nikolaou, V.; Wittmann, J. E.; Nikolaou, A.; Angaridis, P. A.; Charalambidis, G.; Stangel, C.; Kahnt, A.; Coutsolelos, A. G.; Costa, R. D.; Benefits of Using BODIPY-Porphyrin Dyads for Developing Deep-Red Lighting Sources *Chem. Commun.* **2016**, *52*, 1602–1605.

(165) Ho, C.-C.; Chen, H.-F.; Ho, Y.-C.; Liao, C.-T.; Su, H.-C.; Wong, K.-T.; Phosphorescent Sensitized Fluorescent Solid-State near-Infrared Light-Emitting Electrochemical Cells *Phys. Chem. Chem. Phys.* **2011**, *13*, 17729.

(166) Lundberg, P.; Tsuchiya, Y.; Lindh, E. M.; Tang, S.; Adachi, C.; Edman, L.; Thermally Activated Delayed Fluorescence with 7% External Quantum Efficiency from a Light-Emitting Electrochemical Cell *Nat. Commun.* **2019**, *9*, 28810–28816.

(167) Fresta, E.; Dosso, J.; Cabanillas-Gonzalez, J.; Bonifazi, D.; D. Costa, R.; Origin of the Exclusive Ternary Electroluminescent Behavior of BN-Doped Nanographenes in Efficient Single-Component White Light-Emitting Electrochemical Cells *Adv. Funct. Mater.* **2020**, DOI:10.1002/adfm.201906830.

(168) Lin, G.-R.; Cheng, J.-R.; Wang, C.-W.; Sarma, M.; Chen, H.-F.; Su, H.-C.; Chang, C.-H.; Wong, K.-T.; Solid-State White Light-Emitting Electrochemical Cells Based on Scattering Red Color Conversion Layers *J. Mater. Chem. C* **2015**, *3*, 12492–12498.

(169) Akatsuka, T.; Roldán-Carmona, C.; Ortí, E.; Bolink, H. J.; Dynamically Doped White Light Emitting Tandem Devices *Adv. Mater.* **2014**, *26*, 770–774.

(170) Uchida, S.; Takizawa, D.; Ikeda, S.; Takeuchi, H.; Nishimura, S.; Nishide, H.; Nishikitani, Y.; Fabrication of White Light-Emitting Electrochemical Cells with Stable Emission from Exciplexes *J Vis Exp* **2016**, *117*, e54628.

(171) Bastatas, L. D.; Lin, K. Y.; Moore, M. D.; Suhr, K. J.; Bowler, M. H.; Shen, Y.; Holliday, B. J.; Slinker, J. D.; Discerning the Impact of a Lithium Salt Additive in Thin-Film Light-

Emitting Electrochemical Cells with Electrochemical Impedance Spectroscopy *Langmuir* **2016**, *32*, 9468–9474.

(172) Bastatas, L. D.; Moore, M. D.; Slinker, J. D.; The Effect of the Dielectric Constant and Ion Mobility in Light-Emitting Electrochemical Cells *Chempluschem* **2018**, *83*, 266–273.

(173) Nishikitani, Y.; Suga, K.; Uchida, S.; Nishimura, S.; Oyaizu, K.; Nishide, H.; High-Color-Rendering-Index White Polymer Light-Emitting Electrochemical Cells Based on Ionic Host-Guest Systems: Utilization of Blend Films of Blue-Fluorescent Cationic Polyfluorenes and Red-Phosphorescent Cationic Iridium Complexes *Org. Electron.* **2017**, *51*, 168–172.

(174) Nishikitani, Y.; Cho, T.; Uchida, S.; Nishimura, S.; Oyaizu, K.; Nishide, H.; Polymer-Based White-Light-Emitting Electrochemical Cells with Very High Color-Rendering Index Based on Blue-Green Fluorescent Polyfluorenes and Red-Phosphorescent Iridium Complexes *Chempluschem* **2018**, *83*, 463–469.

(175) Fresta, E.; Dosso, J.; Cabanillas-Gonzalez, J.; Bonifazi, D.; Costa, R. D.; Revealing the Impact of Heat Generation Using Nanographene Based Light-Emitting Electrochemical Cells *ACS Appl. Mater. Interfaces* **2020**, DOI:10.1021/acsami.0c06783.

(176) Baumgärtner, K.; Rominger, F.; Mastalerz, M.; Gulf-Selective Postsynthetic Functionalization of a Soluble Hexabenzoovalene *Chem. - A Eur. J.* **2018**, *24*, 8751–8755.

(177) Baumgärtner, K.; Meza Chincha, A. L.; Dreuw, A.; Rominger, F.; Mastalerz, M.; A Conformationally Stable Contorted Hexabenzoovalene *Angew. Chem. Int. Ed.* **2016**, *55*, 15594–15598.

(178) Henwood, A. F.; Pal, A. K.; Cordes, D. B.; Slawin, A. M. Z.; Rees, T. W.; Momblona, C.; Babaei, A.; Pertegás, A.; Ortí, E.; Bolink, H. J.; et al.; Blue-Emitting Cationic Iridium(III) Complexes Featuring Pyridylpyrimidine Ligands and Their Use in Sky-Blue Electroluminescent Devices *J. Mater. Chem. C* **2017**, *5*, 9638–9650.

(179) Blasini, D. R.; Rivnay, J.; Smilgies, D. M.; Slinker, J. D.; Flores-Torres, S.; Abruña, H. D.; Malliaras, G. G.; Observation of Intermediate-Range Order in a Nominally

Amorphous Molecular Semiconductor Film *J. Mater. Chem.* **2007**, *17*, 1458–1461.

(180) Cho, Y. J.; Taylor, S.; Aziz, H.; Increased Electromer Formation and Charge Trapping in Solution-Processed versus Vacuum-Deposited Small Molecule Host Materials of Organic Light-Emitting Devices *ACS Appl. Mater. Interfaces* **2017**, *9*, 40564–40572.

(181) Yu, H.; Zhang, Y.; Cho, Y. J.; Aziz, H.; Exciton-Induced Degradation of Carbazole-Based Host Materials and Its Role in the Electroluminescence Spectral Changes in Phosphorescent Organic Light Emitting Devices with Electrical Aging *ACS Appl. Mater. Interfaces* **2017**, *9*, 14145–14152.

(182) Li, J. Y.; Liu, D.; Ma, C.; Lengyel, O.; Lee, C. S.; Tung, C. H.; Lee, S.; White-Light Emission from a Single-Emitting-Component Organic Electroluminescent Device *Adv. Mater.* **2004**, *16*, 1538–1541.

(183) Yang, S.; Jiang, M.; White Light Generation Combining Emissions from Exciplex, Excimer and Electromer in TAPC-Based Organic Light-Emitting Diodes *Chem. Phys. Lett.* **2009**, *484*, 54–58.

(184) Lee, J. K.; Yoo, D. S.; Handy, E. S.; Rubner, M. F.; Thin Film Light Emitting Devices from an Electroluminescent Ruthenium Complex *Appl. Phys. Lett.* **1996**, *69*, 1686–1688.

(185) Rudmann, H.; Rubner, M. F.; Single Layer Light-Emitting Devices with High Efficiency and Long Lifetime Based on Tris(2,2′ Bipyridyl) Ruthenium(II) Hexafluorophosphate *J. Appl. Phys.* **2001**, *90*, 4338–4345.

(186) Fresta, E.; Volpi, G.; Garino, C.; Barolo, C.; Costa, R. D.; Contextualizing Yellow Light-Emitting Electrochemical Cells Based on a Blue-Emitting Imidazo-Pyridine Emitter *Polyhedron* **2018**, *140*, 129–137.

(187) Charisiadis, A.; Bagaki, A.; Fresta, E.; Weber, K. T.; Charalambidis, G.; Stangel, C.; Hatzidimitriou, A. G.; Angaridis, P. A.; Coutsolelos, A.; Costa, R. D.; Peripheral Substitution of Tetraphenyl Porphyrins: Fine-Tuning of the Self-Assembling towards Enhanced Electroluminescence *Chempluschem* **2018**, *83*, 254–265.

(188) Fresta, E.; Monclus, M.; Bertz, M.; Ezquerro, C.; Molina, J.; Berenguer, J. R.; Kunimoto,

M.; Homma, T.; Costa, R. D.; Key Ionic Electrolytes for Highly Self-Stable Light-Emitting Electrochemical Cells Based on Ir(III) Complexes *Adv. Opt. Mater.* **2020**, DOI:10.1002/adom.202000295.

(189) Ezquerro, C.; Fresta, E.; Serrano, E.; Lalinde Peña, E.; Garcia-Martinez, J.; Berenguer, J. R.; Costa, R. D.; White-Emitting Organometallo-Silica Nanoparticles for Sun-like Light-Emitting Diodes *Mater. Horizons* **2019**, *6*, 130–136.

(190) Fresta, E.; Fernández-Cestau, J.; Gil, B.; Montaño, P.; Berenguer, J. R.; Moreno, M. T.; Coto, P. B.; Lalinde, E.; Costa, R. D.; Versatile Homoleptic Naphthyl-Acetylide Heteronuclear [Pt2M4(C≡C-Np)8] (M = Ag, Cu) Phosphors for Highly Efficient White and NIR Hybrid Light-Emitting Diodes *Adv. Opt. Mater.* **2019**, *8*, 1901126.

(191) Arnosti, N.; Brunner, F.; Susic, I.; Keller, S.; Junquera-Hernández, J. M.; Prescimone, A.; Bolink, H. J.; Sessolo, M.; Ortí, E.; Housecroft, C. E.; et al.; Remote Modification of Bidentate Phosphane Ligands Controlling the Photonic Properties in Their Complexes: Enhanced Performance of [Cu(RN-Xantphos)(N^N)][PF6] in Light-Emitting Electrochemical Cells *Adv. Opt. Mater.* **2020**, *1901689*.

(192) Shafikov, M. Z.; Czerwieniec, R.; Yersin, H.; Ag(i) Complex Design Affording Intense Phosphorescence with a Landmark Lifetime of over 100 Milliseconds *Dalt. Trans.* **2019**, *48*, 2802–2806.

(193) Barbieri, A.; Bandini, E.; Monti, F.; Praveen, V. K.; Armaroli, N.; The Rise of Near-Infrared Emitters: Organic Dyes, Porphyrinoids, and Transition Metal Complexes *Top. Curr. Chem.* **2016**, *374*.

(194) Pashaei, B.; Karimi, S.; Shahroosvand, H.; Pilkington, M.; Molecularly Engineered Near-Infrared Light-Emitting Electrochemical Cells *Adv. Funct. Mater.* **2020**, DOI:10.1002/adfm.201908103.

(195) Mone, M.; Tang, S.; Murto, P.; Abdulahi, B. A.; Larsen, C.; Wang, J.; Mammo, W.; Edman, L.; Wang, E.; Star-Shaped Diketopyrrolopyrrole-Zinc Porphyrin That Delivers 900 Nm Emission in Light-Emitting Electrochemical Cells *Chem. Mater.* **2019**, *31*, 9721–9728.

(196) Pertegás, A.; Wong, M. Y.; Sessolo, M.; Zysman-Colman, E.; Bolink, H. J.; Efficient Light-Emitting Electrochemical Cells Using Small Molecular Weight, Ionic, Host-Guest Systems *ECS J. Solid State Sci. Technol.* **2016**, *5*, 3160–3163.

(197) Wong, M. Y.; La-Placa, M.-G.; Pertegas, A.; Bolink, H. J.; Zysman-Colman, E.; Deep-Blue Thermally Activated Delayed Fluorescence (TADF) Emitters for Light-Emitting Electrochemical Cells (LEECs) *J. Mater. Chem. C* **2017**, *5*, 1699–1705.

(198) Son, M.; Choe, Y.; Phenanthroimidazole Derivatives for Single Component Blue Light-Emitting Electrochemical Cells *Mol. Cryst. Liq. Cryst.* **2017**, *654*, 234–243.

(199) Jongseong, K.; Shanmugasundaram, K.; Chitumalla, R. K.; Jang, J.; Choe, Y.; Phenothiazine Derivatives as an Easily Accessible Emitter for Green Light-Emitting Electrochemical Cells *J. Lumin.* **2018**, *197*, 383–388.

## 8. List of publications

1. Elisa Fresta, Rubén D. Costa, Beyond Traditional Light-Emitting Electrochemical Cells-a Review of new Device Designs and Emitters, *J. Mater. Chem. C*, **2017**, 5, 5643–5675.

2. Asterios Charisiadis, Anthis Bagaki, Elisa Fresta, Katharina T. Weber, Georgios Charalambidis, Christina. Stangel, Anthonios G. Hatzidimitriou, Panagiotis A. Angaridis, Athanassios Coutsolelos and Rubén D. Costa, Peripheral Substitution of Tetraphenyl Porphyrins: Fine-tuning of the Self-assembling towards enhanced Electroluminescence, *Chempluschem*, **2018**, 83, 254–265.

3. Elisa Fresta, Giorgio Volpi, Claudio Garino, Claudia Barolo and Rubén D. Costa, Contextualizing Yellow Light-Emitting Electrochemical Cells Based on a Blue-Emitting Imidazo-Pyridine Emitter, *Polyhedron*, **2018**, 140, 129–137.

4. Michael D. Weber[+], Elisa Fresta[+], Margaux Elie, Matthias E. Miehlich, Jean-Luc Renaud, Karsten Meyer, Sylvain Gaillard and Rubén D. Costa, Rationalizing Fabrication and Design toward highly Efficient and Stable blue Light-Emitting Electrochemical Cells Based on NHC copper(I) complexes, *Adv. Funct. Mater*., **2018**, 28, 1707423.

5. Elisa Fresta, Veronica F. Luna, Pedro B. Coto and Rubén D. Costa, Merging Biology and Solid-state Lighting: recent Advances in Light-emitting Diodes Based on Biological Materials, *Adv. Funct. Mater*., **2018**, 28, 1707011.

6. Elisa Fresta, Giorgio Volpi, Marco Milanesio, Claudio Garino, Claudia Barolo, Rubén D. Costa, Novel Ligands and Device Designs towards Stable Light-Emitting Electrochemical Cells Based on Copper (I) complexes, *Inorg. Chem.* ,**2018**, 57, 10469–10479.

7. Maria Bidikoudi[+], Elisa Fresta[+] and Rubén D. Costa, White-Emitting Perovskite Based Lighting Devices, *Chem Comm.*, **2018**, 54, 8150–8169.

8. Cintia Ezquerro[+], Elisa Fresta[+], Elena Serrano, Elena Lalinde, Javier García Martínez, Jesús R. Berenguer and Rubén D. Costa, White-Emitting Organometallo-Silica Nanoparticles for Sun-like Light-Emitting Diodes, *Mater. Horizons*, **2019**, 6, 130–136.

9. José M. Carbonell-Vilar, E. Fresta, D. Armentano, Rubén D. Costa, Marta Viciano-Chumillas and Joan Cano, Photoluminescent Cu(I) vs Ag(I) Complexes: Slowing Down Emission in Cu(I) Ccomplexes by Pentacoordinate Low-Lying Excited States, *Dalton Trans.*, **2019**, 48, 9765–9775.

10. Elisa Fresta, José M. Carbonell-Vilar, Yiayin Yu, Donatella Armentano, Joan Cano, Marta Viciano-Chumillas, and Rubén D. Costa, Deciphering the Electroluminescence Behavior of Silver(I)-complexes in Light-Emitting Electrochemical Cells: Limitations and Solutions toward Highly Stable Devices, *Adv. Funct. Mater.*, **2019**, 29, 1901797.

11. Babak Pashaei, Soheila Karimi, Hashem Shahroosvand, Parisa Abbasi, Melanie Pilkington, Antonino Bartolotta, Elisa Fresta, Julio Fernández-Cestau, Rubén D. Costa and Francesco Bonaccorso, Polypyridyl Ligands as a Versatile Platform for Solid-State Light-Emitting Devices, *Chem. Soc. Rev*., **2019**, 48, 5033–5139.

12. Elisa Fresta, Michael D. Weber, Julio Fernández-Cestau and Rubén D. Costa, White Light-Emitting Electrochemical Cells Based on Deep-red Cu(I) complexes, *Adv. Opt. Mater.*, **2019**,7, 1900830.

13. Elisa Fresta, Marco Milanesio, Giorgio Volpi, Claudia Barolo, Eleonora Conterosito, Synthesis and Crystal Structure of [Ir(3-(2-methoxyphenyl)-5-methyl-1-(6-methylpyridin-2-yl)H-imidazo[1,5-a]pyridine)(2-phenylpyridine)2]$PF_6$ Showing Three Anion/Cation Couples in the Asymmetric Unit, *Crystals*, **2019**, 9, 617.

14. Elisa Fresta, Julio Fernández-Cestau, Belén Gil, Patricia Montaño, Jesús R. Berenguer, Maria Teresa Moreno, Pedro B. Coto, Elena Lalinde, and Rubén D. Costa, Versatile Homoleptic Naphthyl-Acetylide Heteronuclear [[Pt2M4(C≡C-Np)8] (M = Ag, Cu) Phosphors for Highly Efficient White and NIR Hybrid Light-Emitting Diodes, *Adv. Opt. Mater.*, **2020**, 8, 1901126.

15. Elisa Fresta, Jacopo Dosso, Juan Cabanillas- González, Davide Bonifazi and Rubén D. Costa, On the Origin of Efficient White Light-Emitting Electrochemical Cells with B-N Doped Nanographene as Single Emitter, *Adv. Funct. Mater*., **2020**, DOI: 10.1002/adfm.201906830.

16. Elisa Fresta, Kevin Bäumgartner, Juan Cabanillas-Gonzalez, Michael Mastalerz and Rubén D. Costa, Bright, Stable, and Efficient Red Light-Emitting Electrochemical Cells Using Contorted Nanographenes, *Nanoscale Horiz*., **2020**, 5, 473–480.

17. Elisa Fresta, Miguel A. Monclús, Morten Bertz, Cintia Ezquerro, Jon M. Molina-Aldareguia, Jesús R. Berenguer, Masahiro Kunimoto, Takayuki Homma and Rubén D. Costa, Key Ionic Electrolytes for Highly Self-Stable Light-Emitting Electrochemical Cells Based on Ir(III) Complexes, *Adv. Opt. Mater*, **2020**, DOI:10.1002/adom.202000295.

18. Elisa Fresta and Rubén D. Costa, Advances and Challenges in White Light-Emitting Electrochemical Cells, *Adv. Funct. Mater*., **2020**, DOI: 10.1002/adfm.201908176.

19. Elisa Fresta, Jacopo Dosso, Juan Cabanillas- González, Davide Bonifazi and Rubén D. Costa, Revealing the Impact of Heat Generation Using Nanographene Based Light-Emitting Electrochemical Cells, *ACS Appl. Mater. Inter.*, **2020**, DOI:10.1021/acsami.0c06783.

+ authors contributed equally.

## 9. Publications discussed in this thesis

Section 3.1.1: Rationalizing Fabrication and Design Towards Highly Efficient and Stable Blue Light-Emitting Electrochemical Cells based on NHC Copper(I) Complexes

ADVANCED FUNCTIONAL MATERIALS

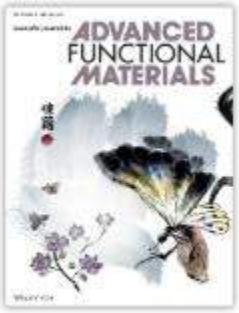


Volume 28, Issue 17
April 25, 2018
1707423

Michael D. Weber,[1+] Elisa Fresta,[2+] Margaux Elie,[3] Matthias E. Miehlich,[4] Jean-Luc Renaud,[3] Karsten Meyer,[4] Sylvain Gaillard,[3]*and Rubén D. Costa[1,2]*

1. Department of Chemistry & Pharmacy at the University of Erlangen-Nuremberg, Egerlandstr. 3, 91058 Erlangen, Germany.
2. IMDEA Materials Institute, Calle Eric Kandel 2, 28906 Getafe, Spain
3. Department of Chemistry & Pharmacy at the University of Erlangen-Nuremberg, Egerlandstr. 5, 91058 Erlangen, Germany.
4. Laboratoire de Chimie Moléculaire et Thioorganique, Université de Caen Basse Normandie, Boulevard du Maréchal Juin 6, 14050 Caen, France.

+ authors contributed equally.

ADVANCED FUNCTIONAL MATERIALS

www.afm-journal.de

# Rationalizing Fabrication and Design Toward Highly Efficient and Stable Blue Light-Emitting Electrochemical Cells Based on NHC Copper(I) Complexes

*Michael D. Weber, Elisa Fresta, Margaux Elie, Matthias E. Miehlich, Jean-Luc Renaud, Karsten Meyer, Sylvain Gaillard,* and Rubén D. Costa**

**Recently, the use of a new family of electroluminescent copper(I) complexes—i.e., the archetypal [Cu(IPr)(3-Medpa)][$PF_6$] complex; IPr: 1,3-bis-(2,6-di-iso-propylphenyl)imidazole-2-ylidene; 3-Medpa: 2,2′-bis-(3-methylpyridyl) amine—has led to blue light-emitting electrochemical cells (LECs) featuring luminances of 20 cd $m^{-2}$, stabilities of 4 mJ, and efficiencies of 0.17 cd $A^{-1}$. Herein, this study rationalizes how to enhance these figures-of-merit optimizing both device fabrication and design. On one hand, a comprehensive spectroscopic and electrochemical study reveals the degradation of this novel emitter in common solvents used for LEC fabrication, as well as the impact on the photoluminescence features of thin-films. On the other hand, spectroelectrochemical and electrochemical impedance spectroscopy assays suggest that the device performance is strongly limited by the irreversible formation of oxidized species that mainly act as carrier trappers and luminance quenchers. Based on all of the aforementioned, device optimization was realized using ionic additives and a hole transporter either as a host–guest or as a multilayered architecture approach to decouple hole/electron injection. The latter significantly enhances the LEC performance, reaching luminances of 160 cd $m^{-2}$, stabilities of 32.7 mJ, and efficiencies of 1.2 cd $A^{-1}$. Overall, this work highlights the need of optimizing both device fabrication and design toward highly efficient and stable LECs based on cationic copper(I) complexes.**

## 1. Introduction

Although the discovery of ionic transition metal complexes (iTMCs) based on copper(I) metal ion by McMillin and co-workers—hereafter abbreviated as Cu-iTMCs—dates back to the mid 1960s,[1,2] this family of luminescent materials has recently emerged as novel emitters for organic light-emitting diodes (OLEDs)[3,4] and light-emitting electrochemical cells (LECs).[5,6] The root interest in Cu-iTMCs sets by (i) the low price and abundance of copper in the earth crust, (ii) the $d^{10}$-electron configuration of Cu(I) that eliminates the quenching mechanism via metal-centered excited states, (iii) the moderately high photoluminescence quantum yields (PLQYs) due to the metal-to-ligand charge transfer (MLCT) nature of the emitting excited state, and (iv) the thermally activated delayed fluorescence (TADF) or singlet harvesting emission mechanism that numerous Cu(I) complexes present and that has recently been exploited to achieve highly efficient lighting devices.[7–12]

As a matter of fact, this sort of electroluminescent materials have recently led to important breakthroughs in OLEDs, catching more and more attention of the scientific community.[3,4,13–25] It is, therefore, surprising that there are few contributions about LECs based on Cu-iTMCs.[26,27,14,28–44] Indeed, there are only three families of Cu-iTMCs that have been explored, namely (i) homoleptic/heteroleptic Cu-iTMCs bearing diimine (N^N), diphosphine (P^P), and phosphineamide (P^N) ligands—i.e., $[Cu(N^N)_2]^+$, $[Cu(P^P)_2]^+$, and $[Cu(N^N)(P^P)]^+$,[14,28,29,33,35–41] (ii) dinuclear Cu-iTMC—i.e., $[Cu_2(P^P)_2]^+$,[26,34] $[Cu_2(P^N)_2]$,[31] and very recently (iii) the NHC Cu-iTMCs—i.e., $[CuNHC(N^N)]^+$ where NHC is N-heterocyclic carbene.[42–44] Despite huge efforts of the LEC community in designing new complexes toward enhanced devices, state-of-the-art performance using the first and second families of Cu-iTMCs involves efficiencies of 0.1–5 and 0.05–0.1 cd $A^{-1}$ in concert with stabilities of several hours and minutes, respectively.[5] The latter were noted for yellowish orange and/or greenish yellow emitting devices. The recent family of NHC Cu-iTMCs has led to blue- and green-emitting LECs, featuring efficiencies up to 0.2 cd $A^{-1}$ with stabilities of a few seconds.[42–44]

M. D. Weber, Dr. R. D. Costa
Department of Chemistry and Pharmacy, Physical Chemistry I
Friedrich-Alexander-University Erlangen-Nürnberg (FAU)
Egerlandstraße 3, D-91058 Erlangen, Germany
E-mail: ruben.costa@imdea.org
E. Miehlich, Prof. K. Meyer
Department of Chemistry and Pharmacy, Inorganic Chemistry
Friedrich-Alexander-University Erlangen-Nürnberg (FAU)
Egerlandstraße 1, D-91058 Erlangen, Germany
E. Fresta, Dr. R. D. Costa
IMDEA Materials Institute
Calle Eric Kandel 2, 28906 Getafe, Spain
Dr. M. Elie, Prof. J.-L. Renaud, Dr. S. Gaillard
Normandie Univ., LCMT
ENSICAEN, UNICAEN, CNRS, 14000 Caen, France
E-mail: sylvain.gaillard@ensicaen.fr
The ORCID identification number(s) for the author(s) of this article can be found under https://doi.org/10.1002/adfm.201707423.

DOI: 10.1002/adfm.201707423

 

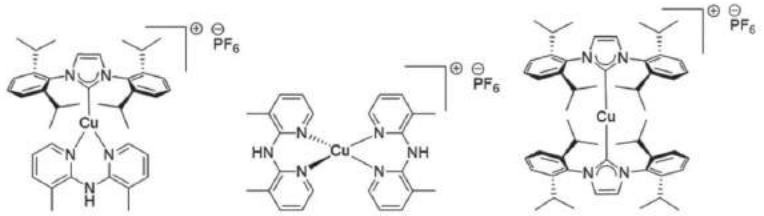


**Figure 1.** Molecular structures of [Cu(IPr)(3-Medpa)][$PF_6$] (**1**), [Cu(3-Medpa)$_2$][$PF_6$] (**2**), and [Cu(IPr)$_2$][$PF_6$] (**3**).

In view of the aforementioned, Cu-iTMC-based LECs have not reached their maximum potential by far, especially if we take into account the recent breakthroughs in OLEDs.[3,4] Strikingly, the underlying reasons are still unanswered. To date, two hints can, however, be elucidated upon close inspection of the literature. First, similar to what has early been noted in OLEDs based on copper(I) complexes, care has to be taken with respect to their degradation using solvent-based deposition techniques. Indeed, OLED breakthroughs have mainly been achieved using films of neutral copper(I) complexes prepared via physical vapor deposition techniques.[23] The latter is not suitable for LEC fabrication as the active layer consists of a blend of the emitter with ionic electrolytes in solution. Here, it is of utmost relevance to point out that, for example, Nierengarten and Armaroli groups have recently stated that, although the synthesis of [Cu(N^N)(P^P)]$^+$ is apparently very simple, [Cu(N^N)$_2$]$^+$ and [Cu$_2$(P^P)$_3$]$^+$ species are easily formed during the synthesis or over time in solution.[45–47] Among them, [Cu(N^N)$_2$]$^+$ species are the major by-product and are also extremely efficient luminescent quenchers. Therefore, traces can dramatically reduce the device performance. In other words, not only the synthesis and purification steps are critical aspects, but also the conditions of preparing the active layer—i.e., type of solvent, aging time, deposition technique, atmosphere, temperature, etc. The latter needs to be carefully optimized to prepare thin films with a homogenous morphology in concert with high PLQYs. Second, the emitter used in LECs is also responsible for both carrier injection and transport processes. As such, the formation of undesired species upon charge injection cannot be ruled out under device operation conditions. They could be detrimental in terms of device efficiency and stability—e.g., irreversible degradation of the emitter, emission quenching, carrier trapping, etc. Thus, it is all important to provide a solid understanding about the changes of the photophysical/electrochemical features of Cu-iTMCs during both device fabrication and operation conditions to optimize the device design—e.g., pretreatment of the solutions, use of neutral and ionic additives, new architectures for the active layer, etc.—toward future breakthroughs in LECs based on Cu-iTMCs.

Herein, this work focuses on rationalizing how to enhance the performance of LECs based on the most recent family of copper(I) emitters—i.e., NHC Cu-iTMCs—with respect to both device fabrication and design. In early works, we have demonstrated how to enhance PLQYs through a fine ligand optimization, leading to devices with a moderate performance—vide supra.[42–44] In this follow-up work, we rationalize how to significantly boost the device performance of more than one order of magnitude revealing three major findings. First, we elucidated for the first time the degradation mechanism of the archetypal NHC Cu-iTMC—i.e., [Cu(IPr)(3-Medpa)][$PF_6$] (**1**) where IPr is 1,3-bis(2,6-di-iso-propylphenyl)imidazole-2-ylidene and 3-Medpa is 2,2′-bis-(3-methylpyridyl)amine, as shown in **Figure 1**—going all the way from the synthesis to the preparation of thin-films using common solvents for LEC fabrication. Second, we determine the underlying reasons for the moderate device performance, combining spectro-electrochemical and electrochemical impedance spectroscopy (EIS) assays. Based on the gathered information, the third major aspect of this work is the investigation of several strategies to optimize the device performance using ionic additives and hole transporters either in a single-layered configuration as a host–guest approach or in a multilayered device architecture to decouple hole/electron injection. Among them, the latter provided LECs with luminances of 160 cd m$^{-2}$, efficiencies of 1.2 cd A$^{-1}$, and stabilities of 32.7 mJ. This optimization represents a significant enhancement compared to the performance of previous LECs elaborated with NHC copper(I) complexes. Finally, we strongly believe that both the device fabrication and design could easily be extrapolated to other families of Cu-iTMCs.

## 2. Results and Discussion

### 2.1. Notes about the Synthesis of NHC-Cu-iTMCs

Complex **1** was synthesized following the reported procedure, starting from [CuCl(IPr)] and the 2,2′-(3-methylpyridyl)amine (3-Medpa).[42] It is worth noting that the synthesis must be performed under argon atmosphere with degassed absolute ethanol to have the pure product as a white precipitate. The CH–$\pi$ interaction between the hydrogen atom in $\alpha$-position of the nitrogen atom of the pyridine ring in 3-Medpa and the *N* aromatic substituent of the NHC plays a pivotal role with respect to the air and moisture stability in solid-state. Moreover, the Cu–$C_{IPr}$ bond has a strong $\sigma$-donor character prompting to decoordinate the NHC via transmetallation reaction.[48] This led us to select the NHC ligand family to tackle the drawback of heteroleptic tetracoordinated copper(I) complexes described by Nierengarten and co-workers—i.e., the dissociation–recombination process that can appear in solution.[30] However, for a better understanding of the complexes' behavior upon device preparation, we synthesized the homoleptic copper(I) complex

$[Cu(3\text{-Medpa})_2][PF_6]$ (**2**)—Figure 1. In short, the synthesis consisted of mixing $[Cu(CH_3CN)_4][PF_6]$ and 2 equivalents of the 3-Medpa ligand in degassed dichloromethane furnishing the expected complex **2** as a yellow precipitate—see the Supporting Information for details about the $^1H$ and $^{13}C$ NMR data shown in Figures S1 and S2, respectively. Finally, the remaining homoleptic copper(I) complex is $[Cu(IPr)_2][PF_6]$ (**3**) (Figure 1) that has been already reported and its spectroscopic features have been used for comparison purposes.[49]

### 2.2. Notes about the Degradation Mechanism of NHC-Cu-iTMCs in Solution

The typical procedure to prepare iTMC-based films for LECs involve the use of solvent-based coating techniques—e.g., spin-coating and doctor-blading—using tetrahydrofuran (THF) and acetonitrile (MeCN) as the most representative solvents.[5,6] Although NHC-Cu-iTMCs shows a sound stability in powder,[42–44] there is little known about its stability in solution. Thus, our first focus was to investigate its stability in both solvents, monitoring the changes of the absorption features over time under ambient conditions—see the Experimental Section for details. As shown in **Figure 2**, the absorption spectrum of fresh solutions consists of two bands in the UV region centered at ≈300 nm and ascribed to $d\pi$–$\pi^*$ MLCT absorption nature independently of the solvent. Upon storage under ambient and dark conditions, a distinct behavior over time was observed for both solutions—Figure 2. While a new well-structured band centered at 350–400 nm evolves in THF after a few minutes reaching a steady plateau after ≈2 h, the absorption features in MeCN solutions remain unchanged during this timeframe, showing the same new low-energy band only after several days upon storage (Figure 2). Three reasons might likely explain the new absorption features, namely, (i) the formation of homoleptic complexes like **2** and **3**,[49] (ii) a solvent-assisted ligand exchange process as both solvents show coordination features,[45,50,51] and (iii) the spontaneous formation of copper(II) compounds.[52–54]

To further investigate this behavior, we firstly compared the changes of the absorption features of **2** over time with those obtained for **1**. The homoleptic complex also shows a quick formation of the low-energy absorption band independently of the solvent (Figure S3, Supporting Information). This suggests that the same reaction takes place over time for both heteroleptic and homoleptic complexes. In other words, we can qualitatively discard the formation of homoleptic complexes, but neither a ligand exchange reaction with surrounding solvent molecules nor the formation of copper(II) complexes. If the former occurs, the new species should not feature low-energy absorption bands, as the coordination of the solvent does not introduce low lying molecular orbitals levels in the electronic structure upon replacing the 3-Medpa ligand. Thus, it is quite unlikely to monitor the new species via steady-state absorption assays. As such, time-dependent $^1H$ nuclear magnetic resonance (NMR) and electron paramagnetic resonance (EPR) spectroscopy experiments were performed in both solvents—see the Experimental Section for details, and **Figures 3** and **4** and Figure S4 (Supporting Information). On one hand, the $^1H$-NMR analysis of **1** was performed every 15 min during 3 h in $CD_3CN$ and $d_8$-THF under ambient conditions—Figure 3 and Figure S4 (Supporting Information). In $CD_3CN$, signals of the coalescence of the 3-Medpa ligand were immediately observed, indicating a fast solvent-assisted dissociation–recombination of the 3-Medpa ligand. In $d_8$-THF, no coalescence of the signals and no new signals were detected after 3 h. Finally, no new proton signals corresponding to both homoleptic complexes **2** and **3** were observed for both solvents, confirming that their formation upon film forming can be discarded. On the other hand, low-temperature, time-dependent EPR assays were performed on $1.1 \times 10^{-3}$ M samples of **1** in THF and MeCN at 90 K—Figure 4. This allowed us to investigate its oxidative degradation in solution at room temperature over aging times of 0, 2, 24, and 48 h. In THF, an axial signal at $g = 2.055$ instantaneously evolved exhibiting hyperfine coupling associated to a Cu ($^{63}Cu$: I = 3/2, 69.17%, $^{65}Cu$: I = 3/2, 30.83%) nucleus. This suggests the presence of copper(II) complexes. As expected, an increase of the signal's intensity was noted over time. A simulation of the EPR spectrum measured after 24 h showed effective g-values at $g_1 = g_2 = 2.055$ and $g_3 = 2.248$, hyperfine coupling with $A_3 = 555$ MHz (18.69 mT), and line-widths of $W_1 = W_2 = 3.3$ mT and $W_3 = 2.4$ mT. Moreover, the high intensity of the signal after 49 h allowed us to obtain an excellent resolution of superhyperfine coupling to four $^{14}N$ (I = 1, 99.6%) nuclei, suggesting the presence of homoleptic copper(II) species as simulated with g-values at $g_1 = 2.045$, $g_2 = 2.060$, and $g_3 = 2.255$, line widths of $W_1 = 0.4$ mT, $W_2 = 0.6$ mT, and $W_3 = 0.2$ mT, hyperfine coupling to a Cu ($^{63}Cu$: I = 3/2, 69.17%, $^{65}Cu$: I = 3/2, 30.83%) nucleus with $A_3(Cu) = 530$ MHz (17.84 mT), and superhyperfine coupling to four N ($^{14}N$: I = 1,

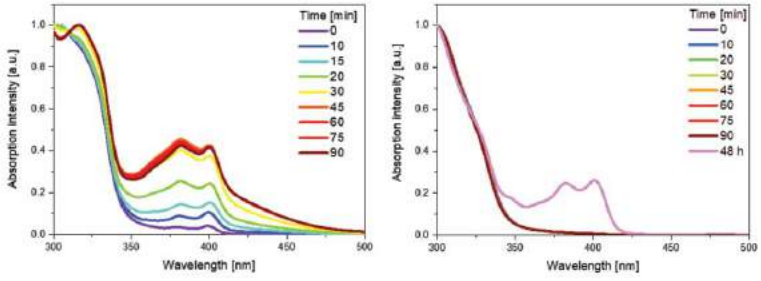


**Figure 2.** Absorption spectra over time of **1** ($1 \times 10^{-6}$ M) in THF (left) and MeCN (right) upon storage under ambient and dark conditions.

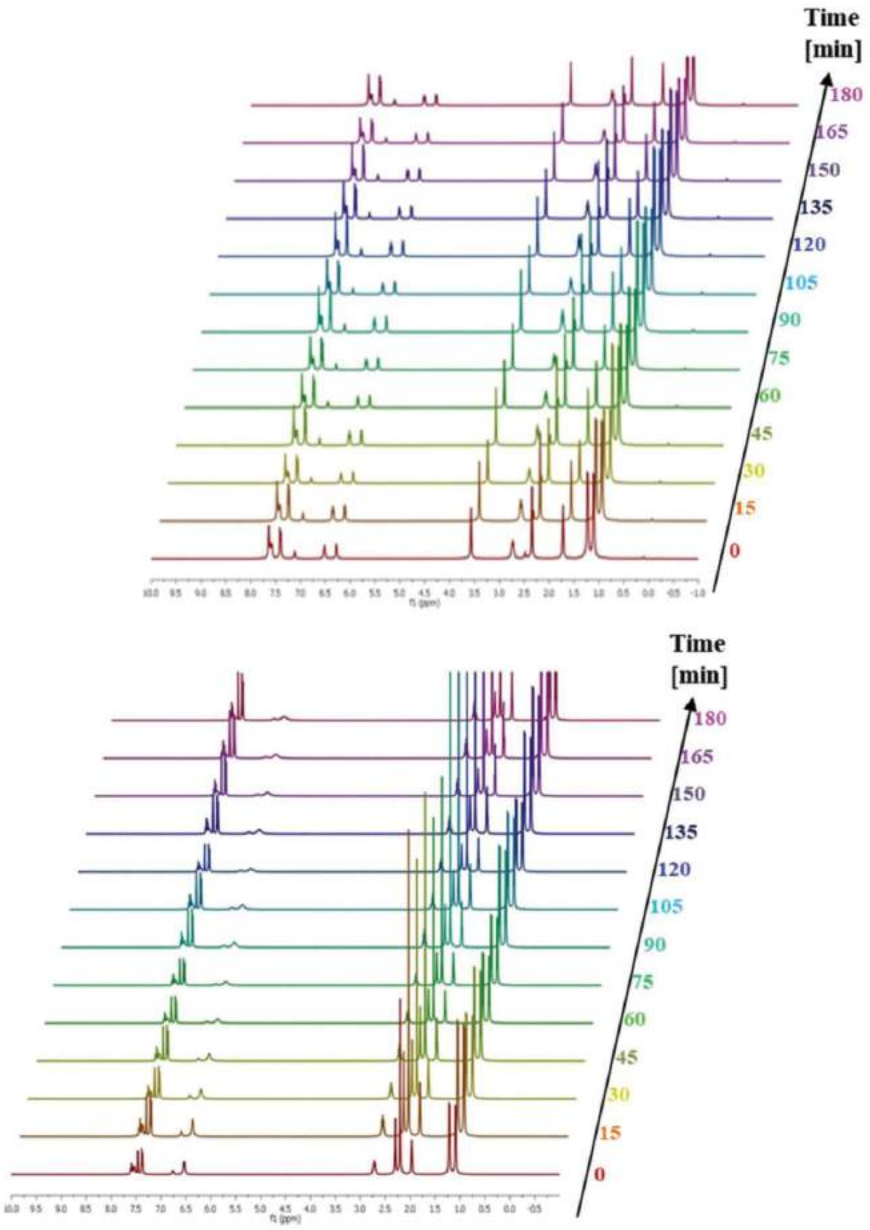


**Figure 3.** $^1$H-NMR spectra (400 MHz, 298 K) over time of **1** in THF-$d_8$ (top) and $CD_3CN$ (bottom).

99.64%) nuclei with $A_1$(N) = 23 MHz (0.77 mT), $A_2$(N) = 29 MHz (0.98 mT), and $A_3$(N) = 38 MHz (1.28 mT) only after long periods of time. On the contrary, MeCN solutions showed the formation of a similar, slightly rhombic EPR signal developing significantly slower than in THF. In detail, the EPR spectrum of MeCN solutions aged for 24 h was simulated with

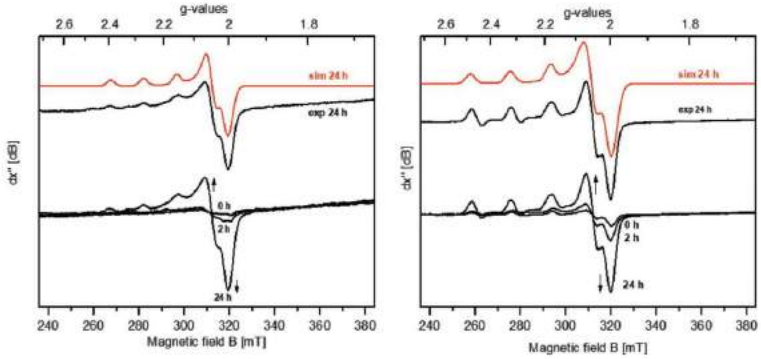


**Figure 4.** CW X-band EPR-monitored time-depending degradation of **1** in $1 \times 10^{-3}$ M frozen solutions of MeCN (left) and THF (right) at 90 K after 0, 2, and 24 h (black traces). Simulation of the measurement in the respective solvent after 24 h is depicted with the red trace. Detailed experimental and simulation parameters can be found in the Experimental Section.

effective g-values of $g_1 = 2.040$, $g_2 = 2.055$, and $g_3 = 2.218$, hyperfine coupling of $A_3 = 450$ MHz (15.27 mT) and line-widths of $W_1 = 2.8$ mT, $W_2 = 3.0$ mT, and $W_3 = 2.0$ mT. Here, the resolution of superhyperfine coupling was not possible due to the low intensity of the signal. Please notice that the slight deviation of the g-values of the predominant oxidation process in both solvents is likely related to different solvent matrices or possible coordination of solvent molecules.

In view of all the aforementioned, there are two prominent degradation mechanisms for NHC-Cu-iTMCs in solution, that is, the irreversible solvent-assisted ligand exchange reaction and the formation of copper(II) species that are prominent in MeCN and THF, respectively. Noteworthy, the typical formation of homoleptic complexes (**2** and **3**) is only noted upon aging the solutions for more than 24 h. As a next step, we turned to investigate the impact of the presence of these species on the morphology and photoluminescence features of thin-films.

### 2.3. Notes about the Morphology and the Photophysical Features of Thin Films

Pristine 100 nm films were prepared from aged solutions of **1** in THF and MeCN via doctor blading—see the Experimental Section for details. The films were stored under dark and ambient conditions. Atomic force microscopy (AFM) assays confirmed that all of them were homogenous with no particular aggregation or phase separation features with a less than 1 nm root mean square (RMS) roughness—**Figure 5** and Figure S5 (Supporting Information). In contrast to the results noted in solution, both absorption and emission features of films prepared from fresh solutions—i.e., less than 1 min aged solutions—are unchanged over long periods of time under ambient conditions (Figure 5), suggesting a significant stability similar to that noted in powder.[43] In addition, the emission features of the films prepared from fresh solutions are similar to those in powder and also stable over time (Figure 5). In detail, thin films featured emission spectra with a well-structured shape centered at 425 and around 470 nm (Figure 5), while PLQYs are superior to 75% regardless of the solvent used. However, striking enough, significant changes of the PLQYs of films prepared from the aged solutions were noted (**Figure 6**). In particular, the aged films prepared from THF show no significant change in the PLQYs after aging time of 1 h, while the PLQYs of films prepared with MeCN dramatically drop in this timeframe. Hence, it is safe to conclude that the irreversible ligand exchange process in MeCN has a dramatic impact on the luminescent features, as these species act as strong quenchers, while the presence of oxidized species has a neglectable impact on the luminescent features. This finding clearly confirms that THF should be considered as the best choice for device fabrication.

### 2.4. Notes about the Performance and Degradation Mechanism of Nonoptimized Devices

As above described, both the morphology and photoluminescence features of pristine films prepared from fresh, degassed, and anhydrous THF solutions of **1** are optimum for device fabrication. The latter were finalized by evaporating a 90 nm aluminium cathode onto the active layer. These devices were probed using a pulsed 2.0 mA current driving scheme based on a block-wave at 1000 Hz and a duty cycle of 50%. As noted in our previous paper,[43] the device color holds upon driving at lower currents, featuring a blue electroluminescent response with a spectrum centered at around 500 nm and $x/y$ Commission Internationale de l'Éclairage 1931 (CIE) color coordinates of 0.23/0.28. These devices show instantaneous luminances of ≈20 cd $m^{-2}$, efficiencies of 0.17 cd $A^{-1}$, and stabilities measured with a total emitted energy ($E_{tot}$) of 4 mJ (**Figure 7**). Here, the device stability is characterized using the $E_{tot}$ parameter taking the time needed to reach one fifth of the maximum luminance as the upper limit. This approach allows a clear stability comparison of devices showing different luminance levels as indicated by Bard and co-workers.[55]

It is important to point out that the brightness decays exponentially, as the profile of the applied voltage remains constant.

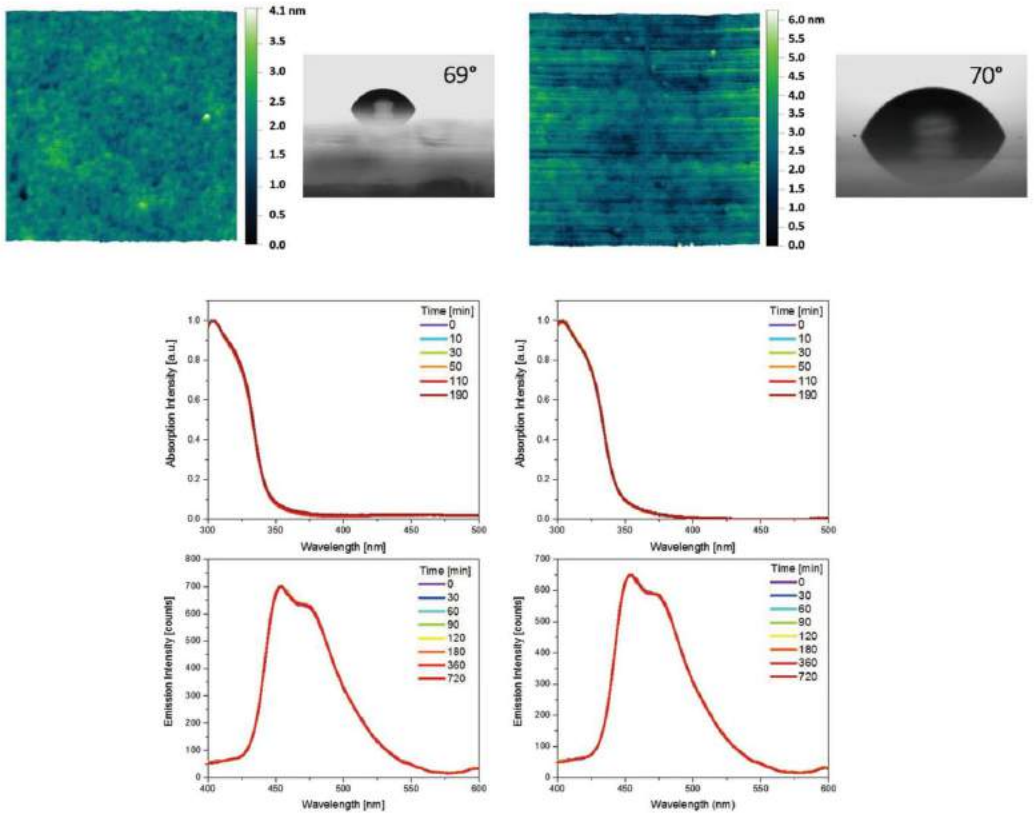


**Figure 5.** Upper part: AFM (left) and water static contact angle (right) measurements of **1** thin-films prepared from THF (left) and MeCN (right) solutions under ambient conditions. Central part: Absorption spectra over time of **1** thin films prepared from fresh THF (left) and MeCN (right) solutions under ambient conditions. Lower part: Emission spectra over time of **1** thin films prepared from fresh THF (left) and MeCN (right) solutions under ambient conditions.

This suggests that the low device stability might be related to a quick reduction of the p–i–n emitting region and/or the formation of degradation species that act as luminescent quenchers of the formed excitons. We discard the formation of black spots or pinholes as a possible reason, as we did not observe their formation using an optical microscope upon the whole lifespan of the device. This is expected because AFM assays have already showed the homogenous morphology of the active layer (Figure 5).

To further study the changes in the electrical behavior of the devices before and after being driven, static EIS assays at different applied voltages were performed in fresh and used devices—see the Experimental Section, and Figure 7 and Figure S6 (Supporting Information). The EIS analysis of the Nyquist plots was conducted using a single resistor/capacitor equivalent circuit model that relates to the two dominant dynamic processes upon increasing the applied voltage (Figure S6, Supporting Information). Typically, Nyquist plots consist of one semicircle whose diameter relates to the resistance associated to the dynamics of the electrical double layer (EDL) formation at the electrode interface under applied voltages lower than the band gap of the emitter (i.e., 3–3.5 eV) and the reduction of the intrinsic nondoped region when charge injection is effective (>3.5 eV). This is related to the formation of the EDLs due to the slow movement of the mobile anions toward the electrode interfaces until charge injection is efficient. At this point, the p- and n-doped regions start to grow reducing the p–i–n region and leading to a linear decrease of the resistance profile due to the ohmic charge injection.[56–61]

By stark contrast, used devices showed an overall increase of the resistance, while the resistance profile decays in a linear fashion. This is in line with the reduction of the total ionic conductivity ($\sigma$) and the dielectrical constant ($\varepsilon$) upon comparing fresh and used devices, i.e., $5.61 \times 10^{-8}$ S m$^{-1}$ and 10.0 and $1.37 \times 10^{-8}$ S m$^{-1}$ and 8.6, respectively. In other words, these findings suggest that the degradation of the devices could

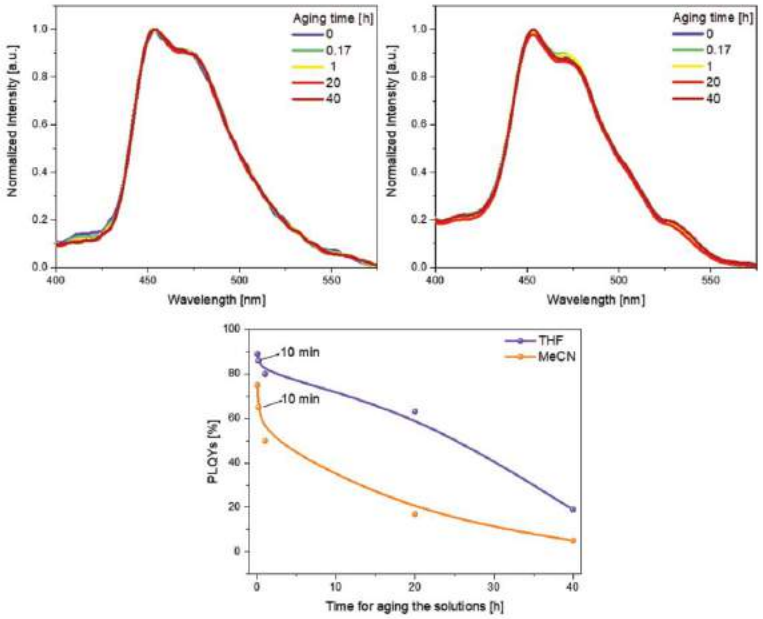


**Figure 6.** Upper part: Emission spectra of **1** films prepared from aged solutions in THF (left) and MeCN (right). Lower part: Changes of the PLQYs of **1** films prepared from aged solutions in THF and MeCN.

involve the formation of species that act as both carrier disrupters and luminescent quenchers.

To further corroborate this notion, we turned to perform cyclovoltammetry and spectro-electrochemistry measurements—see the Experimental Section for details. As shown in Figure 8, **1** shows two quasireversible oxidations at 0.95 and 1.40 V versus $Fc/Fc^+$, while only one quasireversible reduction process at −2.00 V versus $Fc/Fc^+$. Based on previous theoretical studies,[42–44] the first oxidation and reduction processes are located at the dπ–Cu–3-Medpa and the 3-Medpa moieties, respectively. Although both oxidation and reduction processes could be considered as *quasi*-reversible, their impact on the photoluminescence features needs to be determined. Indeed, the effective quenching of the excitons caused by the proximity of oxidized and reduced species is one of the main reasons for the luminance decay in LECs. Therefore, it is of utmost relevance to determine if the redox processes have an impact on the photoluminescence features and whether this is reversible or irreversible. To this end, we performed spectro-electrochemical assays, in which the emission features were monitored upon applying a cyclic voltage loop from 0 to either 1.0 or −2.0 V and back to 0 V to avoid over oxidation and/or reductions processes. Upon oxidation, the emission intensity is significantly reduced, but, more importantly, this is not recovered upon

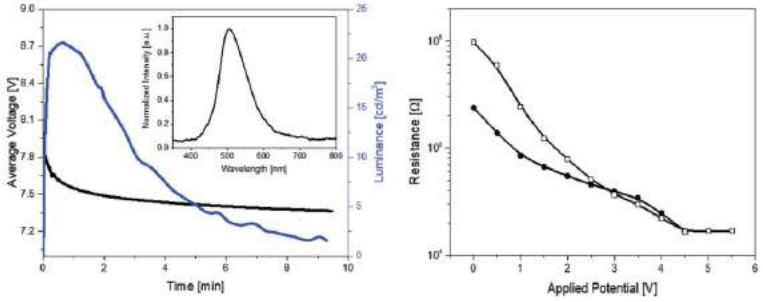


**Figure 7.** Left part: Luminance and average voltage over time of devices with **1** driven at applied pulsed current of 2 mA. The inset graph shows the electroluminescence spectrum of the device. Right part: Resistance changes versus applied potential derived from EIS assays performed on devices with **1** before (solid symbol) and after (open symbol) operation.

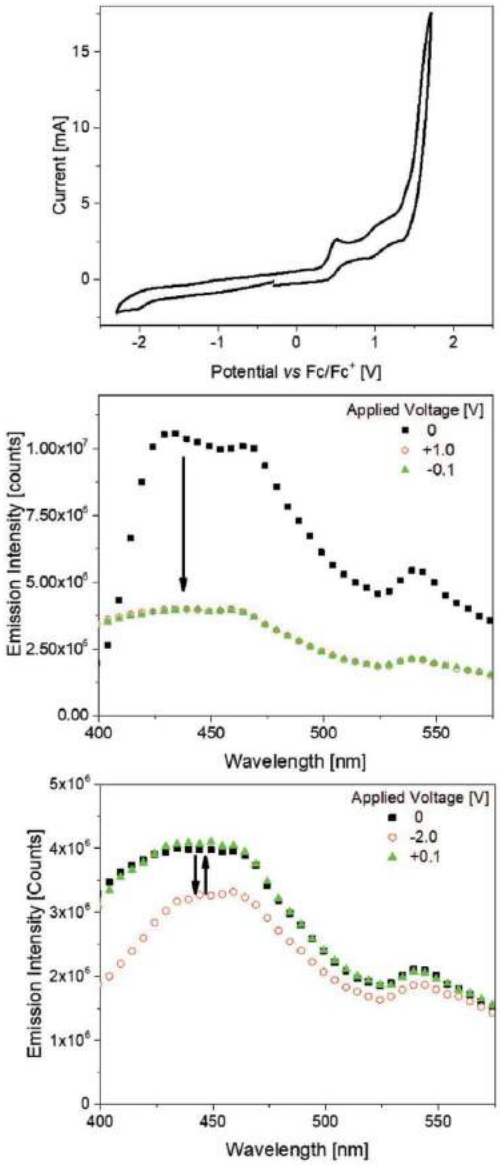


**Figure 8.** Upper part: Cyclovoltammetry of **1** versus standard reference $Fc/Fc^+$ (0.45 V) using 0.1 M tetrabutylammonium hexafluorophosphate ([TBA][$PF_6$]) electrolyte. Central and lower parts: Spectro-electrochemical assays of **1** under different oxidation (central) and reduction (lower) applied voltages upon excitation of 320 nm using conditions above.

applying −0.1 V (Figure 8), suggesting that the *quasi*-reversible formation of the oxidized species has a dramatic impact on the photoluminescence features. In stark contrast, the reduction process shows a total recovery of the emission intensity without showing any change in the emission band shape. In light of these results, we postulate that the injection of holes in **1** leads to the irreversible formation of oxidized species that act as both efficient quenchers of the remaining emitting molecules placed in the p–i–n region and carrier trappers, as indicated by the EIS assays. As such, in order to enhance the device performance, it is necessary to decouple hole/electron injection and transport processes without affecting exciton formation under device operation conditions.

### 2.5. Device Optimization

We explore how to enhance the device performance following two approaches, namely, (i) the use of ionic additives like ionic liquids and ionic polyelectrolytes—i.e., 1,3-butylmethylimidazolium hexafluorophosphate ([BMIM][$PF_6$]) in a 4:1 molar ratio with respect to **1** and an ionic polyelectrolyte that consists of hydroxyl-terminated trimethylolpropane ethoxylate (TMPE) and the inorganic salt lithium trifluoromethanesulfonate ($LiCF_3SO_3$) in a 1:0.1:0.03 mass ratio of **1**:TMPE:$LiCF_3SO_3$—that commonly lead to enhanced brightness and turn-on time values, associated with a detrimental impact on the device stability,[5,6,62–64] and (ii) the use of hole transport compounds implemented either as a host in a single-layered device or as an interlayer in a multi-layered device configuration—*vide infra*.[65,66]

Concerning the first strategy, pristine thin-films based on **1** were compared with those containing different ionic additives—see the Experimental Section. Although all of them seem to be homogeneous to the naked eye, AFM assays show a very different scenario (**Figure 9**). In contrast to the homogenous morphology of pristine **1** films (Figure 5), those with the additives are best described as rough films—i.e., 57.8 and 32.7 nm RMS roughness for films with the ionic liquid and the ionic polyelectrolyte additives, respectively—due to the formation of large orientated aggreates or crystalline domains (Figure 9). This is independent of the type of deposition technique and conditions—see the Experimental Section. Thus, the use of ionic additives was discarded for the optimization of LECs based on NHC copper(I) complexes.

To this end, we decided to use the hole transport material 4,4′-bis(*N*-carbazolyl)-1,1′-biphenyl (CBP) for preparing two sets of devices, as shown in **Figure 10**. In detail, we investigated the use of the common host–guest approach—i.e., a single active layer based on mixture of CBP as host and **1** as guest in mass ratio of 10, 20, 30, and 50 wt%—and a bilayer device architecture, i.e., a device with the configuration indium tin oxide (ITO)/CBP:**1**/Al, in which CBP acts as a hole injection/transport layer and features thicknesses varying from 15 to 25, and to 60 nm, and **1** acts as electron-transport as well electron–hole recombination layer. We selected CBP among other hole transport matrices due to (i) the reversible oxidation and reduction processes that ensure a stable n- and p-electrochemical doping, and (ii) its wide electrochemical band-gap, in which the highest-occupied molecular orbital and lowest-unoccupied molecular orbital levels of **1** are embedded, ensuring the formation of singlet and triplet excitons via efficient electron and hole trapping at only **1**.

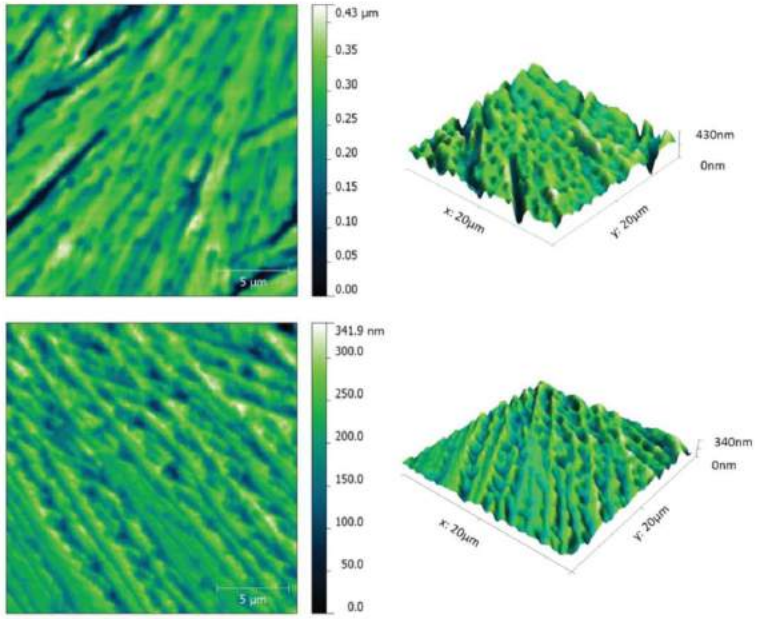


**Figure 9.** AFM images of films based on **1** with either ionic liquids (top) or ionic polyelectrolytes (bottom).

Next, we investigated the morphology of films prepared with mixtures of CBP:**1** in a 90:10, 70:30, and 50:50 mass ratio by means of AFM assays—see the Experimental Section for details. With the exception of the 90:10 films that showed phase separation features, all the blended films presented a homogenous morphology with comparable RMS roughness (Figure S7, Supporting Information). Thus, we finalized the device by evaporating 90 nm of Al as cathode onto the films. **Figure 11** displays representative examples of the electroluminescence spectra of devices with active layers CBP:**1** of 90:10, 80:20, 70:30, and 50:50 wt% under luminance-current-voltage (LIV) sweep experiments. Here, devices with a CBP:**1** (90:10 and 80:20 wt%) active layers feature an electroluminescence spectrum that consists of three peaks centred at ≈430, ≈485, and ≈595 nm, which are ascribed to the CBP electroluminescence response. In other words, the energy transfer process from CBP to **1** seems to be not operative at these active layer compositions. Indeed, devices with a CBP:**1** (70:30 wt%) active layer feature an electroluminescence response with maxima at 430 and 500 nm that are related to the remaining electroluminescence response of the CBP and that of **1**, respectively. Only devices with a CBP:**1** 50:50 wt% start to feature a broad electroluminescence emission band whose maximum corresponds to the EL response of LECs based on **1** (Figures 5 and 11). Overall, these results indicate that, even though the formation of excitons in **1** might be efficient via charge trapping, the other energy transfer processes based on Förster resonance (FRET) and Dexter energy transfer are not efficient. Here, the FRET process mainly depends on (i) the spectral overlap of the emission of the CBP and the absorption spectrum of **1** and (ii) the distance between both compounds, as the efficiency of the FRET is inversely proportional to the sixth power of the distance.[67] As shown in Figure S8 (Supporting Information), there is a very poor spectra-overlapping between both compounds due to the high optical band gap of **1**. In addition, the Dexter mechanism, which is responsible of the triplet exciton transfer from the host to the guest via an electron-exchange process,[68] might be not operative at low amounts of **1**. This might be

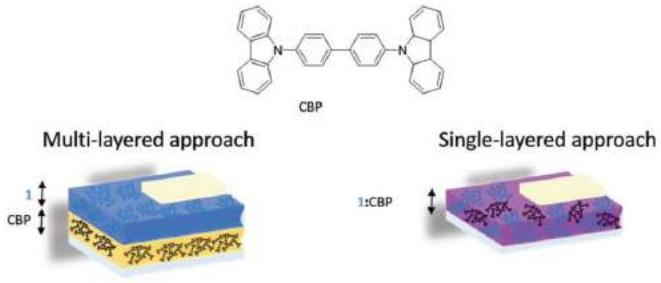


**Figure 10.** Scheme underlying the strategy for the optimization of the device performance using CBP in a single-layered and multi-layered device configuration.

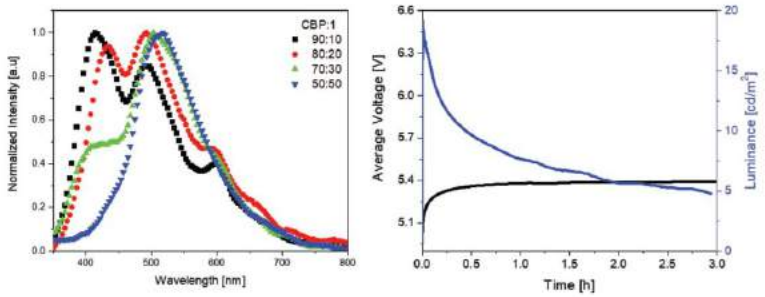


**Figure 11.** Left part: Electroluminescence spectra of devices with different blending ratios of CBP:1. Right part: Luminance and average voltage over time of devices with CBP:1 (50:50 wt%) active layer driven at applied pulsed current of 2 mA.

related to either a lack of overlapping between the wave functions of the excited states of the CBP and 1 or to the emission mechanism of 1 from the singlet excited state after its repopulation via TADF.[43,44] Besides this finding, we probed a CBP:1 (50:50 wt%) active layer by using the same driving scheme as the pristine devices (Figure 11). A direct comparison with the reference device indicates that both the luminance (19 cd $m^{-2}$) and the efficacy (0.15 cd $A^{-1}$) values are similar to those of the reference device, but the device stability is enhanced by a factor of 6, reaching an $E_{tot}$ of 24.6 mJ. This highlights the benefits of adding hole transporting materials to alleviate the degradation process via hole injection and/or transport through the active layer.

Since the CBP might only enhance hole injection and transport processes without showing an efficient energy transfer process to 1, it is more convenient to follow the recent approach of Edman and co-workers,[65,66] that is, to fabricate multi-layered devices, in which pure CBP layers of different thicknesses—i.e., 15, 25, and 60 nm—are previously deposited onto the electrode followed by a deposition of a pristine 1 layer (90 nm) onto the CBP layer—see the Experimental Section for details. The success of our approach was confirmed by the change of the water contact angle from 100° to 70° for CBP and CBP|1 films, respectively (Figure S9, Supporting Information). The latter nicely corresponds to that of pristine films with 1 (Figure 5). Much more importantly, the bilayer devices also showed a similar homogenous morphology to that of the pristine films with 1 (Figure 5 and Figure S9, Supporting Information). This ensures that the underlying layer is at best only partially dissolved providing a smooth gradient at the CBP|1 interface. Overall, these experiments point to the fact that a bilayer structure has been attained.

Next, the devices were finalized by evaporating 90 nm of Al onto the 1 layer and were driven at the same conditions as the reference device (Figure 12). Strikingly enough, the multi-layered devices with 15, 25, and 60 nm CBP bottom layers featured a significant enhanced device performance in terms of luminances of 170, 160, and 47 cd $m^{-2}$, as well as efficacies of 1.3, 1.2, and 0.35 cd $A^{-1}$, respectively. This significantly contrasts with those of the reference device—i.e., 20 cd $m^{-2}$ and 0.17 cd $A^{-1}$. In addition, the device color is not affected consisting of an electroluminescence band centered at ≈500 nm (Figure S10, Supporting Information). Finally, multilayered devices showed $E_{tot}$ values of 4.8, 32.7, and 2 mJ for multi-layered devices with 15, 25, and 60 nm CBP bottom layers, respectively. As a reference, devices lacking the CBP layer featured a stability of 4 mJ. As such, the device architecture CBP|1 (25 nm|90 nm) clearly outperformed the reference devices based on 1 with an almost one order of magnitude enhancement. Please notice that, though fabricated with a multi-layered architecture, our devices cannot be considered solution-processed OLEDs as they show the typical working mechanism of LECs with an initial peak voltage followed by a slow decay to the steady-state regime under constant pulsed current (Figure 12). While the former is related to the formation of the p–i–n junction, the latter is ascribed to the autosustained emission from the p–i–n junction.[69]

## 3. Conclusion

After having presented the first studies on LECs based on NHC copper(I) complexes as a new family of emitters for blue- and green-emitting devices, this follow-up work provides valuable insights on how the handling on this family of compounds in solution significantly impacts both morphology and spectroscopic features of thin films used for LEC fabrication. For instance, we have rationalized that the degradation mechanism in THF involves the quick oxidation of the complexes without affecting the PLQY in short-aged solutions, while the degradation mechanism in MeCN involves an efficient ligand exchange that strongly reduces the PLQY of the thin films prepared with short-aged solutions. Nevertheless, LECs prepared with the archetypal NHC copper(I) complex showed blue emission featuring luminances of 20 cd $m^{-2}$, stabilities of 4 mJ, and efficiencies of 0.17 cd $A^{-1}$. Based on joint spectro-electrochemical and EIS experiments, we were able to determine that the device performance is limited during the hole injection process, forming new species that mainly act as carrier trappers and luminance quenchers. This encouraged us to investigate new device designs using ionic additives and hole transporter either as a host–guest or as a multi-layered architecture approach to decouple hole/electron injection. While traditional ionic additives used in LECs are not suitable for the fabrication of LECs based on NHC copper(I) complexes due to the formation of films with a nonhomogenous morphology, the use of a hole transporter (CBP) provided a reasonable enhancement

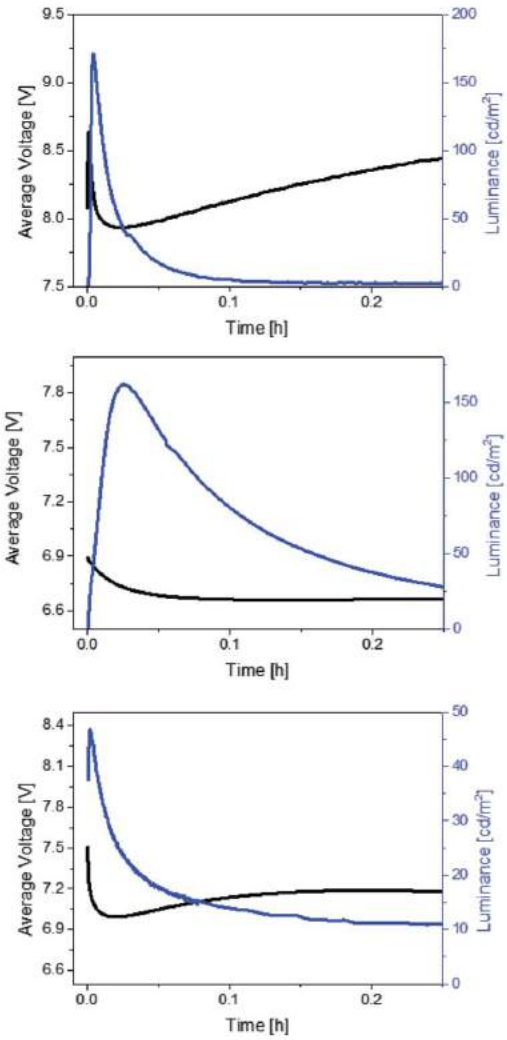


**Figure 12.** Luminance and average voltage over time of CBP|1 devices with 15 nm (upper), 25 nm (central), and 60 nm (lower) CBP bottom layers.

with regard to the device stability—i.e., 4 mJ versus 24.6 and 32.7 mJ for pristine, CBP:1 (50:50 wt%) blended, and CBP|1 (25 nm|90 nm) multi-layered LECs, respectively. However, the use of a hole transporter in a multi-layered architecture turned to be more beneficial in terms of luminances and efficiencies due to both the formation of more homogenous active layers and the accumulation of holes exclusively at the CBP layer interface, while the electron injection, transport and, finally, electron–hole recombination occurs at the layer of **1**. This device design leads to significantly enhanced device figures-of-merit, reaching luminances of 160 cd $m^{-2}$, stabilities of 32.7 mJ, and efficiencies of 1.2 cd $A^{-1}$ that strongly contrast with those of the reference device—vide supra. Overall, this work highlights the need of optimizing both device fabrication and design as new means toward highly efficient and stable LECs based on copper(I) complexes. Here, other neutral and ionic hole transporting materials might be a key to realize this goal and is under investigation in our laboratories.

## 4. Experimental Section

*Materials*: Complex **1** was prepared following the synthesis reported elsewhere.[42] All reactions were carried out using standard Schlenk technique under an atmosphere of dry argon. Solvents were purchased from Carlo Erba and degassed prior to use by bubbling argon gas directly in the solvent. Other materials such as 1-butyl-3-methylimidazolium hexafluorophosphate [BMIM][$PF_6$], $LiCF_3SO_3$ (≥98%), trimethylolpropane ethoxylate ($M_n$≈450 mol wt), acetonitrile, and THF anhydrous (≥99.9%) were purchased from Sigma-Aldrich and used as received. poly(3,4-ethylenedioxythiophene) polystyrene sulfonate (PEDOT:PSS) (Clevios PAI4083) was purchased from Heraeus.

*Characterization Techniques*: Steady-state absorption spectra were recorded with a Perkin Elmer Lambda 35 UV-VIS Spectrophotometer. Steady-state emission spectra were recorded with a Fluoromax-P-spectrometer from HORIBA Jobin Yvon IBH. Photoluminescence quantum yields and emission spectra of thin-films were measured using an Horiba Jobin Yvon Fluoromax-4P spectrofluorometer equipped with an integrating sphere F-3018. Cyclovoltammetry and spectro-electrochemical measurements were carried out in degassed solutions with 0.1 M tetrabutylammonium hexafluorophosphate ([TBA][$PF_6$]) as electrolyte with a Methrom μAutolabIII/FRA3 coupled to an Avantes Avaspec-ULS2048L-USB2 system. Ferrocene was used as internal reference ($Fc/Fc^+$) for all the measurements. NMR spectra were recorded on 500 MHz Bruker spectrometers. Solvents for NMR spectroscopy were dried over molecular sieves. Proton ($^1H$) NMR information is given in the following format: multiplicity (s, singlet; d, doublet; t, triplet; q, quartet; qui, quintet; sex, sextet; sept, septet; m, multiplet), coupling constant(s) (*J*) in Hertz (Hz), number of protons. The prefix app is occasionally applied when the true signal multiplicity was unresolved and *br* indicates that the signal in question is broadened. Carbon ($^{13}C$) NMR spectra are reported in ppm ($\delta$) relative to residual $CHCl_3$ ($\delta$ 77.0) unless noted otherwise.

EPR spectra were recorded on a JEOL continuous wave spectrometer JES-FA200 equipped with an X-band Gunn oscillator bridge, a cylindrical mode cavity, and a nitrogen cryostat. The samples were dissolved in the respective solvent, placed in a quartz EPR tube, frozen in liquid nitrogen, and immediately measured. The spectra of **1** were recorded in $1.1 \times 10^{-3}$ M frozen solutions in MeCN and THF with the following parameters: (i) MeCN: Experimental conditions: $T$ = 90 K, modulation width = 2.0 mT, microwave power = 1 mW, modulation frequency = 100 kHz, time constant = 0.1 s. Spectra were recorded after 0 h ($\nu$ = 8.9536 GHz), 2 h ($\nu$ = 8.9556 GHz), and 24 h ($\nu$ = 8.9560 GHz). Simulation of the measurement after 24 h was performed with the following parameters: $S = 1/2$, $g_1 = 2.040$, $g_2 = 2.055$, $g_3 = 2.218$; $A_1$(Cu) = 0 MHz (0 mT), $A_2$(Cu) = 0 MHz (0 mT), $A_3$(Cu) = 450 MHz (15.27 mT), and $W_1$ = 2.8 mT, $W_2$ = 3.0 mT, $W_3$ = 2.8 mT; (ii) THF: Experimental conditions: $T$ = 90 K, modulation width = 2.0 mT, microwave power = 1 mW, modulation frequency = 100 kHz, time constant = 0.1 s. Spectra were recorded after 0 h ($\nu$ = 8.9554 GHz), 2 h ($\nu$ = 8.9557 GHz), and 24 h ($\nu$ = 8.9556 GHz). Simulation of the measurement after 24 h was performed with the following parameters: $S = 1/2$, $g_1 = g_2 = 2.055$, $g_3 = 2.248$; $A_1$(Cu) = 0 MHz (0 mT), $A_2$(Cu) = 0 MHz (0 mT), $A_3$(Cu) = 555 MHz (18.69 mT), and $W_1 = W_2$ = 3.3 mT, $W_3$ = 2.4 mT. Spectral simulation was performed using the program W95EPR written by Neese.[70] AFM images were performed with VEECO DIMENSION 5000 with probe head from NanoScope V. Water static contact angle measurements were performed in sessile drop mode and DI water (1.0 μL) as probe liquids with a Dataphysics OCA from Data Physics Instruments GmbH.

*Device Fabrication and Characterization*: Devices were fabricated using the following coating protocol: double layer LECs were fabricated with a photo lithographically patterned ITO glass substrate received from Naranjo substrates. The substrates were cleaned by using ultrasonic baths in water/soap, water, ethanol, and propan-2-ol solvents prior to an ozone treatment performed in a Jetlight 42-220 for 8 min. A 90 nm PEDOT:PSS layer was coated by doctor blading technique (Zehtner ZAA 2300 equipped with a ZUA 2000 blade) using a two-step coating process at a speed of 10 and 5 mm $s^{-1}$ on a hotplate at 40 °C and a blade gap of 400 µm to enhance the device preparation yield and to decrease the overall roughness. The emissive layer comprised the pure emitting compound in a concentration of 20 mg $mL^{-1}$ in THF and was coated by means of doctor blading (speed = 2 0 mm $s^{-1}$, HP = 40 °C, blade gap = 600 µm) resulting in films of around 90 nm. Multi-layered devices comprising hole transporting material CBP dissolved in THF at a concentration of 4 mg $mL^{-1}$ were coated via spin-coating in ambient air at three steps with 800, 1000, and 3000 rpm, altering the first step speed to adjust the layer thickness. The devices were backed at 100 °C during 30 min to provide hard films for a second deposition of the layer 1 using the procedure above. For measuring the photophysical properties and imaging the layer morphology in AFM solid state samples on quartz glass were fabricated using the described doctor blading process. All layers were analyzed with a profilometer (DektakxT, Bruker) validating roughness values less than 5% and no apparent optical defects. After this, the samples were transferred into an inert atmosphere glovebox (<0.1 ppm $O_2$ and $H_2O$, Innovative Technology). An Al cathode electrode of 90 nm was thermally evaporated using a shadow mask under high vacuum (<1 × $10^{-6}$ mbar) in an Angstrom Covap evaporator integrated into the inert atmosphere glovebox. Time dependence of luminance, voltage, and current was measured by applying constant and/or pulsed voltage and current by monitoring the desired parameters simultaneously with an Avantes spectrophotometer (Avaspec-ULS2048L-USB2) in conjunction with a calibrated integrated sphere Avasphere 30-Irrad and Botest OLT OLED Lifetime-Test System. Electroluminescence spectra were recorded using the above mentioned spectrophotometer. EIS assays were carried out with a potentiostat/galvanostat (PGSTAT30, Autolab) equipped with a frequency response analyzer module (FRA). Measurements were performed at the applied voltage of 0 V after a LIV sweep from 0 to 6 V. The AC signal amplitude was set to 50 mV, modulated in a frequency range from 1 to $10^6$ Hz. The Nova 1.11 software was used to obtain the parameters from the L-R-R/C equivalent circuit. The film conductivity (S $m^{-1}$) is measured at 0 V with the following equation: $\sigma = d/(AR_i)$, where $d$ is the thickness of the layer, $A$ is the area of the electrodes, and $R_i$ is the resistance of the active layer. The latter was directly obtained from the data at hand.

## Supporting Information

Supporting Information is available from the Wiley Online Library or from the author.

## Acknowledgements

M.D.W. and E.F. contributed equally to this work. This work was supported by the "Ministère de la Recherche et des Nouvelles Technologies," CNRS (Centre National de la Recherche Scientifique) and the LABEX SynOrg (ANR-11-LABX-0029). The authors thank the "Agence Nationale de la Recherche," within the CSOSG program (ANR-12-SECU-0002-02) and the "Région Basse-Normandie" for their funding (M.E.). S.G. thanks Johnson Matthey for the gift of metals. R.D.C. and M.D.W. acknowledge the support by the "Fonds der Chemischen Industrie" (FCI) in the Liebig grant framework. E.F. and R.D.C. acknowledge funding from the Comunidad de Madrid within the frame of the "Atracción de talento Mod 1" with the project 2016-T1/IND-1463 and from the MINECO (RYC-2016-20891).

## Conflict of Interest

The authors declare no conflict of interest.

## Keywords

blue electroluminescence, copper(I) complexes, light-emitting electrochemical cells, multi-layered device design, redox stability

Received: December 21, 2017
Revised: February 1, 2018
Published online: March 8, 2018

[1] M. T. Buckner, D. R. McMillin, *J. Chem. Soc., Chem. Commun.* **1978**, *29*, 759.
[2] R. A. Rader, D. R. Mcmillin, M. T. Buckner, T. G. Matthews, D. J. Casadonte, R. K. Lengel, S. B. Whittaker, L. M. Darmon, F. E. Lytle, *J. Am. Chem. Soc.* **1981**, *103*, 5906.
[3] D. Volz, M. Wallesch, C. Flechon, M. Danz, A. Verma, J. M. Navarro, D. M. Zink, S. Brase, T. Baumann, *Green Chem.* **2015**, *17*, 1988.
[4] F. Dumur, *Org. Electron.* **2015**, *21*, 27.
[5] E. Fresta, R. D. Costa, *J. Mater. Chem. C* **2017**, *5*, 5643.
[6] R. D. Costa, *Light-Emitting Electrochemical Cells: Concepts, Advances, and Challenges*, Springer, Basel **2017**.
[7] X.-L. Chen, C.-S. Lin, X.-Y. Wu, R. Yu, T. Teng, Q.-K. Zhang, Q. Zhang, W.-B. Yang, C.-Z. Lu, *J. Mater. Chem. C* **2015**, *3*, 1187.
[8] E. Cariati, E. Lucenti, C. Botta, U. Giovanella, D. Marinotto, S. Righetto, *Coord. Chem. Rev.* **2016**, *306*, 566.
[9] Y. Tao, K. Yuan, T. Chen, P. Xu, H. Li, R. Chen, C. Zheng, L. Zhang, W. Huang, *Adv. Mater.* **2014**, *26*, 7931.
[10] C. L. Linfoot, M. J. Leitl, P. Richardson, A. F. Rausch, O. Chepelin, F. J. White, H. Yersin, N. Robertson, *Inorg. Chem.* **2014**, *53*, 10854.
[11] M. J. Leitl, V. A. Krylova, P. I. Djurovich, M. E. Thompson, H. Yersin, *J. Am. Chem. Soc.* **2014**, *136*, 16032.
[12] K. Tsuge, Y. Chishina, H. Hashiguchi, Y. Sasaki, M. Kato, S. Ishizaka, N. Kitamura, *Coord. Chem. Rev.* **2016**, *306*, 636.
[13] Y. Ma, C. Che, H. Chao, X. Zhou, W. Chan, *Adv. Mater.* **1999**, *11*, 852.
[14] Q. Zhang, Q. Zhou, Y. Cheng, L. Wang, D. Ma, X. Jing, F. Wang, *Adv. Funct. Mater.* **2006**, *16*, 1203.
[15] L. J. Wen, T. McCormick, Y. Tao, J. P. Lu, S. Wang, *Inorg. Chem.* **2005**, *44*, 5706.
[16] G. Che, Z. Su, W. Li, B. Chu, M. Li, Z. Hu, Z. Zhang, *Appl. Phys. Lett.* **2006**, *89*, 103511.
[17] Z. Su, G. Che, W. Li, W. Su, M. Li, B. Chu, B. Li, Z. Zhang, Z. Hu, *Appl. Phys. Lett.* **2006**, *88*, 213508.
[18] Q. Zhang, J. Ding, Y. Cheng, L. Wang, Z. Xie, X. Jing, F. Wang, *Adv. Funct. Mater.* **2007**, *17*, 2983.
[19] Z. Si, J. Li, B. Li, S. Liu, W. Li, *J. Lumin.* **2009**, *129*, 181.
[20] L. Zhang, B. Li, Z. Su, *J. Phys. Chem. C* **2009**, *113*, 13968.
[21] Z. Liu, M. Qayyum, C. Wu, M. T. Whited, P. I. Djurovich, K. O. Hodgson, B. Hedman, E. I. Solomon, M. E. Thompson, *J. Am. Chem. Soc.* **2011**, *133*, 3700.
[22] M. Hashimoto, S. Igawa, M. Yashima, I. Kawata, M. Hoshino, M. Osawa, *J. Am. Chem. Soc.* **2011**, *133*, 10348.
[23] C.-W. Hsu, C.-C. Lin, M.-W. Chung, Y. Chi, G.-H. Lee, P.-T. Chou, C.-H. Chang, P.-Y. Chen, *J. Am. Chem. Soc.* **2011**, *133*, 12085.
[24] Q. Zhang, T. Komino, S. Huang, S. Matsunami, K. Goushi, C. Adachi, *Adv. Funct. Mater.* **2012**, *22*, 2327.
[25] S. Igawa, M. Hashimoto, I. Kawata, M. Yashima, M. Hoshino, M. Osawa, *J. Mater. Chem. C* **2013**, *1*, 542.
[26] Y. M. Wang, F. Teng, Y. B. Hou, Z. Xu, Y. S. Wang, W. F. Fu, *Appl. Phys. Lett.* **2005**, *87*, 233512.

 

[27] N. Armaroli, G. Accorsi, M. Holler, O. Moudam, J.-F. Nierengarten, Z. Zhou, R. T. Wegh, R. Welter, *Adv. Mater.* **2006**, *18*, 1313.
[28] O. Moudam, A. Kaeser, B. Delavaux-Nicot, C. Duhayon, M. Holler, G. Accorsi, N. Armaroli, I. Séguy, J. Navarro, P. Destruel, J.-F. Nierengarten, *Chem. Commun.* **2007**, 3077.
[29] R. D. Costa, D. Tordera, E. Ortí, H. J. Bolink, J. Schönle, S. Graber, C. E. Housecroft, E. C. Constable, J. A. Zampese, *J. Mater. Chem.* **2011**, *21*, 16108.
[30] A. Kaeser, M. Mohankumar, J. Mohanraj, F. Monti, M. Holler, J.-J. Cid, O. Moudam, I. Nierengarten, L. Karmazin-Brelot, C. Duhayon, B. Delavaux-Nicot, N. Armaroli, J.-F. Nierengarten, *Inorg. Chem.* **2013**, *52*, 12140.
[31] J. J. Cid, J. Mohanraj, M. Mohankumar, M. Holler, F. Monti, G. Accorsi, L. Karmazin-Brelot, I. Nierengarten, J. M. Malicka, M. Cocchi, B. Delavaux-Nicot, N. Armaroli, J. F. Nierengarten, *Polyhedron* **2014**, *82*, 158.
[32] D. Asil, J. A. Foster, A. Patra, X. Dehatten, J. Delbarrio, O. A. Scherman, J. R. Nitschke, R. H. Friend, *Angew. Chem., Int. Ed.* **2014**, *53*, 8388.
[33] S. Keller, E. C. Constable, C. E. Housecroft, M. Neuburger, A. Prescimone, G. Longo, A. Pertegás, M. Sessolo, H. J. Bolink, *Dalton Trans.* **2014**, *43*, 16593.
[34] C. Bizzarri, C. Strabler, J. Prock, B. Trettenbrein, M. Ruggenthaler, C. H. Yang, F. Polo, A. Iordache, P. Brüggeller, L. De Cola, *Inorg. Chem.* **2014**, *53*, 10944.
[35] F. Brunner, L. Martínez-Sarti, S. Keller, A. Pertegás, A. Prescimone, E. C. Constable, H. J. Bolink, C. E. Housecroft, *Dalton Trans.* **2016**, *45*, 15180.
[36] S. Keller, A. Pertegás, G. Longo, L. Martínez, J. Cerdá, J. M. Junquera-Hernández, A. Prescimone, E. C. Constable, C. E. Housecroft, E. Ortí, H. J. Bolink, *J. Mater. Chem. C* **2016**, *4*, 3872.
[37] Y. Zhang, M. Schulz, M. Wächtler, M. Karnahl, B. Dietzek, *Coord. Chem. Rev.* **2018**, *356*, 127.
[38] M. D. Weber, C. Garino, G. Volpi, E. Casamassa, M. Milanesio, C. Barolo, R. D. Costa, *Dalton Trans.* **2016**, *45*, 8984.
[39] S. Keller, F. Brunner, J. M. Junquera-Hernández, A. Pertegás, M.-G. La-Placa, A. Prescimone, E. C. Constable, H. J. Bolink, E. Ortí, C. E. Housecroft, *Chempluschem* **2018**, https://doi.org/10.1002/cplu.201700501.
[40] M. D. Weber, M. Viciano-Chumillas, D. Armentano, J. Cano, R. D. Costa, *Dalton Trans.* **2017**, *46*, 6312.
[41] M. Elie, S. Gaillard, J.-L. Renaud, in *Light-Emitting Electrochemical Cells: Concepts, Advances and Challenges*, Springer, Basel **2017**, pp. 287–327.
[42] R. Marion, R. Daniellou, J. Renaud, M. Linares, M. Hamel, S. Gaillard, *Inorg. Chem.* **2014**, *53*, 9181.
[43] M. Elie, F. Sguerra, F. Di Meo, M. D. Weber, R. Marion, A. Grimault, J. F. Lohier, A. Stallivieri, A. Brosseau, R. B. Pansu, J. L. Renaud, M. Linares, M. Hamel, R. D. Costa, S. Gaillard, *ACS Appl. Mater. Interfaces* **2016**, *8*, 14678.
[44] M. Elie, M. D. Weber, F. Di Meo, F. Sguerra, J.-F. Lohier, R. B. Pansu, J.-L. Renaud, M. Hamel, M. Linares, R. D. Costa, S. Gaillard, *Chem. - Eur. J.* **2017**, *23*, 16328.
[45] A. Kaeser, O. Moudam, G. Accorsi, I. Séguy, J. Navarro, A. Belbakra, C. Duhayon, N. Armaroli, B. Delavaux-Nicot, J. F. Nierengarten, *Eur. J. Inorg. Chem.* **2014**, *2014*, 1345.
[46] N. Armaroli, *Chem. Soc. Rev.* **2001**, *30*, 113.
[47] N. Armaroli, G. Accorsi, F. Cardinali, A. Listorti, in *Photochemistry and Photophysics of Coordination Compounds I*, Vol. *280*, Springer, Berlin Heidelberg **2007**, pp. 69–115.
[48] O. Santoro, F. Lazreg, D. B. Cordes, A. M. Z. Slawin, C. S. J. Cazin, *Dalton Trans.* **2016**, *45*, 4970.
[49] S. Díez-González, N. M. Scott, S. P. Nolan, *Organometallics* **2006**, *25*, 2355.
[50] S.-M. Kuang, D. G. Cuttell, D. R. McMillin, P. E. Fanwick, R. A. Walton, *Inorg. Chem.* **2002**, *41*, 3313.
[51] J. Yuasa, M. Dan, T. Kawai, *Dalton Trans.* **2013**, *42*, 16096.
[52] L. X. Chen, G. B. Shaw, G. Jennings, L. X. Chen, G. B. Shaw, I. Novozhilova, T. Liu, G. Jennings, K. Attenkofer, G. J. Meyer, P. Coppens, *J. Am. Chem. Soc.* **2003**, *125*, 7022.
[53] T. Gunaratne, M. A. J. Rodgers, D. Felder, J.-F. Nierengarten, G. Accorsi, N. Armaroli, *Chem. Commun.* **2003**, *0*, 3010.
[54] G. B. Shaw, C. D. Grant, H. Shirota, E. W. Castner, G. J. Meyer, L. X. Chen, *J. Am. Chem. Soc.* **2007**, *129*, 2147.
[55] G. Kalyuzhny, M. Buda, J. Mcneill, P. Barbara, A. J. Bard, *J. Am. Chem. Soc.* **2003**, *125*, 6272.
[56] S. van Reenen, P. Matyba, A. Dzwilewski, R. A. J. Janssen, L. Edman, M. Kemerink, *J. Am. Chem. Soc.* **2010**, *132*, 13776.
[57] S. Van Reenen, P. Matyba, A. Dzwilewski, R. A. J. Janssen, L. Edman, M. Kemerink, *Adv. Funct. Mater.* **2011**, *21*, 1795.
[58] S. Van Reenen, R. A. J. Janssen, M. Kemerink, *Adv. Funct. Mater.* **2012**, *22*, 4547.
[59] A. Munar, A. Sandström, S. Tang, L. Edman, *Adv. Funct. Mater.* **2012**, *22*, 1511.
[60] S. B. Meier, D. Hartmann, A. Winnacker, W. Sarfert, *J. Appl. Phys.* **2014**, *116*, 104504.
[61] B. M. D. Puscher, M. F. Aygueler, P. Docampo, R. D. Costa, *Adv. Energy Mater.* **2017**, *7*, 1602283.
[62] J. Mindemark, L. Edman, *J. Mater. Chem. C* **2016**, *4*, 420.
[63] R. D. Costa, A. Pertegás, E. Ortí, H. J. Bolink, *Chem. Mater.* **2010**, *22*, 1288.
[64] S. Tang, L. Edman, *J. Phys. Chem. Lett.* **2010**, *1*, 2727.
[65] S. Tang, H. A. Buchholz, L. Edman, *J. Mater. Chem. C* **2015**, *3*, 8114.
[66] S. Tang, A. Sandström, J. Fang, L. Edman, *J. Am. Chem. Soc.* **2012**, *134*, 14050.
[67] T. Förster, *Discuss. Faraday Soc.* **1959**, *27*, 7.
[68] D. L. Dexter, *J. Chem. Phys.* **1953**, *21*, 836.
[69] P. Matyba, K. Maturova, M. Kemerink, N. D. Robinson, L. Edman, *Nat. Mater.* **2009**, *8*, 672.
[70] F. Neese, *Diploma Thesis*, University of Kostanz, **1993**.

 

ADVANCED FUNCTIONAL MATERIALS

# Supporting Information

for *Adv. Funct. Mater.,* DOI: 10.1002/adfm.201707423

## Rationalizing Fabrication and Design Toward Highly Efficient and Stable Blue Light-Emitting Electrochemical Cells Based on NHC Copper(I) Complexes

*Michael D. Weber, Elisa Fresta, Margaux Elie, Matthias E. Miehlich, Jean-Luc Renaud, Karsten Meyer, Sylvain Gaillard,* and Rubén D. Costa**

Submitted to ADVANCED FUNCTIONAL MATERIALS

# Supporting information

**Rationalizing Fabrication and Design Towards Highly Efficient and Stable Blue Light-Emitting Electrochemical Cells based on NHC Copper(I) Complexes**

By *Michael D. Weber, Elisa Fresta, Margaux Elie, Matthias Miehlich, Jean-Luc Renaud, Karsten Meyer, Sylvain Gaillard*, and Rubén D. Costa**

Synthesis of $[Cu(^{3\text{-}Me}dpa)_2][PF_6]$ (**2**):

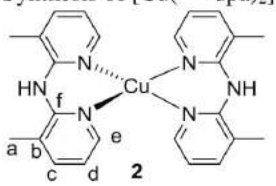


**2**

In a flame-dried Schlenk tube under an atmosphere of dry argon, $[Cu(CH_3CN)_4][PF_6]$ ( 0.2 mmol, 74.5 mg) and 3-Medpa (0.4 mmol, 80.0 mg) were introduced in dry degassed $CH_2Cl_2$ (4 mL). The reaction mixture was stirred at room temperature for 3 hours. Then, the reaction mixture was filtered through a pad of diatomaceous earth, the cake was washed with $CH_2Cl_2$ and pentane was added to afford a yellow precipitate which was collected on a frit and dried under vacuum. The complex $[Cu(3Medpa)_2][PF_6]$ **2** was obtained as a yellow powder with 97% yield (0.19 mmol, 117 mg,). $^1$H-NMR ($CD_2Cl_2$, 500 MHz): 2.42 (s, 12 H, $H_a$), 6.72-6.83 (m, 6H, NH and $H_e$), 7.58 (*app.* s, 4H, $H_d$), 7.87 (*app.* s, 4H, $H_c$) ppm (see Figure S1). $^{13}$C-NMR ($CD_2Cl_2$, 125 MHz): 17.3 (4xq, $C_a$), 117.8 (4xd, $C_d$), 121.5 (4xs, $C_b$), 139.3 (4xd, $C_c$), 145.5 (4xd, $C_e$), 151.8 (4xs, $C_f$) ppm. IR (neat) ν 3449, 1611, 1586, 1520, 1456, 1403, 1427, 1332, 1224, 1114, 1003, 838, 780 cm$^{-1}$. HRMS (ESI): *m/z* calcd for $C_{24}H_{26}CuN_6$ $[M–PF_6]^+$: 461.1515; found: 461.1511 – Figure S2.

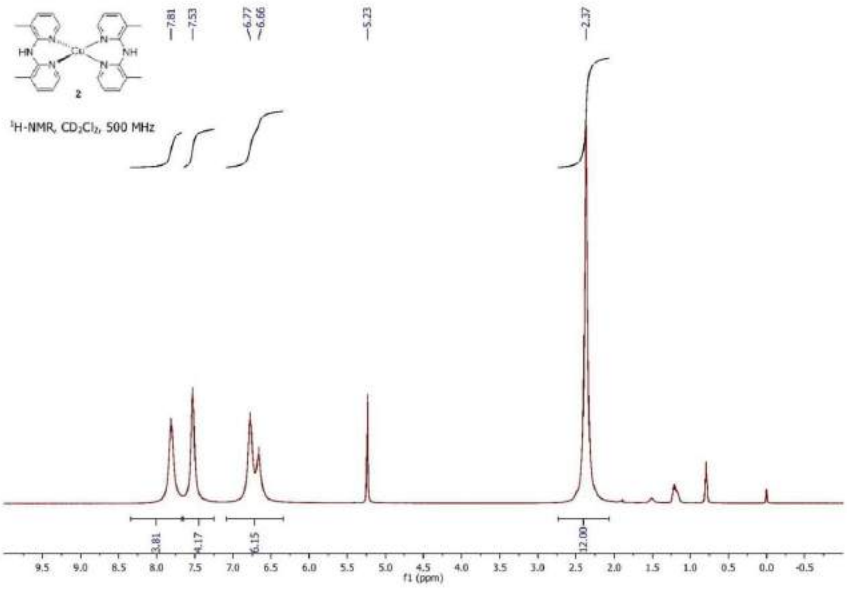


**Figure S1**. $^1$H-NMR spectrum of **2** in $CD_2Cl_2$, 500 MHz.

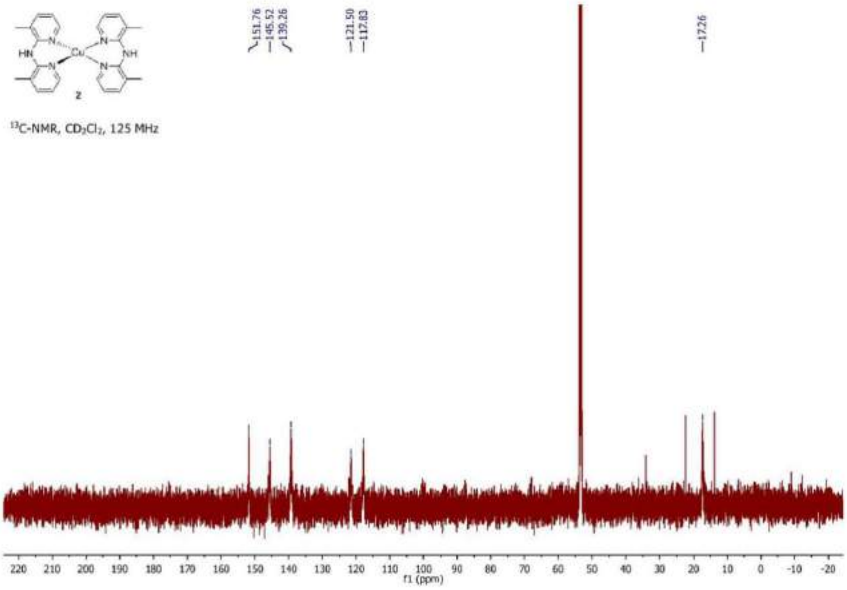


**Figure S2**. $^{13}$C-NMR spectrum of complex spectra of **2** in $CD_2Cl_2$, 125 MHz.

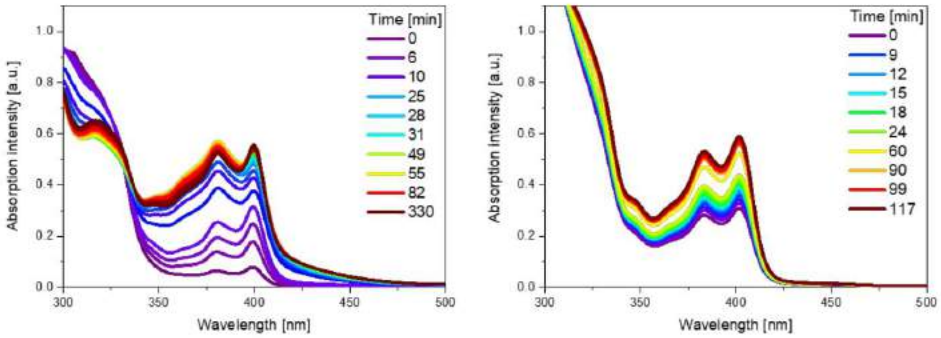


**Figure S3**. Absorption spectra over time of **2** (1 x $10^{-6}$ M) in THF (left) and MeCN (right) upon storage under ambient and dark conditions.

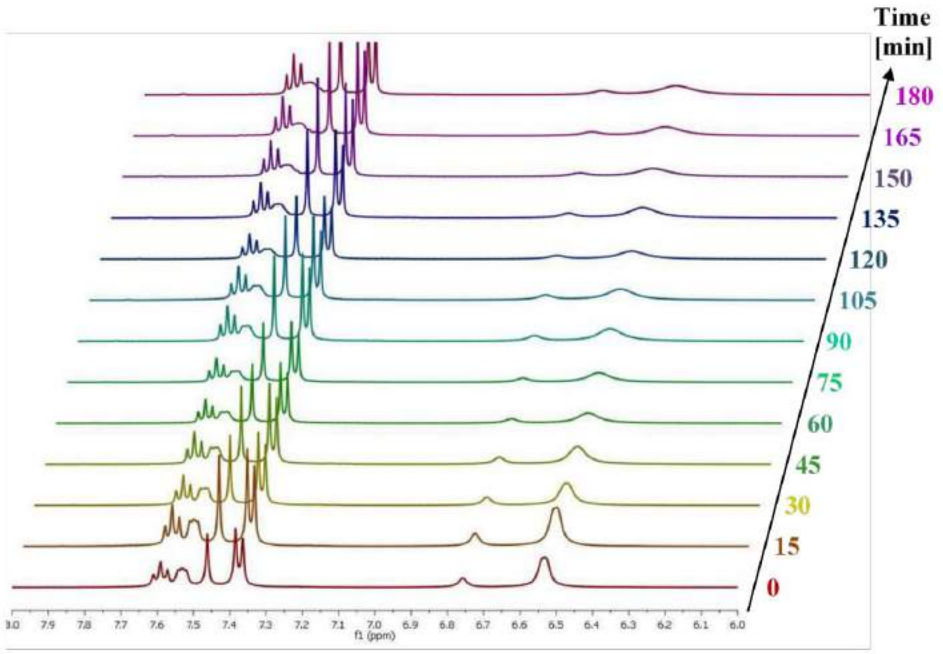


**Figure S4**. $^{1}$H-NMR spectra (400 MHz, 298 K) over time of **1** in $CD_3CN$.

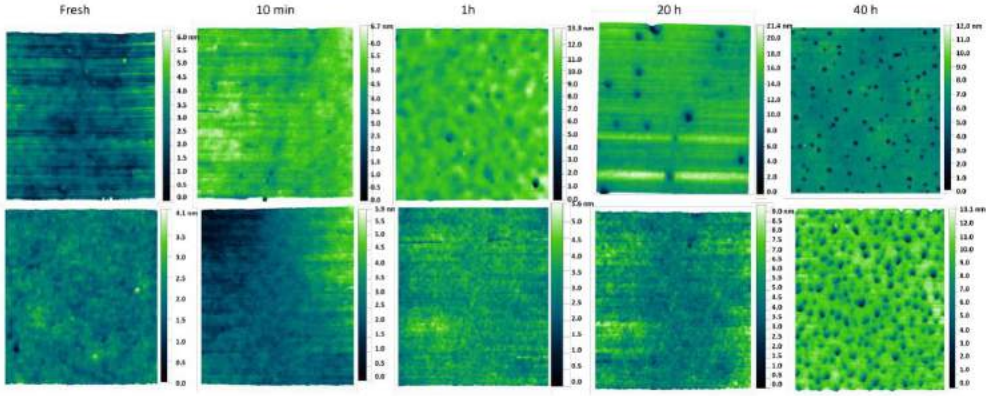


**Figure S5**. AFM images of thin films prepared with aged THF (top) and MeCN (bottom) solutions of **1.**

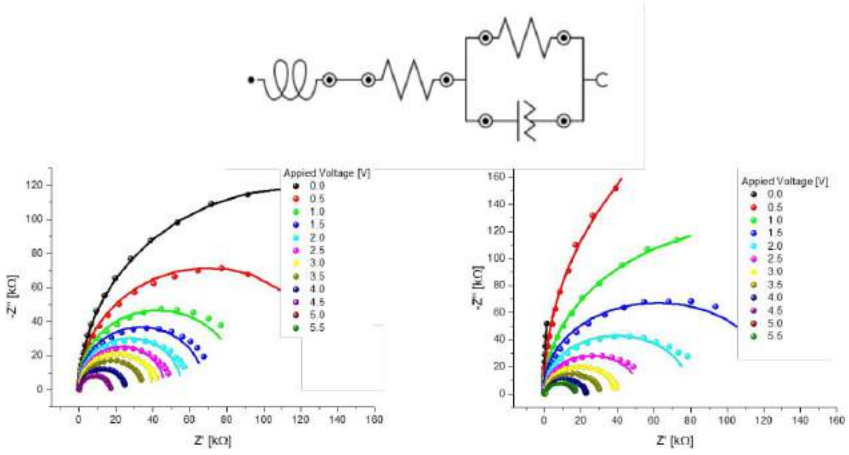


**Figure S6.** Upper part - Equivalent circuit model for EIS fitting used for devices containing **1**. Lower part - Nyquist plots of a freshly prepared device (left) and a device after measurement of the lifetime (right) with the fittings as solid lines.

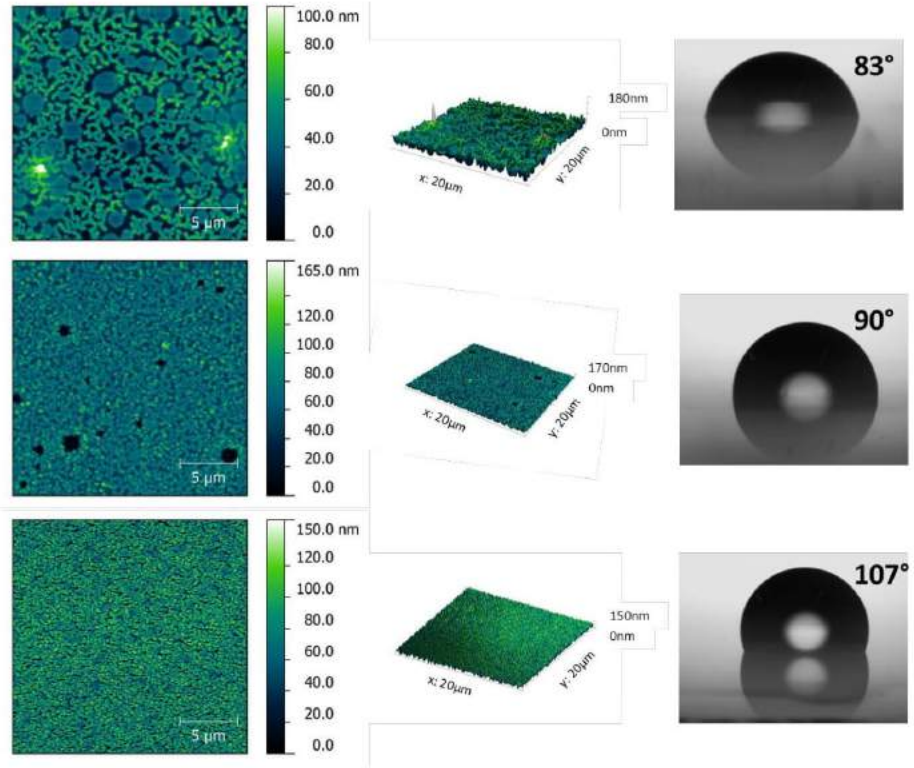


**Figure S7**. AFM (left) and water static contact angle (right) measurements of films with a blend of CBP:**1** in a mass ratio of 90:10 (upper), 70:30 (central) and 50:50 (lower).

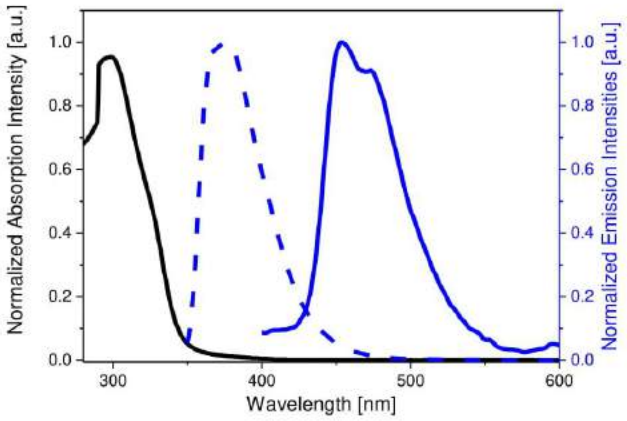


**Figure S8**. Absorption and emission spectra of **1** (solid line) and CBP (dashed line).

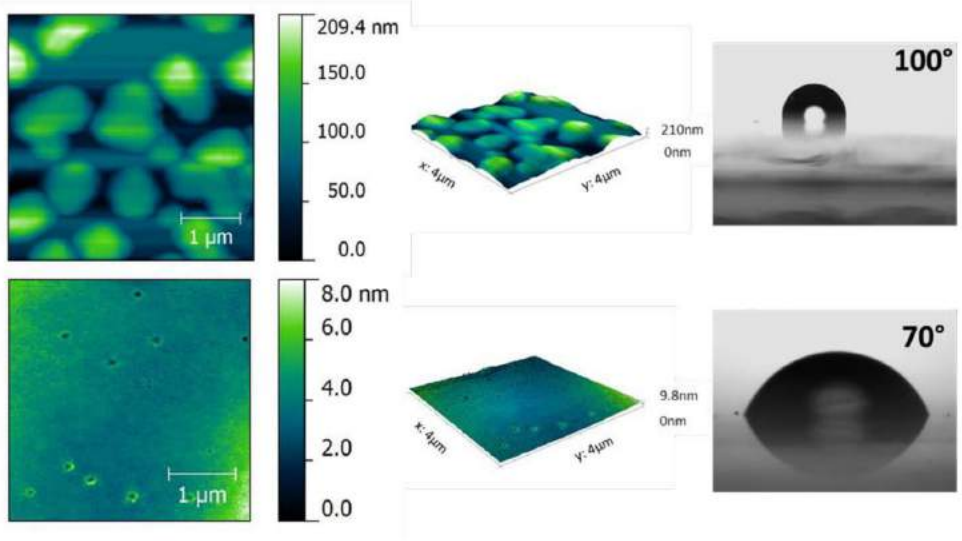


**Figure S9.** AFM (left) and water static contact angle (right) measurements of pure CBP (upper) and CBP|**1** (lower) layers.

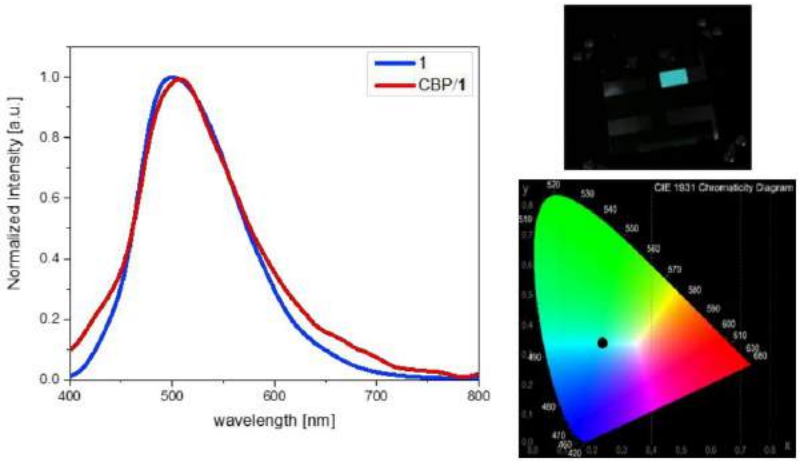


**Figure S10.** Left part - Electroluminescence spectra of devices with **1** and CBP|**1** (25 nm|90 nm) active layers upon pulsed current of 2 mA. Right part – Picture of the running CBP|**1** (25 nm|90 nm) and the corresponding x/y CIE color coordinates.

Section 3.1.2: Novel Ligand and Device Designs for Stable Light-emitting Electrochemical Cells based on Heteroleptic Copper (I) complexes

Inorganic Chemistry

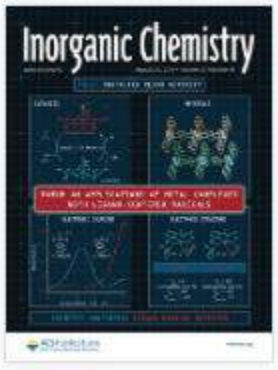


Elisa Fresta,[1] Giorgio Volpi,[2] Marco Milanesio,[3] Claudio Garino,[2] Claudia Barolo,[2,4]* and Rubén D. Costa[1]*

1. IMDEA Materials Institute, Calle Eric Kandel 2, 28906 Getafe, Madrid, Spain.
2. Department of Chemistry, NIS Interdepartmental Centre and INSTM Reference Centre, Università degli Studi di Torino, Via Pietro Giuria 7, 10125, Torino, Italy.
3. Università del Piemonte Orientale Dipartimento di Scienze e Innovazione Tecnologica, Viale T. Michelin 11, I-15121, Alessandria, Italy and CrisDi Interdepartmental Center for Crystallography.
4. ICxT Interdepartmental Centre, Università degli Studi di Torino, Lungo Dora Siena 100, 10153, Torino, Italy.

Inorganic Chemistry
Cite This: Inorg. Chem. 2018, 57, 10469−10479
Article
pubs.acs.org/IC

# Novel Ligand and Device Designs for Stable Light-Emitting Electrochemical Cells Based on Heteroleptic Copper(I) Complexes

Elisa Fresta,[†] Giorgio Volpi,[‡] Marco Milanesio,[§,⊥] Claudio Garino,[‡] Claudia Barolo,*[,‡,∥] and Rubén D. Costa*[,†]

[†]IMDEA Materials Institute, Calle Eric Kandel 2, 28906 Getafe, Madrid, Spain

[‡]Department of Chemistry, NIS Interdepartmental Centre and INSTM Reference Centre, Università degli Studi di Torino, Via Pietro Giuria 7, 10125 Torino, Italy

[§]Dipartimento di Scienze e Innovazione Tecnologica, Università del Piemonte Orientale, Viale T. Michel 11, I-15121 Alessandria, Italy

[∥]ICxT Interdepartmental Centre, Università degli Studi di Torino, Lungo Dora Siena 100, 10153 Torino, Italy

[⊥]CrisDi, Interdepartmental Center for Crystallography, 10125 Turin, Italy

Supporting Information

**ABSTRACT:** This work reports on the positive impact of (i) attaching methoxy groups at the ortho position of the bipyridine ligand (6,6′-dimethoxy-2,2′-bipyridine) in heteroleptic copper(I) complexes belonging to the [Cu(bpy)(POP)]$^+$ family, and (ii) a new device design comprising a multilayered architecture to decouple hole/electron injection and transport processes on the performance of light-emitting electrochemical cells (LECs). In short, the substituted complex showed enhanced thermal- and photostability, photoluminescence, and ionic conductivity features in thin films compared to those of the archetypal complex without substitution. These beneficial features led to LECs outperforming reference devices in terms of luminance, stability, and efficacy. Furthermore, a new device design resulted in a 10-fold enhancement of the stability without negatively affecting the other figures of merit. Here, hole/electron injection and transport processes are performed at two different layers, while electron injection and electron−hole recombination occur at the copper(I) complex layer. As such, this work provides further insights into a smart design of N^N ligands for copper(I) complexes, opening the path to a simple device architecture toward an enhanced electroluminescence response.

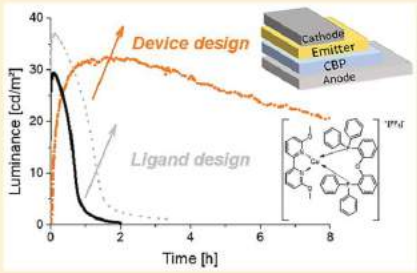


## 1. INTRODUCTION

The final goal in thin-film lighting technologies is to fabricate highly efficient, air-stable, low-cost, and single-layer lighting sources using up-scalable solution-based techniques.[1−4]

Those requirements are fulfilled by the light-emitting electrochemical cell (LEC) technology.[1−3,5,6] LECs are a single-layer lighting device consisting of a mixture of a luminescent material and an ionic electrolyte. When no bias is applied, the mobile ions are randomly distributed in the active layer. Upon biasing the device, the ions drift toward the electrode interfaces, creating the so-called electric double layers (EDLs) that assist charge injection regardless of the nature of the electrodes—for example, air-stable metals, metal oxides, nanocarbon, etc.[2,3,7−9] As a result, highly conductive n- and p-doped regions along with a light-emitting nondoped region are formed.[10−12]

The most attractive LEC features are (i) tolerance with respect to the nature of the electrodes and the thickness of the active layer ranging from a few tens to hundreds of nanometers, (ii) easy fabrication from solution-based techniques under ambient conditions—for example, roll-to-roll,[13] inkjet printing,[14] spray-deposition,[15] etc., and (iii) versatility in emitters, such as polymers, ionic transition-metal complexes (iTMCs), small molecules, quantum dots, and perovskites.[2,3,6,16−20] In addition, the LEC community has also demonstrated the potential applicability of this lighting technology using unconventional conductive substrates—for example, kitchen forks,[15] printing papers,[21] wearable fibers,[22] line-art lighting devices,[23] etc. Finally, numerous research groups focused on the search of sustainable and low-cost emitters to fabricate highly efficient and stable LECs spanning the whole visible range,[1−3] including white-emitting LECs featuring promising performances.[16,24−26]

In this regard, copper(I)-based iTMCs (Cu-iTMCs) are attracting more and more attention, since they are considered as a serious alternative to the well-known iridium(III)-based iTMCs (Ir-iTMCs).[5,6] The interest in Cu-iTMCs is justified

Received: July 13, 2018
Published: August 2, 2018





DOI: 10.1021/acs.inorgchem.8b01914
Inorg. Chem. 2018, 57, 10469−10479

by (i) the absence of metal-centered (MC) excited states that are typical degradative pathways for iridium(III) complexes,[5,27−29] (ii) the emission mechanism involving a thermally activated delayed fluorescence (TADF) that results in high photoluminescence quantum yields (**Φ**),[30−32] (iii) the large number of emitting families,[3,33,34] and (iv) the low production costs related to the use of a relatively abundant and cheaper metal with respect to iridium.

Among the different Cu-iTMC families applied in LECs,[35−41] heteroleptic complexes—that is, $[Cu(N^N)(P^P)]^+$, where N^N and P^P are diimine and diphosphine ligands, respectively—are the most studied ones. Currently, huge efforts have been conducted to elucidate strategies with respect to both the synthesis protocol (purification and yields)[42,43] and the ligand design (*para* or *ortho* substitutions of the N^N ligand),[37−39,44] toward enhancing the performance of yellow- and green-emitting LECs.

Concerning the ligand design, important achievements have been realized attaching $\sigma$-donating groups or halogen atoms at the *para* position of the N^N ligands.[39,44] For instance, a linear correlation between the $\sigma$-Hammett parameter ($\sigma_p$) and an improvement in the LEC figures of merit was recently reported.[44] As far as the substitution at the *ortho* position is concerned, Yersin's group has recently noted a significant enhancement of the photoluminescence upon attaching one or two methyl groups,[30] while Bolink and co-workers proved it in LECs.[37,38] This substitution causes the twisting of the bipyridyl units coupled with a tilting of the heterocyclic ring plane, leading to enhanced luminescence as the photoinduced flattening distortion is limited. Noteworthy, the stabilizing effect is more pronounced in symmetrically substituted complexes, while the substitution with groups that are bulkier than the ethyl moiety does not provide any further enhancement and renders the synthesis of pure complexes more difficult.[38]

Following these works, we propose a rationalized ligand design in which both ortho positions of the 2,2′-bipyridine ligand are functionalized with methoxy groups (6,6′-dimethoxy-2,2′-bipyridine, MeO-bpy). Two reasons compelled us to select this moiety. On one hand, *ortho* substitution with methoxy groups provides a stronger electron-donating effect than that of the methyl group. This should provide an enhanced back-donation that strengthens the metal−ligand coordination, preventing significant structural changes upon excitation. On the other hand, both the steric hindrance and easy rotation motion of the methoxy group further shields the coordination sphere of the Cu(I) metal ion. This should avoid the solvent-assisted ligand exchange process in coordinative solvents, increasing both thermal- and photostabilities.

The above statements were corroborated by comparing the spectroscopic and electrochemical features of two complexes, namely, the archetypal $[Cu(bpy)(POP)][PF_6]$ (**1**) and the novel $[Cu(MeO\text{-}bpy)(POP)][PF_6]$ (**2**), where bpy is 2,2′-bipyridine, MeO-bpy is 6,6′-dimethoxy-2,2′-bipyridine, and POP is bis(2-(diphenylphosphino)phenyl)ether—Figure 1. Here, efficiency and stability of LECs were enhanced up to three- to fourfold (**2** vs **1**). Furthermore, the device stability can be enhanced by 10-fold using a new device architecture to overcome the irreversible oxidation process of the Cu-iTMCs.[34,45−47] Overall, this work illustrates an easy way to improve the performance of LECs based on Cu-iTMCs through both novel ligand and device designs.

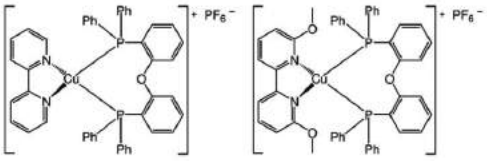


**Figure 1.** Chemical structures of **1** (left) and **2** (right).

## 2. RESULTS AND DISCUSSION

**2.1. Synthesis and X-ray Characterization.** The synthesis of MeO-bpy was performed by one-pot microwave-assisted synthetic protocol with a yield of 80% and short time (90 min) compared to traditional synthetic pathways (74% and 18 h).[48] The formation of the final product was monitored through gas chromatography coupled with mass spectrometry (GC-MS) by stopping the reaction every 30 min, until a maximum in the mass spectrum of the reaction mixture was observed for the final product. The ligand was characterized by mass spectrometry and $^1H$ and $^{13}C$ NMR spectroscopy—Figures S1 and S2. Interestingly, X-ray structure analysis of the ligand showed a planar *anti* conformation with a N1−C1−C1′−N1′ torsion angle of 180.4°—Figure S3 and Tables S1−S3. To explore the energetic cost of the rotation along NC2C2′N′ torsion angle, density functional theory (DFT) calculations were performed. The *trans* conformation resulted to be the more stable, as suggested by the crystal structure. The perfect *cis* conformation corresponds to an energy maximum with a relative energy of 8.0 kcal/mol—Figure S3 and Table S4. This maximum is energetically close to another relative energy minimum with N1−C1−C1′−N1′ torsion angle equal to 35° depicted in Figure S4 with a relative energy of 7.1 kcal/mol.

Complexes **1** and **2** were prepared in an excellent yield following procedures reported in literature.[40,49] $^1H$, $^{13}C$, and $^{31}P$ NMR spectroscopic and mass spectrometric characterizations confirmed the formation of the desired heteroleptic complex **2** with no evidence of either the presence of homoleptic species or free ligands—Figure S5. The new complex **2** was crystallized from a solution of $H_2O$ and acetone 1:1 and its structure solved by X-ray diffraction (XRD), showing a $P2_1/c$ space group—Figures 2 and S6−S8 and Tables 1 and S5−S7. The Cu(I) atom shows a nonplanar *pseudo*-tetrahedral coordination with the two P atoms of the POP moiety and the two N atoms of the bpy moiety—Figure 2, similarly to the parent compound **1**.[40] The Cu−P distances are 2.27 and 2.28 Å. The packing is arranged in planes of molecules of **2** alternated by $PF_6^-$ planes—Figure S8. Rather short CH···F contacts of ∼2.6 Å—that is, closer to the sum of the van der Waals radii of H and F—are observed. This arrangement might explain the preferred growth in two directions to form extended laminae, while in the third direction the growth is probably unfavored, since no regular rows of positive and negative ions are observed. The oxygen bridge between the two phenyls shows C−O distances of 1.39 Å, which are identical to those of an aromatic bond, suggesting a larger electronic delocalization across the bridge than that of **1**.[45] This is reasonable taking into account the strong electron-donor role provided by the methoxy groups.

As such, the ancillary ligand shows an almost planar conformation with a N1−C1−C1′−N1′ torsion angle of 6.22°. As reported elsewhere,[45] the X-ray structure of **1** shows similar Cu−P bond lengths of 2.25 and 2.24 Å, as well as similar Cu−N bond lengths of 2.07 and 2.05 Å. However, it differs from



DOI: 10.1021/acs.inorgchem.8b01914
Inorg. Chem. 2018, 57, 10469−10479

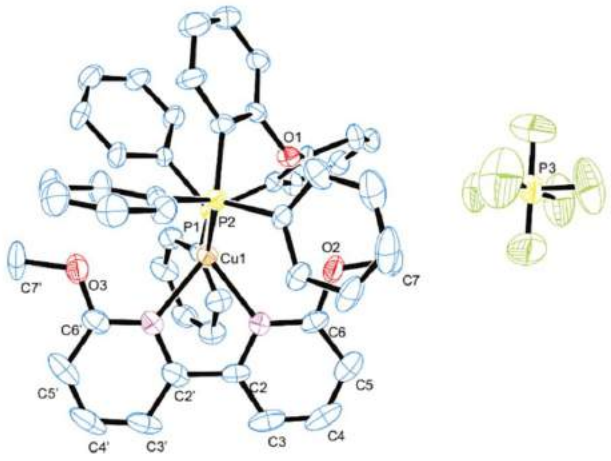


Figure 2. X-ray structure of 2.

**Table 1. Crystal Data and Structure Refinement of 2 and MeO-bpy**

| compound | 2 | MeO-bpy |
|---|---|---|
| empirical formula | $C_{48}H_{40}CuF_6N_2O_3P_3$ | $C_{12}H_{12}N_2O_2$ |
| formula weight | 770.61 | 216.24 |
| temperature | 293(2) K | |
| wavelength | 0.71073 Å | |
| crystal system | monoclinic | orthorhombic |
| space group | $P21/n$ | $Pn21a$ |
| unit cell dimensions (edges in Å and angles in deg) | $a$ = 9.8718(15) | $a$ = 12.5060(14) |
| | $b$ = 29.021(5) | $b$ = 21.731(3) |
| | $c$ = 15.241(2) | $c$ = 3.9733(7) |
| | $\beta$ = 95.469(14) | |
| volume, Å$^3$ | 4346.7(11) | 1079.8(3) |
| $Z$ | 5 | 4 |
| density (Mg/m$^3$ calculated) | 1.472 | 1.330 |
| absorption coefficient (mm$^{-1}$) | 0.684 | 0.092 |
| $F$(000) | 1976 | 456 |
| crystal size (mm$^3$) | 0.120 × 0.040 × 0.020 | 0.410 × 0.220 × 0.040 |
| $\theta$ range for data collection | 2.807 to 28.605° | 3.258 to 28.033° |
| reflections collected | 37 346 | 6417 |
| independent reflections | 10 063 [$R$(int) = 0.2518] | 2396 [$R$(int) = 0.0636] |
| completeness to $\theta$ = 25.242° | 99.8% | 99.9% |
| refinement method | full-matrix least-squares on $F^2$ | |
| data/restraints/parameters | 10 063/0/570 | 2396/1/123 |
| goodness-of-fit on $F^2$ | 0.955 | 1.037 |
| final $R$ indices [$I > 2\sigma(I)$] | R1 = 0.0876, wR2 = 0.1692 | R1 = 0.1122, wR2 = 0.2687 |
| $R$ indices (all data) | R1 = 0.2908, wR2 = 0.2576 | R1 = 0.1875, wR2 = 0.3380 |
| largest diff peak and hole | 0.605 and −0.488 e·Å$^{-3}$ | 0.797 and −0.301 e·Å$^{-3}$ |

2 in the overall distortion of the coordination sphere, assessed by measuring the P−Cu−X bond angles, where point X is defined (using crystallographic coordinates) as the midpoint of the C1−C1′ bond in each complex. Here, no distortion at all from the ideal tetrahedral geometry would result in an angle of 120°. The measured values are of 129.3° and 115.3° for **1**[45] and 125.6° and 118.2° for **2**. The latter are closer to the ideal angle, suggesting an enhanced molecular rigidity in the ground state.

**2.2. Spectroscopic Characterization.** As shown in Figures 3 and 4, fresh acetonitrile solutions of both **1** and **2** showed two well-defined absorption bands corresponding to ligand-centered (LC) and metal-to-ligand charge transfer (MLCT) transitions located at 280−300 and 380−400 nm regions, respectively. In general, the absorption maxima of **2** are red-shifted (15 nm) compared to those of **1**, highlighting the electron-donating features of the methoxy groups—Table 2. In particular, we noted a clear solvatochromic effect while comparing the absorption features of both complexes in dichloromethane and acetonitrile solutions—Figures 3, 4, and S9, as well as Table 2. Blue and red shifts for all the absorption maxima were observed for **1** and **2**, respectively. In addition, the MLCT band of **2** is clearly noted in dichloromethane rather than in acetonitrile. These account for a larger dipole moment in both the excited and ground states of **2** compared to those of **1**.[46] Next, the thermal and photostabilities of both complexes in acetonitrile ($5 \times 10^{-4}$ M), due to its well-known coordinative character, were investigated. First, the absorption features were monitored over time at 70 °C in dark—Figure 3. Under these conditions, ligand exchange of the diimine ligand by solvent molecules is facilitated leading to the formation of undesired $[Cu(POP)(MeCN)_2]^+$ and homoleptic $[Cu(bpy)_2]^+$ species—MeCN refers to acetonitrile.[46,50] This is attested by both a decrease of the MLCT band intensity and the appearance of a new band at ~330 nm that has been previously ascribed to the homoleptic diimine complexes.[33,51] This is only observed for **1** in a time frame of a few hours, while **2** does not show any significant change in this time frame—Figure 3. Thus, both the sterical hindrance and the free motion of the methoxy efficiently prevent the degradation of the complex.

This also holds with regard to the photostability studies. We monitored the changes of the absorption features under constant UV irradiation (302 nm) at room temperature—Figure 4. In stark contrast to the thermal stability study, the MLCT band of **1** disappears within the first minutes, while a progressive red-shift of ~10 nm is noted for the absorption



DOI: 10.1021/acs.inorgchem.8b01914
Inorg. Chem. 2018, 57, 10469−10479

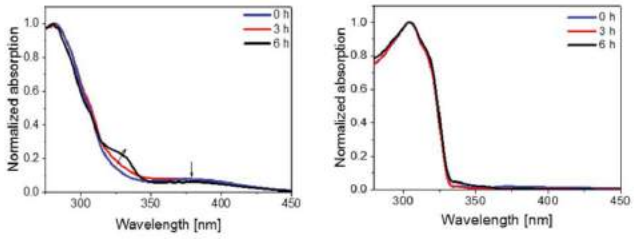


**Figure 3.** Changes of the UV−vis absorption spectra of **1** (left) and **2** (right) measured in acetonitrile over time at 70 °C in dark.

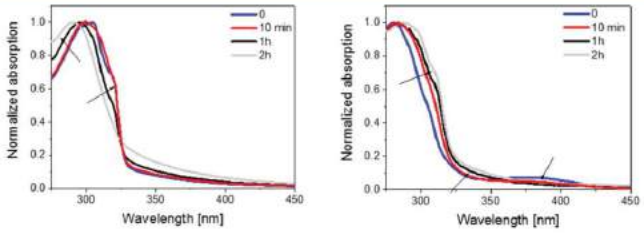


**Figure 4.** Changes of the UV−vis absorption spectra of **1** (left) and **2** UV (right) measured in acetonitrile over time under UV irradiation (302 nm, power density 640 $\mu W/cm^2$).

**Table 2. Photoluminescence and Electrochemical Features of Complexes 1 and 2**

| | absorption | | emission | | | | | electrochemistry | |
|---|---|---|---|---|---|---|---|---|---|
| | $\lambda_{abs}$[a] (nm) | $\lambda_{abs}$[b] (nm) | $\lambda_{em}$[c] (nm) | $\lambda_{em}$[d] (nm) | $\Phi$[e] | $\Phi$[f] | $\tau$[g] ($\mu$s) | $E_{ox}$[g] (V) | $E_{red}$[g] (V) |
| 1 | 289, 388 | 280, 380 | 585 | 590 | 0.06 | 0.09 | 0.83, 0.01 | +0.95 ($_{qr}$) | $-2.00_{(r)}$ |
| | | | | | | | | | $-2.46_{(r)}$ |
| 2 | 294, 415 | 306, 417 | 571 | 575 | 0.14 | 0.20 | 1.22, 0.13 | +1.00 ($_{qr}$) | $-2.12_{(r)}$ |
| | | | | | | | | | $-2.51_{(r)}$ |

[a]Measured at 298 K in dichloromethane. [b]Measured at 298 K in acetonitrile. [c]Photoluminescence spectra measured in powder at room temperature ($\lambda_{exc}$ 370 nm). [d]Photoluminescence spectra measured in thin film at room temperature ($\lambda_{exc}$ 370 nm). [e]Photoluminescence quantum yields measured in powder ($\lambda_{exc}$ 370 nm). [f]Photoluminescence quantum yields measured in thin film ($\lambda_{exc}$ 370 nm); excited-state lifetimes measured in powder ($\lambda_{exc}$ 370 nm). [g]Oxidation and reduction potentials measured versus $Cp_2Fe/Cp_2Fe^+$; qr = quasi reversible, r = reversible.

maxima of the LC band. This goes hand-in-hand with an overall broadening of this band due to the rising of a new shoulder located at ~320 nm. All-in-all, these results suggest the photoinduced formation of new species like $[Cu(POP)(MeCN)_2]^+$ and $[Cu(bpy)_2]^+$—vide supra.[33,46,50,51] Interestingly, the absorption features of **2** hold constant during the first 10 min. For longer periods of time, the LC absorption band narrows, and the absorption maximum shows a blue-shift of ~15 nm. This suggests the partial unbonding of the diimine ligand forming the $[Cu(POP)(MeCN)(MeO\text{-}bpy)]^+$ complex.[51] Noteworthy, we discarded the formation of copper(II) species during the assays above, as the solutions did not turn greenish.

Concerning the photoluminescence features, both complexes are not emitting in both acetonitrile and dichloromethane solutions. However, they are strongly emissive in powder—Figure 5, showing a broad and featureless emission band centered at 580 and 570 nm for **1** and **2**, respectively. The emission shape indicates a similar charge-transfer (CT) nature for the emitting excited state, while the 10 nm blue-shifted emission of **2** compared to that of **1** is related to the difference of the dipole moment of the excited state.[44] The photoluminescence quantum yield ($\Phi$) of **2** is much higher than that of **1**—that is, 0.14 versus 0.06 in the form of powder—

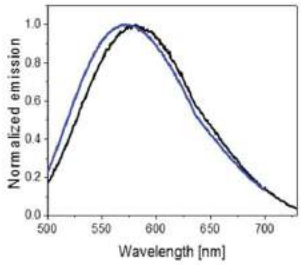


**Figure 5.** Photoluminescence spectra of **1** (black) and **2** (blue) recorded at room temperature ($\lambda_{exc}$ 370 nm).

Table 2, indicating a reduced nonradiative relaxation process in the excited state upon attaching methoxy groups. Importantly, thin films with the same composition as those used in devices also showed the same emission features associated with a similar trend for the $\Phi$, that is, 0.20 versus 0.09 for **2** and **1**, respectively. This is in line with the longer excited-state lifetimes of **2** than those of **1**—Table 2. Overall, **2** features enhanced radiative and



DOI: 10.1021/acs.inorgchem.8b01914
Inorg. Chem. 2018, 57, 10469−10479

reduced nonradiative processes compared to those of **1**, suggesting that a better electroluminescence response with respect to luminance and efficacy might be expected in LECs.

**2.3. Electrochemical Characterization.** Cyclic voltammetry assays were performed for **1** and **2** in acetonitrile—see Experimental Section for further details. The cyclic voltammograms are displayed in Figure 6, while Table 2 summarized the

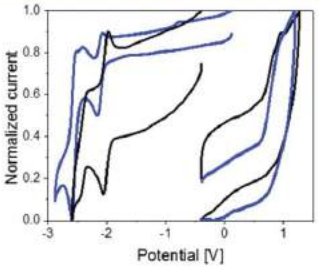


**Figure 6.** Cyclic voltammograms of **1** (black line) and **2** (blue line) in acetonitrile.

oxidation and reduction potentials. In short, both the complexes showed the same *quasi*-reversible oxidation wave at ~1 V versus $Cp_2Fe/Cp_2Fe^+$. This is assigned to the typical metal-centered oxidation that forms copper(II) species.[47] In contrast, both complexes showed two reversible reduction waves located at −2.00/−2.46 V and −2.12/−2.51 V for **1** and **2**, respectively. This is attributed to the reduction of the bipyridyl ligand, and,[47] therefore, it is not surprising that the attachment of electron-donating groups shifts the reduction values toward higher potentials. In light of the electrochemical behavior, we can postulate that hole injection in both complexes could be critical for the device stability due to irreversible formation of oxidized species that can act as both emission quenchers and trap carriers.[52]

**2.4. Electroluminescence Characterization: Effect of the Ligand Design.** The electroluminescence features of **1** and **2** were studied at first in a standard single-layer LEC. Prior to the deposition of the active layer, a first layer of poly(3,4-ethylenedioxythiophene):poly(styrenesulfonate) (PEDOT:PSS) (70 nm) was deposited onto patterned indium tin oxide (ITO) substrate to increase the device preparation yield. The active layer was prepared via spin-coating from fresh solutions of **1** or **2**. The thickness of the active layers was measured with *α*-step technique and was 120 nm. The devices were finalized depositing 90 nm of aluminum as cathode and were driven at various pulsed currents of 2.5, 5, and 7.5 mA, using a 1000 Hz block wave and a 50% duty cycle. Details concerning the device preparation and characterization are provided in the Experimental Section.

Regardless of the applied driving current, all the devices featured the same behavior over time—Figures 7 and 8. In detail, the average voltage profile showed a similar initial voltage peak at ~7 V followed by a slow decay up to a similar steady-state voltage regime at ~4−5 V—Figure 7. The average voltage refers to the half of the maximum voltage amplitude, as a 50% duty cycle is used. It is important to notice that the rise of the average voltage upon applying driving currents beyond 5 mA is quite likely related to over-oxidation processes that generate black spots.[53] Concerning the luminance, all the devices showed an instantaneous emission that increases up to its maximum within the first minutes under operation conditions—Figure 8. The electroluminescence (EL) spectra showed the same broad and unstructured band shape with maxima at 583 (**1**) and 573 (**2**) nm as observed in the photoluminescence measurements—Figure 9. This indicates that the same excited state is involved regardless of the excitation mechanism. The *x*/*y* CIE color coordinates of 0.49/0.53 (**1**) and 0.46/0.52 (**2**) correspond to yellow-emitting devices.

As summarized in Table 3, devices using **2** outperformed the reference devices with **1** in terms of luminance, efficiency, and lifetime. In particular, three- to fourfold higher efficiency was noted for devices with **2**, reaching, for example, 0.4 cd/A at pulsed currents of 2.5 mA. As far as the stability is concerned, devices with **2** also presented a better stability with greater than fivefold longer lifetime using, for example, pulsed currents of 5 mA—Table 3. These results are in line with both the enhanced photoluminescence and stability features upon attaching the methoxy groups at the *ortho* position of diimine ligands—vide supra. On top of all of the aforementioned, it is also important to note that devices with **2** featured an overall low average voltage, while the turn-on time—that is, the time to reach the maximum luminance level—was significantly reduced compared to those with **1**. This suggested that the overall ionic mobility and, in turn, the EDLs formation was more efficient in devices with **2**.

To further shed light onto this aspect, we performed electrochemical impedance spectroscopy (EIS) measurements at different applied voltages ranging from 0 to 5 V and frequencies going from 1 to $1 \times 10^6$ Hz.[20,54,55] EIS analyses of the Nyquist plots were conducted based on the equivalent circuit model provided in Figure S10. As shown in Figure S11, Nyquist plots consist of one semicircle whose diameter relates to

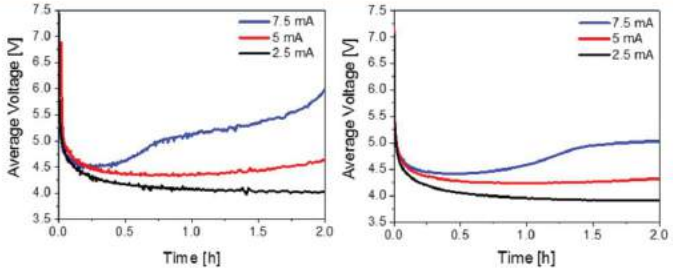


**Figure 7.** Average voltage over time of devices with **1** (left) and **2** (right) driven at various pulsed currents.



DOI: 10.1021/acs.inorgchem.8b01914
Inorg. Chem. 2018, 57, 10469−10479

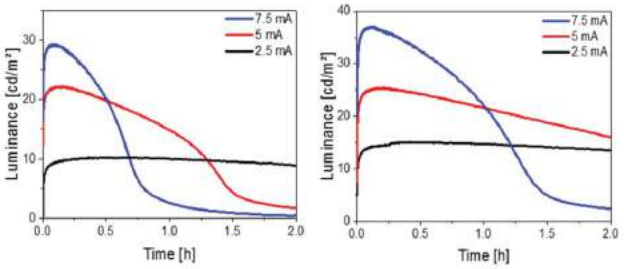


**Figure 8.** Luminance over time of devices with **1** (left) and **2** (right) driven at various pulsed currents.

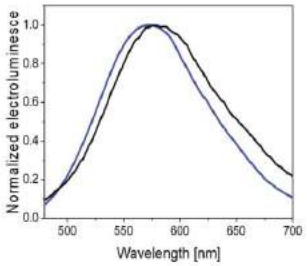


**Figure 9.** Electroluminescence spectra of devices with **1** (black) and **2** (blue) driven at a pulsed current of 7.5 mA.

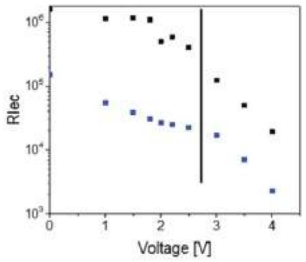


**Figure 10.** Changes in $R_{lec}$ of devices with **1** (black) and **2** (blue) under static EIS measurements. The injection voltage ($V_{inj}$) is indicated with a solid black line.

the resistance associated with the dynamics of the EDLs formation at the electrode interface at applied voltages below the band gap of the emitters (<2.5 V) and the reduction of the intrinsic nondoped region, when charge injection is effective (>2.5 V). The changes of the resistance upon applying different voltages are displayed in Figure 10. At 0 V, devices with **1** show a significantly higher resistance value compared to those of **2**—that is, $1.51 \times 10^6$ versus $1.6 \times 10^5$ Ω. This resistance value is used to calculate the overall ionic mobility ($\sigma$) of the active layer—see Experimental Section for more information. In line with the turn-on time, devices with **2** featured a 10-fold higher $\sigma$ ($5.3 \times 10^{-7}$ S/m) than that of devices with **1** ($5.1 \times 10^{-8}$ S/m). Furthermore, devices with **2** showed the typical exponential decay of the resistance related to the EDL formation until applied voltages close to 2.5 V—Figure 10.[20,54] This indicates that EDLs are easily formed due to the drifting of the mobile anions toward the electrode interfaces. In contrast, devices with **1** showed small changes in the resistance, until high voltages at ~1.7 V are applied, while a similar injection voltage ($V_{inj}$) at ~2.5 V was also noted.

Noteworthy, the resistance values of devices with **1** held 1 order of magnitude higher than those of devices with **2**. This finding could be related to either a different film morphology or a different cation−anion binding energy due to the sterical hindrance of the methoxy groups. The morphology of the active layers was therefore studied by using atomic force microscopy (AFM)—Figure S12. Both layers show the same morphology with a less than 2% roughness and the absence of aggregates, holes, and/or a noticeable phase separation. This left the second hypothesis as the most plausible one that needs, however, a further corroboration.

**2.5. Electroluminescence Characterization: Effect of the Device Design.** The new ligand design of complex **2** provides a significant enhancement with respect to the standard **1** in terms of efficacy and stability features due to the improved photoluminescence and ionic conductivity features in thin films. However, its moderate stability is still a concern. As noted by several authors, one of the major challenges in LECs involves the use of only one active compound for charge injection, transport,

**Table 3. Figures of Merit of Devices Prepared with 1 and 2 Driven at Different Pulsed Currents**

| | driving current (mA) | average voltage (V) | $L_{inst}$[a] (cd/m²) | $L_{max}$[b] (cd/m²) | $t_{on}$[c] (h) | $t_{1/2}$[d] (h) | efficacy (cd/A) | $\lambda_{em}$[e] (x/y CIE coord) |
|---|---|---|---|---|---|---|---|---|
| **1** | 2.5 | 4.0 | 0.3 | 10.2 | 0.90 | 5.5 | 0.1 | 587 (0.51/0.49) |
| **1** | 5.0 | 4.3 | 12.3 | 22.1 | 0.25 | 0.5 | 0.1 | |
| **1** | 7.5 | 4.5 | 16.6 | 28.5 | 0.20 | 0.6 | 0.1 | |
| **2** | 2.5 | 3.9 | 4.8 | 15.2 | 0.31 | 7.2 | 0.4 | 573 (0.46/0.52) |
| **2** | 5.0 | 4.2 | 7.8 | 25.1 | 0.12 | 2.6 | 0.3 | |
| **2** | 7.5 | 4.4 | 20.3 | 36.4 | 0.05 | 1.1 | 0.3 | |

[a]Instantaneous luminance or initial luminance level. [b]Maximum luminance. [c]Time to reach the maximum luminance. [d]Time to decay to the half of the maximum luminance. [e]Maximum in the electroluminescence spectrum of a fresh device (nm).



DOI: 10.1021/acs.inorgchem.8b01914
Inorg. Chem. 2018, 57, 10469−10479

and emission processes.[2,3,6] This is critical in copper(I) complexes, as the oxidation process is irreversible—vide supra. Although the negative impact of forming irreversible oxidized species upon device operation conditions on the device stability has already been claimed, the underlying reasons have not been clarified yet.[41,52,56]

In an attempt to reduce the formation of the oxidized species, we proposed to decouple hole/electron injection and transport using a bilayer device architecture, in which a thin CBP (15 nm)—that is, 4,4′-bis(9-carbazolyl)-1,1′-biphenyl, 4,4-*N*,*N*′-dicarbazole-1,1′-biphenyl)—layer separates the anode and active layer—Figure 11.

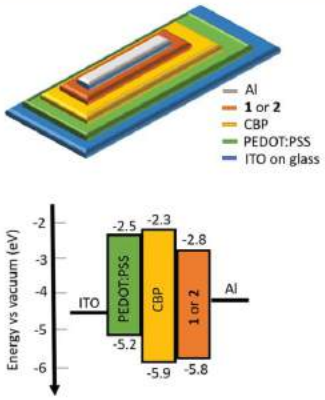


**Figure 11.** Schemes of a bilayer device design (top) and its energy diagram (bottom) as derived from the CV data with the formula $E_{HOMO/LUMO} = e(V_{Cp/Cp^+}) + 4.8$ eV.

This compound was selected among other hole transport matrices due to (i) the reversible oxidation behavior at 1.1 V ensuring a stable p-electrochemical doping,[52] (ii) its wide electrochemical band gap, in which the highest-occupied molecular orbital (HOMO) and lowest-unoccupied molecular orbital (LUMO) levels of both **1** and **2** are embedded—Figure 11, ensuring an efficient electron−hole recombination at the Cu-iTMC layer, and (iii) its low solubility in acetonitrile, allowing the easy fabrication of devices by sequential spin-coating process from orthogonal solvents—see Experimental Section for further details.

We decided to drive these devices at 7.5 mA, which corresponds to the pulsed current that caused the least stability in the single-layer devices, along with a remarkable degradation in the active layer, as highlighted by the rise in the voltage after ∼0.5 and ∼1 h for **1** and **2**, respectively—Table 3 and Figure 11. Similar to the single-layer devices, the LEC behavior was noted by the average voltage and luminance behaviors—Figure 12. While the luminance and efficacy remained very similar to those of the single-layer devices—for example, 32.9 cd/m$^2$ and 0.3 cd/A versus 36.4 cd/m$^2$ and 0.3 cd/A for single and double LECs with **2**, respectively, the stability was significantly enhanced by 1 order of magnitude—Figures 12, 13, and S13, as well as Table 4. Noteworthy, devices with **2** always outperformed those with **1**, regardless of the device architecture.

Since the EL spectra of the double-layer devices are similar to those of the single-layer devices without showing any EL feature of the CBP layer—Figures 13 and S13, we can postulate that electron−hole recombination efficiently occurs in the Cu-iTMC layers close at the interface CBP/Cu-iTMC. Since the hole energy barrier is the lowest one—Figure 11, hole injection occurs in the CBP layer, and then it is transferred to the Cu-iTMC, while electron injection and accumulation is effective in the Cu-iTMC emitting layer. As such, the formation of oxidized Cu-iTMC species is significantly reduced, leading to an enhanced device stability without affecting brightness and efficiency.

## 3. CONCLUSIONS

Two new findings on how to enhance the performance of LECs based on heteroleptic copper(I) complexes with the formula $[Cu(N^N)(P^P)]^+$ have been attained. First, we showed a new ligand design, obtained thanks to the symmetric insertion of two methoxy groups at the *ortho* position of the bpy ligand. The methoxy ligand combines high electron-donating properties, sterical hindrance, and a relatively high rotation freedom. This leads to superior photoluminescence and stability features, as demonstrated by spectroscopic and photo and thermal stability studies and XRD characterizations. These properties were also reflected in the EL features of single-layer LECs. Here, devices with the new emitter showed a significant enhanced luminance, efficiency, and stability compared to those of reference devices with the archetypal copper(I) complex without any substituents. Second, further improvements were achieved introducing a new device design to decouple electron/hole injection and transport from electron−hole recombination. As evidenced by the electrochemical behavior of this family of copper(I) complexes, the formation of oxidized species is nonreversible. In addition,

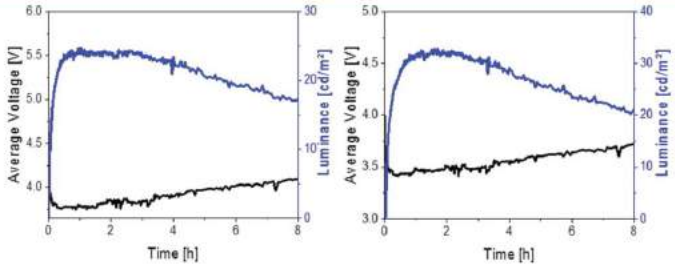


**Figure 12.** Average voltage and luminance over time of devices with CBP/**1** (left) and CBP/**2** (right) driven at a pulsed current of 7.5 mA.



DOI: 10.1021/acs.inorgchem.8b01914
Inorg. Chem. 2018, 57, 10469−10479

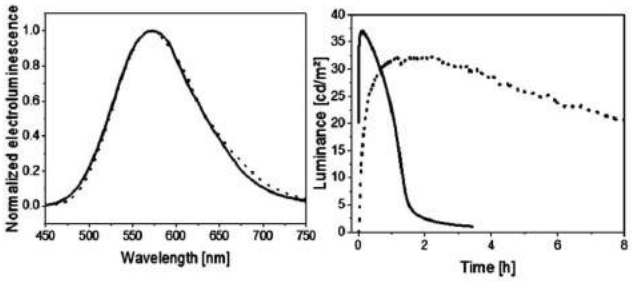


**Figure 13.** EL spectra (left) and luminance (right) over time of the devices with **2** (solid line) and with CBP/**2** (dotted line) active layers driven at a pulsed current of 7.5 mA.

**Table 4. Figures of Merit of Devices with CBP/1 and CBP/2 Architecture under a Pulsed Driving Current of 7.5 mA**

| device | average voltage (V) | $L_{max}$ (cd/m²) | $t_{on}$ (h) | $t_{1/2}$ (h) | efficacy (cd/A) |
|---|---|---|---|---|---|
| CBP/1 | 3.7 | 24.7 | 1.1 | 13 | 0.1 |
| CBP/2 | 3.4 | 32.9 | 1.6 | 10.8 | 0.3 |

the effect of its accumulation under device operation conditions has not been fully understood yet. Herein, the double-layer architecture, in which a bottom CBP-based layer acts as hole injection/transport layer, and the top Cu-iTMC-based layer acts as an electron transport layer and emitting layer. Regardless of the applied Cu-iTMC, this device design leads to 10-fold enhanced stability without affecting the luminance and efficacy levels. As such, we can state that the search of novel device architectures might be key toward future breakthrough in the LECs based on the third generation of emitters.

## 4. EXPERIMENTAL SECTION

**4.1. Materials.** All chemicals were purchased from chemical suppliers and used without further purification. All analytical reagent-grade solvents were purified by distillation. All reactions were performed under inert nitrogen atmosphere using standard vacuum lines techniques. PEDOT:PSS (Clevios PAI4083) was purchased from Heraeus. Microwave-assisted reactions were performed by a Biotage Initiator EXP synthesizer. Reactions were conducted in Biotage microwave vials, which were loaded using dried solvents. $^{1}H$, $^{13}C$, and $^{31}P$ NMR spectra were recorded on a JEOL ECP 400 spectrometer ($^{1}H$ NMR operating frequency 400 MHz) with chemical shifts referenced to residual protons of the solvent. The following abbreviations are used: s (singlet), d (doublet), t (triplet), dd (doublet of doublets), m (multiplet). Mass spectra were recorded on a Thermo-Finnigan Advantage Max Ion Trap Spectrometer equipped with an electrospray ion source (ESI).

**4.2. Syntheses.** *6,6′-Dimethoxy-2,2′-bipyridine.* In a 20 mL Biotage microwave vial, $NiCl_2 \cdot 6\,H_2O$ (0.23 g, 1 mmol) and triphenylphosphine (4 mmol, 1.06 g) were put in 10 mL of dimethylformamide under $N_2$. Zinc powder (3 mmol, 0.19 g) was then added to the solution, which was stirred for 1 h at 50 °C. At this point, 2-bromo-6-methoxypyridine (1 mmol, 0.19 g) was added, and the solution was stirred for 20 h at 50 °C. The reaction mixture was then poured in 4 mL of 17% $NH_3$ and stirred for 1 h, and the aqueous phase was extracted three times with $CH_2Cl_2$. The reunited organic phases were dried with a rotavapor, and the residue was gathered in $CH_2Cl_2$. The product—a white solid—was then purified via flash column chromatography, to give yield to the desired 6,6′-dimethoxy-2,2′-bipyridine (0.17 g, 0.8 mmol, 80%). $^{1}H$ NMR (400 MHz, $CDCl_3$): $\delta$ = 8.02 (d, $J$ = 7.4 Hz, 2H), 7.68 (dd, $J$ = 7.4, $J$ = 8.2 Hz, 2H), 6.75 (d, $J$ = 8.2 Hz, 2H), 4.04 (s, 6H) ppm. $^{13}C$ NMR (100 MHz, $CDCl_3$): $\delta$ = 163.5, 153.6, 139.4, 113.8, 111.0, 53.3 ppm. Mass $m/z$ (ESI⁺) for $C_{12}H_{12}N_2O_2$ calcd 216.09, found 216.07 $[M+H]^+$. Anal. Calcd (%) for $C_{12}H_{12}N_2O_2$: C 66.65, H 5.59, N 12.96, O 14.80; found: C 66.28, H 5.65, N 12.88, O 15.21.

*[Cu(6,6′-dimethoxy-2,2′-bipyridine)(bis[2-(diphenylphosphino)-phenyl]ether))]$PF_6$ (**2**).* In a 50 mL three-necked round-bottom flask $[Cu(CH_3CN)_4]PF_6$ (0.18 g, 0.5 mmol) and POP (0.29 g, 0.5 mmol) were mixed at room temperature under nitrogen. The solid reagents were then dissolved in 15 mL of freshly distilled $CH_2Cl_2$, and the mixture was stirred at room temperature for 30 min. Then 15 mL of a degassed $CH_2Cl_2$ solution of 6,6′-dimethoxy-2,2′-bipyridine (0.11 g, 0.5 mmol) was added in the reaction flask, generating an instantaneous turn of the solution color from colorless to bright yellow. The solution was stirred for additional 30 min under $N_2$ at room temperature. The nitrogen flux was then removed, and the solvent was evaporated, providing a yellow solid powder. The solid was washed with diethyl ether to separate the product from the unreacted ligand. The purification was monitored via thin-layer chromatography (TLC) and afforded complex **2** (0.41 g, 87%). $^{1}H$ NMR: (400 MHz, $CD_2Cl_2$): $\delta$ = 7.93 (t, $J$ = 8.0 Hz, 2H), 7.74 (d, $J$ = 7.6 Hz, 2H), 7.28–7.08 (m, 22H), 6.97 (t, $J$ = 7.5 Hz, 2H), 6.86–6.81 (m, 4H), 6.72 (d, $J$ = 8.3 Hz, 2H), 3.31 (s, 6H) ppm. $^{13}C$ NMR (100 MHz, $CD_2Cl_2$): $\delta$ = 164.0, 158.6 (t, $J$ = 6.1 Hz), 151.1, 141.9, 134.0, 133.5 (t, $J$ = 8.0 Hz), 132.2 (t, $J$ = 16.3 Hz), 131.7, 129.9, 128.6, 125.7 (t, $J$ = 14.4 Hz), 124.7, 120.1, 115.3, 107.3, 55.1 ppm. $^{31}P$ NMR (162 MHz, $CD_2Cl_2$): $\delta$ = −10.55 (broad s), −143.87 ($PF_6$ septet, $J$ = 710.43 Hz) ppm. Mass $m/z$ (ESI⁺) for $C_{48}H_{40}N_2O_3P_2Cu$ calcd 817.18, found 816.20 $[M]^+$. Anal. Calcd (%) for $C_{48}H_{40}N_2O_3F_6P_3Cu$: C 59.85, H 4.19, N 2.91, O 4.98; found: C 59.99, H 4.38, N 2.83, O 5.32.

**4.3. X-ray Crystallography.** Author: Please verify that the changes made to improve the English still retain your original meaning.The crystal structures of **2** and of the ligand MeO-bpy alone were solved, and relevant crystallographic data are available in Table 1. Single-crystal diffraction data were collected using an Oxford Xcalibur CCD area detector diffractometer. Structure solution was performed by SIR2011,[57] and refinement with full-matrix least-squares was by SHELXL-2013.[58] Mercury was used for crystal structure drawing.[59] A suitable crystal was grown by slow evaporation of a 50:50 water/acetone solution of **2**. Despite all crystallization attempts, the crystal grows in aggregates of very thin laminae. After it was checked optically and by a short XRD test a very small lamina was selected—Figure S2. The crystal, despite its reduced size and weakly diffracting nature, was suitable for structure solution and refinement, but it required a very long data collection (~50 h with a single frame acquisition of 200 s). The internal agreement factor ($R_{int}$) and $I/\sigma$ are good up to $2\theta$ = 20 and reasonable up to $2\theta$ = 30—Figure S3. Beyond this limit, the number of unobserved reflections increase dramatically, similarly to $R_{int}$ values, but observed reflections are still present, and cutting these data would decrease the disagreement factors but also the data/parameter ratio. Therefore, all the collected data were used for the refinement, resulting more stable even if this choice generates some alerts in the checkcif. The distribution of distances and of anisotropic displacement parameter



DOI: 10.1021/acs.inorgchem.8b01914
Inorg. Chem. 2018, 57, 10469−10479

values confirms the stability of the refinement and the goodness of the data—Tables S1–S3. The structure that resulted was ordered similarly to that reported by Weber et al.[40] even for the $PF_6^-$ anion, which was often found disordered in similar structures.[60] Relevant XRD data are reported in Table 1, and geometric data are in Tables S1–S6 in the Supporting Information.

A transparent lamina was obtained by slow evaporation of MeO-bpy, dissolved in a 1:1 ethanol/water mixture. MeO-bpy crystallized unexpectedly in the non-centrosymmetric *Pn*21*a* space group. Attempt at solving MeO-bpy structure in *Pnma* space group resulted in a disordered structure with a not interpretable electron density. The good agreement of values and ADP parameters, together with the absence of serious alerts in the checkcif, confirm the space group assignation and the reliability of the structure. These peculiarities, along with some difficulties in its structure solution, might explain the current absence in the CCDC database, despite the molecule simplicity. Constraint of the ADP of corresponding atoms was employed, and a stable refinement was obtained, as indicated by the good agreement values—Table S1, and by the reasonable obtained geometric—Tables S1 and S2, and atomic displacement parameters (ADP)—Table S3. It is worth noting that MeO-bpy crystallizes in its neutral form as indicated by the absence of counteranions and by the packing consistent with a not-protonated nitrogen. In CCDC database most of the 6,6′-dimethoxy-2,2′-bipyridine structures show a cationic form.[61] All the related crystal structures show the stable trans conformation like MeO-bpy, except that reported by Chan et al.,[62] where the NCCN torsion angle is equal to −129°. Concerning MeO-bpy packing, two subsets of parallel $\pi$-stacking of the molecules and CH···O contacts of ∼2.5 Å, with each subset perpendicular to the adjacent subset.

**4.4. Theoretical Calculations.** All the calculations were performed by the Gaussian 09 (G09) program package,[63] employing DFT method,[64] the Becke three-parameter hybrid functional,[65] the Lee–Yang–Parr[66] gradient-corrected correlation functional (B3LYP), and the 6-31G** basis set.[67]

**4.5. Spectroscopic, Electrochemical, and Microscopy Characterization.** The measurements under UV irradiation were performed with a UV lamp UVP 95-0199-01 model UVM-18 EL series hand-held UV lamp. Steady-state absorption spectra were recorded with a PerkinElmer Lambda 35. Steady-state emission spectra, photoluminescence quantum yields, and excited-state lifetimes were recorded with a fluoromax spectrometer from HORIBA Jobin Yvon IBH using an integrating sphere and the fluorescence and phosphorescence mode (measurement after 10 ns). AFM assays were performed with Veeco Dimension 5000 with a NanoScope V probe head and the Gwyddion evaluation software. Cyclic voltammetry was performed in acetonitrile solution, using the redox couple $Cp_2Fe/Cp_2Fe^+$ as internal reference ($E_{1/2}$ = +0.40 V), a solution of tetrabuthylammonium hexafluorophosphate 0.1 M as electrolyte, and a glassy/carbon electrode as working electrode. The scan speed was 100 mV/s. It was measured with a Metrohm $\mu$AutolabIII potentiostat.

**4.6. Device Fabrication and Characterization.** ITO substrates were purchased from Naranjo Substrates with ITO thickness of 130 nm. They were first cleaned with detergent, water, ethanol, and propan-2-ol as solvents in an ultrasonic bath (frequency 37–70 Hz, 30–40 °C) for 15 min each. Afterward, the slides were dried with $N_2$ gas and put in an UV-ozone cleaner for 8 min. A solution of PEDOT:PSS was filtered, sonicated, and mixed with propan-2-ol in a ratio of 3:1. The aforementioned solution (50 $\mu$L) was dropped onto the ITO, while the spin coater was rotating at a speed of 1500 rpm for 60 s giving rise to a thickness of 70 nm after drying the covered substrates for 10 min at 120 °C. The slides were then stored in a glovebox ($O_2$ level < 0.1 ppm, $H_2O$ level < 0.5 ppm). Complexes **1** and **2** were dissolved in acetonitrile with a concentration of 20 mg/mL. They were stirred in a closed vial for 10 min, and, if necessary, it was filtered. To obtain a thickness of ∼120 nm of active layer, the solution (75 $\mu$L) was spread onto the substrate that was later spin-coated with a speed of 1000 rpm for 50 s. The coated slides were then put in a glovebox and dried on a hot plate for 30 min at 90 °C. To obtain the biactive layer devices, a first layer of pristine CBP was deposited using a tetrahydrofuran (THF) solution of 2 mg/mL of the molecule and spin-coating it for 30 s at 3000 rpm; the parameters for **1** and **2** were the same as described before but with a concentration of 15 mg/mL. Once the active layer was deposited, the samples were transferred into an inert atmosphere glovebox (<0.1 ppm of $O_2$ and $H_2O$, Innovative Technology). Aluminum cathode electrode (90 nm) was thermally evaporated using a shadow mask under high vacuum (<1 × $10^{-6}$ mbar) using an Angstrom Covap evaporator integrated into the inert atmosphere glovebox. The device statistics involve up to five different devices—that is, a total number of 20 pixels. Time dependence of luminance, voltage, and current was measured by applying constant and/or pulsed voltage and current by monitoring the desired parameters simultaneously by using Avantes spectrophotometer (Avaspec-ULS2048L-USB2) in conjunction with a calibrated integrated sphere Avasphere 30-Irrad and Botest OLT OLED Lifetime-Test System. Electroluminescence spectra were recorded using the above-mentioned spectrophotometer. Electrochemical impedance spectroscopic assays were performed with a potentiostat/galvanostat (Metrohm $\mu$AutolabIII) equipped with a frequency response analyzer module (FRA2). Measurements were performed at the applied voltage range from 0 to 4 V and fitted with the Nova software using the circuit model shown in Figure S10. The alternating-current (AC) signal amplitude was set to 10 mV, modulated in a frequency range from 10 to 1 MHz. The Nova 1.11 software was used to obtain the parameters from the equivalent circuit. With these data at hand, the resistance of the intrinsic nondoped region ($R_i$) was directly obtained. The film conductivity ($S/m$) is measured at 0 V with the following equation: $\sigma = d/(AR_i)$, where $d$ is the thickness of the layer, $A$ is the area of the electrodes, and $R_i$ is the resistance of the active layer.

## ■ ASSOCIATED CONTENT

### Supporting Information

Supporting Information content: Part 1. The Supporting Information is available free of charge on the ACS Publications website at DOI: 10.1021/acs.inorgchem.8b01914.

Characterization of MeO-bpy: chemical structure, $^1H$ and $^{13}C$ NMR, X-ray data, and theoretical study. Characterization of complex **2**: $^1H$, $^{13}C$, and $^{31}P$ NMR, X-ray, and absorption spectrum. Device characterization. EIS and AFM of the active layer. References. (PDF)

### Accession Codes

CCDC 1588140–1588141 contain the supplementary crystallographic data for this paper. These data can be obtained free of charge via www.ccdc.cam.ac.uk/data_request/cif, or by emailing data_request@ccdc.cam.ac.uk, or by contacting The Cambridge Crystallographic Data Centre, 12 Union Road, Cambridge CB2 1EZ, UK; fax: +44 1223 336033.

## ■ AUTHOR INFORMATION


### Corresponding Authors

*E-mail: claudia.barolo@unito.it. (C.B.)
*E-mail: ruben.costa@imdea.org. (R.D.C.)

### ORCID

Giorgio Volpi: 0000-0002-9695-9202
Claudio Garino: 0000-0002-7854-6076
Claudia Barolo: 0000-0003-0627-2579
Rubén D. Costa: 0000-0003-3776-9158


### Author Contributions

The manuscript was written through contributions of all authors. All authors have given approval to the final version of the manuscript.

### Notes

The authors declare no competing financial interest.



DOI: 10.1021/acs.inorgchem.8b01914
Inorg. Chem. 2018, 57, 10469–10479

## ■ ACKNOWLEDGMENTS

E.F. and R.D.C. acknowledge the program "Ayudas para la atracción de talento investigador−Modalidad 1 of the Consejería de Educación, Juventud y Deporte−Comunidad de Madrid with the reference number 2016-T1/IND-1463". R.D.C. acknowledges Spanish MINECO (RYC-2016-20891) for the Ramón y Cajal program (RYC-2016-20891).

## ■ REFERENCES

(1) Tang, S.; Edman, L. Light-Emitting Electrochemical Cells: A Review on Recent Progress. *Top Curr. Chem.* **2016**, *374*, 40.

(2) Fresta, E.; Costa, R. D. Beyond Traditional Light-Emitting Electrochemical Cells−a Review of New Device Designs and Emitters. *J. Mater. Chem. C* **2017**, *5*, 5643−5675.

(3) Costa, R. D. *Light-Emitting Electrochemical Cells. Concepts, Advances and Challenges*, 1st ed.; Costa, R. D., Ed.; Springer: Basel, Switzerland, 2017.

(4) Nardelli, A.; Deuschle, E.; de Azevedo, L. D.; Pessoa, J. L. N.; Ghisi, E. Assessment of Light Emitting Diodes Technology for General Lighting: A Critical Review. *Renewable Sustainable Energy Rev.* **2017**, *75*, 368−379.

(5) Housecroft, C. E.; Constable, E. C. Over the LEC Rainbow: Colour and Stability Tuning of Cyclometallated Iridium(III) Complexes in Light-Emitting Electrochemical Cells. *Coord. Chem. Rev.* **2017**, *350*, 155−177.

(6) Costa, R. D.; Ortí, E.; Bolink, H. J.; Monti, F.; Accorsi, G.; Armaroli, N. Luminescent Ionic Transition-Metal Complexes for Light-Emitting Electrochemical Cells. *Angew. Chem., Int. Ed.* **2012**, *51*, 8178−8211.

(7) Matyba, P.; Yamaguchi, H.; Chhowalla, M.; Robinson, N. D.; Edman, L. Flexible and Metal-Free Light-Emitting Electrochemical Cells Based on Graphene and PEDOT-PSS as the Electrode Materials. *ACS Nano* **2011**, *5*, 574−580.

(8) Yu, Z.; Niu, X.; Liu, Z.; Pei, Q. Intrinsically Stretchable Polymer Light-Emitting Devices Using Carbon Nanotube-Polymer Composite Electrodes. *Adv. Mater.* **2011**, *23*, 3989−3994.

(9) Liang, J.; Li, L.; Niu, X.; Yu, Z.; Pei, Q. Fully Solution-Based Fabrication of Flexible Light-Emitting Device at Ambient Conditions. *J. Phys. Chem. C* **2013**, *117*, 16632−16639.

(10) Altal, F.; Gao, J. Scanning Photocurrent and PL Imaging of a Frozen Polymer P-I-N Junction. *Phys. Status Solidi RRL* **2015**, *9*, 77−81.

(11) Matyba, P.; Maturova, K.; Kemerink, M.; Robinson, N. D.; Edman, L. The Dynamic Organic P-N Junction. *Nat. Mater.* **2009**, *8*, 672−676.

(12) van Reenen, S.; Matyba, P.; Dzwilewski, A.; Janssen, R. A. J.; Edman, L.; Kemerink, M. A Unifying Model for the Operation of Light-Emitting Electrochemical Cells. *J. Am. Chem. Soc.* **2010**, *132*, 13776−13781.

(13) Sandstrom, A.; Dam, H. F.; Krebs, F. C.; Edman, L. Ambient Fabrication of Flexible and Large-Area Organic Light-Emitting Devices Using Slot-Die Coating. *Nat. Commun.* **2012**, *3*, 1002.

(14) Mauthner, G.; Landfester, K.; Köck, A.; Brückl, H.; Kast, M.; Stepper, C.; List, E. J. W. Inkjet Printed Surface Cell Light-Emitting Devices from a Water-Based Polymer Dispersion. *Org. Electron.* **2008**, *9*, 164−170.

(15) Sandstroem, A.; Asadpoordarvish, A.; Enevold, J.; Edman, L. Spraying Light: Ambient-Air Fabrication of Large-Area Emissive Devices on Complex-Shaped Surfaces. *Adv. Mater.* **2014**, *26*, 4975−4980.

(16) Weber, M. D.; Adam, M.; Tykwinski, R. R.; Costa, R. D. Controlling the Chromaticity of Small-Molecule Light-Emitting Electrochemical Cells Based on TIPS-Pentacene. *Adv. Funct. Mater.* **2015**, *25*, 5066−5074.

(17) Weber, K. T.; Karikis, K.; Weber, M. D.; Coto, P. B.; Charisiadis, A.; Charitaki, D.; Charalambidis, G.; Angaridis, P.; Coutsolelos, A. G.; Costa, R. D. Cunning Metal Core: Efficiency/stability Dilemma in Metallated Porphyrin Based Light-Emitting Electrochemical Cells. *Dalt. Trans.* **2016**, *45*, 13284−13288.

(18) Qian, G.; Lin, Y.; Wantz, G.; Davis, A. R.; Carter, K. R.; Watkins, J. J. Saturated and Multi-Colored Electroluminescence from Quantum Dots Based Light Emitting Electrochemical Cells. *Adv. Funct. Mater.* **2014**, *24*, 4484−4490.

(19) Aygüler, M. F.; Weber, M. D.; Puscher, B. M. D.; Medina, D. D.; Docampo, P.; Costa, R. D. Light-Emitting Electrochemical Cells Based on Hybrid Lead Halide Perovskite Nanoparticles. *J. Phys. Chem. C* **2015**, *119*, 12047−12054.

(20) Puscher, B. M. D.; Aygueler, M. F.; Docampo, P.; Costa, R. D. Unveiling the Dynamic Processes in Hybrid Lead Bromide Perovskite Nanoparticle Thin Film Devices. *Adv. Energy Mater.* **2017**, *7*, 1602283.

(21) Asadpoordarvish, A.; Sandström, A.; Larsen, C.; Bollström, R.; Toivakka, M.; Österbacka, R.; Edman, L. Light-Emitting Paper. *Adv. Funct. Mater.* **2015**, *25*, 3238−3245.

(22) Zhang, Z.; Li, Y.; Guan, G.; Li, H.; Luo, Y.; Zhao, F.; Zhang, Q.; Wei, B.; Pei, Q.; Peng, H.; et al. A Colour-Tunable, Weavable Fibre-Shaped Polymer Light-Emitting Electrochemical Cell. *Nat. Photonics* **2015**, *9*, 233−238.

(23) Lindh, E. M.; Sandström, A.; Andersson, M. R.; Edman, L. Luminescent Line Art by Direct-Write Patterning. *Light: Sci. Appl.* **2016**, *5*, e16050.

(24) Weber, M. D.; Wittmann, J. E.; Burger, A.; Malcioglu, O. B.; Segarra-Marti, J.; Hirsch, A.; Coto, P. B.; Bockstedte, M.; Costa, R. D. From White to Red: Electric-Field Dependent Chromaticity of Light-Emitting Electrochemical Cells Based on Archetypal Porphyrins. *Adv. Funct. Mater.* **2016**, *26*, 6737−6750.

(25) Nishikitani, Y.; Takizawa, D.; Nishide, H.; Uchida, S.; Nishimura, S. White Polymer Light-Emitting Electrochemical Cells Fabricated Using Energy Donor and Acceptor Fluorescent ??-Conjugated Polymers Based on Concepts of Band-Structure Engineering. *J. Phys. Chem. C* **2015**, *119*, 28701−28710.

(26) Tang, S.; Pan, J.; Buchholz, H. a.; Edman, L. White Light from a Single-Emitter Light-Emitting Electrochemical Cell. *J. Am. Chem. Soc.* **2013**, *135*, 3647−3652.

(27) Henwood, A. F.; Zysman-Colman, E. Luminescent Iridium Complexes Used in Light-Emitting Electrochemical Cells (LEECs). *Top. Curr. Chem.* **2016**, *374*, 36.

(28) Minaev, B.; Minaeva, V.; Ågren, H. Theoretical Study of the Cyclometalated Iridium (III) Complexes Used as Chromophores for Organic Light-Emitting Diodes. *J. Phys. Chem. A* **2009**, *113*, 726−735.

(29) Costa, R. D.; Monti, F.; Accorsi, G.; Barbieri, A.; Bolink, H. J.; Ortí, E.; Armaroli, N. Photophysical Properties of Charged Cyclometalated Ir(III) Complexes: A Joint Theoretical and Experimental Study. *Inorg. Chem.* **2011**, *50*, 7229−7238.

(30) Linfoot, C. L.; Leitl, M. J.; Richardson, P.; Rausch, A. F.; Chepelin, O.; White, F. J.; Yersin, H.; Robertson, N. Thermally Activated Delayed Fluorescence (TADF) and Enhancing Photoluminescence Quantum Yields of $[Cu^{I}(Diimine)(diphosphine)]^{+}$ Complexes—Photophysical, Structural, and Computational Studies. *Inorg. Chem.* **2014**, *53*, 10854−10861.

(31) Czerwieniec, R.; Leitl, M. J.; Homeier, H. H. H.; Yersin, H. Cu(I) Complexes − Thermally Activated Delayed Fluorescence. Photophysical Approach and Material Design. *Coord. Chem. Rev.* **2016**, *325*, 2−28.

(32) Onoue, Y.; Hiraki, K.; Nishikawa, Y. Interactions of Solid Supports and Fluorescent Substances in Thermally Activated Delayed Fluorescence. *Anal. Sci.* **1987**, *3*, 509−513.

(33) Armaroli, N.; Accorsi, G.; Cardinali, F.; Listorti, A. Photochemistry and Photophysics of Coordination Compounds: Copper. In *Photochemistry and Photophysics of Coordination Compounds I*; Balzani, V., Campagna, S., Eds.; Springer: Berlin, Germany, 2007; Vol. *280*, pp 69−115.

(34) Lavie-Cambot, A.; Cantuel, M.; Leydet, Y.; Jonusauskas, G.; Bassani, D. M.; McClenaghan, N. D. Improving the Photophysical Properties of Copper(I) Bis(phenanthroline) Complexes. *Coord. Chem. Rev.* **2008**, *252*, 2572−2584.



DOI: 10.1021/acs.inorgchem.8b01914
Inorg. Chem. 2018, 57, 10469−10479

(35) Bizzarri, C.; Strabler, C.; Prock, J.; Trettenbrein, B.; Ruggenthaler, M.; Yang, C. H.; Polo, F.; Iordache, A.; Brüggeller, P.; De Cola, L. Luminescent Dinuclear Cu(I) Complexes Containing Rigid Tetraphosphine Ligands. *Inorg. Chem.* **2014**, *53*, 10944−10951.
(36) Asil, D.; Foster, J. A.; Patra, A.; Dehatten, X.; Delbarrio, J.; Scherman, O. A.; Nitschke, J. R.; Friend, R. H. Temperature- and Voltage-Induced Ligand Rearrangement of a Dynamic Electroluminescent Metallopolymer. *Angew. Chem., Int. Ed.* **2014**, *53*, 8388−8391.
(37) Keller, S.; Constable, E. C.; Housecroft, C. E.; Neuburger, M.; Prescimone, A.; Longo, G.; Pertegás, A.; Sessolo, M.; Bolink, H. J. [Cu(bpy)(PˆP)] + Containing Light-Emitting Electrochemical Cells: Improving Performance through Simple Substitution. *Dalt. Trans.* **2014**, *43*, 16593−16596.
(38) Keller, S.; Pertegás, A.; Longo, G.; Martínez, L.; Cerdá, J.; Junquera-Hernández, J. M.; Prescimone, A.; Constable, E. C.; Housecroft, C. E.; Orti, E.; et al. Correction: Shine Bright or Live Long: Substituent Effects in $[Cu(NˆN)(PˆP)]^+$-Based Light-Emitting Electrochemical Cells Where NˆN Is a 6-Substituted 2,2′-Bipyridine. *J. Mater. Chem. C* **2016**, *4*, 3872−3872.
(39) Brunner, F.; Martínez-Sarti, L.; Keller, S.; Pertegás, A.; Prescimone, A.; Constable, E. C.; Bolink, H. J.; Housecroft, C. E. Peripheral Halo-Functionalization in [Cu(NˆN)(PˆP)](+) Emitters: Influence on the Performances of Light-Emitting Electrochemical Cells. *Dalt. Trans.* **2016**, *45*, 15180−15192.
(40) Weber, M. D.; Garino, C.; Volpi, G.; Casamassa, E.; Milanesio, M.; Barolo, C.; Costa, R. D. Origin of a Counterintuitive Yellow Light-Emitting Electrochemical Cell Based on a Blue-Emitting Heteroleptic Copper(I) Complex. *Dalt. Trans.* **2016**, *45*, 8984−8993.
(41) Elie, M.; Sguerra, F.; Di Meo, F.; Weber, M. D.; Marion, R.; Grimault, A.; Lohier, J. F.; Stallivieri, A.; Brosseau, A.; Pansu, R. B.; et al. Designing NHC-Copper(I) Dipyridylamine Complexes for Blue Light-Emitting Electrochemical Cells. *ACS Appl. Mater. Interfaces* **2016**, *8*, 14678−14691.
(42) Mohankumar, M.; Monti, F.; Holler, M.; Niess, F.; Delavaux-Nicot, B.; Armaroli, N.; Sauvage, J. P.; Nierengarten, J. F. Combining Topological and Steric Constraints for the Preparation of Heteroleptic Copper(I) Complexes. *Chem. - Eur. J.* **2014**, *20*, 12083−12090.
(43) Kaeser, A.; Mohankumar, M.; Mohanraj, J.; Monti, F.; Holler, M.; Cid, J.-J.; Moudam, O.; Nierengarten, I.; Karmazin-Brelot, L.; Duhayon, C.; et al. Heteroleptic Copper(I) Complexes Prepared from Phenanthroline and Bis-Phosphine Ligands. *Inorg. Chem.* **2013**, *52*, 12140−12151.
(44) Weber, M. D.; Viciano-Chumillas, M.; Armentano, D.; Cano, J.; Costa, R. D. σ-Hammett Parameter: A Strategy to Enhance Both Photo- and Electro-Luminescence Features of Heteroleptic Copper(I) Complexes. *Dalt. Trans.* **2017**, *46*, 6312−6323.
(45) Costa, R. D.; Tordera, D.; Orti, E.; Bolink, H. J.; Schönle, J.; Graber, S.; Housecroft, C. E.; Constable, E. C.; Zampese, J. A. Copper(i) Complexes for Sustainable Light-Emitting Electrochemical Cells. *J. Mater. Chem.* **2011**, *21*, 16108−16118.
(46) Kuang, S.-M.; Cuttell, D. G.; McMillin, D. R.; Fanwick, P. E.; Walton, R. A. Synthesis and Structural Characterization of Cu(I) and Ni(II) Complexes That Contain the Bis[2-(Diphenylphosphino)-phenyl]ether Ligand. Novel Emission Properties for the Cu(I) Species. *Inorg. Chem.* **2002**, *41*, 3313−3322.
(47) Andrés-Tomé, I.; Fyson, J.; Baiao Dias, F.; Monkman, A. P.; Iacobellis, G.; Coppo, P. Copper(I) Complexes with Bipyridyl and Phosphine Ligands: A Systematic Study. *Dalt. Trans.* **2012**, *41*, 8669−8674.
(48) Nelson, T. D.; Crouch, R. D. Cu, Ni, and Pd Mediated Homocoupling Reactions in Biaryl Syntheses: The Ullmann Reaction. *Org. React.* **2004**, *63*, 265−555.
(49) Kaeser, A.; Moudam, O.; Accorsi, G.; Séguy, I.; Navarro, J.; Belbakra, A.; Duhayon, C.; Armaroli, N.; Delavaux-Nicot, B.; Nierengarten, J. F. Homoleptic Copper(I), Silver(I), and Gold(I) Bisphosphine Complexes. *Eur. J. Inorg. Chem.* **2014**, *2014*, 1345−1355.
(50) Yuasa, J.; Dan, M.; Kawai, T. Phosphorescent Properties of Metal-Free Diphosphine Ligands and Effects of Copper Binding. *Dalt. Trans.* **2013**, *42*, 16096−16101.
(51) Armaroli, N. Photoactive Mono- and Polynuclear Cu(I)−phenanthrolines. A Viable Alternative to Ru(II)−polypyridines? *Chem. Soc. Rev.* **2001**, *30*, 113−124.
(52) Lundberg, P.; Lindh, E. M.; Tang, S.; Edman, L. Towards Efficient and Metal-Free Emissive Devices: A Solution-Processed Host-Guest Light-Emitting Electrochemical Cell Featuring Thermally Activated Delayed Fluorescence. *ACS Appl. Mater. Interfaces* **2017**, *9*, 28810−28816.
(53) Gao, Y.; MacKenzie, R. C. I.; Liu, Y.; Xu, B.; Van Loosdrecht, P. H. M.; Tian, W. Engineering Ultra Long Charge Carrier Lifetimes in Organic Electronic Devices at Room Temperature. *Adv. Mater. Interfaces* **2015**, *2*, 1400555.
(54) Munar, A.; Sandström, A.; Tang, S.; Edman, L. Shedding Light on the Operation of Polymer Light-Emitting Electrochemical Cells Using Impedance Spectroscopy. *Adv. Funct. Mater.* **2012**, *22*, 1511−1517.
(55) Van Reenen, S.; Janssen, R. A. J.; Kemerink, M. Dynamic Processes in Sandwich Polymer Light-Emitting Electrochemical Cells. *Adv. Funct. Mater.* **2012**, *22*, 4547−4556.
(56) Wågberg, T.; Hania, P. R.; Robinson, N. D.; Shin, J. H.; Matyba, P.; Edman, L. On the Limited Operational Lifetime of Light-Emitting Electrochemical Cells. *Adv. Mater.* **2008**, *20*, 1744−1749.
(57) Burla, M. C.; Caliandro, R.; Camalli, M.; Carrozzini, B.; Cascarano, G. L.; Giacovazzo, C.; Mallamo, M.; Mazzone, A.; Polidori, G.; Spagna, R. SIR2011: A New Package for Crystal Structure Determination and Refinement. *J. Appl. Crystallogr.* **2012**, *45*, 357−361.
(58) Sheldrick, G. M. Experimental Phasing with SHELXC/D/E: Combining Chain Tracing with Density Modification. *Acta Crystallogr., Sect. D: Biol. Crystallogr.* **2010**, *66*, 479−485.
(59) Macrae, C. F.; Bruno, I. J.; Chisholm, J. A.; Edgington, P. R.; McCabe, P.; Pidcock, E.; Rodriguez-Monge, L.; Taylor, R.; Van De Streek, J.; Wood, P. A. Mercury CSD 2.0-New Features for the Visualization and Investigation of Crystal Structures. *J. Appl. Crystallogr.* **2008**, *41*, 466−470.
(60) Gobetto, R.; Nervi, C.; Romanin, B.; Salassa, L.; Milanesio, M.; Croce, G. X-Ray Structures and Complete NMR Assignment by DFT Calculations of [Os(bpy)2(CO)Cl]PF6 and [Os(bpy)2(CO)H]PF6 Complexes. *Organometallics* **2003**, *22*, 4012−4019.
(61) Bator, G.; Sawka-Dobrowolska, W.; Sobczyk, L.; Grech, E.; Nowicka-Scheibe, J.; Pawlukojć, A.; Wuttke, J.; Baran, J.; Owczarek, M. 4,4′-, 5,5′-, and 6,6′- Dimethyl-2,2′-Bipyridyls: The Structures, Phase Transitions, Vibrations, and Methyl Group Tunneling of Their Complexes with Chloranilic Acid. *J. Chem. Phys.* **2011**, *135*, 44509.
(62) Chan, B. C. K.; Baird, M. C. Reactions of 6,6′-Dimethyl-2,2′-Bipyridyl with Iron(II) in Aqueous and Non-Aqueous Media. *Inorg. Chim. Acta* **2004**, *357*, 2776−2782.
(63) Frisch, M. J.; Trucks, G. W.; Schlegel, H. B.; Scuseria, G. E.; Robb, M. A.; Cheeseman, J. R.; G. Scalmani, V.; Barone, B.; Mennucci, G. A.; Petersson, H.; et al. *Gaussian09*, Revision E.01; Gaussian, Inc.: Wallingford, CT, 2009.
(64) Casida, M. E.; Jamorski, C.; Casida, K. C.; Salahub, D. R. Molecular Excitation Energies to High-Lying Bound States from Time-Dependent Density-Functional Response Theory: Characterization and Correction of the Time-Dependent Local Density Approximation Ionization Threshold. *J. Chem. Phys.* **1998**, *108*, 4439−4449.
(65) Becke, A. D. Density-functional Thermochemistry. III. The Role of Exact Exchange. *J. Chem. Phys.* **1993**, *98*, 5648−5652.
(66) Lee, C.; Yang, W.; Parr, R. G. Development of the Colle-Salvetti Correlation-Energy Formula into a Functional of the Electron Density. *Phys. Rev. B: Condens. Matter Mater. Phys.* **1988**, *37*, 785−789.
(67) McLean, A. D.; Chandler, G. S. Contracted Gaussian Basis Sets for Molecular Calculations. I. Second Row Atoms, $Z = 11−18$. *J. Chem. Phys.* **1980**, *72*, 5639−5648.



DOI: 10.1021/acs.inorgchem.8b01914
*Inorg. Chem.* 2018, 57, 10469−10479

SUPPORTING INFORMATION FOR:

# Novel ligand and device designs for stable light-emitting electrochemical cells based on heteroleptic copper (I) complexes

*Elisa Fresta,[a] Giorgio Volpi,[b] Marco Milanesio,[c] Claudio Garino,[b] Claudia Barolo*,[b,d] Rubén D. Costa*[a]*

a. IMDEA Materials Institute, Calle Eric Kandel 2, 28906 Getafe, Madrid, Spain.

b. Department of Chemistry, NIS Interdepartmental Centre and INSTM Reference Centre, Università degli Studi di Torino, Via Pietro Giuria 7, 10125, Torino, Italy.

c. Università del Piemonte Orientale Dipartimento di Scienze e Innovazione Tecnologica, Viale T. Michelin 11, I-15121, Alessandria, Italy and CrisDi Interdepartmental Center for Crystallography.

d. ICxT Interdepartmental Centre, Università degli Studi di Torino, Lungo Dora Siena 100, 10153, Torino, Italy.

claudia.barolo@unito.it, ruben.costa@imdea.org

*Part 1.*

a)

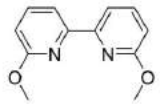
N
N
O
O

b)

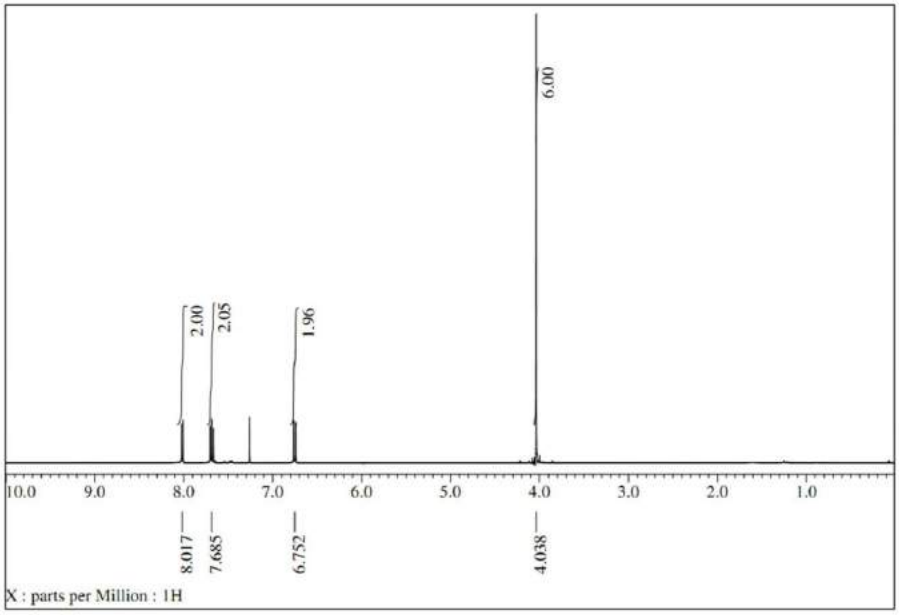
6.00
2.00
2.05
1.96
10.0
9.0
8.0
7.0
6.0
5.0
4.0
3.0
2.0
1.0
8.017
7.685
6.752
4.038
X : parts per Million : 1H

c)

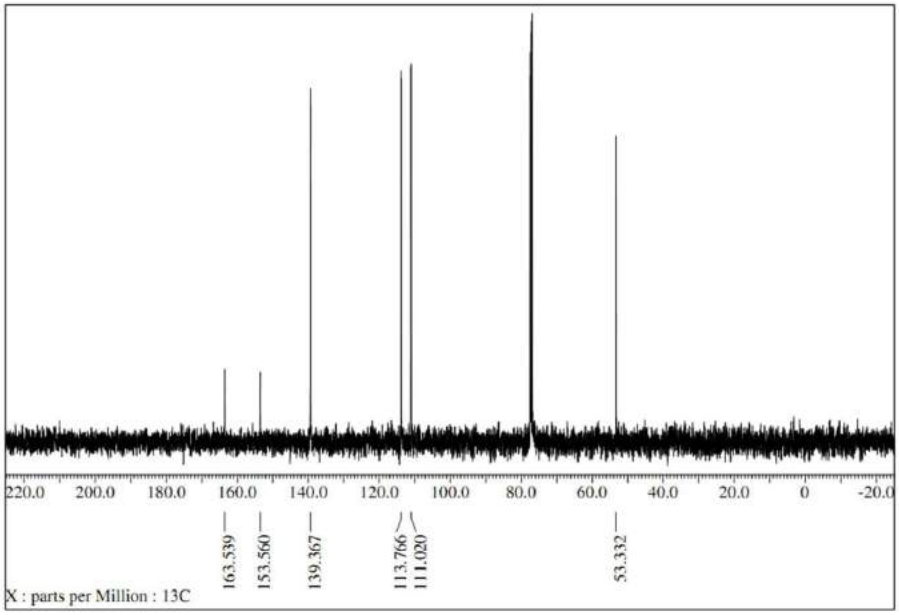


**Figure S1**. Chemical structure of MeO-bpy (a), $^{1}$H- and $^{13}$C-NMR spectra of MeO-bpy in $CDCl_3$ (b) and (c).

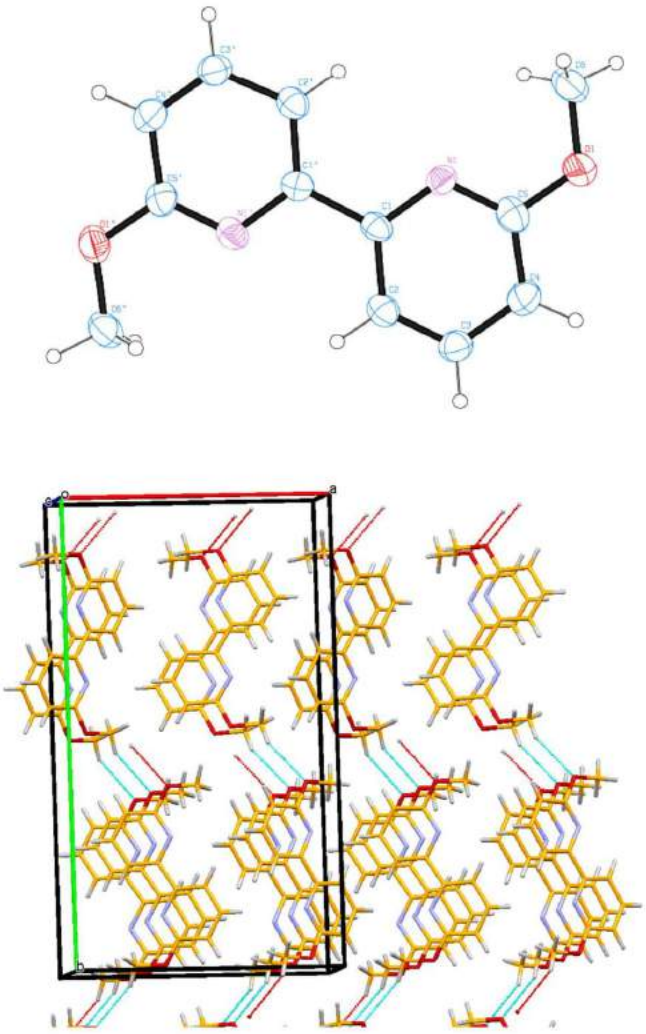

**Figure S2**. ORTEP plot (top) and crystal packing (bottom) of MeO-bpy.

**Table S1**. Atomic coordinates (x $10^4$) and equivalent isotropic displacement parameters ($Å^2$ x $10^3$)for MeO-bpy. U(eq) is defined as one third of the trace of the orthogonalized Uij tensor.

| | x | y | z | U(eq) |
|---|---|---|---|---|
| N(1) | 3941(5) | 7131(3) | 4327(16) | 45(2) |
| N(1') | 3619(5) | 8768(3) | 5473(19) | 52(2) |
| C(1') | 4090(6) | 8236(4) | 4550(20) | 44(2) |
| C(2) | 2492(8) | 7669(5) | 6890(30) | 51(1) |
| O(1') | 3701(5) | 9827(3) | 5830(20) | 74(3) |
| C(1) | 3485(6) | 7661(4) | 5250(30) | 45(2) |
| C(5') | 4142(6) | 9282(4) | 4920(20) | 50(2) |
| C(3) | 1956(7) | 7142(7) | 7490(20) | 55(1) |
| O(1) | 3850(5) | 6073(3) | 3920(20) | 74(2) |
| C(3') | 5603(7) | 8780(6) | 2550(20) | 55(1) |
| C(4') | 5166(7) | 9304(5) | 3460(30) | 62(2) |
| C(2') | 5074(8) | 8213(4) | 2990(20) | 51(1) |
| C(4) | 2426(7) | 6587(5) | 6530(30) | 62(2) |
| C(5) | 3421(7) | 6617(4) | 4900(30) | 56(2) |
| C(6) | 4843(9) | 6085(7) | 2210(30) | 71(2) |
| C(6') | 2672(9) | 9803(7) | 7450(30) | 71(2) |

**Table S2**. Bond lengths [Å] and angles [°] of MeO-bpy.

| | |
|---|---|
| N(1)-C(5) | 1.314(12) |
| N(1)-C(1) | 1.336(10) |
| N(1')-C(5') | 1.313(12) |
| N(1')-C(1') | 1.349(9) |
| C(1')-C(2') | 1.379(13) |
| C(1')-C(1) | 1.487(9) |
| C(2)-C(3) | 1.348(18) |
| C(2)-C(1) | 1.402(14) |
| C(2)-H(2) | 0.9300 |
| O(1')-C(5') | 1.356(11) |
| O(1')-C(6') | 1.439(14) |
| C(5')-C(4') | 1.406(13) |
| C(3)-C(4) | 1.394(18) |
| C(3)-H(3) | 0.9300 |
| O(1)-C(5) | 1.354(10) |
| O(1)-C(6) | 1.416(13) |
| C(3')-C(4') | 1.313(18) |
| C(3')-C(2') | 1.410(17) |
| C(3')-H(3') | 0.9300 |
| C(4')-H(4') | 0.9300 |
| C(2')-H(2') | 0.9300 |
| C(4)-C(5) | 1.406(14) |
| C(4)-H(4) | 0.9300 |
| C(6)-H(6A) | 0.9600 |
| C(6)-H(6B) | 0.9600 |
| C(6)-H(6C) | 0.9600 |
| C(6')-H(6'1) | 0.9600 |
| C(6')-H(6'2) | 0.9600 |
| C(6')-H(6'3) | 0.9600 |
| C(5)-N(1)-C(1) | 118.4(7) |
| C(5')-N(1')-C(1') | 117.8(7) |
| N(1')-C(1')-C(2') | 123.0(8) |
| N(1')-C(1')-C(1) | 116.5(6) |
| C(2')-C(1')-C(1) | 120.5(7) |
| C(3)-C(2)-C(1) | 120.9(10) |
| C(3)-C(2)-H(2) | 119.6 |
| C(1)-C(2)-H(2) | 119.6 |

| | |
|---|---|
| C(5')-O(1')-C(6') | 116.8(9) |
| N(1)-C(1)-C(2) | 121.0(8) |
| N(1)-C(1)-C(1') | 117.1(6) |
| C(2)-C(1)-C(1') | 121.9(7) |
| N(1')-C(5')-O(1') | 119.8(8) |
| N(1')-C(5')-C(4') | 123.4(9) |
| O(1')-C(5')-C(4') | 116.8(9) |
| C(2)-C(3)-C(4) | 118.5(9) |
| C(2)-C(3)-H(3) | 120.8 |
| C(4)-C(3)-H(3) | 120.8 |
| C(5)-O(1)-C(6) | 118.0(10) |
| C(4')-C(3')-C(2') | 121.9(10) |
| C(4')-C(3')-H(3') | 119.1 |
| C(2')-C(3')-H(3') | 119.1 |
| C(3')-C(4')-C(5') | 117.7(11) |
| C(3')-C(4')-H(4') | 121.2 |
| C(5')-C(4')-H(4') | 121.2 |
| C(1')-C(2')-C(3') | 116.2(9) |
| C(1')-C(2')-H(2') | 121.9 |
| C(3')-C(2')-H(2') | 121.9 |
| C(3)-C(4)-C(5) | 117.4(10) |
| C(3)-C(4)-H(4) | 121.3 |
| C(5)-C(4)-H(4) | 121.3 |
| N(1)-C(5)-O(1) | 119.9(9) |
| N(1)-C(5)-C(4) | 123.8(9) |
| O(1)-C(5)-C(4) | 116.3(9) |
| O(1)-C(6)-H(6A) | 109.5 |
| O(1)-C(6)-H(6B) | 109.5 |
| H(6A)-C(6)-H(6B) | 109.5 |
| O(1)-C(6)-H(6C) | 109.5 |
| H(6A)-C(6)-H(6C) | 109.5 |
| H(6B)-C(6)-H(6C) | 109.5 |
| O(1')-C(6')-H(6'1) | 109.5 |
| O(1')-C(6')-H(6'2) | 109.5 |
| H(6'1)-C(6')-H(6'2) | 109.5 |
| O(1')-C(6')-H(6'3) | 109.5 |
| H(6'1)-C(6')-H(6'3) | 109.5 |
| H(6'2)-C(6')-H(6'3) | 109.5 |

**Table S3**. Anisotropic displacement parameters ($Å^2$ x $10^3$) of MeO-bpy. The anisotropic displacement factor exponent takes the form: $-2^2[h^2a^{*2}U^{11} + ... + 2\ h\ k\ a^*\ b^*\ U^{12}]$.

| | $U^{11}$ | $U^{22}$ | $U^{33}$ | $U^{23}$ | $U^{13}$ | $U^{12}$ |
|---|---|---|---|---|---|---|
| N(1) | 41(3) | 46(4) | 47(4) | -3(4) | 3(3) | -7(3) |
| N(1') | 48(3) | 49(4) | 58(5) | -5(4) | -5(4) | 9(4) |
| C(1') | 44(4) | 51(5) | 37(5) | -2(4) | -2(4) | 2(4) |
| C(2) | 49(3) | 50(3) | 55(3) | -1(2) | -3(2) | 7(2) |
| O(1') | 57(4) | 48(5) | 116(8) | -17(4) | -6(4) | 3(3) |
| C(1) | 36(4) | 49(5) | 50(5) | -7(4) | -6(4) | 8(4) |
| C(5') | 47(5) | 51(5) | 53(5) | -5(5) | -12(4) | -3(5) |
| C(3) | 46(3) | 59(3) | 59(3) | 2(3) | 3(3) | -2(2) |
| O(1) | 59(4) | 52(5) | 110(7) | -12(5) | 15(4) | -1(3) |
| C(3') | 46(3) | 59(3) | 59(3) | 2(3) | 3(3) | -2(2) |
| C(4') | 50(3) | 56(3) | 79(5) | 2(3) | 2(3) | -8(2) |
| C(2') | 49(3) | 50(3) | 55(3) | -1(2) | -3(2) | 7(2) |
| C(4) | 50(3) | 56(3) | 79(5) | 2(3) | 2(3) | -8(2) |
| C(5) | 58(5) | 52(5) | 60(6) | -8(5) | -8(5) | 6(5) |
| C(6) | 57(3) | 60(3) | 95(5) | -19(4) | 2(4) | 12(2) |
| C(6') | 57(3) | 60(3) | 95(5) | -19(4) | 2(4) | 12(2) |

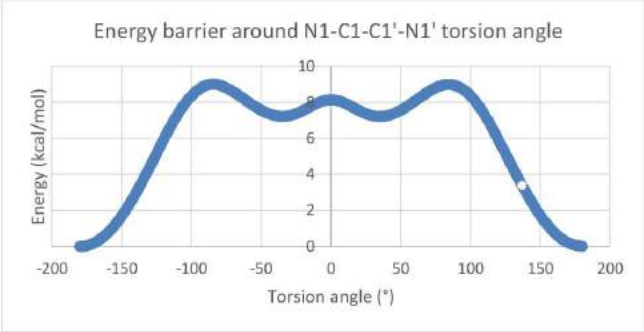


**Figure S3**. Calculated energy barrier for the rotation along the N1–C1–C1'–N1' torsion angle in MeO-bpy.

**Table S4**. Energetic and geometric data of conformers of MeO-bpy.

| Structure | N1–C1–C1'–N1' (°) | Relative stability (Kcal/mol) |
|---|---|---|
| Trans (Absolute minimum) | 180 | 0.0 |
| Staggered1 (Relative minimum) | 35 | 7.1 |
| Staggered2 (Relative minimum) | -35 | 7.1 |
| Cis (Energy maximum) | 0 | 8.0 |

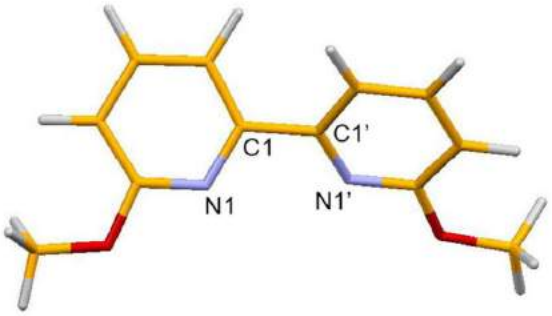


**Figure S4.** Relative minimum energy conformation for the isolated molecule of MeO-bpy (N1–C1–C1'–N1' = +/–35°).

*Part 2.*

a)

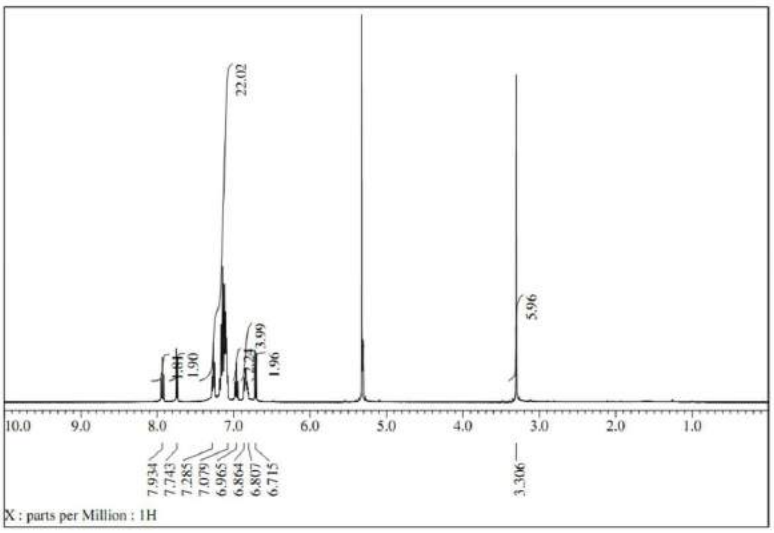
22.02
5.96
3.99
1.96
1.90
10.0
9.0
8.0
7.0
6.0
5.0
4.0
3.0
2.0
1.0
7.934
7.743
7.285
7.079
6.965
6.864
6.807
6.715
3.306
X : parts per Million : 1H

b)

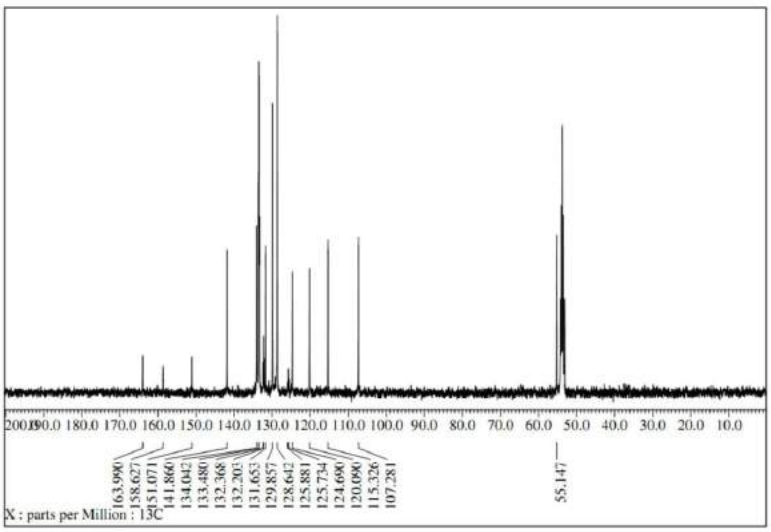
200.0
190.0
180.0
170.0
160.0
150.0
140.0
130.0
120.0
110.0
100.0
90.0
80.0
70.0
60.0
50.0
40.0
30.0
20.0
10.0
163.990
158.627
151.071
141.860
134.042
133.480
132.368
132.203
131.653
129.857
128.642
125.881
125.734
124.690
120.098
115.326
107.281
55.147
X : parts per Million : 13C

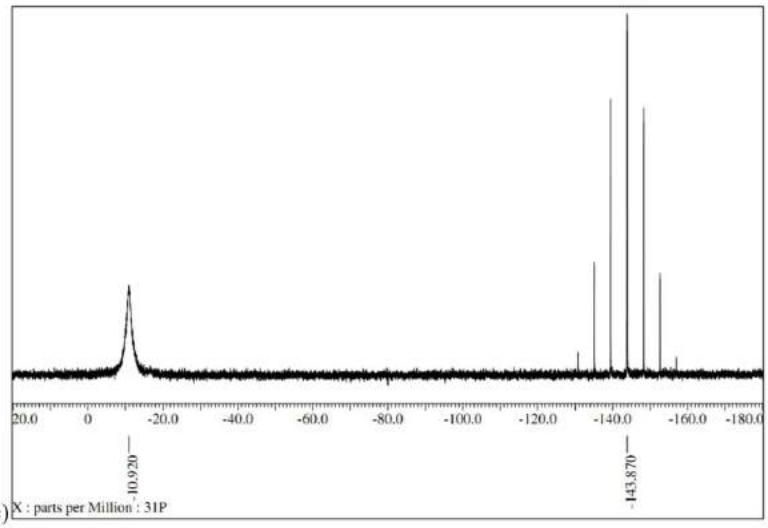


c)

**Figure S5**. $^{1}$H-NMR (a), $^{13}$C-NMR (b) and (c) $^{31}$P-NMR spectra of **2** in $CD_2Cl_2$.

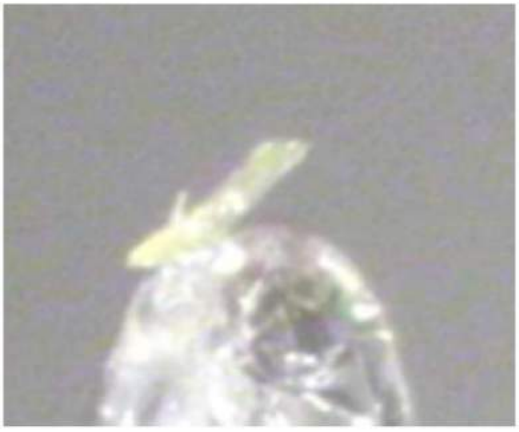

**Figure S6**. The crystal employed for the x-ray structure determination of **2**.

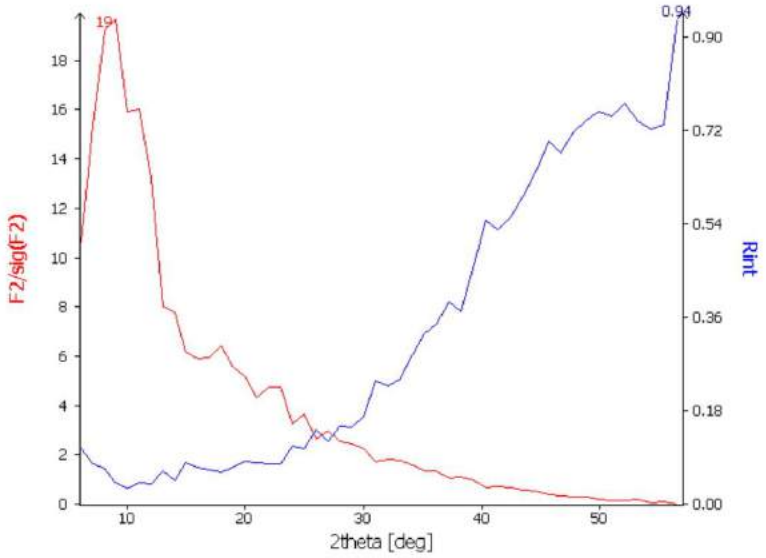


**Figure S7**. $R_{Int}$ and I/σ vs. 2θ for the collected XRD data of **2**.

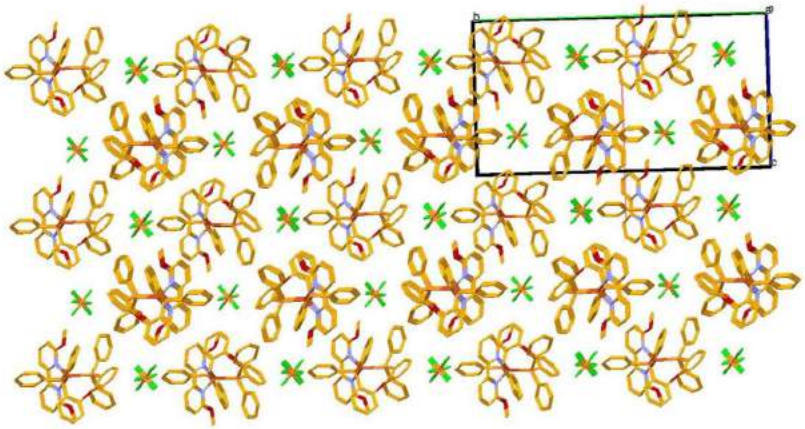

**Figure S8**. Crystal packing of **2**.

**Table S5**. Atomic coordinates (x $10^4$) and equivalent isotropic displacement parameters ($Å^2$ x $10^3$) of **2**. U(eq) is defined as one third of the trace of the orthogonalized Uij tensor.

| | x | y | z | U(eq) |
|---|---|---|---|---|
| Cu(1) | 403(1) | 919(1) | 7315(1) | 44(1) |
| P(1) | 2611(2) | 705(1) | 7525(1) | 42(1) |
| P(2) | 14(2) | 1690(1) | 7270(1) | 42(1) |
| O(1) | 2220(5) | 1550(2) | 8572(3) | 44(1) |
| O(2) | 280(6) | 936(2) | 9321(4) | 69(2) |
| O(3) | -25(6) | 771(2) | 5271(4) | 76(2) |
| N(1) | -713(6) | 559(2) | 8179(5) | 47(2) |
| C(2) | -1551(8) | 239(3) | 7822(7) | 56(2) |
| C(3) | -2271(9) | -44(3) | 8348(9) | 82(3) |
| C(4) | -2145(11) | 17(4) | 9242(10) | 96(4) |
| C(5) | -1307(11) | 349(4) | 9612(7) | 80(3) |
| C(6) | -614(8) | 607(3) | 9042(7) | 56(2) |
| C(7) | 283(10) | 1112(4) | 10207(6) | 86(3) |
| N(1') | -824(7) | 493(2) | 6470(5) | 51(2) |
| C(2') | -1686(9) | 213(3) | 6862(7) | 62(3) |
| C(3') | -2614(10) | -65(3) | 6382(9) | 84(3) |
| C(4') | -2722(12) | -47(4) | 5497(10) | 107(5) |
| C(5') | -1878(11) | 232(4) | 5097(8) | 90(4) |
| C(6') | -935(9) | 494(3) | 5589(7) | 62(3) |
| C(7') | -80(11) | 828(4) | 4330(6) | 101(4) |
| C(8) | 3731(7) | 942(2) | 6757(5) | 39(2) |
| C(9) | 5122(8) | 985(3) | 6967(6) | 61(2) |
| C(10) | 5917(10) | 1155(3) | 6348(7) | 72(3) |
| C(11) | 5349(13) | 1285(3) | 5526(8) | 81(3) |
| C(12) | 3994(13) | 1248(3) | 5337(6) | 82(3) |
| C(13) | 3198(9) | 1073(3) | 5943(6) | 64(3) |
| C(14) | 2891(8) | 84(3) | 7474(5) | 45(2) |
| C(15) | 3911(8) | -115(3) | 7067(6) | 61(2) |
| C(16) | 4055(10) | -585(3) | 7044(7) | 75(3) |
| C(17) | 3157(11) | -868(3) | 7429(7) | 72(3) |
| C(18) | 2123(10) | -671(4) | 7822(7) | 75(3) |
| C(19) | 2003(9) | -200(3) | 7827(6) | 68(3) |
| C(20) | 3480(7) | 845(2) | 8608(5) | 40(2) |
| C(21) | 4398(7) | 557(3) | 9064(6) | 50(2) |

| | | | | |
|---|---|---|---|---|
| C(22) | 4989(8) | 678(3) | 9883(6) | 58(2) |
| C(23) | 4657(8) | 1083(3) | 10274(5) | 56(2) |
| C(24) | 3742(8) | 1378(3) | 9823(5) | 54(2) |
| C(25) | 3203(7) | 1266(3) | 9003(5) | 40(2) |
| C(26) | 2600(8) | 1883(3) | 7992(5) | 44(2) |
| C(27) | 3874(8) | 2070(3) | 8057(6) | 55(2) |
| C(28) | 4113(10) | 2424(4) | 7488(7) | 82(3) |
| C(29) | 3106(11) | 2588(4) | 6910(7) | 90(3) |
| C(30) | 1845(9) | 2388(3) | 6839(6) | 72(3) |
| C(31) | 1575(7) | 2022(3) | 7381(5) | 46(2) |
| C(32) | -897(8) | 1941(3) | 6297(5) | 48(2) |
| C(33) | -438(9) | 1851(3) | 5491(6) | 69(3) |
| C(34) | -1105(12) | 2020(4) | 4726(6) | 88(3) |
| C(35) | -2230(12) | 2279(4) | 4769(8) | 81(3) |
| C(36) | -2697(10) | 2371(3) | 5543(8) | 77(3) |
| C(37) | -2029(8) | 2203(3) | 6308(6) | 55(2) |
| C(38) | -936(7) | 1887(3) | 8161(5) | 42(2) |
| C(39) | -1989(8) | 1615(3) | 8407(6) | 58(2) |
| C(40) | -2751(10) | 1742(5) | 9060(7) | 84(3) |
| C(41) | -2471(13) | 2149(6) | 9493(7) | 101(5) |
| C(42) | -1454(13) | 2422(4) | 9282(7) | 96(4) |
| C(43) | -695(10) | 2298(3) | 8597(6) | 70(3) |
| P(3) | 2205(3) | 1448(1) | 12538(2) | 78(1) |
| F(1) | 987(8) | 1144(4) | 12446(6) | 198(4) |
| F(2) | 1613(9) | 1730(3) | 13265(5) | 184(4) |
| F(3) | 3466(12) | 1752(4) | 12606(8) | 248(6) |
| F(4) | 2802(8) | 1160(3) | 11816(4) | 139(3) |
| F(5) | 1526(13) | 1753(3) | 11825(6) | 226(5) |
| F(6) | 2882(9) | 1142(3) | 13245(5) | 167(3) |

**Table S6.** Bond lengths [Å] and angles [°] of **2**.

| | |
|---|---|
| Cu(1)-N(1) | 2.078(7) |
| Cu(1)-N(1') | 2.087(7) |
| Cu(1)-P(1) | 2.260(2) |
| Cu(1)-P(2) | 2.271(2) |
| P(1)-C(8) | 1.820(7) |
| P(1)-C(14) | 1.826(8) |
| P(1)-C(20) | 1.831(8) |
| P(2)-C(32) | 1.811(8) |
| P(2)-C(31) | 1.812(8) |
| P(2)-C(38) | 1.815(8) |
| O(1)-C(26) | 1.386(9) |
| O(1)-C(25) | 1.389(8) |
| O(2)-C(6) | 1.342(10) |
| O(2)-C(7) | 1.444(9) |
| O(3)-C(6') | 1.331(10) |
| O(3)-C(7') | 1.439(10) |
| N(1)-C(6) | 1.317(10) |
| N(1)-C(2) | 1.324(9) |
| C(2)-C(3) | 1.390(12) |
| C(2)-C(2') | 1.458(12) |
| C(3)-C(4) | 1.367(14) |
| C(4)-C(5) | 1.359(14) |
| C(5)-C(6) | 1.378(12) |
| N(1')-C(6') | 1.336(11) |
| N(1')-C(2') | 1.357(10) |
| C(2')-C(3') | 1.377(12) |
| C(3')-C(4') | 1.344(15) |
| C(4')-C(5') | 1.349(15) |
| C(5')-C(6') | 1.369(12) |
| C(8)-C(13) | 1.356(10) |
| C(8)-C(9) | 1.385(10) |
| C(9)-C(10) | 1.376(11) |
| C(10)-C(11) | 1.375(13) |
| C(11)-C(12) | 1.346(13) |
| C(12)-C(13) | 1.366(11) |
| C(14)-C(19) | 1.352(10) |
| C(14)-C(15) | 1.361(10) |

| | |
|---|---|
| C(15)-C(16) | 1.371(12) |
| C(16)-C(17) | 1.379(12) |
| C(17)-C(18) | 1.359(11) |
| C(18)-C(19) | 1.370(11) |
| C(20)-C(21) | 1.373(9) |
| C(20)-C(25) | 1.402(9) |
| C(21)-C(22) | 1.373(10) |
| C(22)-C(23) | 1.371(11) |
| C(23)-C(24) | 1.381(10) |
| C(24)-C(25) | 1.350(10) |
| C(26)-C(27) | 1.365(10) |
| C(26)-C(31) | 1.369(10) |
| C(27)-C(28) | 1.377(12) |
| C(28)-C(29) | 1.351(13) |
| C(29)-C(30) | 1.370(11) |
| C(30)-C(31) | 1.385(10) |
| C(32)-C(37) | 1.352(10) |
| C(32)-C(33) | 1.374(11) |
| C(33)-C(34) | 1.375(12) |
| C(34)-C(35) | 1.348(13) |
| C(35)-C(36) | 1.333(12) |
| C(36)-C(37) | 1.375(11) |
| C(38)-C(43) | 1.376(11) |
| C(38)-C(39) | 1.385(10) |
| C(39)-C(40) | 1.353(12) |
| C(40)-C(41) | 1.368(14) |
| C(41)-C(42) | 1.342(15) |
| C(42)-C(43) | 1.389(13) |
| P(3)-F(1) | 1.487(8) |
| P(3)-F(6) | 1.502(7) |
| P(3)-F(5) | 1.509(8) |
| P(3)-F(3) | 1.521(9) |
| P(3)-F(2) | 1.537(7) |
| P(3)-F(4) | 1.543(7) |
| N(1)-Cu(1)-N(1') | 77.4(3) |
| N(1)-Cu(1)-P(1) | 109.50(18) |
| N(1')-Cu(1)-P(1) | 114.81(18) |
| N(1)-Cu(1)-P(2) | 114.66(18) |
| N(1')-Cu(1)-P(2) | 118.60(19) |

| | |
|---|---|
| P(1)-Cu(1)-P(2) | 115.68(8) |
| C(8)-P(1)-C(14) | 103.9(4) |
| C(8)-P(1)-C(20) | 103.6(3) |
| C(14)-P(1)-C(20) | 101.4(3) |
| C(8)-P(1)-Cu(1) | 116.2(3) |
| C(14)-P(1)-Cu(1) | 114.4(3) |
| C(20)-P(1)-Cu(1) | 115.4(2) |
| C(32)-P(2)-C(31) | 102.4(4) |
| C(32)-P(2)-C(38) | 103.6(4) |
| C(31)-P(2)-C(38) | 105.0(4) |
| C(32)-P(2)-Cu(1) | 119.3(3) |
| C(31)-P(2)-Cu(1) | 112.4(3) |
| C(38)-P(2)-Cu(1) | 112.6(3) |
| C(26)-O(1)-C(25) | 119.7(5) |
| C(6)-O(2)-C(7) | 119.4(7) |
| C(6')-O(3)-C(7') | 118.0(8) |
| C(6)-N(1)-C(2) | 118.0(8) |
| C(6)-N(1)-Cu(1) | 125.9(6) |
| C(2)-N(1)-Cu(1) | 116.1(6) |
| N(1)-C(2)-C(3) | 120.6(10) |
| N(1)-C(2)-C(2') | 116.3(8) |
| C(3)-C(2)-C(2') | 123.0(10) |
| C(4)-C(3)-C(2) | 119.8(11) |
| C(5)-C(4)-C(3) | 119.9(11) |
| C(4)-C(5)-C(6) | 116.3(11) |
| N(1)-C(6)-O(2) | 112.1(8) |
| N(1)-C(6)-C(5) | 125.3(10) |
| O(2)-C(6)-C(5) | 122.5(10) |
| C(6')-N(1')-C(2') | 116.7(8) |
| C(6')-N(1')-Cu(1) | 127.3(6) |
| C(2')-N(1')-Cu(1) | 115.7(6) |
| N(1')-C(2')-C(3') | 122.0(10) |
| N(1')-C(2')-C(2) | 114.2(8) |
| C(3')-C(2')-C(2) | 123.9(10) |
| C(4')-C(3')-C(2') | 119.8(11) |
| C(3')-C(4')-C(5') | 118.9(11) |
| C(4')-C(5')-C(6') | 120.2(12) |
| O(3)-C(6')-N(1') | 112.0(8) |
| O(3)-C(6')-C(5') | 125.7(11) |

| | |
|---|---|
| N(1')-C(6')-C(5') | 122.3(10) |
| C(13)-C(8)-C(9) | 118.4(7) |
| C(13)-C(8)-P(1) | 119.2(6) |
| C(9)-C(8)-P(1) | 122.4(6) |
| C(10)-C(9)-C(8) | 119.5(8) |
| C(11)-C(10)-C(9) | 120.9(9) |
| C(12)-C(11)-C(10) | 118.9(9) |
| C(11)-C(12)-C(13) | 120.6(10) |
| C(8)-C(13)-C(12) | 121.7(9) |
| C(19)-C(14)-C(15) | 117.3(8) |
| C(19)-C(14)-P(1) | 118.6(6) |
| C(15)-C(14)-P(1) | 124.1(7) |
| C(14)-C(15)-C(16) | 121.1(9) |
| C(15)-C(16)-C(17) | 120.6(9) |
| C(18)-C(17)-C(16) | 118.5(9) |
| C(17)-C(18)-C(19) | 119.4(10) |
| C(14)-C(19)-C(18) | 123.1(9) |
| C(21)-C(20)-C(25) | 117.4(7) |
| C(21)-C(20)-P(1) | 123.4(6) |
| C(25)-C(20)-P(1) | 119.1(5) |
| C(20)-C(21)-C(22) | 120.5(8) |
| C(23)-C(22)-C(21) | 121.1(8) |
| C(22)-C(23)-C(24) | 119.3(8) |
| C(25)-C(24)-C(23) | 119.5(8) |
| C(24)-C(25)-O(1) | 119.4(7) |
| C(24)-C(25)-C(20) | 122.1(7) |
| O(1)-C(25)-C(20) | 118.0(7) |
| C(27)-C(26)-C(31) | 123.2(8) |
| C(27)-C(26)-O(1) | 122.4(7) |
| C(31)-C(26)-O(1) | 114.4(7) |
| C(26)-C(27)-C(28) | 117.6(9) |
| C(29)-C(28)-C(27) | 120.9(9) |
| C(28)-C(29)-C(30) | 120.5(10) |
| C(29)-C(30)-C(31) | 120.2(9) |
| C(26)-C(31)-C(30) | 117.4(7) |
| C(26)-C(31)-P(2) | 118.3(6) |
| C(30)-C(31)-P(2) | 124.1(6) |
| C(37)-C(32)-C(33) | 117.5(8) |
| C(37)-C(32)-P(2) | 124.1(7) |

| | |
|---|---|
| C(33)-C(32)-P(2) | 118.4(7) |
| C(32)-C(33)-C(34) | 121.2(9) |
| C(35)-C(34)-C(33) | 119.2(10) |
| C(36)-C(35)-C(34) | 120.8(10) |
| C(35)-C(36)-C(37) | 120.0(10) |
| C(32)-C(37)-C(36) | 121.3(9) |
| C(43)-C(38)-C(39) | 117.6(8) |
| C(43)-C(38)-P(2) | 123.8(7) |
| C(39)-C(38)-P(2) | 118.6(6) |
| C(40)-C(39)-C(38) | 121.8(9) |
| C(39)-C(40)-C(41) | 119.3(11) |
| C(42)-C(41)-C(40) | 121.0(10) |
| C(41)-C(42)-C(43) | 119.8(11) |
| C(38)-C(43)-C(42) | 120.4(10) |
| F(1)-P(3)-F(6) | 91.0(6) |
| F(1)-P(3)-F(5) | 88.8(7) |
| F(6)-P(3)-F(5) | 179.6(6) |
| F(1)-P(3)-F(3) | 178.2(6) |
| F(6)-P(3)-F(3) | 89.4(7) |
| F(5)-P(3)-F(3) | 90.8(7) |
| F(1)-P(3)-F(2) | 91.4(5) |
| F(6)-P(3)-F(2) | 88.4(5) |
| F(5)-P(3)-F(2) | 92.0(5) |
| F(3)-P(3)-F(2) | 90.4(5) |
| F(1)-P(3)-F(4) | 88.4(5) |
| F(6)-P(3)-F(4) | 91.0(4) |
| F(5)-P(3)-F(4) | 88.7(5) |
| F(3)-P(3)-F(4) | 89.8(5) |
| F(2)-P(3)-F(4) | 179.3(5) |

**Table S7**. Anisotropic displacement parameters ($Å^2$ x $10^3$) of **2**. The anisotropic displacement factor exponent takes the form: $-2^2[h^2a^{*2}U^{11} + ... + 2\ h\ k\ a^*\ b^*\ U^{12}]$

| | $U^{11}$ | $U^{22}$ | $U^{33}$ | $U^{23}$ | $U^{13}$ | $U^{12}$ |
|---|---|---|---|---|---|---|
| Cu(1) | 42(1) | 49(1) | 43(1) | 0(1) | 3(1) | -3(1) |
| P(1) | 40(1) | 46(1) | 39(1) | 1(1) | 2(1) | 0(1) |
| P(2) | 38(1) | 50(1) | 38(1) | 4(1) | -1(1) | -1(1) |
| O(1) | 31(3) | 49(3) | 49(4) | 7(3) | -4(2) | 1(3) |
| O(2) | 66(4) | 104(5) | 38(4) | 6(4) | 11(3) | -7(4) |
| O(3) | 72(4) | 103(5) | 51(5) | -7(4) | 2(3) | -5(4) |
| N(1) | 47(4) | 48(4) | 45(5) | 1(4) | 5(3) | 5(3) |
| C(2) | 48(5) | 38(5) | 84(8) | 8(5) | 10(5) | -7(4) |
| C(3) | 45(6) | 65(7) | 141(11) | 16(8) | 30(7) | 0(5) |
| C(4) | 71(8) | 92(9) | 134(12) | 43(9) | 54(8) | 7(7) |
| C(5) | 75(8) | 92(8) | 77(8) | 32(7) | 25(6) | 15(6) |
| C(6) | 37(5) | 60(6) | 72(8) | 22(5) | 8(5) | 4(4) |
| C(7) | 91(8) | 125(9) | 41(7) | -12(6) | 8(5) | -8(7) |
| N(1') | 46(4) | 51(4) | 53(5) | -8(4) | -1(4) | 6(4) |
| C(2') | 43(6) | 59(6) | 84(8) | -28(6) | 10(5) | 4(5) |
| C(3') | 61(7) | 60(7) | 131(11) | -32(7) | 10(7) | -22(5) |
| C(4') | 80(8) | 102(10) | 134(13) | -60(9) | -16(9) | -28(7) |
| C(5') | 75(8) | 92(8) | 96(9) | -41(7) | -36(7) | 10(7) |
| C(6') | 36(5) | 70(7) | 80(8) | -18(6) | 3(5) | 3(5) |
| C(7') | 121(9) | 153(11) | 29(6) | -7(6) | 7(6) | 16(8) |
| C(8) | 41(5) | 44(5) | 32(5) | -2(4) | 3(4) | 1(4) |
| C(9) | 50(6) | 82(7) | 50(6) | 10(5) | 4(4) | -3(5) |
| C(10) | 57(6) | 83(7) | 79(8) | 3(6) | 27(6) | -16(5) |
| C(11) | 98(9) | 80(7) | 71(8) | 9(6) | 36(7) | -10(7) |
| C(12) | 107(9) | 101(8) | 40(6) | 25(6) | 15(6) | -13(7) |
| C(13) | 63(6) | 90(7) | 36(6) | 11(5) | -1(5) | -8(5) |
| C(14) | 40(5) | 50(5) | 46(5) | -9(4) | 0(4) | -2(4) |
| C(15) | 46(5) | 67(7) | 70(7) | 2(5) | 8(5) | 3(5) |
| C(16) | 60(7) | 58(7) | 105(9) | -21(6) | 1(6) | 14(6) |
| C(17) | 78(7) | 49(6) | 87(8) | -6(6) | -8(6) | 0(6) |
| C(18) | 69(7) | 69(7) | 88(8) | 4(6) | 8(6) | 0(6) |
| C(19) | 65(7) | 55(6) | 86(8) | -3(6) | 18(5) | 7(5) |
| C(20) | 37(4) | 42(5) | 41(5) | 4(4) | 8(4) | 5(4) |
| C(21) | 46(5) | 57(6) | 47(6) | 5(4) | -2(4) | 13(4) |

| | | | | | | |
|---|---|---|---|---|---|---|
| C(22) | 51(5) | 70(7) | 51(6) | 11(5) | -2(5) | 8(5) |
| C(23) | 45(5) | 86(7) | 34(5) | 2(5) | -10(4) | -5(5) |
| C(24) | 57(6) | 67(6) | 36(5) | -7(4) | -4(4) | 5(5) |
| C(25) | 35(5) | 59(5) | 26(5) | 3(4) | 4(4) | 4(4) |
| C(26) | 38(5) | 48(5) | 46(5) | -9(4) | 1(4) | -5(4) |
| C(27) | 42(5) | 66(6) | 58(6) | -12(5) | 5(4) | -7(5) |
| C(28) | 59(7) | 107(9) | 82(8) | -5(7) | 15(6) | -41(6) |
| C(29) | 84(8) | 90(8) | 92(9) | 32(7) | -7(7) | -28(7) |
| C(30) | 60(6) | 80(7) | 73(7) | 32(6) | -8(5) | -29(5) |
| C(31) | 35(5) | 48(5) | 54(6) | 6(4) | 1(4) | -4(4) |
| C(32) | 58(6) | 48(5) | 37(5) | -2(4) | -3(4) | -1(4) |
| C(33) | 79(7) | 81(7) | 46(6) | 10(5) | -5(5) | 19(5) |
| C(34) | 120(10) | 101(9) | 40(7) | 20(6) | -2(6) | 8(8) |
| C(35) | 86(8) | 93(8) | 60(8) | 31(6) | -15(6) | 4(7) |
| C(36) | 67(7) | 77(7) | 83(9) | 16(6) | -10(6) | 10(5) |
| C(37) | 52(6) | 58(6) | 54(6) | 11(5) | 0(5) | 9(5) |
| C(38) | 36(5) | 57(5) | 34(5) | 12(4) | -3(4) | 5(4) |
| C(39) | 50(6) | 72(6) | 53(6) | 10(5) | 14(4) | 10(5) |
| C(40) | 51(6) | 140(11) | 66(8) | 23(7) | 29(6) | 22(7) |
| C(41) | 74(9) | 178(14) | 53(8) | -16(8) | 16(6) | 57(9) |
| C(42) | 92(9) | 124(11) | 70(9) | -32(7) | 6(7) | 22(8) |
| C(43) | 72(7) | 62(6) | 73(8) | -16(6) | -6(6) | 11(5) |
| P(3) | 103(2) | 69(2) | 61(2) | 1(2) | 7(2) | 10(2) |
| F(1) | 126(6) | 311(12) | 160(8) | -31(8) | 23(6) | -110(7) |
| F(2) | 186(8) | 222(8) | 142(7) | -91(6) | 10(6) | 106(7) |
| F(3) | 286(13) | 205(10) | 262(13) | -67(9) | 77(11) | -162(10) |
| F(4) | 164(7) | 167(7) | 93(5) | -38(5) | 46(5) | 2(5) |
| F(5) | 330(14) | 184(9) | 163(9) | 79(7) | 17(9) | 122(9) |
| F(6) | 218(9) | 192(8) | 83(5) | 15(5) | -27(5) | 99(7) |

*Part 3.*

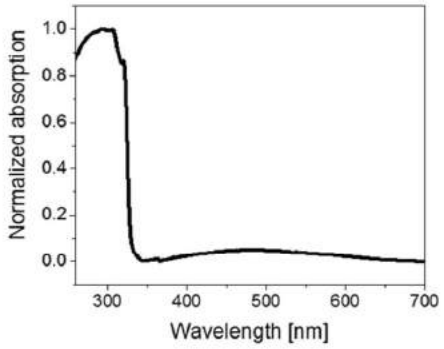


**Figure S9**. Absorption spectrum of **2** ($10^{-4}$ M) in dichloromethane at room temperature.

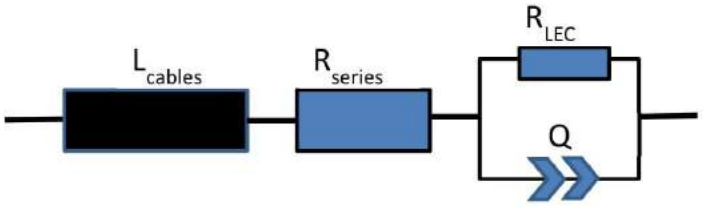


**Figure S10**. Simplified circuit model with inductance ($L_{cables}$), series resistor ($R_{series}$) electrical resistance ($R_{LEC}$), and constant phase element Q used for static EIS assays.[1,2]

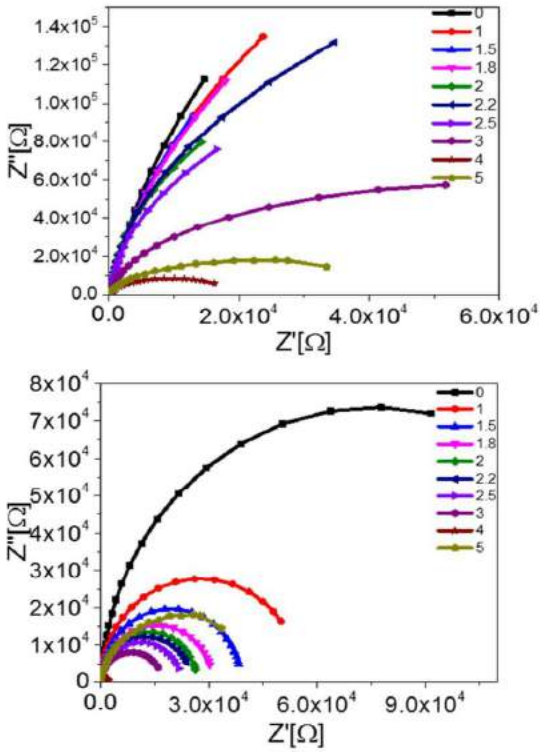


**Figure S11**. Nyquist plots of fresh devices with **1** (top) and **2** (bottom) measured upon constant bias (see legend). The fittings are shown in solid lines.

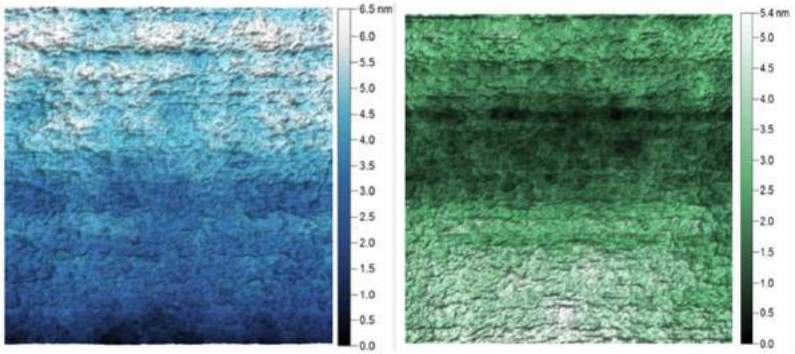


**Figure S12**. AFM image of thin film (120 nm) of **1** (left) and **2** (right).

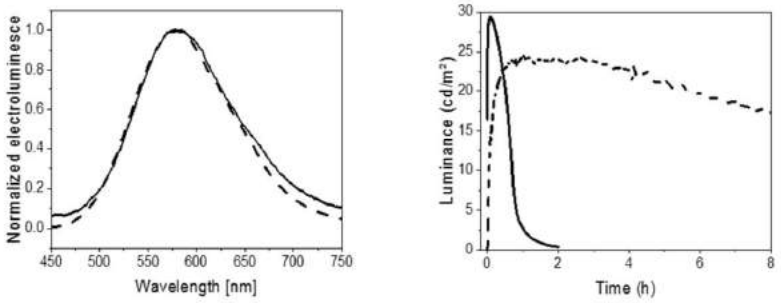


**Figure S13**. Electroluminescence spectrum (left) of and luminance (right) over time of devices with **1** (solid line) and with CBP/**1** (dotted line) active layers driven at a pulsed current of 7.5 mA.

*Part 4.*

(1) Meier, S. B.; Hartmann, D.; Winnacker, A.; Sarfert, W.; The Dynamic Behavior of Thin-Film Ionic Transition Metal Complex-Based Light-Emitting Electrochemical Cells *J. Appl. Phys.* **2014**, *116*, 104504.

(2) Puscher, B. M. D.; Aygueler, M. F.; Docampo, P.; Costa, R. D.; Unveiling the Dynamic Processes in Hybrid Lead Bromide Perovskite Nanoparticle Thin Film Devices *Adv. Energy Mater.* **2017**, *7*, 1602283.

Section 3.1.3: White Light-emitting Electrochemical Cells based on Deep-red Cu(I) complexes

ADVANCED OPTICAL MATERIALS

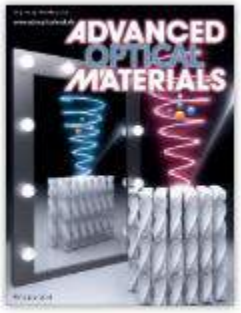


Volume 7, Issue 23
December 3, 2019
1900830

Elisa Fresta,[1,2] Michael D. Weber,[3] Julio Fernández-Cestau[1] and Rubén D. Costa[1,3]*

1. IMDEA Materials Institute, Calle Eric Kandel 2, E-28906 Getafe, Madrid, Spain. ruben.costa@imdea.org
2. Department of Applied Physics, Faculty of Science M12, Universidad Autónoma de Madrid, 28049 Madrid, Spain
3. Department of Chemistry and Pharmacy, Chair of Physical Chemistry I, University of Erlangen-Nürnberg, Egerlandstrasse 3, 91058, Erlangen, Germany

ADVANCED OPTICAL MATERIALS
www.advopticalmat.de

# White Light-Emitting Electrochemical Cells Based on Deep-Red Cu(I) Complexes

*Elisa Fresta, Michael D. Weber, Julio Fernandez-Cestau, and Rubén D. Costa**

**The synthesis and characterization, as well as photoluminescent and electrochemical features of a series of ionic copper(I) complexes—, i.e., $[Cu(N^N)(P^P)]^+$, where N^N is 4,4′-diethylester-2,2′-biquinoline (dcbq) and P^P is bis-triphenylphosphine, bis[2-(diphenylphosphino)phenyl)ether] (POP), or 4,5-bis(diphenylphosphino)-9,9-dimethylxanthene (Xantphos)—are reported along with their application to achieve both deep-red and white light-emitting electrochemical cells (LECs). In short, the first deep-red Cu(I)-based LECs featuring high irradiances (≈100 μW cm$^{-2}$) and excellent color stability (*x*/*y* CIE color coordinates of 0.66/0.32) over days are reported. This is achieved by comparing the electroluminescent behavior of this series of complexes with respect to the irradiance and stability, as well as the impact of introducing supporting electrolytes on the device performance. This is rationalized using spectroscopic and electrochemical studies. Finally, the first white-emitting LEC is manufactured with red-emitting copper(I) complexes, achieving *x*/*y* CIE color coordinates of 0.31/0.32 and a high color rendering index of 92.**

## 1. Introduction

One of the main challenges in solid-state lighting (SSL) technologies is the search of stable and sustainable efficient emitters for large-area lighting applications.[1] A viable approach is to implement low-cost earth-abundant materials—, e.g., copper[2–11]—in single-layered thin-film lighting devices based on the light-emitting electrochemical cell (LEC) concept.[12–14]

LECs consist of an ionic-based active layer sandwiched between electrodes.[15] Both the solution-based coating protocols and good tolerance to thickness and type of electrodes significantly reduce fabrication time and costs.[16–18] For this reason, the use of soluble ionic transition metal complexes (iTMCs) as emitters has intensively been investigated throughout the last decade.[15,19,20] However, up to date, the most efficient devices are based on Ir(III)-iTMCs.[15,21–25] While these emitters yield light that spans the whole visible range,[15,26,27] the high cost and low abundance of iridium in the Earth's crust[28] do not match the future needs for sustainable large-area lighting. In this context, ionic copper(I) complexes—, i.e., Cu(I)-iTMCs—represent an appealing alternative to Ir(III)-iTMCs for LECs. Indeed, copper resources are abundant and considered as low-cost, while Cu(I)-iTMCs chemistry is well-known in literature,[29,30] allowing to tailor the features of the emitter—, e.g., redox stability, photoluminescence quantum yields (PLQYs), and/or the shift of the emission and the device color. As a matter of fact, Cu(I)-iTMCs have led to interesting results in LECs, achieving moderate stable and efficient blue and yellow devices.[13,31–36]

As in early works on Ir(III)-iTMC-LECs,[27] one of the major challenge is to identify possible complexes whose luminescent response covers the whole visible range. This has to be complemented with the right balance between efficiency, brightness, and stability, in order to achieve well-performing white LECs in the near future.[37–39] In contrast to Ir(III)-iTMCs, the state-of-the-art of Cu(I)-iTMC-LECs just involves yellow- and blue-emitting complexes. In short, Costa and co-workers have explored the possibility to prepare heteroleptic blue-emitting compounds with N^N ligands with high energy lowest unoccupied molecular orbital (LUMO) levels, achieving yellow-emitting devices due to the lack of a thermally activated delayed fluorescence (TADF) process.[40] However, the same authors proposed to use another family of Cu(I) complexes bearing different *N*-heterocyclic carbenes and dipyridylamine ligands–, i.e., di-iso-propylphenyl)imidazole-2-ylidene and 2,2′-bis-(3-methylpyridyl)amine, showing an effective TADF emission that led to the first blue-emitting Cu(I)-iTMC LECs.[34,41,42] Other studies by Zhang et al.,[43] Bolink and co-workers,[31,33,44] and Costa and co-workers[36,45,46] showed green- and yellow-emitting Cu(I)-iTMC based devices by changing the pattern substitution of heteroleptic diamine and diphosphine ligands.

In light of the current art, deep-red LECs based on Cu(I)-iTMCs are still missing, hampering the preparation of white-emitting LECs. In this context, we report the synthesis and

E. Fresta, Dr. J. Fernandez-Cestau, Dr. R. D. Costa
IMDEA Materials Institute
Calle Eric Kandel 2, E-28906 Getafe, Madrid, Spain
E-mail: ruben.costa@imdea.org
E. Fresta
Department of Applied Physics
Faculty of Science M12
Universidad Autónoma de Madrid
28049 Madrid, Spain
Dr. M. D. Weber, Dr. R. D. Costa
Department of Chemistry and Pharmacy
Chair of Physical Chemistry I
University of Erlangen-Nürnberg
Egerlandstrasse 3, 91058 Erlangen, Germany
The ORCID identification number(s) for the author(s) of this article can be found under https://doi.org/10.1002/adom.201900830.

DOI: 10.1002/adom.201900830

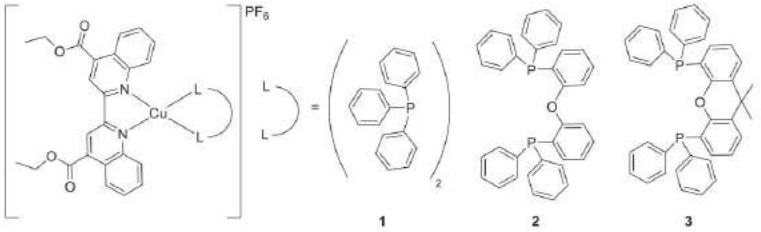


**Figure 1.** Chemical structures of complexes **1–3**.

the application of a series of deep-red emitting heteroleptic [Cu(N^N)(P^P)](PF$_6$) complexes. The complexes have the same N^N ligand, namely dcbq ( = 4,4′-diethylester-2,2′-biquinoline), and different P^P ligands; namely, $(PPh_3)_2$ or bis-triphenylphosphine, POP or (bis(2-(diphenylphosphino)phenyl)ether), and Xantphos or (4,5-Bis(diphenylphosphino)-9,9-dimethylxanthene), named **1**, **2**, and **3** (**Figure 1**), respectively. The rigidity of the P^P ligand increases from **1** to **3**, leading to (i) higher chemical stabilities, and (ii) a lower nonradiative deactivation suppressing the flattening in the emitting excited state. Based on spectroscopic and electrochemical studies, optimized LECs based on **3** feature efficient (0.23 lm W$^{-1}$) and stable (up to several days) deep-red response—, i.e., $x/y$ CIE color coordinates of 0.66/0.32, $\lambda_{max}$ 671 nm—achieving irradiances of ≈100 μW cm$^{-2}$. To the best of our knowledge, this is the first example of deep-red-emitting LECs based on the heteroleptic [Cu(N^N)(P^P)]$^+$ complexes. We further changed the device chromaticity towards white LECs using a host:guest approach comprising a hole transporting material (HTM) as host, namely 4,4′-bis(*N*-carbazolyl)-1,1′-biphenyl (CBP), and **3** as guest. The optimized device showed white light peaking at 379, 478, and 653 nm associated to $x/y$ CIE color coordinates of 0.31/0.32 and a color rendering index (CRI) of 92.

## 2. Results and Discussion

### 2.1. Synthesis and Characterization of the Emitters

A detailed description of the synthesis and the characterization of the complexes can be found in the Experimental Section. In brief, the syntheses of Cu(I)-iTMCs was carried out following a standard 2-steps/1-pot method in $CH_2Cl_2$ at room temperature—Figure 1. First, tetrakis-acetonitrile copper(I) react with the phosphine ligand, then dcbq is subsequently added. Evaporation of the solvent and addition of diethylether allows for the crystallization of the complexes as deep-red solids in good yields. The most relevant feature of the NMR characterization is the broad singlet of the phosphine in the $^{31}P\{^1H\}$ NMR (−2.02 ppm **1**, −10.66 ppm **2**, −11.06 ppm **3**), that, in all cases, integrates 2:1 with respect to the septuplet of the $PF_6$ anion—Figures S1–S3 in the Supporting Information. While complexes **2** and **3** are isolated as pure solids, the $^1H$ NMR spectra of **1** shows that, in solution, the complex is in equilibrium with the homoleptic side products $[Cu(dcbq)_2]^+$ and $Cu(PPh_3)_4]^+$—Figures S1–S3 in the Supporting Information. This type of ligand exchange has been previously reported with copper(I) complexes based on N^N and P^P bidentate ligands.[47] Therefore, it is not surprising that such exchange can be also be observed in the particular case of **1**, as the absence of chelating diphosphine surely favours the ligand reorganization in solution.

### 2.2. Photophysical Characterization of the Emitters

The UV–vis absorption spectra of **1–3** in $CH_2Cl_2$ solution are characterized by strong high-energy bands at ≈280 nm followed by a less intense band at around 375 nm and a weak band in the green-yellow region—**Figure 2**. The high-energy absorptions present a ligand-centered (LC) energy transfer character, representing an intraligand $\pi \rightarrow \pi^*$ transition. The low-energy bands at 370–500 nm are characteristic of the formation of the complexes and responsible of the deep-red color in solution. These bands are attributed to metal-to-ligand charge-transfer transitions (MLCT) involving the Cu(I) metal core and the bcbq ligand.[31,45,48–50] As was mentioned before, the NMR characterization of **1** in $CDCl_3$ reveals the presence of an equilibrium process of the complex with $[Cu(dcbq)_2]^+$ and $Cu(PPh_3)_4]^+$. In concordance, the UV–vis absorption spectrum of **1** in $CH_2Cl_2$ shows an additional absorption band located at ≈577 nm that is attributed to the homoleptic $[Cu(N^N)_2]^+$.

These complexes show intense photoluminescence in both fluid and rigid media. **Table 1** summarizes the photophysical properties of the complexes and selected examples are shown in Figure 2. In $CH_2Cl_2$ solution, the complexes exhibit featureless bands centered at $\lambda_{max}$ = 704 nm (**1**), 709 nm (**2**), and 701 nm (**3**) that are remarkable blue-shifted in powder ($\lambda_{max}$ = 669 nm **1**; 676 nm **2**; 671 nm **3**). This may be attributed to common J-type aggregates noted for this family of compounds in powder, which typically lead to a hypsochromic shift due to a change in the molecular geometry in the excited state.[10] The PLQY in powder corresponds to 26% **1**, 36% **2**, and 56% **3**, increasing as the P^P moiety becomes more rigid. This highlights the well-known impact of a proper ligand design on preventing a flattening of the complex in the excited emitting state.[45,49,51–56] The excited state decay profiles revealed average lifetimes $\langle\tau\rangle$ of 0.71, 0.58, and 0.63 μs for **1**, **2** and **3**, respectively. The average radiative rate constants $\langle k_r\rangle$ increases in line with the PLQY values—Table 1 and Figure S4 (Supporting Information). Similar photophysical trends for PLQYs, $\langle\tau\rangle$, and $\langle k_r\rangle$ are noted in thin films prepared for devices—Table 1. In light of the aforementioned, complex **3** turns to be the best emitter candidate for lighting devices.

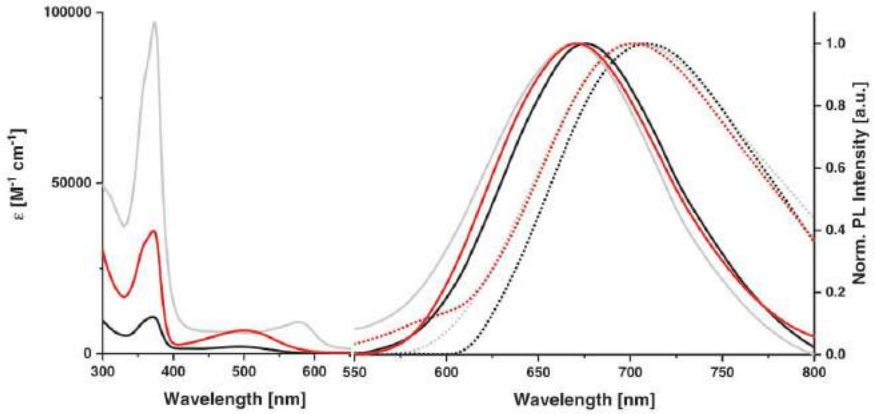


**Figure 2.** Left: Absorption spectra of **1** (grey line), **2** (black line), and **3** (red line) at a concentration of $10^{-4}$ M. Right: Emission in DCM (dotted lines) at excitation wavelength of 490 nm (bottom left) recorded in DCM solution and in powder (solid lines) at excitation at 420 nm of complexes **1** (grey lines), **2** (black lines), and **3** (red lines).

### 2.3. Electrochemical Characterization of the Emitters

Considering the LEC mechanism—vide infra, the emitter must be stable towards repetitive oxidation and reduction processes. We, therefore, studied the redox-features of **1–3** with cyclovoltammetric (CV) and square wave voltammetry (SWV) assays in acetonitrile ($CH_3CN$)—Table 1 and Figures S5 and S6 (Supporting Information). All compounds show a *quasi*-reversible redox behavior with a small shift of the oxidation potential in the row **3** < **2** < **1** towards lower potentials going from 0.91 V (**3**), to 0.87 V (**2**), and to 0.83 V (**1**) versus $Fc/Fc^+$. This is in line with the rigidity of the P^P ligand Xantphos > POP > $PPh_3$ and supported by a linear trend associated to the highest occupied molecular orbital (HOMO), which is usually located across the Cu(I) central atom and the P^P ligand.

The three complexes present a first reduction wave at −1.3 V versus $Fc/Fc^+$, which is ascribed to the N^N ligand (dcbq), upon which the LUMO is presumably located—Table 1. Additionally, the complexes present a second reduction wave at −1.51 V, −1.70 V, and −1.76 V versus $Fc/Fc^+$ for **1**, **2**, and **3**, respectively. This second reduction is assigned to the P^P ligand, which presents additional accessibility for electronic reduction. In order to identify the level of *quasi*-reversibility of the series, we further corroborated the ratio of the first oxidation and reduction peak of the SWV assays by integrating the peak derived in forward and reverse scanning directions—, i.e., upon scanning from the cathodic to the anodic direction and vice versa—Figure S6 in the Supporting Information. The obtained ratio increases linearly from **1** to **3** with respect to both the oxidation and reduction processes. Thus, the stability towards hole transport under device operation in the compounds points to a clear trend that goes again hand-in-hand with the rigidity of the present P^P ligand—Figure 1. Thus, **3** also shows the best electrochemical behavior for LECs.

### 2.4. Electrical Behavior of Thin Films

To fabricate good performing LECs, homogeneous and defect-free active layers are essential. In this context, we prepared

**Table 1.** Photophysical and electrochemical characterization of **1–3** emitters.

| Compound | Molar absorptivity | Photoluminescence | | | | | | Cyclovoltammetry | | |
|---|---|---|---|---|---|---|---|---|---|---|
| | $\varepsilon$ [$10^4$ L mol$^{-1}$ cm$^{-1}$][a] ($\lambda_{max}$ [nm]) | $\lambda_{em}$[b] [nm] | $\lambda_{solid}$[c] [nm] | $\phi$[d] [%] | $\phi$[e] [%] | $\langle\tau\rangle$[f] [μs] $\langle\tau\rangle$[g] [μs] | $\langle k_r\rangle$ [$10^9$ s$^{-1}$] | $\langle k_{nr}\rangle$ [$10^{12}$ s$^{-1}$] | $E_{ox}$ [V][h] | $E_{red}$ [V][h] |
| **1** | 24.1 (277), 9.69 (373), 0.93 (577) | 704 | 669 | 26 | 1 | 0.71 0.88 | 3.65 | 1.41 | 0.91 | −1.26 |
| **2** | 13.3 (277), 1.08 (371), 0.21 (497) | 709 | 676 | 35 | 13 | 0.58 1.96 | 6.06 | 1.71 | 0.87 | −1.30 |
| **3** | 12.4 (276), 3.61 (372), 0.68 (501) | 701 | 671 | 56 | 23 | 0.63 1.85 | 8.87 | 1.59 | 0.83 | −1.26 |

[a]in $CH_2Cl_2$, concentration $10^{-5}$ mol L$^{-1}$; [b]in $CH_2Cl_2$, concentration $10^{-4}$ mol L$^{-1}$ at excitation of 490 nm; [c]in powder at excitation of 420 nm; [d]first reduction and oxidation peak versus $Fc/Fc^+$; [e]in powder versus $[Ru(bpy)_3][PF_6]_2$ reference (error ±10%); [f]in thin film; [g]excited state-lifetimes measured in powder upon excitation at 355 nm; [h]excited state-lifetimes measured in thin film upon excitation at 355 nm.

layers comprising the respective compound on a glass/indium tin oxide (ITO)/poly(3,4-ethylenedioxythiophene) polystyrene sulfonate (PEDOT:PSS) (90 nm)/active layer (120 nm)—see the Experimental Section for details. First, the morphology of the layers was studied by atomic force microscopy (AFM) and both ionic and electronic behavior was investigated by electrochemical impedance spectroscopy (EIS) technique. Regardless of the complex, we were able to prepare homogeneous layers with an active layer thickness of 120 nm and very low root mean square (RMS) roughness values of around 0.2 nm in a 5 $\mu m^2$ sample area. This accounts for a similar layer morphology as shown in **Figure 3**. Please notice that the photophysical features—, i.e., PLQY and excited state lifetime—of the thin-films are similar to those of powder—vide supra—and are summarized in Table 1.

The LEC operation implies that the emitter is responsible of charge injection, transport, and emission processes.[57–59] In

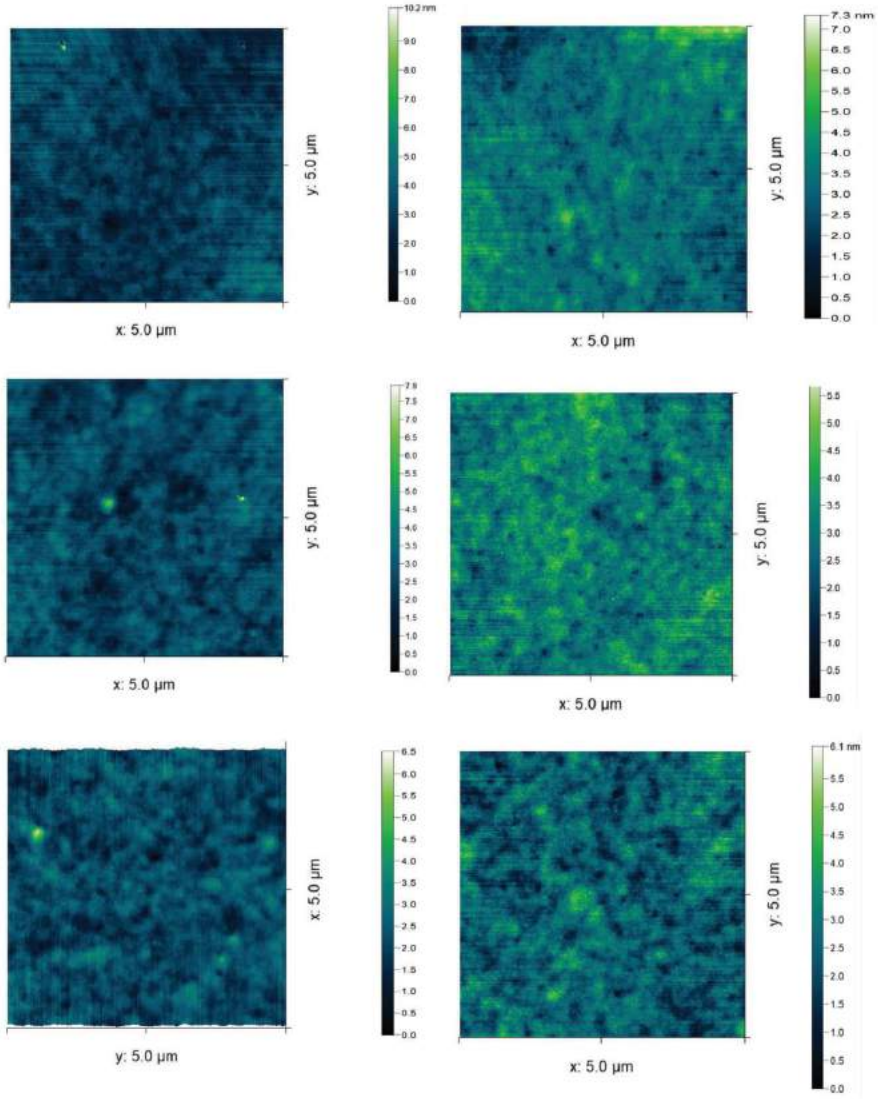


**Figure 3.** AFM microscopy graphs of a) layers prepared from pristine **1**–**3** (top, center and bottom left, respectively) and layers prepared with **1**–**3**:IL in 4:1 molar ratio (top, center and bottom right, respectively).

short, mobile ions are at first randomly distributed throughout the entire active layer. After biasing the device, the ions move towards the respective electrodes, forming EDLs at the electrode/active layer interfaces. Thus, Ohmic contacts form, leading to a heavy doping of the active layer and to an efficient increase in current and electroluminescence emission. This unique feature allows the use of different electrodes fairly independent to their work functions response.[60] By further biasing the device, injection of electrons and holes occurs leading to n- and p-doped regions, which grow towards each other, creating an intrinsic region in between, where holes and electrons recombine under emission of light.

As a step further, we focus on static EIS analysis of devices prepared **1**–**3**, putting special emphasis on comparing freshly versus after prebiasing the layers. Here, **1** shows an abrupt decrease of the resistance—, e.g., $9.1 \times 10^4$ Ω at 0 V versus $1.9 \times 10^3$ at 1.5 V; this is followed by a rapid increase of the resistance at biases higher than injection voltage ($V_{inj}$), which indicates the formation of degraded species—Figure S7 in the Supporting Information. As well, prebiased devices show five-times increased resistance compared to fresh ones—, i.e., $9.1 \times 10^5$ versus $5 \times 10^6$ Ω for fresh and prebiased devices, respectively. Furthermore, the resistance steadily increases for applied voltages > 1.8 V.

On the contrary, fresh devices of **2** and **3** show standard trends in resistance upon increasing the applied voltages. In short, a similar ionic conductivity of $4.1 \times 10^9$ and $3.6 \times 10^9$ S m$^{-1}$ at 0 V for **2** and **3** was noted, respectively. However, devices with **3** show a quicker electrical double layers (EDL) formation than devices with **2**, as it is shown by the steeper slope of the resistance versus applied voltage curve at voltages lower than the $V_{inj}$ (<2 V)—inset of **Figure 4**. This goes hand-in-hand with a more prominent lower resistance at any further applied voltage for **3** compared to **2**—, e.g., $2.3 \times 10^5$ versus $6.5 \times 10^4$ Ω at 2.5 V; Table S1 (Supporting Information) and Figure 4. This is, indeed, in perfect agreement with the dielectric constant ($\varepsilon_r$) values, which are almost twice for **3** compared to **2**—, i.e., 9.8 versus 5.3, despite both show the same ionic conductivity at 0 V. Since there is a direct relationship between the rearrangement of a molecule and its dipole moment and $\varepsilon_r$, we can state that **3** rearranges faster upon applying an external electric field, and, therefore, it is more suitable for enhancing charge injection.[61] This may be related to a different cation–anion distribution in Cu(I)-iTMCs upon changing the P^P ligand from POP to Xantphos. Thus, the electrically induced polarization is different for each complex leading to different ionic conductivity and electrical susceptibility. In addition, also the charge transport should be more favorable in **3**, since the overall resistance gradually decreases upon increasing applied voltage. This is further corroborated upon inspection of the electrical behavior of prebiased devices. Here, **3** shows a similar trend for the resistance upon increasing the applied voltage, but the overall resistance values are lower—, i.e., $3.2 \times 10^4$ versus $3.25 \times 10^5$ at 1.8 V for **3** and **2**, respectively—caused by the polarization of the active layer. Indeed, $\varepsilon_r$ increases up to 12.6. In stark contrast, **2** shows a significant increase of the overall resistance, highlighting the irreversible formation of new species that are hampering charge transport. This is in line with the electrochemical stability above described and could result in a lower device stability.[34,62]

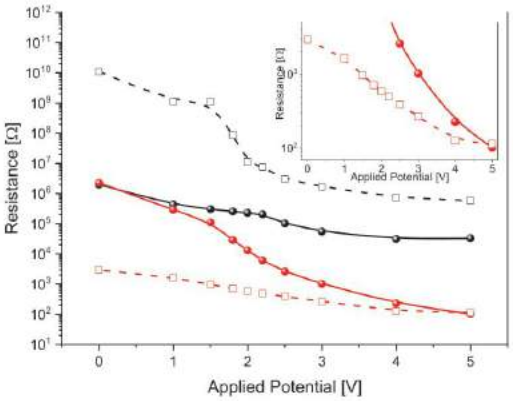


**Figure 4.** Resistance change derived from EIS data in a solid-state configuration for pristine **2** (black) and **3** (red) in fresh (solid line) and prebiased condition (dashed line). Inset shows the detailed zoom-in for compound **3**.

### 2.5. Electroluminescent Response of Deep-Red LECs Based on Cu(I)-iTMCs

LECs with **1**–**3** were prepared in a sandwich-like device architecture based on a Al metal cathode and an active layer comprising **1**–**3** on top of a glass/ITO anode coated with a PEDOT:PSS layer—see the Experimental Section for details. Upon luminance–current–voltage (*L*–*I*–*V*) assays in the form of five cycles with a scan at 300 mV s$^{-1}$, the current density holds constant for devices with **2** and **3**, while devices with **1** feature an enhancement up to the 4th scan cycle. The luminescence increases with the number of cycles for devices with **2** and **3**, while devices with **1** show a decrease upon injection over time. This might be related to the different electrochemical stability of the complexes, but it must be mentioned that devices with **1** also contain impurities that surely affect the properties of the layer in great extent. The devices show stable deep-red emission with *x*/*y* CIE color coordinates of 0.52/0.33 (**1**), and 0.66/0.32 (**2** and **3**). In addition, the highest value of irradiance follows the PLQY trend in thin films—, i.e., 0.89, 29, and 40 μW cm$^{-2}$ for **1**, **2**, and **3**, respectively—**Figure 5** and Figure S8 (Supporting Information). Devices with **3** show the lowest injection voltage of 2.5 V to note light response, as expected from the easier formation of the EDLs as discussed in Section 2.4.

With this data at hand, we turned to lifetime measurements of the devices—Figure 5 and Figure S10 (Supporting Information). We therefore applied a driving mode based on an average current of either 15 or 20 mA in a pulsed current scheme at a standard block wave of 1 kHz and a duty cycle of 50%—**Table 2**. The pulsed driving scheme led to best performing LECs with fast turn-on times and long-time stabilities.[15,59] For all the three complexes, the voltage profile follows the typical LEC behavior, i.e., the rapid drop of the initial average voltage due to the EDL formation and of the doping process in the active layer,

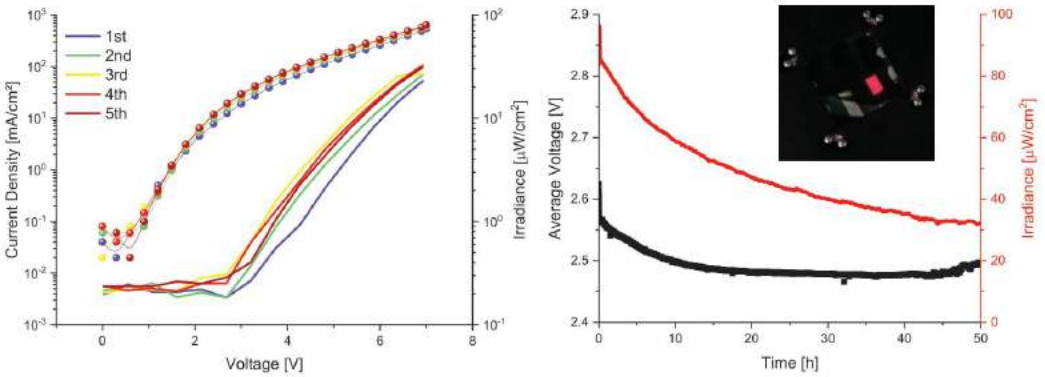


**Figure 5.** Repetitive current–voltage sweeps (left) and light output in pulsed galvanostatic driving scheme at an average current of 15 mA (right) of devices prepared with **3**. The inset shows a picture of a device under operation conditions.

thus reducing the voltage until reaching steady state conditions, whereby the voltage reaches a stable plateau.

As was expected, the maximum irradiance and stability—, i.e., $t_{1/2}$ or time to reach half of the maximum irradiance—, of devices with **3** overcomes those of **2** and **1** (97.9 μW cm$^{-2}$, 20.9 h **3**; 41.5 μW cm$^{-2}$, 6.5 h **2**; 0.77 μW cm$^{-2}$, 1.7 × 10$^{-3}$ h **1**). Since all the devices show different irradiance levels,[63] the stability is better studied analyzing the total emitted energy, obtained by taking the time needed to reach one fifth of the maximum luminance as the upper limit. Devices with **3** also shows the best stability behavior—Table 2. In particular, the total emitted energy of **3** devices increases up to eight orders of magnitude compared to **1**, resulting in stable deep-red-emitting LECs with broad shape EL and CIE 1931 coordinates of *x*/*y* of 0.66/0.32 and lifetimes of almost a day—Figure 5, Table 2, and Figure S10 (Supporting Information). This supports by EIS assays, as devices with **2** present an inefficient charge mobility shortly after prebiasing the device, which generates charge unbalance upon applied voltage and a fast drop of the irradiance. The stability trends are, therefore, related to the formation of (i) degradative species promoted by ligand-exchange reactions during the fabrication process, owing to the poor stability of **1** in coordinative solvents—vide infra, and (ii) Cu(II) species promoted by geometrical distortions—, e.g., flattening, rocking, and wagging distortions—caused by photo- and electrical-excitations. Figure S9 in the Supporting Information illustrates these degradative pathways in Cu(I)-iTMCs.[50,64]

Overall, the device data supports the previous discussion, corroborating the superior performance of **3** emitters in LECs—Figure 5 and Figure S10 (Supporting Information). Thereby, the key figures-of-merit preferentially ruling the device performance are considered to be (i) the PLQY, (ii) the redox stability, (iii) the film morphology, and (iv) the stable electronic device behavior.

As in iTMCs the cation is mostly bulkier than the small counter-anion—, i.e., $PF_6$, the charge migration is unfavorably balanced, leading to a shift of the emission zone away from the center as shown in planar devices.[65] In this context, the introduction of supporting electrolytes and/or the use of double-layer architectures have proved to be effective strategies to enhance device performance.[22,34,36,45]

We elucidated the effect of a supporting electrolyte introduced to the active layer in order to enhance the device response. Therefore, we used the ionic liquid (IL) 1-ethyl-3-methylimidazolium hexafluorophosphate, EMIM $PF_6$, mixed in a molar ratio of 4:1 with compounds **1**–**3**, and studied the effect on the device. One can usually expect to enhance the overall performance by effectively assisting the EDL formation and, thus, the doping process, leading to a faster and higher light output—vide supra. As reported in many studies, the

**Table 2.** Figures-of-merit of **1**–**3** devices.

| Device | Current density [mA cm$^{-2}$] | Average current [mA] | Irradiance [μW cm$^{-2}$] | $t_{1/2}$[a] [h] | $t_{1/5}$[b] [h] | $E_{tot}$[c] [J] | Eff[d] [lm W$^{-1}$] | $\lambda_{max}$ [nm] | CIE 1931 coordinates *x*/*y* |
|---|---|---|---|---|---|---|---|---|---|
| **1** | 133.1 | 20 | 0.77 | 1.4*E*−3 | 3.1*E*−3 | 3.74*E*−05 | 5.54*E*−4 | 670 | 0.524/0.334 |
| | 100.4 | 15 | 0.90 | 1.7*E*−3 | 4.7*E*−3 | 7.15*E*−05 | 1.00*E*−4 | | |
| **2** | 132.1 | 20 | 50.1 | 1.3 | 5.7 | 5.50E+01 | 0.04 | 672 | 0.661/0.323 |
| | 99.85 | 15 | 41.1 | 6.5 | 20.0 | 1.39E+02 | 0.05 | | |
| **3** | 133.35 | 20 | 129.8 | 3.12 | 24.8 | 5.46E+02 | 0.19 | 675 | 0.660/0.320 |
| | 99.92 | 15 | 97.9 | 20.9 | 81.2 | 1.34E+03 | 0.23 | | |

[a]time to reach 50% of the initial irradiance; [b]time to reach 20% of the initial irradiance; [c]total emitted energy; [d]Power efficiency.

mixtures of ILs and Cu-iTMCs are prone to crystallization upon film forming.[41,45] Hence, we first studied the layer quality for the device architecture ITO/PEDOT:PSS/Cu(I)-iTMC:IL in molar ratios of 4:1 and 1:1. Contrary to what has been observed in the literature,[15,34,66] the blended ones showed no significant difference in layer quality featuring a thickness of 120 nm and an active layer RMS roughness of <0.2 nm—Figure 3. Additionally, the PL features of pristine devices and devices with the IL in molar ratio 4:1 and 1:1 were recorded, highlighting no significant difference in the emission maxima ($\lambda_{max}$ = ≈677 nm for **1** and ≈680 nm for **2** and **3**)—Figure S11 in the Supporting Information.

Devices with IL showed similar electroluminescence emission and CIE $x/y$ color coordinates to those of the pristine device—Table S2 in the Supporting Information. As a general trend, the irradiance and lifetime are, however, dramatically reduced—Figure S12 and Table S2 in the Supporting Information. EIS assays shed light onto this behavior—Figure 4; Figures S13 and S14 and Table S2 in the Supporting Information. For instance, devices with **3** blended with two different molar ratios of IL, i.e., 4:1 and 1:1. As expected, samples comprising ILs showed a higher ionic conductivity than pristine ones, owing to the higher concentration of mobile ions provided by the electrolyte. Likewise, the dielectric constant $\varepsilon$ reduces from 9.79, to 8.54, and to 7.53 going from pure **3**, to 4:1, and to 1:1 of **3**:IL—Table S1 in the Supporting Information. Devices with an increasing amount of IL show a prominent drop of the overall resistance upon increasing the applied voltage. However, prebiased devices with 1:1 molar ratio show an overall higher resistance at any applied voltage than that of the fresh devices. Thus, we conclude that the introduction of additional mobile ions leads to either an excessive charge density and, in turn, a fast electrochemical degradation of the emitters, or a significant phase separation phenomena between the emitter and the IL. In both cases, charge transport across the emissive layer remains limited, and thus the doping at the interface does not significantly lower the bulk resistance. The earlier might be dominant in our case, as we do not observe differences neither in film morphology nor in their photoluminescence response—Figure 3; Figure S11 and Table S1 in the Supporting Information. This explains the drop in lifetime and light output as summarized by the total emitted energy, which decreases for a driving mode of 15 mA from 135.4 J, to 5.1 J, and to $7.0 \times 10^{-3}$ J for pristine **3**, 4:1, and 1:1 **3**:IL devices, respectively. Increasing the amount of IL, therefore, reduces the overall figures-of-merit expressed in a lower stability and light output.

### 2.6. White-Emitting LECs Based on Cu(I)-iTMCs

Complex **3** shows the most efficient deep-red electroluminescence and it is the best candidate among this series to act as guest with a blue emitting host material towards manufacturing white LECs. Following our previous reports, we used the hole transport material (HTM) CBP or 4,4′-Bis(*N*-carbazolyl)-1,1′-biphenyl, since it features a suitable electrochemical bandgap and a bluish photoluminescence and electroluminescence response that perfectly fit to the absorption of **3**. Indeed, a good charge and energy transfer in a traditional host:guest system is expected, given the HOMO–LUMO energy levels of CBP and **3**—**Figure 6**.

The device architecture ITO/PEDOT:PSS/**3**:CBP/Al was analyzed changing the blending ratio in a range 1%–30% wt. of **3**—see the Experimental Section for details. As shown in Figure 6, the electroluminescence response can be tuned to obtain a white light output. For instance, devices with 1% wt. of **3** show only the CBP electroluminescence response centered at around 390 and 490 nm, but as the amount of **3** increases the emission features of **3** become more efficient—Figure 6. A 15% wt. of **3** is enough to generate white response with $x/y$ CIE color coordinates of 0.31/0.32 and CRI of 92. The device response is stable over the lifetime showing a moderate luminance of 4 cd $m^{-2}$ at 25 mA puled current driving—Figure 6. Although the luminance value is moderate, this must be put into the right context, considering that CBP:TMPE:LiOTf devices only produce a maximum luminance of 5 cd $m^{-2}$ at the same driving conditions—Figure S15 in the Supporting Information.

Finally, it is interesting to point out that devices with 30% wt. of **3** showed the expected deep-red emission ($\lambda_{max}$ 670 nm; $x/y$ CIE color coordinates of 0.66/0.32) with slightly lower irradiances (79 μW $cm^{-2}$) compared to pure **3** devices, but with an outstanding stability of 170 h—**Figure 7**. Overall, these examples shows the potential of effectively mixing [Cu(dcbq)(Xantphos)]($PF_6$) **3** with other emissive materials to build highly stable deep-red or white-emitting LECs.

## 3. Conclusions

First, a novel family of [Cu(dcbq)(P^P)]($PF_6$) complexes (P^P = 2 $PPh_3$ **1**, POP **2**, or Xantphos **3**) has been synthesized and characterized, as well as the photophysical and electrochemical properties studied. We described that increasing the rigidity of the diphosphine ligand provides enhanced electrochemical stability, reversibility, and higher PLQYs. The same trend is reflected in the stability and light output of **1**–**3** based LEC devices. In particular, the complex bearing Xantphos as P^P ligand showed a promising electroluminescent response—, i.e., stable deep-red emission centered at around 675 nm, $x/y$ CIE color coordinates of 0.66/0.32, irradiance of ≈100 μW $cm^{-2}$, and stabilities of almost a day.

Optimization with the IL $EMIMPF_6$ showed no significant difference in layer quality as corroborated by AFM assays. However, these devices showed decreased stability and irradiance values compared to the pristine ones. Quite likely, this is related to an excessive charge accumulation at the electrode interface.

Finally, the optimization mixing **3** with the HTM CBP in a host-guest approach allow to achieve proof-of-concept white-emitting LECs (85:15% wt. of CBP:**3**) featuring $x/y$ CIE color coordinates of 0.31/0.32 and a high CRI of 92. Last but not less, devices with 70:30% wt. of CBP:**3** show a similar deep-red emission to those of the pristine **3** devices with slightly reduced irradiances of 79 μW $cm^{-2}$ and outstanding improved stabilities of 170 h.

Overall, this work provides the first example of deep-red- and white-emitting LECs based on Cu(I) complexes, bridging the gap to explore emitters covering the whole visible range for future applications.

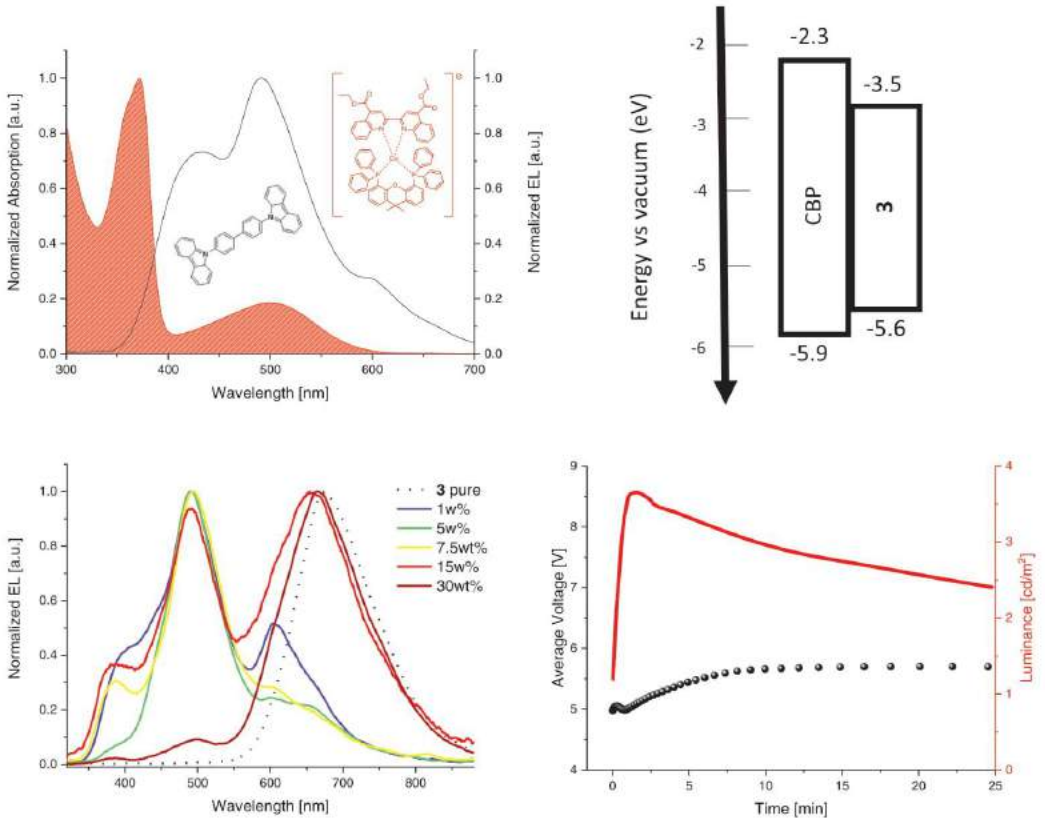


**Figure 6.** Top: Normalized absorption of **3** (red) showing an overlap to the electroluminescence (black) of CBP (left), energy levels of CBP and **3** as derived from the CV data with the formula $E_{HOMO/LUMO} = e(VFc/Fc^{+}) + 4.8$ eV (right). Bottom: electroluminescence response of different blending ratios in %wt. of **3** with CBP (left), and lifetime measurement at pulsed galvanostatic driving scheme at an average current of 25 mA (right) of a white-emitting device containing compound **3** at 15% wt. blended in CBP.

## 4. Experimental Section

*Synthesis and Characterization*: When required, manipulations were performed using standard Schlenk techniques under dry argon or using a M. Braun glove box. Solvents were obtained from a solvent purification system (M-BRAUN MB SPS-800). All commercial chemicals were used without further purification. Elemental analyses were carried out with a Carlo Erba EA1110 CHNS-O microanalyzer. NMR spectra were recorded on a Bruker ARX 300 spectrometers at 298 K. Chemical shifts are reported in parts per million (ppm) relative to external standards, and all coupling constants are given in hertz (Hz). Mass spectra were recorded on a Micromass ZABspec spectrometer utilizing electrospray ionization with a MeOH or $CH_3CN$ mobile phase.

The ligand 4,4′-diethylester-2,2′-bipyridine was prepared as reported in reference.[67] Briefly, at 0 °C sulfuric acid in excess (20 mL) was dropwise added to 4,4′-dicarboxylic acid-2,2′-biquinoline (6 g, 17 mmol) in ethanol (80 mL). The reaction mixture was heated to reflux temperature overnight. The grey mixture was neutralized with NaOH (aq. 25%) and the grey precipitate obtained filtered, washed with water and cold EtOH and air dried. $^1$H NMR (300 MHz, $CDCl_3$) $\delta$ 9.31 (s, 2H), 8.80 (dd, $J$ = 8.6, 1.5 Hz, 2H), 8.33 (dd, $J$ = 8.4, 1.4 Hz, 2H), 7.84 (ddd, $J$ = 8.4, 6.9, 1.5 Hz, 2H), 7.70 (ddd, $J$ = 8.4, 6.9, 1.4 Hz, 2H), 4.60 (q, $J$ = 7.1 Hz, 4H), 1.55 (t, $J$ = 7.2 Hz, 6H).

$$\left[Cu(dcbq)(PPh_3)_2\right](PF_6) \quad (1)$$

$[Cu(NCCH_3)_4](PF_6)$ (100 mg, 0.26 mmol) and $PPh_3$ (136 mg, 0.52 mmol) are mixed in 10 mL of dry $CH_2Cl_2$ and the reaction mixture stirred at room temperature for 20 min. After this time, dcbq (107 mg, 0.26 mmol) was added, what causes a noticeable color change from colorless to dark red. The mixture was filtered through diatomaceous earth (celite) and the filtrate concentrated to ≈2 mL by rotatory evaporation. The addition of diethyl ether caused the precipitation of a dark red solid that was filtered, washed with diethylether and dried under vacuum to give **1** (225 mg, 77%). Anal. Calcd. For $C_{68}H_{50}N_2CuF_6O_4P_3$ (1133.51): C, 63.58; H, 4.45; N, 2.47. Found: C, 63.71; H, 4.57; N, 2.43. TOF-MS (ES+): [M] + $m/z$ = 987.2, calculated $m/z$ = 987.25. $^1$H NMR (300 MHz, $CDCl_3$, 298K) (only signals attributed to **1** are given) $\delta$ 8.95 (s, 2H, $H^3$, dcbq), 8.72 (br, d, 2H, dcbq), 8.03 (br, m, 2H, dcbq), 7.66 (br, m, 2H, dcbq), 7.38 (br, t, 6H, $PPh_3$ + 2H, dcbq), 7.17 (br, m, 12H, $PPh_3$),

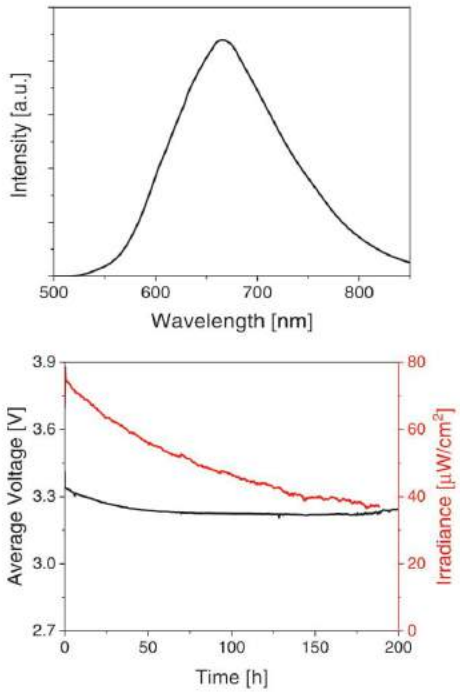


**Figure 7.** Electroluminescence spectrum (top) and device performance of CBP:**3** in 65:35 wt% at an average driving current of 15 mA (bottom).

7.05 (br, m, 12H, $PPh_3$), 4.68 (br, q, 4H, $CH_2$, dcbq), 1.58 (br, t, 6H, dcbq). $^{31}P\{^1H\}$ NMR (121.5 MHz, $CDCl_3$, 298K): −2.02 (br, 2P, $PPh_3$), −144.27 (sept, 1P, $PF_6$, $^1J$(P-F) = 712 Hz).

$$[Cu(dcbq)(POP)](PF_6) \quad (2)$$

This complex was prepared following the same procedure described for **1**, but starting from $[Cu(NCCH_3)_4](PF_6)$ (100 mg, 0.26 mmol), POP (140 mg, 0.26 mmol), and dcbq (107 mg, 0.26 mmol). Complex **2** was isolated as a red solid (264 mg, 88%). Anal. Calcd. For $C_{60}H_{48}N_2CuF_6O_5P_3$ (1147.49): C, 62.80; H, 4.22; N, 2.44. Found: C, 62.71; H, 4.27; N, 2.42. TOF-MS (ES+): [M]+ $m/z$ = 1001.2, calculated $m/z$ = 1001.23. $^1H$ NMR (300 MHz, $CDCl_3$, 298K) $\delta$ 8.70 (d, $J$ = 8.5 Hz, 2H, POP), 8.65 (s, 2H, $H^3$, dcbq), 8.41 (d, $J$ = 8.6 Hz, 2H, dcbq), 7.63 (m, 2H, dcbq), 7.45–7.37 (m, 2H), 7.23 (br, t, 2H), 7.22–7.19 (m, 4H), 7.18–7.10 (m, 6H), 6.91 (br, dd, 8H, POP), 6.79 (br, dd, 8H, POP), 4.65 (q, $^3J$ = 7.2 Hz, 4H, $CH_2$, dcbq), 1.56 (t, $^3J$ = 7.2 Hz, 6H, $CH_3$, dcbq). $^{31}P\{^1H\}$ NMR (121.5 MHz, $CDCl_3$, 298K): −10.66 (br, 2P, POP), −144.28 (sept, 1P, $PF_6$, $^1J$(P-F) = 712 Hz).

$$[Cu(dcbq)(POP)](PF_6) \quad (3)$$

This complex was prepared following the same procedure described for **1**, but starting from $[Cu(NCCH_3)_4](PF_6)$ (100 mg, 0.26 mmol), Xantphos (150 mg, 0.26 mmol), and dcbq (107 mg, 0.26 mmol). Complex **3** was isolated as a red solid (250 mg, 81%). Anal. Calcd. For $C_{63}H_{52}CuF_6N_2O_5P_3$ (1187.55): C, 63.72; H, 4.41; N, 2.36. Found: C, 63.74; H, 4.47; N, 2.35. TOF-MS (ES+): [M]+ $m/z$ = 1041.2, calculated $m/z$ = 1041.26. $^1H$ NMR (300 MHz, $CDCl_3$, 298K) $\delta$ 8.86 (s, 2H, $H^3$, dcbq), 8.73 (d, $J$ = 8.6 Hz, 2H, dcbq), 7.96 (d, $J$ = 8.5 Hz, 2H), 7.75 (d, $J$ = 7.8 Hz, 2H), 7.61 (t, $J$ = 7.7 Hz, 2H), 7.32–7.26 (m, 4H), 7.14–7.06 (m, 10H), 7.01 (m, 2H), 4.67 (q, $J$ = 7.1 Hz, 4H, $CH_2$, dcbq), 1.90 (s, 6H, $CH_3$, Xantphos), 1.58 (t, $J$ = 7.1 Hz, 6H, $CH_3$, dcbq). $^{31}P\{^1H\}$ NMR (121.5 MHz, $CDCl_3$, 298K): −11.06 (br, 2P, Xantphos), −144.28 (sept, 1P, $PF_6$, $^1J$(P-F) = 712 Hz).

*Photophysical and Electrochemical Characterization*: Absorption spectra were recorded with a Shimadzu UV/2600 spectrometer. The $\phi$ values were measured with a FS5 Spectrofluorometer with integrating sphere SC-30 (Edinburgh Instruments). Cyclic voltammetry and SWV performed with a Metrohm μAutolabIII/FRA3, a glassy carbon electrode as working electrode, a silver wire as pseudo-reference electrode and a platinum wire as counter electrode. All spectra were recorded in $CH_3CN$ at a concentration of $5 \times 10^{-5}$ M with tetrabutylammonium hexafluorophosphate (0.1 M) as electrolyte and corrected versus $Fc/Fc^+$ redox couple. PLQY measurements in powder were performed and referenced against $[Ru(bpy)_3][PF_6]_2$. Excited-state lifetimes were measured using nanosecond laser flash photolysis transient absorption measurements, which were carried out with an Nd/YAG laser (third harmonic, 355 nm, 10 mJ) from Brilliant B, Quantel. The optical detection is based on a pulsed (pulser MSP 05 – Müller Elektronik Optik) xenon lamp (XBO 450, Osram), a monochromator (Spectra Pro 2300i, Acton Research), a fast InGaAs photodiode (Nano 5, Coherent) with 300 MHz amplification, and a 1 GHz digital oscilloscope (WavePro7100, LeCroy). The average lifetime can be obtained by using the depicted formula reported in literature:[68] $R(t) = \sum_{i=1}^{2} A_i e^{-t/\tau_i}$ where $A_i$ is constant. The average lifetime can be obtained with: $\langle\tau\rangle = \frac{A_1\tau_1^2 + A_2\tau_2^2}{A_1\tau_1 + A_2\tau_2}$.

*Device Fabrication and Analysis*: LECs were fabricated as follows: ITO coated glass plates were patterned by conventional photolithography (Naranjo Substrates). The substrates were cleaned by using sequential ultrasonic baths, namely in water-soap, water, ethanol, and propan-2-ol solvents. After drying, the substrates were placed in an UV-ozone cleaner (Jetlight 42-220) for 8 min. A 80 nm layer of PEDOT:PSS was doctor-bladed onto the ITO-glass substrate to increase the device preparation yield (400 μm substrate distance and a speed of 10 mm $s^{-1}$). The luminescent layer was entirely prepared with **1**–**3** dissolved in THF at a concentration of 20 mg $mL^{-1}$ or by mixing **3** with CBP in different weight ratios. To achieve white-emitting devices, 5 mg of CBP were mixed with 0.75 mg of **3** and dissolved in 290 μL of THF to achieve a total concentration of 20 mg $mL^{-1}$. The mixture was stirred until complete dissolution of both components, and afterwards filtered. The active layer was deposited in all cases by means of spin-coating in a three steps process of 800/1200/3000 rpm for 60 s reaching a thickness of 120 nm. These conditions resulted in homogenous thin films with a RMS less than 0.20 nm, having no apparent optical defects. The latter was determined by AFM Park XE150 instrument (Park Systems Corp., Suwon, South Korea) in tapping mode, and using the profilometer DektakxT (Bruker). Once the active layer was deposited, the samples were transferred into an inert atmosphere glovebox (<0.1 ppm $O_2$ and $H_2O$, Angstrom Engineering). Physical vapor deposition of aluminum cathode electrodes (90 nm) was carried out using a shadow mask under high vacuum (<1 × $10^{-6}$ mbar) in an Angstrom Covap evaporator integrated into the inert atmosphere glovebox. Time dependence of irradiance, voltage, and current measured by applying constant and/or pulsed voltage and current by monitoring the desired parameters simultaneously by using Avantes spectrophotometer (Avaspec-ULS2048L-USB2) in conjunction with a calibrated integrated sphere Avasphere 30-Irrad and Botest OLT OLED Lifetime-Test System. Electroluminescence spectra were recorded using the above mentioned spectrophotometer. EIS assays were carried out with a potentiostat/galvanostat (PGSTAT30, Autolab) equipped with a frequency response analyzer module (FRA). Measurements were performed at the applied voltage range from 0 to 5 V. The AC signal amplitude was set to 50 mV, modulated in a frequency range from 10 to $10^6$ Hz. The software "Nova 1.11" was used to obtain the parameters from the equivalent circuit[69,70] following the procedure reported by Brug et al.[71] and Hirschorn et al.[72] The effective capacitance ($C_{eff}$) was calculated using $C_{eff} = Q^{(1/\alpha)} R^{(1-\alpha)/\alpha}$

where $R$ the resistance, $Q$ and $\alpha$ being frequency independent parameters. With this data at hand, the $R$ (active layer) was directly obtained and the relative dielectric constant ($\varepsilon_r$) was calculated by means of $\varepsilon_r = (C_{eff}\, d)/(\varepsilon_0\, A)$ where $\varepsilon_0$ is the permittivity of free space, $A$ is the device area, and $d$ is the thickness of the active layer. Finally, the ionic conductivity ($\sigma$) was calculated using $\sigma = d/(R \times A)$. The equivalent circuit model for the fittings is shown in the Supporting Information.

An inductance parameter was included in the circuit to improve the quality of the fittings by taking into account noise generated by the impedance setup cables.

## Supporting Information

Supporting Information is available from the Wiley Online Library or from the author.

## Acknowledgements

E.F., J.F-C., and R.D.C. acknowledge the program "Ayudas para la atracción de talento investigador – Modalidad 1 of the Consejería de Educación, Juventud y Deporte – Comunidad de Madrid with the reference number 2016-T1/IND-1463." R.D.C. acknowledges Spanish MINECO for the Ramón y Cajal program (RYC-2016-20891), the Europa Excelencia program (ERC2019-092825), the 2018 Leonardo Grant for Researchers and Cultural Creators from BBVA Foundation, and FOTOART-CM project funded by Madrid region under programme P2018/NMT-4367. R.D.C. and M.D.W. acknowledge funding by the 'Fonds der Chemischen Industrie' (FCI) in the Liebig grant framework and the Cluster of Excellence 'Engineering of Advanced Materials' (EAM). J.F.-C. acknowledges the Marie Skłodowska-Curie Individual Fellowships (H2020-MSCA-IF-2017). The authors are thankful to Y. Lao, X. Zhang, E. Baranoff for the preliminary work on the synthesis.

## Conflict of Interest

The authors declare no conflict of interest.

## Keywords

copper (I) complexes, deep-red emitters, light-emitting electrochemical cells, thin film lighting, white-emitting devices

Received: May 17, 2019
Revised: August 12, 2019
Published online: September 16, 2019

[1] C. J. Humphreys, *MRS Bull.* **2008**, *33*, 459.
[2] D. Volz, M. Wallesch, C. Fléchon, M. Danz, A. Verma, J. M. Navarro, D. M. Zink, S. Bräse, T. Baumann, *Green Chem.* **2015**, *17*, 1988.
[3] R. Czerwieniec, H. Yersin, *Inorg. Chem.* **2015**, *54*, 4322.
[4] Y. Tao, K. Yuan, T. Chen, P. Xu, H. Li, R. Chen, C. Zheng, L. Zhang, W. Huang, *Adv. Mater.* **2014**, *26*, 7931.
[5] F. Dumur, *Org. Electron.: Phys., Mater. Appl.* **2015**, *21*, 27.
[6] S. Igawa, M. Hashimoto, I. Kawata, M. Yashima, M. Hoshino, M. Osawa, *J. Mater. Chem. C* **2013**, *1*, 542.
[7] K. Tsuge, Y. Chishina, H. Hashiguchi, Y. Sasaki, M. Kato, S. Ishizaka, N. Kitamura, *Coord. Chem. Rev.* **2016**, *306*, 636.
[8] E. Cariati, E. Lucenti, C. Botta, U. Giovanella, D. Marinotto, S. Righetto, *Coord. Chem. Rev.* **2016**, *306*, 566.
[9] A. Chihaya, *Jpn. J. Appl. Phys.* **2014**, *53*, 060101.
[10] H. Yersin, A. F. Rausch, R. Czerwieniec, T. Hofbeck, T. Fischer, *Coord. Chem. Rev.* **2011**, *255*, 2622.
[11] G. Cheng, G. K.-M. So, W.-P. To, Y. Chen, C.-C. Kwok, C. Ma, X. Guan, X. Chang, W.-M. Kwok, C.-M. Che, *Chem. Sci.* **2015**, *6*, 4623.
[12] Q. Pei, Y. Yang, G. Yu, C. Zhang, A. J. Heeger, *Science* **1995**, *269*, 1086.
[13] E. Fresta, R. D. Costa, *J. Mater. Chem. C* **2017**, *5*, 5643.
[14] R. D. Costa, *Light-Emitting Electrochemical Cells. Concepts, Advances and Challenges*, Springer International Publishing, Basel **2017**.
[15] R. D. Costa, E. Ortí, H. J. Bolink, F. Monti, G. Accorsi, N. Armaroli, *Angew. Chem., Int. Ed.* **2012**, *51*, 8178.
[16] A. Asadpoordarvish, A. Sandström, C. Larsen, R. Bollström, M. Toivakka, R. Österbacka, L. Edman, *Adv. Funct. Mater.* **2015**, *25*, 3238.
[17] A. Sandström, L. Edman, *Energy Technol.* **2015**, *3*, 329.
[18] A. Sandstroem, A. Asadpoordarvish, J. Enevold, L. Edman, *Adv. Mater.* **2014**, *26*, 4975.
[19] H. Rudmann, S. Shimada, M. F. Rubner, *J. Am. Chem. Soc.* **2002**, *124*, 4918.
[20] L. Flamigni, A. Barbieri, C. Sabatini, B. Ventura, F. Barigelletti, *Top. Curr. Chem.* **2007**, *281*, 143.
[21] T. Hu, L. He, L. Duan, Y. Qiu, *J. Mater. Chem.* **2012**, *22*, 4206.
[22] D. Tordera, S. Meier, M. Lenes, R. D. Costa, E. Ortí, W. Sarfert, H. J. Bolink, *Adv. Mater.* **2012**, *24*, 897.
[23] M. Martínez-Alonso, J. Cerdá, C. Momblona, A. Pertegás, J. M. Junquera-Hernández, A. Heras, A. M. Rodríguez, G. Espino, H. Bolink, E. Ortí, *Inorg. Chem.* **2017**, *56*, 10298.
[24] L. He, L. Duan, J. Qiao, R. Wang, P. Wei, L. Wang, Y. Qiu, *Adv. Funct. Mater.* **2008**, *18*, 2123.
[25] R. D. Costa, E. Ortí, H. J. Bolink, S. Graber, C. E. Housecroft, E. C. Constable, *Adv. Funct. Mater.* **2010**, *20*, 1511.
[26] C. E. Housecroft, E. C. Constable, *Coord. Chem. Rev.* **2017**, *350*, 155.
[27] A. F. Henwood, E. Zysman-Colman, *Top. Curr. Chem.* **2016**, *374*, 36.
[28] J. Emsley, *Nature's Building Blocks: An A-Z Guide to the Elements*, Oxford University Press, Oxford **2011**.
[29] D. R. McMillin, M. T. Buckner, *J. Chem. Soc., Chem. Comm.* **1978**, *29*, 759.
[30] C. Balzani, S. Campagna, N. Armaroli, G. Accorsi, F. Cardinali, A. Listorti, *Top. Curr. Chem.* **2007**, *281*, 143.
[31] S. Keller, E. C. Constable, C. E. Housecroft, M. Neuburger, A. Prescimone, G. Longo, A. Pertegás, M. Sessolo, H. J. Bolink, *Dalton Trans.* **2014**, *43*, 16593.
[32] S. Keller, A. Pertegás, G. Longo, L. Martínez, J. Cerdá, J. M. Junquera-Hernández, A. Prescimone, E. C. Constable, C. E. Housecroft, E. Ortí, H. J. Bolink, *J. Mater. Chem. C* **2016**, *4*, 3857.
[33] F. Brunner, L. Martínez-Sarti, S. Keller, A. Pertegás, A. Prescimone, E. C. Constable, H. J. Bolink, C. E. Housecroft, *Dalton Trans.* **2016**, *45*, 15180.
[34] M. D. Weber, E. Fresta, M. Elie, M. E. Miehlich, J.-L. Renaud, K. Meyer, S. Gaillard, R. D. Costa, *Adv. Funct. Mater.* **2018**, *28*, 1707423.
[35] M. Elie, F. Sguerra, F. Di Meo, M. D. Weber, R. Marion, A. Grimault, J. F. Lohier, A. Stallivieri, A. Brosseau, R. B. Pansu, J. L. Renaud, M. Linares, M. Hamel, R. D. Costa, S. Gaillard, *ACS Appl. Mater. Interfaces* **2016**, *8*, 14678.
[36] E. Fresta, G. Volpi, M. Milanesio, C. Garino, C. Barolo, R. D. Costa, *Inorg. Chem.* **2018**, *57*, 10469.
[37] M. D. Weber, M. Adam, R. R. Tykwinski, R. D. Costa, *Adv. Funct. Mater.* **2015**, *25*, 5066.
[38] M. D. Weber, J. E. Wittmann, A. Burger, O. B. Malcıoğlu, J. Segarra-Martí, A. Hirsch, P. B. Coto, M. Bockstedte, R. D. Costa, *Adv. Funct. Mater.* **2016**, *26*, 6737.

 

[39] S. Tang, J. Pan, H. a Buchholz, L. Edman, *J. Am. Chem. Soc.* **2013**, *135*, 3647.
[40] M. D. Weber, C. Garino, G. Volpi, E. Casamassa, M. Milanesio, C. Barolo, R. D. Costa, *Dalton Trans.* **2016**, *45*, 8984.
[41] M. Elie, F. Sguerra, F. Di Meo, M. D. Weber, R. Marion, A. Grimault, J.-F. Lohier, A. Stallivieri, A. Brosseau, R. B. Pansu, J.-L. Renaud, M. Linares, M. Hamel, R. D. Costa, S. Gaillard, *ACS Appl. Mater. Interfaces* **2016**, *8*, 14678.
[42] M. Elie, M. D. Weber, F. Di Meo, F. Sguerra, J.-F. Lohier, R. B. Pansu, J.-L. Renaud, M. Hamel, M. Linares, R. D. Costa, S. Gaillard, *Chem. - Eur. J.* **2017**, *23*, 16328.
[43] Q. Zhang, Q. Zhou, Y. Cheng, L. Wang, D. Ma, X. Jing, F. Wang, *Adv. Funct. Mater.* **2006**, *16*, 1203.
[44] S. Keller, F. Brunner, J. M. Junquera-Hernández, A. Pertegás, M.-G. La-Placa, A. Prescimone, E. C. Constable, H. J. Bolink, E. Ortí, C. E. Housecroft, *ChemPlusChem* **2018**, *83*, 217.
[45] R. D. Costa, D. Tordera, E. Ortí, H. J. Bolink, J. Schönle, S. Graber, C. E. Housecroft, E. C. Constable, J. A. Zampese, *J. Mater. Chem.* **2011**, *21*, 16108.
[46] M. D. Weber, M. Viciano-Chumillas, D. Armentano, J. Cano, R. D. Costa, *Dalton Trans.* **2017**, *46*, 6312.
[47] A. Kaeser, M. Mohankumar, J. Mohanraj, F. Monti, M. Holler, J.-J. Cid, O. Moudam, I. Nierengarten, L. Karmazin-Brelot, C. Duhayon, B. Delavaux-Nicot, N. Armaroli, J.-F. Nierengarten, *Inorg. Chem.* **2013**, *52*, 12140.
[48] M. Nishikawa, S. Sawamura, A. Haraguchi, J. Morikubo, K. Takao, T. Tsubomura, *Dalton Trans.* **2015**, *44*, 411.
[49] Q. Zhang, J. Ding, Y. Cheng, L. Wang, Z. Xie, X. Jing, F. Wang, *Adv. Funct. Mater.* **2007**, *17*, 2983.
[50] N. Armaroli, G. Accorsi, F. Cardinali, A. Listorti, *Photochemistry and Photophysics of Coordination Compounds: Copper*, Springer, Berlin, Heidelberg **2007**.
[51] C. E. McCusker, F. N. Castellano, *Inorg. Chem.* **2013**, *52*, 8114.
[52] I. Andrés-Tomé, J. Fyson, F. Baiao Dias, A. P. Monkman, G. Iacobellis, P. Coppo, *Dalton Trans.* **2012**, *41*, 8669.
[53] R. D. Costa, E. Ortí, H. J. Bolink, S. Graber, C. E. Housecroft, M. Neuburger, S. Schaffner, E. C. Constable, *Chem. Commun.* **2008**, 2029.
[54] O. Moudam, A. Kaeser, B. Delavaux-Nicot, C. Duhayon, M. Holler, G. Accorsi, N. Armaroli, I. Séguy, J. Navarro, P. Destruel, J.-F. Nierengarten, *Chem. Commun.* **2007**, *3092*, 3077.
[55] L. Zhang, B. Li, Z. Su, *Langmuir* **2009**, *113*, 13968.
[56] G. Che, Z. Su, W. Li, B. Chu, M. Li, Z. Hu, Z. Zhang, *Appl. Phys. Lett.* **2006**, *89*, 103511.
[57] R. D. Costa, E. Ortí, H. J. Bolink, *Pure Appl. Chem.* **2011**, *83*, 2115.
[58] J. Mindemark, L. Edman, *J. Mater. Chem. C* **2016**, *4*, 420.
[59] S. B. Meier, D. Tordera, A. Pertegás, C. Roldán-Carmona, E. Ortí, H. J. Bolink, *Mater. Today* **2014**, *17*, 217.
[60] J. Xu, A. Sandström, E. M. Lindh, W. Yang, S. Tang, L. Edman, *ACS Appl. Mater. Interfaces* **2018**, *10*, 33380.
[61] L. D. Bastatas, M. D. Moore, J. D. Slinker, *ChemPlusChem* **2018**, *83*, 266.
[62] L. D. Bastatas, K. Y. Lin, M. D. Moore, K. J. Suhr, M. H. Bowler, Y. Shen, B. J. Holliday, J. D. Slinker, *Langmuir* **2016**, *32*, 9468.
[63] G. Kalyuzhny, M. Buda, J. Mcneill, P. Barbara, A. J. Bard, *J. Am. Chem. Soc.* **2003**, *125*, 6272.
[64] M. Iwamura, S. Takeuchi, T. Tahara, *Acc. Chem. Res.* **2015**, *48*, 782.
[65] S. Höfle, T. Lutz, A. Egel, F. Nickel, S. W. Kettlitz, G. Gomard, U. Lemmer, A. Colsmann, *ACS Photonics* **2014**, *1*, 968.
[66] E. Fresta, G. Volpi, C. Garino, C. Barolo, R. D. Costa, *Polyhedron* **2018**, *140*, 129.
[67] P. G. Hoertz, A. Staniszewski, A. Marton, G. T. Higgins, C. D. Incarvito, A. L. Rheingold, G. J. Meyer, *J. Am. Chem. Soc.* **2006**, *128*, 8234.
[68] C. M. Luk, L. B. Tang, W. F. Zhang, S. F. Yu, K. S. Teng, S. P. Lau, *J. Mater. Chem.* **2012**, *22*, 22378.
[69] S. B. Meier, D. Hartmann, A. Winnacker, W. Sarfert, *J. Appl. Phys.* **2014**, *116*, 104504.
[70] A. Munar, A. Sandström, S. Tang, L. Edman, *Adv. Funct. Mater.* **2012**, *22*, 1511.
[71] G. J. Brug, A. L. G. van den Eeden, M. Sluyters-Rehbach, J. H. Sluyters, *J. Electroanal. Chem. Interfacial Electrochem.* **1984**, *176*, 275.
[72] B. Hirschorn, M. E. Orazem, B. Tribollet, V. Vivier, I. Frateur, M. Musiani, *Electrochim. Acta* **2010**, *55*, 6218.

 

ADVANCED OPTICAL MATERIALS

# Supporting Information

for *Adv. Optical Mater.*, DOI: 10.1002/adom.201900830

## White Light-Emitting Electrochemical Cells Based on Deep-Red Cu(I) Complexes

*Elisa Fresta, Michael D. Weber, Julio Fernandez-Cestau, and Rubén D. Costa**

WILEY-VCH



# Supporting Information

## White light-emitting electrochemical cells based on deep-red Cu(I) complexes

Elisa Fresta, Michael D. Weber, Julio Fernández-Cestau and Rubén D. Costa*

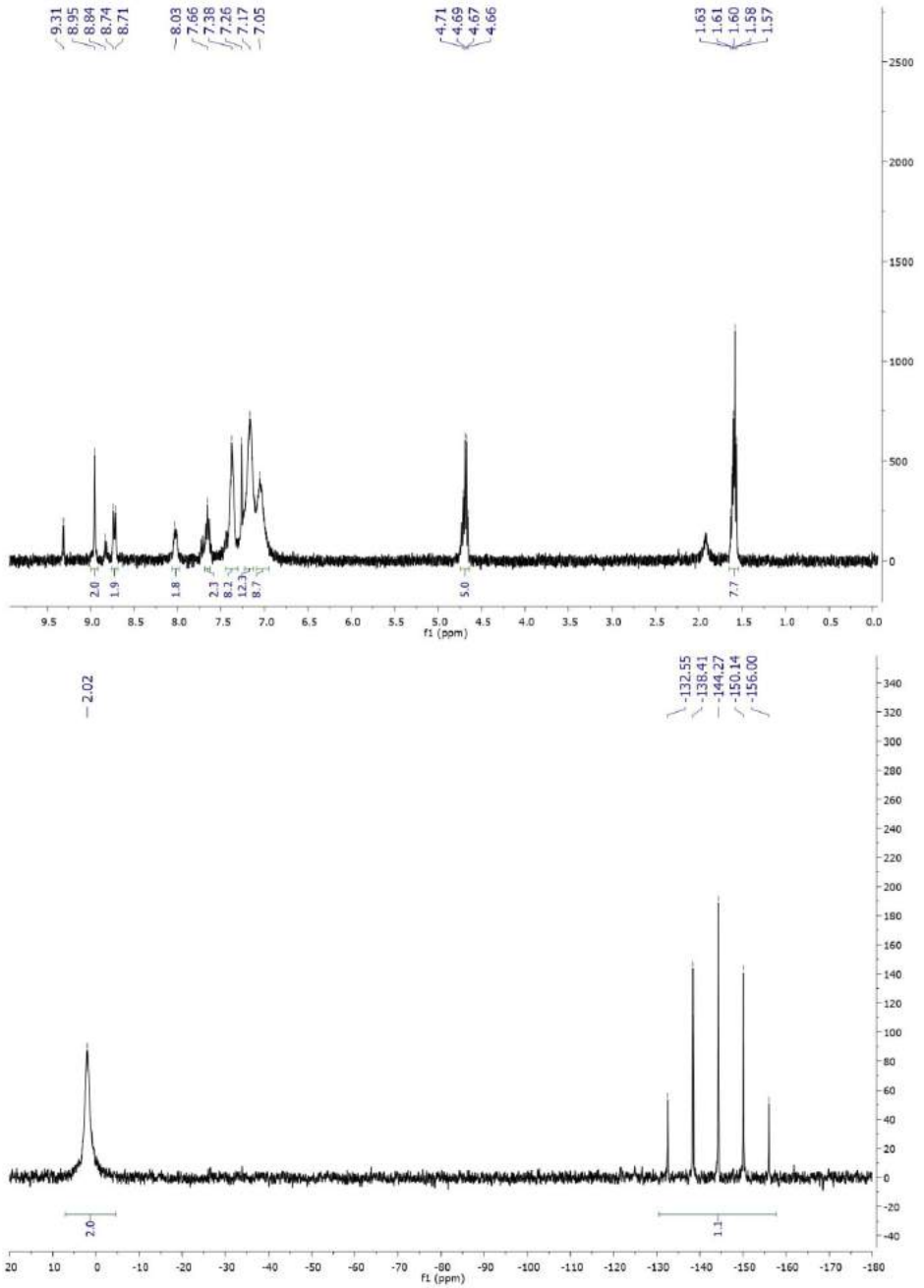


**Figure S1:** $^{1}H$ and $^{31}P\{^{1}H\}$ NMR spectra of complex $[Cu(dcbq)(PPh_3)_2](PF_6)$ **(1)**.

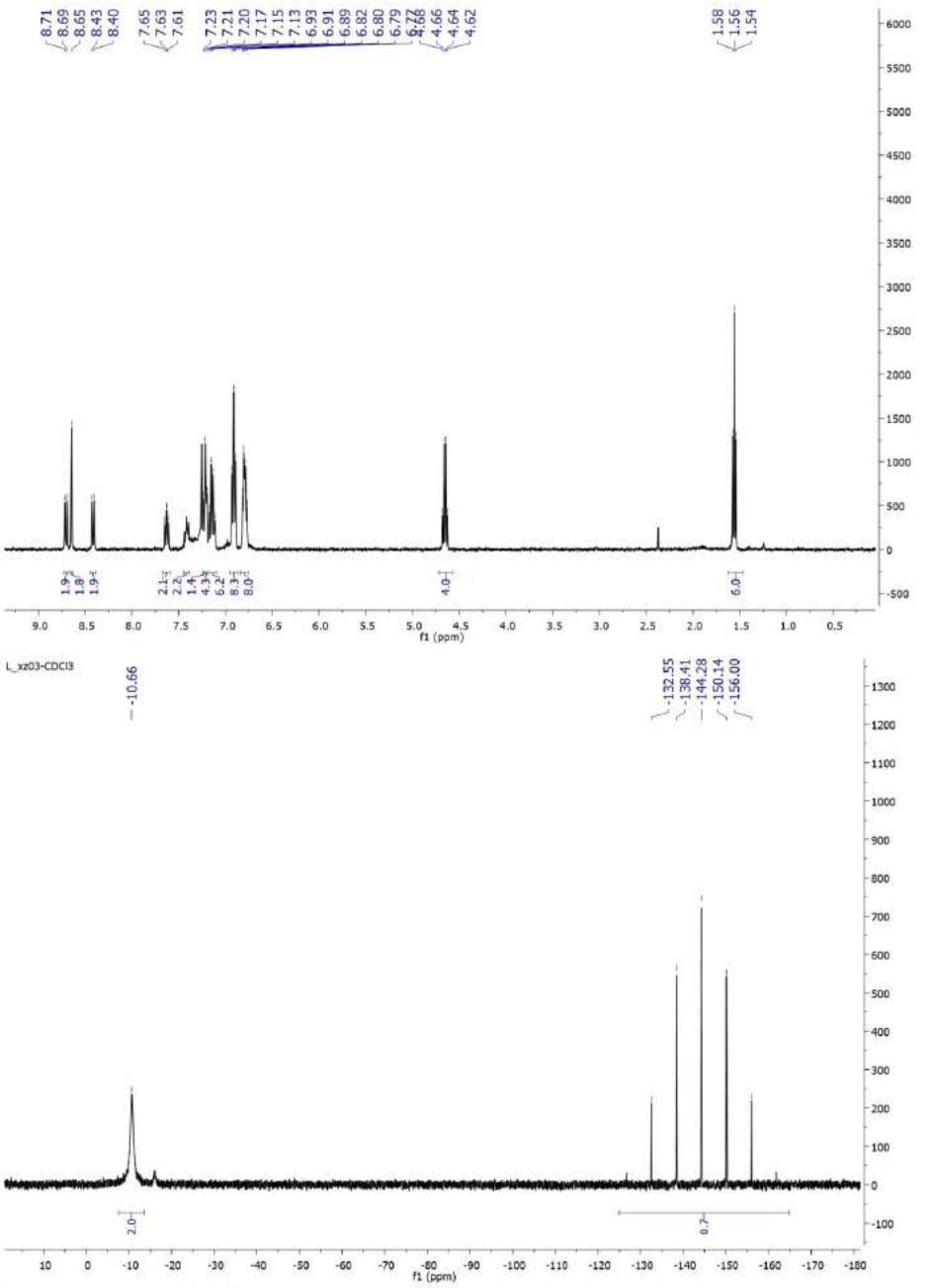


**Figure S2:** $^{1}H$ and $^{31}P\{^{1}H\}$ NMR spectra of complex [Cu(dcbq)(POP)]($PF_6$) (**2**).

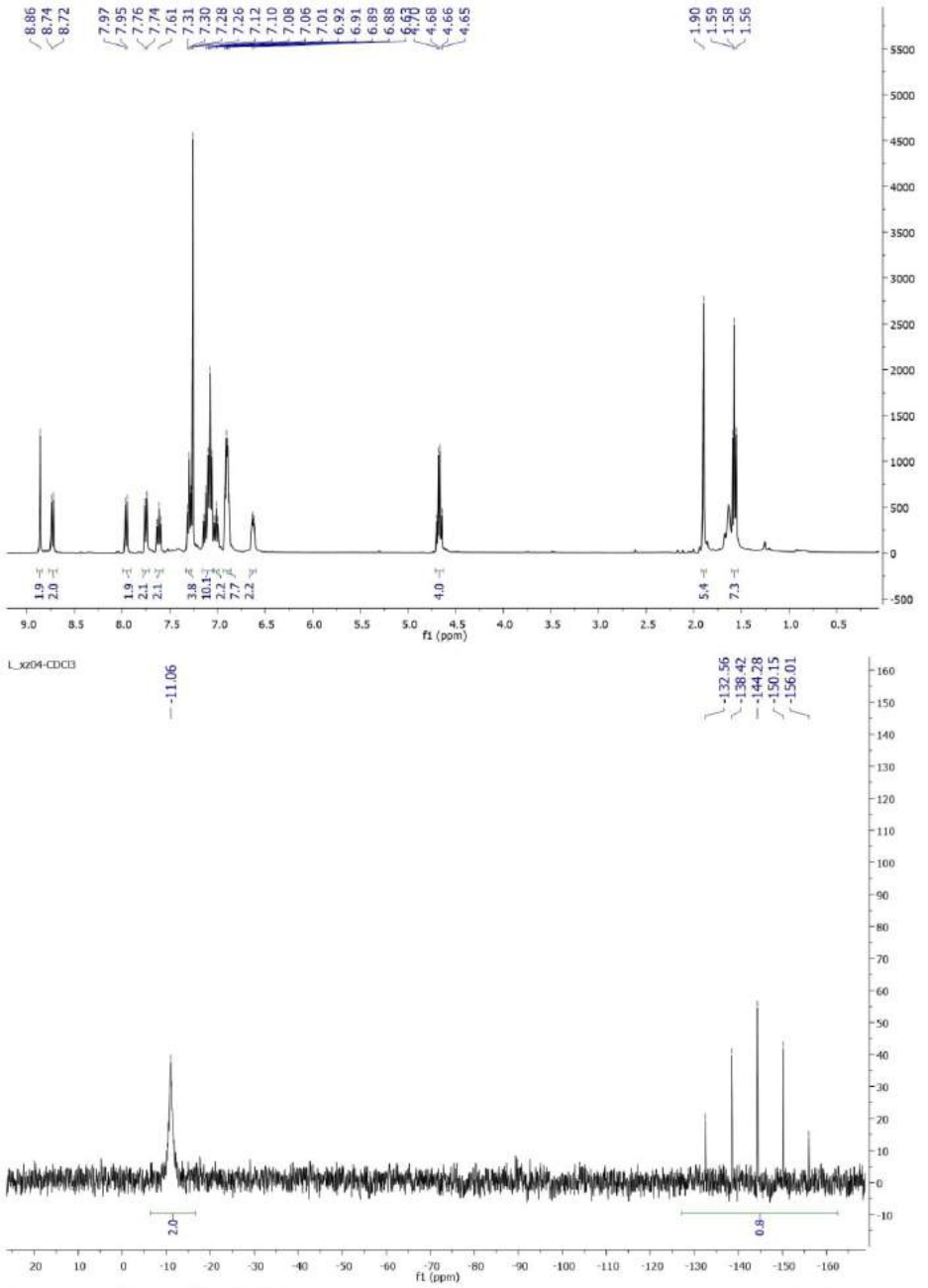


**Figure S3:** $^{1}H$ and $^{31}P\{^{1}H\}$ NMR spectra of complex [Cu(dcbq)(Xantphos)]($PF_6$) **(3)**.

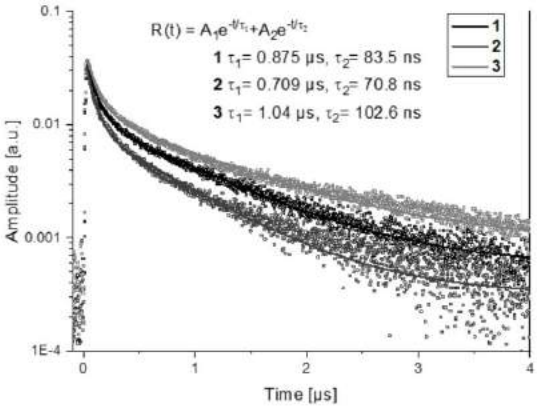


**Figure S4**. Excited-state decay profile for compounds **1-3** (symbol) and bi-exponential fittings (line).

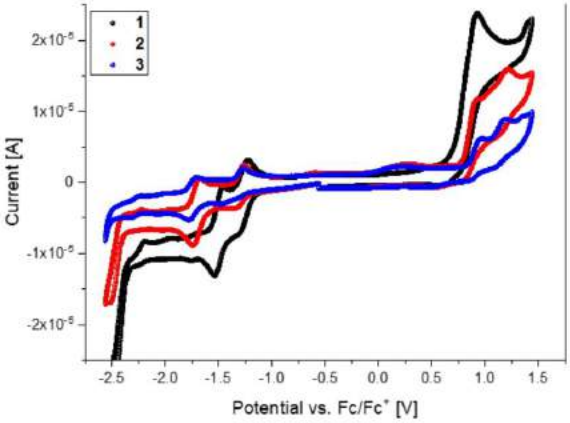


**Figure S5.** Cyclovoltammetry with scan rate 100 mV/s for compounds **1-3** in $CH_3CN$.

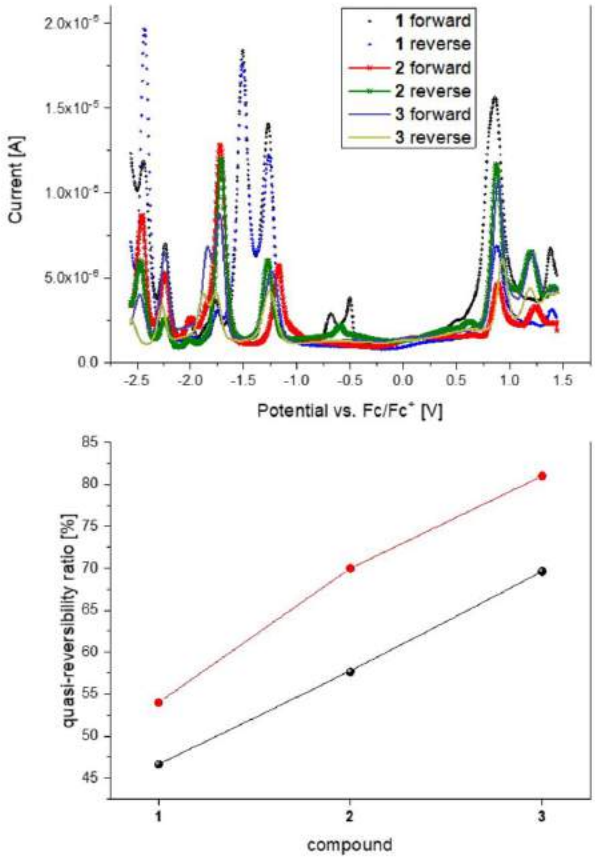


**Figure S6.** Top: Square wave voltammetry at 25 Hz scan frequency in forward and reverse scan direction, see legend. Bottom: the quasi-reversibility of **1-3** expressed by the ratio of their integrated peak area of the first oxidation (black) and reduction (red).

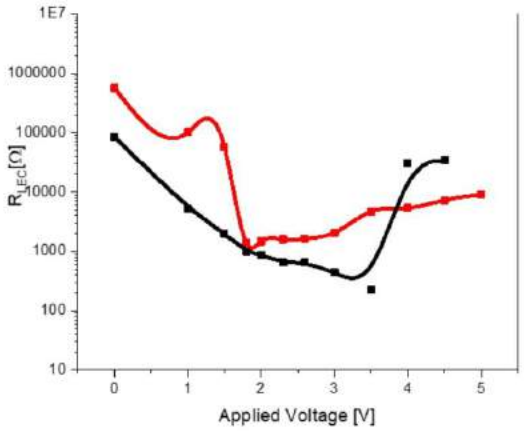


**Figure S7.** Resistance change derived from EIS data in a solid-state configuration for pristine 1 (black) and pre-biased condition (dashed line).

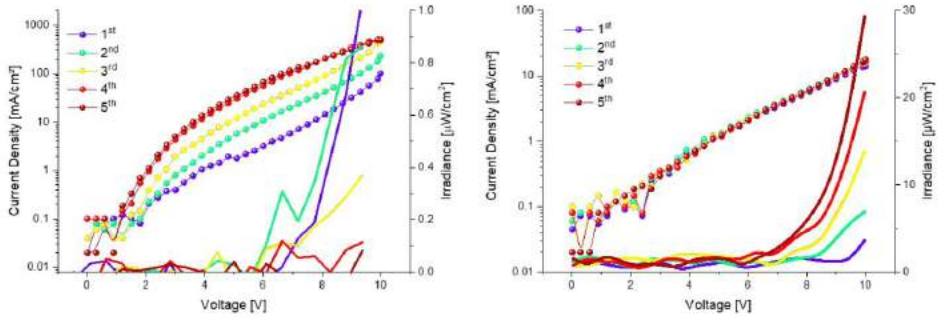


**Figure S8.** Current-voltage-irradiance (LIV) sweeps with 5 repetitions at a potential step of 300mV for devices prepared from compound **1** (left) and **2** (right).

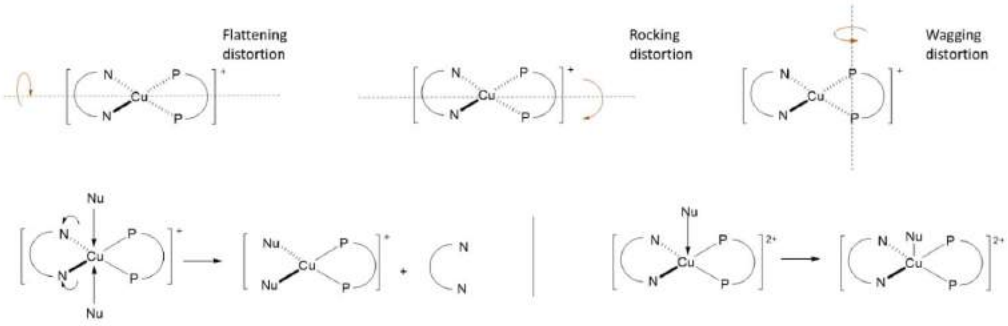


**Figure S9.** Typical degradation pathways caused by photo and electrochemically induced geometrical distortions (top) leading to either ligand exchange reactions (bottom, left) or formation Cu(II) species (bottom, right).

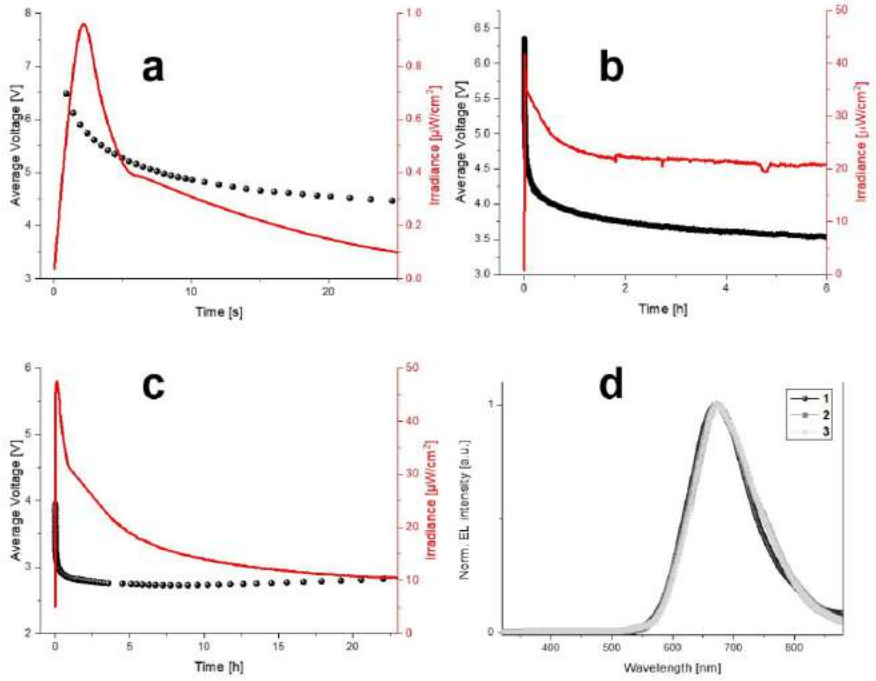


**Figure S10.** Device performance of compounds **1** (a), **2** (b) at an average driving current of 15 mA and **3** (c) at 20 mA and the EL response of the compounds (d).

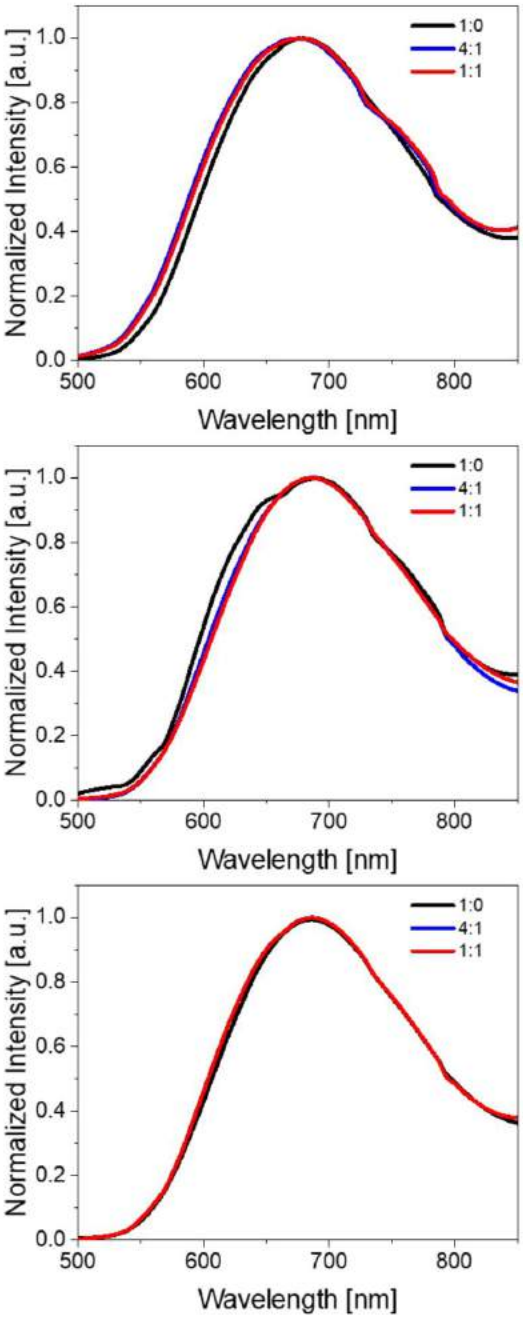


**Figure S11.** Photoluminescence spectra ($\lambda_{exc}$= 370 nm) of **1** (top), **2** (centre), and **3** (bottom) in thin film with different **1**-**3**:IL molar ratios (see legend)

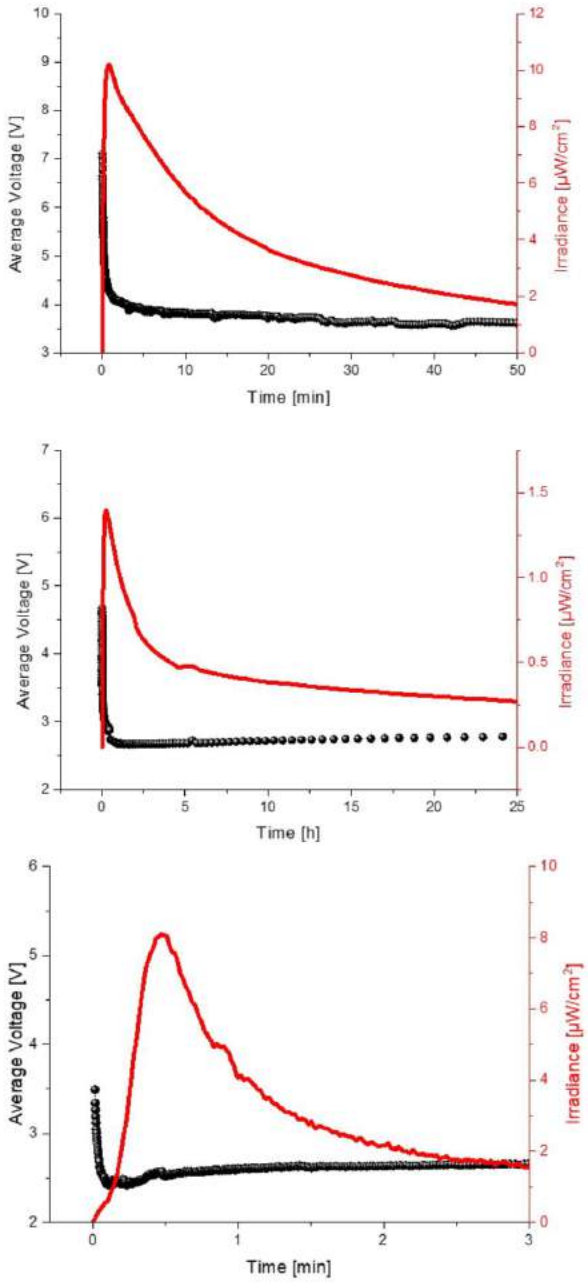


**Figure S12.** Device performance with EMIM $PF_6$ in a ratio of 4:1 of compounds **2** (top) and **3** (center) and 1:1 (bottom) at an average driving current of 15mA.

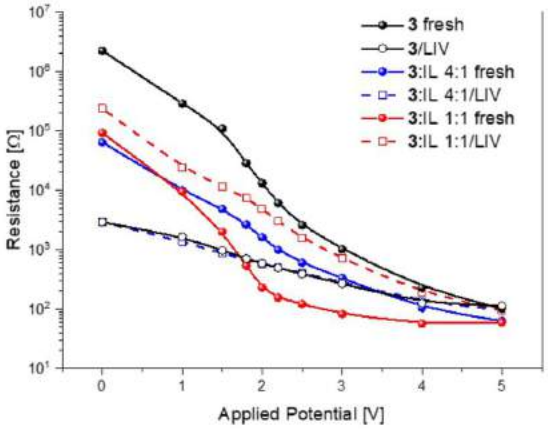


**Figure S13.** Resistance change derived from EIS data in a solid-state configuration for compound **3** pristine or mixed with EMIM $PF_6$ (see legend).

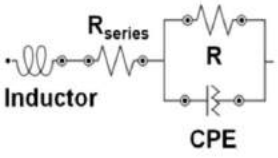


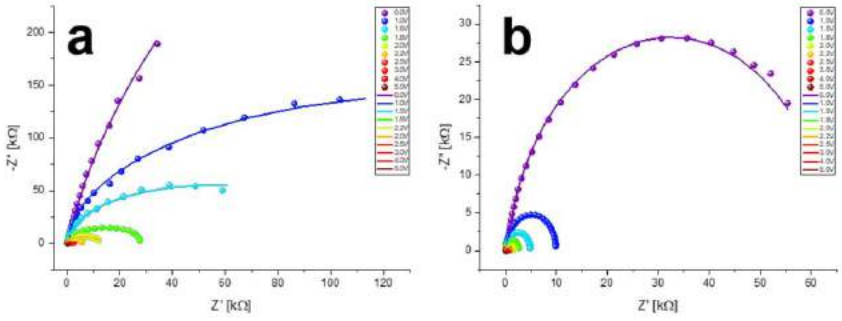

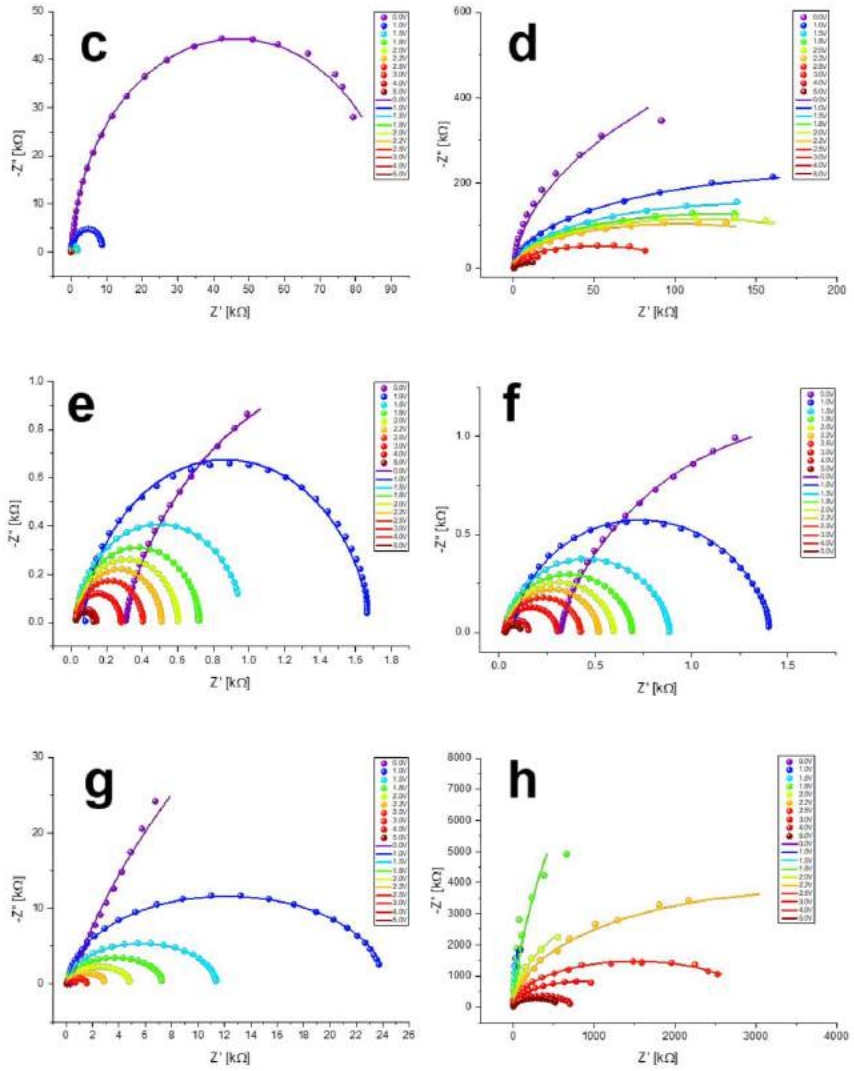


**Figure S14:** Equivalent fitting circuit (top) and Nyquist plots (symbol) and corresponding fittings (solid line) of fresh (a-d) and pre-biased (e-h) devices prepared from pure **2** (d, h), pure **3** (a, g) and **3** mixed with EMIM $PF_6$ in a molar ratio of 4:1 (b, e) and 1:1 IL (c, f).

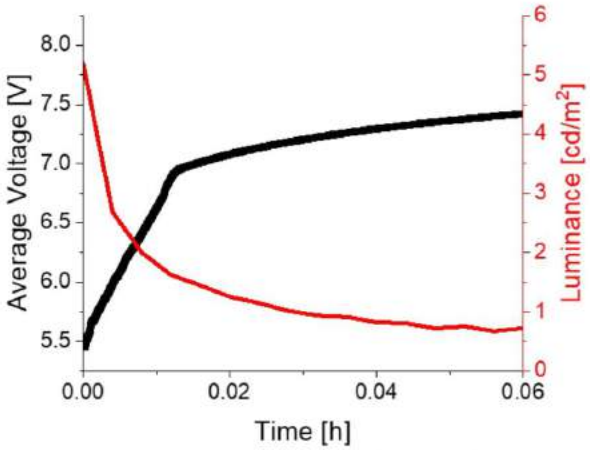


**Figure S15.** Device performance of CBP:TMPE:LiOTf (1:0.15:0.05) at an average driving current of 25 mA.

**Table S1.** Parameters obtained from electrochemical impedance spectroscopy

| Compound | Molar ratio complex : EMIM $PF_6$ | Condition | R[a] [Ω] | $C_{eff}$[b] [F] | $\varepsilon_r$[b] | σ[c] [S/m] |
|---|---|---|---|---|---|---|
| **2** | 1:0 | fresh | 1.96E+06 | 5.85E-09 | 5.29 | 4.07E-09 |
| | | pre-biased | 1.10E+10 | 6.18E-11 | 5.21E-02 | 7.27E-12 |
| **3** | 1:0 | fresh | 2.25E+06 | 1.08E-08 | 9.79 | 3.56E-09 |
| | | pre-biased | 2918.3 | 1.39E-08 | 12.57 | 2.74E-06 |
| **3** | 4:1 | fresh | 64186 | 9.45E-09 | 8.54 | 1.25E-07 |
| | | pre-biased | 2933.4 | 1.21E-08 | 10.91 | 2.73E-06 |
| **3** | 1:1 | fresh | 92323 | 8.34E-09 | 7.53 | 8.67E-08 |
| | | pre-biased | 237280 | 1.63E-08 | 14.71 | 3.37E-08 |

a values obtained at 0V. b effective capacitance calculated from equation 1-3 (see experimental section). c effective conductivity calculated from equations 1-3 (see experimental section).

**Table S2.** Figures-of-merit of devices prepared from compounds **1-3** mixed with EMIM $PF_6$

| Compound | Current Density [mA/cm²] | Average Current [mA] | Irradiance [μW/cm²] | $t_{1/2}$[d] [h] | $t_{1/5}$[e] [h] | $E_{tot}$[f] [J] | Eff.[g] [lm/W] | $\lambda_{max, EL}$ [nm] | CIE 1931 coordinates x / y |
|---|---|---|---|---|---|---|---|---|---|
| **1**[a] | 134.54 | 20 | 0.22 | 1.9E-3 | 0.01 | 5.0E-05 | 1.58E-5 | 670 | 0.524 / 0.334 |
| | 101.7 | 15 | 0[b] | 0[c] | 0[c] | 0[c] | - | | |
| **2**[a] | 133.36 | 20 | 89.0 | 3.5E-3 | 6.0E-3 | 7.9E-01 | 0.13 | 672 | 0.641 / 0.320 |
| | 100.09 | 15 | 114.3 | 3.4E-3 | 0.01 | 1.5E+00 | 0.20 | | |
| **3**[a] | 133.2 | 20 | 7.8 | 2.40 | 21.2 | 2.3E+00 | 0.01 | 675 | 0.641 / 0.316 |
| | 99.97 | 15 | 15.6 | 2.09 | 23.5 | 5.0E+00 | 0.03 | | |
| **3**[b] | 134.2 | 20 | 62.2 | 0.47 | 0.8 | 3.3E-03 | 0.09 | | |
| | 99.49 | 15 | 7.8 | 1.16 | 2.9 | 7.0E-04 | 0.01 | | |

[a] molar ratio 4:1. [b] molar ratio 1:1. [c] no values detectable. [d] time to reach 50% of the initial irradiance. [e] time to reach 20% of the initial irradiance. [f] total emitted energy [g] Power efficiency

Section 3.1.4: Deciphering the Electroluminescence Behavior of Silver (I)-complexes in Light-emitting Electrochemical Cells: Limitations and Solutions toward highly Stable Devices

ADVANCED FUNCTIONAL MATERIALS

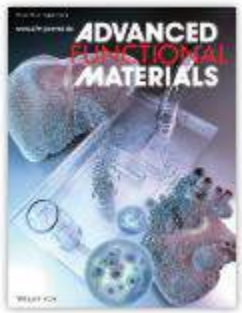


Volume 29, Issue 31
August 1, 2019
1901797

Elisa Fresta,[1,2] José M. Carbonell-Vilar,[3] Jiayin Yu,[1] Donatella Armentano,[4] Joan Cano,[3] Marta Viciano-Chumillas,[3*] and Rubén D. Costa[1]*

1. IMDEA Materials Institute, Calle Eric Kandel 2, E-28906 Getafe, Madrid, Spain. ruben.costa@imdea.org
2. Universidad Autónoma de Madrid, Departamento de Física Aplicada, Calle Francisco Tomás y Valiente, 7, 28049 Madrid, Spain.
3. Instituto de Ciencia Molecular (ICMol), Universidad de Valencia, Calle Catedrático José Beltrán, 2, E-46980 Paterna, Valencia, Spain.
4. Dipartimento di Chimica e Tecnologie Chimiche (CTC), Università della Calabria, 87030 Rende, Cosenza, Italy.

ADVANCED FUNCTIONAL MATERIALS
www.afm-journal.de

# Deciphering the Electroluminescence Behavior of Silver(I)-Complexes in Light-Emitting Electrochemical Cells: Limitations and Solutions toward Highly Stable Devices

*Elisa Fresta, José M. Carbonell-Vilar, Jiayin Yu, Donatella Armentano, Joan Cano, Marta Viciano-Chumillas,* and Rubén D. Costa**

**Ionic transition-metal complexes based on silver(I) metal core (Ag-iTMCs) represent an appealing alternative to other iTMCs in solid-state lighting owing to (i) their low cost and well-known synthesis, (ii) the tunable bandgap, and (iii) the highly efficient photoluminescence. However, their electroluminescence behavior is barely studied. Herein, the archetypal green-emitting Ag-iTMCs, namely [Ag(4,4′-dimethoxy-2,2′-bipyridine)(Xantphos)]X (X = $BF_4$, $PF_6$, and $ClO_4$), are thoughtfully investigated, revealing their electroluminescent features in light-emitting electrochemical cells (LECs). Despite optimizing device fabrication and operation, luminance of 40 cd $m^{-2}$, efficacy of 0.2 cd $A^{-1}$, and a very poor stability of 30 s are achieved. This outcome encourages the comprehensive study of the degradation mechanism combining electrochemical impedance spectroscopy, X-ray diffraction, and cyclic voltammetry techniques. These results point out the irreversible formation of silver nanoclusters under operation strongly limiting the device performance. As such, LECs are further optimized by (i) changing the counterions ($PF_6^-$ and $ClO_4^-$) and (ii) decoupling electron injection and exciton formation using a double-layered architecture. The synergy of both approaches leads to a broad exciplex-like whitish electroluminescence emission (x/y CIE of 0.40/0.44 and color rendering index of 85) with an outstanding improved stability of ≈4 orders of magnitude (>80 h) without losing brightness (35 cd $m^{-2}$).**

## 1. Introduction

Light-emitting electrochemical cells (LECs) are thin-film single-layer devices consisting of an electroluminescent material blended with an ionic electrolyte.[1] Owing to the presence of mobile ions, LECs are fairly tolerant with respect to the working function of the electrodes, allowing for a low-cost production involving solution-based techniques.[2] This renders them an interesting candidate for thin-film lighting applications.[3,4] There are three main types of LECs depending on the electroluminescent material; namely, (i) conjugated polymers mixed with inorganic salts,[5] (ii) ionic transition-metal complexes (iTMCs),[1,6] (iii) small-molecules mixed with ionic polyelectrolytes or ionic liquids,[4,7–11] and (iv) quantum-dots mixed with ionic polyelectrolytes.[4,7–10] In particular, iTMC-based LECs have attracted considerable interest as a result of their easily tunable color, high-performance levels, stabilities of thousands of hours, and high power efficiencies.[1,12,13] The most widely used iTMCs are based on cationic iridium(III) complexes with counterions, such as hexafluorophosphate or tetrafluoroborate.[6,12–17] However, iridium is one of the least abundant elements in the earth's crust (0.001 ppm), with a current price of around 45 000 $ per kg.[18] Therefore, iTMCs based on cheap and earth-abundant metals are highly desired for producing low-cost, large-area panels based on LEC technology.

In this context, copper(I) complexes (Cu-iTMCs) have attracted much attention owing to their (i) low cost, (ii) well-known chemistry, (iii) the presence of a thermally activated delayed fluorescence (TADF) behavior in many of them, and (iv) the good photoluminescence features spanning the whole visible spectrum.[4,19–22] The most studied Cu-iTMCs are related to the family $[Cu(N^N)(P^P)]^+$, where the N^N ligand is usually bipy (2,2′-bipyridine) or phen (1,10-phenantroline) derivatives and P^P is usually POP (bis(2-(diphenylphosphino)phenyl) ether) or Xantphos (4,5-bis(diphenylphosphino)-9,9-dimethylxanthene).[23–25] However, these materials suffer from two main limitations. First, the pseudotetrahedral geometry of the

E. Fresta, J. Yu, Dr. R. D. Costa
IMDEA Materials Institute
Calle Eric Kandel 2, E-28906 Getafe, Madrid, Spain
E-mail: ruben.costa@imdea.org
E. Fresta
Departamento de Física Aplicada
Universidad Autónoma de Madrid
Calle Francisco Tomás y Valiente, 7, 28049 Madrid, Spain
J. M. Carbonell-Vilar, Dr. J. Cano, Dr. M. Viciano-Chumillas
Instituto de Ciencia Molecular (ICMol)
Universidad de Valencia
Calle Catedrático José Beltrán, 2, E-46980 Paterna, Valencia, Spain
E-mail: marta.viciano@uv.es
Dr. D. Armentano
Dipartimento di Chimica e Tecnologie Chimiche (CTC)
Università della Calabria
87030 Rende, Cosenza, Italy
The ORCID identification number(s) for the author(s) of this article can be found under https://doi.org/10.1002/adfm.201901797.

DOI: 10.1002/adfm.201901797

 

Cu(I) ion changes to a flatter conformation upon both photo- and electrical-excitation stimuli, forming other species that dramatically reduce the luminescence properties and device stability.[26–28] Second, blue-emitting members of this family have typically led to yellow LECs due to ligand-centered nature of the emitting excited state, lacking an effective TADF emission.[29] The only so far reported blue-emitting Cu-iTMC LEC involves a tricoordinated NHC-Cu complex, which is intrinsically subjected to limited device stability.[21,30,31] Recently, much more attention has evolved with ionic Ag(I) complexes or Ag-iTMCs owing to (i) their straight-forward synthesis (ii) the ease of providing high energy-gap iTMCs with well-known, easily synthesizable ligands, such as bipy and phen, (iii) their high photoluminescence quantum yields ($\phi$) in solid-state, and (iv) their relatively low-cost compared to iridium (current silver price 470 $ per kg).[1,32–34]

Despite all of those mentioned above, they have received less attention compared to Cu-iTMCs in the thin-film lighting field. This might be related to (i) their light sensitivity, as they spontaneously decompose to Ag(0) in solution,[35] and (ii) the high oxidation potential of Ag(I) that implies charge transport issues.[36] Therefore, it is not surprising that the electroluminescence behavior of Ag-iTMCs remains poorly studied. To the best of our knowledge, organic light-emitting diodes (OLEDs) have, however, achieved high external quantum efficiencies of 14%,[37] while LECs[32] showed interesting green-emitting devices with $[Ag(bipy)(POP)]^+$ ($\lambda_{max}$ = 520 nm; compared to $\lambda_{max}$ = 590 nm for LECs with $[Cu(bipy)(POP)]^+$).[33,38] Strikingly enough, the device stability has not been discussed in both device concepts.

Herein, we provide a thorough study revealing the electroluminescence behavior of an archetypal member of Ag-iTMCs using the LEC concept as a technological platform. Thus, we selected the green-emitting Ag-iTMC, namely [Ag(4,4′-$(MeO)_2$-bipy)(Xantphos)]X (**1·X**, X = $BF_4$, $PF_6$, and $ClO_4$ and 4,4′-$(MeO)_2$-bipy = 4,4′-dimethoxy-2,2′-bipyridine). For reference purposes, please notice that Cu-iTMC analogues and their photophysical and electrochemical features properties were recently published.[19]

This work provides four major contributions. First, the synthesis and structural characterization of **1·X** (X = $PF_6$ and $ClO_4$) complements our previous work on the reference **1·$BF_4$** complex.[39] Second, we disclose the best conditions for device preparation (e.g., solvent, deposition, baking temperatures, exposure to room light, etc.) taking into account the thermal- and photostabilities of **1·$BF_4$** in both solution and thin films. The latter was selected by studying the stability and degradation mechanism of **1·$BF_4$** with the aid of spectroscopic and microscopic techniques. Besides optimizing device fabrication and operation, LECs featured moderate luminances of 40 cd $m^{-2}$ in concert with very poor stabilities of 30 s (0.008 h). As such, we turned to elucidate the device degradation mechanism with the aid of electrochemical impedance spectroscopy (EIS), X-ray diffraction (XRD), and cyclic voltammetry (CV); this constitutes the third relevant aspect of this work. The irreversible and rapid formation of reduced Ag(0) species under device operation conditions strongly limits the device performance, significantly reducing the overall electrical resistance, causing a quick collapse of the p- and n-doped regions and a deterioration of the luminance properties. To the best of our knowledge, this limitation has never been highlighted in other thin-film lighting devices based on Ag-iTMCs.[32,37] Based on these results, the fourth relevant aspect states a double-layered device architecture to decouple electron injection and exciton formation, which led to comparable luminances and efficiencies as the state-of-the-art Ag-iTMC-LECs, but with an outstanding improved stability of around four orders of magnitude compared to traditional LEC architectures (≈80 h vs 30 s). This solution is ascribed to the (i) suppression of the formation of Ag(0) species under device operation conditions, and (ii) the change of the electroluminescence mechanism for an exciplex-like emission, as highlighted by a broad whitish electroluminescence emission (x/y CIE of 0.40/0.44 and color rendering index (CRI) of 85).

Overall, our work sheds light for the first time onto the electroluminescence behavior of the new family of $d^{10}$ emitters (Ag-iTMCs), stating essential information for their implementation in solid-state lighting based on a comprehensive discussion about their limitations and solutions to provide highly stable devices. Even though the device stability is still moderate, its significant enhancement from seconds to several days paves the way toward the use of Ag-iTMCs in thin-film lighting.

## 2. Results and Discussion

### 2.1. Notes about the Synthesis and X-Ray Structure Description of $[Ag(4,4'\text{-}(MeO)_2\text{-bipy})(Xantphos)]^+$ Complexes

Similar to the recent preparation of the reference compound **1·$BF_4$**,[19] compounds **1·X** (X = $ClO_4$ and $PF_6$) were obtained by the reaction between the corresponding silver(I) salt and Xantphos in dichlorometane and methanol, with the subsequent addition of 4,4′-$(MeO)_2$-2,2′-bipy. Their complete characterization by $^1H$, $^{13}C$, and $^{31}P$ NMR, high-resolution electrospray mass spectroscopy (HR-ESI-MS), thermogravimetric analysis (TGA), and differential scanning calorimetry (DSC) analysis (Figures S1–S10, Supporting Information) is provided in the Supporting Information, while the theoretical characterization of both ground and excited states were recently reported.[39] The diethyl ether content was confirmed by TGA in **1·$ClO_4$**. The 5.3% weight loss below 119 °C corresponds to the removal of the lattice diethyl ether. Single crystals of **1·X** (X = $ClO_4$ and $PF_6$) were obtained by slow diffusion of diethyl ether or hexane into a dichloromethane solution of the compounds. **1·X** (X = $ClO_4$ and $PF_6$) crystallize in the triclinic space group *P*–*1*, showing a distorted tetrahedral coordination geometry with a $N_2P_2$ chromophore formed by Xantphos and 4,4′-$(MeO)_2$-2,2′-bipy ligands, as shown in **Figure 1**. The charge of **1** is counterbalanced by one anion (X = $ClO_4$ and $PF_6$). Moreover, **1·$ClO_4$** contains one crystallization diethyl ether solvent molecule. In **1·$PF_6$**, two crystallographically distinct moieties are present at the asymmetric unit. The distortion degree for all compounds were calculated with the continuous shape measure theory and the SHAPE software.[40] A zero and large value of the minimal distortion path analysis are obtained for an ideal and a distorted polyhedron, respectively. The values of the deviation from a minimal distortion pathway corresponding to a tetrahedron (T-4) and square-planar geometry (SP-4) are 6.01 (T-4) and 20.96

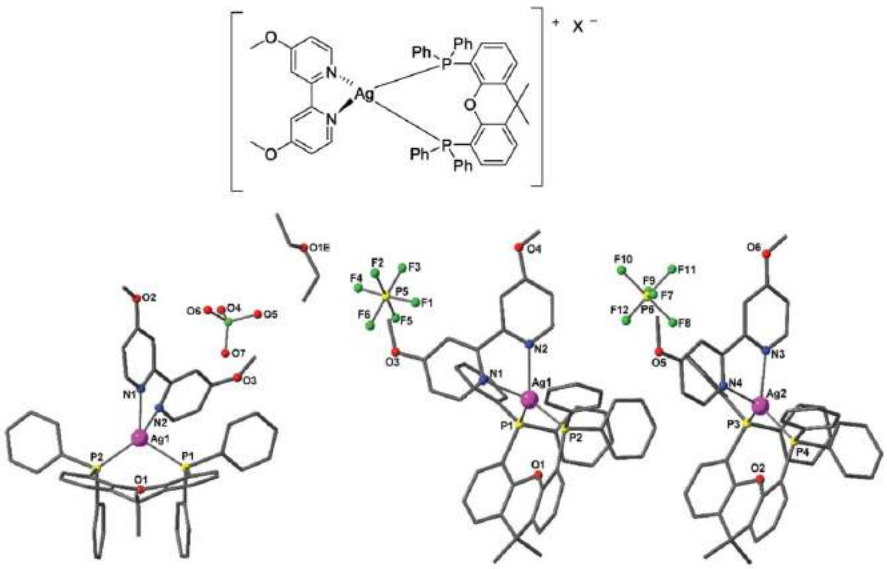


**Figure 1.** Top: chemical structure of **1·X**. Bottom: X-ray structures of **1·ClO$_4$·Et$_2$O** (left) and **1·PF$_6$** (center and right). Hydrogen atoms are omitted for clarity. Color code: magenta, silver; blue, nitrogen; yellow, phosphorus; green, halogen (chloride or fluoride); red, oxygen; gray, carbon.

(SP-4) for **1·ClO$_4$**, as well as 4.79 (T-4) and 26.89 (SP-4) for Ag1 and 4.68 (T-4) and 25.49 (SP-4) for Ag2 of **1·PF$_6$**. Selected distances and angles are listed in **Table 1** and Figure S1 (Supporting Information). The Ag–P and the Ag–N distances are in the range of 2.40–2.53 and 2.31–2.41 Å for all compounds, respectively. The Ag···O1 distance is large enough for the oxygen atom of the Xantphos ligand not being coordinated with values of 3.24 Å (**1·ClO$_4$**), as well as 3.28 and 3.18 Å (**1·PF$_6$**). The bite P–Ag–P angles are between 110.0° and 115.0°, whereas the N–Ag–N angles are between 70.3° and 71.7°. The two aromatic rings of the 4,4′-(MeO)$_2$-2,2′-bipy ligand form an angle of 34.18° (**1·ClO$_4$**), as well as 16.79° and 5.35° (for each **1·PF$_6$** present in the unit cell), whereas the central aromatic rings of the Xantphos ligand has a folding angle of 152.99° (**1·ClO$_4$**), as well as 152.77° and 158.03° (**1·PF$_6$**). The dihedral angles between the phenyl rings of the same phosphorous atom are 80.25° and 81.25°, and 80.98°, 68.17°, 76.65°, and 83.51° for compounds **1·ClO$_4$**, and **1·PF$_6$**, respectively. Intramolecular $\pi$–$\pi$ interactions, are present between two phenyl rings from two different phosphorous atoms of the Xantphos ligand for all compounds, except for the Ag2 unit of **1·PF$_6$** (Table S2, Supporting Information). The shortest intermolecular Ag···Ag distances are 9.765, and 9.841 Å for **1·ClO$_4$** and **1·PF$_6$**, respectively. In all compounds, the anions are involved in C–H···X (X = F, O) interactions (Figure S11 and Table S3, Supporting Information). In **1·ClO$_4$**, the $ClO_4^-$ anions are between two 4,4′-(MeO)$_2$-2,2′-bipy ligands of two complexes in a lineal supramolecular chain with Ag···Ag distances of 10.242 Å (Figure S11, Supporting Information), whereas in **1·PF$_6$**, the $PF_6^-$ anions interactions involve several complexes with Ag···Ag distances in the range of 10.427–14.858 Å (Figure S12, Supporting Information).

### 2.2. Notes about the Degradation Mechanism of [Ag(4,4′-(MeO)$_2$-bipy)(Xantphos)]$^+$ Complexes in Solution

The typical procedure to prepare iTMC-LECs involves solvent-based coating techniques—e.g., spin-coating and doctor-blading—using acetonitrile (MeCN) as one of the most representative solvents.[1,4] Although it is known that silver(I) complexes may show degradation under sunlight or thermal stress,[41–43] there is little known about their impact on (i) thin film morphology, (ii) $\phi$ values, and (iii) the final device performance. Thus, our first focus was to investigate the stability of our reference **1·BF$_4$** in MeCN, monitoring the changes of the absorption features over time under different conditions—i.e., dark or UV-irradiation and thermal stress. The absorption spectrum of fresh solutions consists of a band centered at 254 nm flanked by a shoulder at 277 nm, which are ascribed to a mixture of metal-to-ligand charge-transfer (MLCT) from bipy derivative and $\pi$–$\pi^*$ ligand centered (LC) absorption nature. **1·BF$_4$** shows sound stability when kept in solution under dark at room temperature (Figure S13, Supporting Information). This fact is encouraging as it suggests that the LEC preparation should not be relatively affected by the delay time required to prepare the active layers. To fasten eventual degradation processes, the absorption features were monitored at 60 °C over time in dark and under normal sunlight. Here, three different scenarios are possible: (i) the formation of homoleptic complexes like [Ag(N^N)$_2$]$^+$ or [Ag(P^P)$_2$]$^+$, (ii) a solvent-assisted ligand exchange process as MeCN shows coordination features,[44–46] and (iii) the formation of silver nanoclusters.[47] In detail, the measurement under dark shows a sound stability of the complex even when the solution is kept at 60 °C for 4 h (**Figure 2**). However, the situation completely changes combining

**Table 1.** Selected bond lengths (Å) and angles (°) for compounds [Ag(Xantphos)(4,4′-$(MeO)_2$-2,2′-bipy)]X (**1-X**) being X = $ClO_4$ and $PF_6$.

| Compound | 1-$ClO_4$ | 1-$PF_6$ |
|---|---|---|
| Bond lengths | | |
| Ag1–P1 | 2.532(3) | 2.5010(13) |
| Ag1–P2 | 2.437(3) | 2.4042(13) |
| Ag1–N1 | 2.350(10) | 2.312(4) |
| Ag1–N2 | 2.408(10) | 2.356(5) |
| Ag1···O1 | 3.240(5) | 3.280(3) |
| P1···P2 | 4.071(5) | 4.078(3) |
| Ag2–P3 | | 2.4535(13) |
| Ag2–P4 | | 2.4537(14) |
| Ag2–N3 | | 2.368(5) |
| Ag2–N4 | | 2.315(4) |
| Ag2···O2 | | 3.184(2) |
| P3···P4 | | 4.138(3) |
| Bond angles | | |
| P1–Ag1–P2 | 110.01(11) | 112.45(4) |
| N1–Ag1–N2 | 70.4(3) | 71.65(19) |
| N1–Ag1–P1 | 115.5(3) | 102.83(11) |
| N1–Ag1–P2 | 121.6(3) | 130.07(11) |
| P1–Ag1–N2 | 98.2(3) | 106.80(11) |
| P2–Ag1–N2 | 135.9(2) | 125.68(10) |
| P3–Ag2–P4 | | 114.96(5) |
| N3–Ag2–N4 | | 70.49(16) |
| N3–Ag2–P3 | | 112.99(11) |
| N3–Ag2–P4 | | 118.77(10) |
| P4–Ag2–N4 | | 112.60(11) |
| P3–Ag2–N4 | | 119.98(10) |

both thermal and UV-irradiation stress. In this case, two new absorption bands at 310 and 346 nm evolved after 4 h (Figure 2). These are not related to the formation of the analogue homoleptic complexes, which feature an absorption band centered at 251 nm with a shoulder at 295 nm (Figure S14, Supporting Information). Additionally, they cannot be attributed to the formation of solvent-coordinating species as the coordination of the solvent does not introduce low lying molecular orbitals levels in the electronic structure upon replacing one of the ligands. As such, we attribute them to the formation of silver nanoclusters. As reported by Mulvaney and Henglein, the absorption features at around 300 and 350 nm are characteristic of nonmetallic $Ag_n$ nanoclusters with $n = 3$, and $n >> 3$, respectively.[47] Further confirmation was provided with $^1$H NMR revealing that the above-mentioned species are not evolving under these conditions.

### 2.3. Notes about the Preparation, Morphology, and Photophysical Features of [Ag(4,4′-$(MeO)_2$-bipy)(Xantphos)]$^+$ Thin Films

Thin films of pristine **1**·$BF_4$ obtained by spin-coating MeCN solutions present the same shapeless emission with a maximum

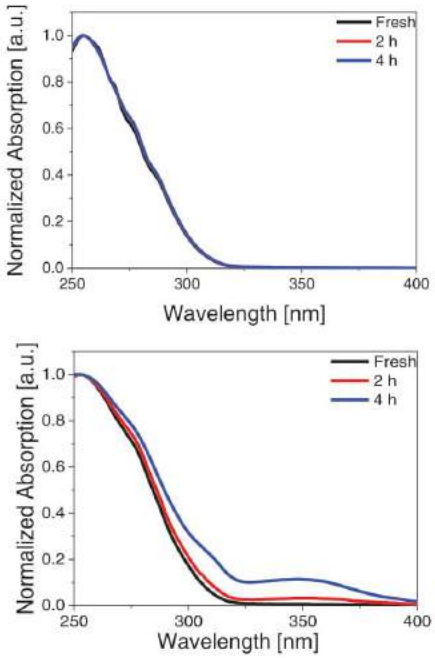


**Figure 2.** Changes of the UV–vis absorption spectra of **1**·$BF_4$ measured in MeCN over time at 60 °C in dark (top) and under UV-irradiation (bottom).

wavelength emission ($\lambda_{max}$) red-shifted 20 nm compared to that in powder ($\lambda_{max}$ = 490 nm) caused by the formation of aggregates (**Figure 3** and **Table 2**). Indeed, while **1**·$BF_4$ powder feature $\phi$ of ≈55%, thin films show $\phi$ of around 20%. Please notice that this value is, however, fivefold higher than for its Cu-iTMC counterpart, which features a $\phi$ of 4% in neat thin films.[15]

In order to enhance the performance of Ir-iTMC-LECs, it is highly recommended to dry the freshly prepared films at high temperature (from 50° to 90 °C) under an inert and dry

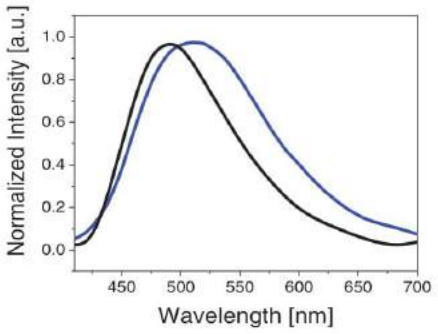


**Figure 3.** Photoluminescence spectra of **1**·$BF_4$ in powder (black) and thin film (blue) recorded at room temperature ($\lambda_{exc}$ = 300 nm).

**Table 2.** Photoluminescence and electrochemical features of **1·BF$_4$**.

| State | Absorption[a] | Emission[b] | | Cyclovoltammetry[c] | |
|---|---|---|---|---|---|
| | $\lambda_{max}$ [nm] | $\lambda_{max}$ [nm] | $\phi$ [%] | $E_{ox}$ [V] | $E_{red}$ [V] |
| Solution (MeCN) | 250,277 (shoulder) | 500 | – | 1.2 (qr) | −2.0 (irr) |
| Thin film | 250 | 520 | 20 | – | – |

[a]Measured at 298 K; [b]Measured at room temperature ($\lambda_{exc}$ = 365 nm); [c]Oxidation and reduction potentials measured versus $Fc/Fc^+$; qr = quasi reversible, irr = irreversible.

atmosphere ($N_2$) to remove any solvent. However, this procedure can impact both the photoluminescence and morphology features. As such, thin films prepared from fresh solutions were dried, increasing the temperature in a step-wise fashion (10 °C steps from 40 to 90 °C holding the temperature for 30 min each step) while monitoring eventual changes in $\phi$ values. Surprisingly, this figure remarkably and steadily decreases during the entire measurement timespan, reaching a 42% loss after baking the thin films at 90 °C for 30 min (**Figure 4**). This decrease was related to morphological changes as highlighted by atomic force microscopic (AFM) (**Figure 5**). Here, fresh layers show a neat, homogeneous morphology with a root mean square roughness of 4 nm. However, thin films baked at 90 °C exhibit more defined channels and mountain-like structures with a 25-times increased roughness. Thus, active layers must be prepared directly from MeCN solutions via spin-coating and stored under dark without any baking process. Noteworthy, morphological changes that are correlated to degradation were already observed in early works on Ru(II)-iTMC LECs upon exposition to moisture.[48]

### 2.4. Notes about the Stability Limitations of [Ag(4,4′-(MeO)$_2$-bipy)(Xantphos)]$^+$ Based LECs

As above described, both the photoluminescence and morphology features of pristine films prepared from fresh, degassed, and anhydrous MeCN solutions of **1·BF$_4$** are optimum for device fabrication. The latter were finalized by evaporating a 90 nm thin aluminum cathode onto the

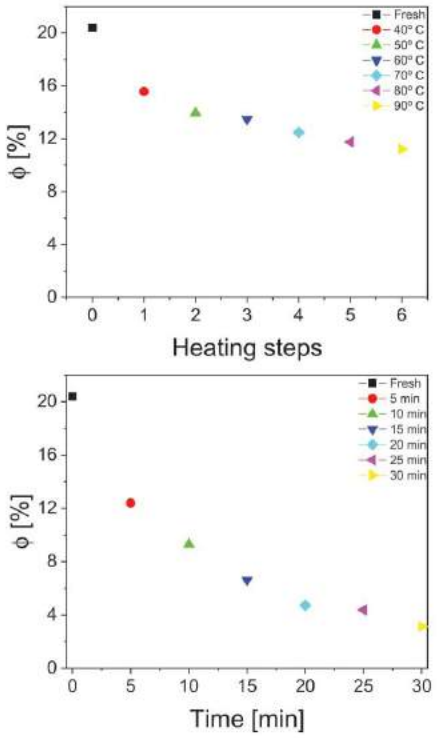


**Figure 4.** $\phi$ values of **1·BF$_4$** thin films after different baking steps (top) and UV light irradiation (302 nm, 640 µW cm$^{-2}$) over time (bottom).

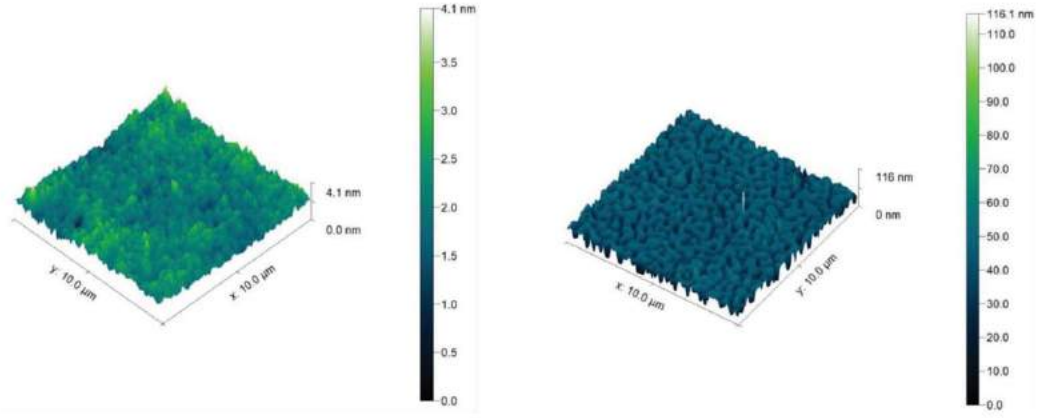


**Figure 5.** AFM images of **1·BF$_4$** thin films before (left) and after (right) baking at 90 °C.

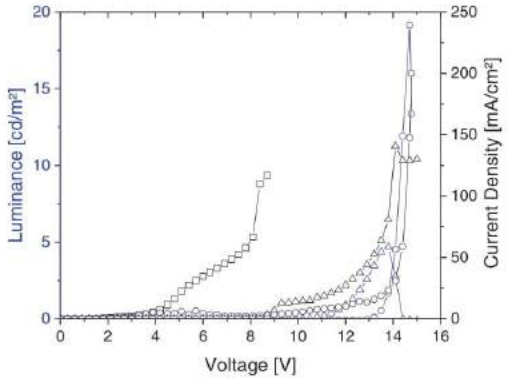


**Figure 6.** Luminance (blue) and current density (black) of repetitive *L–I–V* scans of **1·BF$_4$** devices. The first, second, and third *L–I–V* scans are represented by circles, triangles, and squares, respectively.

active layer. The devices were first tested via consecutive luminance–current–voltage (*L–I–V*) scans highlighting two findings (**Figure 6**). First, the injection voltage is quite high (≈10 V), which leads to overoxidation and/or over-reduction issues in stability assays, as the average applied voltage will be high compared to, for example, Ir- or Cu-iTMC-LECs.[1] Second, the luminance reached during the first *L–I–V* scan (20 cd m$^{-2}$) is fourfold reduced during the second scan and is absent during the third one. However, current injection is still observed and occurs at lower voltages of ≈9 V for the second and ≈4 V for the third scan. This accounts for a poor stability upon electrical stimuli. Nonetheless, the devices showed a green electroluminescence response with a spectrum centered at around 520 nm and x/y CIE color coordinates of 0.29/0.45, indicating that the same emitting excited state is involved in both photoluminescence and electroluminescence processes (**Figure 7**).

Next, we measured **1·BF$_4$** devices at different pulsed currents of 5, 7.5, 10, 15, and 20 mA using driving schemes based on a block-wave at 1000 Hz and a duty cycle of 50% (Figure S15, Supporting Information). Pulsed currents of 15 mA were selected for further optimizations, as it yielded the best-balanced performance with respect to luminance, efficiency, and stability, e.g., luminance of 40 cd m$^{-2}$, efficacies of 0.2 cd A$^{-1}$, and very poor stability of 30 s (Figure 7 and **Table 3**).

Upon close inspection of the electroluminescent behavior, the luminance follows a monoexponential decay while the applied voltage still shows the initial decay due to the formation of the electric double-layers (EDL) at the electrode interface. This decline is followed by a second linear decay that is also unusual in iTMC-LECs driven at these conditions (Figure 7).[1] The earlier reduction of the luminance before the average voltage profile reaches a plateau indicates a fast collapse

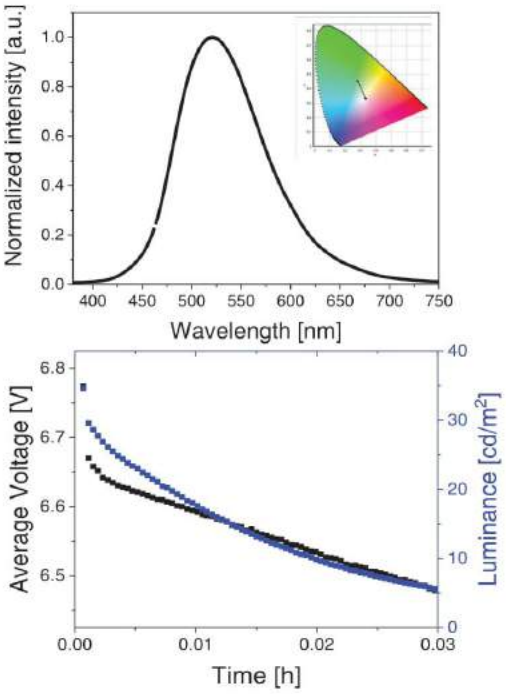


**Figure 7.** Electroluminescence spectrum of **1·BF$_4$** (top) and x/y CIE color coordinates as inset are shown. Average voltage and luminance over time (bottom) of **1·BF$_4$** devices driven at pulsed current of 15 mA.

of the p- and n-regions and/or a prominent degradation at the electrode interface. A possible way to slow down the growth of the p- and n-doped regions is to change the duty cycle (25%, 50%, 75%, and 100%).[49] However, driving at 50% duty cycle still show the best balance between luminance and stability (Figure S16, Supporting Information), suggesting that the formation of strong luminance quenchers rules the device stability. We discard the formation of black spots or pin-holes, as

**Table 3.** Figures-of-merit of single- and double-layered devices prepared with 1·BF$_4$ devices and their optimizations.

| | Average voltage[V] | $L_{inst}$[a)][cd m$^{-2}$] | $L_{max}$[b)][cd m$^{-2}$] | $t_{on}$[c)][s] | $t_{1/2}$[d)][h] | Efficacy[cd A$^{-1}$] |
|---|---|---|---|---|---|---|
| 1·BF$_4$ | 6.5 | 40 | 40 | Subsec | 0.008 | 0.2 |
| 1·PF$_6$ | 6.9 | 71 | 131 | 4.0 | 0.003 | 0.6 |
| 1·ClO$_4$ | 6.0 | 4 | 4 | Subsec | 0.01 | 0.1 |
| CBP/1·BF$_4$ | 5.4 | 4 | 41 | 21.5 | 0.03 | 0.2 |
| 1·BF$_4$/PBD | 4.5 | 2 | 7 | 0.12 h | 7.2 | 0.04 |
| 1·PF$_6$/PBD | 4.2 | 2 | 35 | 1.5 h | 80 | 0.1 |
| 1·ClO$_4$/PBD | 5.9 | 1 | 3 | 288 | 1.6 | 0.01 |

[a)]Instantaneous luminance or initial luminance level; [b)]Maximum luminance; [c)]Time to reach the maximum luminance; [d)]Time to decay to the half of the maximum luminance.

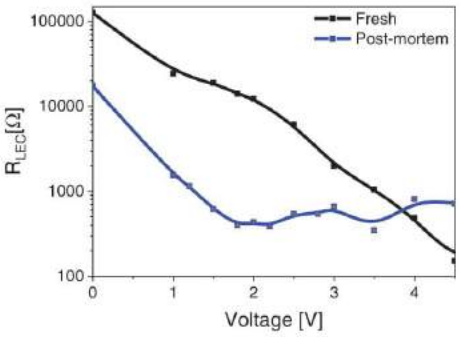


**Figure 8.** Changes in $R_{LEC}$ of **1·BF$_4$** devices under static EIS measurements (0–4.5 V).

we did not observe their formation using an optical microscope upon the whole lifespan of the device, as expected since AFM assays have already demonstrated the homogenous morphology of fresh active layers (Figure 5), while the applied voltage does not rise over time. To discard the eventual effect of room light, we compared devices prepared under both dark conditions and room light, and subsequently subjected to the direct sun irradiation (Air Mass-AM-1.5) for 30 min and 1 h. All the devices feature comparable performances in terms of luminance and stability (Figure S17, Supporting Information).

To further study the changes in the electrical behavior between fresh and used devices, static EIS assays were performed—see the Experimental Section for details and **Figure 8** and Figures S18–S20 (Supporting Information). The EIS analysis of the Nyquist plots was conducted by using a single resistor/capacitor equivalent circuit model that relates to the two dominant dynamic processes upon increasing the applied voltage (Figure S18, Supporting Information). Typically, under applied voltages lower than the injection voltage ($V_{inj}$) of the emitter—i.e., 2.5–3 eV corresponding to the energy bandgap of **1·BF$_4$**—an exponential decrease of the resistance occurs, being related to the formation of EDLs due to the slow movement of the mobile anions toward the electrode interfaces until charge injection is efficient. At this point, the p- and n-doped regions start to grow reducing the p–i–n region, leading to a linear decrease profile of the resistance due to ohmic charge injection.[50–55] In stark contrast to this scenario, the overall resistance linearly decreases in Ag-iTMC-LECs (Figure 8). The measurement performed at 0 V is of particular importance as the active layer has not been affected in any way. The total ionic resistance of $1.26 \times 10^5$ Ω and the dielectric constant ($\varepsilon$) of 7.8 are in line with values found for other iTMC-LECs.[33,56,57] However, used devices also show an unusual behavior with a significant decrease in the active layer ionic resistance ($1.7 \times 10^4$ Ω) and increased $\varepsilon$ (9). Additionally, the resistance further decreases during the voltage scan, approaching very low values (≈1000 Ω) at only 1 V, which is far below the bandgap of **1·BF$_4$**. By comparison, fresh devices showed ionic resistances of $2.4 \times 10^4$ Ω at the same applied bias (Figure 8). The overall electrical behavior contrasts with that of used LECs, in which EDL and charge injection are typically noted.[57]

Having in mind the degradation species above described (Section 2.2), the nature of the resistance drop could be related to the irreversible formation of metallic Ag(0) nanoclusters upon charge injection, ruling the electrical behavior of the devices. In order to confirm this hypothesis, we first turned our attention to CV assays in solution (**Figure 9**). **1·BF$_4$** shows a broad quasireversible oxidation peak at 1.1 V and one irreversible reduction wave at −2.05 V (both vs $Fc/Fc^+$ couple). Additional waves—i.e., sharp peak at −0.09 V, were noted on a consecutive scan (Figure 9). This is ascribed to the deposition of Ag(0) on the working electrode, corroborating the formation of silver nanoparticles upon reduction in solution. Much more striking, we also confirmed the presence of Ag(0) nanoclusters in used devices using XRD assay—see the Experimental Section for details concerning the measuring setup. In detail, fresh devices show an amorphous based structure with crystalline peaks belonging only to the ITO substrate—i.e., 30.2°, 35.2°, 50.5°, and 60.2°, in good agreement with literature (**Figure 10**).[58] This scenario changes, however, when the used devices are measured. Diffraction peaks were observed at $2\theta$ values of 38.1°, 44.4°, 64.5°, 77.5°, and 81.6° and clearly evidence the presence of Ag(0) nanoclusters.[41] The diffraction peaks are indexed as the (111), (200), (220), (311), and (222) crystal planes of the face-centered cubic (fcc) crystal structure (JCPDS No. 4–783). Thus, we can safely state that the formation of Ag(0) nanoclusters is electrochemically produced upon driving. Curiously, the use of silver nanoclusters in LECs was pioneered by Wong and co-workers, whom applied them as a plasmonic notch filter embedded in the anode to obtain white

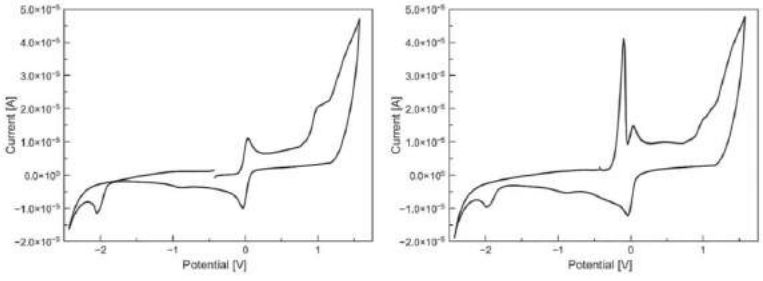


**Figure 9.** Cyclic voltammogram of **1·BF$_4$** in acetonitrile versus $Fc/Fc^+$, left: first scan, right: second scan. Scan rate is 100 mV $s^{-1}$.

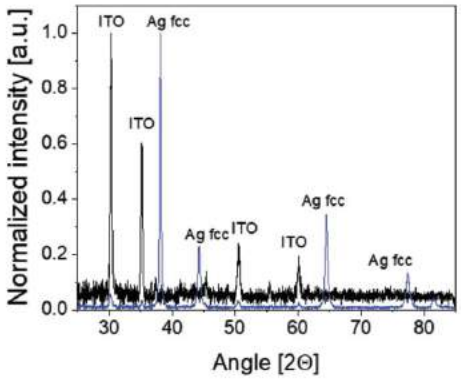


**Figure 10.** XRD measurements of fresh (blue) and used (black) **1·BF$_4$** devices. The peaks related to ITO and to metallic silver (fcc crystalline cell) are marked above.

emitting stable LECs.[59] However, our result shows that their formation in the active layer upon degradation of the emitter is detrimental for the device performance.

### 2.5. Notes about Strategies to Provide Stable [Ag(4,4′-(MeO)$_2$-bipy)(Xantphos)]$^+$ Based LECs

Having elucidated the main degradation mechanism in Ag-iTMC-LECs, we explored how to enhance the device performance following three approaches, namely (i) the use of ionic additives like ionic liquids and ionic polyelectrolytes—see the Experimental Section for details, (ii) the exchange of the $BF_4^-$ counterion in $1^+$ with other two commonly used counterions, namely hexafluorophosphate ($PF_6^-$) and perchlorate ($ClO_4^-$) affording **1·PF$_6$** and **1·ClO$_4$**—vide supra, and (iii) new device architectures to decouple the charge injection and recombination processes—vide infra.[60,61]

Concerning the first strategy, pristine thin films based on **1·BF$_4$** were compared with those with different ionic additives. In contrast to the homogenous morphology of pristine **1·BF$_4$** films (Figure 5), those with the ionic liquid and the ionic polyelectrolyte exhibit large orientated aggregates and crystalline domains, showing a high surface roughness of 179 and 174 nm (Figure S20, Supporting Information). Consequently, the $\phi$ values reduced to 16.9% and 11.6%, respectively; a fact that is independent of the type of deposition technique and conditions (see the Experimental Section). Thus, the use of ionic additives was discarded for the optimization of Ag-iTMC-LECs.

Next, the impact of different counterions on the device performances was studied (**Figure 11** and Table 3). Here, **1·PF$_6$** devices featured higher luminances of ≈130 cd m$^{-2}$ along with similar stabilities in the second regime, while **1·ClO$_4$** devices showed lower brightness (4 cd m$^{-2}$) and similar stabilities. The huge differences in device performance are neither related to photoluminescence features nor caused by the thin film morphology, as **1·PF$_6$**, **1·ClO$_4$**, and **1·BF$_4$** thin films show similar

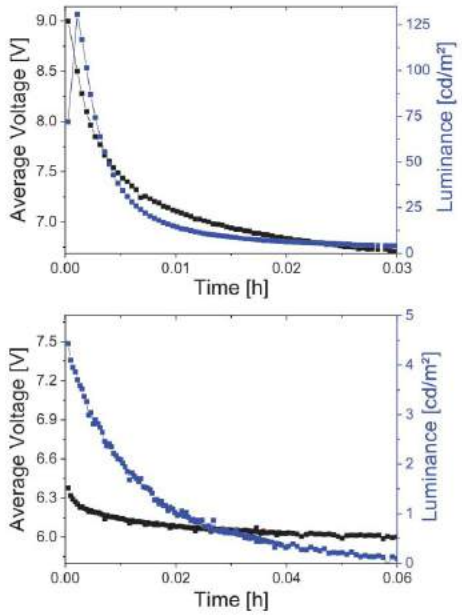


**Figure 11.** Average voltage and luminance over time of **1·PF$_6$** (top) and **1·ClO$_4$** (bottom) devices driven at pulsed current of 15 mA.

emission bands with $\phi$ of around 25% and less than 5 nm roughness (Figure S21, Supporting Information). As such, it may be related to changes in the device mechanism ruled by the ionic mobility and/or the growing of the doped regions, as already reported in literature.[62] To confirm this hypothesis, we performed EIS measurements of fresh and used **1·PF$_6$** and **1·ClO$_4$** devices (**Figure 12**). The ionic resistance at 0 V increases from **1·BF$_4$** ($1.26 \times 10^5$ Ω) to **1·PF$_6$** ($1.66 \times 10^5$ Ω), and finally to **1·ClO$_4$** ($1.88 \times 10^6$ Ω) due to the reduced ionic mobility of the progressively bulkier nature of the anions.

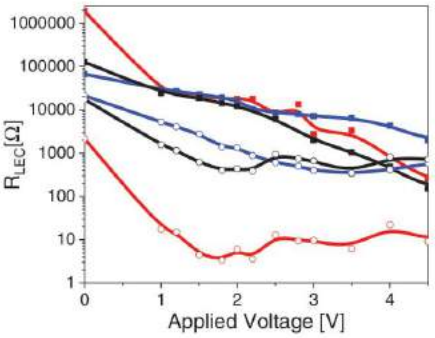


**Figure 12.** Changes in $R_{LEC}$ of **1·BF$_4$** (black), **1·PF$_6$** (blue), and **1·ClO$_4$** (red) devices under static EIS measurements (0–5 V). The full squares and empty circles refer to fresh and used devices, respectively.

However, $1 \cdot BF_4$ and $1 \cdot ClO_4$ devices show a linear decrease of the resistance upon applied voltage, regardless of the $V_{inj}$. In stark contrast, $1 \cdot PF_6$ devices shows a fast decrease of the resistance up to 2.5 V and the resistance holds almost constant at higher applied voltages up to 5 V. This indicates a better stability toward forming Ag(0) species upon charge injection, which leads to a slower collapse of the doped regions, allowing improved luminance levels.

In the case of used devices, $1 \cdot ClO_4$ devices exhibit even lower resistances compared to $1 \cdot BF_4$ devices at 0 V ($1.7 \times 10^4$ Ω), which suggest the prominent formation of conductive species in line with the reduced luminance. By contrast, used $1 \cdot PF_6$ devices feature higher overall resistance compared to the others, but showing the same linear decay of the resistance upon applying voltage. As such, we can conclude that this counterion slows down the degradation mechanism, but it does not solve the stability issue. This was further confirmed with the aid of XRD, which highlighted the formation of Ag nanoparticles regardless of the counterion (Figure S22, Supporting Information).

Finally, to decouple charge injection/recombination processes, we focused on tailored device architectures that have already provided excellent results in Cu-iTMC-LECs.[30,33] In Ag-iTMCs, oxidation is considered as quasi-reversible, while the irreversible reduction must dramatically present a strong impact on the device performance. Nevertheless, we were diligent to study both hole–electron injection and recombination decoupling on the device performance.

Following our recent contributions in Cu-iTMC-LECs,[30,33] we first opted for a device architecture possessing 4,4′-bis(N-carbazolyl)-1,1′-biphenyl (CBP) as a hole transporter. The double-layered device was built as ITO/CBP/$1 \cdot BF_4$/Al—see the Experimental Section for further details. Devices driven at 15 mA pulsed current reached luminance of ≈40 cd $m^{-2}$, stability of 0.03 h, and efficacy of 0.2 cd $A^{-1}$ (Figure S23, Supporting Information; Table 3). Furthermore, the instantaneous luminance (measured at time 0) does not correspond to the maximum luminance as in the previous measurements, but increases up to the maximum within the first seconds of operation and starts decaying exponentially afterward, following the common LEC behavior. Since the electroluminescence spectra of the double-layer devices are similar to those of the single-layered devices without showing any emission feature of the CBP layer (Figure S23, Supporting Information), we can postulate that electron–hole recombination efficiently occurs in $1 \cdot BF_4$ layer close at the interface CBP/$1 \cdot BF_4$. Hole injection occurs in the CBP layer (Figure S23, Supporting Information), and then it is transferred to $1 \cdot BF_4$, while electron injection and accumulation are effective in $1 \cdot BF_4$. As such, the formation of oxidized $1 \cdot BF_4$ species is reduced, leading to enhanced device stability. Nonetheless, the improvement is still moderate compared to pristine devices. In line with the CV data, this result suggests that hole injection and transport processes are not the major bottlenecks toward enhancing device stability.

Next, we turned our attention to a device architecture possessing an electron transport layer onto the Ag-iTMCs layer. We selected the well-known electron transport 2-(4-*tert*-butylphenyl)-5-(4-biphenylyl)-1,3,4-oxadiazole (PBD) and investigated a device architecture with the configuration ITO/$1 \cdot BF_4$/PBD/Al (**Figure 13**). We used PBD among other electron transport matrices due to (i) the reversible oxidation and reduction processes that ensure a stable n- and p-electrochemical doping and (ii) its well-known electron transport properties.[63,64] The PBD layer thickness was optimized to be 15 nm, ensuring enhanced performances by balancing luminance, efficacy, and stability values (Figure S24 and Table S4, Supporting Information).

The optimized devices showed moderate luminances of 7 cd $m^{-2}$ and about three orders of magnitude enhanced stability, reaching 7.2 h at the driving pulsed current of 15 mA (Figure 13). More importantly, the luminance increases during the first minutes, until it reaches its maximum values, and starts to decrease slowly. The voltage, in turn, exponentially decreases until it reaches a plateau that holds constant over time until starting to rise as the luminance deteriorates. This behavior is expected for a LEC device. Interestingly, these devices showed broad whitish electroluminescence with a full-width to half-maximum (FWHM) of 206 nm that is centered at 540 nm and shows x/y CIE coordinates of 0.40/0.44 in concert with a high CRI of 85 (Figure 13). As a reference purpose, pristine $1 \cdot BF_4$ devices show an FWHM of 126 nm centered at 520 nm and x/y CIE coordinates of 0.29/0.45.

We can discard the presence of aggregation as a reason for the broad electroluminescence. In fact, the thin films presented photoluminescence emission maxima centered at 377 and 394 nm, with a shoulder at 520 nm upon top excitation (Figure S25, Supporting Information). The low contribution of $1 \cdot BF_4$ emission is reasonable as the top PBD layer mostly absorbs the excitation source light. Indeed, upon bottom excitation, only a broad emission of $1 \cdot BF_4$ centered at 520 nm is noted, highlighting that not only any aggregation phenomenon is absent, but also that the device presents a double-layered architecture, as the emission from the top and bottom sides are related mostly to the component closer to the surface. In the eventuality of a mixed layer, emission from both components would be equally present on each side.

We can, therefore, assume that an exciplex is at the origin of the broad emission, as widely described in the literature.[65–67] In short, exciplex emission takes place between the bound upper and the unbound ground states of the two compounds. The latter is not subjected to quantization for vibrational states, which typically leads to a broad emission. A further proof is provided by the energy levels reported in Figure 13. Here, the HOMO of $1 \cdot BF_4$ is around 0.3 eV lower in energy than the one of PBD, leading to an exciplex bandgap of 2.4 eV, which nicely corresponds to the broad emission band centered at 540 nm. The peculiarity of this emission mechanism assures that the reduction process is happening at the PBD layer, while the recombination happens at the interface between $1 \cdot BF_4$ and PBD layers.

Similar electroluminescent features are noted regardless of the counterion (Figure 13). In line with trends noted for pristine devices, the configuration $1 \cdot PF_6$/PBD led to the maximum brightness of 35 cd $m^{-2}$ and an extrapolated stability of ≈80 h (**Figure 14**; Figure S26, Supporting Information), thereby reaching four order of magnitude stability enhancement compared to both $1 \cdot PF_6$ and $1 \cdot BF_4$ devices. $1 \cdot ClO_4$/PBD devices showed a slight loss in luminance compared to $1 \cdot ClO_4$, but

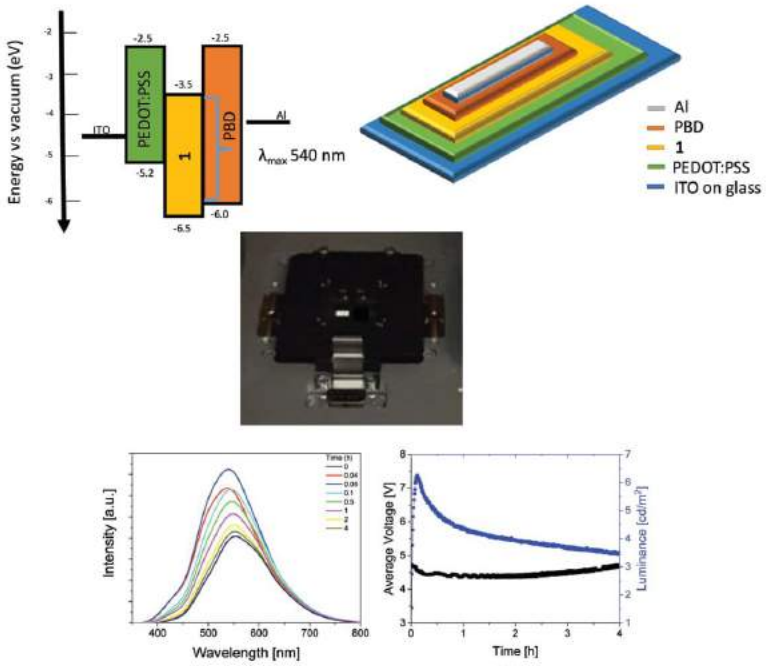


**Figure 13.** Top: schemes of a multilayered device design (right) and its energy diagram (left) as derived from the CV data using the formula $E_{HOMO/LUMO} = e(V_{Fc/Fc+}) + 5.1$ eV. The energy gap of the exciplex emission ($\lambda_{max} = 540$ nm) is highlighted with a blue brace. Middle: a picture of the device under operation. Bottom: electroluminescence spectra over time (left), as well as average voltage and luminance over time of **1**·$BF_4$/PBD devices driven at pulsed current of 15 mA (center), and a picture of **1**·$BF_4$/PBD devices upon operation (right).

with a similar enhancement on the device stability (Figure 14 and Table 1). It is important to notice that the effect on the counterion on the luminance and stability is not fully understood yet. Future works based on transient absorption spectroscopy to determine the impact of the counterion onto the radiative decay channels of the exciplex are on-going in our laboratories.

Besides this finding, we performed EIS assays of fresh and used devices to corroborate the success of preventing Ag(0) nanocluster formation (Figure S27, Supporting Information). Here, fresh double-layered devices show an electrical behavior related to a standard LECs, showing a <10% loss in the resistance comparing fresh and used devices (Figure S28, Supporting Information). Finally, we performed XRD experiments to confirm the lack of Ag(0) formation under device operation (Figure S29, Supporting Information). As expected, no XRD peak related to metallic silver in double-layered devices was detected.

Even though the degradation mechanism has been suppressed, the luminance is slightly reduced using the multilayered approach and the device lifetime is still moderate but comparable to that reported in Cu-iTMC LECs.[4] Therefore, further enhancements are envisaged controlling the Ag-iTMCs/PBD interface and combining other electron transport layers and counterions.

## 3. Conclusions

The electroluminescent behavior of Ag-iTMCs is revealed for the first time studying the archetypal ionic silver(I) complex with the formula [Ag(4,4′-dimethoxy-2,2′-bipyridine)(Xantphos)]X (X = $BF_4$, $PF_6$, and $ClO_4$). Despite the establishment of the best preparation route and driving mode, the LEC performance is moderate with stabilities that do not go beyond a few seconds. Hence, the degradation was thoroughly studied with the aid of EIS, XRD, and CV techniques. The results suggested that the device performance is strongly limited by the irreversible formation of Ag(0) nanoclusters upon electron injection, ruling the device mechanism quickly decreasing the intrinsic emitting region. Thus, the device was optimized by both selecting a better performing counterion ($PF_6^-$) and decoupling electron injection and exciton formation using an electron transport layer to hinder the direct reduction of the Ag-iTMCs. The synergy of both approaches led to a broad whitish electroluminescence emission (x/y CIE of 0.40/0.44 and CRI of 85) along with luminance of 35 cd $m^{-2}$ and outstanding improved stability (>80 h). Overall, this work provides novel insights into the electroluminescent properties of a barely studied family of iTMCs, highlighting both limitations and solutions to increase device stability.

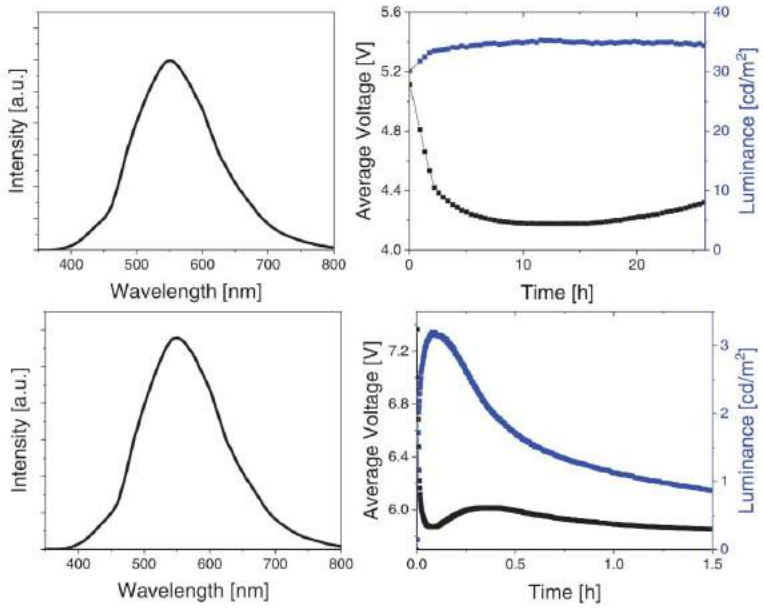


**Figure 14.** Electroluminescence spectrum (left) and average voltage and luminance over time (right) of **1·PF$_6$**/PBD (top) and **1·ClO$_4$**/PBD (bottom) devices driven at pulsed current of 15 mA.

## 4. Experimental Section

*Materials*: All chemicals were purchased from chemical suppliers and used without further purification. Solvents were reagent grade and stored over activated 3 Å molecular sieves. All reactions were carried out under inert nitrogen atmosphere using standard vacuum lines techniques. **1·BF$_4$** was synthesized as reported previously.[39]

*Synthesis: General Synthetic Procedure of [Ag(Xantphos(4,4′-(MeO)$_2$-2,2′-bipy)]X* (**1·X**): The corresponding silver salt, $AgClO_4$ or $AgPF_6$, (0.20 mmol), and Xantphos (0.20 mmol) were dissolved in a mixture of dry dichloromethane (5 mL) and methanol (2.5 mL) and stirred in the absence of light at room temperature for 30 min. Then, 4,4′-(MeO)$_2$-2,2′-bipy (0.20 mmol) was added affording a colorless solution. Addition of hexane or diethylether gave a white precipitate, which was isolated by filtration, washed with diethyl ether and dried. Single white crystals suitable for X-ray diffraction were grown by slow diffusion of diethyl ether or hexane into a dichloromethane solution at room temperature.

*[Ag(Xantphos)(4,4′-(MeO)$_2$-2,2′-bipy)]ClO$_4$·Et$_2$O* (**1·ClO$_4$·Et$_2$O**): Yield: 172 mg (80%). $^1$H NMR (300 MHz, d$_6$-dmso, 300 K): $\delta$ = 8.43 (d, 2H, $J$ = 6 Hz, C*H* bipy), 7.95 (d, 2H, $J$ = 3 Hz, C*H* bipy), 7.80 (dd, 2H, $J$ = 3, 9 Hz, C*H* arom), 7.42 (m, 12H, C*H* arom), 7.27 (m, 10H, C*H* arom), 7.04 (dd, 2H, $J$ = 3 Hz, 6 Hz, C*H* bipy), 6.69 (m, 2H, C*H* arom), 3.92 (s, 6H, OC$H_3$), 1.60 (s, 6H. Ar-C$H_3$). $^{13}$C NMR (75 MHz, d$_6$-dmso, 300 K): $\delta$ = 166.9, 155.2, 152.6 (t, $J$ = 7 Hz), 151.1, 133.1 (t, $J$ = 9 Hz), 132.3, 131.4, 131.0 (t, $J$ = 16 Hz), 130.4, 129.0 (t, $J$ = 5 Hz), 128.6, 125.0, 119.0 (t, $J$ = 11 Hz), 111.1, 108.4, 55.9, 34.9, 29.7. $^{31}$P NMR (121 MHz, d$_6$-dmso, 300 K): $\delta$ = −9.44 (2d, $^1J_{^{31}P,\ ^{109}Ag}$ = 452 Hz, $^1J_{^{31}P,\ ^{107}Ag}$ = 391 Hz). Anal. Calcd for **1·ClO$_4$·Et$_2$O** ($C_{55}H_{54}AgClN_2O_8P_2$): C, 61.38; H, 5.06; N, 2.60. Found: C, 61.21; H, 4.36; N, 2.50. IR ($\nu_{max}$ cm$^{-1}$): 3449(br), 3068(w), 2972(w), 1605(s), 1561(m), 1479(m), 1462(w), 1435(s), 1405(vs), 1311(m), 1280(w), 1229(s), 1181(w), 1150(w), 1091(vs), 1032(m), 998(w), 876(w), 816(w), 776(w), 746(s), 695(s), 623(s), 533(w), 511(s). ESI-MS ($m/z$): 901 [Ag(Xantphos)(4,4′-(MeO)$_2$-2,2′-bipy)]$^+$, 685 [Ag(Xantphos)]$^+$.

*[Ag(Xantphos)(4,4′-(MeO)$_2$-2,2′-bipy)]PF$_6$* (**1·PF$_6$**): Yield: 172 mg (82%). $^1$H NMR (300 MHz, d$_6$-dmso, 300 K): $\delta$ = 8.47 (d, 2H, $J$ = 6 Hz, C*H* bipy), 7.94 (d, 2H, $J$ = 3 Hz, C*H* bipy), 7.80 (dd, 2H, $J$ = 1, 9 Hz, C*H* arom), 7.42 (m, 12H, C*H* arom), 7.29 (m, 10H, C*H* arom), 7.04 (dd, 2H, $J$ = 3 Hz, 6 Hz, C*H* bipy), 6.71 (m, 2H, C*H* arom), 3.92 (s, 6H, OC$H_3$), 1.60 (s, 6H. Ar-C$H_3$). $^{13}$C NMR (75 MHz, d$_6$-dmso, 300 K): $\delta$ = 166.9, 155.2, 152.7 (t, $J$ = 7 Hz), 151.1, 133.1 (t, $J$ = 9 Hz), 132.3, 131.4, 131.0 (t, $J$ = 16 Hz), 130.4, 129.0 (t, $J$ = 5 Hz), 128.6, 125.0, 119.0 (t, $J$ = 10 Hz), 111.2, 108.5, 55.9, 34.9, 29.7. $^{31}$P NMR (121 MHz, d$_6$-dmso, 300 K): $\delta$ = −9.40 (2d, $^1J_{^{31}P,\ ^{109}Ag}$ = 449 Hz, $^1J_{^{31}P,\ ^{107}Ag}$ = 389 Hz. Anal. Calcd for **1·PF$_6$** ($C_{53}H_{44}AgF_6N_2O_3P_3$): C, 58.47; H, 4.23; N, 2.67. Found: C, 58.84; H, 4.73; N, 2.70. IR ($\nu_{max}$ cm$^{-1}$): 3432(br), 3056(w), 2960(w), 1603(vs), 1562(s), 1495(m), 1480(m), 1463(m), 1436(s), 1404(vs), 1364(w), 1338(m), 1316(m), 1281(m), 1221(s), 1183(w), 1151(w), 1097(m), 1045(m), 1025(m), 1007(w), 998(w), 918(w), 841(vs), 791(w), 777(w), 748(s), 694(s), 609(w), 557(s), 534(w), 510(s). ESI-MS ($m/z$): 901 [Ag(Xantphos)(4,4′-(MeO)$_2$-2,2′-bipy)]$^+$, 685 [Ag(Xantphos)]$^+$.

*X-Ray Crystallography*: Single-crystal X-ray diffraction data of **1·X** (X = $ClO_4$ and $PF_6$) were collected on a Bruker-Nonius X8APEXII CCD area detector diffractometer using graphite-monochromated Mo-K$\alpha$ radiation ($\lambda$ = 0.7173 Å) at 90 K. All calculations for data reduction, structure solution, and refinement were done through the SAINT[68] and SADABS[69] programs. The structures were solved with the SHELXS structure solution program, using the Patterson method. The models were refined with version 2018/3 of SHELXL against F2 on all data by full-matrix least squares.[70,71] All non-hydrogen atoms were refined with anisotropic displacement parameters. In **1·PF$_6$** the diffuse electron density, most likely related to messy lattice solvent molecules, was not modelled. Hence, the contribution to the diffraction pattern from the highly disordered atoms located in the voids was subtracted from the observed data through the SQUEEZE method, implemented in PLATON.[72] The hydrogen atoms on the Xantphos ligand and on the lattice solvent molecules (**1·ClO$_4$**) were included at geometrically calculated positions and refined using a riding model.

The final geometrical calculations and the graphical manipulations were carried out with the PLATON package[73] implemented in WinGX Farrugia,[74] and Crystal Maker programs,[75] respectively. Crystallographic data for compounds **1·X** are given in Table S1 of the Supporting Information. Crystallographic data for the structures reported in this paper are supplied as CIFs files and have been deposited with the Cambridge Crystallographic Data Centre as supplementary publication CCDC–1897434 (**1·$PF_6$**) and CCDC–1897435 (**1·$ClO_4$**).

*Spectroscopic, Electrochemical, and Microscopy Characterization*: $^1H$, $^{13}C$, and $^{31}P$ NMR spectra were recorded at room temperature on a Bruker AC 300 spectrometer. Chemical shifts are reported in ppm. $d_6$-dmso was used as the solvent. Infrared spectra (4000–500 $cm^{-1}$) were recorded with a Nicolet 5700 spectrophotometer as KBr pellets. ESI-MS in methanol solution were obtained on an AB SCIEX TripleTOF 5600 LC/MS/MS System. TGA and DSC were performed using TA-TGA 550 and TA DSC Q20 instruments, respectively. Absorption spectra were recorded with a Perkin Elmer Lambda 35. The $\phi$ values were measured with a FS5 Spectrofluorometer with integrating sphere SC-30 (Edinburgh Instruments. Cyclic voltammetry measurements were carried out at 25 °C using an AUTOLAB PGSTAT 204 potentiostat. A three-electrode system was used, consisting of a static glassy carbon working electrode, a platinum wire auxiliary electrode and an Ag/AgCl reference electrode. Solutions of **1·$BF_4$** was prepared in dried acetonitrile with a concentration of $1 \times 10^{-3}$ M, and were measured with [$n$Bu$_4$N][$PF_6$] (0.10 M) as a supporting electrolyte and ferrocene as an internal standard. AFM measurements were carried out with a Park XE150 instrument (Park Systems Corp., Suwon, South Korea), and the Gwyddion evaluation software. XRD measurements in devices were conducted using an XRD-6000 X-ray diffractometer (Shimadzu, Kyoto, Japan) operated at a voltage of 40 kV and 30 mA with Cu K$\alpha$ radiation (1.5406 nm) in $\theta$–2$\theta$ configurations. The crystallite sizes of the metallic silver clusters in the films were calculated using the Bragg equation $d = n\lambda/2\sin\theta$ where d is the distance among planes, $\lambda$ is the X-ray wavelength (Cu-K$\alpha$ 0.15418 nm), $\theta$ is the Bragg angle, and $n$ is the order of diffraction, 1 in the case. For an fcc crystal structure, the cell parameter $a$ can be calculated as $a = \sqrt{h^2+k^2+l^2}$ where $h$, $k$, and $l$ are the Miller index of the diffraction peak. A linear fitting among the five diffractions peaks was performed to find a cell parameter value of $a = 4.0$ Å, which is in perfect agreement with literature data.[76]

*Device Fabrication and Characterization*: ITO substrates were purchased from Naranjo Substrates with an ITO thickness of 130 nm. They were extensively cleaned using detergent, water, ethanol, and propan-2-ol as solvents in an ultrasonic bath (frequency 37–70 Hz) for 15 min each. Afterward, the slides were dried with $N_2$ gas and put in an UV-ozone cleaner for 8 min. Then, the clean plates were coated with 70 nm PEDOT:PSS layers using spin coating. To this end, an aqueous solution of PEDOT:PSS was filtered and mixed with propan-2-ol in a ratio of 3:1. From this solution 50 µL were dropped onto the substrate at a rotation speed of 2000 rpm and spun for 60 s. The resulting layers were dried on a hotplate at 120 °C and stored under $N_2$. On top of the PEDOT:PSS layer solutions containing 12 mg $mL^{-1}$ of 1·X were spin-coated at 800 rpm for 30 s, at 1500 rpm for 30 s and at 3000 rpm for an additional 10 s. Before the coating procedure, the solutions were filtered, resulting in a thickness of 70 nm. Thermal stress measurements were performed with a laboratory hotplate and the actual temperature of the thin films was monitored with the Infrared Thermal Imaging camera T420 (FLIR Instruments). Sun irradiation stress assay was performed with a solar simulator LSH-7320 (Newport Ltd.) with 1 sun intensity and AM 1.5. Some experiments required a combination of 1·X with an ionic polyelectrolyte matrix in a mass ratio of 1:0.15:0.06 (1·X:TMPE: LiOTf), which was prepared using solutions of LiOTf (10 mg $mL^{-1}$) and TMPE (20 mg $mL^{-1}$) in acetonitrile and spin-coated with the same procedure as above, resulting in 80 nm of active layer thickness. In case of the combination of 1·X with ionic liquid, the former was mixed with [BMIM]$PF_6$ in a molar ratio of 4:1 (1·X: IL) and spin-coated at 1000 rpm for 60 s and 2000 rpm for 30 s, yielding thicknesses of 70 nm. In the case of double-layered devices, the previously prepared layers were dried under vacuum (30 mbar) for 2 h. Then, a THF solution of either CBP or PBD (2 mg $mL^{-1}$) was spin-coated before or after 1·X layers at 3000 rpm for 60 s, yielding thicknesses of 15 nm. In all cases, after the deposition of the active layer the devices were transferred to an inert atmosphere glovebox (<0.1 ppm $O_2$ and $H_2O$, Angstrom Engineering). Onto all devices, aluminum cathode electrode (90 nm) was thermally evaporated onto all devices using a shadow mask under high vacuum ($<1 \times 10^{-6}$ mbar) in an Angstrom Covap evaporator integrated into the inert atmosphere glovebox. The device statistics involve up to five different devices-, i.e., a total number of 20 pixels. Time dependence of luminance, voltage, and current was measured by applying constant and/or pulsed voltage and current by monitoring the desired parameters simultaneously by using Avantes spectrophotometer (Avaspec-ULS2048L-USB2) in conjunction with a calibrated integrated sphere Avasphere 30-Irrad and Botest OLT OLED Lifetime-Test System. Electroluminescence spectra were recorded using the above mentioned spectrophotometer. EIS assays were carried out with a potentiostat/galvanostat (Metrohm µAutolabIII) equipped with a frequency response analyzer module (FRA2). Measurements were performed at the applied voltage range from 0 to 5 V and fitted with the Nova software using the circuit model shown in Figure S19 of the Supporting Information. The AC signal amplitude was set to 10 mV, modulated in a frequency range from 10 to 1 MHz. The Nova 1.11 software was used to obtain the parameters from the equivalent circuit. With this data at hand, the resistance of the intrinsic non-doped region ($R_{LEC}$) was directly obtained. The film conductivity (S $m^{-1}$) is measured at 0 V with the following equation: $\sigma = d/(AR_{LEC})$, where d is the thickness of the layer, $A$ is the area of the electrodes, and $R_{LEC}$ is the resistance of the active layer. The dielectric constant $\varepsilon_r$ was calculated with the formula $\varepsilon_r = CL/(\varepsilon_0 A)$, where $C$ is the effective capacitance, $L$ the thickness of the active layer, $\varepsilon_0$ is the vacuum permittivity ($8.85 \times 10^{-12}$ F $m^{-1}$), and $A$ is the active area of the device (15 $mm^2$).

## Supporting Information

Supporting Information is available from the Wiley Online Library or from the author.

## Acknowledgements

E.F. and R.D.C. acknowledge the program "Ayudas para la atracción de talento investigador—Modalidad 1 of the Consejería de Educación, Juventud y Deporte—Comunidad de Madrid with the Reference No. 2016-T1/IND-1463." R.D.C. acknowledges Spanish MINECO for the Ramón y Cajal program (RYC-2016-20891), the Europa Excelencia program (ERC2019-092825), and the 2018 Leonardo Grant for Researchers and Cultural Creators from BBVA Foundation and the FOTOART-CM project funded by Madrid region under programme P2018/NMT-4367. This work was financially supported by the MCCC (CTQ2016-75068-P and CTQ2016-75671-P), the Generalitat Valenciana (Project PROMETEOII/2014/070), "María de Maeztu" Excellence Unit by Mineco (MDM-2014-0538). M.V.-C. and J.M.C.-V. acknowledge MINECO for their research fellowships (MDM-2015-0538-16-2 and Juan de la Cierva). D.A. thanks the Italian MIUR and the Fondo per il finanziamento delle attività base di ricerca." R.D.C. and E.F. are heartily grateful for the assistance of Dr. Javier García for the XRD measurements.

## Conflict of Interest

The authors declare no conflict of interest.

## Keywords

decoupling charge injection and recombination, degradation mechanism, electroluminescence mechanism, light-emitting electrochemical cells, silver(I) complexes

Received: March 1, 2019
Revised: May 9, 2019
Published online: May 30, 2019

[1] R. D. Costa, *Light-Emitting Electrochemical Cells: Concepts, Advances and Challenges*, 1st ed., Springer International Publishing, Basel **2017**.
[2] J. Xu, A. Sandström, E. M. Lindh, W. Yang, S. Tang, L. Edman, *ACS Appl. Mater. Interfaces* **2018**, *10*, 33380.
[3] S. Tang, L. Edman, *Top. Curr. Chem.* **2016**, *374*, 40.
[4] E. Fresta, R. D. Costa, *J. Mater. Chem. C* **2017**, *5*, 5643.
[5] J. Gao, *Curr. Opin. Electrochem.* **2018**, *7*, 87.
[6] C. E. Housecroft, E. C. Constable, *Coord. Chem. Rev.* **2017**, *350*, 155.
[7] M. D. Weber, M. Adam, R. R. Tykwinski, R. D. Costa, *Adv. Funct. Mater.* **2015**, *25*, 5066.
[8] E. Fresta, G. Volpi, C. Garino, C. Barolo, R. D. Costa, *Polyhedron* **2018**, *140*, 129.
[9] S. Tang, W.-Y. Tan, X.-H. Zhu, L. Edman, *Chem. Commun.* **2013**, *49*, 4926.
[10] M. D. Weber, J. E. Wittmann, A. Burger, O. B. Malcioglu, J. Segarra-Martinez, A. Hirsch, P. B. Coto, M. Bockstedte, R. D. Costa, *Adv. Funct. Mater.* **2016**, *26*, 6737.
[11] M. D. Weber, V. Nikolaou, J. E. Wittmann, A. Nikolaou, P. A. Angaridis, G. Charalambidis, C. Stangel, A. Kahnt, A. G. Coutsolelos, R. D. Costa, *Chem. Commun.* **2016**, *52*, 1602.
[12] R. D. Costa, E. Ortí, H. J. Bolink, F. Monti, G. Accorsi, N. Armaroli, *Angew. Chem., Int. Ed.* **2012**, *51*, 8178.
[13] A. F. Henwood, E. Zysman-Colman, *Top. Curr. Chem.* **2016**, *374*, 36.
[14] J. Slinker, D. Bernards, P. L. Houston, H. Abruna, S. Bernhard, G. G. Malliaras, *Chem. Commun.* **2003**, 2392.
[15] J. L. Rodríguez-Redondo, R. D. Costa, E. Ortí, A. Sastre-Santos, H. J. Bolink, F. Fernández-Lázaro, *Dalton Trans.* **2009**, *44*, 9787.
[16] R. D. Costa, F. J. Céspedes-Guirao, J. B. Henk, F. Fernández-Lázaro, Á. Sastre-Santos, E. Ortí, J. Gierschner, *J. Phys. Chem. C* **2009**, *113*, 19292.
[17] G.-Y. Chen, B.-R. Chang, T.-A. Shih, C.-H. Lin, C.-L. Lo, Y.-Z. Chen, Y.-X. Liu, Y.-R. Li, J.-T. Guo, C.-W. Lu, Z.-P. Yang, H.-C. Su, *Chem. - A Eur. J.* **2019**, *25*, 5489.
[18] http://www.infomine.com/investment/metal-prices/ (accessed).
[19] M. D. Weber, M. Viciano-Chumillas, D. Armentano, J. Cano, R. D. Costa, *Dalton Trans.* **2017**, *46*, 6312.
[20] S. Keller, E. C. Constable, C. E. Housecroft, M. Neuburger, A. Prescimone, G. Longo, A. Pertegás, M. Sessolo, H. J. Bolink, *Dalton Trans.* **2014**, *43*, 16593.
[21] M. Elie, F. Sguerra, F. Di Meo, M. D. Weber, R. Marion, A. Grimault, J. F. Lohier, A. Stallivieri, A. Brosseau, R. B. Pansu, J. L. Renaud, M. Linares, M. Hamel, R. D. Costa, S. Gaillard, *ACS Appl. Mater. Interfaces* **2016**, *8*, 14678.
[22] R. Czerwieniec, M. J. Leitl, H. H. H. Homeier, H. Yersin, *Coord. Chem. Rev.* **2016**, *325*, 2.
[23] M. Alkan-Zambada, S. Keller, L. Martínez-Sarti, A. Prescimone, J. M. Junquera-Hernández, E. C. Constable, H. J. Bolink, M. Sessolo, E. Ortí, C. E. Housecroft, *J. Mater. Chem. C* **2018**, *6*, 8460.
[24] C. E. Housecroft, E. C. Constable, E. Orti, H. J. Bolink, S. Keller, A. Prescimone, M. Sessolo, G. Longo, L. Martinez-Sarti, J. M. Junquera-Hernandez, *Dalton Trans.* **2018**, *47*, 14263.
[25] S. Keller, A. Pertegás, G. Longo, L. Martínez, J. Cerdá, J. M. Junquera-Hernández, A. Prescimone, E. C. Constable, C. E. Housecroft, E. Ortí, H. J. Bolink, *J. Mater. Chem. C* **2016**, *4*, 3872.
[26] O. Moudam, A. Kaeser, B. Delavaux-Nicot, C. Duhayon, M. Holler, G. Accorsi, N. Armaroli, I. Séguy, J. Navarro, P. Destruel, J.-F. Nierengarten, *Chem. Commun.* **2007**, *3092*, 3077.
[27] M. Elie, S. Gaillard, J.-L. Renaud, *Light-Emitting Electrochemical Cells: Concepts, Advances and Challenges*, Springer International Publishing, Basel **2017**, pp. 287–327.
[28] A. Kaeser, M. Mohankumar, J. Mohanraj, F. Monti, M. Holler, J.-J. Cid, O. Moudam, I. Nierengarten, L. Karmazin-Brelot, C. Duhayon, B. Delavaux-Nicot, N. Armaroli, J.-F. Nierengarten, *Inorg. Chem.* **2013**, *52*, 12140.
[29] M. D. Weber, C. Garino, G. Volpi, E. Casamassa, M. Milanesio, C. Barolo, R. D. Costa, *Dalton Trans.* **2016**, *45*, 8984.
[30] M. D. Weber, E. Fresta, M. Elie, M. E. Miehlich, J.-L. Renaud, K. Meyer, S. Gaillard, R. D. Costa, *Adv. Funct. Mater.* **2018**, *28*, 1707423.
[31] M. Elie, M. D. Weber, F. Di Meo, F. Sguerra, J.-F. Lohier, R. B. Pansu, J.-L. Renaud, M. Hamel, M. Linares, R. D. Costa, S. Gaillard, *Chem. - Eur. J.* **2017**, *23*, 16328.
[32] O. Moudam, A. C. Tsipis, S. Kommanaboyina, P. N. Horton, S. J. Coles, *RSC Adv.* **2015**, *5*, 95047.
[33] E. Fresta, G. Volpi, M. Milanesio, C. Garino, C. Barolo, R. D. Costa, *Inorg. Chem.* **2018**, *57*, 10469.
[34] C. Bizzarri, F. Hundemer, J. Busch, S. Bräse, *Polyhedron* **2018**, *140*, 51.
[35] J. Chen, T. Teng, L. Kang, X. L. Chen, X. Y. Wu, R. Yu, C. Z. Lu, *Inorg. Chem.* **2016**, *55*, 9528.
[36] M. Z. Shafikov, A. Suleymanova, A. Schinabeck, H. Yersin, *J. Phys. Chem. Lett.* **2018**, *9*, 702.
[37] A. S. Romanov, S. T. E. Jones, L. Yang, P. J. Conaghan, D. Di, M. Linnolahti, D. Credgington, M. Bochmann, *Adv. Opt. Mater.* **2018**, *6*, 1801347.
[38] R. D. Costa, D. Tordera, E. Ortí, H. J. Bolink, J. Schönle, S. Graber, C. E. Housecroft, E. C. Constable, J. A. Zampese, *J. Mater. Chem.* **2011**, *21*, 16108.
[39] J. M. Carbonell-Vilar, E. Fresta, D. Armentano, J. Cano, R. D. Costa, M. Viciano-Chumillas, *Dalton Trans.* **2019**, https://doi.org/10.39/C9DT00772E.
[40] M. Llunel, D. Casanova, J. Cirera, P. Alemany, S. Alvarez, *SHAPE 2.1*, Universitat de Barcelona **2013**.
[41] W. Yang, C. Wang, V. Arrighi, *J. Mater. Sci. Mater. Electron.* **2018**, *29*, 2771.
[42] M. Ganguly, A. Pal, Y. Negishi, T. Pal, *Langmuir* **2013**, *29*, 2033.
[43] C.-W. Hsu, C.-C. Lin, M.-W. Chung, Y. Chi, G.-H. Lee, P.-T. Chou, C.-H. Chang, P.-Y. Chen, *J. Am. Chem. Soc.* **2011**, *133*, 12085.
[44] S.-M. Kuang, D. G. Cuttell, D. R. McMillin, P. E. Fanwick, R. A. Walton, *Inorg. Chem.* **2002**, *41*, 3313.
[45] J. Yuasa, M. Dan, T. Kawai, *Dalton Trans.* **2013**, *42*, 16096.
[46] A. Kaeser, O. Moudam, G. Accorsi, I. Séguy, J. Navarro, A. Belbakra, C. Duhayon, N. Armaroli, B. Delavaux-Nicot, J. F. Nierengarten, *Eur. J. Inorg. Chem.* **2014**, *2014*, 1345.
[47] P. Mulvaney, A. Henglein, *J. Phys. Chem.* **1990**, *94*, 4182.
[48] D. R. Blasini, J. Rivnay, D. M. Smilgies, J. D. Slinker, S. Flores-Torres, H. D. Abruña, G. G. Malliaras, *J. Mater. Chem.* **2007**, *17*, 1458.
[49] D. Tordera, J. Frey, D. Vonlanthen, E. Constable, A. Pertegás, E. Ortí, H. J. Bolink, E. Baranoff, M. K. Nazeeruddin, *Adv. Energy Mater.* **2013**, *3*, 1338.
[50] S. van Reenen, P. Matyba, A. Dzwilewski, R. A. J. Janssen, L. Edman, M. Kemerink, *J. Am. Chem. Soc.* **2010**, *132*, 13776.
[51] S. Van Reenen, P. Matyba, A. Dzwilewski, R. A. J. Janssen, L. Edman, M. Kemerink, *Adv. Funct. Mater.* **2011**, *21*, 1795.
[52] S. Van Reenen, R. A. J. Janssen, M. Kemerink, *Adv. Funct. Mater.* **2012**, *22*, 4547.
[53] A. Munar, A. Sandström, S. Tang, L. Edman, *Adv. Funct. Mater.* **2012**, *22*, 1511.
[54] S. B. Meier, D. Hartmann, A. Winnacker, W. Sarfert, *J. Appl. Phys.* **2014**, *116*, 104504.
[55] B. M. D. Puscher, M. F. Aygueler, P. Docampo, R. D. Costa, *Adv. Energy Mater.* **2017**, *7*, 1602283.
[56] L. D. Bastatas, M. D. Moore, J. D. Slinker, *ChemPlusChem* **2017**, *83*, 266.
[57] L. D. Bastatas, K. Y. Lin, M. D. Moore, K. J. Suhr, M. H. Bowler, Y. Shen, B. J. Holliday, J. D. Slinker, *Langmuir* **2016**, *32*, 9468.
[58] H. Kim, C. M. Gilmore, A. Piqué, J. S. Horwitz, H. Mattoussi, H. Murata, Z. H. Kafafi, D. B. Chrisey, *J. Appl. Phys.* **1999**, *86*, 6451.
[59] Y.-J. Lee, C.-C. Lin, H.-C. Lee, Y.-C. Yao, M. Sarma, H.-C. Su, Z.-P. Yang, K.-T. Wong, *J. Mater. Chem. C* **2016**, *4*, 1599.

 

[60] S. Tang, H. A. Buchholz, L. Edman, *J. Mater. Chem. C* **2015**, *3*, 8114.
[61] S. Tang, A. Sandström, J. Fang, L. Edman, *J. Am. Chem. Soc.* **2012**, *134*, 14050.
[62] H. Rudmann, S. Shimada, M. F. Rubner, *J. Am. Chem. Soc.* **2002**, *124*, 4918.
[63] C. Zhang, P. Chen, W. Hu, *Small* **2016**, *12*, 1252.
[64] A. Kulkarni, C. J. Tonzola, A. Babel, S. A. Jenekhe, *Chem. Mater.* **2004**, *16*, 4556.
[65] Y. Nishikitani, D. Takizawa, H. Nishide, S. Uchida, S. Nishimura, *J. Phys. Chem. C* **2015**, *119*, 28701.
[66] H.-C. Su, C.-Y. Cheng, *Isr. J. Chem.* **2014**, *54*, 855.
[67] S. Uchida, D. Takizawa, S. Ikeda, H. Takeuchi, S. Nishimura, H. Nishide, Y. Nishikitani, *J. Vis. Exp.* **2016**, *117*, e54628.
[68] SAINT, version 6.45, *Bruker Analytical X-ray Systems*, Madison, WI **2003**.
[69] L. Krause, R. Herbst-Irmer, G. M. Sheldrick, D. Stalke, *J. Appl. Crystallogr.* **2015**, *48*, 3.
[70] G. M. Sheldrick, *Acta Crystallogr., Sect. A: Found. Crystallogr.* **2008**, *64*, 112.
[71] G. M. Sheldrick, *Acta Crystallogr., Sect. C: Struct. Chem.* **2015**, *71*, 3.
[72] A. L. Spek, *Acta Crystallogr., Sect. C: Struct. Chem.* **2015**, *71*, 9.
[73] A. L. Spek, *Acta Crystallogr., Sect. D: Biol. Crystallogr.* **2009**, *65*, 148.
[74] L. J. Farrugia, *J. Appl. Crystallogr.* **1999**, *32*, 837.
[75] D. Palmer, *CRYSTAL MAKER*, Cambridge University Technical Services **1996**.
[76] W. P. Davey, *Phys. Rev.* **1925**, *25*, 753.

 

ADVANCED FUNCTIONAL MATERIALS

# Supporting Information

for *Adv. Funct. Mater.,* DOI: 10.1002/adfm.201901797

## Deciphering the Electroluminescence Behavior of Silver(I)-Complexes in Light-Emitting Electrochemical Cells: Limitations and Solutions toward Highly Stable Devices

*Elisa Fresta, José M. Carbonell-Vilar, Jiayin Yu, Donatella Armentano, Joan Cano, Marta Viciano-Chumillas,* and Rubén D. Costa**

# Supporting Information

Deciphering the electroluminescence behaviour of Silver (I) complexes in light-emitting electrochemical cells: limitations and solutions towards highly stable devices

*By Elisa Fresta, José-Miguel Carbonell-Vilar, Jiayin Yu, Donatella Armentano, Joan Cano, Marta Viciano-Chumillas*, and Rubén D. Costa**

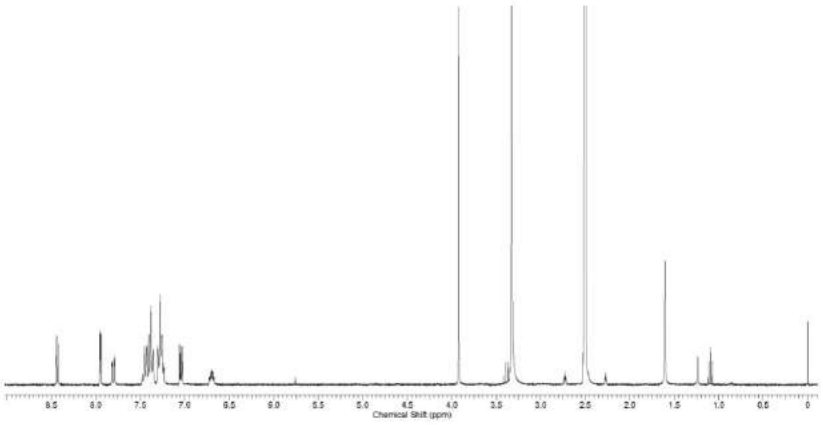


**Figure S1.** $^{1}$H NMR spectrum of **1·ClO$_4$·Et$_2$O** in d$_6$-dmso at room temperature.

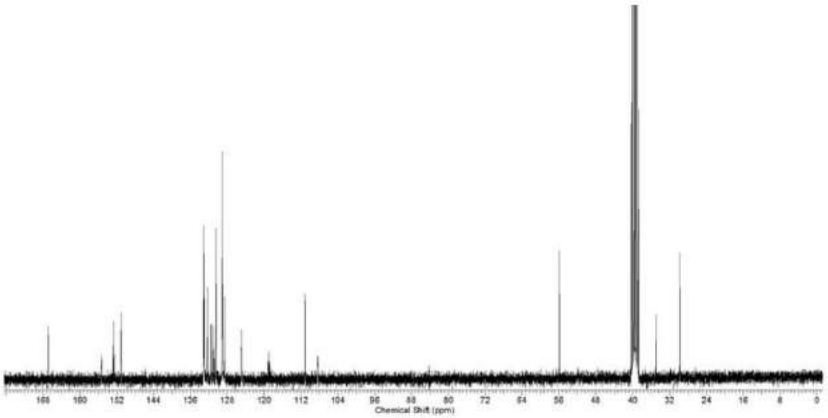

**Figure S2.** $^{13}C$ NMR spectrum of **1·ClO$_4$·Et$_2$O** in $d_6$-dmso at room temperature.

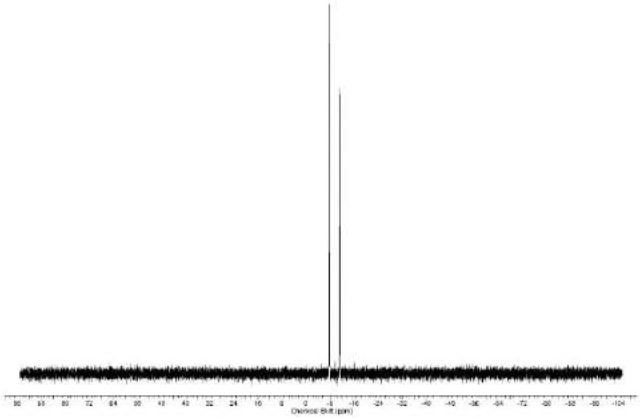

**Figure S3.** $^{31}P$ NMR spectrum of **1·ClO$_4$·Et$_2$O** in $d_6$-dmso at room temperature.

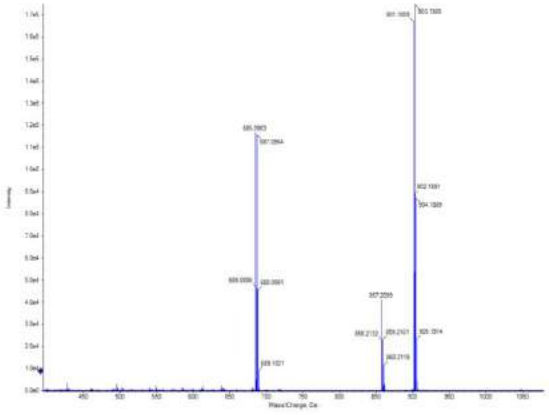

**Figure S4.** ESI-MS spectrum of **1·ClO$_4$·Et$_2$O**.

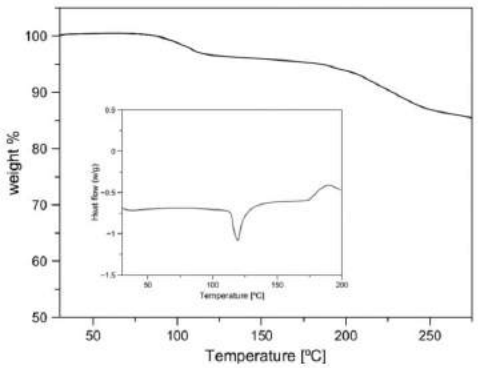


**Figure S5.** TGA and DSC (inset) curves of **1·ClO$_4$·Et$_2$O**.

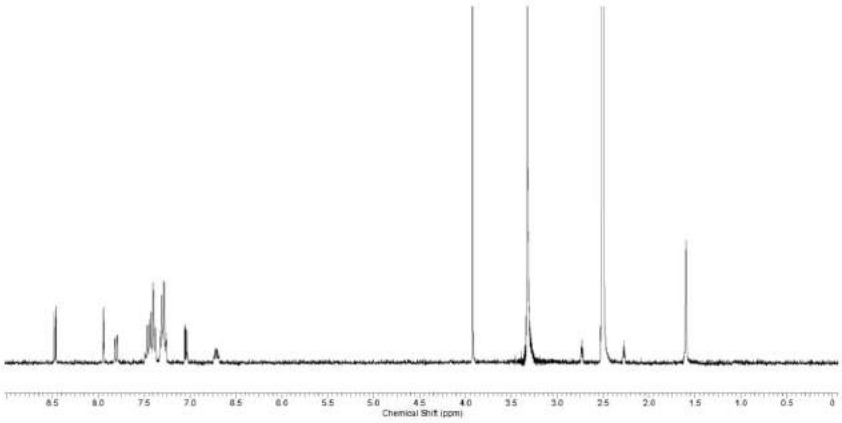


**Figure S6.** $^1$H NMR spectrum of **1·PF$_6$** in d$_6$-dmso at room temperature.

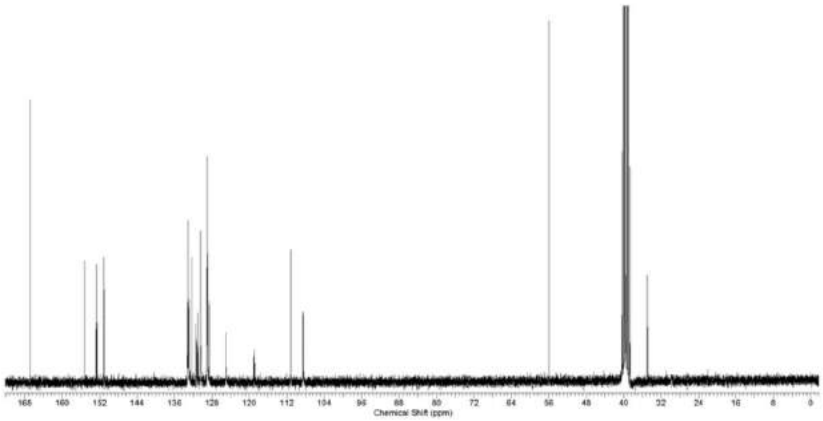

**Figure S7.** $^{13}C$ NMR spectrum of **1·PF$_6$** in $d_6$-dmso at room temperature.

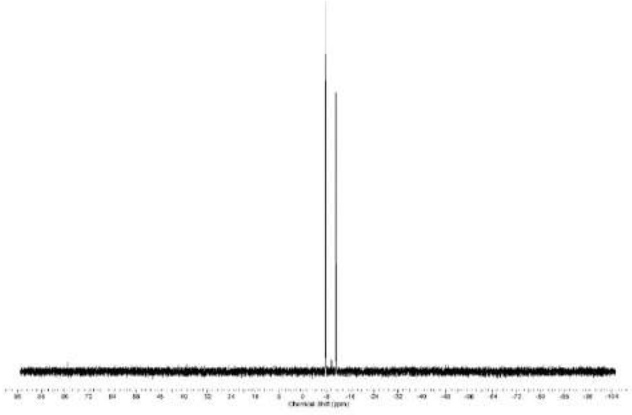

**Figure S8.** $^{31}P$ NMR spectrum of **1·PF$_6$** in $d_6$-dmso at room temperature.

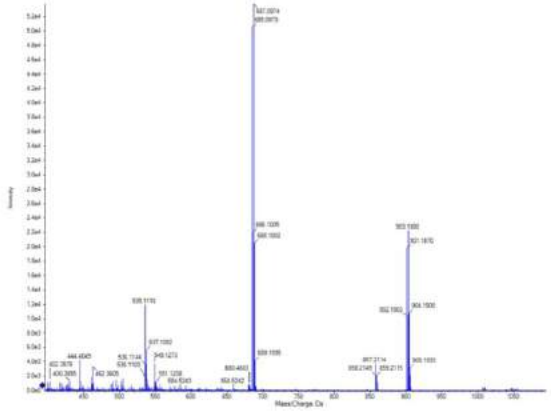

**Figure S9.** ESI-MS spectrum of **1·PF$_6$**.

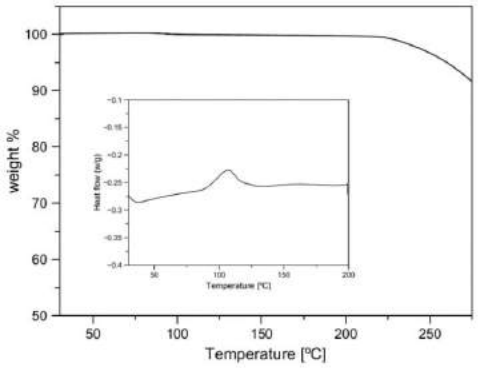


**Figure S10.** TGA and DSC (inset) curves of **1·PF$_6$**.

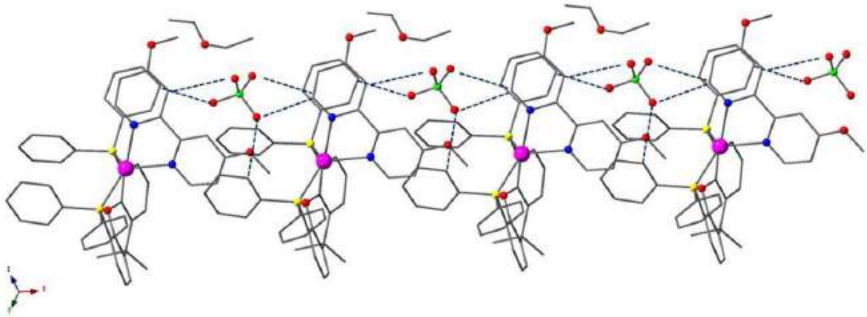

**Figure S11.** View of the C–H···O interactions in compound **1·ClO$_4$·Et$_2$O**. Hydrogen atoms are omitted for clarity. Color code: magenta, silver; blue, nitrogen; yellow, phosphorous; green, halogen (chloride or fluoride); red, oxygen; grey, carbon.

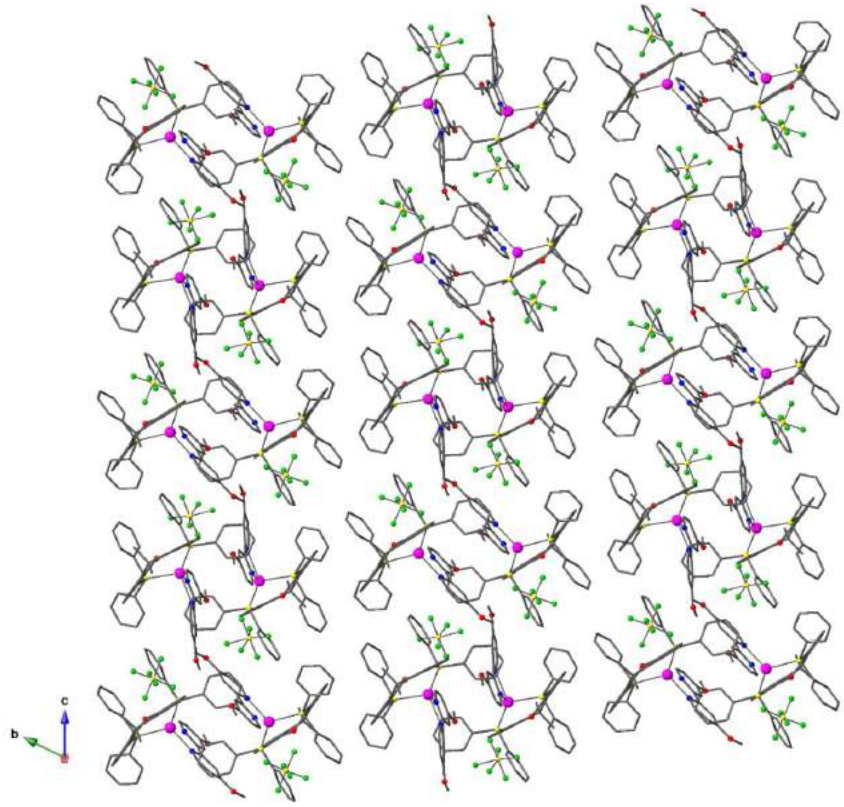


**Figure S12.** View of a portion of the crystal packing of **1·PF$_6$** along the crystallographic a axis.

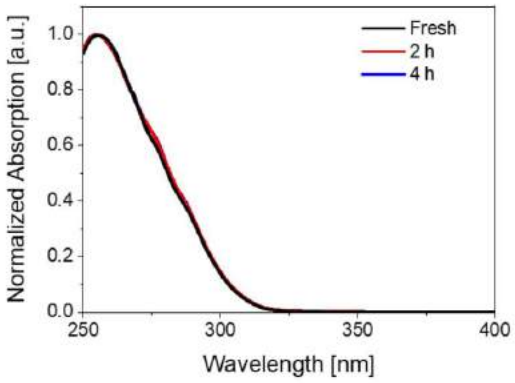


**Figure S13.** UV/vis absorption spectra of **1·BF$_4$** in MeCN (1 x $10^{-4}$ M) measured over time at room temperature.

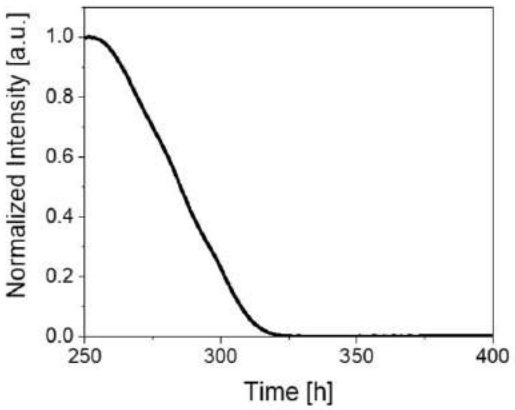


**Figure S14.** UV/vis absorption spectrum of $[Ag(Xantphos)_2]ClO_4$ in MeCN ($1 \times 10^{-4}$ M) at room temperature.

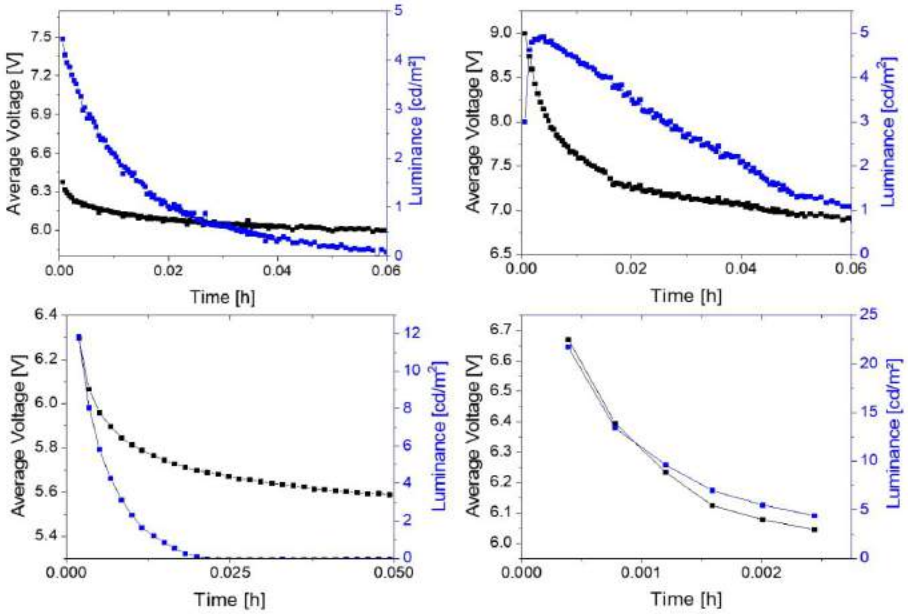


**Figure S15.** Average Voltage and Luminance over time of **1·BF$_4$** devices measured at the pulsed current of 5 mA (top left), 7.5 mA (top right), 10 mA (bottom left), and 20 mA (bottom right).

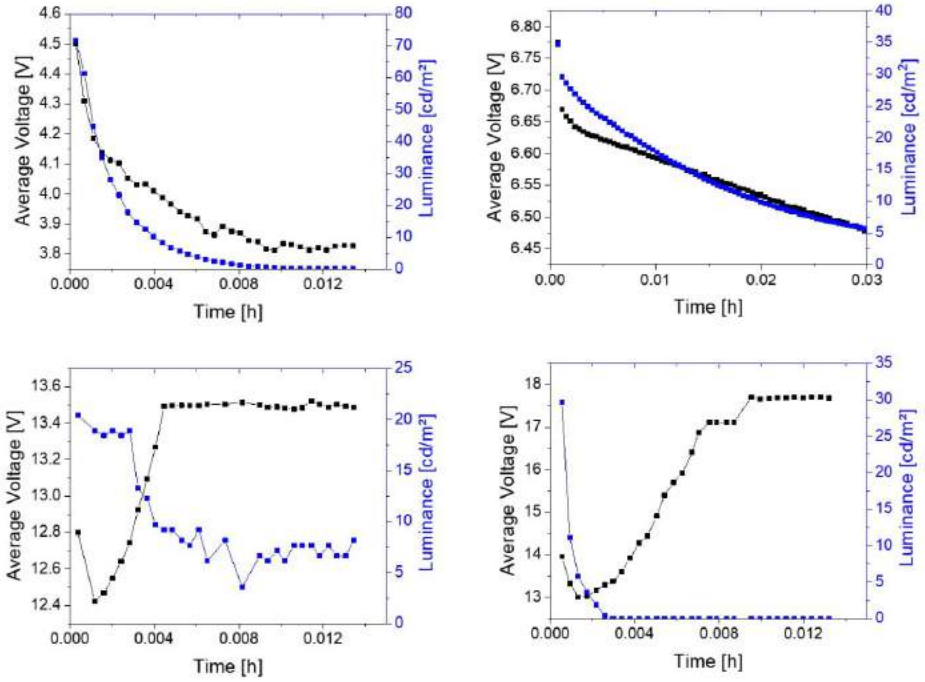


**Figure S16.** Average voltage and luminance over time of **1·BF$_4$** devices driven at 15 mA pulsed mode with a 25% duty cycle (top left), and 50% duty cycle (top right), 75% duty cycle (bottom left), and 100% duty cycle (bottom right).

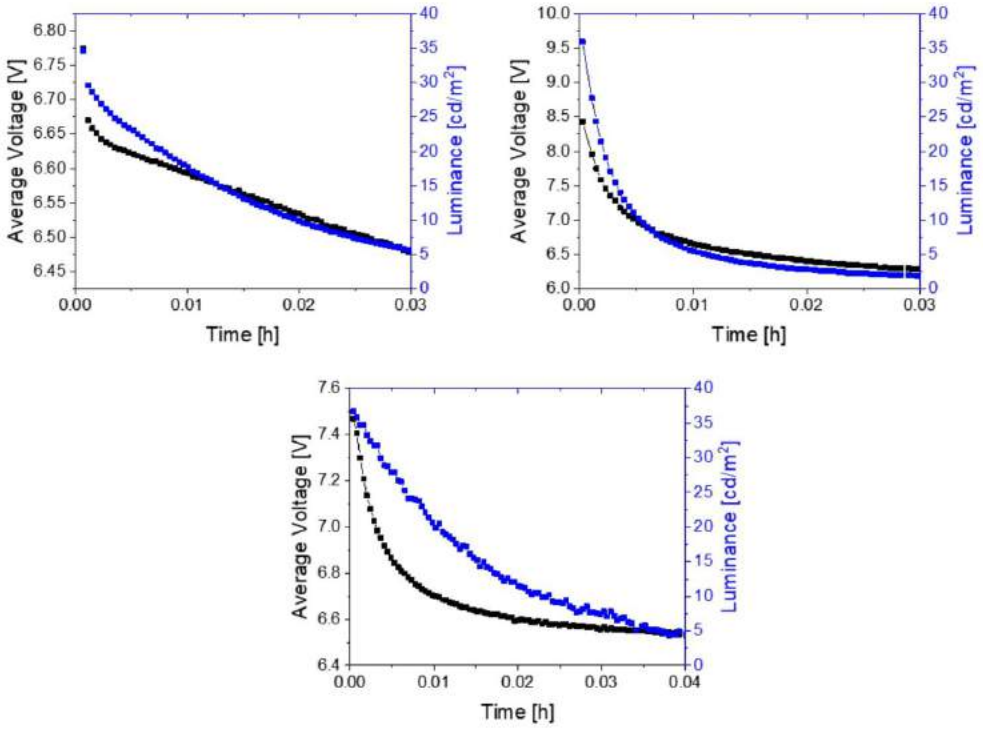


**Figure S17.** Average voltage and luminance over time of **1·BF$_4$** devices (15 mA pulsed mode) fabricated under normal light and freshly evaporated (top left), and irradiated with 1 sun light for 30 min (top right), and 1 h (bottom).

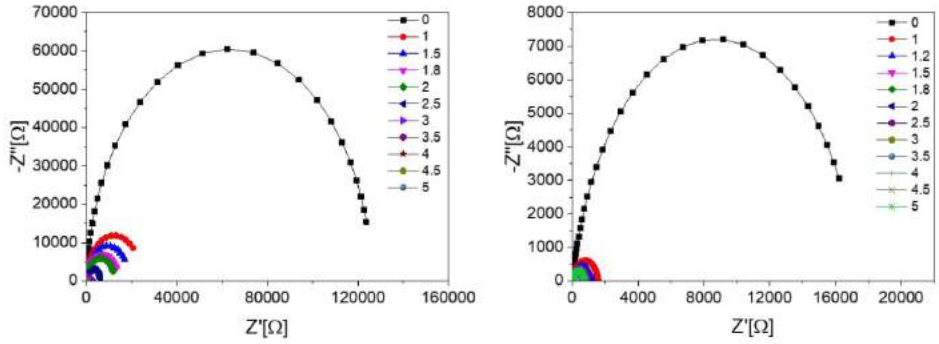


**Figure S18.** Nyquist plots of fresh (left) and used (right) **1·BF$_4$** devices measured upon constant bias (see legend). The fittings are shown in solid lines.

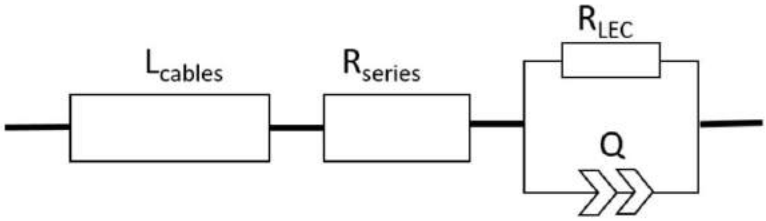


**Figure S19.** Simplified circuit model with only electrical resistance ($R_{LEC}$) and admittance Q used for static EIS assays. A series resistor ($R_{series}$) and inductor elements for the cables ($L_{cables}$) were also included in the model.

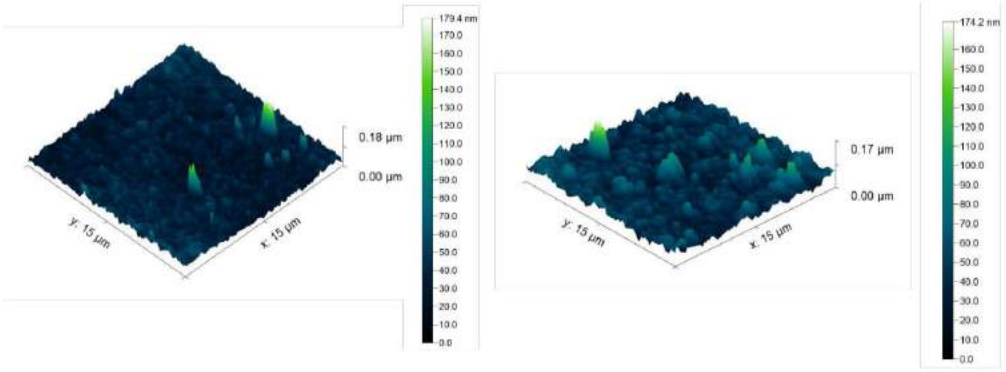


**Figure S20.** AFM images of **1·BF$_4$** thin films with ionic liquid (left) and ionic polyelectrolyte (right).

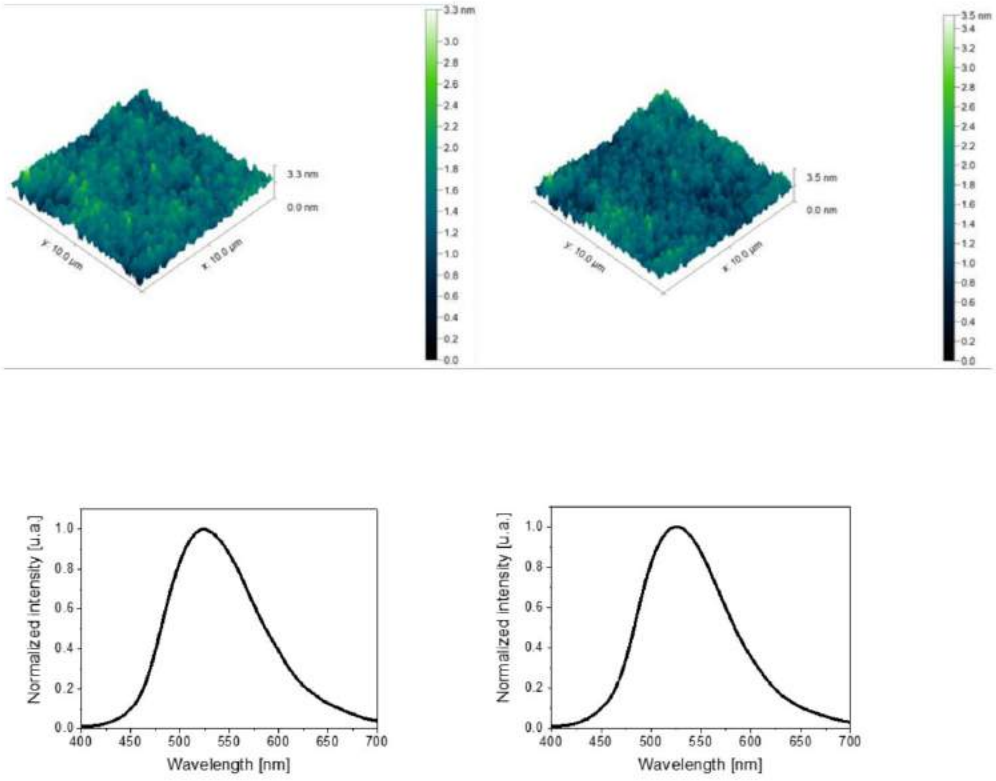


**Figure S21.** AFM images (top) and photoluminescence (bottom) of **1·PF$_6$** (left) and **1·ClO$_4$** (right) thin films.

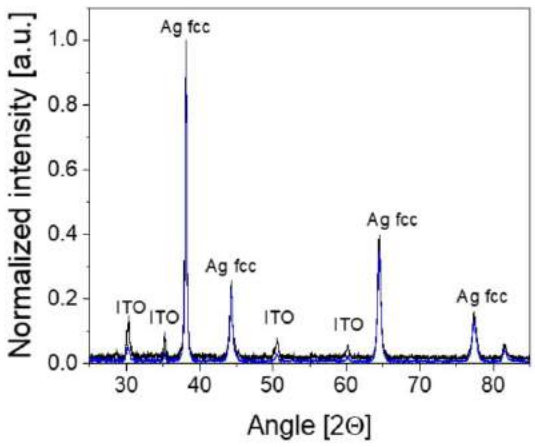

**Figure S22.** XRD measurement of used **1·PF$_6$** (black) and **1·ClO$_4$** (blue) devices. The peaks related to ITO and the Ag fcc crystalline structure are marked above.

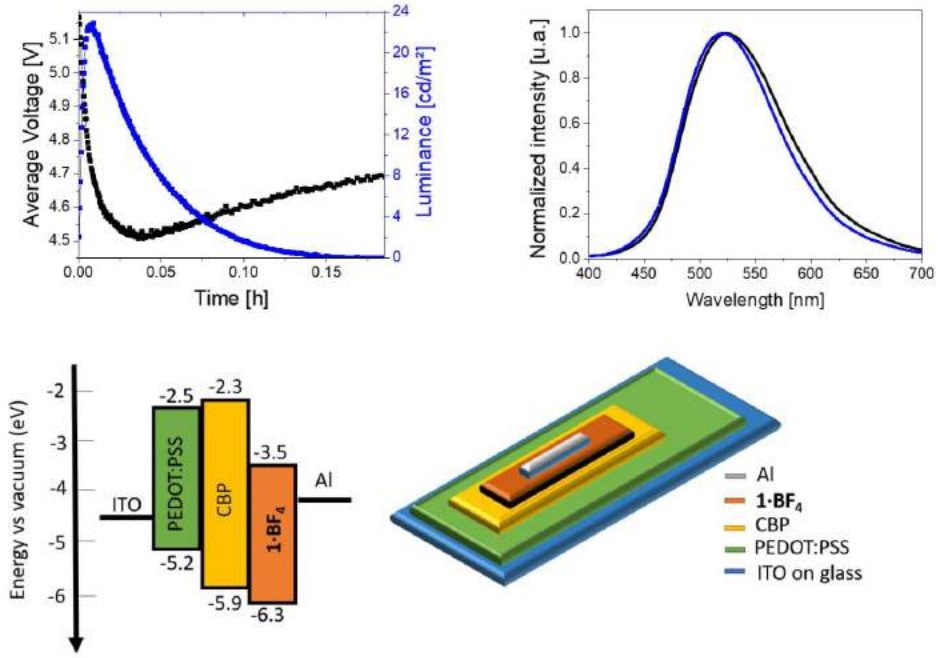


**Figure S23.** Top: Average Voltage and Luminance over time of CBP/**1·BF$_4$** devices driven at pulsed 15 mA (left), and the electroluminescence spectra (right) of **1·BF$_4$** (black) and CBP/**1·BF$_4$** (blue). Bottom: Schemes of the CBP/**1·BF$_4$** device design (left) and its energy diagram (right) as derived from the CV data using the formula $E_{HOMO/LUMO} = e(V_{Fc/Fc^+}) + 5.1$ eV.

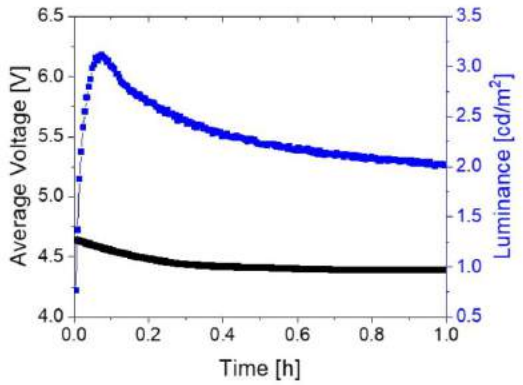


**Figure S24.** Average Voltage and Luminance over time of **1·BF$_4$**/PBD devices driven at the pulsed current of 15 mA (left), featuring a thickness of the PBD layer of 35 nm. **1·BF$_4$**/PBD devices with a PBD layer thickness of 50 nm showed no current injection and luminance.

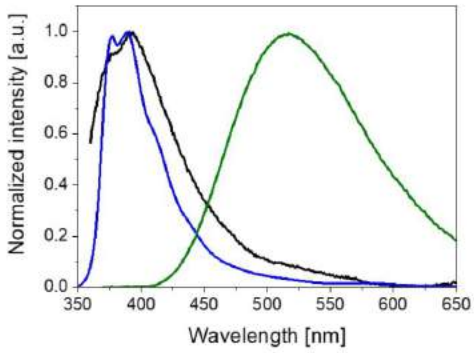


**Figure S25.** Emission spectra of **1·BF$_4$**/PBD from top (black) and bottom (green) excitation, and PBD (blue) thin films. ($\lambda_{exc}$ = 330 nm).

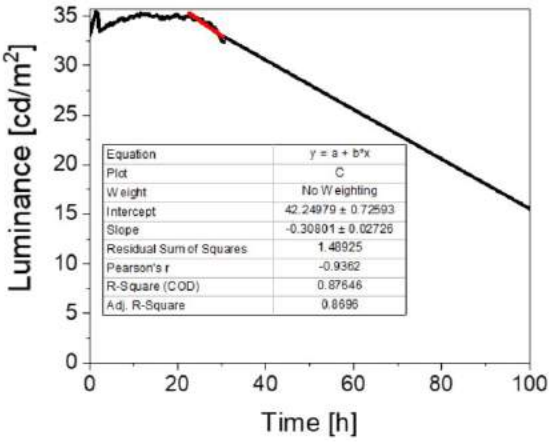


**Figure S26.** Luminance over time of **1·PF$_6$**/PBD devices driven at pulsed 15 mA, showing a linear fit decay extrapolation (red). The linear fit brings to a $t_{1/2}$ of 81 hours.

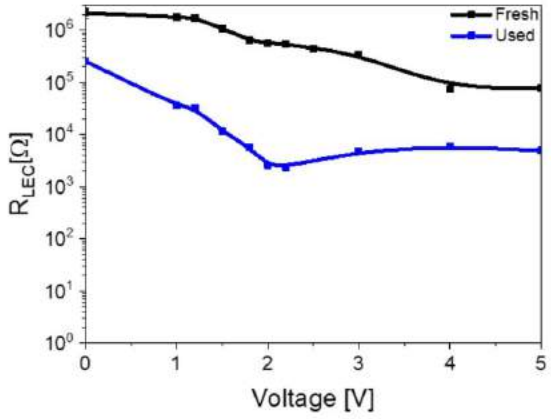


**Figure S27.** Changes in $R_{LEC}$ of **1·BF$_4$**/PBD devices under static EIS measurements (0-5 V).

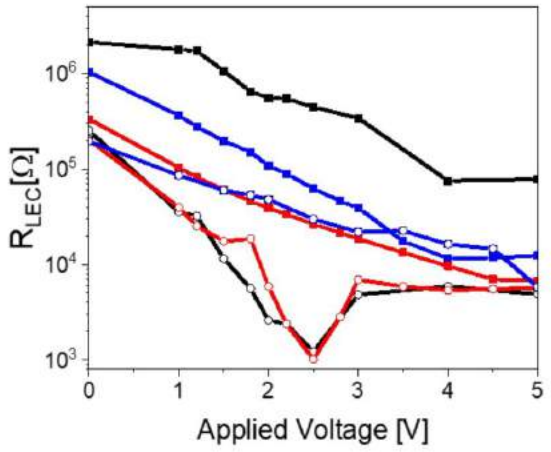


**Figure S28.** Changes in $R_{LEC}$ of **1·BF$_4$**/PBD (black), **1·PF$_6$**/PBD (blue) and **1·ClO$_4$**/PBD (red) devices under static EIS measurements (0-5 V). The full squares and empty circles refer to fresh and used devices, respectively.

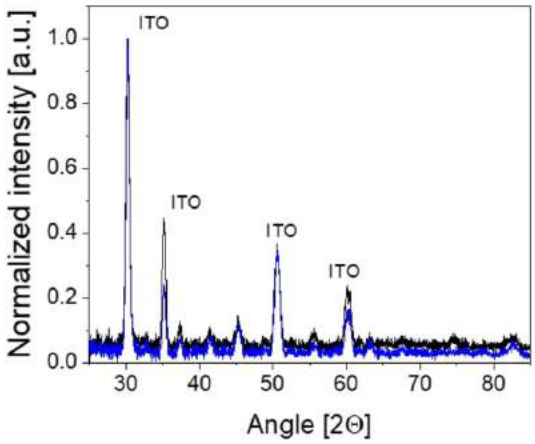


**Figure S29.** XRD measurement of fresh (blue) and used (black) **1·BF$_4$**/PBD devices. The peaks related to ITO are marked above.

**Table S1.** Crystal data for **1·X** (X = $ClO_4$ and $PF_6$).

| | $C_{51}H_{44}AgN_2O_3P_2$, $ClO_4 \cdot C_4H_{10}O$ (**1·ClO$_4$**·Et$_2$O) | $C_{51}H_{44}AgN_2O_3P_2$, $PF_6$ (**1·PF$_6$**) |
|---|---|---|
| Formula weight [g/mol] | 1076.26 | 1047.66 |
| Crystal system | Triclinic | Triclinic |
| Space group | *P*–1 | *P*–1 |
| *a* [Å] | 10.2416(7) | 14.8578(8) |
| *b* [Å] | 14.1143(10) | 21.1157(14) |
| *c* [Å] | 17.8297(14) | 21.6247(18) |
| α [°] | 99.238(4) | 61.851(3) |
| β [°] | 99.110(4) | 78.555(4) |
| γ [°] | 99.233(4) | 69.945(2) |
| V [Å$^3$] | 2465.7(3) | 5613.7(7) |
| Z | 2 | 4 |
| $D_{calc}$ [g/cm$^3$] | 1.450 | 1.240 |
| μ [mm$^{-1}$] | 0.586 | 0.502 |
| Number of collected reflections (unique) | 32067(5514) | 113783(22780) |
| Number of observed reflections ($I_o > 2\sigma(I_o)$) | 43634 | 16113 |
| Internal R factor | 0.996 | 0.056 |
| Number of parameters | 61328 | 1197 |
| Goodness-of-fit S on $F^2$ | 1.143 | 1.11 |
| Largest peak and hole in final difference Fourier map (e Å$^{-3}$) | −1.208 and 2.4538 | −1.40 and 2.37 |
| $R_1$[a] [*I*> 2.0σ(*I*)] | 0.0904 | 0.0664 |
| $wR_2$[b] [all data] | 0.2490 | 0.1986 |
| T [K] | 90 | 90 |

**Table S2.** Details (distances [Å] and angles [°]) of the π···π interactions in [Ag(Xantphos)(4,4'-(MeO)$_2$-2,2'-bipy)]X (**1·X**), being X = $ClO_4$ and $PF_6$.

| Compound | Cg···Cg[a] | Cg···Cg | α[b] |
|---|---|---|---|
| **1·$ClO_4$** | Cg6···Cg8 intram | 3.831(8) | 21.2(6) |
| **1·$PF_6$** | Cg8[a]···Cg10 intram | 3.875(3) | 20.3(3) |

[a] Cg are the six-membered rings: Cg6, C19–C24; Cg8, C31–C36; Cg8[a], C22–C27; Cg10, C34–C39. [b] α is the dihedral angle between each pair of mean ring planes.

**Table S3.** C–H···X (X = F, O) interactions details (distances [Å] and angles [°]) for compounds **1·X** (X = $ClO_4$ and $PF_6$).

| Donor–H···Acceptor | D–H | H···A | D···A | D–H···A |
|---|---|---|---|---|
| **1·$ClO_4$** | | | | |
| C7–H7···O4 | 0.95 | 2.43 | 3.369(14) | 172 |
| C10–H10···O5 | 0.95 | 2.45 | 3.177(17) | 133 |
| C10–H10···O6 | 0.95 | 2.44 | 3.314(17) | 153 |
| C17–H17···O7 | 0.95 | 2.54 | 3.190(17) | 126 |
| C36–H36···O6 | 0.95 | 2.59 | 3.401(15) | 143 |
| **1·$PF_6$** | | | | |
| C102–H10A···F2 | 0.98 | 2.47 | 3.431(15) | 166 |
| C102–H10C···F7 | 0.98 | 2.10 | 3.005(16) | 152 |
| C11–H11···F10 | 0.95 | 2.54 | 3.243(8) | 131 |
| C46–H46···F7 | 0.95 | 2.52 | 3.451(11) | 166 |
| C48–H48···F10 | 0.95 | 2.45 | 3.309(8) | 149 |
| C50–H50A···F11 | 0.98 | 2.43 | 3.399(13) | 170 |
| C91–H91···F6 | 0.95 | 2.47 | 3.314(9) | 149 |
| C92–H92···F2 | 0;95 | 2.47 | 3.270(9) | 142 |

**Table S4.** Figures of merit of devices prepared with **1·BF$_4$**/PBD devices driven at pulsed 15 mA featuring a different thickness of the PBD layer.

| PBD layer thickness [nm] | Average Voltage [V] | $L_{inst}$[a] [cd/m$^2$] | $L_{max}$[b] [cd/m$^2$] | $t_{on}$[c] [h] | $t_{1/2}$[d] [h] | Efficacy [cd/A] |
|---|---|---|---|---|---|---|
| 15 | 4.5 | 2 | 7 | 0.12 | 7.2 | 0.04 |
| 35 | 5.2 | 0.1 | 3 | 0.1 | 1 | 0.02 |
| 50 | 7.5 | No luminance observed | No luminance observed | - | - | - |

a. Instantaneous luminance or initial luminance level; b. Maximum luminance; c. Time to reach the maximum luminance; d. Time to decay to the half of the maximum luminance.

Section 3.2.1: Revealing the Impact of Heat Generation using Nanographene based Light-emitting Electrochemical cells.

Elisa Fresta,[1,2] Jacopo Dosso,[3] Juan Cabanillas-Gonzalez,[4] Davide Bonifazi,[3,5] and Rubén D. Costa*[1,6]

1. IMDEA Materials Institute, Calle Eric Kandel 2, E-28906 Getafe, Madrid, Spain.
2. Universidad Autónoma de Madrid, Departamento de Física Aplicada, Calle Francisco Tomás y Valiente, 7, 28049 Madrid, Spain.
3. School of Chemistry, Cardiff University, CF10 3AT Cardiff, Great Britain.
4. IMDEA Nanoscience, Calle Faraday 9, 28049 Madrid, Spain.
5. Institute of Organic Chemistry, Faculty of Chemistry, University of Vienna, Währinger Strasse 38, 1090 Vienna, Austria.
6. Chair of Biogenic Functional Materials, Technical University of Munich, Schulgasse 22, 94315 Straubing.

ACS APPLIED MATERIALS & INTERFACES

www.acsami.org Research Article

# Revealing the Impact of Heat Generation Using Nanographene-Based Light-Emitting Electrochemical Cells

Elisa Fresta, Jacopo Dosso, Juan Cabanillas-Gonzalez, Davide Bonifazi, and Rubén D. Costa*

Cite This: https://dx.doi.org/10.1021/acsami.0c06783 Read Online

ACCESS | Metrics & More | Article Recommendations | Supporting Information

**ABSTRACT:** Self-heating in light-emitting electrochemical cells (LECs) has been long overlooked, while it has a significant impact on (i) device chromaticity by changing the electroluminescent band shape, (ii) device efficiency because of thermal quenching and exciton dissociation reducing the external quantum efficiency (EQE), and (iii) device stability because of thermal quenching of excitons and formation of doped species, phase separation, and collapse of the intrinsic emitting zone. Herein, we reveal, for the first time, a direct relationship between self-heating and the early changes in the device chromaticity as well as the magnitude of the error comparing theoretical/experimental EQEs—that is, an overestimation error of *ca.* 35% at usual pixel working temperatures of around 50 °C. This has been realized in LECs using a benchmark nanographene—that is, a substituted hexa-peri-hexabenzocoronene—as an emerging class of emitters with outstanding device performance compared to the prior art of small-molecule LECs—for example, luminances of 345 cd/m$^2$ and EQEs of 0.35%. As such, this work is a fundamental contribution highlighting how self-heating is a critical limitation toward the optimization and wide use of LECs.

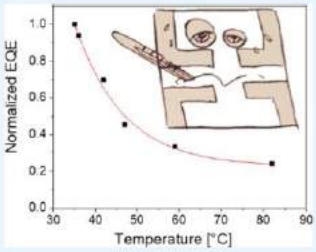


**KEYWORDS:** *small molecules, nanographenes, self-heating, light-emitting electrochemical cells, device efficiency*

## 1. INTRODUCTION

Light-emitting electrochemical cells (LECs) are simple and low-cost solid-state emissive devices that consist of a thin-film active layer sandwiched between two air-stable electrodes.[1,2] The active layer comprises a blend of mobile ions and an electroactive emitter. The presence of mobile ions leads to a peculiar working mechanism, in which charge injection and carrier transport depend on ion arrangements under operating conditions. This also allows us to easily fabricate devices with a good tolerance toward the active layer thickness, the type of electrodes/substrates, and the type of deposition techniques. Indeed, LECs could be applied to a myriad of lighting applications, including labeling, decorative, and medical applications, among others.[3−5] However, their wide implementation must also take into account not only a simple device architecture and a low-cost solvent-based fabrication process[5,6] but also an excellent self-stability upon storage and mechanical stress[7] and the right operating conditions to meet the performance criteria for each application.[3,7−15]

In this context, the effect of the temperature in the LEC performance is a critical aspect that has barely been considered in the literature until date.[16−18] In brief, Friend *et al.* reported on the reversible color changes in LECs based on copper(I) complexes upon externally applying temperature,[16] while Slinker and co-workers nicely studied the relationship between the thermal stability of LECs with iridium(III) and ruthenium(II) complexes and the presence of their degradative metal-centered excited states.[17] Finally, Gao and collaborators stated that poor thermally conductive substrates, such as glass, have a dramatic effect on both electroluminescence and driving voltage that can only be explained by the effect of self-heating.[9] In a following contribution, they abruptly cooled the devices to −73 °C, thereby freezing the p−i−n junction and allowing for the study of a static doping profile.[19] We have also described how gentle thermal drying under different atmospheres significantly changes the film morphology, affecting the photoluminescence, electrical, and ion conductivity features in LECs with small molecules and d$^{10}$-complexes as emitters.[18,20−24]

Much less considered is the impact of the self-heating in LECs caused by the operating conditions.[25] Similar to other thin-film organic/inorganic lighting diodes,[26] the instantaneous heat generation upon driving is related to (i) the resistances associated to the interfaces and the bulk of the active layer (Joule effect) and (ii) the nonradiative deactivation process of excitons (formation of dark/quenched excitons and self-absorption). In LECs, self-heating might also be a source of emitter degradation, exciton dissociation, quick collapse of the intrinsic emitting zone, and morphological changes because the

Received: April 13, 2020
Accepted: June 1, 2020
Published: June 1, 2020

  

https://dx.doi.org/10.1021/acsami.0c06783
ACS Appl. Mater. Interfaces XXXX, XXX, XXX−XXX

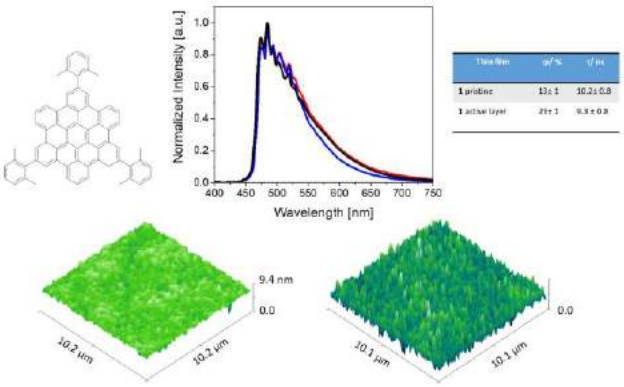


**Figure 1.** Top: Chemical structure of **1** (left), photoluminescence spectra (centre) of **1** films without (black) and with (blue) an ionic polyelectrolyte, and without a polyelectrolyte at 77 K (red) and a table summarizing the photophysical properties of the abovementioned **1** films (right). Bottom: AFM images of **1** films without (right) and with (left) an ionic polyelectrolyte.

internal temperature of the devices can reach values close to 80 °C.[18] Furthermore, the increase in the temperature has a direct impact on (i) the device chromaticity as the emission band shape is broadened because of radiative decay from upper vibrational modes and (ii) the reduction of the external quantum efficiency (EQE) because of the typical thermal quenching leading to decreased photoluminescence quantum yields ($\phi$) of the active layer.

As an example for the former, we have recently deciphered the origin of efficient and stable white LECs based on blue-emitting BN-doped nanographenes.[18] We described how the spontaneous heat generation, which led to pixel temperatures of *ca.* 80 °C, activates a ternary radiative mechanism, leading to efficient white photo- and electroluminescence responses. Thus, self-heating must be considered a synergistic effect to others, such as unbalanced doping and movement of the emitting p−i−n region,[27] as well as microcavity and scattering effects,[28−31] for the changes of the electroluminescence spectrum before the operation steady state is reached. Concerning the device efficiency, theoretical EQE values are regularly calculated with $\phi$ values obtained at room temperature. Because the device temperature can reach values of up to 80 °C,[18] a significant error with respect to the experimental EQE is committed. Thus, the pixel temperature should also be considered upon optimizing the device performance with respect to layer thickness, substrates, driving modes, and so forth. Overall, a full understanding of the temperature influence on the electroluminescence response in LECs would help to focus efforts toward realizing improved emitters and smart device architectures to meet highly efficient and stable devices. In particular, this aspect must be of utmost relevance toward designing lighting devices for medical applications and labeling, as heat dissipation architectures have not been implemented in LECs yet.

Along these lines, the major thrust of this work is the unveiling of the impact of the self-heating on the chromaticity and efficiency of LECs using a benchmark nanographene—that is, hexa-peri-hexabenzocoronene or **1**[32]—as an emerging class of emitters with outstanding device performance. Because LECs show a high versatility with respect to the type of emitters,[4,23,33−39] the impact of self-heating can, indeed, be considered as universal. For instance, Figure S1 displays the working pixel temperature of 40−50 °C LECs with $d^6$-/$d^{10}$-complexes and small molecules operating at pulsed 100 mA/cm$^2$,[7,24,40] while Edman's group has recently showed that polymer-LECs reach 50 °C at 50 mA/cm$^2$.[25] Our interest on nanographenes lies on their high $\phi$, ambipolar carrier properties, sound thermal and redox stabilities, and a good solubility in common organic solvents.[32,41,42] Despite these appealing properties, they have barely been investigated as emitters in thin-film lighting devices.[41] In stark contrast, we have recently reported highly stable and efficient red-emitting LECs with contorted nanographenes[24] and highly efficient white-emitting LECs with B−N-doped nanographenes—*vide supra*.[18] In this line, **1**-LECs show one of the best-performing green-emitting LECs based on small-molecule emitters regardless of the chosen driving mode—for example, maximum luminances of 345 cd/m$^2$ and EQEs of 0.35%.[4] Finally, the electroluminescent behavior of **1**-LECs allowed us to contextualize clear relationships between self-heating and the early changes of the electroluminescence spectra as well as the source and magnitude of the error in the experimental/theoretical EQE calculations, accounting for values of up to 40% depending on the driving modes and pixel temperatures.

Overall, this work states the relevance of self-heating as a critical limitation in the optimization of both, device performance (color and efficiency) and device application (medicine, labeling, *etc.*), regardless of the type of the emitter.

## 2. RESULTS AND DISCUSSION

The synthesis and photophysical characterization of **1** in solution was reported elsewhere,[32] showing blue-green fluorescence and yellow-orange phosphorescence at room temperature and 77 K, respectively—as shown in Figure S2. We have further prepared thin films with only **1** and with blends of **1** with the polymer electrolyte mixture used in devices—that is, 1/PS/PEO/LiOTf in a mass ratio 10:0.9:2.6:0.78, being PS (polystyrene), PEO (polyethylene oxide), and LiOTf (lithium triflate); see the Supporting Information for more details. Atomic force microscopy (AFM) assays confirm that both films show a similar homogeneous morphology with a root-mean-square roughness of around 2 fl


https://dx.doi.org/10.1021/acsami.0c06783
ACS Appl. Mater. Interfaces XXXX, XXX, XXX−XXX

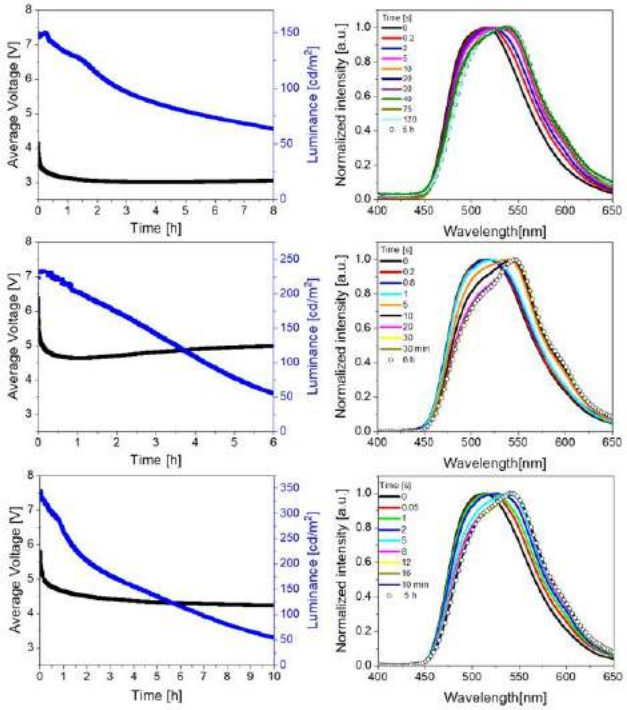


**Figure 2.** Average voltage and luminance *vs* time (left) and selected electroluminescence bands over time (right) of **1**-LECs driven at pulsed currents of 15 (top), 25 (center), and 55 (bottom) mA.

**Table 1. Figures of Merit of 1-LECs Driven at Pulsed Current and Constant Voltage**

| driving mode [mA] | luminance [cd/m²] | $t_{on}$[c] [min] | $t_{1/2}$[d] [h] | $E_{tot}$[e] [J] | efficiency [cd/A] | EQE[f] [%] | *x*/*y* CIE color coordinates (fresh-final) |
|---|---|---|---|---|---|---|---|
| 15 mA[a] | 157 ± 13 | 0.48 ± 0.03 | 5.8 ± 0.6 | 483 ± 51 | 0.20 ± 0.02 | $8.6 \times 10^{-2} \pm 1.1 \times 10^{-2}$ | 0.31–0.37/0.49–0.52 |
| 25 mA[a] | 233 ± 21 | 0.24 ± 0.02 | 3.8 ± 0.3 | 469 ± 49 | 0.18 ± 0.02 | $2.5 \times 10^{-2} \pm 2.7 \times 10^{-3}$ | 0.31–0.38/0.49–0.52 |
| 55 mA[a] | 343 ± 28 | 0.18 ± 0.02 | 3.0 ± 0.2 | 545 ± 56 | 0.12 ± 0.01 | $7.2 \times 10^{-3} \pm 9 \times 10^{-4}$ | 0.31–0.36/0.49–0.54 |
| 3.5 V[b] | 12 ± 2 | 12.0 ± 0.01 | 5.5 ± 0.6 | 35 ± 4 | 0.12 ± 0.01 | $3.5 \times 10^{-1} \pm 3.8 \times 10^{-2}$ | 0.29–0.32/0.44–0.44 |
| 4.5 V[b] | 36 ± 4 | 3.1 ± 0.03 | 0.23 ± 0.2 | 4.4 ± 0.5 | 0.20 ± 0.02 | $1.9 \times 10^{-1} \pm 2.2 \times 10^{-2}$ | 0.30–0.33/0.44–0.46 |
| 6 V[b] | 133 ± 14 | 0.60 ± 0.05 | 0.17 ± 0.02 | 12 ± 0.1 | 0.11 ± 0.01 | $1.3 \times 10^{-2} \pm 1.7 \times 10^{-3}$ | 0.30–0.34/0.44–0.53 |

[a]Pulsed mode. [b]Constant mode. [c]Turn on time: time to reach the maximum luminance. [d]Lifetime: time to reach 50% of the maximum luminance. [e]Total emitted energy: calculated from integration of the radiant flux of the device *vs* time from $t = 0$ (application of bias) to $t = t_{1/2}$. [f]External quantum efficiency: ratio of emitted photons per injected electrons.

fi

nm—as shown in Figure 1. Similar to the photoluminescence in solution, both films exhibit a well-structured emission centered at *ca.* 500 nm with associated $\phi$ values of 23 and 14% with and without a polymer electrolyte, respectively—as shown in Figure 1, while it is very interesting to note the lack of phosphorescence in thin films at 77 K.

To study the electroluminescence behavior of **1**, a series of devices with the architecture ITO/PEDOT:PSS (70 nm)/**1**/PS/PEO/LiOTf (10:0.9:2.6:0.78; 70 nm)/Al were prepared—see the Supporting Information for more details. Here, this polymer electrolyte mixture was already proposed by Edman and co-workers to avoid phase separation upon film forming and over time.[43] Indeed, it was selected as other commonly used matrices [*i.e.*, trimethylol propane ethoxylate (TMPE)/LiOTf] led to phase separation upon device fabrication. These devices were driven at a pulsed current of 15, 25, and 55 mA, monitoring luminance, color, and electrical features over time—as shown in Figure 2 and Table 1. Regardless of the f2t1 applied current, they exhibited the typical LEC behavior with a high initial average voltage that exponentially reduces, reaching a plateau close to the energy band gap of **1**. This goes hand-in-hand with an initial increase in the luminance toward its maximum value that then slowly decreases, realizing stabilities—that is, lifetime/total emitted energy—of 5.8 h/483 J, 3.8 h/469 J, and 3 h/545 J for 15, 25, and 55 mA, respectively. Finally, the device efficiency linearly decreases from 0.20, 0.18, and 0.12 cd/A upon increasing the applied current. Contextualizing the abovementioned device performance, **1**-LECs stand among the best in the prior art of green-emitting small-molecule LECs.[44−47]



https://dx.doi.org/10.1021/acsami.0c06783
ACS Appl. Mater. Interfaces XXXX, XXX, XXX−XXX

Interesting are the changes in the electroluminescence spectra under operation—as shown in Figure 2. At the very early stage, a broad emission band with a slightly red-shifted maximum peak that is associated to a green emission—that is, $\lambda_{max}$ = 510 nm; $x/y$ CIE color coordinates of 0.31/0.49—was noted at any applied current—as shown in Figures 2 and 3.

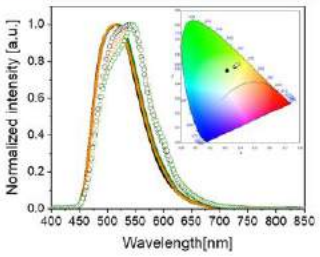


**Figure 3.** Electroluminescence emission bands and their respective $x/y$ CIE color coordinates (inset) of fresh (solid) and after 1 h of driving (open) 1-LECs driven at 15 (black), 25 (orange), and 55 (green) mA.

The differences between the photo- and electroluminescence responses might be attributed to the electric polarization effect that modifies the radiative vibrational deactivation rates and provokes the stabilization of the excited state.[48] However, the electroluminescence band quickly sharpens—as shown in Figure 2, featuring a final structured yellowish green emission—that is, $\lambda_{max}$ at 545 nm with a shoulder at 505 nm; $x/y$ CIE color coordinates of 0.34/0.50, as shown in Figure 3. Interestingly, the time to reach a stable electroluminescence spectrum depends on the applied current. For instance, Figure 2 shows that the electroluminescence spectrum stabilizes after 120 s, 30 s, and 8 s for devices driven at 15, 25, and 55 mA, respectively. Common to all the devices, the electroluminescence energy onset of the band and the full width at half-maximum values of the electroluminescence spectra hold constant at *ca.* 2.75 eV and *ca.* 95 nm, pointing out that the same excited state is responsible for the initial and final emission features. At this point, we can discard the contribution of triplet excited states to the electroluminescence. On the one hand, phosphorescence was not observed at 77 K in thin films—as shown in Figure 1. On the other hand, electroluminescence and phosphorescence from frozen solutions are clearly dissimilar; the latter consists of a band centered at $\lambda_{max}$ at 580 nm with shoulders at 630 and 680 nm—as shown in Figure S2.

Because observed electroluminescence changes rapidly occur before the electrical steady-state regime of the device is reached and hold over the lifespan of the devices, we ruled out effects related to (i) variations in the internal local electric field distribution[24,49−52] and (ii) microcavity effects due to the movement of the emitting p−i−n region.[27] In addition, the formation of emitting degradative species was also discarded using spectroscopic techniques. In short, static electrochemical impedance spectroscopy (EIS) measurements—that is, the frequency scan at increasing applied voltages from 0 to 5 V, as shown in Figures 4, S3, and S4—of fresh devices show a common LEC behavior: (i) an initial decrease in the resistance at biases below the energy band gap (*ca.* 3.0 V), indicating the formation of electrical double layers at the electrode interfaces, and (ii) a further resistance decrease that holds at higher

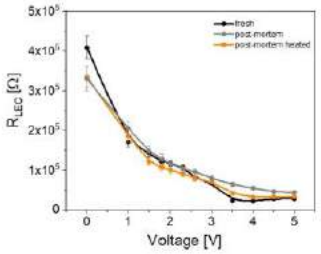


**Figure 4.** Resistance values *vs* applied voltage of fresh, used (pulsed 25 mA), and heated (60 °C for 1 h) 1-LECs.

biases, which accounts for the formation of the doped regions and the autosustained charge recombination.[7,24,39,53−55] In contrast, used devices have been polarized, featuring slightly decreased resistance values than fresh devices and a linear decrease in the resistance upon biasing from 0 to 5 V. By heating them at 60 °C for 1 h, the polarization induced by previous biasing is erased and the resistance *versus* applied voltage resembles that of fresh devices with a clear drop at *ca.* 3.5−4 V. Here, the slightly higher resistance observed above the threshold voltage in used devices may suggest slight degradation. However, the absorption and emission features of fresh and used devices are similar—as shown in Figure S5. Therefore, we discard degradation as the responsible for the change in electroluminescence over time.

Next, the electroluminescence behavior is put into context with the direct comparison with the photoluminescence of the films. The PL spectrum features a rich vibrational structure covering a spectral range from 476 to 590 nm—as shown in Figures 1 and 5. As a matter of fact, the vibrational structure

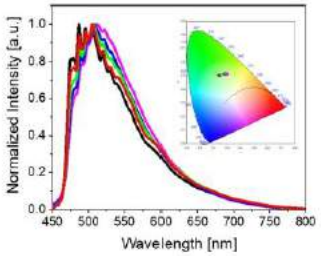


**Figure 5.** Photoluminescence spectra ($\lambda_{exc}$ = 405 nm) of **1** thin films with the same composition as **1**-LECs upon heating at rt (black), 50 °C (red), 100 °C (green), 150 °C (blue), and 200 °C (magenta), with their respective $x/y$ CIE coordinates (inset).

can easily be altered applying heat or electric fields. To shed light onto temperature-dependent emission, we studied the photoluminescence of **1**-films with the same composition as **1**-LECs under vacuum upon increasing temperature from rt to 200 °C—as shown in Figure 5. Uncommonly, the emission intensity is fivefold increased at high temperatures. This is corroborated by the improvement of $\phi$ upon increasing the temperature—as shown in Figure S6. The reasons leading to this rare increase are not fully understood yet. This could be related to a reduced vibrational exchange energy between singlet excited states or temperature-induced short-range morphological changes in the films, reducing intermolecular


https://dx.doi.org/10.1021/acsami.0c06783
ACS Appl. Mater. Interfaces XXXX, XXX, XXX−XXX

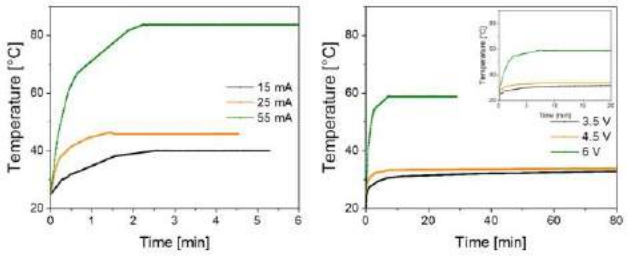


**Figure 6.** Temperature rise in 1-LECs using pulsed currents (left) and constant voltage (right). Inset: zoom on the first 20 min of measurement. The error in the temperature measurement is of ±2 °C.

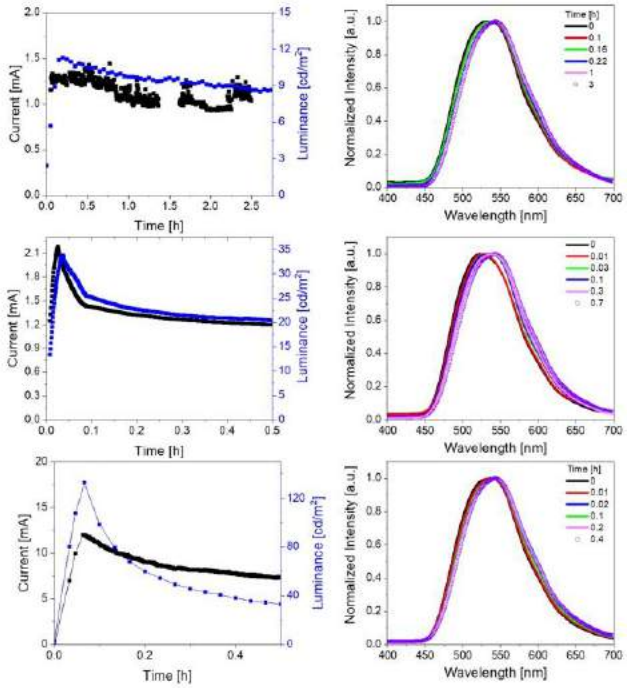


**Figure 7.** Current and luminance *vs* time (left) and selected electroluminescence bands over time (right) of 1-LECs driven at a constant voltage of 3.5 (top), 4.5 (center), and 6.5 (bottom) V.

interactions like aggregates.[56,57] As far as the emission band shape is concerned, the high-energy vibrational features ($\lambda$ < 500 nm) decrease, while the low-energy vibrational peaks ($\lambda$ > 530 nm) are enhanced upon increasing the temperature. This leads to a color emission change from blue to yellow−green that resembles those in the devices. Finally, the $\tau$ ($\lambda_{exc}$ = 405 nm) values at 486 and 600 nm upon heating were similar in the nanosecond regime—as shown in Table S1, corroborating the exclusive presence of fluorescence on the overall emission.

In view of the above-described results, the reason underlying the electroluminescence changes might imply (i) the modification of the radiative deactivation rate of excited vibrational states promoted by the synergistic effect of the external electric field and the increased pixel temperature and (ii) doping-induced self-absorption.[58] Regarding the first point, the pixel temperature might be considered as the dominant process because the average voltage showed a similar slow decay and plateau—as shown in Figure 2, indicating that the applied electric field distribution across the active layer might follow a similar evolution. As for the second point, self-absorbing species would cause a continuous variation in the electroluminescence response, which, however, does not change relevantly after, on average, minutes of measurements. In addition, the temperature-dependent photoluminescence shows the same behavior as the electroluminescence, while self-absorption does not apply here.

Further corroboration comes from the correlation between the increase in the pixel temperature and the spectral changes


https://dx.doi.org/10.1021/acsami.0c06783
ACS Appl. Mater. Interfaces XXXX, XXX, XXX−XXX

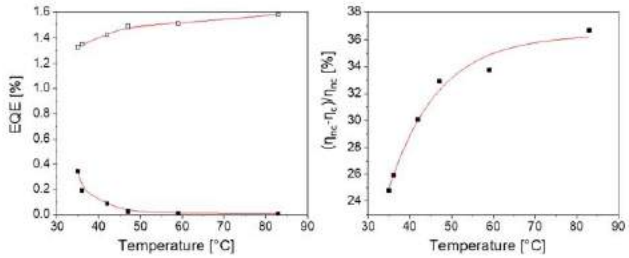


**Figure 8.** Left: Experimental (solid symbol) and theoretical (open symbol) EQE values *vs* pixel working temperature of **1**-LECs operating at pulsed current and constant voltage driving modes. Right: Error *vs* pixel working temperature of **1**-LECs operating at pulsed current and constant voltage driving modes. The red lines display the fittings. The fitting models are presented in the Supporting Information.

using different driving conditions. In particular, operating at pulsed 15 mA leads to an exponential increase in temperature up to 40 °C during the first 2 min—as shown in Figure 6, holding constant over time. The increase in the current compliance leads to both, a quicker heat generation—for example, 40 °C is reached at 24 s (25 mA) and 7 s (55 mA)—and higher maximum temperature values of *ca.* 50 °C (25 mA) and 90 °C (55 mA). The increase in the pixel temperature nicely fits with the time to stabilize the electroluminescence response under the pulsed driving mode—that is, 2 min, 20 s, and 8 s, for 15, 25, and 55 mA, respectively, as shown in Figure 2. Noteworthy, the temperature rise profile is similar to that commented by Edman and co-workers.[25]

Finally, we also analyzed devices driven at constant applied voltage—that is, 3.5, 4.5, and 6 V, as shown in Figure 7 and Table 1. In line with the literature,[8] these devices exhibited similar efficiencies and lower luminance and stability values compared to those driven at pulsed current—as shown in Table 1. Likewise, all the devices show (i) the same initial green and broad electroluminescence spectrum—that is, $\lambda_{max}$ = 520 nm; $x/y$ CIE color coordinates of 0.29/0.44—independent of the driving voltage and (ii) a slow change until a stable yellowish green electroluminescence band is reached—that is, $\lambda_{max}$ = 548 nm; $x/y$ CIE color coordinates of 0.44/0.53. The time to reach a stable emission band decreases from 32 to 13.2 and to 7.2 min for devices driven at 3.5, 4.5, and 6 V, respectively. This behavior corresponds to the time to reach the plateau temperature observed in devices, that is, 30 min (3.5 V), 12 min (4.5 V), and 8 min (6 V).—as shown in Figure 6. The highest temperature values of 35, 36, and 59 °C are reached for 3.5, 4.5, and 6 V, respectively—as shown in Figure 6. This might be related to the reduced density of the injected carrier compared to the pulsed driving mode—for example, 12.5 mA at 6 V.

As mentioned above, **1** shows a peculiar enhancement of the $\phi$ values with the temperature—see the Experimental Section, Figure S6, and Table S2 for details. Taking the $\phi$ of *ca.* 23% at 25 °C as the reference, this figure exponentially increases up to 37% at 83 °C—as shown in Figure S6. This must be translated into an increase in the fraction of excitons that decay radiatively ($\varphi$) under operating conditions. In **1**-LECs, the maximum $\varphi$ is 1/4 of $\phi$ in thin films, as, statistically, 1/4 of the electron−hole recombination produces singlets. Thus, the EQE, which is defined as EQE = $b\varphi/2n^2$, where $b$ is the recombination efficiency (equal to 1 for two ohmic contacts) and $n$ is the refractive index of the glass substrate and is equal to 1.5 (the factor $1/2n^2$ represents the light out-coupling of the device, while we assume that the change in refractive index with temperature is negligible), is also temperature-dependent and must be calculated taking into account the temperature dependence of $\phi$ with respect to the pixel temperature under operation. For instance, after gathering all the abovementioned devices measured at different driving modes, as $\phi$ increases with the temperature, the theoretical EQE increases from 1.28% (rt) to 1.58% (83 °C), in a manner that can be described using a Gompertz growth model—as shown in Figure 8 and Table S3, while the experimental value decreases with the working temperature in a manner that is well-described using a $y = 1/(x + A)$ function—as shown in Figure 8 and Table S4.

The ratio between experimental and theoretical EQE values ($\eta$ = $EQE_{exp}/EQE_{theo}$) is typically used to determine the optimization degree of the devices using different driving modes. At pulsed currents of 15, 25, and 55 mA, $\eta$ values are 0.067, 0.019, and 0.0057 considering $\phi$ at 25 °C, while $\eta$ values of 0.047, 0.013, and 0.0036 are recalculated taking into account the pixel working temperature. Likewise, devices driven at a constant bias of 3.5, 4.5, and 6 V show a $\eta$ value of 0.27, 0.15, and 0.010 and 0.20, 0.11, and 0.0067 with and without considering pixel temperature, respectively. We can contextualize all these results calculating the % error—that is, $((\eta_{nc}-\eta_c)/\eta_{nc}) \times 100$—between the uncorrected ($\eta_{nc}$) and corrected ($\eta_c$) values with the temperature, regardless of the driving mode—as shown in Tables S5 and S6 and Figure 8. Thus, the error *versus* pixel temperature obeys an exponential rise similar to that of $\phi(T)$, accounting for an overestimation error of *ca.* 35% at usual working temperatures (50 °C) that has been long neglected. This simple analysis testifies that self-heating is critical for the optimization of devices driven at pulsed modes as high working temperatures of 40−60 °C are typically reached—as shown in Figure S1. In contrast, the optimization using a constant voltage driving mode seems to be more reliable as long as carrier density is low.

## 3. CONCLUSIONS

This work provides the first comprehensive study about the impact of the self-heating on the device chromaticity and efficiency in LECs. To this end, we have focused on a benchmark nanographene as an emerging class of emitters that lead to outstanding device performances (luminance of 345 cd/m$^2$ and EQE of 0.35%) compared to the prior art in small-molecule-based LECs. The relevance of this work lies on two important findings. On the one hand, a direct relationship between the rise of the pixel temperature (self-heating) and the


https://dx.doi.org/10.1021/acsami.0c06783
ACS Appl. Mater. Interfaces XXXX, XXX, XXX−XXX

changes of the device electroluminescence band shape over time is provided. Thus, a rationale about early chromaticity changes in LECs might also include the heat generation under operating conditions, as a synergistic parameter to others related to optical and electrical phenomena. On the other hand, a source and magnitude of the error upon optimizing the device with respect to $\eta$ as the ratio theoretical/experimental EQE is highlighted. As a matter of fact, $\phi$ values are temperature-dependent and, in turn, the theoretical EQE must be also recalculated taking into account the pixel temperature. Regardless of the driving mode, we have estimated errors of up to *ca.* 35% at usual working temperatures of 40−50 °C in nanographene LECs.

Overall, this work represents a key contribution, highlighting how self-heating is a critical parameter that must be taken into consideration toward (i) rationalizing the design of emitters and device architectures to optimize device performance (color and efficiency) and (ii) engineering of smart devices for applications in medicine and labeling applications, among others.

## 4. EXPERIMENTAL SECTION

**4.1. Materials.** All chemicals were purchased from chemical suppliers and used without further purification. All analytical reagent-grade solvents were purified by distillation. All reactions were carried out under an inert nitrogen atmosphere using standard vacuum line techniques.

**4.2. Synthesis and Spectroscopic, Electrochemical, and Microscopy Characterization.** **1** was synthesized as reported in a previous contribution.[32] Absorption spectra were recorded with a PerkinElmer Lambda 35 ultraviolet (UV)−vis spectrometer. The photoluminescence spectra and $\phi$ values at 25 °C were measured with an FS5 Spectrofluorometer with an integrating sphere SC-30 (Edinburgh Instruments). Photoluminescence measurements at temperatures ranging from 25 to 202 °C were performed upon enclosing HBC films in a CFV-Optistat (Oxford Instruments) equipped with a temperature controller. Films were photoexcited with a TEEM Photonics passive Q-switch Nd:YAG laser (405 nm, 300 ps pulse duration, 170 Hz, pulse energy < 1 mJ) mildly focused on the sample (fluence < 10 mJ/cm$^2$). The photoluminescence emitted by the samples was dispersed using a grating inside a spectrometer (SP2500, Acton Research) and spectrally recorded with a liquid $N_2$-cooled back-depleted CCD (Princeton Instruments). Long-pass filters were employed to reject stray light from the photoexcitation beam into the spectrometer. The photoluminescence spectra were acquired 10 min after the sample reached the desired temperature in order to ensure complete sample thermalization. The temperature dependence of the $\phi$ values by recalculating considering the differences in the integration of the absorption and emission spectra at different temperatures with respect to that measured at rt. Excited state lifetimes ($\tau$) were obtained with a time-correlated single-photon counting (TCSPC) with $\lambda_{exc}$ = 405 nm and the corresponding exponential fitting: $R(t) = \sum_{i=1}^{2} A_i e^{-t/\tau_i}$. The average lifetime values $\langle\tau\rangle$ were obtained with: $\langle\tau\rangle = \frac{A_1\tau_1^2 + A_2\tau_2^2 + A_3\tau_3^2}{A_1\tau_1 + A_2\tau_2 + A_3\tau_3}$.

Device and film temperature was obtained using an FLIR-430sc thermal camera and the absorption scan was performed in 30 s to avoid excessive cooling. Thin films (75 nm) were prepared onto cleaned quartz slides from a filtered solution of **1** (10 mg/mL in THF; without or with an ion-doped matrix, as below described) using a spin-coated matrix at 800 rpm for 30 s, at 1500 rpm for 30 s, and at 3000 rpm for an additional 10 s. AFM measurements were carried out with a Park XE150 instrument (Park Systems Corp., Suwon, South Korea) and the Gwyddion evaluation software.

**4.3. Device Fabrication and Characterization.** Indium−tin oxide (ITO) substrates were purchased from Naranjo Substrates with an ITO thickness of 130 nm. They were extensively cleaned using detergent, water, ethanol, and propan-2-ol as solvents in an ultrasonic bath (frequency 37−70 Hz) for 15 min each. Afterward, the slides were dried with $N_2$ gas and put in a UV−ozone cleaner for 8 min and used directly as described in the main text. As PEDOT:PSS was used to increase reproducibility, the clean plates were coated with 70 nm PEDOT:PSS layers *via* spin-coating. To this end, an aqueous solution of PEDOT:PSS was filtered and mixed with propan-2-ol in a ratio of 3:1. From this solution, 50 $\mu$L was dropped onto the substrate at a rotation speed of 2000 rpm and spun for 60 s. The resulting layers were dried on a hotplate at 120 °C and stored under $N_2$. Thick active layers (100 nm) were deposited from 10 mg/mL **1** combined with a ion-doped matrix consisting of **1**/PS/PEO/LiOTf 10:1.81:2.6:0.78 mass ratio. This was prepared using THF solutions of PS (polystyrene) with $M_w$ 900,000 (10 mg/mL), PEO (polyethylene oxide) (20 mg/mL), and LiOTf (lithium triflate) (10 mg/mL) and spin-coated at 800 rpm for 30 s, at 1500 rpm for 30 s, and at 3000 rpm for an additional 10 s, resulting in 70 nm of the active layer thickness. In all cases, after the deposition of the active layer, the devices were dried under vacuum for 2 h and transferred to an inert atmosphere glovebox (<0.1 ppm $O_2$ and $H_2O$, Angstrom Engineering). Finally, aluminum cathodes (90 nm) were thermally evaporated onto the active layer using a shadow mask under high vacuum (<1 × $10^{-6}$ mbar) in an Angstrom Covap evaporator integrated into the inert atmosphere glovebox. The device statistics involve up to five different devices—that is, a total number of 20 pixels. Time dependence of luminance, voltage, and current was measured by applying constant and/or pulsed voltage and current by monitoring the desired parameters simultaneously using an Avantes spectrophotometer (Avaspec-ULS2048L-USB2) in conjunction with a calibrated integrated sphere Avasphere 30-Irrad and Botest OLT OLED Lifetime-Test System. Electroluminescence spectra were recorded using the abovementioned spectrophotometer. The temperature of the devices upon driving was recorded with a FLIR 430-sc thermal camera. EIS assays were carried out with a potentiostat/galvanostat (Metrohm $\mu$AutolabIII) equipped with a frequency response analyzer module (FRA2). Measurements were performed at the applied voltage range from 0 to 6 V and fitted with the Nova software using the circuit model, as shown in Figure S3. The ac signal amplitude was set to 15 mV and modulated in a frequency range from 10 to 1 MHz. The Nova 1.11 software was used to obtain the parameters from the equivalent circuit. With this data at hand, the resistance of the intrinsic nondoped region ($R_{LEC}$) was directly obtained. The temperature of the devices upon driving was recorded with a FLIR 430-sc thermal camera.

## ■ ASSOCIATED CONTENT

### Supporting Information

The Supporting Information is available free of charge at https://pubs.acs.org/doi/10.1021/acsami.0c06783.

Thermal pictures of selected LECs, absorption spectrum of **1**, EIS circuits used to fit EIS data, absorption spectrum of 1-LECs (fresh and used), $\Phi/\Phi_{rt}$ ratio at different temperatures, photoluminescence features of **1**: electrolyte matrix at different temperatures, $\tau$ values measured at different temperatures, model and parameters employed to describe EQE-related figures of merit of **1**-LECs, and experimental and theoretical EQE-related figures of merit of **1**-LECs (PDF)

## ■ AUTHOR INFORMATION

### Corresponding Author

Rubén D. Costa − *IMDEA Materials Institute, E-28906 Getafe, Spain;* orcid.org/0000-0003-3776-9158; Email: ruben.costa@imdea.org



https://dx.doi.org/10.1021/acsami.0c06783
ACS Appl. Mater. Interfaces XXXX, XXX, XXX−XXX

# Supporting Information

**Revealing the impact of heat generation using nanographene based light-emitting electrochemical cells**

*Elisa Fresta,[ab] Jacopo Dosso,[c] Juan Cabanillas-Gonzalez,[d] Davide Bonifazi,[c] and Rubén D. Costa*[a]*

a. IMDEA Materials Institute, Calle Eric Kandel 2, E-28906 Getafe, Madrid, Spain. ruben.costa@imdea.org

b. Universidad Autónoma de Madrid, Departamento de Física Aplicada, Calle Francisco Tomás y Valiente, 7, 28049 Madrid, Spain.

c. School of Chemistry, Cardiff University, CF10 3AT Cardiff, Great Britain.

d. IMDEA Nanoscience, Calle Faraday 9, 28049 Madrid, Spain.

**Outline**

## 1. Figures

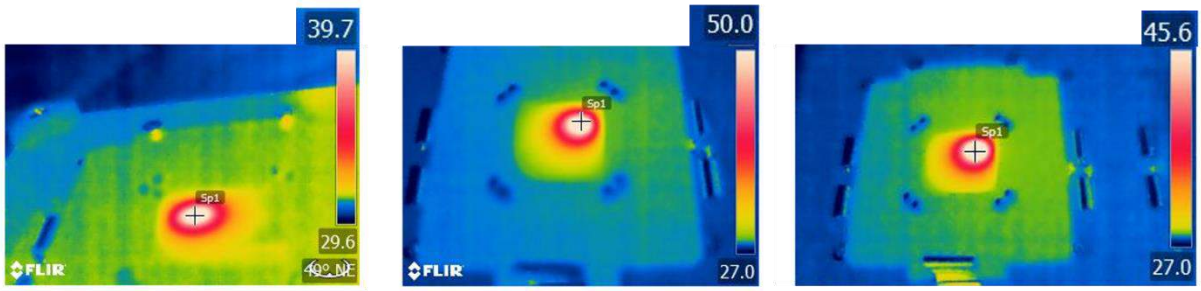


**Figure S1**. Thermal pictures of LECs based on Ir-iTMCs (left, maximum temperature reached: 39.7 °C; ITO/PEDOT:PSS(70 nm)/[Ir(ppy)(tbbpy)]$PF_6$(100 nm)/Al), with ppy: phenylpyridine, tbbpy:tert-butyl pyridine, small molecules (center, maximum temperature reached 50 °C; ITO/PEDOT:PSS(70 nm)/hexa-peri-hexa-benzoborazinocoronene (70 nm)/Al), and Cu-iTMCs (right, maximum temperature reached 45.6 °C; ; ITO/PEDOT:PSS(70 nm)/[Cu(bpy)(POP)]$PF_6$ (110 nm)/Al), with POP: (bis(2-(diphenylphosphino)phenyl)ether) all driven at pulsed current of 100 mA/cm$^2$.

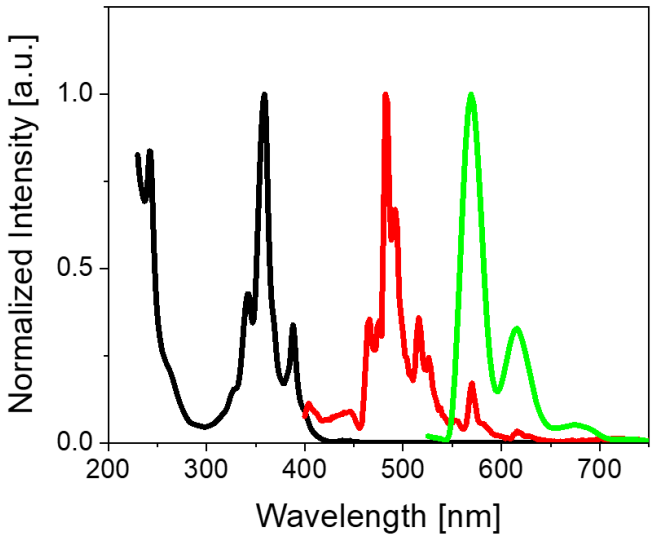


**Figure S2.** UV-Vis absorption spectrum in $CH_2Cl_2$ (black) and emission spectrum ($\lambda_{exc}$=355 nm) at rt. in $CH_2Cl_2$ (red) and at 77 K in frozen matrix of $CH_2Cl_2$ (green) of **1**.

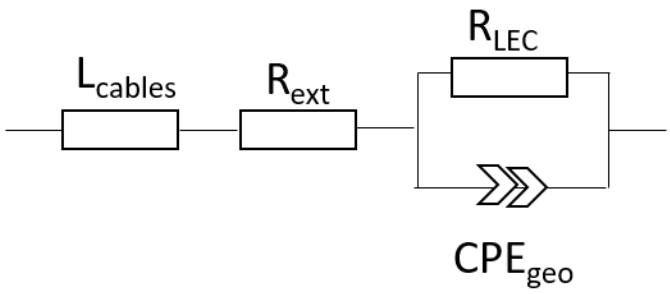


**Figure S3.** Simplified circuit model with only electrical resistance ($R_{LEC}$) and geometrical capacitance ($CPE_{geo}$) used for static EIS assays. An external resistor ($R_{ext}$) and inductor elements for the cables ($L_{cables}$) were also included in the model.

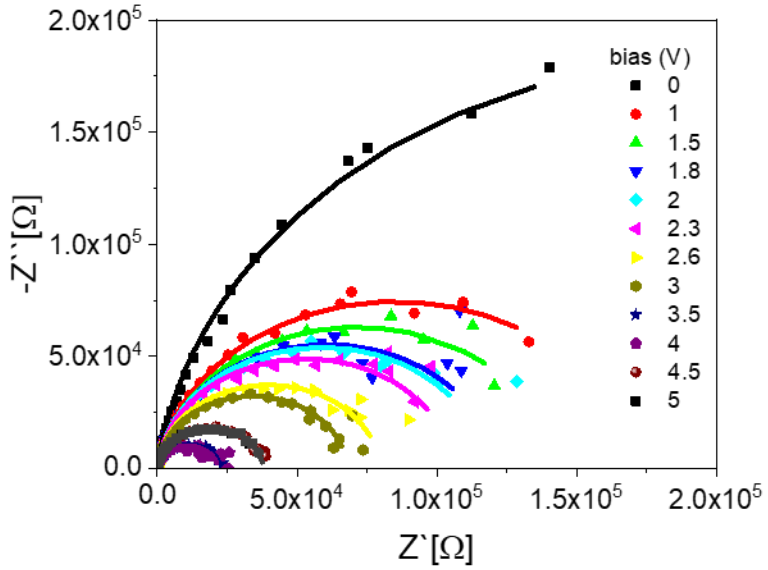
2.0x10^5
1.5x10^5
1.0x10^5
5.0x10^4
0.0
-Z``[Ω]
0.0
5.0x10^4
1.0x10^5
1.5x10^5
2.0x10^5
Z`[Ω]
bias (V)
0
1
1.5
1.8
2
2.3
2.6
3
3.5
4
4.5
5

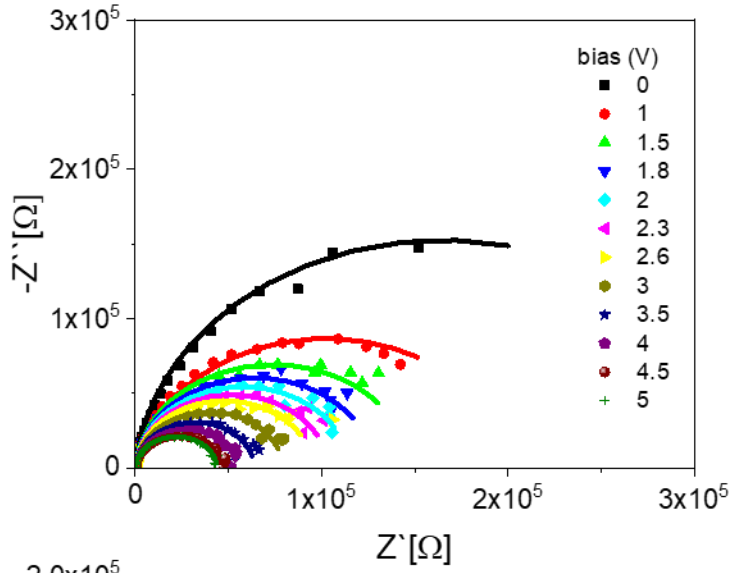
3x10^5
2x10^5
1x10^5
0
-Z``[Ω]
0
1x10^5
2x10^5
3x10^5
Z`[Ω]
bias (V)
0
1
1.5
1.8
2
2.3
2.6
3
3.5
4
4.5
5

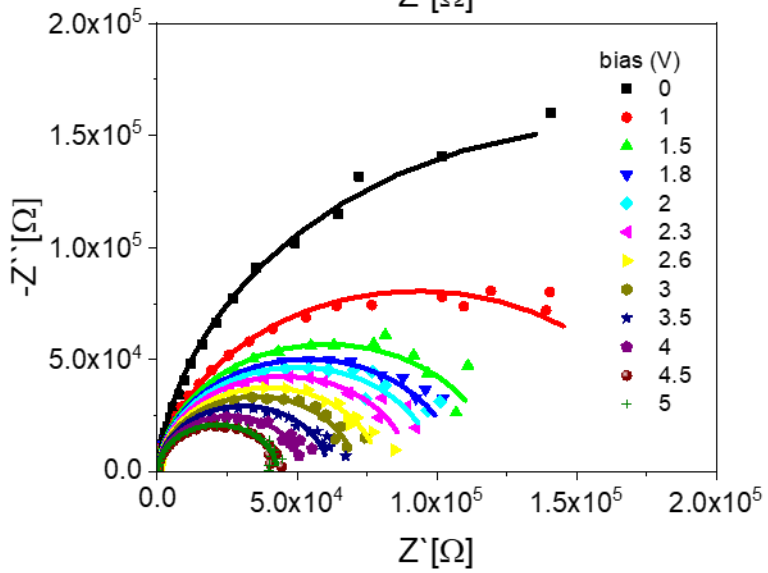
2.0x10^5
1.5x10^5
1.0x10^5
5.0x10^4
0.0
-Z``[Ω]
0.0
5.0x10^4
1.0x10^5
1.5x10^5
2.0x10^5
Z`[Ω]
bias (V)
0
1
1.5
1.8
2
2.3
2.6
3
3.5
4
4.5
5

**Figure S4.** Nyquist plots of fresh (top), used at 25 mA (middle), and heated at 60°C (bottom) **1**-LECs measured upon constant bias (see legend). The fittings are shown in solid lines.

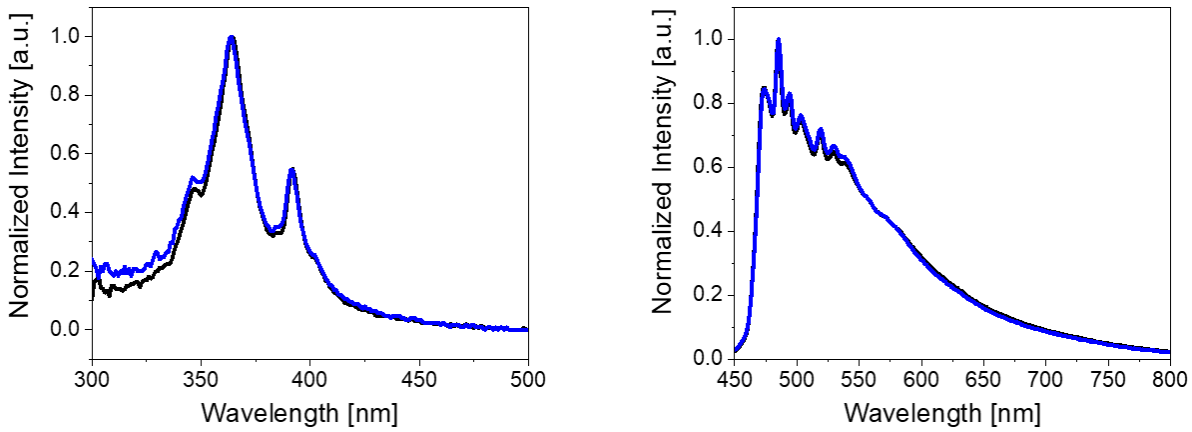


**Figure S5.** Absorption (left) and photoluminescence (right) spectra of fresh (black) and used (blue) **1**-LECs.

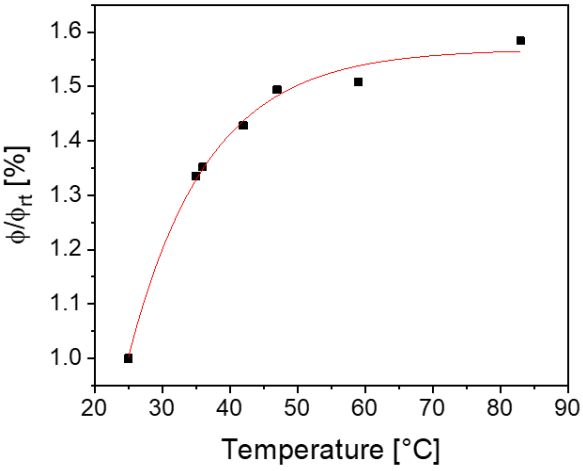


**Figure S6.** $\phi/\phi_{rt}$ of **1**-films upon increasing temperature. The red line displays the fitting, which are detailed in the table on the right.

**Table S1.** $\tau$ values measured at different temperatures ($\lambda_{exc}$=405 nm).

| Temperature | $\tau_x$ | $\tau$ *at* 486 nm [ns] | $\tau$ *at* 600 nm [ns] | $A_x$ | *A at* 486 nm | *A at* 600 nm |
|---|---|---|---|---|---|---|
| rt | $\tau_1$ | 8.6 | 7.39 | $A_1$ | 7591 | 10069 |
| | $\tau_2$ | 3.3 | 0.71 | $A_2$ | 3120 | -5011 |
| | $\tau_3$ | 17.3 | 16.0 | $A_3$ | 1505 | 2449 |
| | $<\tau>$ | 8.3 | 14.7 | - | - | - |
| 325 K | $\tau_1$ | 8.8 | 8.25 | $A_1$ | 6007 | 10499 |
| | $\tau_2$ | 3.7 | 1.00 | $A_2$ | 2654 | -4768 |
| | $\tau_3$ | 17.5 | 17.3 | $A_3$ | 1085 | 2303 |
| | $<\tau>$ | 8.4 | 15.2 | - | - | - |
| 375 K | $\tau_1$ | 9.0 | 8.4 | $A_1$ | 5955 | 10448 |
| | $\tau_2$ | 3.9 | 1.2 | $A_2$ | 2846 | -3982 |
| | $\tau_3$ | 17.0 | 16.5 | $A_3$ | 990 | 2341 |
| | $<\tau>$ | 8.3 | 13.8 | - | - | - |
| 425 K | $\tau_1$ | 8.4 | 8.8 | $A_1$ | 6261 | 10570 |
| | $\tau_2$ | 3.3 | 1.4 | $A_2$ | 2603 | -2966 |
| | $\tau_3$ | 15.3 | 16.6 | $A_3$ | 1154 | 1882 |
| | $<\tau>$ | 7.9 | 12.6 | - | - | - |
| 475 K | $\tau_1$ | 7.29 | 8.8 | $A_1$ | 6066 | 11963 |
| | $\tau_2$ | 2.6 | 1.4 | $A_2$ | 2023 | -3843 |
| | $\tau_3$ | 13.0 | 18.0 | $A_3$ | 1472 | 972 |
| | $<\tau>$ | 7.1 | 12.9 | - | - | - |

**Table S2**. Models and parameters employed to describe $\phi/\phi_{rt}$ at different device temperatures.

| Model | ExpGrowth1 |
|---|---|
| Equation | Y=a*exp(x/t)+ b |
| a | -4.83028±0.93039 |
| t | -11.66134±1.07521 |
| b | 1.56854±0.01703 |
| R-square | 0.99307 |

**Table S3**. Models and parameters employed to describe the theoretical EQE) at different device temperatures.

| Model | Gompertz |
|---|---|
| Equation | Y=a*exp(-exp(-k*(x-xc) |
| a | 1.5585±0.00175 |
| xc | 12.62739±0.45394 |
| k | 0.08267±0.00176 |
| R-square | 0.99274 |

**Table S4**. Models and parameters employed to describe the experimental EQE) at different device temperatures.

| Model | Reciprocal |
|---|---|
| Equation | Y=1/(x+A) |
| a | -31.90311±0.039 |
| R-square | 0.9704 |

**Table S5.** Models and parameters employed to describe the % error $((\eta_{nc}-\eta_c)/\eta_{nc}) \times 100$ (right) at different device temperatures.

| Model | ExpGrowth1 |
|---|---|
| Equation | Y=a*exp(x/t)+ b |
| a | -215.46492±135.28644 |
| t | -11.91689±2.67395 |
| b | 36.3932±0.87596 |
| R-square | 0.9821 |

**Table S6.** Experimental and theoretical EQE-related figures-of-merit of **1**-LECs driven at pulsed current and constant voltage.

| Driving Mode | $T$ [°C] | $\phi/\phi_{rt}$ | Exp[b] *EQE* [%] | Theo[c] *EQE* [%] | $\eta_c$ | $\eta_{nc}$ |
|---|---|---|---|---|---|---|
| 3.5 V | 35±2 | 1.33±0.02 | 0.35±0.038 | 1.69±0.21 | 0.20±0.02 | 0.27±0.03 |
| 4.5 V | 36±2 | 1.35±0.02 | 0.19±0.022 | 1.72±0.21 | 0.11±0.01 | 0.15±0.02 |
| 15 mA[a] | 42±2 | 1.43±0.02 | 0.086±0.001 | 1.83±0.22 | 0.047±0.005 | 0.067±0.001 |
| 25 mA[a] | 47±2 | 1.49±0.02 | 0.025±0.0027 | 1.90±0.22 | 0.013±0.001 | 0.019±0.002 |
| 6 V | 59±2 | 1.51±0.03 | 0.013±0.0017 | 1.93±0.23 | 0.0067±0.0008 | 0.010±0.001 |
| 55 mA[a] | 83±2 | 1.58±0.03 | 0.0072±0.0009 | 2.04±0.23 | 0.0036±0.0004 | 0.0057±0.0006 |

a: measured in pulsed mode. b: experimental. c: theoretical.

Section 3.2.2: Origin of the Exclusive Ternary Electroluminescent Behavior of BN-Doped Nanographenes in Efficient Single-Component White Light-Emitting Electrochemical Cells

ADVANCED FUNCTIONAL MATERIALS

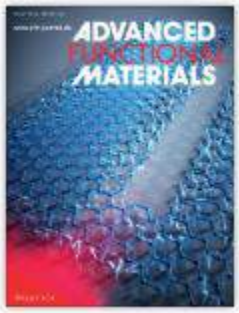


Early View
Online Version of Record before inclusion in an issue
1906830

Elisa Fresta,[1,2] Jacopo Dosso,[3] Juan Cabanillas-Gonzalez,[4] Davide Bonifazi,[3,5] and Rubén D. Costa[*1]

1. IMDEA Materials Institute, Calle Eric Kandel 2, E-28906 Getafe, Madrid, Spain.
2. Universidad Autónoma de Madrid, Departamento de Física Aplicada, Calle Francisco Tomás y Valiente, 7, 28049 Madrid, Spain.
3. School of Chemistry, Cardiff University, CF10 3AT Cardiff, Great Britain.
4. IMDEA Nanoscience, Calle Faraday 9, 28049 Madrid, Spain.
5. Institute of Organic Chemistry, Faculty of Chemistry, University of Vienna, Währinger Strasse 38, 1090 Vienna, Austria.

ADVANCED FUNCTIONAL MATERIALS
www.afm-journal.de

# Origin of the Exclusive Ternary Electroluminescent Behavior of BN-Doped Nanographenes in Efficient Single-Component White Light-Emitting Electrochemical Cells

*Elisa Fresta, Jacopo Dosso, Juan Cabanillas-González, Davide Bonifazi, and Rubén D. Costa**

**White-light-emitting electrochemical cells (WLECs) still represent a significant milestone, since only a few examples with moderate performances have been reported. Particularly, multiemissive white emitters are highly desired, as a paradigm to circumvent phase separation and voltage-dependent emission color issues that are encountered following host:guest and multilayered approaches. Herein, the origin of the exclusive white ternary electroluminescent behavior of BN-doped nanographenes with a $B_3N_3$ doping pattern (hexa-perihexabenzoborazinocoronene) is rationalized, leading to one of the most efficient (≈3 cd $A^{-1}$) and stable-over-days single-component and single-layered WLECs. To date, BN-doped nanographenes have featured blue thermally activated delayed fluorescence (TADF). This doping pattern provides, however, white electroluminescence spanning the whole visible range (*x*/*y* CIE coordinates of 0.29–31/0.31–38 and average color rendering index (CRI) of 87) through a ternary emission involving fluorescence and thermally activated dual phosphorescence. This temperature-dependent multiemissive mechanism is operative for both photo- and electroluminescence processes and holds over the device lifespan, regardless of the device architecture, active layer composition, and operating conditions. As such, this work represents a new stepping-stone toward designing a new family of multiemissive white emitters based on BN-doped nanographenes that realizes one of the best-performing single-component white-emitting devices compared to the prior-art.**

## 1. Introduction

White light-emitting electrochemical cells (WLECs) have recently been attracting much interest as they offer low-cost, single-layer, and air-stable alternatives for lighting applications, such as signaling, panels, and labeling.[1–5] However, efficient and stable single-component and single-layered WLECs still represent a significant milestone.[6–8] Up to date, there are four approaches to fabricate WLECs. First, host:guest active layers mixing a high-energy emitting host with a low-energy emitting guest are subjected to several drawbacks, such as phase separation, poor color stability over time, extreme sensitivity to the layer thickness and the ratio between emitters, as well as voltage-dependent color emission.[9–11] Second, multilayered architectures based on either tandem or color down-converting schemes suffer from the high production costs due to complicate architectures and the low feasibility to customize tailored emitters.[12,13] A third strategy is to exploit white-emitting excimers or exciplex species.[14,15] This has, however, given poorly efficient devices due to the intrinsic low photoluminescence quantum yields ($\phi$) of these emitting species. Finally, the most desired approach is the use of intrinsically white-emitting molecules for single-component WLECs. Up to date, there are a handful number of contributions involving conjugated polymers (CPs)[16,17] and small molecules (SMs).[18,19] Edman and Pei groups have reported excellent examples in CP-WLECs designing emitters with different multifluorophoric units.[16,17] They achieved encouraging LEC performances with efficiencies of ≈3 cd $A^{-1}$, color rendering index (CRI) of ≈80, and stabilities of few hours. Recently, devices with low efficiencies (<0.5 cd $A^{-1}$), CRI of around 90, and stabilities of <1 d have been realized with TIPs-functionalized pentacenes[18] and free-base porphyrins[19] controlling the photoinduced degradation upon film forming and the strength of local electric-fields under operation, respectively.

In parallel, a few groups working in single-component white organic light-emitting diodes (WOLEDs) have unraveled new white emission mechanisms using SMs.[20–22] For instance, Li's group and others have reported on a low-energy electromeric

E. Fresta, Dr. R. D. Costa
IMDEA Materials Institute
Calle Eric Kandel 2, Getafe, E-28906 Madrid, Spain
E-mail: ruben.costa@imdea.org
E. Fresta
Departamento de Física Aplicada
Universidad Autónoma de Madrid
Calle Francisco Tomás y Valiente 7, 28049 Madrid, Spain
J. Dosso, Prof. D. Bonifazi
School of Chemistry
Cardiff University
CF10 3AT Cardiff, UK
Dr. J. Cabanillas-González
IMDEA Nanoscience
Calle Faraday 9, 28049 Madrid, Spain
The ORCID identification number(s) for the author(s) of this article can be found under https://doi.org/10.1002/adfm.201906830.

DOI: 10.1002/adfm.201906830

 

emission that was highly favored upon the influence of the electric field,[20] while Mazzeo et al. have reported on the formation of low-energy emitting cross-like dimers upon film forming.[21] Finally, Park and collaborators prepared a white-emitting SM with two fluorophores, in which the energy transfer between them was blocked allowing electroluminescence from both moieties.[22] All-in-all, these examples show similar performances to those of WLECs, achieving high CRI values (70–85) and efficiencies of ≈1 cd $A^{-1}$. Despite the excellent color features of SM-based lighting devices, the efficiency is highly limited by the low $\phi$ value in thin films and the 25% electron-hole recombination yield.

In light of the above mentioned, single-component white-emitting devices based on a multiemissive electroluminescent response—i.e., equally efficient dual or ternary emission—has not been accomplished yet. Indeed, the molecular design of emitters featuring ternary photoluminescence mechanisms is still in its infancy with one of the very first examples recently reported by Yang and co-workers;[23] though it has not been proven in lighting devices so far. Hence, both the molecular design of multiemissive compounds and its effective use toward white devices represent one of the most significant milestones in the thin-film lighting field.

In this context, this work provides the first example that fully meets the requirements to open a new approach toward single-component and single-layered white-emitting devices. In short, we deciphered the electroluminescent features of a BN-doped nanographene with the $B_3N_3$ doping pattern—i.e., hexa-peri-hexabenzoborazinocoronene or **1** as shown in **Figure 1**—in thin films using the LEC concept. Despite its blue fluorescence in both solution and thin films at room temperature,[24] efficient (≈3 cd $A^{-1}$) and stable over days WLECs with a broad white spectrum peaking at 435, 505, 550, 695, and 750 nm—i.e., $x/y$ CIE color coordinates of 0.28–0.31/0.31–0.38 and average CRI = 87—were easily achieved regardless of active layer composition—i.e., type of ion-doped matrix and its interaction with **1** –, device architecture and operation—i.e., thickness, electrodes, and driving conditions. The origin of this exclusive white electroluminescent response is a highly desired multiemissive mechanism involving a ternary emission that includes

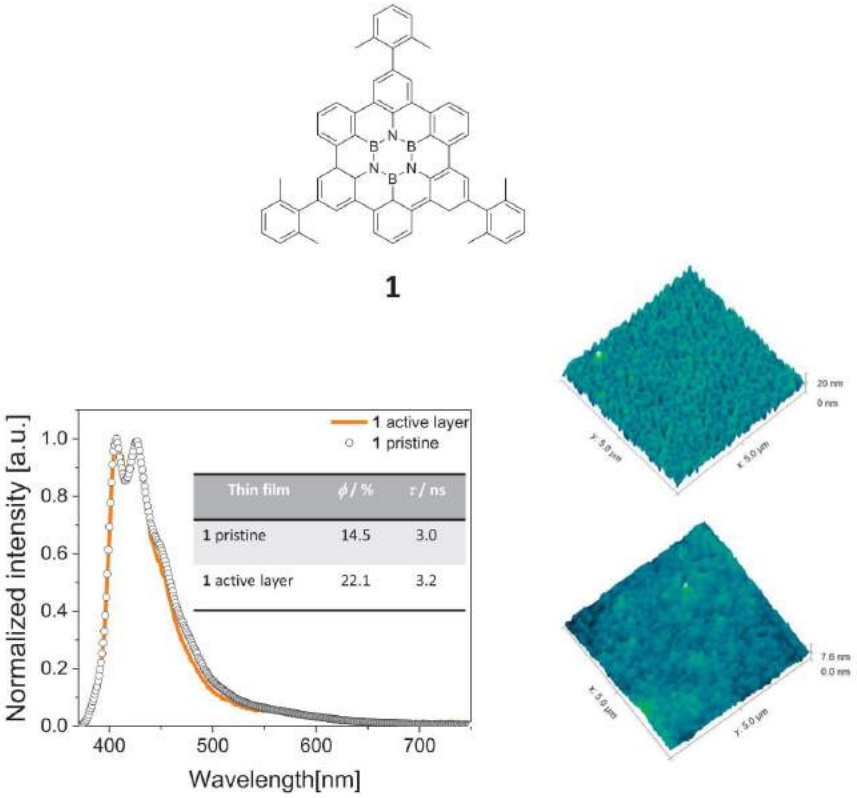


**Figure 1.** Top: chemical structure of **1**. Bottom, left: photoluminescence spectra ($\lambda_{exc}$ = 355 nm) of thin films based on **1** with (active layer) and without (pristine) ionic matrix onto ITO/PEDOT:PSS substrates in air at room temperature. Inset: table summarizing the photoluminescence figures-of-merit, namely, $\phi$ and $\tau$. Bottom, right: AFM pictures of thin films based on **1** with (active layer; top) and without ionic matrix (pristine; bottom).

fluorescence and a thermally activated dual phosphorescence. This temperature dependent multiemissive mechanism is an intrinsic feature of **1** as it is operative for both photo- and electroluminescence processes.

Hence, this work shows an exclusive emission behavior of BN-doped nanographenes with the $B_3N_3$ doping pattern, leading to one of the most efficient and stable WLECs compared to the prior-art. This will represent a landmark toward the designing a new family of white emitters based on BN-doped nanographenes for highly efficient single-component and single-layered white-emitting devices.

## 2. Results and Discussion

Capitalizing on the BN-doping approach[24–40] to tailor the physical[24,41–44] and chemical[40,45,46] properties of polycyclic aromatic hydrocarbons (PAHs) and nanographenes, we have recently developed the first rational synthesis of a $B_3N_3$-doped nanographene, hexa-peri-hexabenzoborazinocoronene or **1**.[24] The characterization of **1** is provided in a previous contribution[24] and in the Supporting Information. Its purity is confirmed by both $^1$H-NMR, HPLC (high-performance liquid chromatography) and excitation spectra (Figures S1–S3, Supporting Information). Please notice that below results were obtained from three batches, confirming the lack of artifacts related to impurities. The photophysical characterization of **1** in solution showed blue fluorescence (wavelength maxima or $\lambda_{max}$ = 415 nm) and green phosphorescence ($\lambda_{max}$ = 525 nm) at room temperature and 77 K (Figure S4, Supporting Information), respectively. Inspired by recent developments describing the first use of BN-doped molecular materials in electroluminescent devices,[47–50] and the exploitation of thermally activated delayed fluorescence (TADF)[31] in BN-doped nanographene, we engineered LECs containing **1** as the active emitter to elucidate its electroluminescence behavior.

As a first step, we prepared thin films containing only **1** and mixed with the ionic matrix as those used in devices—i.e., **1**:PS:PEO:LiOTf in a mass ratio 10:0.9:2.6:0.78 being PS (polystyrene), PEO (polyethylene oxide) and LiOTf (lithium triflate); see the Supporting Information for more details. Atomic force microscopy (AFM) assay confirm that both films show a similar homogenous morphology with root-mean-square roughness of 2 nm (Figure 1). Likewise, the photoluminescence features are similar at room temperature and in air, involving a well-structured blue emission band centered at 415 nm (Figure 1), $\phi$ = 22.1%, and excited state lifetimes ($\tau$) of ≈3 ns (Figure 1).

Next, the electroluminescent behavior **1** was studied in "thin" devices built as indium-tin oxide (ITO)/poli(3,4-etilendioxitiofeno)-poli(estireno sulfonato) (PEDOT:PSS) (70 nm)/**1**:PS:PEO:LiOTf 10:0.9:2.6:0.78 (100 nm)/Al(90 nm)—see the Supporting Information for more details on the device preparation. The devices were driven at pulsed current of 5 mA monitoring the luminance, color, and electrical behavior over time. In stark contrast with the blue photoluminescence features of the thin films, these devices exhibit a white electroluminescence response covering the whole visible range (**Figure 2**). Specifically, the electroluminescence spectral envelop consists of three well-defined peaks located at 435, 505, and 695 nm along with shoulders at 550 and 750 nm that are associated to $x/y$ CIE coordinates of 0.28/0.31 and CRI value of 89. Notably, the shape of the electroluminescence emission changes until the maximum luminance is reached (Figure 2), showing i) an intensity decrease of the high-energy peak ($\lambda_{max}$ = 435 nm), ii) an intensity increase and broadening of the mid-energy peak leading to a red-shifted $\lambda_{max}$ (530 nm), and iii) an intensity increase of the low-energy peak ($\lambda_{max}$ = 695 nm). This results in a peak intensity pattern that corresponds to final $x/y$ CIE coordinates of 0.31/0.38 and CRI of 85 holding until the device is dead (Figure 2). Despite of the changes of the emission bands, the overall white response of the devices lays on the daylight white region—i.e., averaged color correlated temperature of 5500 K—during the whole lifespan (Figure 2). As far as the device performance is concerned, **1**-WLECs stand out compared to other single-component WLECs.[16–19,51] In detail, the average voltage exponentially decreases up to ≈4 V during the first hour due to the formation of the electrical double layers (EDLs) at the electrode interfaces, allowing both charge injection and stabilization of the doped regions. At the same time, the luminance slowly increases reaching a remarkable value of ≈50 cd m$^{-2}$ associated with an efficacy of 2.6 cd A$^{-1}$ and a lifetime superior to 40 h. Here, the average applied voltage remains fairly constant ($\Delta V$ < 100 mV), suggesting that the decay of the luminance is likely related to the reduction of the thickness of the emitting p-i-n region.

Small electroluminescence color changes over time can be ascribed to multiple reasons in LECs, namely i) unbalanced doping and movement of the emitting p–i–n regions,[1] ii) increase of the operation temperature,[52,53] iii) changes in the local electric field distribution and intensity,[19,20,54,55] and iv) microcavity and scattering effects.[6,56,57] Though the nature of the excited states involved in the mid- and low-energy electroluminescent bands—i.e., $\lambda_{max}$ of 505 and 695 nm, respectively—is puzzling compared to the blue photoluminescence at room temperature that just matches to the high-energy electroluminescent peak—i.e., $\lambda_{max}$ = 435 nm. However, this peak slowly disappears, while the mid-energy spectrum evolves into a broad band centered at 530 nm (Figure 2). Compared to the photoluminescence emission in frozen solvent matrix (77 K; Figure S4, Supporting Information), the maximum wavelength value of the mid-energy band (530 nm) hints at the presence of a phosphorescence mechanism. This was further confirmed in thin film (vide infra). However, the well-structured low-energy band, which is the key emissive feature providing high quality white lighting, has not been observed in both photophysical characterizations in solution,[25–30,34–44,46–48] and lighting devices.[31,44,49,50]

Based on the prior art in both single-component WLECs and WOLEDs,[17–22,51,54,55,58] three hypothesis can be postulated regarding the origin the low-energy emission band, namely i) ion-doped matrix-molecule interactions, ii) lower-energy emitting degradative species of **1**, and iii) exciplex, electromeric, and/or aggregation phenomena. At first, we focused on probing any interactions between **1** and the ion-doped matrix components. Although the photoluminescence profiles are very similar for pristine films and the active layers (Figure 1), we performed $^1$H-NMR analysis of **1**, the ion-doped matrix, and mixtures of **1**:ion-doped matrix in solution at increasing concentrations (up to 100 times) of the ion-doped matrix (Figure S5, Supporting

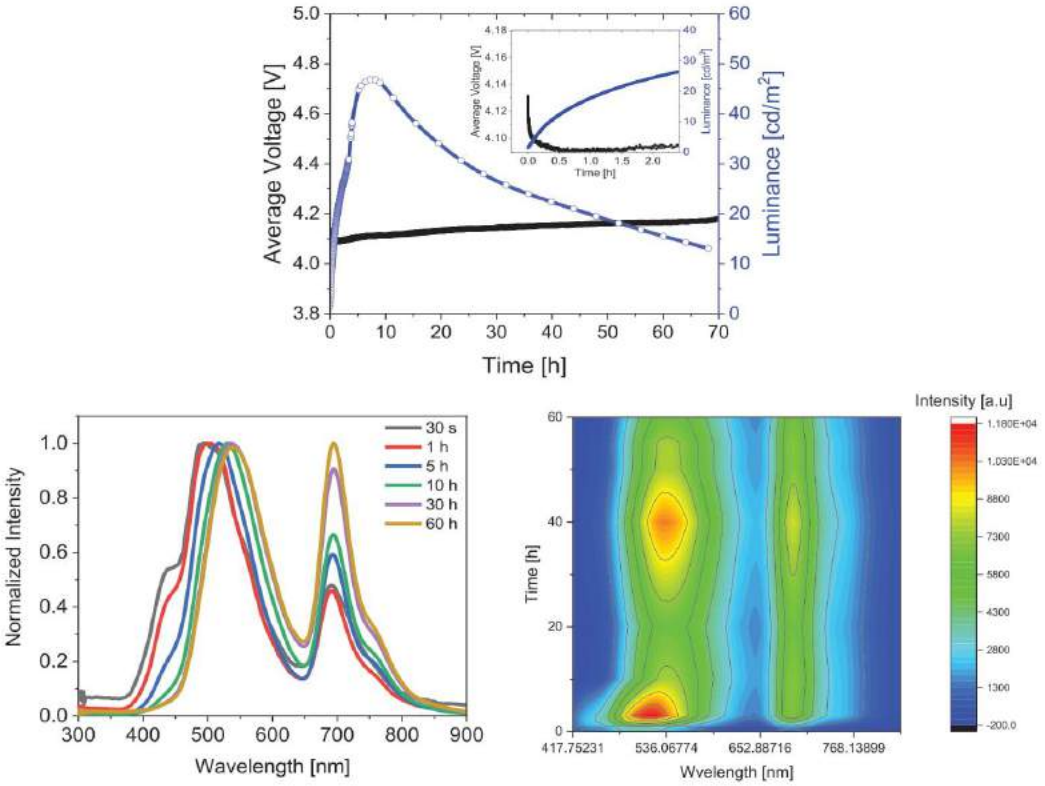


**Figure 2.** Top: luminance and applied voltage over time of thin 1-WLECs driven at pulsed 5 mA. The inset graph highlights the device behavior during the first 2 h. Bottom: electroluminescence changes over time highlighted by representative spectra (left) taken at different times (see legend) and 2D electroluminescence map evolution (right).

Information). The high concentration of the matrix resembles a quasi-solid-state configuration in which 1 is heavily diluted into the matrix. No noticeable differences in the $^1$H-NMR spectra were observed, suggesting the absence of any interactions between 1 and the ion-doped matrix. Noteworthy, the absence of dimers or multiple emitting species was also confirmed by performing excitation spectra in the range $\lambda = 290–430$ nm as well as emission spectra of highly concentrated solutions at high and low temperatures (Figure S2, Supporting Information). In addition, preliminary theoretical calculations were performed for single and dimer molecules. While a reasonable agreement with the experimental absorption and the high and mid-energy peak emission spectra was noted, no emission band in the red region (≈700 nm) was inferred. This might indicate that the nature of this band is not related to a new thermally activated radiative pathway involving a monomer or dimer structure of 1 (vide infra). In spite of the degree of agreement found with the experimental results, known limitations of the theoretical methods used for the description of these type of systems[59,60] cast some doubts on the reliability of the results. Thus, further information has not been provided in the text.

To discard any chemical degradation of **1** upon both device fabrication and operation,[18,19,61,62] we first looked for any relationship between the intensity changes for each band over the whole device lifespan. Figure S6 (Supporting Information) displays that the intensity of the high-energy peak increases during the first hour until it starts to decay. Unrelatedly, the behavior of both mid- and low-energy bands is similar, showing a slow exponential increase at different rates followed by a slow decrease over time. This indicates that the three bands are independent, and their changes are not related to the formation of degradative species of **1**. Nevertheless, we further compared the spectroscopic features of fresh and used devices (Figure S7, Supporting Information). For instance, both absorption and emission spectra are very similar, confirming the lack of new species formed under electrical stimuli. At last, we tackle this study using electrochemical impedance spectroscopy (EIS) to investigate the electrical behavior of fresh and used devices. Under static EIS measurements (**Figure 3**, Figures S8 and S9, Supporting Information), fresh devices show a common LEC behavior, namely i) an initial decrease of the electronic resistance at biases below the energy

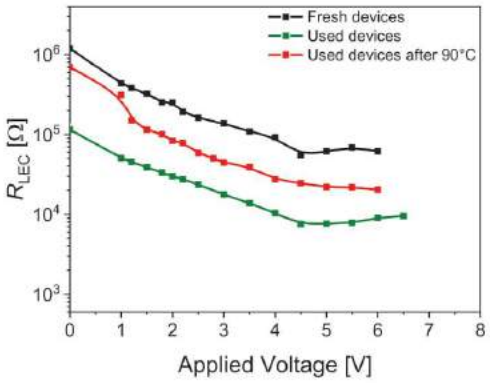


**Figure 3.** Static EIS assays applied to 1-WLECs to monitor the changes of the device behavior of fresh, used, and after heating at 90 °C devices with respect to the resistance values associated with the EDL and doped region formations upon increasing the applied voltage from 0 to 6 V.

band-gap (≈3.5–4 V), which corresponds to the formation of the EDL formation, and ii) a further resistance decrease that holds at higher biases, which accounts for the formation of the doped regions and the auto-sustained charge recombination (Figure 3). In addition, fresh and used devices showed ionic resistance ($\sigma$) values of $1 \times 10^6$ and $1 \times 10^5$ Ω at 0 V, respectively. A decrease of the $\sigma$ in used devices indicates the lack of degradative events at the electrodes interfaces,[19,61,63–65] while it is attributed to the remaining polarization upon forming the p- and n-doped regions. Upon heating the used devices at 90 °C for 30 min, the value of $\sigma$ is significantly recovered (78% or $0.78 \times 10^6$ Ω), indicating that no electrochemical degradation processes are taking place.[19,61,63] In line with the recovery of $\sigma$, the shape of the Nyquist plots of fresh devices consists of flattened semicircles, as expected from the poor charge storage capacity and $\sigma$ values. In contrast, used devices show quasi-perfect semicircles due to the polarization effect of the electrochemical doping. After the heating treatment, the Nyquist shape resembles those of fresh devices, indicating that the polarization has been erased.

Finally, we examine the possible formation of exciplex species at the electrode interfaces,[14,15] aggregates at the active layer,[21] and/or the formation of electromeric emitters.[20,54,55] The exciplex emission was discarded preparing a single-layer device changing the electrodes for bare ITO and Ag (Figure S10, Supporting Information). The electroluminescence response corresponds to a white emission as observed for the classical device configuration, showing the same behavior over time with respect to device color—i.e., $x/y$ CIE color coordinates 0.28/0.31 and 0.31/0.38 in concert with CRI values of 89 and 85 at the beginning and the end of the device lifespan, respectively. Noteworthy, these devices also show a high luminance of around 70 cd $m^{-2}$ and efficiency of 3.1 cd $A^{-1}$. In line with the above experiments (Figures S5–S10, Supporting Information), the observed steady electroluminescence behavior further confirms the lack of degradation upon evaporating different metal cathodes.

Aggregated species usually feature either a low efficient and broad emission spectrum or an enhanced emission depending on the type of aggregates and/or aggregated-induced emission takes over.[14,15,66,67] However, the ion-doped matrix has been designed to avoid the formation of aggregates, including a high amount of PS. Indeed, the mixture of **1** and the standard matrix—i.e., **1**:PEO:LiOTf in a mass ratio 1:0.15:0.06—leads to nonhomogeneous films with big crystalline-like aggregates and a similar photoluminescence response, but with a strongly reduced $\phi$ compared to that measured for pristine films and device active layers (Figure S11, Supporting Information). Indeed, these devices did not show any electroluminescence response, indicating that crystalline-like aggregates are effective non-radiative electron-hole recombination centers. The presence of crystalline-like aggregates disrupts the homogeneity of the thin film, leading to the formation of shorts whenever the device is run. Finally, the low-energy band in the electroluminescence spectrum shows a well-defined structure with a maximum at 695 nm and a shoulder at 750 nm; features that are not expected from an emission originated from aggregates.

The formation of electromeric emitting species is related to the presence of a pair of statistically independent **1** molecules, combining an ionic and cationic forms—i.e., $(\mathbf{1}^-/\mathbf{1}^+)^*$ singlet or triplet states—under the presence of high electric fields. Similar to the exciplex- and aggregated-like electroluminescence, they are sensitive to the emitter concentration, but even more to the externally applied electric field.[20,54,55] Thus, we decided to prepare a new set of devices increasing the amount of PS and thickness to further avoid the presence of any aggregate species and to significantly reduce the built-up electric field at the active layer—i.e., ITO/PEDOT:PSS(70 nm)/1:PS:PEO:LiOTf 10:1.8:2.6:0.78(100 nm)/Al(90 nm). In addition, these devices were driven at 9 V pulsed voltage to study if the driving operation has any effect on the electroluminescence behavior. As shown in **Figure 4**, the electrical device behavior is common for all LECs—vide supra, while the white response is preserved showing a broad band with maxima at 435, 560, 690, and 750 nm. The initial emission corresponds to $x/y$ CIE color coordinates of 0.29/0.35 and CRI of 87, which quickly change to 0.33/0.38 and CRI of 85 after 30 s, remaining constant throughout the lifespan of the device. In addition, these devices also show good luminance levels of ≈30 cd $m^{-2}$, efficiency of 2.5 cd $A^{-1}$, and stabilities over days. As such, the white response and device performance hold regardless the device architecture—i.e., active layer composition, thickness, and type of electrodes—as well as the driving modes, excluding all of the known reasons to reveal the nature of the low-energy emitting band.

A remaining aspect long overlooked in LECs is the heat generation under operation conditions. Indeed, 1-WLECs feature an increase of the pixel temperature between 45–65 °C holding constant during the measurements (Figure S12, Supporting Information). Thus, we decided to investigate the temperature dependence of the photoluminescence of **1** films. Surprisingly, two new well-structured bands centered at 530 and 700 nm evolved upon heating, leading to a whitish photoluminescence spectrum that is very similar to that observed in all the above described devices (**Figure 5**). This experiment is indeed crucial as it allows to correlate the unexpected electroluminescence response with the photoluminescence features, indicating that

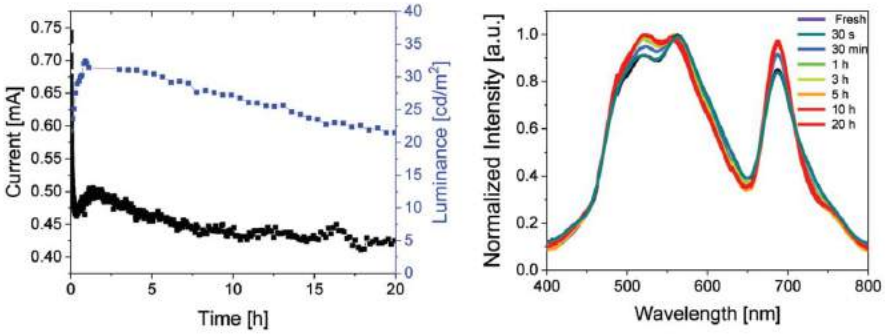


**Figure 4.** Left: luminance and applied voltage over time of thick **1**-WLECs driven at pulsed 9 V. Right: electroluminescence changes over time highlighted by representative spectra taken at different times (see legend).

the same radiative mechanism is operative regardless of the nature of excitation. To elucidate the nature of these emitting excited states, the $\tau$ values were determined at 400, 525, and 700 nm corresponding to 3.2 ns, 5.8 µs, and 12.3 µs (Figure S13, Supporting Information). Please note that the emission related to the mid- and low-energy bands is strongly quenched in air even at the high temperature of 400 K (Figure S14, Supporting Information), highlighting its sensitivity toward oxygen and suggesting a triplet-based emission. This points out a unique multiemissive mechanism involving fluorescence at high energies and thermally activated dual phosphorescence at the mid- and low-energy parts of the visible spectrum. These findings are also valid for the temperature dependence photoluminescence of **1** devices. Notably, the film morphology (Figure S15, Supporting Information) and the above $\tau$ values (Table S1, Supporting Information) of **1** devices are not affected upon heating for long periods of time—i.e., 60 °C for 7 d. These findings allow us to discard long-range changes of the chemical and structural surroundings of **1**, as well as effects of the substrates. In addition, the theoretical description of the manifold of excited states of **1** and its related dimers discards that the low-emission band is a figure for the BN doping pattern of **1**. Therefore, we conclude that the low emission must be related to temperature-induced short-range molecular and/or domain conformations in thin films. Further studies using transient spectroscopy coupled to both temperature and electric fields are ongoing in our laboratories.

As Figure 5 displays, the ternary white emission might be even more prominent in devices, as the spin statistics upon charge recombination promotes the formation of triplets (75%) over singlets (25%). Differences in the device temperature and the statistics formation rate of mid- and low-energy emitting triplets under different electric fields could explain the discrepancies between the intensity peaks upon comparing both photo- and electroluminescence responses (Figure 5), as well as the electroluminescence spectra between devices with different architectures and driving conditions (Figures 2,4, and 5). For instance, thick devices driven at pulsed voltage featured 65 °C, exhibiting a very small high-energy intensity and a well-balanced emission intensity between the mid- and low-energy bands, while thin devices operating at pulsed current reached 40 °C, showing a more prominent high-energy band and less intense low-energy bands. Please note that the previously commented time-dependent redshift of the low-energy electroluminescence peak was ascribed to the rise in temperature upon device driving, which takes place in the first stage of device operation (Figure S12, Supporting Information).

## 3. Conclusions

This work presents one of the most outstanding performances in single-component SM-WLECs, encompassing white color (average $x/y$ CIE color coordinates of 0.28–31/0.31–0.38 and CRI of 87), luminance values around 50–70 cd $m^{-2}$, efficiencies of ≈3 cd $A^{-1}$, and stabilities of days. This has been realized applying, for the first time, BN-doped nanographenes with the $B_3N_3$ doping pattern as single emitters. After discarding prior reported reasons for a white electroluminescence using non-white-emitting compounds in single-component WLECs and WOLEDs—i.e., device architecture, driving conditions, presence of degradative and aggregated species, as well as excimeric and electromeric emissions –, we concluded that the origin of the white electroluminescent response is a unique ternary emission mechanism involving a fluorescence and a thermally activated dual phosphorescence.

The relevance of this finding is clearly stated by three facts. First, the presence of ternary photoluminescence in engineered emitters has just been announced,[23] while this work presents the first example rationalizing how the $B_3N_3$ doping pattern in BN-doped nanographenes leads to a highly desired white multiemissive photo- and electroluminescence responses. Second, this exclusive ternary emission mechanism leads to one of the best performing thin-film white-emitting devices compared to the prior-art. Third, this contribution sheds light onto the prospect of the BN doping approach to design new functional nanographenes with tailored photo- and electroluminescent features. In particular, we highlight, that the replacement of the C=C bonds with B=N couples in a $B_3N_3$ fashion is a powerful approach to design white-emitting nanographenes for efficient single-component white-emitting devices. Other groups like Bettinger, Bragg,[28–30] Piers,[32] Hatakeyama[31,44] have also

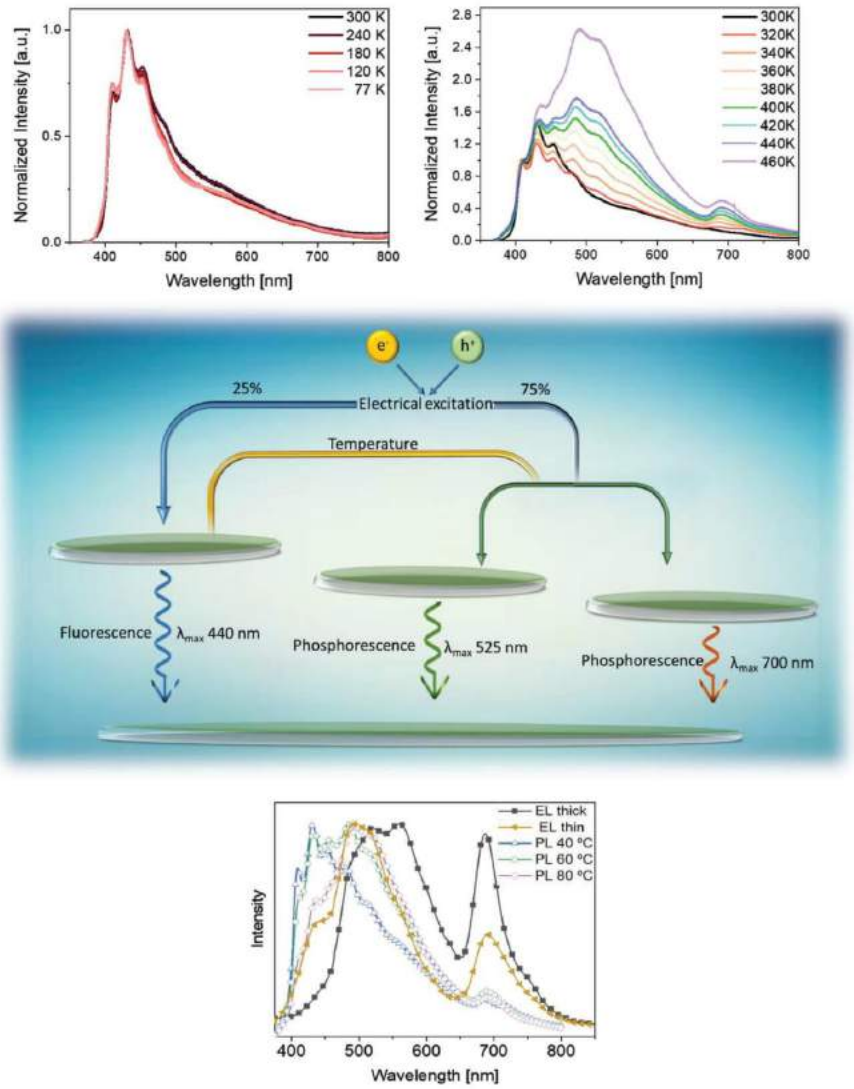


**Figure 5.** Top: photoluminescence spectra ($\lambda_{exc}$ = 355 nm) of **1** films on quartz upon heating from 77 to 300 K (left) and from 300 to 460 K (right). Middle: sketch highlighting the ternary electroluminescence mechanism involving fluorescence and thermally activated dual phosphorescence. Bottom: comparison of the photoluminescence spectra (open symbols) of **1** thin films at different temperatures (see legend) and the electroluminescence spectra (full symbols) of both thin and thick **1**-WLECs.

provided excellent examples about the effect of the B-N doping pattern on the emission features, showing several examples of high-energy TADF emission.

Overall, the designing principle to program BN-doped molecular graphenes is still in its infancy, opening new horizons in using this doping approach for the preparation of functional nanographenes with tailored photo- and electroluminescent properties. As shown in this work, this family of compounds exhibits, in addition, an interesting photoluminescence behavior in thin films with regard to externally applied temperature and electric field. A solid understanding of the emission mechanism in thin films under the above conditions is still highly desired. Transient spectroscopy coupled to both temperature and electric fields are ongoing studies in our laboratories. These aspects

 

represent the challenge of our forthcoming activities in the field of molecular BN-doped materials toward realizing highly efficient and stable single-component and single-layered white-emitting devices.

## Supporting Information

Supporting Information is available from the Wiley Online Library or from the author.

## Acknowledgements

E.F. and R.D.C. acknowledge the program "Ayudas para la atracción de talento investigador – Modalidad 1 of the Consejería de Educación, Juventud y Deporte—Comunidad de Madrid with the Reference No. 2016-T1/IND- 1463." R.D.C. also acknowledges the Spanish MINECO for the Ramón y Cajal program (RYC-2016-20891), the Europa Excelencia program (ERC2019- 092825), and HYNANOSC (RTI2018-099504-A-C22), as well as the 2018 Leonardo Grant for Researchers and Cultural Creators from BBVA Foundation and the FOTOART-CM project funded by Madrid region under programme P2018/NMT-4367. D.B. and J.D. gratefully acknowledge the EU through the MC-RISE project "INFUSION" (734834) and Cardiff University for the financial support. The authors heartily thank Pedro B. Coto for his efforts on the theoretical characterization of **1** and Julio Fernandez-Cestau for his assistance with spectroscopic measurements. J.C.-G. is grateful to the Spanish Ministry of Economy and Competitiveness and to the Regional Government of Madrid for funding through projects RTI2018-097508-B-I00 (AMAPOLA) and S2018/NMT-4511 (NMAT2D-CM) respectively. IMDEA Nanociencia acknowledges support from the "Severo Ochoa" Programme for Centers of Excellence in R&D (MINECO, Grant SEV-2016-0686).

## Conflict of Interest

The authors declare no conflict of interest.

## Keywords

BN-doped nanographene, single-component white lighting, small molecules, ternary electroluminescent mechanism, white light-emitting electrochemical cells

Received: August 19, 2019
Revised: December 10, 2019
Published online:

[1] S. Tang, A. Sandström, P. Lundberg, T. Lanz, C. Larsen, S. Van Reenen, M. Kemerink, L. Edman, *Nat. Commun.* **2017**, *8*, 1190.
[2] Z. Zhang, Y. Li, G. Guan, H. Li, Y. Luo, F. Zhao, Q. Zhang, B. Wei, Q. Pei, H. Peng, Z. Zhang, K. Guo, Y. Li, X. Li, G. Guan, H. Li, Y. Luo, F. Zhao, Q. Zhang, B. Wei, Q. Pei, H. Peng, *Nat. Photonics* **2015**, *9*, 233.
[3] A. Sandstroem, A. Asadpoordarvish, J. Enevold, L. Edman, *Adv. Mater.* **2014**, *26*, 4975.
[4] G. Hernandez-Sosa, S. Tekoglu, S. Stolz, R. Eckstein, C. Teusch, J. Trapp, U. Lemmer, M. Hamburger, N. Mechau, *Adv. Mater.* **2014**, *26*, 3235.
[5] A. Asadpoordarvish, A. Sandström, C. Larsen, R. Bollström, M. Toivakka, R. Österbacka, L. Edman, *Adv. Funct. Mater.* **2015**, *25*, 3238.
[6] H.-C. Su, C.-Y. Cheng, *Isr. J. Chem.* **2014**, *54*, 855.
[7] E. Fresta, R. D. Costa, *J. Mater. Chem. C* **2017**, *5*, 5643.
[8] R. D. Costa, *Light-Emitting Electrochemical Cells. Concepts, Advances and Challenges*, 1st ed., Springer International Publishing, Basel **2017**.
[9] H. C. Su, H. F. Chen, F. C. Fang, C. C. Liu, C. C. Wu, K. T. Wong, Y. H. Liu, S. M. Peng, *J. Am. Chem. Soc.* **2008**, *130*, 3413.
[10] L. He, J. Qiao, L. Duan, G. Dong, D. Zhang, L. Wang, Y. Qiu, *Adv. Funct. Mater.* **2009**, *19*, 2950.
[11] M. L. Wu, G. Y. Chen, T. A. Shih, C. W. Lu, H. C. Su, *Phys. Chem. Chem. Phys.* **2018**, *20*, 18226.
[12] G.-R. Lin, J.-R. Cheng, C.-W. Wang, M. Sarma, H.-F. Chen, H.-C. Su, C.-H. Chang, K.-T. Wong, *J. Mater. Chem. C* **2015**, *3*, 12492.
[13] T. Akatsuka, C. Roldán-Carmona, E. Ortí, H. J. Bolink, *Adv. Mater.* **2014**, *26*, 770.
[14] Y. Nishikitani, H. Takeuchi, H. Nishide, S. Uchida, S. Yazaki, S. Nishimura, *J. Appl. Phys.* **2015**, *118*, 225501.
[15] S. Uchida, D. Takizawa, S. Ikeda, H. Takeuchi, S. Nishimura, H. Nishide, Y. Nishikitani, *J. Visualized Exp.* **2016**, *117*, e54628.
[16] Y. Yang, Q. Pei, *J. Appl. Phys.* **1997**, *81*, 3294.
[17] S. Tang, J. Pan, H. a. Buchholz, L. Edman, *J. Am. Chem. Soc.* **2013**, *135*, 3647.
[18] M. D. Weber, M. Adam, R. R. Tykwinski, R. D. Costa, *Adv. Funct. Mater.* **2015**, *25*, 5066.
[19] M. D. Weber, J. E. Wittmann, A. Burger, O. B. Malcioglu, J. Segarra-Martínez, A. Hirsch, P. B. Coto, M. Bockstedte, R. D. Costa, *Adv. Funct. Mater.* **2016**, *26*, 6737.
[20] J. Y. Li, D. Liu, C. Ma, O. Lengyel, C. S. Lee, C. H. Tung, S. Lee, *Adv. Mater.* **2004**, *16*, 1538.
[21] M. Mazzeo, V. Vitale, F. Della Sala, M. Anni, G. Barbarella, L. Favaretto, G. Sotgiu, R. Cingolani, G. Gigli, *Adv. Mater.* **2005**, *17*, 34.
[22] S. Park, J. E. Kwon, S. H. Kim, J. Seo, K. Chung, S.-Y. Park, D.-J. Jang, B. M. Medina, J. Gierschner, S. Y. Park, *J. Am. Chem. Soc.* **2009**, *131*, 14043.
[23] C. Zhou, S. Zhang, Y. Gao, H. Liu, T. Shan, X. Liang, B. Yang, Y. Ma, *Adv. Funct. Mater.* **2018**, *28*, 1802407.
[24] J. Dosso, J. Tasseroul, F. Fasano, D. Marinelli, N. Biot, A. Fermi, D. Bonifazi, *Angew. Chem., Int. Ed.* **2017**, *56*, 4483.
[25] Z. X. Giustra, S. Y. Liu, *J. Am. Chem. Soc.* **2018**, *140*, 1184.
[26] X. Y. Wang, J. Y. Wang, J. Pei, *Chem. - Eur. J.* **2015**, *21*, 3528.
[27] D. Bonifazi, F. Fasano, M. M. Lorenzo-Garcia, D. Marinelli, H. Oubaha, J. Tasseroul, *Chem. Commun.* **2015**, *51*, 15222.
[28] J. A. Snyder, P. Grüninger, H. F. Bettinger, A. E. Bragg, *J. Phys. Chem. A* **2017**, *121*, 5136.
[29] J. A. Snyder, P. Grüninger, H. F. Bettinger, A. E. Bragg, *J. Phys. Chem. A* **2017**, *121*, 8359.
[30] S. A. Brough, A. N. Lamm, S. Y. Liu, H. F. Bettinger, *Angew. Chem., Int. Ed.* **2012**, *51*, 10880.
[31] K. Matsui, S. Oda, K. Yoshiura, K. Nakajima, N. Yasuda, T. Hatakeyama, *J. Am. Chem. Soc.* **2018**, *140*, 1195.
[32] M. J. D. Bosdet, W. E. Piers, T. S. Sorensen, M. Parvez, *Angew. Chem., Int. Ed.* **2007**, *46*, 4940.
[33] A. Abengózar, P. García-García, D. Sucunza, A. Pérez-Redondo, J. J. Vaquero, *Chem. Commun.* **2018**, *54*, 2467.
[34] M. M. Lorenzo-García, D. Bonifazi, *CHIMIA Int. J. Chem.* **2017**, *71*, 550.
[35] L. Brown, C.-J. Kim, R. W. Havener, D. A. Muller, P. Y. Huang, J. Park, M. P. Levendorf, *Nature* **2012**, *488*, 638.
[36] P. M. Ajayan, S. Lei, A. Babakhani, X. Yang, W. Zhou, K. P. Hackenberg, J. Zhang, Y. Gong, J.-C. Idrobo, Z. Liu, R. Vajtai, G. Shi, J. Lou, L. Ma, J. Yu, *Nat. Nanotechnol.* **2013**, *8*, 119.
[37] M. Krieg, F. Reicherter, P. Haiss, M. Ströbele, K. Eichele, M. J. Treanor, R. Schaub, H. F. Bettinger, *Angew. Chem., Int. Ed.* **2015**, *54*, 8284.

[38] Z. Liu, T. B. Marder, *Angew. Chem., Int. Ed.* **2008**, *47*, 242.
[39] H. Helten, *Chem. - Eur. J.* **2016**, *22*, 12972.
[40] X. Chen, H. Yang, B. Wu, L. Wang, Q. Fu, Y. Liu, *Adv. Mater.* **2019**, *31*, 1805582.
[41] M. Fan, J. Wu, J. Yuan, L. Deng, N. Zhong, L. He, J. Cui, Z. Wang, S. K. Behera, C. Zhang, J. Lai, B. M. I. Jawdat, R. Vajtai, P. Deb, Y. Huang, J. Qian, J. Yang, J. M. Tour, J. Lou, C. W. Chu, D. Sun, P. M. Ajayan, *Adv. Mater.* **2019**, *31*, 1805778.
[42] U. Hahn, E. Maisonhaute, J. F. Nierengarten, *Angew. Chem., Int. Ed.* **2018**, *57*, 10635.
[43] X. Y. Wang, A. Narita, X. Feng, K. Müllen, *J. Am. Chem. Soc.* **2015**, *137*, 7668.
[44] S. Nakatsuka, T. Hatakeyama, T. Ikuta, K. Kinoshita, S. Nomura, Y. Ono, J. Ni, K. Nakajima, K. Shiren, *Adv. Mater.* **2016**, *28*, 2777.
[45] D. Portehault, D. Liu, Y. Chen, S. Qin, J. Hao, J. Wang, Y. Li, W. Lei, *ACS Energy Lett.* **2017**, *2*, 306.
[46] A. M. Abdalla, S. Hossain, O. B. Nisfindy, A. T. Azad, M. Dawood, A. K. Azad, *Energy Convers. Manage.* **2018**, *165*, 602.
[47] B. Li, Z. Liu, M. Vasiliu, A. Chrostowska, S.-Y. Liu, J. S. A. Ishibashi, A. Dargelos, D. A. Dixon, C. Darrigan, *J. Am. Chem. Soc.* **2017**, *139*, 6082.
[48] J. Y. Wang, J. Pei, *Chin. Chem. Lett.* **2016**, *27*, 1139.
[49] S. Nakatsuka, N. Yasuda, T. Hatakeyama, *J. Am. Chem. Soc.* **2018**, *140*, 13562.
[50] S. Kervyn, O. Fenwick, F. Di Stasio, Y. S. Shin, J. Wouters, G. Accorsi, S. Osella, D. Beljonne, F. Cacialli, D. Bonifazi, *Chem. - Eur. J.* **2013**, *19*, 7771.
[51] S. Tang, J. Pan, H. Buchholz, L. Edman, *ACS Appl. Mater. Interfaces* **2011**, *3*, 3384.
[52] D. Asil, J. A. Foster, A. Patra, X. Dehatten, J. Delbarrio, O. A. Scherman, J. R. Nitschke, R. H. Friend, *Angew. Chem., Int. Ed.* **2014**, *53*, 8388.
[53] M. H. Bowler, T. Guo, L. Bastatas, M. D. Moore, A. V Malko, J. D. Slinker, *Mater. Horiz.* **2017**, *4*, 657.
[54] H. Yu, Y. Zhang, Y. J. Cho, H. Aziz, *ACS Appl. Mater. Interfaces* **2017**, *9*, 14145.
[55] Y. J. Cho, S. Taylor, H. Aziz, *ACS Appl. Mater. Interfaces* **2017**, *9*, 40564.
[56] G. R. Lin, H. R. Chen, H. C. Shih, J. H. Hsu, Y. Chang, C. H. Chiu, C. Y. Cheng, Y. S. Yeh, H. C. Su, K. T. Wong, *Phys. Chem. Chem. Phys.* **2015**, *17*, 6956.
[57] N. Kaihovirta, C. Larsen, L. Edman, *ACS Appl. Mater. Interfaces* **2014**, *6*, 2940.
[58] G. M. Farinola, R. Ragni, *Chem. Soc. Rev.* **2011**, *40*, 3467.
[59] S. Huang, Q. Zhang, Y. Shiota, T. Nakagawa, K. Kuwabara, K. Yoshizawa, C. Adachi, *J. Chem. Theory Comput.* **2013**, *9*, 3872.
[60] D. Hait, T. Zhu, D. P. McMahon, T. Van Voorhis, *J. Chem. Theory Comput.* **2016**, *12*, 3353.
[61] M. D. Weber, E. Fresta, M. Elie, M. E. Miehlich, J.-L. Renaud, K. Meyer, S. Gaillard, R. D. Costa, *Adv. Funct. Mater.* **2018**, *28*, 1707423.
[62] E. Fresta, J.-M. Carbonell-Vilar, J. Yu, D. Armentano, J. Cano, M. Viciano-Chumillas, R. D. Costa, *Adv. Funct. Mater.* **2019**, *29*, 1901797.
[63] L. D. Bastatas, K. Y. Lin, M. D. Moore, K. J. Suhr, M. H. Bowler, Y. Shen, B. J. Holliday, J. D. Slinker, *Langmuir* **2016**, *32*, 9468.
[64] E. Fresta, K. Baumgärtner, J. Cabanillas-Gonzalez, M. Mastalerz, R. D. Costa, *Nanoscale Horiz.* **2020**, https://doi.org/10.1039/C9NH00641A.
[65] E. Fresta, M. D. Weber, J. Fernández-Cestau, R. D. Costa, *Adv. Opt. Mater.* **2019**, *7*, 1900830.
[66] E. Fresta, G. Volpi, C. Garino, C. Barolo, R. D. Costa, *Polyhedron* **2018**, *140*, 129.
[67] J. Mei, N. L. C. Leung, R. T. K. Kwok, J. W. Y. Lam, B. Z. Tang, *Chem. Rev.* **2015**, *115*, 11718.

 

ADVANCED FUNCTIONAL MATERIALS

# Supporting Information

for *Adv. Funct. Mater.,* DOI: 10.1002/adfm.201906830

## Origin of the Exclusive Ternary Electroluminescent Behavior of BN-Doped Nanographenes in Efficient Single-Component White Light-Emitting Electrochemical Cells

*Elisa Fresta, Jacopo Dosso, Juan Cabanillas-González, Davide Bonifazi, and Rubén D. Costa**

WILEY-VCH

# Supporting Information

**Origin of the exclusive ternary electroluminescent behavior of BN-doped nanographenes in efficient single-component white light-emitting electrochemical cells**

Elisa Fresta, Jacopo Dosso, Juan Cabanillas-González, Davide Bonifazi, and Rubén D. Costa*

Elisa Fresta and Dr. Rubén D. Costa*
IMDEA Materials Institute, Calle Eric Kandel 2, E-28906 Getafe, Madrid, Spain.
ruben.costa@imdea.org

Elisa Fresta
Universidad Autónoma de Madrid, Departamento de Física Aplicada, Calle Francisco Tomás y Valiente, 7, 28049 Madrid, Spain.

Jacopo Dosso and Prof. Davide Bonifazi
School of Chemistry, Cardiff University, CF10 3AT Cardiff, Great Britain.

Dr. Juan Cabanillas
IMDEA Nanoscience, Calle Faraday 9, 28049 Madrid, Spain.

**Outline**



## 1. Experimental

*Materials*

All chemicals were purchased from chemical suppliers and used without further purification. All analytical reagent grade solvents were purified by distillation. All reactions were carried out under inert nitrogen atmosphere using standard vacuum lines techniques. Deuterated solvents were purchased from Eurisotop and Sigma Aldrich.

*Synthesis, spectroscopic, and microscopy characterization*

**1** was synthesized as reported in a previous contribution.[1] Its purification was carried out using two consecutive SCC (size exclusion chromatography) (eluent: Petroleum ether/$CH_2Cl_2$ 8/2). When recycling HPLC was performed, it was necessary to use a Petroleum Ether/$CH_2Cl_2$ 6/4 eluent due to solubility issues in order to avoid precipitation in the column. To further purify the desired product, three consecutive preparative TLCs (thin layer chromatography) with petroleum ether/$CH_2Cl_2$ 8/2 as eluent were carried out, allowing for the obtainment of **1** as a clean product. Excitation emission analyses were then performed to exclude the presence of other emissive species (Figure S2). This was done in combination with $^1$H-NMR experiments (Figure S3). Please note that a clear correspondence between the absorption and emission peaks (within experimental error of ± 2 nm) can be noticed from the excitation envelope. (e.g., Absorption: 314 nm, 335 nm, 354 nm, 373 nm; Emission: 383 nm, 404 nm (max), 426 nm, 452 nm. This confirms that **1** is the only emitting specie.

Absorption spectra were recorded with a Perkin Elmer Lambda 35 UV-Vis spectrometer. The photoluminescence spectra and photoluminescence quantum yield values were measured with a FS5 Spectrofluorometer with integrating sphere SC-30 (Edinburgh Instruments). Thin films (75 nm) were prepared onto cleaned quartz slides from a filtered solution of **1** (15 mg/mL in THF; without ion-doped matrix or with as below described) by spin-coating them at 800 rpm for 30 s, at 1500 rpm for 30 s and at 3000 rpm for an additional 10 s. Excited states lifetimes of fluorescence emission were obtained with a TCSPC laser ($\lambda_{exc}$ 377.6 nm), while the phosphorescence lifetimes at 550 nm and 700 nm were carried with a microsecond lamp using phosphorescence mode with a delay of 1.6 µs. The average lifetime can be obtained by using the $< \tau > = \frac{A_1\tau_1^2+A_2\tau_2^2}{A_1\tau_1+A_2\tau_2}$ formula reported in literature.[68]

Photoluminescence measurements at temperatures ranging from 77 K to 475 K were performed upon enclosing **1** films in a CFV-Optistat (Oxford Instruments) equipped with a

temperature controller. Films were photoexcited with a TEEM Photonics passive Q-switch Nd:YAG laser (405 nm, 300 ps pulse duration, 170 Hz, pulse energy < 1 mJ) mildly focused on the sample (fluence < 10 mJ/cm$^2$). The photoluminescence emitted by the samples was dispersed by a grating inside a spectrometer (SP2500, Acton Research) and spectrally recorded with a liquid $N_2$-cooled back depleted CCD (Princeton Instruments). Long pass filters were employed to reject stray light from the photoexcitation beam into the spectrometer. The photoluminescence spectra were acquired 10 minutes after the sample reached the desired temperature in order to ensure complete sample thermalization.

$^1$H NMR spectra were recorded on a Bruker Fourier 300 MHz spectrometer equipped with a dual ($^{13}$C, $^1$H) probe. $^1$H spectra were obtained at 300 MHz. All spectra were obtained at rt if not otherwise stated. Chemical shifts were reported in ppm according to tetramethylsilane using the solvent residual signal as an internal reference ($CDCl_3$: $\delta_H$ = 7.26 ppm, THF-*d*8: $\delta_H$ = 3.58, 1.73 ppm). Coupling constants (*J*) were given in Hz. Resonance multiplicity was described as *s* (singlet), *d* (doublet), *t* (triplet), *dd* (doublet of doublets), *dt* (doublet of triplets), *td* (triplet of doublets), *q* (quartet), *m* (multiplet) and *bs* (broad signal).

AFM measurements were carried out with a Park XE150 instrument (Park Systems Corp., Suwon, South Korea), and the Gwyddion evaluation software.

*Device fabrication and characterization*

ITO substrates were purchased from Naranjo Substrates with an ITO thickness of 130 nm. They were extensively cleaned using detergent, water, ethanol, and propan-2-ol as solvents in an ultrasonic bath (frequency 37-70 Hz) for 15 min each. Afterwards, the slides were dried with $N_2$ gas and put in an UV-ozone cleaner for 8 min and used directly as described in the main text. If PEDOT:PSS was used to increase reproducibility, the clean plates were coated with 70 nm PEDOT:PSS layers via spin coating. To this end, an aqueous solution of PEDOT:PSS was filtered and mixed with propan-2-ol in a ratio of 3:1. From this solution, 50 µL were dropped onto the substrate at a rotation speed of 2000 rpm and spun for 60 s. The resulting layers were dried on a hotplate at 120 °C and stored under $N_2$. Thick active layers (100 nm) were deposited from a 15 mg/mL of **1** combined with a ion-doped matrix consisting of **1**:PS:PEO:LiOTf 10:1.81:2.6:0.78 mass ratio. This was prepared using THF solutions of PS with $M_w$ 900,000 (10 mg/mL), PEO with $M_w$ 8,000,000 (20 mg/mL) and LiOTf (10 mg/ml) and spin coated at 800 rpm for 30 s, at 1500 rpm for 30 s and at 3000 rpm for an additional 10 s, resulting in 100 nm of active layer thickness. The thin active layers (70 nm) were achieved by employing a ratio **1**:PS:PEO:LiOTf 10:0.9:2.6:0.78 mass ratio, following

the same procedure as above. In all cases, after the deposition of the active layer the devices were dried under vacuum for 2 h and transferred to an inert atmosphere glovebox (<0.1 ppm $O_2$ and $H_2O$, Angstrom Engineering). Finally, either Aluminum or Silver cathodes (90 nm) were thermally evaporated onto the active layer using a shadow mask under high vacuum (<1 x $10^{-6}$ mbar) in an Angstrom Covap evaporator integrated into the inert atmosphere glovebox. The device statistics involve up to five different devices – *i.e.*, a total number of 20 pixels. Time dependence of luminance, voltage, and current was measured by applying constant and/or pulsed voltage and current by monitoring the desired parameters simultaneously by using Avantes spectrophotometer (Avaspec-ULS2048L-USB2) in conjunction with a calibrated integrated sphere Avasphere 30-Irrad and Botest OLT OLED Lifetime-Test System. Electroluminescence spectra were recorded using the above mentioned spectrophotometer. Electrochemical impedance spectroscopic assays (EIS) were carried out with a potentiostat/galvanostat (Metrohm μAutolabIII) equipped with a frequency response analyser module (FRA2). Measurements were performed at the applied voltage range from 0 to 6 V and fitted with the Nova software using the circuit model shown in Figure S8. The AC signal amplitude was set to 10 mV, modulated in a frequency range from 10 to 1 MHz. The Nova 1.11 software was used to obtain the parameters from the equivalent circuit. With this data at hand, the resistance of the intrinsic non-doped region ($R_{LEC}$) was directly obtained. The film conductivity (S/m) is measured at 0 V with the following equation: $\sigma=d/(AR_{LEC})$, where $d$ is the thickness of the layer, $A$ is the area of the electrodes, and $R_{LEC}$ is the resistance of the active layer. The temperature of the devices upon driving was recorded with a FLIR 430-sc thermal camera.

## 2. Figures

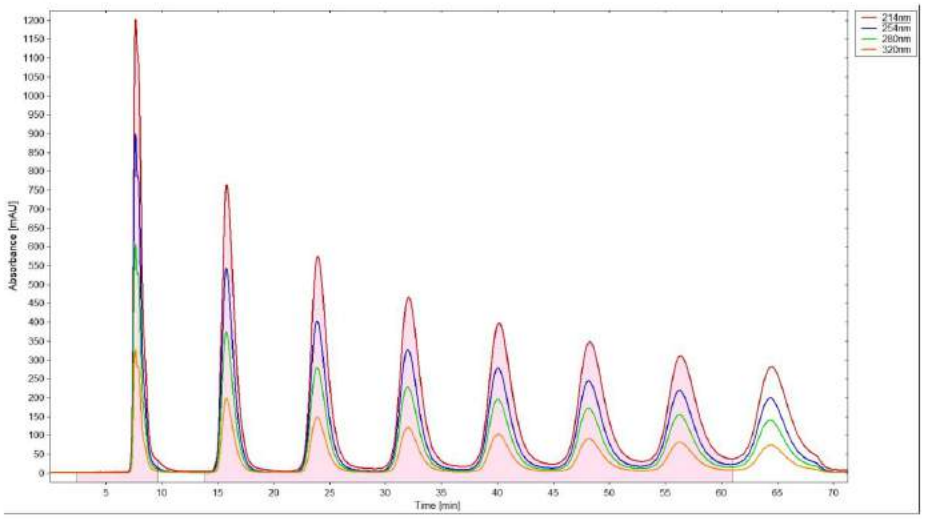


**Figure S1.** Absorption intensity *versus* retention times for **1** under recycling HPLC with petroleum ether/$CH_2Cl_2$ 6/4 as eluent. The detector wavelengths are reported in the legend.

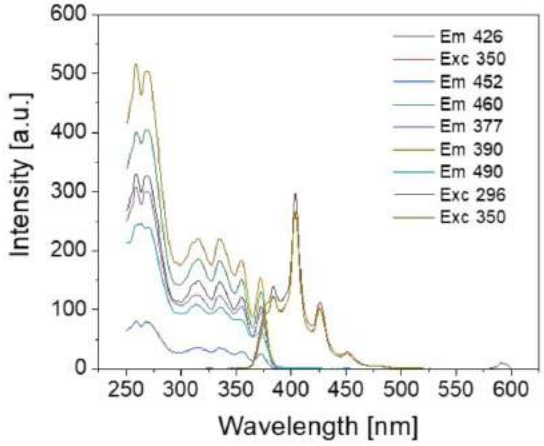

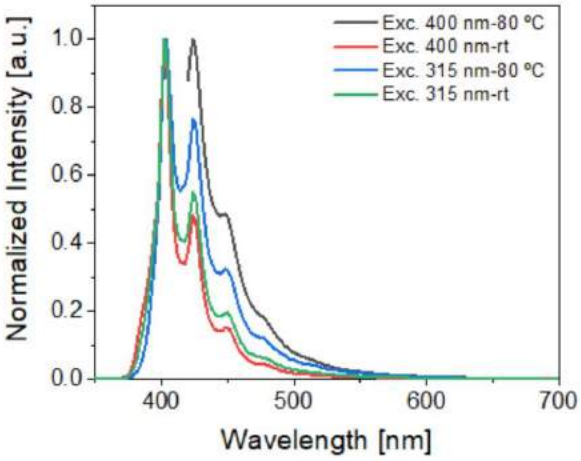


**Figure S2**. Top: Excitation-emission spectra of **1** recorded in $CH_2Cl_2$ at rt. The various emission (Em) and excitation (Exc) wavelengths (in nm) are reported in the legend. Bottom: Emission spectra at various excitation wavelengths of **1** in degassed chlorobenzene recorded at rt and 80 °C (see legend).

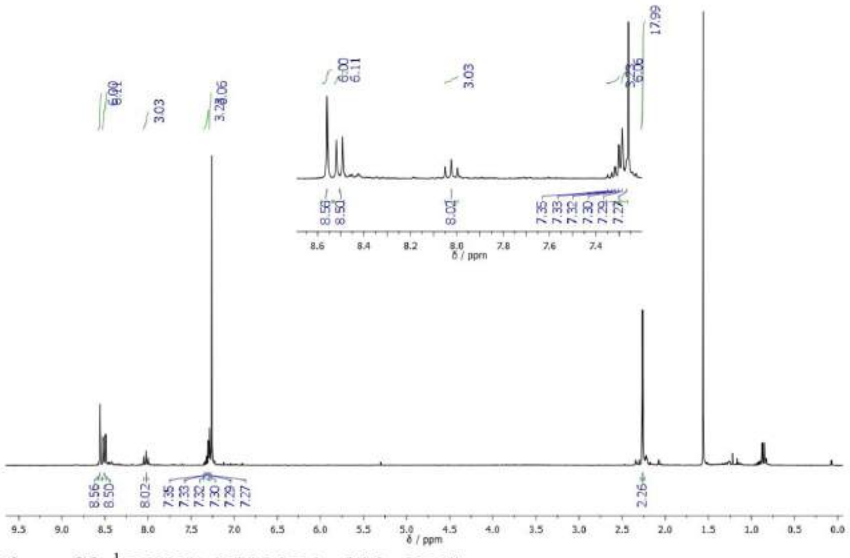


**Figure S3.** $^1$H-NMR (300 MHz) of **1** in $CDCl_3$.

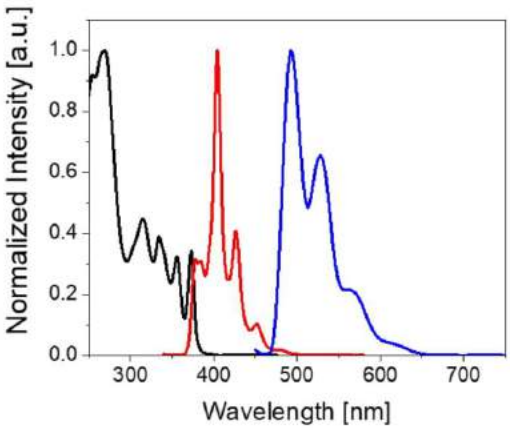


**Figure S4**. Normalized absorption (black; in air equilibrated $CH_2Cl_2$ at rt), fluorescence (red; $\lambda_{exc}$=315 nm in air equilibrated $CH_2Cl_2$ at rt), and phosphorescence (blue; $\lambda_{exc}$=315 nm at 77 K in a 1:1, v/v $CH_2Cl_2$:$CH_3OH$) spectra of **1**.

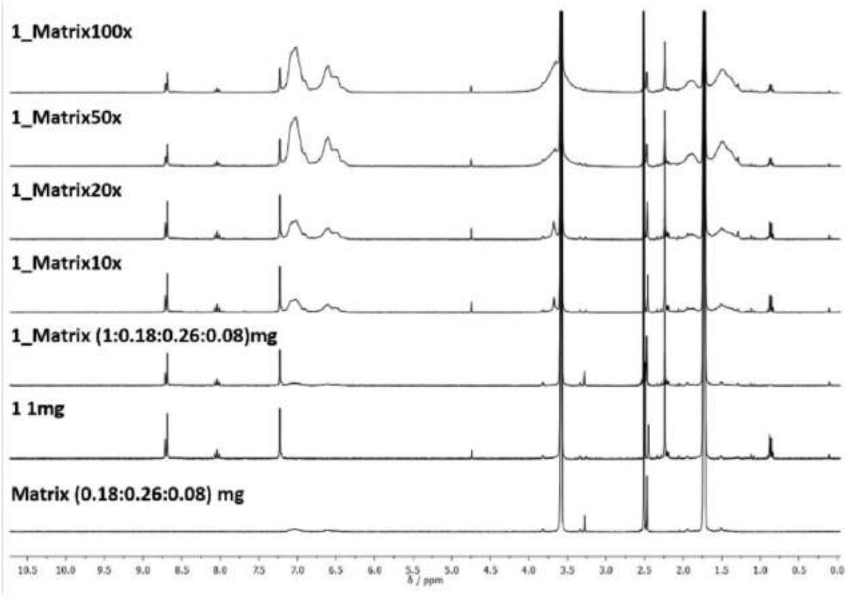
1_Matrix100x
1_Matrix50x
1_Matrix20x
1_Matrix10x
1_Matrix (1:0.18:0.26:0.08)mg
1 1mg
Matrix (0.18:0.26:0.08) mg
δ / ppm

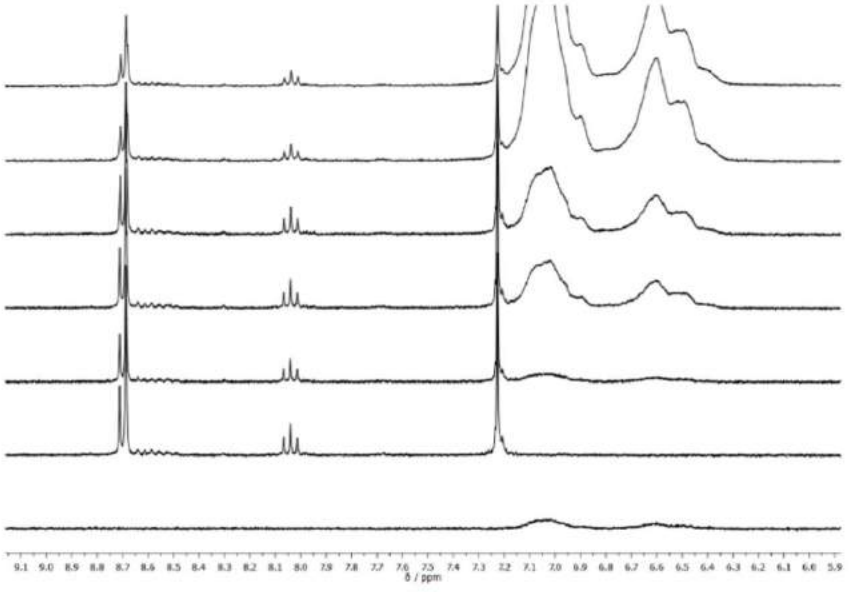
δ / ppm

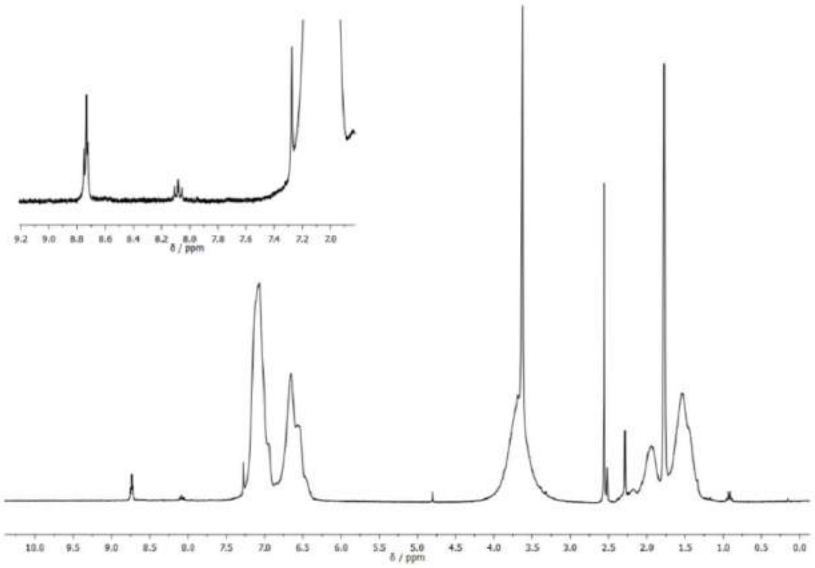


**Figure S5**. Top: Stacked $^{1}$H NMR 300 MHz study in THF-*d*8 showing **1** (1.0 mg) in the presence of increasing amounts of matrix 1×, 10×, 20×, 50× and 100× (starting from 0.18:0.26:0.08 mg PS:PEO:LiOTf). Center: inset on the aromatic region of the spectra highlighting the absence of changes in the signals. Bottom: $^{1}$H NMR 300 MHz of the 100× matrix concentration sample after 24h.

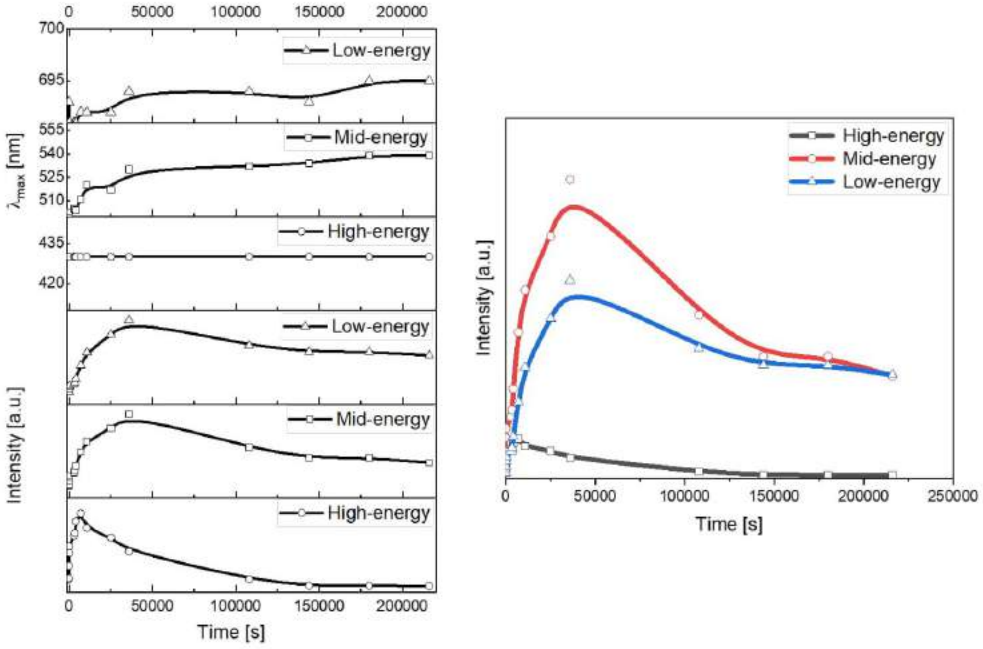


**Figure S6**. Intensity and $\lambda_{max}$ changes for the high-, mid-, and low-energy peaks over time of **1**-WLECs driven at pulsed 5 mA.

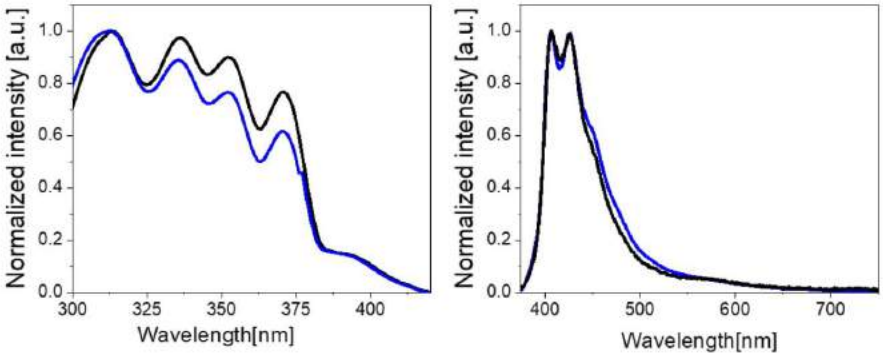


**Figure S7**. Absorption (left) and emission (right) spectra of fresh (black) and used (blue) devices.

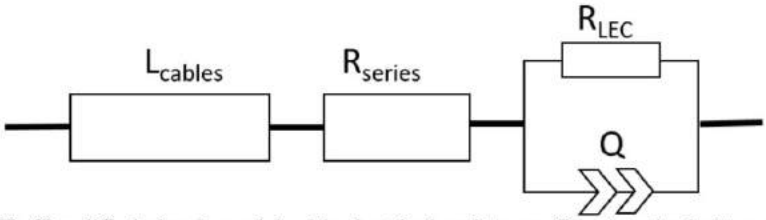


**Figure S8.** Simplified circuit model with electrical resistance ($R_{LEC}$) and admittance Q used for static EIS assays. A series resistor ($R_{series}$) and inductor elements for the cables ($L_{cables}$) were also included in the model.

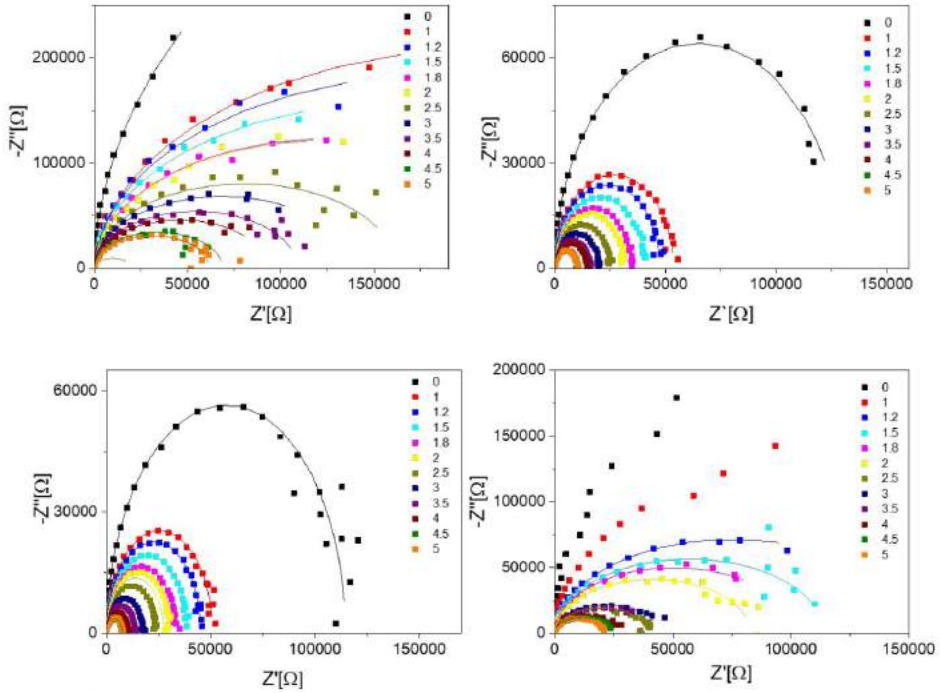


**Figure S9**. Nyquist plots of fresh (top left), used (top right), used heated at 60°C (bottom left) and used heated at 90°C (bottom right) **1** devices measured upon constant bias (see legend, the values are in V). The fittings are shown in solid lines.

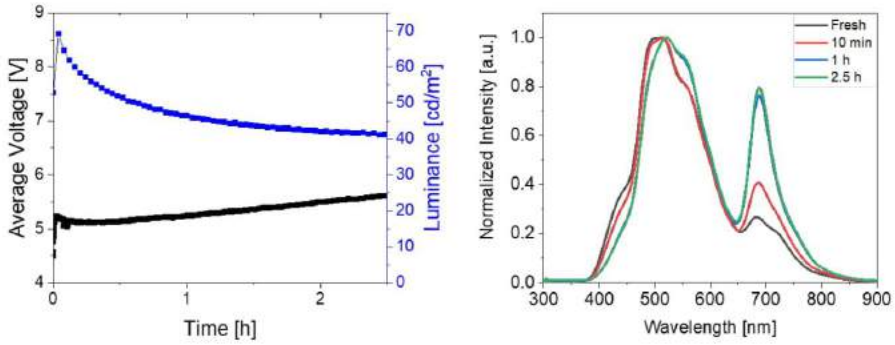


**Figure S10.** Left: Luminance and applied voltage over time of thin **1**-WLECs driven at pulsed 5 mA. Right: Electroluminescence changes over time highlighted by representative spectra taken at different times (see legends).

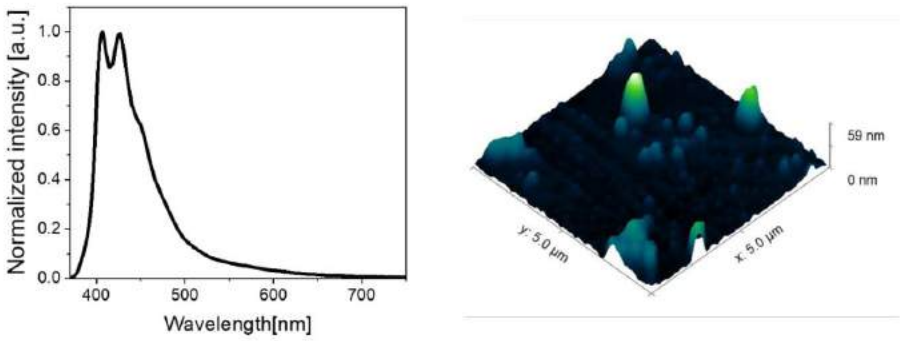


**Figure S11**. Left: Photoluminescence spectra ($\lambda_{exc}$=350 nm) of thin films based on **1**:PEO:LiOTf in air at room temperature. Right: AFM pictures of thin films based on **1**:PEO:LiOTf.

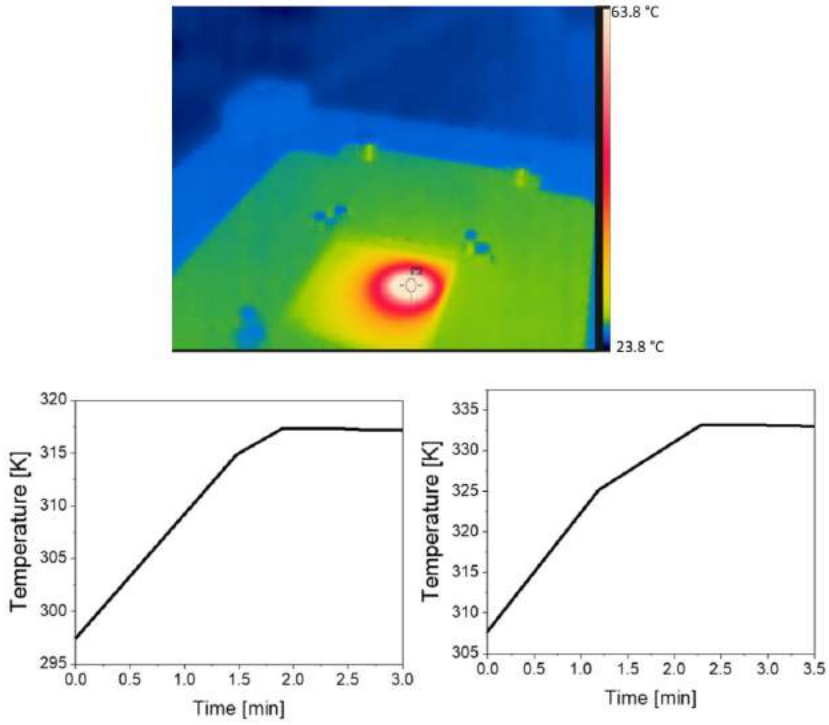


**Figure S12**. Top: Representative thermal picure of a 1-WLEC operating at pulsed voltage (9V). Bottom: Temperature rise in the first minutes of measurements for thin and thick **1**-WLECs driven at pulsed current of 5 mA (left) and voltage of 9 V (right), respectively.

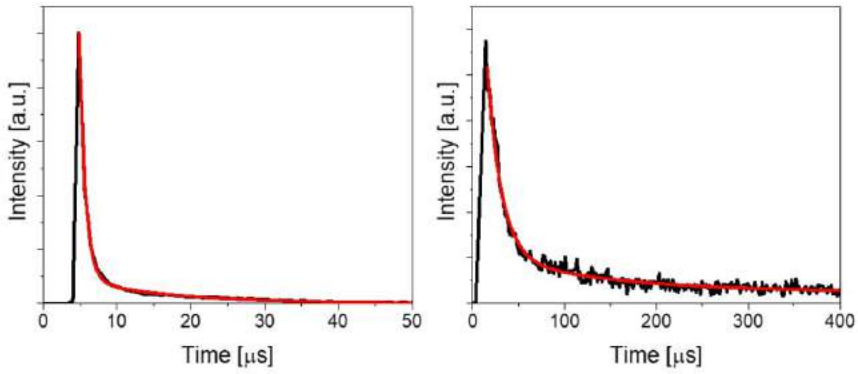


| $\langle\tau\rangle$ $\lambda_{max}$ 550 nm | $\langle\tau\rangle$ $\lambda_{max}$ 720 nm |
|---|---|
| 5.8 μs | 12.3 μs |

**Figure S13**. Excited-state decay profile ($\lambda_{exc}$ = 355 nm at 60ºC) of **1** films on quartz at $\lambda_{em}$ of 550 nm (left) and 720 nm (right) and the respective fitting (red). The averaged $\langle\tau\rangle$ are reported below.

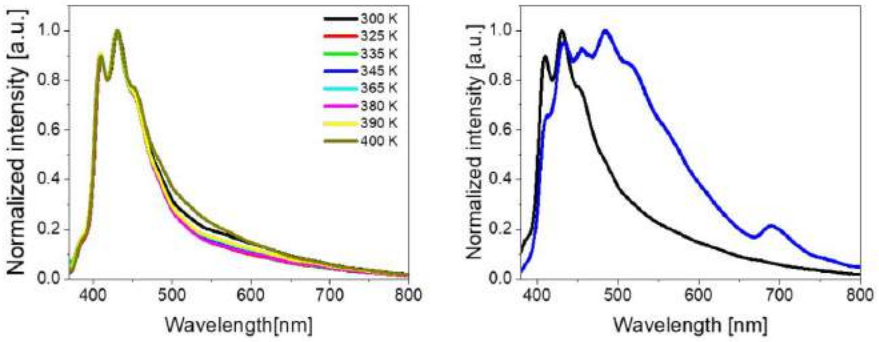


**Figure S14.** Photoluminescence features of **1** thin films performed in air at different temperatures (left) and comparison at 400 K between the photoluminescence in air (black) and in vacuum (blue).

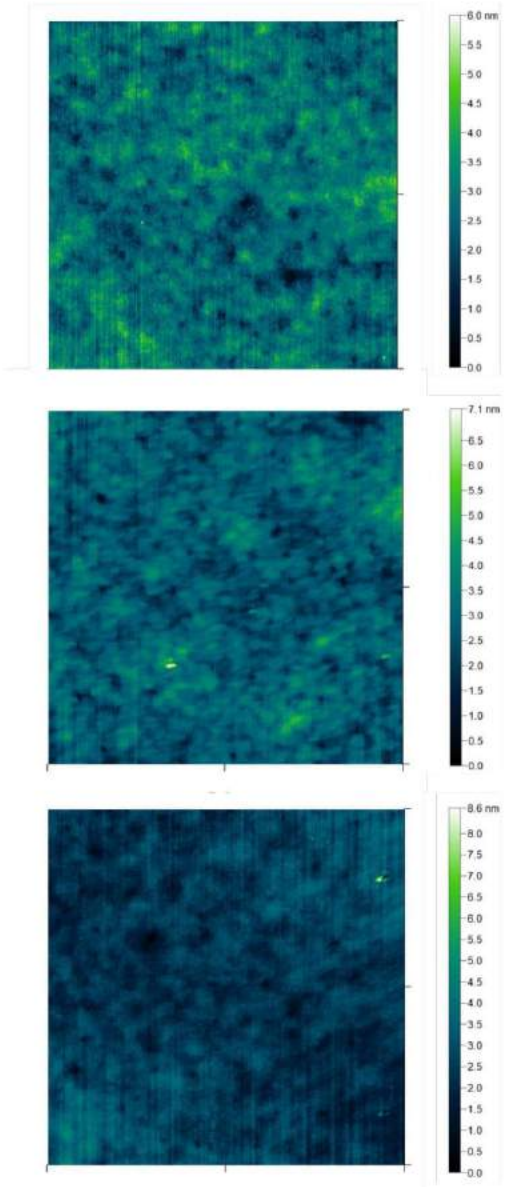


**Figure S15.** AFM pictures of **1** devices fresh (top), kept at 60°C fresh for 1 day (center), and for 10 days (bottom).

## 3. Tables

**Table S1.** Average excited state lifetimes ($\lambda_{exc}$ = 355 nm at 60 °C) of **1** devices fresh and kept at 60°C over time.

| Time | $\langle\tau\rangle$ $\lambda_{max}$ 425 nm | $\langle\tau\rangle$ $\lambda_{max}$ 550 nm | $\langle\tau\rangle$ $\lambda_{max}$ 720 nm |
|---|---|---|---|
| fresh | 3.2 ns | 5.9 µs | 12.3 µs |
| 1 day | 3.1 ns | 5.9 µs | 12.2 µs |
| 7 days | 3.3 ns | 5.8 µs | 12.2 µs |

## 4. References

[1] J. Dosso, J. Tasseroul, F. Fasano, D. Marinelli, N. Biot, A. Fermi, D. Bonifazi, *Angew. Chem. Int. Ed.* **2017**, *56*, 4483.

[2] C. M. Luk, L. B. Tang, W. F. Zhang, S. F. Yu, K. S. Teng, S. P. Lau, *J. Mater. Chem.* **2012**, *22*, 22378.

Section 3.2.3: Bright, Stable, and Efficient Red Light-emitting Electrochemical Cells using Contorted Nanographenes

Nanoscale Horizons

Issue 3, 2020


Elisa Fresta,[1,2] Kevin Baumgärtner,[3] Juan Cabanillas-Gonzalez,[4] Michael Mastalerz,[3] and Rubén D. Costa[1]

1. IMDEA Materials Institute, Calle Eric Kandel 2, E-28906 Getafe, Madrid, Spain.
2. Universidad Autónoma de Madrid, Departamento de Física Aplicada, Calle Francisco Tomás y Valiente, 7, 28049 Madrid, Spain.
3. Organisch-Chemisches Institut, Ruprecht-Karls-Universität Im Neuenheimer Feld 270, 69120 Heidelberg, Germany.
4. IMDEA Nanoscience, Calle Faraday 9, 28049 Madrid, Spain.

Volume 5
Number 3
March 2020
Pages 377–588

# Nanoscale Horizons

The home for rapid reports of exceptional significance in nanoscience and nanotechnology

rsc.li/nanoscale-horizons

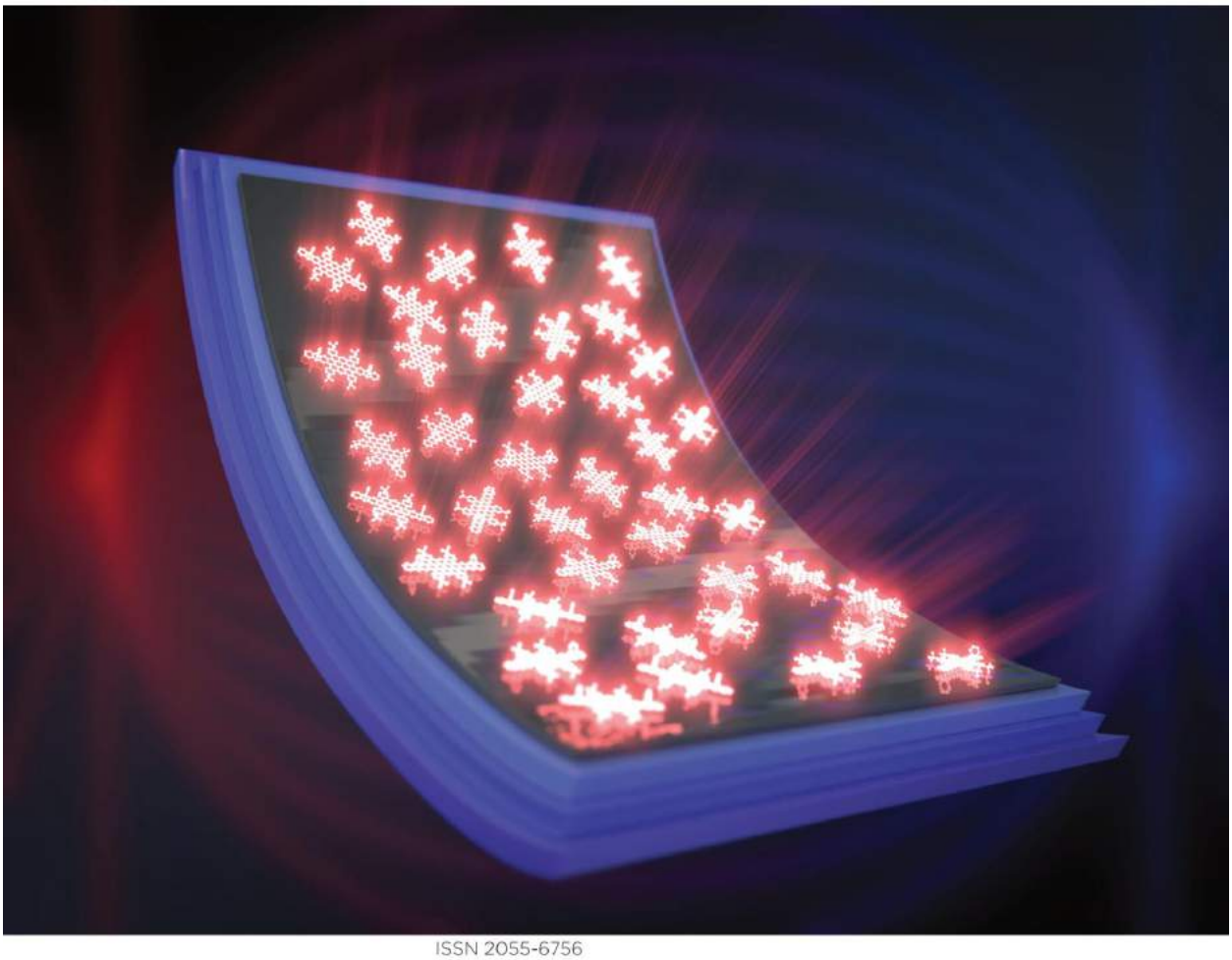

ISSN 2055-6756

ROYAL SOCIETY OF CHEMISTRY

**COMMUNICATION**
Rubén D. Costa *et al.*
Bright, stable, and efficient red light-emitting electrochemical cells using contorted nanographenes

NCNST

Nanoscale Horizons

ROYAL SOCIETY OF CHEMISTRY

COMMUNICATION

View Article Online
View Journal | View Issue





Cite this: *Nanoscale Horiz.*, 2020, 5, 473

Received 3rd October 2019,
Accepted 5th December 2019

DOI: 10.1039/c9nh00641a

rsc.li/nanoscale-horizons

# Bright, stable, and efficient red light-emitting electrochemical cells using contorted nanographenes†

Elisa Fresta,[ab] Kevin Baumgärtner,[c] Juan Cabanillas-Gonzalez,[d] Michael Mastalerz[c] and Rubén D. Costa[*ae]

**This work rationalizes, for the first time, the electroluminescent behavior of a representative red-emitting contorted nanographene – *i.e.*, hexabenzoovalene derivative – in small molecule light-emitting electrochemical cells (SM-LECs). This new emitter provides devices with irradiances of *ca.* 220 μW cm$^{-2}$ (242 cd m$^{-2}$), external quantum efficiencies (EQE) of 0.78% (<25% loss of the maximum theoretical EQE), and stabilities over 200 h. Upon optimizing the device architecture, the stability increased up to 3600 h (measured) and 13 000 h (extrapolated) at a high brightness of *ca.* 30 μW cm$^{-2}$ (34 cd m$^{-2}$). This represents a record stability at a high brightness level compared to the state-of-the-art SM-LECs (1000 h at 0.3 μW cm$^{-2}$). In addition, we rationalized one of the very rare LEC examples in which the changes of the electroluminescence band shape relates to the dependence of the relative intensity of the vibrational peaks with electric field, as corroborated by dynamic electrochemical impedance spectroscopy assays. Nevertheless, this exclusive electroluminescence behavior does not affect the device color, realizing one of the most stable, bright, and efficient red-emitting SM-LECs up to date.**

**New concepts**

Stable, bright, and efficient red-emitting small molecule light-emitting electrochemical cells (SM-LECs) still represent a challenge (1000 h at 0.3 μW cm$^{-2}$). Aggregation quenching and electrochemical formation of quenchers and trap carriers are responsible for the commonly observed poor performances. Herein, SM-LECs featuring high irradiances of *ca.* 220 μW cm$^{-2}$, external quantum efficiencies of 0.78% (<25% loss of the theoretical maximum), and stabilities over 200 h are demonstrated using a representative red-emitting contorted nanographene – *i.e.*, hexabenzoovalene derivative. Its distorted molecular structure avoids aggregation leading to highly emissive thin films, while its excellent electrochemical stability results in high stabilities. Upon optimization of the device architecture, outstanding stabilities of 3600 h (measured) and 13 000 h (extrapolated) at a high brightness of *ca.* 30 μW cm$^{-2}$ were achieved. Besides this new performance record compared to the SM-LEC prior-art, this works decipheres a very rare elecroluminescence behavior that is ruled by an electric-field dependence of the intensity for the radiative deactivation of the excited vibrational modes without changing the nature of the emitting excited state. This is supported by using different device architectures, driving modes as well as *in operando* electrochemical techniques.

Light-emitting electrochemical cells (LECs) consist of ionic-based active layers sandwiched between two electrodes.[1] The presence of mobile ions allows for solution-based deposition techniques and low driving voltages using air-stable electrodes.[2–4] Thus, LECs represent an easy-to-fabricate and low-cost alternative to the well-known organic light-emitting diodes (OLEDs). Indeed, good stabilities (320 h at 100 cd m$^{-2}$) along with remarkable efficiencies (99.2 cd A$^{-1}$ at 1910 cd m$^{-2}$) have recently been achieved after optimizing quenching and exciton diffusion processes in a host–guest LEC.[5]

As a curse and a blessing, LECs hold a high versatility toward a huge variety of emitters, such as ionic transition metal complexes (iTMCs), conjugated polymers (CPs), small molecules (SMs), perovskites, and quantum dots.[1,3,6–12] However, each emitter requires the optimization of the type and amount of the mobile ion source, such as ionic liquids,[13] ionic polyelectrolytes,[14,15] inorganic salts,[16,17] as well as the device architecture with respect to thickness,[18] injection layers,[10,11,19] *etc.* Along these lines, LECs based on iTMCs and CPs have extensively been optimized, reaching outstanding efficiency and brightness values.[9,20] However, these emitters usually present low photoluminescence quantum yields ($\varphi$) in the low-energy emitting region, as well as low electrochemical stabilities, leading to devices with poor efficiencies and stabilities.[21–23] Therefore, stable and efficient red-emitters are highly desired. Towards this

[a] *IMDEA Materials Institute, Calle Eric Kandel 2, E-28906 Getafe, Madrid, Spain. E-mail: ruben.costa@imdea.org*
[b] *Universidad Autónoma de Madrid, Departamento de Física Aplicada, Calle Francisco Tomás y Valiente, 7, 28049 Madrid, Spain*
[c] *Organisch-Chemisches Institut, Ruprecht-Karls-Universität, Im Neuenheimer Feld 270, 69120 Heidelberg, Germany*
[d] *IMDEA Nanoscience Institute, Calle Faraday 9, 28049 Madrid, Spain*
[e] *Research Institute for Science and Engineering, Waseda University, 3-4-1 Okubo, Shinjuku, Tokyo 165-8555, Japan. E-mail: ruben.costa@aoni.waseda.jp*
† Electronic supplementary information (ESI) available. See DOI: 10.1039/c9nh00641a

end, red-emitting SMs like perylenes, benzothiadiazoles, pentacenes, porphyrins, BODIPY–porphyrin dyads, and cyanines have recently been applied to LECs.[24–29] However, SM-LECs combining high irradiances along with stabilities of hundreds of hours have not been realized yet. Indeed, while the best stabilities (~1000 hours) are accompanied by low irradiances (0.1–1 μW cm$^{-2}$),[26,27] the best luminances (750 cd m$^{-2}$) come at the price of low stabilities (15 hours).[25]

Herein, we investigate the electroluminescent behavior of a highly contorted nanographene, namely a hexabenzoovalene (HBO) – *i.e.*, **1** as shown in Fig. 1,[30] highlighting its excellent prospect as an emerging family of red-emitters for SM-LECs. In general, interest in the optoelectronic application of 2D-annulated nanographenes has enormously grown in recent years.[31–34] In particular, distorted nanographenes are soluble in organic solvents, as they do not present efficient π–π stacking, allowing them to be suitable candidates for solution processed devices.[30,34–36] In addition, this family of SMs shows high $\varphi$, good electrochemical and thermal stabilities, and ambipolar carrier mobilities.[31,37,38] Despite these excellent features, their electroluminescent behavior has barely been investigated, as highlighted by only a few interesting OLED and LEC examples.[28,39]

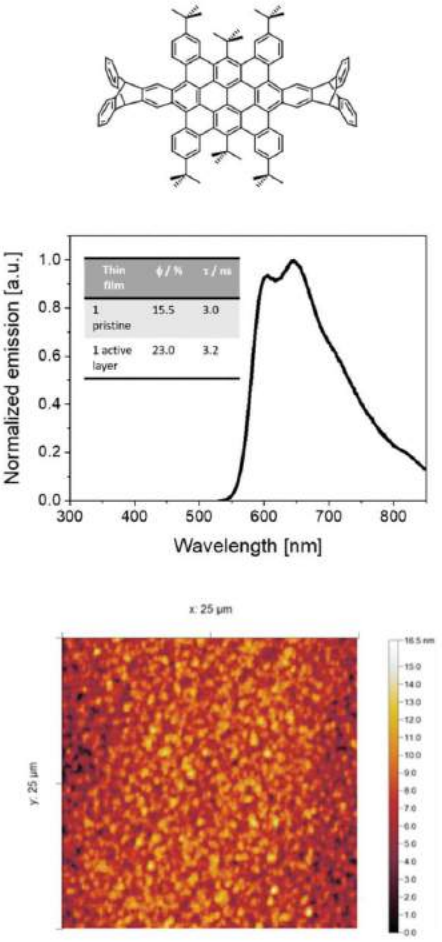


**Fig. 1** Top: Chemical structure of **1**. Centre: Photoluminescence spectra ($\lambda_{exc}$ = 450 nm) of thin films based on **1** with ionic matrix onto ITO substrates in air at rt. Inset: Photophysical properties ($\varphi$ and $\langle\tau\rangle$) of **1** thin films. Bottom: AFM picture of **1** thin films used in devices.

To shed light onto the electroluminescent behavior of contorted nanographenes and its prospect in the lighting field, we decided to comprehensively investigate both photo- and electro-luminescent features of the representative HBO in thin films.[30,40] The impact of this work is two-fold. On one hand, **1**-LECs achieved irradiances of *ca.* 220 μW cm$^{-2}$ (242 cd m$^{-2}$) external quantum efficiencies (EQEs) of 0.78% (76% the theoretical maximum EQE), and stabilities over 200 h. Upon optimizing the active layer thickness, the devices feature stabilities of 3600 h (measured) and >13 000 h (extrapolated) at a high brightness level (30 μW cm$^{-2}$ or 34 cd m$^{-2}$). Thus, these devices represent one the most stable and bright red-emitting SM-LECs so far reported (*e.g.*, 1000 h at 0.3 μW cm$^{-2}$).[1,41] On the other hand, we encountered that, regardless of the device architecture and driving conditions, the electroluminescence behavior is highlighted by an arrangement of the vibrational intensities caused by the steady increase of the internal electric field across the active layer. This leads to minimal changes in the color quality of the devices. However, this behavior represents one of the very rare examples of electric field dependent chromaticity in single-component and single-layered lighting devices, in general, and SM-LECs, in particular.

As reported previously,[30,40] HBO or **1** shows an orange-red fluorescence (maximum emission wavelength ($\lambda_{max}$) at around 600 nm with a shoulder at 640 nm) associated to $\varphi$ of 54% and excited state-lifetimes ($\tau$) of 4 ns in solution. Thin-films of **1** mixed with TMPE (trimethylolpropane ethoxylate), PEO (polyethylene oxide), and LiOTf (lithium triflate) as ionic matrices were used as the active layers in devices – *i.e.*, **1** : TMPE : LiOTf in a mass ratio 1 : 0.15 : 0.06; see Experimental section for more details. Investigating the thin-films by atomic force microscopy (AFM) revealed a homogenous morphology with a root-mean-square roughness of 2–3 nm (Fig. 1). The photoluminescence features of these thin-films consist of a broad emission band with peaks at 598 nm and 647 nm associated to $\varphi$ of 23% and $\tau$ of 3.2 ns (Fig. 1). The presence of a well-defined vibrational structure implies that thin films are not formed upon aggregation, which usually leads to broad and shapeless emission. Indeed, both the excitation spectra and $\tau$ values centered at either 598 nm or 647 nm and measured at 298 K and 77 K are similar, highlighting the lack of aggregates (Fig. S1–S4, ESI†). All-in-all, these results are in line with the well-thought molecular design that leads to a desired contorted molecular structure of **1**, providing high solubilities with a low aggregation behavior even upon film forming.

After having investigated **1** and thin-films thereof in ionic matrices, the promising photophysical data encouraged us to

 

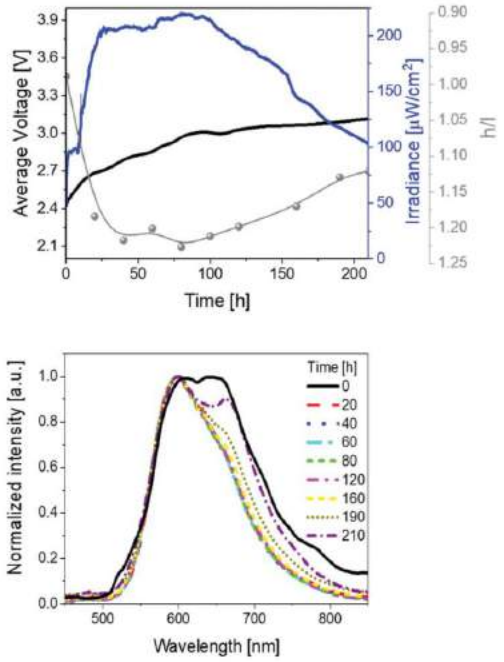


Fig. 2 Average voltage, irradiance, and h/l (high/low energy peak) ratio (top), as well as electroluminescence spectra (bottom) over time (see legend) for **1** devices driven at a pulsed 25 mA current.

transfer **1** to devices with the architecture ITO/PEDOT:PSS (70 nm)/**1**:TMPE:LiOTf 1:0.15:0.05 (70 nm)/Al (90 nm) – see Experimental section.

These devices were driven at pulsed currents of 25 mA monitoring the luminance, color, and electrical behavior over time (Fig. 2). The measurements involved the use of a pulsed driving scheme based on a block-wave at 1000 Hz and a duty cycle of 50%. In detail, the device behavior shows the typical LEC features, that is, an initial decrease of the applied voltage along with an increase of the luminance due to the formation of electrical double layers (EDLs) that assist the charge injection at the doped fronts growing from the respective electrodes. Similar to the LIV assays, the initial electroluminescence spectrum consists of a broad emission featuring the two above peaks at 600 and 650 nm. The device brightness achieved values of *ca.* 220 μW cm$^{-2}$ in concert with stabilities over 200 h. In addition, luminous efficiency and EQE values of 0.74 lm W$^{-1}$ and 0.78% were noted. Importantly, the EQE values account for 76% of the theoretical EQE (1.15%; Fig. 2 and Table 1). This is remarkable when considering the prior state-of-the-art of SM-LECs (33%),[29,42] especially if taking into account that no host–guest optimization has been performed yet – *e.g.*, EQE optimization from 33% up to 94% has recently been reported in host:guest CPs.[42]

Besides the excellent device performance, it is important to point out that the chromaticity changes over time (Fig. 2). This behavior has already been noticed in several LECs,[1,3] showing either large $\lambda_{max}$ shifts (10–100 nm) or changes of the spectrum shape that have been attributed to a strong polarization of the emitting excited state[43,44] and/or a change of nature of the emitting excited states,[45–47] respectively. In contrast to these examples, the electroluminescence spectra of **1**-LEC feature neither a $\lambda_{max}$ shift for both peaks nor a change of the $E_{0\text{-}0}$ energy (Fig. S5, ESI†), indicating that the nature of the excited state holds upon electrical excitation over time. In short, just the intensity ratio between the high-energy vibrational peak (h-peak; 600 nm) and low-energy vibrational peak (l-peak; 650 nm), herein called h/l, changes over time, increasing from 0.99 to 1.23 during the first 40 hours, holding constant up to 100 h, and then abruptly decreasing (1.13) until the device lifetime is reached (Fig. 2). This translates to a marginal color change during the first 80 h – *i.e.*, *x*/*y* CIE color coordinates move from 0.59/0.40 to 0.59/0.41, and then a slight change towards the red region – *i.e.*, *x*/*y* CIE color coordinates of 0.61/0.39; Fig. S5 (ESI†). Overall, this is accompanied by a change in the correlated color temperature (CCT) of $<300$ K.

The reason underlying the interplay among the chromaticity changes in **1**-LEC is, therefore, not trivial. Since changes in the nature of the excited state are not involved, other reasons, such as (i) unbalanced doping and movement of the emitting p–i–n regions,[5] (ii) increase of the operation temperature,[48,49] and (iii) microcavity and scattering effects,[50–52] could explain the color evolution. They can be meaningful until the luminance reaches a steady-state regime and they are highly dependent to the thickness of the active layer. However, **1**-LECs show a constant and very slow color change that extend itself throughout the entire lifetime of the device, regardless of the device architecture – *vide infra*. This is a hint for other reasons, such as degradation,[19,53] phase separation or film morphology changes,[11,54] and/or changes in the local electric field distribution and intensity.[55–58]

The formation of new species acting as either quenchers or emitters upon device operation may induce slow and irreversible

Table 1 Figures-of-merit of devices prepared from **1**

| Active layer thickness [nm] | Driving current [mA] | Irradiance [μW cm$^{-2}$] | $t_{1/2}$[a] [h] | $t_{on}$[b] [h] | Efficiency [lm W$^{-1}$] | EQE [%] |
|---|---|---|---|---|---|---|
| 70 | 25 mA, PM | 222.8 | 204 | 27 | 0.74 | 0.78 |
| 70 | 50 mA, PM | 369.9 | 25 | 2 | 0.50 | 0.51 |
| 30 | 25 mA, PM | 31.2 | >13 000 | 260 | 0.10 | 0.12 |
| 70 | 3 V | 150 | 7 | 0.40 | 0.30 | 0.43 |

PM = pulsed mode. [a] Time to reach 50% of the initial irradiance. [b] Time to reach the maximum irradiance.

changes over time, leading to a traceable relationship between the intensity changes of the h- and l-peaks. However, Fig. S6 (ESI†) shows that the intensity changes of the two peaks are equally affected over time. Furthermore, the $E_{0-0}$ band does not shift over time, remaining constant at 2.38 eV (520 nm) (Fig. S6, ESI†). In addition, we compared the spectroscopic features of fresh and used devices (Fig. S7, ESI†), showing that both emission and UV-Vis absorption spectra, do not show any relevant change after device operation. Both findings suggest the lack of the formation of new species under electrical stimuli. As a further confirmation, we carried out static electrochemical impedance spectroscopy (EIS) of both fresh and used devices (Fig. S8–S10, ESI†). Fresh devices show a common LEC behavior, namely (i) an initial decrease of the electronic resistance at biases below the energy band-gap (*ca.* 2–3 V), which corresponds to the formation of the EDLs, and (ii) a further resistance decrease that holds at higher biases, which corresponds to the formation of the doped regions and the auto-sustained charge recombination (Fig. S9, ESI†). In addition, fresh and used devices showed ionic resistance values of $1 \times 10^5$ Ω and $1 \times 1.9 \times 10^4$ Ω at 0 V, respectively. A decrease of the resistance in used devices suggests the lack of degradative events at the electrodes interfaces,[17,59] being instead attributed to the remaining polarization upon forming the p- and n-doped regions. Upon heating the used devices at 60 °C for 30 min, the resistance is significantly recovered (82% or $0.82 \times 10^5$ Ω), indicating that electrochemical degradation processes are not taking place.[17,53] Finally, we measured the figures-of merit of 1-LEC driven as described above until lifetime and heated at 60 °C for 30 min (Fig. S11 and S12, ESI†). Here, the h/l ratio of 0.85 is drastically different compared to the value at lifetime (1.15), being more similar to the one found for a fresh device (1.00). In addition, it follows the same trend over time as for fresh devices. This indicates the reversibility of the h/l change over time, as well as the absence of degradation processes.

As noticed in previous contributions, heat generation occurs under operation conditions.[48] Indeed, 1-LEC experiences a temperature rise up to 65 °C during the first minutes, holding constant for the entire measurement (Fig. S13, ESI†). This contrasts with the above described behavior, in which the h/l peak intensity ratio constantly changes over much longer periods of time. Nonetheless, we also investigated the temperature dependence photoluminescence behavior of pristine films as well as device active layers (Fig. S13, ESI†). Pristine films show a broadening of the photoluminescence spectrum upon heating from 298 K to 475 K. This is expected since the thermal energy promotes excited electrons to higher vibration levels with the temperature increase, leading to new radiative transitions, which typically cause the emission band broadening.[60] In contrast, the photoluminescence response of the devices does not experience significant spectral shape changes other than a slight linewidth broadening. Regardless of the surroundings of 1 in the thin-films, the increase of the temperature induces a reduction of the emission intensity. Finally, no changes in $\varphi$ and layer morphology were noticed upon time when keeping the devices for several days at 353 K (Fig. S14, ESI†). Thus, we can discard temperature as a possible reason for the above-described electroluminescence response.

Finally, we investigated the relationship between electrical and chromaticity changes over time. Here, small changes in the local electric field to which the emitter is subjected may induce structural changes affecting the internal dipole moment and the reorientation of the emitter, modifying the radiative decay from vibronic states and emission quenching over time, respectively. Indeed, we have recently rationalized that the white electroluminescence in free base porphyrin LECs is related to the presence of two regioisomers, in which the inner H atoms are arranged in collinear and vicinal fashions upon increasing the electric field.[53]

To further confirm this hypothesis, we increased the applied electric field using four different approaches, namely (i) measuring consecutive luminance–current–voltage (LIV) assays, in which the voltage is changed over time in a ramp-manner, (ii) increasing the driving current, which is directly correlated to the average driving voltage,[23,61] (iii) changing the duty cycle, as it also correlates with the duration of the applied voltage and electric field, and (iv) reducing the thickness of the active layer from 70 nm (thick) to 30 nm (thin).[18,53,62]

Firstly, we performed a series of LIV scans in the range of 0–6 V with a scan rate of 300 mV $s^{-1}$. The devices showed a red emission response starting at low applied voltages of ~3 V (Fig. S15, ESI†). The electroluminescence spectrum consists of a broad emission band with two peaks at 600 nm and 650 nm, indicating that the same excited state is radiative active, regardless of the type of excitation. They do not change in intensity upon consecutive scans, highlighting the sound stability of 1 upon electrical stimuli. Noteworthy, the h/l ratio changes over time assuming the same values at each step during the entire LIV measurements, indicating the reversibility of the voltage effect on the electroluminescence (Fig. S16, ESI†).

Secondly, devices driven at 50 mA pulsed current showed the same trend as above described (Fig. 3 and Table 1). In short, irradiances of 370 μW $cm^{-2}$, EQEs of 0.52%, and stabilities of 24 h were noted. The electroluminescence band shows a similar trend with regard to the changes of the h/l peak intensity ratios over time, reaching a higher h/l ratio value – *i.e.*, 1.25 *vs.* 1.40 at pulsed 25 and 50 mA, respectively – that hints a relationship between the electrical and chromaticity changes.

Next, the duty cycle was varied in the following manner: devices were driven at 4 different duty cycle values (25, 50, 75, and 100%) for a short time (<5 minutes), in order not to generate over oxidized/reduced species that could hamper the measurement (Fig. S17, ESI†). The duty cycle scan was repeated three times. Here, two points are noteworthy, namely (i) h/l changes with the duty cycle – *i.e.*, from 1.02 at 25% duty cycle to 0.89 at 100% duty cycle, highlighting voltage and electric field dependence, and (ii) h/l showed always similar values for the different duty cycles in each scan, indicating the reversibility of the voltage-dependency and the possibility of controlling the chromaticity with the applied electric field.

Finally, devices with thin active layers (30 nm) driven at pulsed current of 25 mA were studied (Fig. 4 and Table 1). Compared to thick devices (70 nm) (Fig. 2), the irradiance is reduced to approx. 30 μW $cm^{-2}$ and the overall stability is

 

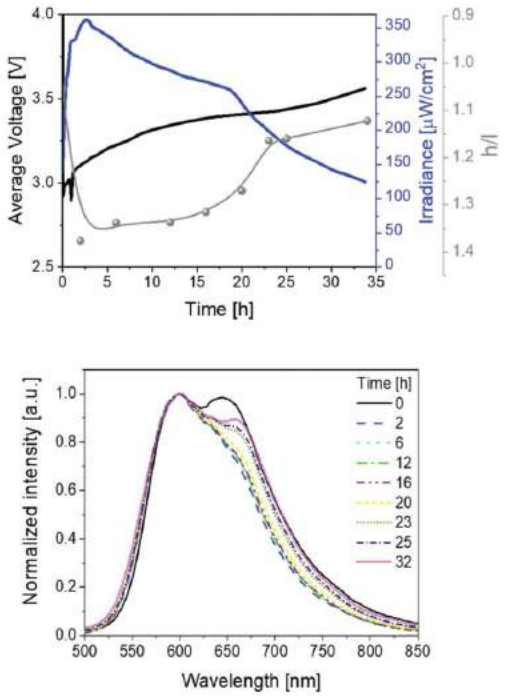


Fig. 3 Average voltage, irradiance, and h/l (h = high energy peak, l = low energy peak) ratio (top), as well as electroluminescence spectra (bottom) over time (see legend) for **1** devices driven at a pulsed 50 mA current.

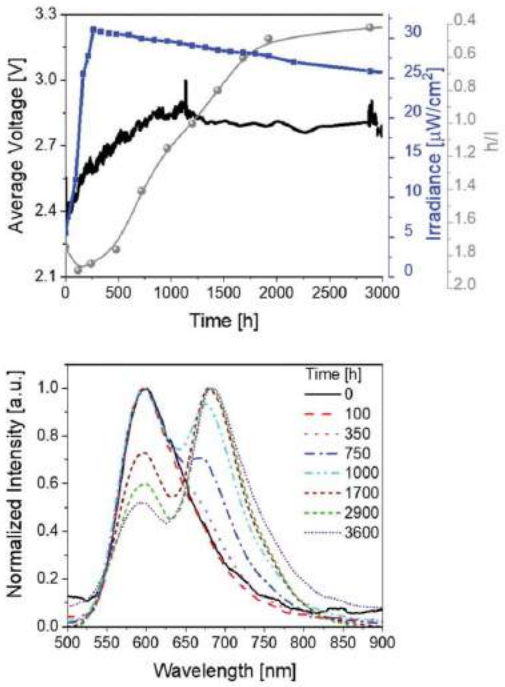


Fig. 4 Average voltage, irradiance, and h/l (h = high energy peak, l = low energy peak) ratio (top), as well as electroluminescence spectra (bottom) over time for **1** devices driven at a pulsed 25 mA current.

significantly increased to >3600 h with extrapolated lifetimes of >13 000 h. The device optimization with regard to the stability is also confirmed by comparing the total emitted energy of thick and thin devices – *i.e.*, 732 J *vs.* 6560 J, respectively. Notice that the total emitted energy is calculated by integrating the radiant flux of the device *vs.* time from $t = 0$ (application of bias) to $t = t_{1/5}$. This approach allows a clear stability comparison of devices showing different luminance levels as indicated by Bard and co-workers.[63] As such, the optimized devices represent one of the most stable and bright red-emitting SM-LECs reported so far.[1]

Besides the excellent stability performance of thin **1**-LECs, the same behavior for the changes of the electroluminescence spectrum over time were observed over the whole lifetime (Fig. 4 and Table 1). In detail, the h/l ratio value increases – *i.e.*, 1.25 *vs.* 1.90 for thin and thick devices, respectively. Indeed, the magnitude of the h/l peak intensity ratio is linearly correlated with respect to the externally applied electric field changing device architecture and driving conditions (Fig. S18, ESI†). Besides this aspect, the emission band shape of thin devices significantly changes showing an initial dominant emission centered at 600 nm with a low intensity shoulder at 670 nm that gets more prominent over time. After 1000 h, the l-peak becomes the major feature of the emission band. This leads to a change in the *x*/*y* CIE color coordinates from initial 0.59/0.40 to final 0.63/0.36 (Fig. S19, ESI†). After 2500 h of measurement, the h/l peak intensity ratio reaches a plateau until the end of the measurement. Noteworthy, this change accounts for a change of CCT <400 K, which is barely perceived by the human eye. As above described, the electroluminescence changes are in line with those of the applied voltage, which firstly decreases, then increases until it reaches a long plateau and then slightly decreases again, keeping its value at around 2.15 V over time (Fig. 4).

The above described relationship between the emission band shape changes and the electrical behavior over time prompted us to precisely determine the correlation with the changes of the internal electric field at the emitting neutral zone measured with dynamic EIS (see Experimental section).[64] To this end, we focused on thick devices driven at constant voltage of 3 V. Their electroluminescence response shows the typical behavior of LECs driven at constant voltage, that is, a slow rise of both current and brightness followed by a slight decrease over the measuring time (Fig. 5). On top of this measurement, we carried out EIS assays at certain time intervals. The EIS data were fitted using the full electric circuit (Fig. S20, ESI†), while the figures-of-merit are gathered in Table S1 and Fig. S21 (ESI†). Details on the data calculation is provided in the ESI.† As shown

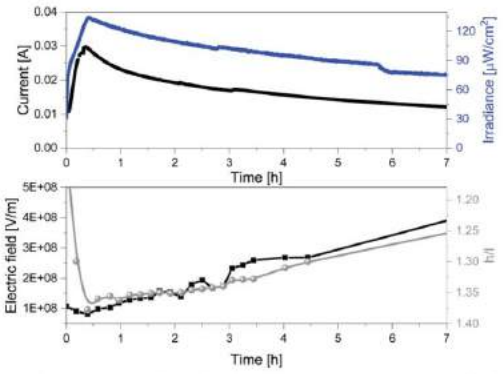


**Fig. 5** Current *vs.* irradiance (top) and internal electric field *vs.* h/l ratio (h = high energy peak, l = low energy peak) (bottom) of **1** devices driven at constant 3 V.

in Fig. 5, the same trend is noted for the changes of both the h/l peak intensity ratios and the internal electric field experience by the emitters. In short, the internal electric field is high at the beginning, but it rapidly decreases, reaching its minimum value after 0.42 h. This is related to the growth of the doped regions as shown by both the reduction of the resistance from 86.8 Ω to 25.9 Ω and the increase of the capacitance C from $8.35 \times 10^{-9}$ to $8.85 \times 10^{-9}$ F (Table S1, ESI†). This nicely corresponds to a time required to reach the maximum in the h/l peak intensity ratio (Fig. 5). Subsequently, the neutral region slowly shrinks, leading to an increase of the internal electrical field that is also well-correlated to a slow decrease of the h/l peak intensity ratio over time (Fig. 5). Hence, we concluded that the electroluminescence behavior of the contorted HBO in LECs is ruled by a rare electric-field dependence of the intensity between excited vibrational modes without changing the nature of the emitting excited state.

Please notice that a possible explanation of the different chromaticity trends over time could be related to changes in the recombination dynamics moving between regions of high and low electric fields as well as changes of the average internal electric field upon changing thickness of the active layer, composition, and driving modes.

## Conclusions

To sum up, the electroluminescent behavior of a representative red-emitting contorted HBO has, for the first time, been investigated using the LEC technology as a platform. Overall, this work provides two major findings. On one hand, this new family of emitters provides SM-LECs with outstanding performances, such as irradiances of *ca.* 220 μW $cm^{-2}$ and stabilities of over 200 h in thick devices and irradiances of *ca.* 30 μW $cm^{-2}$ and stabilities of 3600 h (measured) and 13 000 h (extrapolated) in thin devices. They account for one of the most stable and bright red SM-LECs reported so far.[1,26,28,29,53] On the other hand, we rationalize that the electroluminescent behavior of contorted HBO in LECs is ruled by a very rare electric-field dependence of the intensity for the radiative deactivation of the excited vibrational modes. This behavior is observed regardless of the device architecture and driving modes, while degradation, presence of aggregates, morphology changes over time, and temperature effects were excluded. It is worth mentioning that red shifted emission and broadening of the electroluminescence spectrum over time have typically been described in LECs based on iTMCs[22,45] and CPs.[65,66] However, they have been attributed to either a change of the nature of the excited state, or to a strong polarization as highlighted by change of the $E_{0-0}$ position along with large shifts in the maximum wavelength. This contrasts to the chromaticity changes in HBO based LECs, that are ascribed to the gradual change of the internal electric field affecting the radiative rate of the excited vibrational modes without changing the nature of the excited emitting state. Finally, it is important to point out that voltage-induced changes in the electroluminescence response have also been noticed in both multi-component or multi-layered architectures.[67–70] However, to the best of our knowledge, this type of electroluminescent behavior in a single-component single-layered SM-LECs has not been reported yet. Hence, this work deciphers, for the first time, the electroluminescent behavior of HBO as a new family of emitters for SM-LECs, highlighting one of the very rare examples of electric field dependent vibrational electroluminescence and one of the most efficient, stable, and bright red-emitting SM-LECs reported to date. Both aspects are of utmost relevance to design new emitters in the emerging field of SM-LECs. With this goal in mind, we illustrate the state-of-art of red-emitting LECs in Table S2 (ESI†), highlighting recent major achievements in the field.

## Conflicts of interest

There are no conflicts to declare.

## Acknowledgements

E. F. and R. D. C. acknowledge the program "Ayudas para la atracción de talento investigador – Modalidad 1 of the Consejería de Educación, Juventud y Deporte—Comunidad de Madrid with the Reference No. 2016-T1/IND-1463". R. D. C. also acknowledges the Spanish MINECO for the Ramón y Cajal program (RYC-2016-20891), the Europa Excelencia program (ERC2019-092825), and HYNANOSC (RTI2018-099504-A-C22), as well as the 2018 Leonardo Grant for Researchers and Cultural Creators from BBVA Foundation, the FOTOART-CM project funded by Madrid region under programme P2018/NMT-4367, and the Ministerio Project HYNANOSC with reference number RTI2018-099504-A-C22. K. B. and M. M. are thankful to 'Deutsche Forschungsgemeinschaft' supporting this project within the collaborative research center SFB 1249 "N-heteropolycyclic compounds as functional materials" (TP-A04). J. C.-G. acknowledges financial support from the Spanish Ministry of Science, Innovation and Universities (RTI2018-097508-B-I00), and

from the Regional Government of Madrid (S2018/NMT4511). IMDEA Nanociencia acknowledges support from the "Severo Ochoa" Programme for Centres of Excellence in R&D (MINECO, Grant No. SEV-2016-0686).

## References

1 E. Fresta and R. D. Costa, *J. Mater. Chem. C*, 2017, **5**, 5643–5675.
2 J. Xu, A. Sandström, E. M. Lindh, W. Yang, S. Tang and L. Edman, *ACS Appl. Mater. Interfaces*, 2018, **10**, 33380–33389.
3 R. D. Costa, *Light-emitting electrochemical cells. Concepts, advances and challenges*, Springer International Publishing, Basel, 1st edn, 2017.
4 S. Van Reenen, R. A. J. Janssen and M. Kemerink, *Org. Electron.*, 2011, **12**, 1746–1753.
5 S. Tang, A. Sandström, P. Lundberg, T. Lanz, C. Larsen, S. Van Reenen, M. Kemerink and L. Edman, *Nat. Commun.*, 2017, **8**, 1190.
6 E. Fresta, G. Volpi, C. Garino, C. Barolo and R. D. Costa, *Polyhedron*, 2018, **140**, 129–137.
7 M. F. Aygüler, M. D. Weber, B. M. D. Puscher, D. D. Medina, P. Docampo and R. D. Costa, *J. Phys. Chem. C*, 2015, **119**, 12047–12054.
8 M. S. Subeesh, K. Shanmugasundaram, C. D. Sunesh, R. K. Chitumalla, J. Jang and Y. Choe, *J. Phys. Chem. C*, 2016, **120**, 12207–12217.
9 J. Gao, *Curr. Opin. Electrochem.*, 2018, **7**, 87–94.
10 E. Fresta, G. Volpi, M. Milanesio, C. Garino, C. Barolo and R. D. Costa, *Inorg. Chem.*, 2018, **57**, 10469–10479.
11 E. Fresta, J.-M. Carbonell-Vilar, J. Yu, D. Armentano, J. Cano, M. Viciano-Chumillas and R. D. Costa, *Adv. Funct. Mater.*, 2019, **29**, 1901797.
12 E. Fresta, M. D. Weber, J. Fernández-Cestau and R. D. Costa, *Adv. Opt. Mater.*, 2019, **7**, 1900830.
13 S. T. Parker, J. D. Slinker, M. S. Lowry, M. P. Cox, S. Bernhard and G. G. Malliaras, *Chem. Mater.*, 2005, **17**, 3187–3190.
14 S. Van Reenen, P. Matyba, A. Dzwilewski, R. A. J. Janssen, L. Edman and M. Kemerink, *Adv. Funct. Mater.*, 2011, **21**, 1795–1802.
15 J. Mindemark, S. Tang, H. Li and L. Edman, *Adv. Funct. Mater.*, 2018, **28**, 1801295.
16 K. Y. Lin, L. D. Bastatas, K. J. Suhr, M. D. Moore, B. J. Holliday, M. Minary-Jolandan and J. D. Slinker, *ACS Appl. Mater. Interfaces*, 2016, **8**, 16776–16782.
17 L. D. Bastatas, K. Y. Lin, M. D. Moore, K. J. Suhr, M. H. Bowler, Y. Shen, B. J. Holliday and J. D. Slinker, *Langmuir*, 2016, **32**, 9468–9474.
18 J. K. Lee, D. S. Yoo, E. S. Handy and M. F. Rubner, *Appl. Phys. Lett.*, 1996, **69**, 1686–1688.
19 M. D. Weber, E. Fresta, M. Elie, M. E. Miehlich, J. L. Renaud, K. Meyer, S. Gaillard and R. D. Costa, *Adv. Funct. Mater.*, 2018, **28**, 1707423.
20 B. Pashaei, S. Karimi, H. Shahroosvand, P. Abbasi, M. Pilkington, A. Bartolotta, E. Fresta, J. Fernandez-Cestau, R. D. Costa and F. Bonaccorso, *Chem. Soc. Rev.*, 2019, **48**, 5033–5139.
21 C. E. Housecroft and E. C. Constable, *Coord. Chem. Rev.*, 2017, **350**, 155–177.
22 A. F. Henwood and E. Zysman-Colman, *Top. Curr. Chem.*, 2016, **374**, 36.
23 R. D. Costa, E. Orti, H. J. Bolink, F. Monti, G. Accorsi and N. Armaroli, *Angew. Chem., Int. Ed.*, 2012, **51**, 8178–8211.
24 Z. B. Hill, D. B. Rodovsky, J. M. Leger and G. P. Bartholomew, *Chem. Commun.*, 2008, 6594–6596.
25 S. Tang, W.-Y. Tan, X.-H. Zhu and L. Edman, *Chem. Commun.*, 2013, **49**, 4926–4928.
26 K. T. Weber, K. Karikis, M. D. Weber, P. B. Coto, A. Charisiadis, D. Charitaki, G. Charalambidis, P. Angaridis, A. G. Coutsolelos and R. D. Costa, *Dalton Trans.*, 2016, **45**, 13284–13288.
27 M. D. Weber, V. Nikolaou, J. E. Wittmann, A. Nikolaou, P. A. Angaridis, G. Charalambidis, C. Stangel, A. Kahnt, A. G. Coutsolelos and R. D. Costa, *Chem. Commun.*, 2016, **52**, 1602–1605.
28 M. D. Weber, M. Adam, R. R. Tykwinski and R. D. Costa, *Adv. Funct. Mater.*, 2015, **25**, 5066–5074.
29 A. Pertegás, D. Tordera and J. Serrano-Pérez, *J. Am. Chem. Soc.*, 2013, **135**, 18008–18011.
30 K. Baumgärtner, A. L. Meza Chincha, A. Dreuw, F. Rominger and M. Mastalerz, *Angew. Chem., Int. Ed.*, 2016, **55**, 15594–15598.
31 H. Seyler, B. Purushothaman, D. J. Jones, A. B. Holmes and W. W. H. Wong, *Pure Appl. Chem.*, 2012, **84**, 1047–1067.
32 G. Eda, G. Fanchini and M. Chhowalla, *Nat. Nanotechnol.*, 2008, **3**, 270–274.
33 Y. Zhong, B. Kumar, S. Oh, M. T. Trinh, Y. Wu, K. Elbert, P. Li, X. Zhu, S. Xiao, F. Ng, M. L. Steigerwald and C. Nuckolls, *J. Am. Chem. Soc.*, 2014, **136**, 8122–8130.
34 C. Nuckolls, C. Schenck, S. Xiao, M. Steigerwald, M. Ball, Y. Zhong, F. Ng and Y. Wu, *Acc. Chem. Res.*, 2014, **48**, 267–276.
35 B. Kohl, F. Rominger and M. Mastalerz, *Chem. – Eur. J.*, 2015, **21**, 17308–17313.
36 B. Kohl, F. Rominger and M. Mastalerz, *Angew. Chem., Int. Ed.*, 2015, **54**, 6051–6056.
37 E. Nestoros and M. C. Stuparu, *Chem. Commun.*, 2018, **54**, 6503–6519.
38 J. Mack, P. Vogel, D. Jones, N. Kaval and A. Sutton, *Org. Biomol. Chem.*, 2007, **5**, 2448–2452.
39 J. Vollbrecht, C. Wiebeler, H. Bock, S. Schumacher and H. S. Kitzerow, *J. Phys. Chem. C*, 2019, **123**, 4483–4492.
40 K. Baumgärtner, F. Rominger and M. Mastalerz, *Chem. – Eur. J.*, 2018, **24**, 8751–8755.
41 A. F. Henwood and E. Zysman-Colman, *Top. Curr. Chem.*, 2016, **374**, 36.
42 S. Tang, P. Murto, J. Wang, C. Larsen, M. R. Andersson, E. Wang and L. Edman, *Adv. Opt. Mater.*, 2019, 1900451.
43 Y.-M. Wang, F. Teng, Y.-B. Hou, Z. Xu, Y.-S. Wang and W.-F. Fu, *Appl. Phys. Lett.*, 2005, **87**, 233512.
44 J. D. Slinker, A. A. Gorodetsky, M. S. Lowry, J. Wang, S. Parker, R. Rohl, S. Bernhard and G. G. Malliaras, *J. Am. Chem. Soc.*, 2004, **126**, 2763–2767.

45 S. B. Meier, W. Sarfert, J. M. Junquera-Hernández, M. Delgado, D. Tordera, E. Ortí, H. J. Bolink, F. Kessler, R. Scopelliti, M. Grätzel, M. K. Nazeeruddin and E. Baranoff, *J. Mater. Chem. C*, 2013, **1**, 58–68.
46 H. J. Bolink, L. Cappelli, E. Coronado, A. Parham and P. Stössel, *Chem. Mater.*, 2006, **18**, 2778–2780.
47 H. J. Bolink, L. Cappelli, S. Cheylan, E. Coronado, R. D. Costa, N. Lardiés, M. K. Nazeeruddin and E. Ortí, *J. Mater. Chem.*, 2007, **17**, 5032–5041.
48 D. Asil, J. A. Foster, A. Patra, X. Dehatten, J. Delbarrio, O. A. Scherman, J. R. Nitschke and R. H. Friend, *Angew. Chem., Int. Ed.*, 2014, **53**, 8388–8391.
49 M. H. Bowler, T. Guo, L. Bastatas, M. D. Moore, A. V. Malko and J. D. Slinker, *Mater. Horiz.*, 2017, **4**, 657–664.
50 H.-C. Su and C.-Y. Cheng, *Isr. J. Chem.*, 2014, **54**, 855–866.
51 G. R. Lin, H. R. Chen, H. C. Shih, J. H. Hsu, Y. Chang, C. H. Chiu, C. Y. Cheng, Y. S. Yeh, H. C. Su and K. T. Wong, *Phys. Chem. Chem. Phys.*, 2015, **17**, 6956–6962.
52 N. Kaihovirta, C. Larsen and L. Edman, *ACS Appl. Mater. Interfaces*, 2014, **6**, 2940–2947.
53 M. D. Weber, J. E. Wittmann, A. Burger, O. B. Malcioglu, J. Segarra-Martínez, A. Hirsch, P. B. Coto, M. Bockstedte and R. D. Costa, *Adv. Funct. Mater.*, 2016, **26**, 6737–6750.
54 D. R. Blasini, J. Rivnay, D. M. Smilgies, J. D. Slinker, S. Flores-Torres, H. D. Abruña and G. G. Malliaras, *J. Mater. Chem.*, 2007, **17**, 1458–1461.
55 Y. J. Cho, S. Taylor and H. Aziz, *ACS Appl. Mater. Interfaces*, 2017, **9**, 40564–40572.
56 H. Yu, Y. Zhang, Y. J. Cho and H. Aziz, *ACS Appl. Mater. Interfaces*, 2017, **9**, 14145–14152.
57 J. Y. Li, D. Liu, C. Ma, O. Lengyel, C. S. Lee, C. H. Tung and S. Lee, *Adv. Mater.*, 2004, **16**, 1538–1541.
58 S. Yang and M. Jiang, *Chem. Phys. Lett.*, 2009, **484**, 54–58.
59 M. D. Weber, J. E. Wittmann, A. Burger, O. B. Malcıoğlu, J. Segarra-Martí, A. Hirsch, P. B. Coto, M. Bockstedte and R. D. Costa, *Adv. Funct. Mater.*, 2016, **26**, 6737–6750.
60 B. Henderson and G. F. Imbusch, *Optical Spectroscopy of Inorganic Solids*, Clarendon Press, Oxford, UK, 1989.
61 H. J. Bolink, E. Coronado, R. D. Costa, E. Orti, M. Sessolo, S. Graber, K. Doyle, M. Neuburger, C. E. Housecroft and E. C. Constable, *Adv. Mater.*, 2008, **20**, 3910–3913.
62 H. Rudmann and M. F. Rubner, *J. Appl. Phys.*, 2001, **90**, 4338–4345.
63 G. Kalyuzhny, M. Buda, J. Mcneill, P. Barbara and A. J. Bard, *J. Am. Chem. Soc.*, 2003, **125**, 6272–6283.
64 B. M. D. Puscher, M. F. Aygueler, P. Docampo and R. D. Costa, *Adv. Energy Mater.*, 2017, **7**, 1602283.
65 F. Habrard, T. Ouisse, O. Stéphan, L. Aubouy, P. Gerbier, L. Hirsch, N. Huby and A. Van der Lee, *Synth. Met.*, 2006, **156**, 1262–1270.
66 G. Mauthner, M. Collon, E. J. W. List, F. P. Wenzl, M. Bouguettaya and J. R. Reynolds, *J. Appl. Phys.*, 2005, **97**, 063508.
67 A. J. Norell Bader, A. A. Ilkevich, I. V. Kosilkin and J. M. Leger, *Nano Lett.*, 2011, **11**, 461–465.
68 J. M. Leger, S. A. Carter and B. Ruhstaller, *J. Appl. Phys.*, 2005, **98**, 124907.
69 M. L. Wu, G. Y. Chen, T. A. Shih, C. W. Lu and H. C. Su, *Phys. Chem. Chem. Phys.*, 2018, **20**, 18226–18232.
70 J. Wang, S. Tang, A. Sandström and L. Edman, *ACS Appl. Mater. Interfaces*, 2015, **7**, 2784–2789.

Electronic Supplementary Material (ESI) for Nanoscale Horizons.


# Supporting Information

**Bright, Stable, and Efficient Red Light-emitting Electrochemical Cells using Contorted Nanographenes**

Elisa Fresta, Kevin Baumgärtner, Juan Cabanillas-Gonzalez, Michael Mastalerz and Rubén D. Costa*

## Preparation and characterization of thin films

**1** was synthesized as reported previously.[1,2] Absorption spectra were recorded with a Perkin Elmer Lambda 35 UV-Vis spectrometer. The emission spectra and photoluminescence quantum yields ($\phi$) values were measured with a FS5 Spectrofluorometer with integrating sphere SC-30 (Edinburgh Instruments). Excited states lifetimes ($\tau$) of fluorescence emission were obtained with a TCSPC module ($\lambda_{exc}$ 377.6 nm).

The average lifetime can be obtained by using the depicted formula:

$$R(t) = \sum_{i=1}^{2} A_i e^{-t/\tau_i}$$

where $A_i$ is constant. The average lifetime can be obtained with:

$$< \tau > = \frac{A_1\tau_1^2 + A_2\tau_2^2}{A_1\tau_1 + A_2\tau_2}.$$

Photoluminescence measurements at temperatures ranging from 77 K to 425 K were performed upon enclosing the **1** films in a CFV-Optistat (Oxford Instruments) equipped with a temperature controller. Thin-films were photoexcited with a TEEM Photonics passive Q-switch Nd:YAG laser (405 nm, 300 ps pulse duration, 170 Hz, pulse energy < 1 mJ) mildly focused on the sample (fluence < 10 mJcm$^{-2}$). The photoluminescence emitted by the samples was dispersed by a grating inside a spectrometer (SP2500, Acton Research) and spectrally recorded with a liquid $N_2$-cooled back depleted CCD (Princeton Instruments). Long pass filters were employed to reject stray light from the photoexcitation beam into the spectrometer. Photoluminescence spectra were acquired 10 minutes after the sample reached the desired temperature in order to ensure complete sample thermalization.

Thin films were prepared onto cleaned quartz slides from a filtered solution of **1** (15 mg/mL in THF to achieve 70 nm thickness or 5 mg/mL to achieve 30 nm thickness) by spin-coating them at 800 rpm for 30 s, at 1500 rpm for 30 s and at 3000 rpm for an additional 10 s. AFM measurements were carried out with a Park XE150 instrument (Park Systems Corp., Suwon, South Korea), and the Gwyddion evaluation software.

**Device fabrication and characterization**

ITO substrates were purchased from Naranjo Substrates with an ITO thickness of 130 nm. They were extensively cleaned using detergent, water, ethanol, and propan-2-ol as solvents in an ultrasonic bath (frequency 37-70 Hz) for 15 min each. Afterwards, the slides were dried with $N_2$ gas and put in an UV-ozone cleaner for 8 min and used directly as described in the main text. If PEDOT:PSS is used to increase reproducibility, the clean plates were coated with 70 nm PEDOT:PSS layers via spin coating. To this end, an aqueous solution of PEDOT:PSS was filtered and mixed with propan-2-ol in a ratio of 3:1. From this solution, 50 μL were dropped onto the substrate at a rotation speed of 2000 rpm and spun for 60 s. The resulting layers were dried on a hotplate at 120 °C and stored under $N_2$. Thick active layers (70 nm) were deposited from a 10 mg/mL THF solution of **1** combined with a ion-doped matrix consisting of **1**:TMPE:LiOTf 1:0.15:0.05 mass ratio. This was prepared using THF solutions of TMPE with $M_w$ 450,000 (20 mg/mL), and LiOTf (10 mg/ml) and spin coated at 800 rpm for 30 s, at 1500 rpm for 30 s and at 3000 rpm for an additional 10 s, resulting in 70 nm of active layer thickness. The thin active layers (30 nm) were achieved by employing a 5 mg/mL solution of **1**, following the same procedure as above. In all cases, after the deposition of the active layer the devices were dried under vacuum for 2 h and transferred to an inert atmosphere glovebox (<0.1 ppm $O_2$ and $H_2O$, Angstrom Engineering). Finally, Aluminum cathodes (90 nm) were thermally evaporated onto the active layer using a shadow mask under high vacuum (<1 x $10^{-6}$ mbar) in an Angstrom Covap evaporator integrated into the inert atmosphere glovebox. The device active area was of 10 $mm^2$. The device statistics involve up to five different devices – *i.e.*, a total number of 20 pixels. Time dependence of luminance, voltage, and current was measured by applying constant and/or pulsed voltage and current by monitoring the desired parameters simultaneously by using Avantes spectrophotometer (Avaspec-ULS2048L-USB2) in conjunction with a calibrated integrated sphere Avasphere 30-Irrad and Botest OLT OLED Lifetime-Test System. Electroluminescence spectra were recorded using the above mentioned spectrophotometer. Electrochemical impedance spectroscopic assays (EIS) were carried out with a potentiostat/galvanostat (Metrohm μAutolabIII) equipped with a frequency response analyser module (FRA2). Measurements were performed at the applied voltage range from 0 to 5 V and fitted with the Nova software using the circuit model shown in Figure S9. The AC signal amplitude was set to 10 mV, modulated in a frequency range from 10 Hz to 1 MHz. The Nova 1.11 software was used to obtain the parameters from the equivalent circuit. With this

data at hand, the resistance of the intrinsic non-doped region ($R_{LEC}$) was directly obtained. The film conductivity (S/m) is measured at 0 V with the following equation: $\sigma=d/(AR_{LEC})$, where $d$ is the thickness of the layer, $A$ is the area of the electrodes, and $R_{LEC}$ is the resistance of the active layer. Dynamic EIS measurement were performed at the constant voltage of 3 V and fitted using the circuit model shown in Figure S20. Upon performing the fitting, the capacitance was replaced with a constant phase element (CPE), which is the equivalent electrical circuit component that models the behavior of an imperfect capacitor. This is assumed to be caused by non-uniform current density distribution and/or reaction rates along the electrode surface, usually caused by an inhomogeneous surface. [4,5] The CPE's impedance is defined as $C= Q^{1/\alpha} x\ R_{LEC}^{(1-\alpha)/\alpha}$, and $\alpha$ ($0 \leq \alpha \leq 1$). Q corresponds to $1/|Z|$ at $\omega = 1$ rad/s, where Z is the impedance; it represents no direct meaningful physical value. However, the CPE acts as pure resistor for $\alpha = 0$ and pure capacitor for $\alpha = 1$. The thickness of the doped regions is calculated taking into account that $d_{EDL}C_{EDL}=dC_{geo}$, where $d_{EDL}$=thickness of the doped regions, $C_{EDL}$=capacitance associated to the doped regions, d=device thickness and $C_{geo}$=geometric capacitance obtained by fitting the circuit at 0 V.[4]. The intensity of the internal electric field is then calculated with $E=V/d_{EDL}$, where V is the constant applied voltage and $d_{EDL}$ the thickness of the doped regions. The temperature of the devices upon driving was recorded with a FLIR 430-sc thermal camera. The EQE is defined as $EQE=b\varphi/2n^2$, where b is the recombination efficiency (equal to 1 for two ohmic contacts), $\varphi$ is the fraction of excitons that decay radiatively, and n is the refractive index of the glass substrate and is equal to 1.5 (the factor $1/2n^2$ represent the light out-coupling of the device). As **1** can only presents fluorescence emission, $\varphi$ is equal to ¼ of the PL efficiency, as, statistically, ¼ of the electron-hole recombination produces singlets.

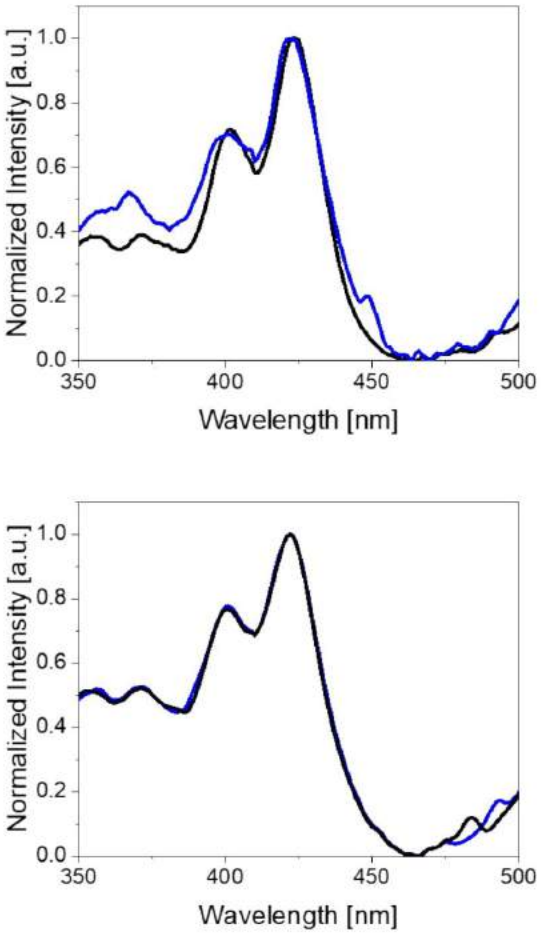


**Figure S1**. Excitation spectra at rt. of pristine **1** thin-film (top) and those used in devices with polyelectrolyte matrix (bottom) at $\lambda_{em}$ of 598 nm (black) and 647 nm (blue).

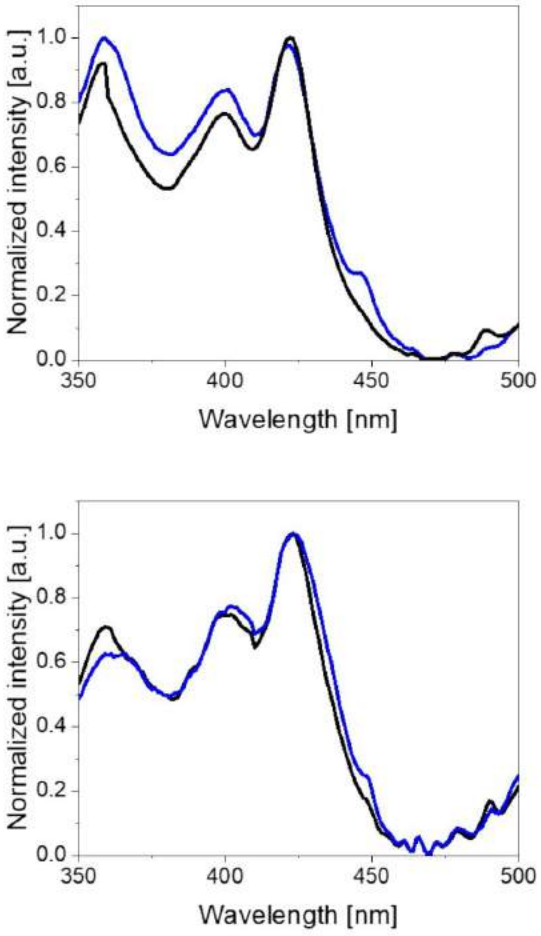


**Figure S2**. Excitation spectra at 77 K of pristine **1** thin-film (top) and those used in devices with polyelectrolyte matrix (bottom) at $\lambda_{em}$ of 598 nm (black) and 647 nm (blue).

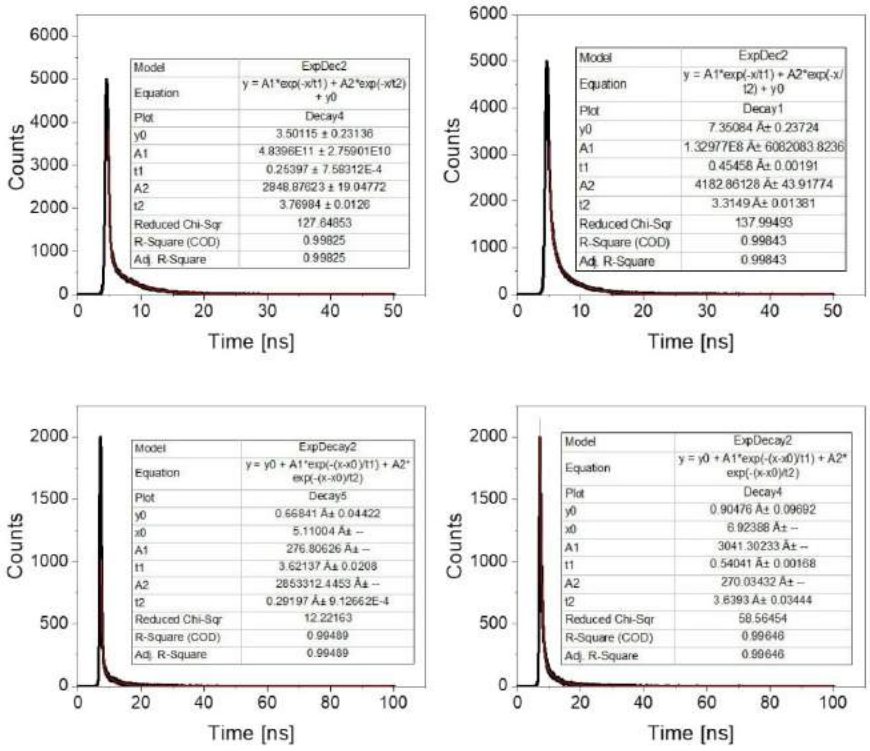


**Figure S3**. Excited-state decay profile ($\lambda_{exc}$ = 377.6 nm) measured at rt. of pristine **1** thin films pure (top) and those used in devices with polyelectrolyte matrix (bottom) at $\lambda_{em}$ of 600 nm (left) and 650 nm (right). The exponential fittings are highlighted in red, while the parameters are gathered in the inset table.

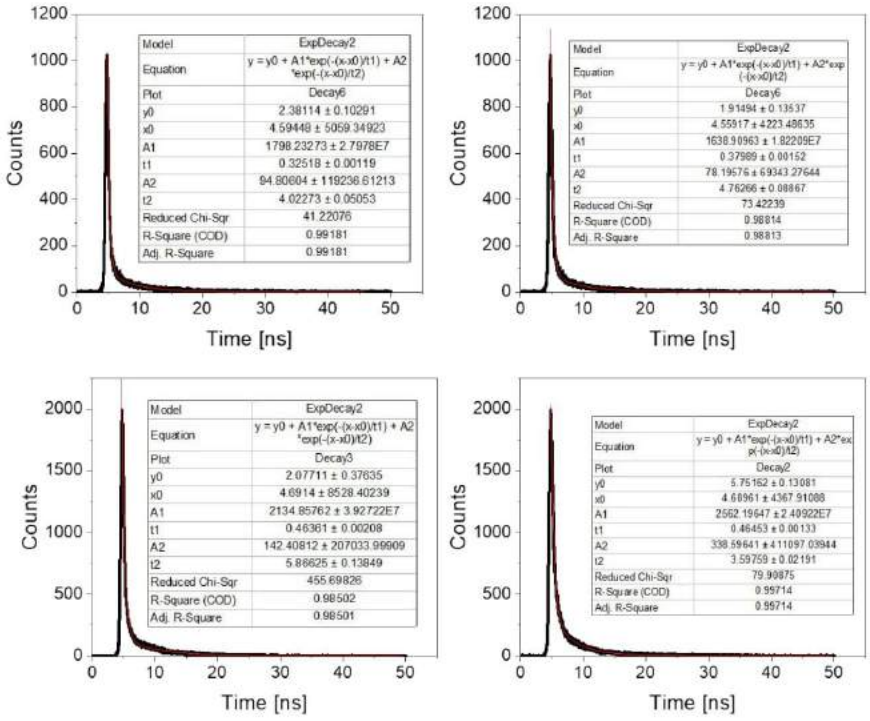


**Figure S4**. Excited-state decay profile ($\lambda_{exc}$ = 377.6 nm) measured at 77K of pristine **1** thin films pure (top) and those used in devices with polyelectrolyte matrix (bottom) at $\lambda_{em}$ of 600 nm (left) and 650 nm (right). The exponential fittings are highlighted in red, while the parameters are gathered in the inset table.

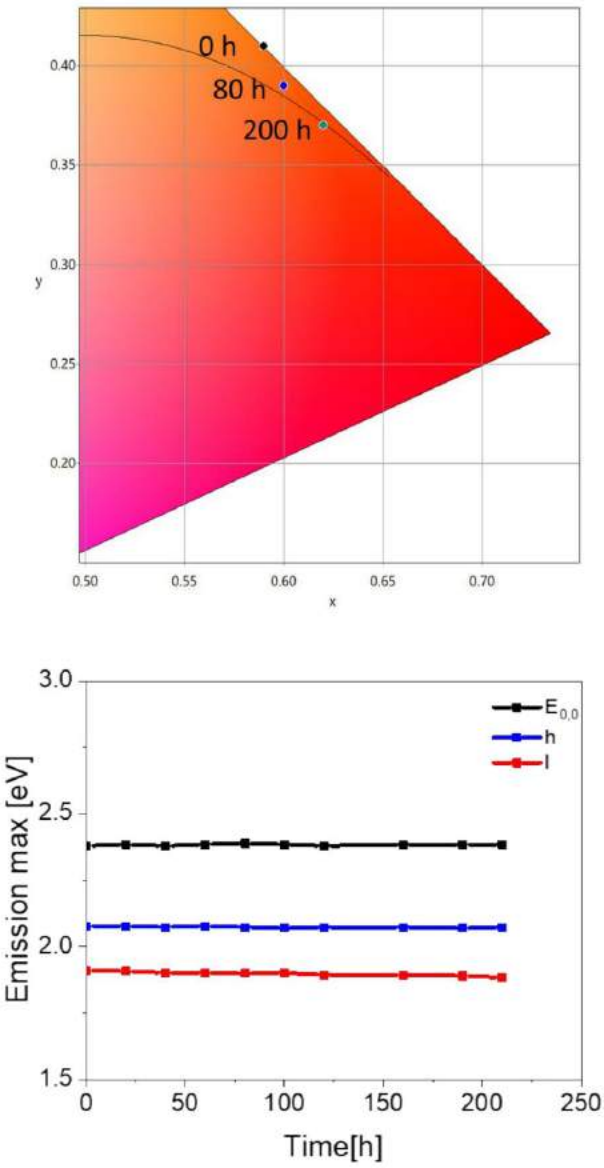


**Figure S5**. Top: Changes of the x/y CIE coordinates of **1** devices corresponding to the electroluminescence response of fresh (black), after 80 h (blue), and after 200 h (green) at a pulsed 25 mA current. Bottom: Changes in $E_{0,0}$ band and emission wavelength maxima of h and l peaks (h=high energy, l=low energy) over time in **1** devices driven at a pulsed 25 mA current.

**Figure S6.** Changes of the intensity of the h and l peaks as well as their difference (h-l) over time (left) over time in **1** devices driven at a pulsed 25 mA current.

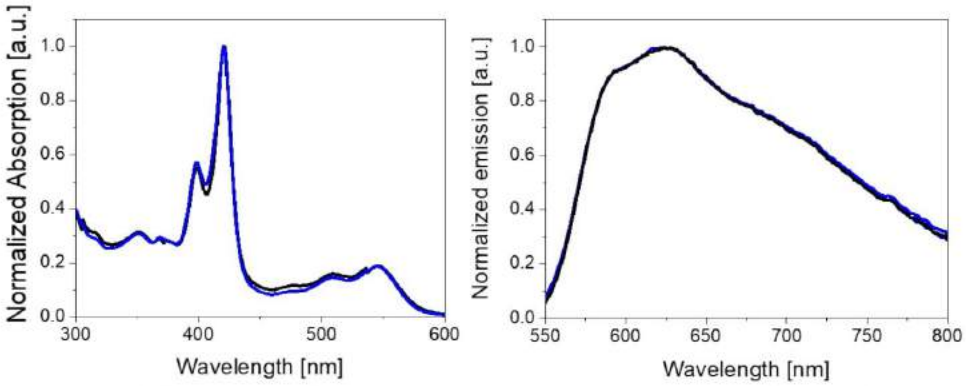


**Figure S7**. UV-Vis absorption (left) and emission (right) spectra of fresh (black) and used (blue) **1** devices.

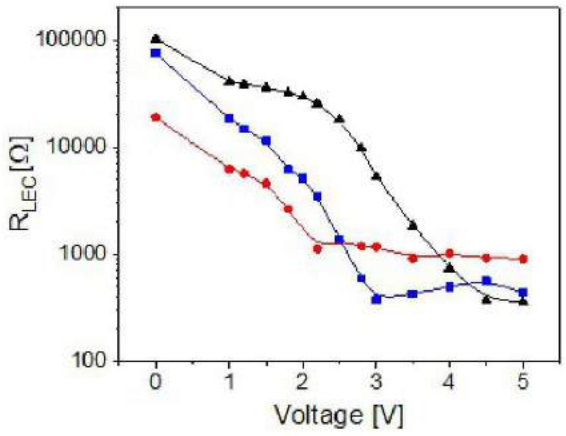


**Figure S8.** Static EIS assays applied to **1** devices to monitor the changes of the device behavior of fresh (black), used (red), and after heating at 60 ºC (blue) devices with respect to resistance associated to the EDL and doped region formations upon increasing the applied voltage from 0 to 5 V.

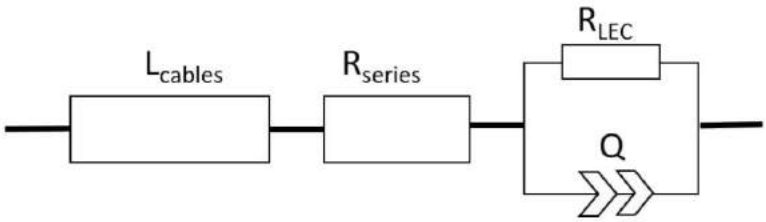


**Figure S9**. Simplified circuit model with electrical resistance ($R_{LEC}$) and admittance Q used for static EIS assays. A series resistor ($R_{series}$) and inductor elements for the cables ($L_{cables}$) were also included.

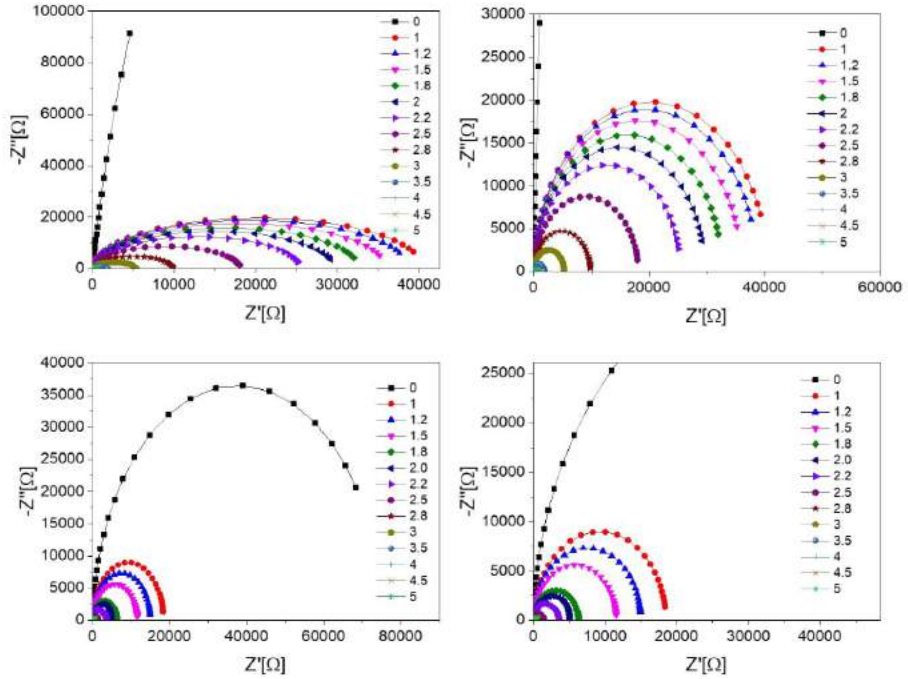


**Figure S10**. Nyquist plots of fresh (top left), with zoom into the 1-5 V region (top right), and used heated at 60°C (bottom left), with zoom into the 1-5 V region (bottom right), **1** devices measured upon constant bias (see legend). The fittings are shown in solid lines.

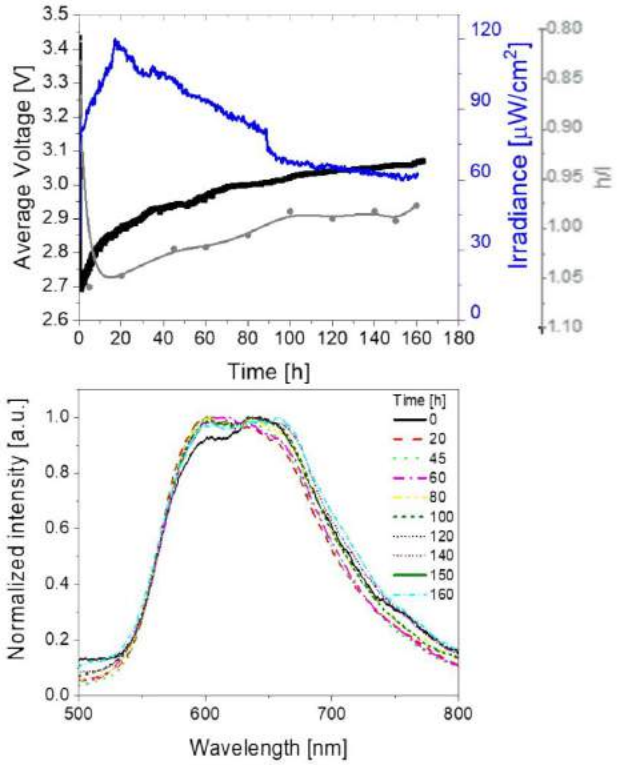


**Figure S11.** Average voltage, irradiance, and h/l ratio (h=high energy peak and l=low energy peak) (top), as well as electroluminescence spectra (bottom) over time (see legend) for used **1** devices driven at pulsed 25 mA current.

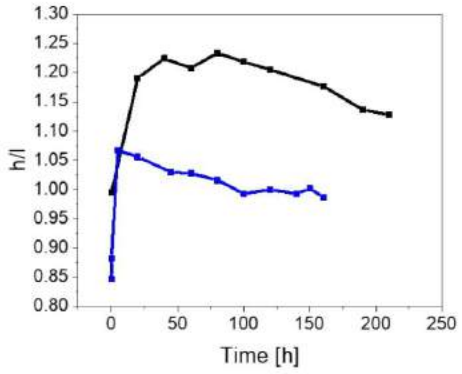

**Figure S12.** h/l (h=high energy peak and l=low energy peak) ratio over time for fresh (black) and used (blue) **1** devices run until lifetime at the pulsed current of 25 mA.

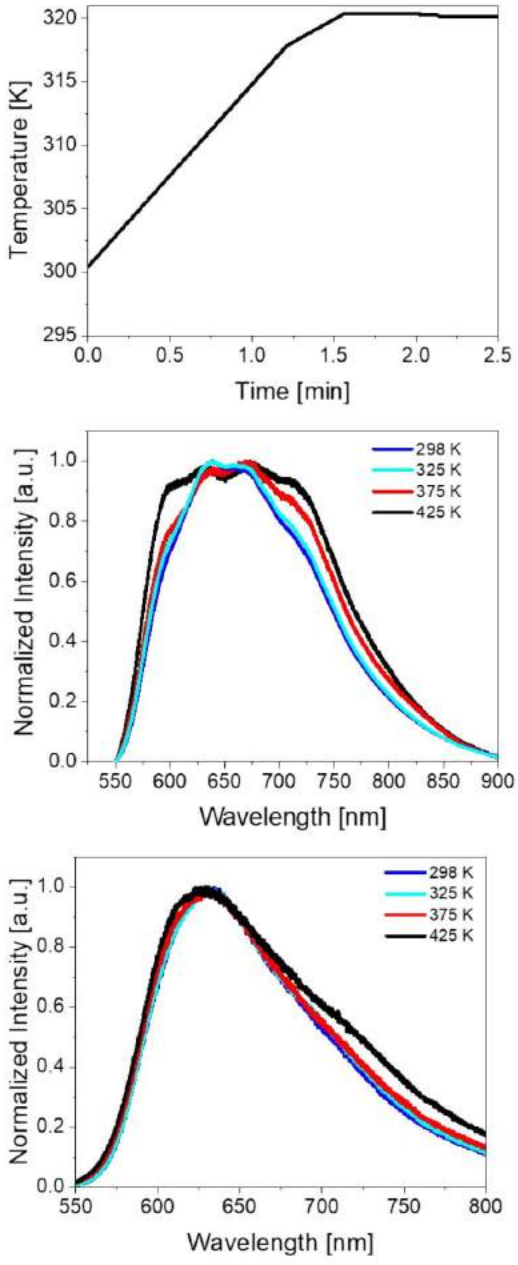

**Figure S13**. Top: Temperature rise of **1** device at 25 mA. Bottom: photoluminescence at different temperatures of pristine **1** thin films (center) and those used in devices with the ionic polyelectrolyte matrix (bottom). The films were prepared onto quartz slides.

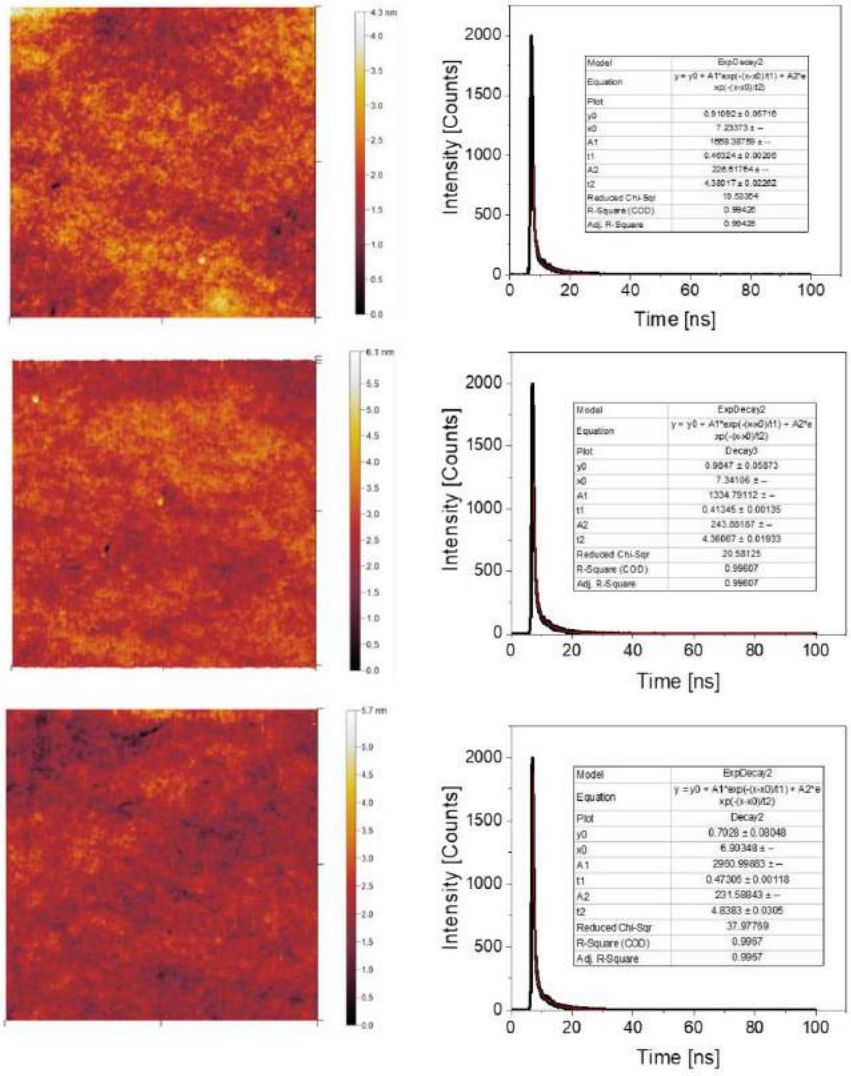


**Figure S14**. AFM measurements (left) and excited-state decay profile ($\lambda_{exc}$ = 377.6 nm; $\lambda_{em}$ 600 nm) (right) of fresh **1** devices (top) and those kept at 60°C for 1 day (centre) and for 10 days (bottom). The exponential fittings are highlighted in red and the parameter are gathered in the inset table.

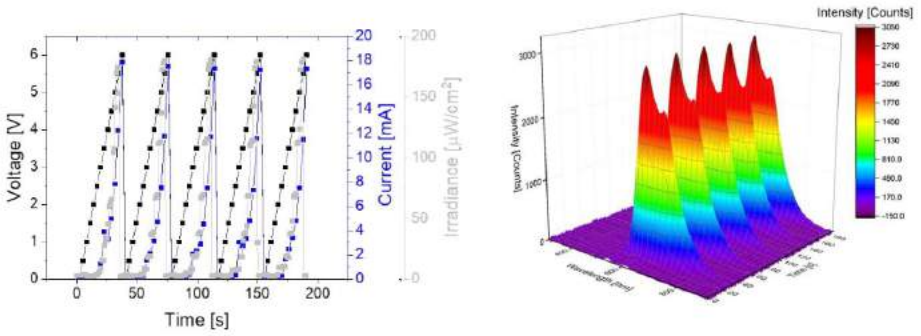


**Figure S15**. Voltage, current and irradiance profiles (left) and electroluminescent spectra (right) of **1** devices under repetitive LIV scans.

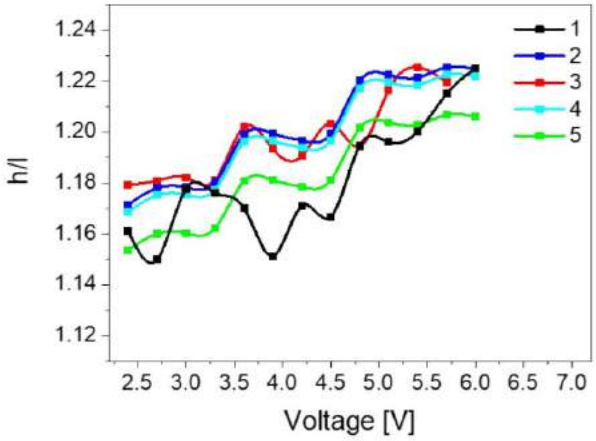


**Figure S16.** h/l (h=high energy peak and l=low energy peak) changes over applied voltage ramp upon different L-I-V (300 mV/s, 0-6 V) scans (see legend).

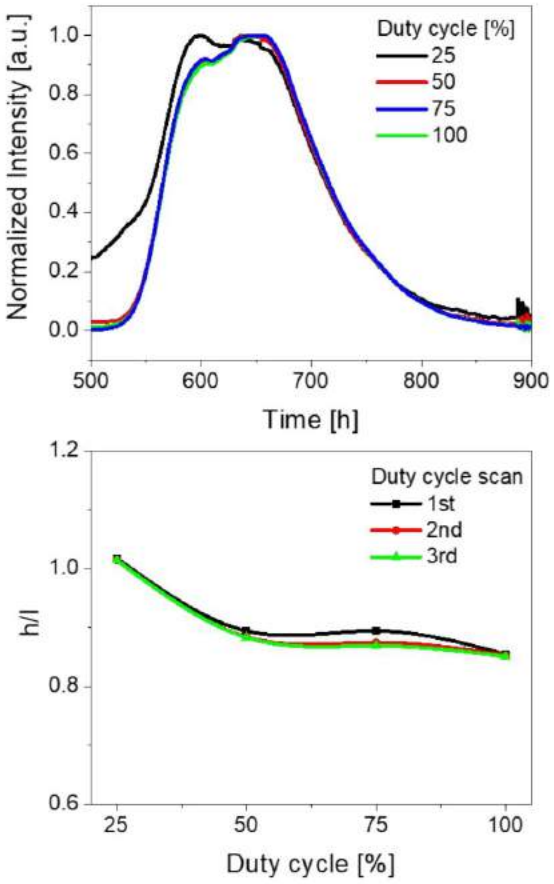


**Figure S17**. Electroluminescence response at different duty cycles (see legend) and h/l (h=high energy peak and l=low energy peak) ratio upon different duty cycle scans (see legend).

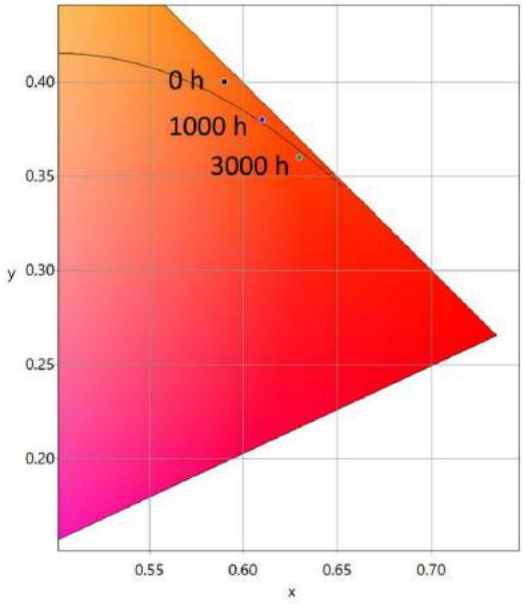


**Figure S18**. Changes of the x/y CIE coordinates of **1** devices corresponding to the electroluminescence response of fresh (black), after 1000 h (blue), and after 3000 h (green) at a pulsed 25 mA current.

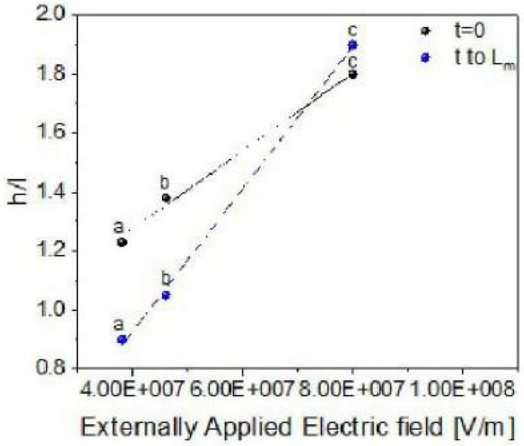


**Figure S19**. h/l (h=high energy peak and l=low energy peak) ratio *vs*. external applied electric field at time 0 and time needed to reach the maximum luminance ($L_m$) of thick devices driven at pulsed 25 mA current (a), thick devices driven at pulsed 50 mA current (b), and thin devices driven at pulsed 25 current (c). The linear fittings ($R^2$= 0.9999) are highlighted in dashed lines.

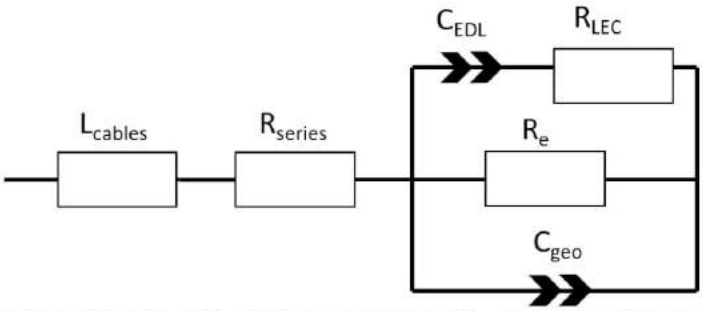


**Figure S20**. Circuit model with EDL related capacitance ($C_{EDL}$), ionic resistance ($R_{LEC}$), electrical resistance ($R_e$), and geometric capacitance ($C_{geo}$) used for dynamic EIS assays.

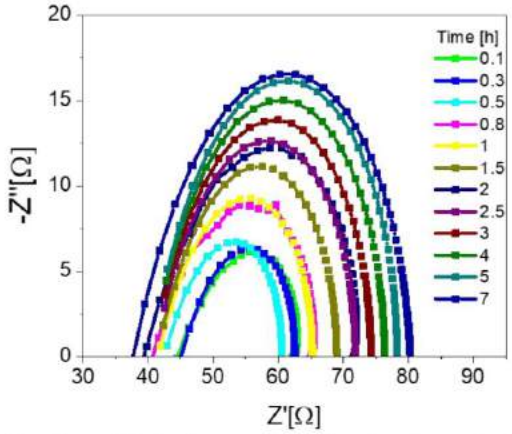


**Figure S21**. Nyquist plots of **1** devices measured under dynamic EIS at 3 V upon time (see legend). The fittings are shown in solid lines.

**Table S1. Data obtained from dynamic EIS performed at 3 V.**

| Time [h] | Electrical field [V] | Doped region width [nm] | $R_{LEC}$ [Ω] | $C_{eff}$ [F] | $\varepsilon_r$ |
|---|---|---|---|---|---|
| 0 | 1.08E+08 | 27.5 | 86.8 | 8.35E-09 | 4.4 |
| 0.15 | 8.69E+07 | 33.4 | 26.9 | 8.83E-09 | 4.7 |
| 0.41 | 7.8E+07 | 38.1 | 25.9 | 8.86E-09 | 4.7 |
| 0.58 | 1.04E+08 | 30.3 | 31.9 | 8.75E-09 | 4.6 |
| 1.35 | 1.17E+08 | 26.0 | 35.6 | 8.60E-09 | 4.6 |
| 2.1 | 1.34E+08 | 23.2 | 39.1 | 8.55E-09 | 4.6 |
| 3.5 | 2.58E+08 | 11.9 | 57.9 | 8.46E-09 | 4.5 |
| 4.4 | 2.61E+08 | 11.7 | 59.5 | 8.45E-09 | 4.5 |
| 7.0 | 3.96E+08 | 7.7 | 71.9 | 8.36E-09 | 4.4 |

**Table S2. State-of-art overview of red-emitting LECs.**

| Type of emitter | LEC structure | Driving mode[a] | $L_{max}$ ($cd/m^2$)[b] [$\lambda_{max}$ (nm)] | Turn-on time (h)[c] | Lifetime (h)[d] | Efficacy (cd/A) | EQE (%) | x/y CIE | Ref. |
|---|---|---|---|---|---|---|---|---|---|
| SM **1** | ITO/PEDOT:PSS(70 nm)/**1**:TMPE:LiOTf 1:0.15:0.05(70 nm)/Al(90 nm) | 25 mA[a] | 242 | 24 | 204 | - | 0.78 | 0.61/0.39 | This work |
| Ir-iTMC **2** | ITO/PEDOT:PSS (80 nm)/**Ir-iTMC**: [BMIM][$PF_6$] 4:1 molar ratio(100 nm)/Al (70 nm) | 100 $A/m^2$ [a] | 200 [642] | 870 | >6000 | 2.0 | 2.0 | 0.63/0.37 | 3 |
| Ir-iTMC **3** | ITO/PEDOT:PSS (40 nm)/**Ir-iTMC**: [BMIM][$PF_6$] 80:20 wt%/Ag | 2.2 V | 9 [663] | - | - | 3.4 | 7.4 | 0.69/0.31 | 4 |
| Ir-iTMC **4** | ITO/PEDOT:PSS (80 nm)/**Ir-iTMC**: [BMIM][$PF_6$] 4:1 molar ratio(100 nm)/Al (70 nm) | 700 $A/m^2$ [a] | 85 [654] | - | 220 | - | 0.16 | 0.63/0.35 | 5 |
| Ru-iTMC **5** | ITO/**Ru-iTMC** /Ga:In | 7.7 V | 742 [690] | 87 s | 0.2 | - | 0.68 (5.9 V) | 0.63/0.30 | 6 |
| Ru-iTMC **6** | ITO/**Ru-iTMC** /Ga:In | 6 V | 2250 [685] | - | - | 0.39 | 0.61 | 0.66/0.32 | 7 |
| Cu-iTMC **7** | ITO/PEDOT:PSS (80 nm)/**Cu-iTMC** (120 nm)/Al (70 nm) | 15 mA[a] | 100 $\mu W/cm^2$ [673] | - | 20.9 | - | - | 0.66/0.32 | 8 |
| ZnTPP **8** | ITO/PEDOT:PSS (80 nm)/ZnTPP: TMPE:LiOTf 1:0.15:0.06 (60 nm)/Al (90 nm) | 7.5 mA[a] | ~1 [650] | 20 | >250 | 0.001 | - | 0.65/0.32 | 9 |
| SM **9,10** | ITO/PEDOT:PSS/SM 7,8 100:0.1 /Al | 100 A $m^{2}$[a] | 0.6 $W/m^2$ [706] | 0.1 | >100 | - | 0.44 | - | 10 |
| SM **11** | ITO/PEDOT:PSS (80 nm)/SM **9**: TMPE:LiOTf 1:0.10:0.06/Al (90 nm) | 7.7 mA[a] | 750 [618] | - | 15 | 1.1 | - | - | 11 |
| Red QDs | ITO/PEDOT:PSS (35 | 2.0 | 581 [620] | - | - | 1.5 | - | 0.67/0.33 | 12 |

| | |
|---|---|
| | nm)/**Red QDs**: [BMIM][$PF_6$]:PVK[f] (150-200 nm)/Al |

a. Constant mode. b. Highest luminance achieved during the entire measurement. c. Time to reach the highest luminance. d. Time to decay to ½ of the maximum luminance. e. [BMIM][PF6]: buthyl methyl imidazolium hexafluorophosphate. f. PVK: Poly (9-vinylcarbazole).

**1**: Hexabenzoovalene in this work

**2**: $[Ir(ppy)_2(N^{\wedge}N)][PF_6]$, with ppy=phenylpyridine, N^N=2-(6-phenylpyridin-2-yl)benzo[d]thiazole

**3**: $[Ir(C^{\wedge}N)_2(N^{\wedge}N)][PF_6]$, with C^N=1-(4-(tert-butyl)phenyl)-1H-pyrazole, N^N=2, 2'-biquinoline

**4**: $[Ir(C^{\wedge}N)2(N^{\wedge}N)][PF_6]$. With C^N=1-phenylisoquinoline, N^N= 2-(pyridine-2-yl)benzo[d]thiazole

**5**: $[Ru_2(4,4'\text{-dimethylbpy})_2(\text{bathophen})][ClO_4]_4$, with dimethylbpy: dimethylbipyridine, bathophen: 4,7-Diphenyl-1,10-phenanthroline

**6**: $[Ru(\text{hpbpip})(4,4'\text{-dimethylbpy})_2](ClO_4)_2$, with hpbpip 2-(2-hydroxyphenyl)-1-(4-bromophenyl)-1*h*-imidazo[4,5-*f*][1,10]phenanthroline

**7**: $[Cu(N^{\wedge}N)(P^{\wedge}P)]^+$, with N^N is 4,4′ -diethylester-2,2′ -biquinoline (dcbq) and P^P is 4,5-bis(diphenylphosphino)-9,9-dimethylxanthene (Xantphos)

**8**: ZnTPP Zinc-tetraphenylporphyrin

**9**: 1-ethyl-2-[3-(1- ethyl-1,3-dihydro-3,3-dimethyl-2H-indol-2-ylidene)-propenyl]- 3,3-dimethyl-3H-indolium hexafluorophosphate

**10**: 1-butyl-2-[5-(1-butyl-1,3-dihydro-3,3-dimethyl-2H- indol-2-ylidene)-penta-1,3-dienyl]-3,3-dimethyl-3H-indolium hexafluorophosphate

**11**: 4,7-bis(4-(4-sec-butoxyphenyl)-5-(3,5-di(1- naphthyl)phenyl)thiophen-2-yl)-2,1,3-benzothiadiazole

## References


1 K. Baumgärtner, A. L. Meza Chincha, A. Dreuw, F. Rominger and M. Mastalerz, *Angew. Chem. Int. Ed.*, 2016, **55**, 15594–15598.

2 K. Baumgärtner, F. Rominger and M. Mastalerz, *Chem. - A Eur. J.*, 2018, **24**, 8751–8755.

3 C. D. Ertl, C. Momblona, A. Pertegás, J. M. Junquera-Hernández, M. G. La-Placa, A. Prescimone, E. Ortí, C. E. Housecroft, E. C. Constable and H. J. Bolink, *J. Am. Chem. Soc.*, 2017, **139**, 3237–3248.

4 G. X. Yu, C. H. Lin, Y. X. Liu, R. H. Yi, G. Y. Chen, C. W. Lu and H. C. Su, *Chem. - A Eur. J.*, 2019, 13748–13758.

5 C. Momblona, C. D. Ertl, A. Pertegás, J. M. Junquera-Hernández, H. J. Bolink, E. C. Constable, M. Sessolo, E. Ortí and C. E. Housecroft, *J. Mater. Chem. C*, 2018, **6**, 12679–12688.

6 B. Nemati Bideh and H. Shahroosvand, *Sci. Rep.*, 2017, **7**, 15739.

7 B. Nemati Bideh, C. Roldán-Carmona, H. Shahroosvand and M. K. Nazeeruddin, *Dalt. Trans.*, 2016, **45**, 7195–7199.

8 E. Fresta, M. D. Weber, J. Fernández-Cestau and R. D. Costa, *Adv. Opt. Mater.*, 2019, DOI: 10.1002/adom.201900830.

9 K. T. Weber, K. Karikis, M. D. Weber, P. B. Coto, A. Charisiadis, D. Charitaki, G.

Charalambidis, P. Angaridis, A. G. Coutsolelos and R. D. Costa, *Dalt. Trans.*, 2016, **45**, 13284–13288.

10 S. Jenatsch, L. Wang, N. Leclaire, E. Hack, R. Steim, S. B. Anantharaman, J. Heier, B. Ruhstaller, L. Penninck, F. Nüesch and R. Hany, *Org. Electron.*, 2017, **48**, 77–84.

11 S. Tang, W.-Y. Tan, X.-H. Zhu and L. Edman, *Chem. Commun.*, 2013, **49**, 4926–4928.

12 G. Qian, Y. Lin, G. Wantz, A. R. Davis, K. R. Carter and J. J. Watkins, *Adv. Funct. Mater.*, 2014, **24**, 4484–4490.